THE UNIVERSITY *of* EDINBURGH

Radio AGN Evolution with Low Frequency Radio Surveys

Louise M. Ker

A thesis submitted in fulfilment of the requirements
for the degree of Doctor of Philosophy
to the
University of Edinburgh
August 2012

Abstract

Supermassive black holes are leading candidates for the regulation of galaxy growth and evolution over cosmic time, via 'feedback' processes, whereby outflows from the Active Galactic Nuclei (AGN) halt star formation within the galaxy. AGN feedback is generally thought to occur in two modes, high-excitation (HERG, or 'quasar-mode') and low-excitation (LERG or 'radio-mode') each having a different effect on the host galaxy. LERGs curtail the growth of the most massive galaxies, whereas HERGs are thought to be activated by mergers/interactions, switching off star formation at high redshift. A critical problem in current extragalactic astrophysics lies in understanding the precise physical mechanisms by which these feedback processes operate, and how they evolve over cosmic time.

Radio-loud AGN are an essential tool for studying major feedback mechanisms, as they are found within the largest ellipticals, and hence are beacons for the most massive black holes across the bulk of cosmic time. In this thesis I develop and study existing complete radio samples with extensive new multi-wavelength data in the radio, optical and infrared, aiming to investigate the evolution of AGN feedback modes, and methods to locate and study such systems at the very highest redshifts. This will serve to inform further studies of radio-AGN planned with next generation radio instruments such as the LOw Frequency ARray (LOFAR).

Very few radio-loud AGN systems are currently known at high redshifts, and the effectiveness of traditional high redshift selection techniques, such as selection based on steep spectral index, have not been well quantified. A purely evidence-based approach to determining the efficiency of various high redshift selection techniques is presented, using nine highly spectroscopically complete radio samples; although weak correlations are confirmed between spectral index and linear size and redshift, selection first of infrared-faint radio sources remains by far the most efficient method of selecting high-z radio galaxies from complete samples. Radio spectral curvature in four of the complete samples is analysed and the effect of radio spectral shape on the measurement of the radio luminosity function (RLF) of steep-spectrum radio sources is investigated. Below z=1, curvature has negligible effect on the measurement of the RLF, however at higher redshifts, where source numbers are low, the shape of the radio spectrum should be taken into account, as individual source luminosities can change up to 0.1-0.2 dex, and this can in some cases introduce errors in space density measurements of up to a factor of 2-3 where source numbers are low.

Building upon these samples, the very first independent determinations of the separate RLFs for high and low excitation radio sources across the bulk of cosmic time are made, out to z=1.

Here it is shown that HERGs show very clear signs of strong evolution, in line with theoretical predictions. LERGs also show some very weak evolution with redshift, showing increases in space density of typically around a factor of 2. These measurements are also used to estimate the contribution of LERGs, which typically show weak or no emission lines to the 'missing redshift' population, which are sources within the complete samples not identifiable spectroscopically. Complementary to this, a pilot study is presented in selecting 'missing redshift' sources which are classed as infra-red faint (IFRS), which show no optical or near-IR identification, and are compact in the radio. Follow up spectroscopy on these candidate high z sources detected no line emission.

Finally, work carried out towards the testing and commissioning of the new LOFAR telescope is presented. The findings from this thesis will serve to both streamline and inform high redshift radio-AGN searches and studies planned to be carried out with LOFAR and other multi-wavelength complementary surveys in the near future, and help to open up an as yet unexplored epoch in radio-AGN formation and evolution.

Declaration

I hereby declare that this thesis is not substantially the same as any that I have submitted for a degree or diploma or other qualification at any other University. No part of my thesis has already been or is being concurrently submitted for any such degree, diploma or other qualification.

Parts of the work contained in this thesis have been published, or are due to be published, in refereed scientific journals, and are referenced accordingly in the text.

I further state that this thesis is the sole composition of myself, and the work presented is my own except where specifically indicated in the text. Any and all remaining errors and omissions are my own.

This thesis was completed with support from a Science and Technology Facilities Council Research Studentship.

L. M. Ker
August 2012

Acknowledgements

There are many people without whose help and support this thesis would not have been possible. My thanks first and foremost to my supervisor Philip Best for his patient and constant support, inspiration and encouragement throughout. There can't be many supervisors who happily and enthusiastically check how things are going from half way round the world at 4am during an observing run! Emma Rigby and Melanie Gendre for patiently reading many paper and proposal drafts and their very much appreciated help and support, Pepe Sabater Montes for checking my maths at 1am up a mountain in Chile and the late Tim Garn for always being happy to help with the intricacies of radio data reduction. The IfA has been a warm, friendly and supportive place to work over the last few years, and I am particularly indebted to John, Horst and Ed for always rescuing my machine when needed, and Jane, Nathalie and Paula for helping with all the formal things.

Thanks to Huub Röttgering, my summer project supervisors and fellow students at ASTRON, & many others involved in the LOFAR project for enabling me to take part in the early operations of a brand new instrument. A fantastic opportunity that has allowed me to participate in a major new telescope project over the last four years, and a great privilege to both work with and learn from an enthusiastic and dedicated expert international team.

Thanks too must go to all the AW and HA friends I made at Pollock Halls, home for seven years and almost two degrees! A very sincere thank-you to my two honourable colleagues in CC. Charles, for all his help, support, integrity, wise words and excellent cooking! I suppose too that Dr Nick should get some time in the spotlight, firstly for being brave enough to become the flatmate of a final year PhD student and her thesis, and secondly, for offering unlimited hugs, love and constant encouragement, and generally managing to annoy me sufficiently to finish.

Mr and the very much missed late Mrs Treehugger need a mention too, as they bear the onerous responsibility for getting me started through the extragalactic gateway in the first place. Thanks too to my parents Moira and David & (now not so) little brother Stephen, for all their unconditional love and support from home. Stephen, graduating as a farmer in 2011 in the face of incredible adversity over the last 18 years makes the four years effort in undertaking a thesis seem very short, and you set the benchmark for both courage and endeavour in undertaking any new challenge, big or small, including this one.

This thesis has made use of data products from the following facilities, and I acknowledge these here, along with grateful thanks to the respective Observatory staff for their assistance.

European Southern Observatory (ESO): Observations made with ESO Telescopes at the La Silla and Paranal Observatories under programmes ID 086.A-0770(A), 086.A-0770(B), 088.A-0389(A), 088.A-0455(A).

Isaac Newton Group (ING): Observations made with the William Herschel Telescope operated on the island of La Palma by the Isaac Newton Group in the Spanish Observatorio del Roque de los Muchachos of the Instituto de Astrofsica de Canarias.

Tata Institute of Fundamental Research (TIFR): Observations made with the GMRT, proposal reference 05MBa01. The GMRT is run by the National Centre for Radio Astrophysics of the Tata Institute of Fundamental Research.

National Radio Astronomy Observatory (NRAO): Observations made with the Very Large Array (VLA), New Mexico. The National Radio Astronomy Observatory is a facility of the National Science Foundation operated under cooperative agreement by Associated Universities, Inc.

Netherlands Institute for Radio Astronomy (ASTRON): LOFAR, the Low Frequency Array designed and constructed by ASTRON, has facilities in several countries, that are owned by various parties (each with their own funding sources), and that are collectively operated by the International LOFAR Telescope (ILT) foundation under a joint scientific policy.

CDS: This research has made use of the SIMBAD database, operated at CDS, Strasbourg, France.

NED: This research has made use of the NASA/IPAC Extragalactic Database (NED) which is operated by the Jet Propulsion Laboratory, California Institute of Technology, under contract with the National Aeronautics and Space Administration.

Contents

List of Figures

List of Tables

Chapter 1

Introduction

Radio astronomy is currently undergoing a renaissance, with the EVLA, e-MERLIN, LOFAR, and SKA pathfinders all soon to come (if not already) online. With similarly ground-breaking optical and near-infrared surveys in progress such as Pan-STARRS and VISTA, the opportunities for simultaneously investigating diverse major science topics will be countless.

A key science driver of many of these upcoming surveys centres around understanding the role of central supermassive black holes (SMBH) in galaxy formation and evolution over cosmic time. A fundamental relationship between the mass of a galaxy's SMBH and the bulge luminosity and stellar velocity dispersion was first noted by Magorrian *et al.* [1998] and by Ferrarese and Merritt [2000] and Gebhardt *et al.* [2000] respectively, and is now accepted as evidence for the central supermassive black hole having a controlling influence on the development of the host galaxy, via 'feedback'. Complex models of galaxy evolution rely on this feedback for curtailing the growth of the most massive galaxies, and influencing conditions in the surrounding cluster/protocluster [cf. Croton *et al.*, 2006; Bower *et al.*, 2006]. It is thought that outflows from an actively accreting central black hole, via radio jets, can remove gas from the centre of the galaxy, halting star formation and preventing large-scale cluster cooling flows [Best *et al.*, 2007]. What is very poorly understood however, are the precise physical mechanisms by which active galactic nuclei (AGN) feedback operates.

In order to understand how galaxies evolved over cosmic time, and how active galactic nuclei influence conditions on a much larger scale in their surrounding clusters, these physical processes must be identified and understood, and the associated energetics measured over a large range in redshift. Radio-loud AGN provide an ideal means of studying major feedback mechanisms, as they trace the most massive ellipticals, and hence the most massive black holes across the bulk of cosmic time.

In this thesis I develop and study existing complete radio samples with extensive new multi-wavelength data in the radio, optical and infrared with the aim of investigating the evolution of AGN feedback modes, and methods to locate and study such systems at the very highest redshifts. I also present and discuss some examples of commissioning activities for LOFAR, a next generation instrument with superb potential for making further, ground-breaking progress

in the understanding of AGN influence on galaxy evolution.

1.1 Cosmology

In this section, I briefly outline our current understanding of the structure and evolution of the Universe, and the currently accepted cosmological framework to describe the evolution of observed physical properties of galaxies with cosmic time. For further details of the derivations of the equations presented here, [see e.g. Peacock, 1998]. The currently accepted model of the Universe, which best fits all the available observational data, is the Λ Cold Dark Matter model, in which the Universe is flat, and filled with baryons, cold dark matter, neutrinos and requires a cosmological constant [Dunkley *et al.*, 2008].

The key set of observations, which marked the shift in the belief of a steady state to an expanding and evolving Universe, with a beginning in time, were made by Slipher, beginning in 1912, measuring Doppler shifts of many galaxies. The realisation of the significance of these is often erroneously attributed to a paper by Edwin Hubble in 1929 [Way and Nussbaumer, 2011], in which he presented Cepheid distances for a subset of nearby galaxies. Observing what looked to be a linear relationship between the recession velocities and distances - that the more distant galaxies had higher redshifts, he then made the connection that the redshifts observed were not due solely to Newtonian Doppler shifts. In fact this had been realised two years earlier by Georges Lemaître, using essentially the same observational data as Hubble, and he put forward the observations as possible evidence of recent theoretical predictions of an expanding Universe made by Einstein.

$$V = H_0 d \tag{1.1}$$

where V is the recession velocity and d is the distance of the galaxy. H_0 is the Hubble constant at the current epoch.

1.1.1 Redshift

If the Universe is expanding, then the light detected from more distant galaxies will be shifted to longer (redder) wavelengths as the space between the observer and galaxy expands over the journey time of the photon. This is cosmological redshift, and should not be confused with the Doppler effect seen for example, in the peculiar motions of local galaxies, or gravitational redshift, whereby light is stretched in the presence of a strong gravitational field. If the Universe is assumed to be homogeneous and isotropic, as introduced by Einstein and later verified by observations of large scale structure, the more distant the galaxy, the more the light is redshifted. The redshift, z, is hence given by:

$$z = \frac{\lambda_{obs} - \lambda_{emit}}{\lambda_{emit}} \tag{1.2}$$

Observationally, the light curves of Type 1a supernovae provide direct evidence that the redshift measured is truly due to cosmological expansion, as distant supernovae have light curves slower by (1+z), than those observed in the local Universe, [see for example Riess *et al.*, 2009].

1.1.2 Friedmann's Equation and the Robertson-Walker Metric

Hubble's Law was in fact in error, due to difficulties in calibrating the Cepheid luminosities, and the observed relation is somewhat misleading, as the Hubble constant H_0 changes with time. However, it does clearly illustrate the concept of an expanding Universe, and leads to the most widely accepted modern view of the expanding Universe, as described by Friedmann's equation. Friedmann's equation can be derived directly from Einstein's field equations, assuming a homogeneous and isotropic Universe, and implies a fundamental connection between the density and geometry of the Universe. To begin with, a means of describing the global structure of time and space is required, and this can be derived from Einstein's field equations in the form of the Robertson-Walker Metric, again assuming the Universe is homogeneous and isotropic.

$$c^2 d\tau^2 = c^2 dt^2 - R^2(t)[dr^2 + S_k^2(r) d\psi^2] \tag{1.3}$$

The term on the left represents the invariant proper time. On the right hand side, the first term represents the universal cosmic time, R(t) the scale factor, and the first term inside the brackets the co-moving radial distance, the second, the co-moving angular distance. In the case of a flat universe, $S_k(r) = r$. The constant k is the curvature term, with k=0 indicating a flat universe. k=+1 describes an open universe, and k=-1 a closed universe.
The Friedmann equation is;

$$(\frac{\dot{a}}{a})^2 = \frac{8\pi G}{3}\rho - \frac{kc^2}{a^2} + \frac{\Lambda}{3} \tag{1.4}$$

where

$$a(t) = \frac{R(t)}{R_0} \tag{1.5}$$

a(t) is known as the scale factor. Friedmann's equation is effectively the equation of motion for a(t) and is set to be dimensionless by setting a(t)=1 at the present time t_0, with the set of comoving coordinates R_0. As space expands the co-moving coordinates R_0 do not change, but the physical coordinates R(t) do change with time. R(t) and R_0 are both proper distances.

All current observational data points towards a flat universe model, and hence I discuss only the k=0 case here. From equations 1.1, 1.4 and 1.5, it can be seen that H=$\dot{a}/a$. In the case of a flat universe, where k=0, the Friedmann equation may be written in terms of the critical density ρ_c.

$$\rho_c = \frac{3H^2}{8\pi G} \tag{1.6}$$

Defining a dimensionless density parameter as the ratio of density to critical density gives:

$$\Omega_M = \frac{\rho}{\rho_c} = \frac{8\pi G}{3H^2}\rho \tag{1.7}$$

Similarly, the other terms in the Friedmann equation can be defined in terms of a density parameter as:

$$\Omega_\Lambda = \frac{\Lambda}{3H^2} \tag{1.8}$$

where Ω_Λ describes the dark energy component of the Universe.

$$\Omega_k = \frac{-kc^2}{a^2H^2} \tag{1.9}$$

Re-writing the Friedmann equation in this manner, gives:

$$\Omega_M + \Omega_\Lambda + \Omega_k = 1 \tag{1.10}$$

1.1.3 Cosmological Parameters

The cosmological parameters described above can be measured by three main observational methods; measurements of Type 1a supernovae, large scale structure, and the cosmic microwave background (CMB). Type 1a supernovae have very similar properties, in that there is a characteristic rise to a peak luminosity, followed by a fall over approximately 30 days, and by measuring both the height and the width of the measured lightcurve, type 1a supernovae can be used as standard candles out to a redshift z $\sim$ 1, allowing an estimation of H_0, and other key cosmological parameters [see for example Riess *et al.*, 2009]. Large scale galaxy redshift surveys can also be utilised for precise estimates by measuring density perturbations. They are excellent tools to test the hypothesis that the structure that is observed in the Universe, such as superclusters, voids, filaments, is formed from the gravitational instability of small initial density perturbations in the early Universe. If this is indeed the case, then newly forming superclusters of galaxies would be expected to trigger systematic infall of other galaxies, giving rise to a pattern in the recession velocities. Therefore there should be a measurable anisotropy in the calculated spatial clustering of galaxies, allowing an estimate of the cosmological mass density parameter [cf. Peacock and 2dFGRS Team, 2001; Susperregi, 2001].

By far the most precise current estimates of cosmological parameters have come from measurements of the cosmic microwave background. The cosmic microwave background marks the time of recombination, when the ionised plasma in the early Universe dropped to a low enough temperature to form neutral atoms. This is also the first time when photons can travel freely: when free electrons are present, photons are Thomson scattered, but when the temperature drops sufficiently to allow neutral atoms to form, the photons are no longer scattered. So in all directions photons are expected to be seen that originate from this last scattering, estimated to be at a redshift z $\sim$ 1100, with measurable fluctuations indicating early matter perturbations. These early perturbations then later go on to form gravitational instabilities seeding the very first galaxies. The CMB has an almost perfect blackbody spectrum; it appears the same in all directions on the sky, ruling out any recent astrophysical activity as the cause. Small temperature fluctuations do appear in the blackbody spectrum of the CMB, and these indicate some of the very earliest processes that took place in the early Universe, for example fluctuations arising due to competition between photon pressure, which tends to smooth out anisotropies, and baryon gravitational attraction, tending to collapse into distinct structures. Measuring these fluctuations on different angular scales give estimates of the cosmological parameters. The Wilkinson Microwave Anisotropy Probe (WMAP), launched in

2001, measured the CMB to a very high precision, and in combination with the other estimators outlined above, gives the currently accepted cosmological values. Best-fitting cosmological parameters for a Λ CDM Universe from seven years worth of data have recently been determined by Komatsu *et al.* [2011].

$$\Omega_\Lambda = 0.728 \pm 0.016 \tag{1.11}$$

$$\Omega_M(\text{baryon}) = 0.0456 \pm 0.0016 \tag{1.12}$$

$$\Omega_M(\text{darkmatter}) = 0.227 \pm 0.014 \tag{1.13}$$

$$H_0 = 70.4 \text{kms}^{-1}\text{Mpc}^{-1} \tag{1.14}$$

In this thesis, the cosmological parameters for a Λ CDM Universe assumed are; Ω_Λ=0.7, Ω_M=0.3 and H_0=70km s^{-1} Mpc^{-1} for ease of comparison with other work in the literature. The cosmocalc python script by Tom Aldcroft[1] is used to compute cosmological results with these values as input throughout.

Ellis [2007] summarises the reasons we currently have for believing the ΛCDM model is acceptable. Measurements of the CMB fluctuations, large scale redshift surveys and some gravitational lensing studies concur on the low matter density, and both the CMB fluctuations and measurement of primordial abundances of light elements such as helium provide a measure of the total baryon component, consistent with a ΛCDM model. The ΛCDM model fits the growth of structure from CMB fluctuations to the large scale distribution of galaxies seen in redshift surveys impressively well and also has good agreement with numerical simulations of structure growth.

Having briefly described the current understanding and best fit cosmological model to the observed Universe, how is this framework applied to observations of distant objects? The basic observational data that can be measured are the redshift, z, the flux density and the angular distance between two points on the sky dψ. Using the RW metric, the Friedmann equation and assuming a ΛCDM model allows derivation of further intrinsic properties of the objects under study.

1.1.4 Line of Sight Co-moving Distance

The first key measure that can be inferred is that between the redshift and co-moving distance. Since 1+z=R_0/R(z), this can be used along with the Friedmann equation, and the equation of motion for a photon, R dr = c dt to obtain the following expression for the co-moving distance D_c.

$$D_C = R_0 dr = \frac{c}{H(z)} dz = \frac{c}{H_0}[(1-\Omega)(1+z)^2 + \Omega_\Lambda + \Omega_M(1+z)^3]^{-1/2} dz \tag{1.15}$$

The transverse co-moving distance, or the proper distance between two events at the same redshift, for a k=0 universe is just;

$$D_T = D_C \delta\theta \tag{1.16}$$

[1] cosmocalc.py is available at `http://cxc.harvard.edu/contrib/cosmocalc/`, and is based on the web calculator by Wright [2006]

1.1.5 Co-moving Volume

The co-moving volume is measured by surveying an area of sky, A, in units of solid angle with a particular range in co-moving distance.

$$dV = AR(z)^3 S_k(r)^2 dr \tag{1.17}$$

1.1.6 Luminosity-Flux Density Relation

In order to relate the observed fluxes at a particular frequency to the intrinsic luminosity of a source, a luminosity flux relation is required, this is given by.

$$S_\nu(\nu_0) = \frac{P_\nu([1+z]\nu_0)}{4\pi R_0^2 S_k^2(r)(1+z)} \tag{1.18}$$

where $S_\nu(\nu_0)$ is the flux density [2] and P_ν is the luminosity.

1.1.7 Angular Distance

From the above expressions, we can define an angular-diameter distance D_A and a luminosity distance D_L via

$$D_A = (1+z)^{-1} R_0 S_k(r) \tag{1.19}$$

$$D_L = (1+z) R_0 S_k(r) \tag{1.20}$$

1.1.8 The K Correction

From the above, it is clear to see that the luminosity we measure of a high redshift object at a particular frequency will not be the same as the luminosity measured in the object's rest frame. Using the traditional system of measuring luminosities in astronomy, magnitudes, the absolute magnitude is defined as the apparent magnitude observed if the source lay at a distance of 10pc. The k-correction is utilised to correct broad band photometric magnitudes to their rest frame values, see Hogg *et al.* [2007]. The absolute rest frame magnitude is

$$m = M + 5log_{10}(\frac{D_L}{10pc}) + K(z) \tag{1.21}$$

where K(z) is the k correction and is given by

$$K(z) = -2.5log\left[\frac{P(\nu_0(1+z))}{P(\nu_0)}\right] \tag{1.22}$$

For a spectrum where $P(\nu_0)$ is proportional to $\nu^{-\alpha}$, as is approximately the case for example, in the radio spectrum of galaxies, where emission is dominated by the synchrotron process, the

[2] Flux density is defined as the radiation energy received per unit time, per unit area per unit frequency range. The most commonly used unit in radio astronomy is the Jansky, where $1\text{Jy}=10^{-26}\text{Wm}^{-2}\text{Hz}^{-1}$.

k correction becomes

$$K(z) = 2.5(\alpha - 1)log_{10}(1 + z) \tag{1.23}$$

1.1.9 Galaxy Formation & Evolution

How the first galaxies were formed, how they evolved over time and interacted with one another, what physical processes drove this evolution and how the present distribution of galaxies that we observe today came to be, form some of the most fundamental questions in astronomy. Having outlined the current cosmological framework, I now address the current understanding of the processes of galaxy formation and evolution, both through observation and simulation, and discuss where some of the key gaps in the current knowledge are, and how they may be addressed.

Observations and simulations of galaxy formation and evolution have a symbiotic relationship in furthering our understanding of the history of the Universe. Simulations provide a crucial means to test theories of the physics involved: if a simulation can reproduce many different observations, this implies that the modeled physical theory may well be important in reality. Simulations based on a ΛCDM Universe can reproduce large scale structure at z=0, starting from the initial fluctuations in the CMB. In the Universe, baryonic 'normal' matter constitutes only a small proportion of Ω_M; the rest is composed of dark matter, the existence of which is inferred by many methods, for example by observations of clusters of galaxies, or by measuring the rotation curves of galaxies. Simulations of the ΛCDM Universe can reproduce the inferred dark matter distributions well, but have more difficulty in reproducing the baryonic structure. In addition, the nature of the major components of the model, namely the cold dark matter and dark energy have yet to be confirmed, although it should be noted that there are many as yet undetected candidate particles for the cold dark matter predicted by the standard model of particle physics. So while the ΛCDM model is one of the most successful we have, it is not perfect and does not account for/predict all observations, and the observational data available are by no means complete.

At the very simplest level, galaxies are composed of a group of stars and gas and dust, within a halo of gravitationally bound dark matter, usually with evidence for a supermassive black hole at the centre. The galaxies we see at the present time are a complex mix of morphological types, ranging from giant red ellipticals, containing old stellar populations to blue spirals such as our own Milky Way. The challenge is to reconcile the simulations of galaxy formation and evolution with observations of the galaxy population made over the range of observable redshifts. Depending on the nature of the dark matter, galaxies can form embedded in dark matter halos, from the initial density fluctuations in one of two scenarios, bottom up (the hierarchical cosmology) or top down. In the top down scenario the very largest structures, such as superclusters etc are formed first, and then proceed to fragment. In the bottom up scenario, the smallest structures form first and proceed to merge via gravitational attraction.

In the ΛCDM model Universe galaxies form in the bottom up, hierarchical scenario. N-body simulations of a ΛCDM model have been carried out for decades with some of the earliest work being carried out by Press and Schechter [1974]. White and Rees [1978] introduced the idea of a

two-stage galaxy formation process, with dark matter halos forming from gravitational collapse of the initial density fluctuations, and galaxies forming inside the halos. At that time, N-body simulations were known to reproduce the large scale structure very well with a hierarchical scenario, when *no* non-gravitational effects were incorporated [White and Rees, 1978]. However, as argued by White and Rees [1978], this purely gravitational approach did not account for the characteristic sizes and masses of observed galaxies, suggesting gas dynamical/feedback effects were also important. Semi-analytical models were soon introduced, to take the simulations one step further [e.g. White and Frenk, 1991]. N-body simulations work by direct integration of the dynamical equations, and semi-analytics are complementary to these, in that they use a modular approach which takes the best known approximations for the physics, and are often combined with N-body simulations [see, e.g. Baugh, 2006, for a comprehensive review]. They build on the N-body simulations of dark matter, using them to determine the location and evolution of dark matter halos, where the first galaxies form. The evolution of normal baryonic matter in galaxies is then modeled using approximate, observationally motivated physical processes, as unlike dark matter, most of these processes are non-linear. This allows observed properties such as star formation history, gas cooling, supernovae feedback and dust extinction to be included [e.g. De Lucia, 2009].

These two methods of simulation each have their own advantages and disadvantages; N-body, or hydrodynamical simulations, use an 'exact' approach, solving equations of motion/thermodynamics for dark matter and gas, using particles or grid cells to represent each constituent. This precision gives the technique its main limitation; that it is extremely computationally expensive, and hence large volumes of space cannot be simulated at high resolution. In addition, although N-body simulations are very good at simulating the inferred dark matter distribution, they are currently poor at reproducing observed galaxy characteristics, as many of the physical processes involved on galaxy scales are inherently non-linear, for example star formation, AGN feedback, as outlined by White and Rees [1978].

The true power of these simulations comes about when the two techniques are combined. Examples of such codes include the N-body code GADGET, used to produce the famous 'Millennium Simulation', [Springel, 2005], which used more than 10 billion particles, each representing a billion solar masses of dark matter to trace the evolution of the matter distribution in a cube of space with sides 2 billion light years long. The output of this N-body simulation was then used by semi-analytic codes to model the growth of galaxies and their central supermassive black holes, through a volume comparable in size to several existing galaxy redshift surveys [Croton *et al.*, 2006].

The review on hierarchical galaxy formation by Baugh [2006] summarises much of the progress made by these models, and also highlights their shortcomings. Until recently, ΛCDM simulations failed to reproduce the massive galaxies observed at high redshift, and have difficulty reconciling the zero point of the Tully-Fisher relation with the luminosity function. They also under-predict the number of disk galaxies formed. The present day galaxy luminosity function has also proved difficult to reproduce, and requires feedback effects to be incorporated in order to produce a good match to the observed data. Without feedback incorporated, models

consistently overestimate the number of very luminous galaxies and the number of very faint galaxies in the present epoch. Introduction of supernova feedback allows the observed faint end to be reproduced: supernovae heat and expel bubbles of surrounding gas, suppressing star formation in smaller galaxies. However this process is not efficient in larger galaxies, and incorporating supernovae feedback alone into the models increases the amount by which the bright end of the luminosity function is over-predicted, as the gas ejected this way by low mass galaxies ends up cooling onto the central massive galaxies, increasing their luminosities [De Lucia, 2009]. This has led to the introduction of other energy sources into the models, such as AGN feedback. Incorporation of AGN feedback, whereby relativistic jets from the central black hole in massive galaxies heat the surrounding gas, switching off the cooling process, has proved very successful, and suggests that although AGN are relatively rare, they may have an important role to play in galaxy formation and evolution.

In order to progress these simulations, and to further our understanding of galaxy formation and evolution, deeper, and wider observations are required across the electromagnetic spectrum to determine whether there is strong observational evidence to support the process of AGN feedback being crucial to halting the growth of the most massive galaxies.

In what follows I give a brief introduction to active galactic nuclei and their observational characteristics, along with the physical processes thought to underpin their evolution, concentrating particularly on radio AGN. I also outline some key areas where current knowledge is sparse and observational data is lacking, and argue that new upcoming, low frequency radio source samples (such as from LOFAR or the GMRT), will greatly contribute to current understanding of radio AGN, and will allow an observational quantification of how radio AGN, which pinpoint AGN feedback processes in the most massive galaxies, contribute to galaxy evolution as a whole.

1.2 The Zoo of Active Galactic Nuclei

The term ‘active galaxy’, or active galactic nuclei is generally used to describe a galaxy with a bright luminosity, which at some wavelength is not dominated by starlight [Robson, 1996]. This activity is generally accepted to come from a super massive black hole in the centre, and observational characteristics of traditional AGN may include an incredibly high luminosity, small angular size of emission, broadened emission lines, variability, radio emission, the presence of jets, and polarised emission. In comparison with the ‘normal’ galaxy spectrum, a typical AGN will have excess ultraviolet, infra-red and X-ray flux density and a flat broadband spectrum. Not all AGN will have all these characteristics, and what is observed is also heavily dependent on viewing angle, the mass of the central black hole and the accretion rate of the black hole. Historical classification of AGNs created a ‘zoo’ of different AGN, as observational biases crept in, and different populations were defined for almost every wavelength regime, for example radio galaxies, Seyferts, LINERS etc. However many of these can be unified into one single model, illustrated in Figure 1.1, if we take into account the fact that we see AGN at different viewing angles.

Despite the obvious selection effects which come in to play with viewing the active galaxy at different angles, a great deal of information can be amassed by multi-wavelength surveys of these objects, as AGN have some form of emission in almost every wavelength range, see for example the review by Andernach [1999].

1.2.1 Observational Characteristics of AGN

The basic model for a traditional AGN is a supermassive black hole residing at the centre of the galaxy. A supermassive black hole exists at the centre of nearly every galaxy, and a remarkable correlation between the mass of the black hole and the mass of the bulge observed, the Magorrian relation, which shows that as the black hole mass increases, so does the mass of the bulge. This suggests that central black hole and galaxy formation are intimately linked [e.g. Kormendy, 2001; Gültekin *et al.*, 2009]. There is some evidence that this relation holds true even to high redshifts [e.g. McLure and Dunlop, 2002; Daddi *et al.*, 2007; Rafferty *et al.*, 2011]; such findings are consistent with the concurrent growth of both the black hole mass and bulge in the precursors to today's massive galaxies.

The current view is that active galactic nuclei are a phase during which the black hole is rapidly accreting and which all massive galaxies go through, implying that the study of these rare objects is key to understanding the lifecycle of galaxies. But which came first, the black hole, or the galaxy? Kormendy [2001] suggest the latter, the galaxy formed first and the black hole later. They reach the conclusion that the defining events that form a bulge and the major growth phases of its black hole when it shone as an AGN were the same events. A run of dissipative mergers that fuelled both starbursts and AGN activity were most likely to be the key formation processes. This is still very much an area of active investigation.

Recent observational results from McLure *et al.* [2006], using the 3CRR [Laing *et al.*, 1983] sample of radio galaxies are in contrast to this idea, and they suggest that black holes evolve ahead of the galaxy, with findings from Targett *et al.* [2012] using a sample of the most luminous z$\sim$4 quasars supporting this. However a study presented by Alexander *et al.* [2008] using a sample of submillimetre selected galaxies suggested the opposite: that the growth of the central black hole is slower than that of the host galaxy. It is likely that the starkly different findings of these two studies arise due to selection effects (e.g. samples of radio galaxies preferentially select the most evolved, massive galaxies at any given epoch and require the presence of a massive black hole, whereas submillimetre selection highlights massive galaxies undergoing early growth via intense phases of star formation), and scatter in the observed relations. Simulations by Merritt and Quinlan [1998] suggest that black hole growth is self-limiting: after a certain mass is reached, the surrounding stars are pushed into circular orbits, and hence safely out of reach. However, this is still uncertain, as is the question of what triggers AGN activity in the first place. As material is accreted by the central black hole, transfer of angular momentum between the particles ensures that the accretion disk heats up, and it will radiate in the X-ray, uv, and optical via Compton scattering [Robson, 1996]. The surrounding gas is ionised by this emission, and the emission lines produced by gas close to the black hole will be Doppler-broadened to produce the broad line region or BLR. Likewise ionised gas away from the black hole produces

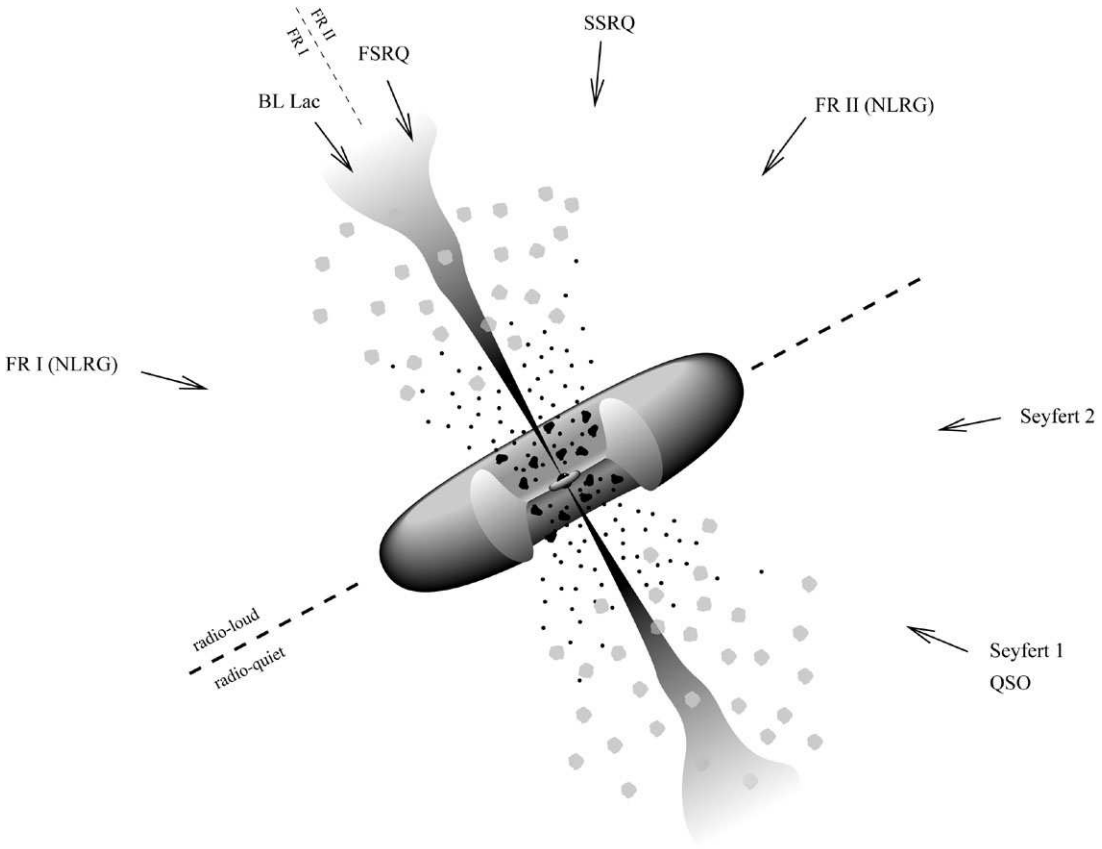

Figure 1.1: This figure illustrates the current understanding of what composes an active galactic nucleus. The observationally diverse range of objects identified as AGN are thought to be different aspects of the same phenomena, the differences arising due to viewing angle. Viewing the jet directly along the line of sight gives rise to flat spectrum radio galaxies or BL Lacs in the case of radio-loud objects, and for radio-quiet objects, the AGN would be observed as a Seyfert 1 quasar. For radio-loud objects, viewing the jet at a relatively small angle to the line of sight, directly towards the broad-line region, gives rise to steep spectrum radio quasars (SSRQ), and at a larger angle, narrow line radio galaxies (NLRG). For radio-quiet sources, the AGN viewed at an angle to the jet gives rise to a Seyfert 2. This figure is reproduced from Torres and Anchordoqui [2004].

narrow emission lines: the NLR region. The generally accepted view is that AGNs often have a surrounding obscuring torus of gas and dust, and collimated jets of accelerated particles driven by the central AGN are often observed (cf. Figure 1.1).

In the optical regime, the continuum emission is composed of starlight from the galaxy, and light from the central accretion disk, and emission lines from the BLR and NLR. If the accretion disk is viewed directly along the line of sight, then optical synchrotron emission from the jets dominates, and a blazar is seen. An accretion disk viewed almost to the line of sight, with broad line emission is classed as a Type 1 Seyfert, or quasar. A Type II Seyfert occurs if the galaxy is viewed edge on and the central AGN obscured by the surrounding torus of dust and gas. The optical emission is then mainly starlight, but with the presence of NLR emission lines, betraying the presence of an AGN.

The manner in which the AGN is accreting material also has a significant influence on its observational characteristics. As gas is accreted, energy is either dissipated as radiation, or is 'advected' inward. AGN accreting close to the Eddington limit in a standard thin disk are very radiatively efficient, and hence display strong X-ray, uv and radio emission, along with bright emission lines [Evans *et al.*, 2008], similarly to the observables described above. These sources are interchangably known as 'cold-mode', 'high-excitation' or 'quasar-mode'. For this mode of accretion to occur, a constant supply of cold gas is required, expected to be brought into the galaxy via mergers or interactions, and indeed, many of these sources show observational evidence for recent collision [Heckman *et al.*, 1986].

Another class of AGN show faint, or no emission lines, and are present predominately at low radio luminosities, although they do exist at higher luminosities [see e.g. Jackson and Rawlings, 1997, for some examples of these]. Only an unabsorbed power law in the X-ray is generally seen, in contrast to the high-excitation sources, which usually show an accretion disk contribution (see Evans *et al.* [2008] for a detailed summary of observational characteristics of both high and low excitation sources). This at first seems inconsistent with the orientation-based model as illustrated in Figure 1.1. However, these sources have no evidence for an obscuring torus [Ogle *et al.*, 2006], and an explanation which has slowly gathered more weight in recent years is that of a central engine powered by a radiatively inefficient accretion.

AGN with sub-Eddington accretion rates are cooled by advection (Advection Dominated Accretion Flows, or ADAFs), via heat captured in matter and not by radiation: in other words, the gas in the accretion disk falls into the black hole *before* it can radiate away it's thermal energy. Such sources are referred to as 'low-excitation', 'hot-mode', or 'radio-mode' in the literature (see Figure 1.2 for an example). Allen *et al.* [2006] showed that very low luminosity radio sources in the centre of clusters could be powered by an ADAF, with the hot gas of the intra-cluster medium as the fuel source. Hardcastle *et al.* [2007] build on this, and show via some simple numerical tests that it is possible that such an accretion mode could be responsible for running even powerful low-excitation radio sources. This observed dichotomy in AGN accretion mode has important implications for radio-AGN feedback (cf. Section 1.3).

1.2.2 Radio Observations of AGN

Radio emission in AGN arises through three main mechanisms: synchrotron, inverse-Compton and adiabatic losses. Here I give a brief summary of each [see e.g. Longair, 2011, for further details]. Radio emission via the synchrotron process arises through a charged particle circling around a magnetic field line in the source. An electron accelerated this way radiates according to

$$F = \frac{d\mathbf{p}}{dt} = e\mathbf{v} \times \mathbf{B} \tag{1.24}$$

where the electron momentum is $\mathbf{p}=\gamma m_0\mathbf{v}$ and m_0 is the rest mass of the electron. Whilst the velocity of the electron parallel to the magnetic field is constant, the velocity component perpendicular to the magnetic field accelerates circularly with angular frequency

$$\omega_B = \frac{eB}{\gamma m_0} \tag{1.25}$$

The loss rate of synchrotron radiation may be determined by combining this result with the relativistic Larmor formula for the total power radiated from an accelerating relativistic charge (see e.g. Jackson [1962] for complete derivation). From equation 1.24 above, it can be seen that the magnitude of the electron's acceleration will be evBsinθ/γm$_0$. This gives a loss rate from synchrotron emission of

$$\frac{dE}{dt} = \frac{\gamma^2 e^4 B^2 sin^2\theta}{6\pi\epsilon_0 c m_0^2} \tag{1.26}$$

Replacing γ by γ=E/m$_0$c^2 shows that the loss rate given in Equation 1.26 above is proportional to E^2. Therefore highly energetic electrons will lose their energy faster. When calculating the loss rate, it is also necessary to consider beaming effects: electrons moving at relativistic velocity with circular motion will give rise to beamed radiation along the direction of travel, as seen in the observers frame. This gives rise to a critical frequency of

$$\nu_c = \frac{3}{4\pi}\gamma^2\omega_g sin\theta \tag{1.27}$$

at which most of the radiation is emitted. The extent of the emitted radiation around the critical frequency is very much narrower than the breadth of the electron energy spectrum, so the assumption that all radiation from a particular electron with energy E is emitted at the critical frequency for that energy is valid.

As the observed spectra of sources whose emission is thought to be synchrotron are predominately non-thermal power-law in form, the underlying energy distribution of the originating ensemble of electrons must also be a power law.

$$N(E)dE = N_0 E^{-x} dE \tag{1.28}$$

where N(E)dE is the number of electrons in the radiating source with an energy between E and

E+dE. Over a frequency range ν to ν+dν, the rate of energy radiation becomes

$$P_\nu d\nu = N(E)dE \times \left(\frac{-dE}{dt}\right)_{\text{single electron at E}} \tag{1.29}$$

This eventually leads to a synchrotron radiation spectrum generated by an ensemble of relativistic electrons, described by

$$S_\nu \propto \nu^{-\alpha} \tag{1.30}$$

where α is related to the slope of the electron energy distribution by $\alpha = (x-1)/2$, and giving rise to the classic power-law shape.

In practice, the observed spectrum is not always a power-law across the observed radio frequency range. Radio spectra of synchrotron sources often 'turn-over' at low frequencies. This arises due to synchrotron self-absorption, which occurs where there is more energy present in the emitted radiation, than the electrons themselves. The electrons absorb this radiation, leading to a turn-over in the spectrum between the optically thin higher frequencies, and the optically thick lower frequencies.

The lifetime of synchrotron radiation is given by

$$\tau = \frac{E}{-dE/dt} \tag{1.31}$$

which for radio emitting electrons equates to roughly a few million years for the magnetic field strengths estimated for radio jets [Condon, 1992]. As radio jets can extend to Mpc scales, this implies that further acceleration processes outside the core take place, e.g. Fermi acceleration at the hotspot [Longair, 2011].

Inverse Compton Scattering also induces losses. This arises when relatively low-energy photons from starlight, or the cosmic microwave background, are scattered by highly energetic electrons. By considering the scattering of such a photon from a high energy electron, the electron loss rate for Inverse Compton can be shown to be

$$-\frac{dE}{dt} = \frac{4}{3}\gamma^2 U_{photon}\sigma_T c \tag{1.32}$$

which has the same E^2 dependence on electron energy as synchrotron radiation.

Finally, losses may also occur adiabatically, where the electrons do work to generate expansion. If the population of accelerating electrons is limited to the volume V within the radio lobes, then over time they will fuel a pressure increase, and subsequent expansion of the jets. Simple thermodynamical arguments [see e.g. Longair, 2011] give a loss rate for adiabatic expansion of

$$-\frac{dE}{dt} = \left(\frac{1}{R}\frac{dR}{dt}\right)E \tag{1.33}$$

where R is the radius of the source, showing that the electron energy loss rate scales with energy. The loss processes outlined above influence the evolution of the radio spectrum of a source in a predictable fashion. If an initial power-law distribution of electron energies is assumed, the

electron energy loss loss rate represents a flow of electrons from high energy to low energy in the source. This can be described in the form of a continuity equation

$$\frac{\delta N}{\delta t} = \frac{\delta}{\delta E}[N(E)\dot{E}] \tag{1.34}$$

If, as is likely, the source of electrons is constantly replenished (e.g. via shocks) this gives

$$\frac{\delta N}{\delta t} = \frac{\delta}{\delta E}[N(E)\dot{E}] + Q(E) \tag{1.35}$$

where Q(E) is the source of new high energy electrons. For a power-law energy electron injection spectrum, as would be expected from shock acceleration, $\mathrm{Q(E)} \propto \mathrm{E}^{-x}$.

Adiabatic losses simply cause a shift of the spectrum, with no change in shape. Observationally, if a loss rate dominated by synchrotron and Inverse Compton scattering is assumed, this gives rise to a characteristic spectrum of two power-laws, with a smooth break, as the spectrum steepens at high frequencies (energies) due to enhanced losses. Assuming that these losses overall dominate over further particle acceleration in the source, the break in the spectrum may be used to gain an estimation of the age of the source [as in, e.g. Machalski *et al.*, 2009]. The radio power of the source will lessen also if these losses dominate, as the radio source grows larger [see e.g. Kaiser and Best, 2007]. Differences in the observed spectrum may also be seen for radio sources operating in markedly different environments. For example, a source in the centre of a cluster may be in a region of such high density that the radio lobes become pressure confined. With the source expansion inhibited, adiabatic expansion losses will slow, and Inverse Compton/synchroton losses will dominate, leading to a steeper spectrum. The lower overall loss rate will lead to a brighter source. Sources in a more isolated environment will continue to have adiabatic expansion losses, and will fade on a much quicker timescale than those in clusters [Klamer *et al.*, 2006].

At higher redshift, changes in environment may give rise to differences in the observed spectra, compared to similar sources locally. For Inverse Compton scattering, the density of the CMB depends as $(1+\mathrm{z})^4$ [Klamer *et al.*, 2006], and so spectral losses will be enhanced, leading to a lower break frequency. There is also a cosmological argument that the environment at high redshift will be denser, and that this will lead again to steeper spectra. However, this is uncertain, as the density of gas around high redshift radio galaxies has been observed to be highly inhomogeneous [Miley and De Breuck, 2008]. At high redshift, there are other factors which could give rise to primarily steep spectra being observed, such as the 'youth-redshift' degeneracy, whereby radio sources observed at high redshift are more likely to be young [Blundell and Rawlings, 1999]. This is discussed further in Chapter 4.

Physically as demonstrated above, the synchrotron processes, Inverse Compton Scattering, and adiabatic processes should result in characteristic spectra (e.g. pure synchrotron giving rise to simple power-law). However, for many studies involving perhaps only 5 or 6 data-points in the frequency-flux plane [e.g. Blundell *et al.*, 1999], first/second order polynomials are chosen as a matter of simplicity/convenience, as they describe the majority of source spectra well and provide a straightforward means of comparing spectra. To attempt more complex

functions would result in over-fitting, unless there are a large number of data points available [e.g. Murgia *et al.*, 1999]. It is also interesting to note that some authors have recently argued that the radio spectra of AGN may arise from an intrinsically curved, rather than power-law underlying electron distribution, naturally giving rise to a polynomial form which appears to fit so many radio spectra well [Duffy and Blundell, 2012].

Radio observations of AGN constitute one of the most basic classification schemes, as almost all AGN can be classified as either radio loud, or radio quiet objects. In radio loud AGN the radio emission traces the jets driven by the central engine, from synchrotron emission in the lobes, and the shocks or 'hotspots' occurring at the lobe ends [Kellermann, 1998]. Synchrotron emission gives a steep power-law radio spectrum, which is observed in the lobes, of order $\alpha \sim$-0.8, where $S_\nu \propto \nu^\alpha$. However in the core, the spectral index is flatter as a result of superposition of synchrotron self-absorbed spectra from individual components of the jet, generally $\alpha \sim -0.5$, and as flat as $\alpha \sim 0.0$ at low redshift.

In contrast radio-quiet AGN show small, usually sub-kiloparsec scale, weak jets (if any), which contribute very little to the total energy output of the galaxy, which is primarily thermal [Padovani *et al.*, 2011]. Whilst the radio emission from radio-loud AGN is clearly powered by the jets, the origin of the radio emission in radio-quiet AGN is less clear: a weaker version of the radio-loud AGN mechanism, disk winds and star formation have all been suggested as possible sources. Recent evidence points towards star formation being a key contributor [e.g. Padovani *et al.*, 2011; Sargent *et al.*, 2010], as radio-quiet AGN have a similar far-infrared to radio ratio as star-forming galaxies, and the luminosity function is also much more consistent with that of star-forming galaxies, rather than radio-loud AGN.

The difference in contribution of the radio AGN to the total bolometric luminosity constitutes the main difference between the radio-loud and radio-quiet classes. However, there are differences in environment seen for the two classes as well, as summarised by Wilson and Colbert [1995]. Radio-loud AGN tend to be almost exclusively found in elliptical galaxies, whilst radio quiet AGN favour spiral galaxies. Radio-loud AGN are also much less numerous, their space density is estimated to be a factor of 10 lower than that of radio quiet AGN. There are differing methods of deciding where the cutoff between a radio quiet and radio loud AGN occurs in the literature, see for example Jarvis and McLure [2002]. One of the most commonly used is a radio to optical luminosity ratio greater than 10, and pure radio luminosity cuts are also used, as in e.g. Croston *et al.* [2005]. More usually a combination of criteria are used, as despite slightly confusing nomenclature, radio-quiet AGN can still have relatively high radio luminosities, and may be easily confused with genuine radio-loud AGN, based solely on a simple cut in radio luminosity.

Wilson and Colbert [1995] suggest that given the thermal emissions from both radio quiet and radio loud AGN are relatively similar, the wide variation observed in AGN radio power is due to black hole spin, and not the black hole mass/accretion rate. Martínez-Sansigre and Rawlings [2011] discuss this in more detail. They suggest that black hole spin is an attractive progenitor of the large variation in radio power observed in radio AGN, as spinning black holes can reach very high efficiencies, capable of powering strong jets in radio-loud AGN. The normal

accretion process via a disk as in spiral galaxy will lead to either a slowly or non-rotating black hole. However a violent merger event of two galaxies, the product of which is an elliptical, could lead to a rapidly spinning central black hole, a strong contender for the progenitor of a radio loud AGN. Whether this is indeed the case is still very uncertain, and constitutes an active area of research in radio astronomy.

Historically, radio loud resolved jet-dominated sources can further be split into two morphological types, Farnaroff -Riley class I and II. Fanaroff and Riley [1974] measured the ratio of the distance between the highest brightness regions on either side of the host galaxy to the total radio galaxy size, using a sample of classical double radio galaxies from the 3CR catalogue. They found a clear correlation of this ratio with luminosity, a higher ratio implying a higher luminosity. Sources were split into class I with a ratio less than 0.5, and class II with a ratio greater than 0.5. As described in Urry and Padovani [1995], as a consequence of this Faranoff-Riley class I (FRI) tend to display luminosities which peak close to the galaxy core, and may include disturbed or anisotropic radio structures. Faranoff-Riley class II (FRII) have well defined morphologies, with clear lobes and outer hotspots, and jets that are more collimated in general than FRIs. FRIs have lower luminosities, whereas FRIIs tend to have high radio luminosities, typically $P_{178MHz} > 5 \times 10^{24} WHz^{-1}sr^{-1}$.

The most popular interpretation of the difference between FRI and FRIIs is that it can be explained by the density of the Intergalactic Medium (IGM) in which they exist. Jets produced by the central engine will be disrupted, and reach very much shorter distances due to entrainment (mixing) of the surrounding medium in regions of high density IGM, producing FRIs. The denser the environment, the more powerful the jet is needed to be in order to prevent disruption, and produce a classic FRII. However, the reasons for the divide may not be solely confined to this simple idea, as FRIIs have been found in clusters, i.e. regions of high density IGM [see for example Wan and Daly, 1996].

Based on the fact that FRIIs have 10-50 times more emission line luminosities than FRIs [Wilson and Colbert, 1995], some early studies suggested that differing accretion modes (i.e. HERGs and LERGs) were responsible for the observed FRI and FRII classes [e.g Baum *et al.*, 1995]. However Hardcastle *et al.* [2007] state that if different accretion modes are present, then they will not be responsible for the observed FRI/FRII divide, noting that the two classes appear similar in other wavelengths, FRIIs can display weak as well as strong emission lines and that the main difference is in their radio morphology. Thus it now seems likely that the observed emission line difference is a result of FRI/FRII and LERG/HERG common population overlap, rather than an intrinsic dependence of FRI/FRII morphology on accretion mode. Recent work by Gendre *et al.* [2012] at low redshift suggests that indeed, the FRI/FRII differences are not likely to be dependent on accretion mode. This suggests that the FRI/FRII divide arises from environmental constraints, whereas the high/low excitation states observed in the optical are caused by different accretion modes.

It is also worth briefly mentioning two further sub divisions of radio AGN, namely compact steep spectrum (CSS) and giga-hertz peaked spectrum (GPS) sources. These are powerful radio sources with a turnover in the radio spectrum (at approximately 1GHz for GPS, <100 MHz

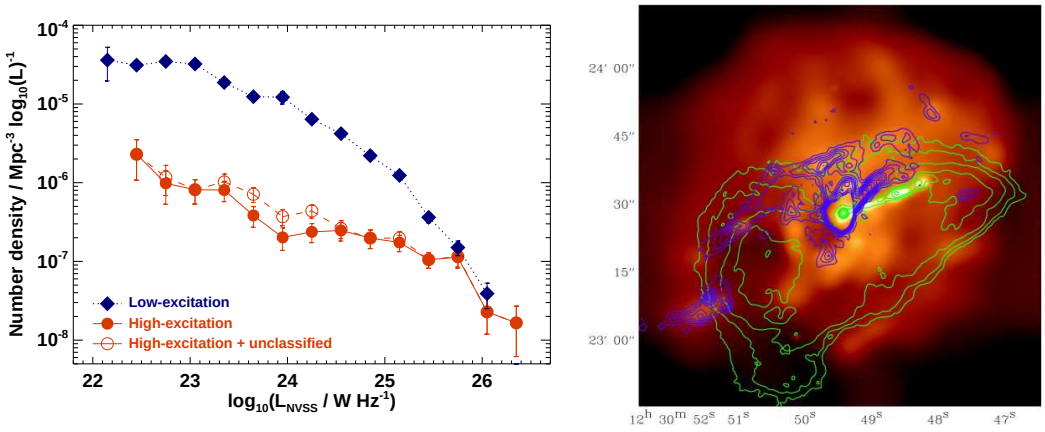

Figure 1.2: On the left, the radio luminosity functions of HERGs (red) and LERGs (blue) out to z∼0.3, as determined by Best and Heckman [2012]. Despite LERGs clearly dominating at low luminosities and HERGs at high, both populations are present over the entire studied luminosity range. Figure reproduced from Best and Heckman [2012]. On the right, an X-ray image of M87 (central galaxy in the Virgo cluster, and one of the brightest radio sources in the sky) which is a classic example of a Low Excitation galaxy. Green contours show 1.4 GHz radio emission, neatly tracing the cavities in the X-ray emitting gas. Figure reproduced from Young *et al.* [2002].

CSS). The difference between these and classical FRI/FRII is that they are very much more compact, their radio morphologies look very much like miniature FRIIs, and Jackson [2006] suggest that they are either young FRI/FRII, or enmeshed in a very dense environment. Data from radio Very Long Baseline Interferometric (VLBI) observations allows measurement of the rate of advance of the hotspots of these sources, allowing age estimates which are consistent with these sources being very young [e.g. Schilizzi *et al.*, 2000].

1.3 AGN Feedback

AGN feedback has been mentioned in the preceding sections as a physical mechanism which could potentially have profound implications for the way that galaxy formation is modelled, and is a process that is not yet fully understood. The very basic view of galaxy evolution in a 'bottom-up' evolution scenario is that star forming young blue galaxies, evolve and undergo mergers over time into red massive elliptical galaxies. The stage between these two points appears on the colour magnitude diagram of a sample of galaxies as the 'green valley'. One of the key problems modeling of galaxy evolution, as outlined earlier, is that the number of both massive blue and red galaxies that we should see is consistently overestimated.

Despite the relatively small numbers of powerful radio AGN, by incorporating radio AGN feedback into the models, this problem can be overcome. As discussed previously, in recent years two types of feedback scenarios have emerged in the literature, e.g. Smolčić [2009], Hardcastle *et al.* [2007]. Firstly high excitation (HERG), or 'quasar mode' in which quasar winds (triggered by mergers) remove gas from the galaxy and hence slow star formation. Secondly low excitation

(LERG), or 'radio mode', which refers to radio outflows from AGN in massive galaxies. These outflows do work against the surrounding gas, preventing more star formation in the galaxy and halting the growth of the massive galaxy. This mechanism will generally only be possible in massive galaxies, where the cooling time of the accreting material is longer than its dynamical time, giving a extended halo of cooling gas surrounding the source against which it can do work [see e.g. Best *et al.*, 2007].

As outlined in Section 1.2.1, the exact circumstances in which these two types of feedback can be effective depend on how the energetic outflows behave close to the central black hole [Fabian, 2012]. Material being accreted on to the black hole heats up and radiates energy, and eventually a limit of the central black hole's luminosity will be reached when the pressure of this emitted radiation balances the gravitational pull of the black hole on the accreting material: the Eddington limit. When this limit is reached, any further infalling matter will be blown away from the central black hole [Blandford]. In the case of quasars, operating at the Eddington limit, it can be shown that it is possible for these to halt accretion at the maximum possible rate [Silk and Rees, 1998]. However, as discussed in Fabian [2012], this cannot be the entire story, as when the mass of the host galaxy is also considered, it must collectively be operating below the Eddington limit. Jets from the AGN can power winds, either by shock heating the gas, or pushing it away. Radiation pressure on dust can also be important, even far away from the black hole, due to the high absorption cross-section of dust [Cattaneo *et al.*, 2009]. As discussed further in Cattaneo *et al.* [2009], there is convincing observational evidence that these processes do occur and are related to star formation: optical and X-ray spectroscopy show winds present in post-starburst galaxies, higher than those generally observed in starburst galaxies.

'Radio-mode', or kinetic feedback occurs in galaxy clusters. In this case the accretion rate of the central galaxy black hole is low, and it radiates inefficiently, in the form of jets. Contrary to 'quasar-mode', outflows from the central black hole occur regularly, and heating by these ensures that the hot gas surrounding the cluster is not able to cool and sink inwards towards the cluster centre. Large bubbles and cavities in the gas inflated by the jets are often observed in these sources (see Figure 1.2).

Over the last few years, observational evidence for this AGN feedback effect in galaxies has increased. Best [2007] summarises some of the key evidence of interaction between the AGN and host galaxy, including the observed high velocity widths of emission line gas surrounding the central radio source, gas outflows, with measurable blueshift seen towards radio galaxies and cavities created by the radio lobes visible in the surrounding hot X-ray emitting gas (see Figure 1.2). The evidence that AGN feedback occurs in galaxies is very strong, and recent observational studies suggest that feedback episodes occur relatively often, and theoretically, with enough energy to stall gas cooling in the galaxy.

Comparing low luminosity radio loud AGN and optically selected emission line AGN, it is clear that the physical processes behind the activity observed are different. In contrast to the host galaxies of radio loud AGN, emission line AGN are often strongly associated with bursts of star formation in the host, fuelled by the accretion in a thin disk of cold gas, and hence imply a growing galaxy [see for example Kauffmann *et al.*, 2003]. There appears to be little

dependence of emission line AGN fraction on black hole mass. If the low luminosity radio loud AGN are being refuelled by accretion of hot gas from surrounding X-ray halos onto the disk, and given that the central black holes are already massive and well established, then this would explain the observed power law dependence of radio loud fraction with black hole mass. Best *et al.* [2006] were able to show that for massive galaxies, the heating by the central radio source is approximately equal to the radiative energy losses from the hot gas halo surrounding the galaxy, utilising previous work relating the 1.4GHz radio luminosity of a source to the mechanical luminosity of the source through study of cavities [Birzan *et al.*, 2004], and X-ray studies of gas cooling rates.

While this represents substantial progress in verifying the existence of physical mechanisms which can control the growth of a massive galaxy that is consistent with both modeling of galaxy evolution and observations, our current understanding is limited by the lack of depth in existing radio and optical surveys, and a lack of deep, comprehensive, and fully identified samples of powerful radio galaxies to provide robust statistics. The occurrence of the feedback processes identified above need to be measured out to high redshift in order to understand their potentially crucial contribution to galaxy evolution over cosmic time. The most recent, comprehensive determination of the radio luminosity function (RLF) out to high redshift by Rigby *et al.* [2011] finds differential cosmic evolution between the high and lower power radio sources - the latter showing only weak evolution, and the former very strong evolution, substantiating earlier findings [e.g. Willott *et al.*, 2003; Dunlop and Peacock, 1990]. The temptation following this has been to classify all low luminosity AGN as LERGs, and high luminosity AGN as HERGs. An early study by Hine and Longair [1979] using the 3CR sample showed that over 70% of high luminosity sources displayed bright emission lines, in contrast to only 10% of low power sources. However, they also cautioned that 'the presence of strong emission lines in the spectrum of the galaxy does not necessarily imply that the galaxy will be a powerful radio source'. More recent work by Best and Heckman [2012], presenting the first separate measurement of the HERG and LERG luminosity functions locally over a wide luminosity range has confirmed that HERGs and LERGs are not separated by radio luminosity. Although LERGs do dominate at lower radio luminosities and HERGs at higher, examples of both are seen over all studied radio luminosities (cf. Figure 1.2). Their work suggests that at least locally ($z<0.3$), HERGs evolve strongly, and LERGs do not, and that this may account for the differential evolution seen in the radio luminosity function as a whole.

The most massive luminous AGN with the highest rates of active star formation have been shown to be most numerous at redshifts of around $z\sim2$-4, with lower luminosity radio-AGN peaking at successively lower redshift [Rigby *et al.*, 2011]. In other words, massive galaxies appear to evolve considerably faster than smaller galaxies. In the case of massive galaxies, it naively makes sense for numbers to increase with decreasing redshift, as in a λCDM hierarchical scenario, it takes some time for smaller galaxies to merge into larger ones. However, at first glance, for numbers to peak, and then decline with decreasing redshift seems contrary to what might be expected for a hierarchical scenario.

Observationally, studies of the cosmic star formation rate have shown this to also peak

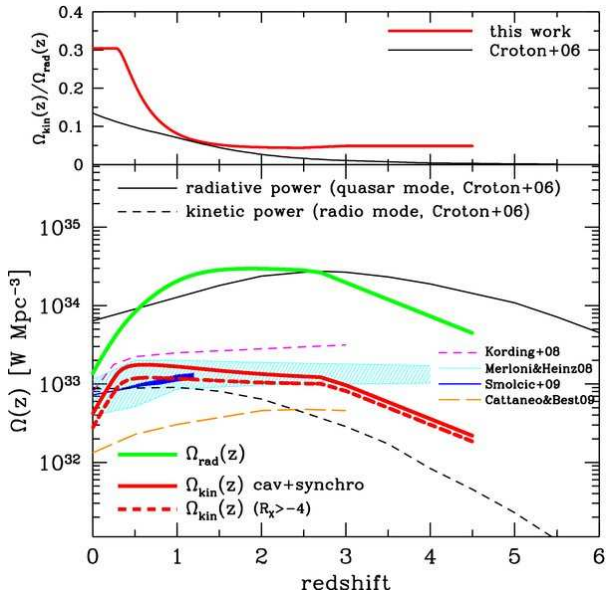

Figure 1.3: This Figure, reproduced from La Franca *et al.* [2010], shows the power density of kinetic and radiative modes with redshift,as measured from an X-ray selected sample both from their data (in red and green), and those expected by current models, as discussed further in the text.

at redshifts around z∼2, in addition to the estimated galaxy merger rate peaking around this epoch [Khochfar and Silk, 2011]. Thus something is switching off star formation at high redshift. If both radiative and kinetic feedback are considered, it is possible to reconcile the observed evolution of galaxies, and thus to infer the expected evolution of HERGs and LERGs. For the most massive galaxies, a larger black hole at the centre means that radiative feedback only becomes effective when enough cold gas is accreted (perhaps as in the case of a merger). During this phase, cold gas is removed from the host galaxy, and the source continues to evolve into a giant red elliptical, with star formation halted. If kinetic feedback is then evoked to maintain the gas surrounding the massive galaxy in its cluster at a high temperature, preventing a cooling flow, then the observed evolution of massive galaxies is expected, and no longer at odds with a λCDM model. For lower mass galaxies, radiative feedback becomes effective much sooner as the black hole has a smaller shallower potential well from which gas needs to be blown away, and star formation proceeds at a much lower rate, leading to a slower evolution [see Cattaneo *et al.*, 2009, for a detailed review].

Assuming that the above is correct, HERGs and LERGs, tracing radio AGN in radiative and kinetic mode respectively, would then be expected to evolve differently, following the interplay between the cosmic evolution of black holes, and their gas fuel. Positive evolution for HERGs out to z∼ 2 would be expected before a decline for the most luminous, mirroring the evolution seen in the cosmic star formation rate, and massive galaxies generally. As LERGs are found only in the most massive cluster galaxies, which take time to grow, the numbers of these would be expected to grow from close to nothing at z∼5 to a moderate number density in the present

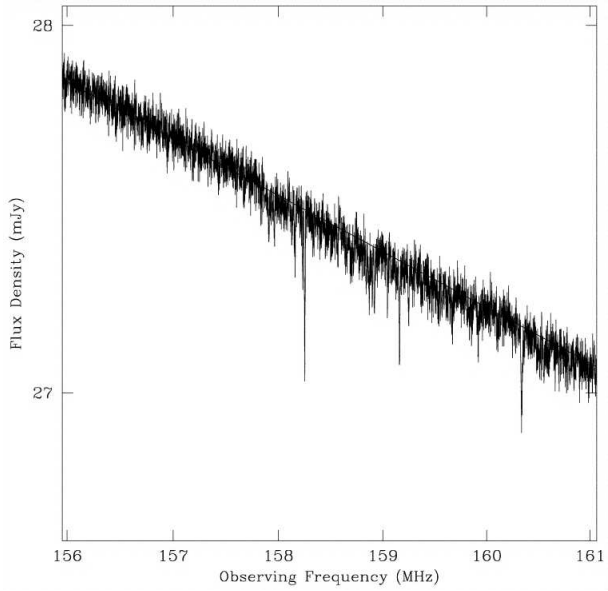

Figure 1.4: This Figure shows the simulated radio spectrum (based on Cygnus A)for a 35 mJy at 120 MHz radio source at z=8, after a 10 day integration with the SKA. The signature of neutral hydrogen should be clearly detected in the low frequency radio spectrum. Figure reproduced from Carilli *et al.* [2007].

day, following the observed decline in the most massive back holes [see e.g. Wen and Han, 2011] and hot gas halos with redshift.

Several recent studies, e.g. Croton *et al.* [2006], Merloni and Heinz [2008], confirm this predicted evolution. La Franca *et al.* [2010] present a determination of the kinetic mode luminosity function from a sample of X-ray selected sources, and compare this to the available galaxy evolution models of Croton *et al.* [2006] and Merloni and Heinz [2008]. In Figure 1.3, this is reproduced. It can be seen that above z=0.5, most are in qualitative agreement: namely a clear decline after z$\sim$2 for the radiative mode, and a gradual decline after z=0.5 for the kinetic mode. Below z=0.5, there are some differences between the models and observations for the kinetic mode. La Franca *et al.* [2010] observe a sharp decrease in kinetic power density between z=0.5 and the present day, slightly stronger than that predicted by Merloni and Heinz [2008]. The Croton *et al.* [2006] model is most at odds with the others, and La Franca *et al.* [2010] suggest that this could be due to the assumption of Croton *et al.* [2006] that both types of feedback come from constant accretion on to the AGN, leading to flat kinetic powers below z=0.5. Thus whilst the expected evolution of HERGs is clear, there remains some uncertainty as to how LERGs evolve at low redshift. There have as yet been no studies attempting to measure the evolution of HERGs and LERGs beyond z=0.3.

Measuring accurate luminosity functions of radio AGN and determining the expected relative numbers of HERGs and LERGs out to high redshift has implications for a number of important related studies, several of which are key science projects for next-generation instruments. Perhaps one of the most exciting, is that of locating powerful radio galaxies

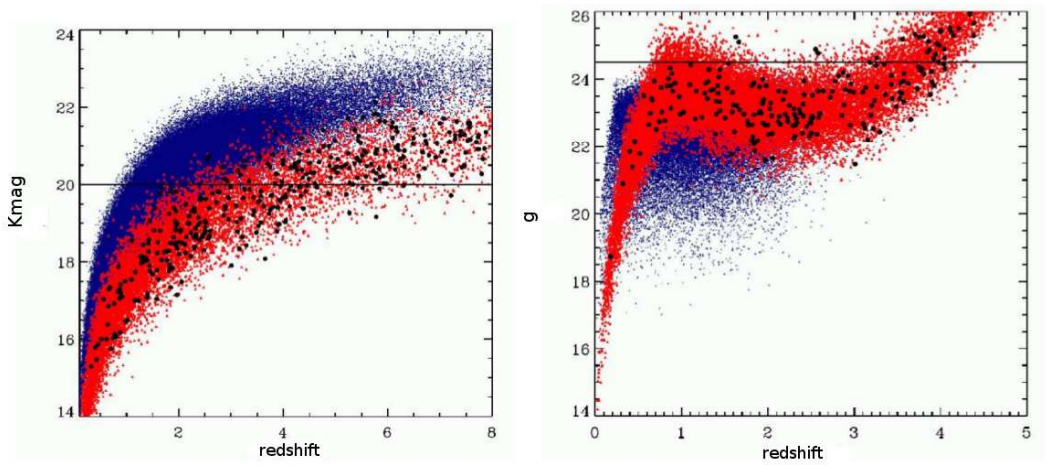

Figure 1.5: This Figure, reproduced from Best and the LOFAR-UK Consortium [2008], shows the simulated K-magnitude - redshift and g magnitude - redshift expected from the planned LOFAR Deep survey and deep optical and K-band surveys. The LOFAR Deep survey will reach a depth of 6μJy at 200 MHz over an area of 250 square degrees. Shown in black are FRIIs, red are FRIs and starbursts in blue. The simulation is over 100 square degrees for the FRIIs, and 1 square degree for the others. The horizontal line on the K-z diagram on the left shows a K=20 limit. The line on the g-z figure shows the limit in g reached by the Pan-STARRS 3π survey specifications.

at very high redshift (z>6), close to, or within the Epoch of Reionisation (EoR). Locating such sources would allow detailed studies of early, as yet unknown, populations of radio galaxies, which will comprise some of the most massive interacting structures in the early Universe. Any radio galaxy located at z>6 could be used to constrain how conditions in the EoR evolved with time by studying redshifted 21cm absorption features along the line of sight in the low frequency radio regime (cf. Figure 1.4). However, as of yet, the highest redshift radio galaxy known is located at a redshift of 'only' z=5.2. The very low numbers of sources expected to be at high redshift makes searching for such sources very challenging. A number of methods are currently employed to 'pre-select' good candidates for spectroscopic follow-up, most commonly based on a steep radio spectrum, or faint K-band magnitude, traits which known high redshift sources favour. However, how efficient these methods are remains open to question, particularly as historically, spectral index cuts were the only practical means of filtering surveys down to managable sizes, due to a lack of deep, wide near-infrared surveys. This is now not the case, with the UKIDSS LAS [Lawrence *et al.*, 2007] survey providing wide coverage in the K-band down to K$\sim$18 (photometric redshift of z$\sim$2), and the Pan-STARRS Medium Deep Survey soon to be completed in 2012 (see Figure 1.5). A new class of radio sources which are faint or undetected in the optical and near-infrared, infra-red faint radio sources (IFRS) have been proposed as strong candidates for very high redshift radio sources, but as these can have a wide

range of radio fluxes, from sub-mJy upwards, it is important to determine how many of these could be moderate redshift LERGs with no emission lines, as opposed to genuine high redshift radio galaxies with emission lines shifted out of the optical range.

With the advent of LOFAR and the SKA, heralding a new generation in radio astronomy, unprecedented volumes of multi-frequency survey data will become available of both a sensitivity and resolution unachievable by current instruments. The planned LOFAR Deep Surveys alone will be sensitive to nearly all radio loud AGN in the Universe out to high redshift [Best and the LOFAR-UK Consortium, 2008]. It is crucial therefore to identify the areas of most interest in radio AGN studies, and to lay the groundwork for the studies planned to be carried out with LOFAR and the SKA, in order to be able to target and collate objects of interest efficiently.

1.4 Thesis Outline

This thesis will address four key currently outstanding questions in radio AGN astrophysics from the wealth of important areas of study outlined above. These have been carefully chosen to both enhance knowledge of radio-AGN influence on galaxy evolution through studying and expanding existing substantial complete radio galaxy samples, whilst also maximising potential input into studies of radio AGN planned to be completed with LOFAR and the SKA, and associated complementary optical (e.g. Pan-STARRS) and near-infrared (e.g. VISTA) surveys, coming online in the very near future.

- What is the most efficient means of assembling samples of very high redshift (z>2, 3) radio AGN?
- What effect does the shape of the radio spectrum have on the determination of the radio luminosity function, particularly at high redshift?
- How does the relative number density of the two main AGN fuelling modes (HERG, and LERG) evolve over the bulk of cosmic time (z∼1)?
- How can the findings above be used to inform efficiently future studies with data intensive instruments such as LOFAR and the SKA?

Chapter 2 gives an introduction to the technique of radio interferometry, particularly as it applies to low frequency radio work, and presents new low frequency radio observations at 610 MHz and 325 MHz of the CENSORS complete radio sample, and new host galaxy identifications. Chapter 3 gives new long-slit optical and near-infrared IFU spectroscopic observations for the CENSORS sources currently without a spectroscopic redshift. Chapter 4 utilises the new CENSORS data in conjunction with eight other existing complete samples to carry out a detailed evidence-based study of the efficiency of common techniques used in the literature to locate powerful radio galaxies at high redshift. Chapter 5 presents radio spectra for CENSORS and three other complete radio samples, and investigates what effect radio spectral curvature has on the determination of the radio luminosity function, and whether spectral curvature can be used as a means of identifying young radio sources at high redshift. Chapter 6 presents the

very first observational measurement of the evolution of high and low excitation radio sources out to z$\sim$1, along with new spectroscopic data for the samples used, and also presents a short exploratory study of deep spectroscopic follow-up of infra-red faint radio sources as possible very high redshift radio galaxy candidates. In Chapter 7, an introduction to LOFAR is given, along with an outline of commissioning activities currently underway in order for new deep low frequency surveys to begin, and finally in Chapter 8 the conclusions from these studies are presented, along with a discussion of future directions.

Chapter 2

Radio Observations of the CENSORS Sample

2.1 An Introduction to Radio Interferometry

Radio interferometers constitute some of the world's most iconic telescopes, but the principles behind their operation are very different to those of a traditional single dish instrument. To understand this, it is helpful to return to the basic requirements for any instrument used to observe astronomical sources at any wavelength. Good resolution, and excellent sensitivity are essential. An optical telescope measures the number of photons collected, and hence the signal to noise achievable depends on the diameter of the dish. A radio receiver measures the voltage induced by the radio signal received, and again, the larger the collecting area, the stronger the signal. Looking at the resolution however, classical optical diffraction theory limits the angular resolution achievable by a single dish telescope to

$$\theta \sim \frac{\lambda}{D} \tag{2.1}$$

where λ is the wavelength of the radiation received, and D is the diameter of the telescope. In the optical, a 6m aperture theoretically provides $\sim$0.025 arcsec resolution, however a single radio dish observing at low frequencies can achieve at best only a few arcminutes resolution. For example, the FAST telescope currently being built in China will be the largest single dish radio telescope in the world with a 500m dish diameter, and yet will only achieve a resolution of $\sim$2 arcminutes in the L band [see Zhao, 2009]. Much of the desired science in radio astronomy relies on obtaining radio source positions with enough precision to enable cross-matching with data at other wavelengths. It was this poor resolution able to be achieved by the largest single dish long wavelength radio telescopes, that provided the initial motivation behind the development of radio interferometry.

The very basic key concept behind an interferometer is that one can link many single radio dishes together, combining the signal received at each, and effectively simulating a large single

radio telescope dish, with a diameter equivalent to the largest distance (baseline) between the smaller dishes.

2.1.1 The Radio Interferometry Problem

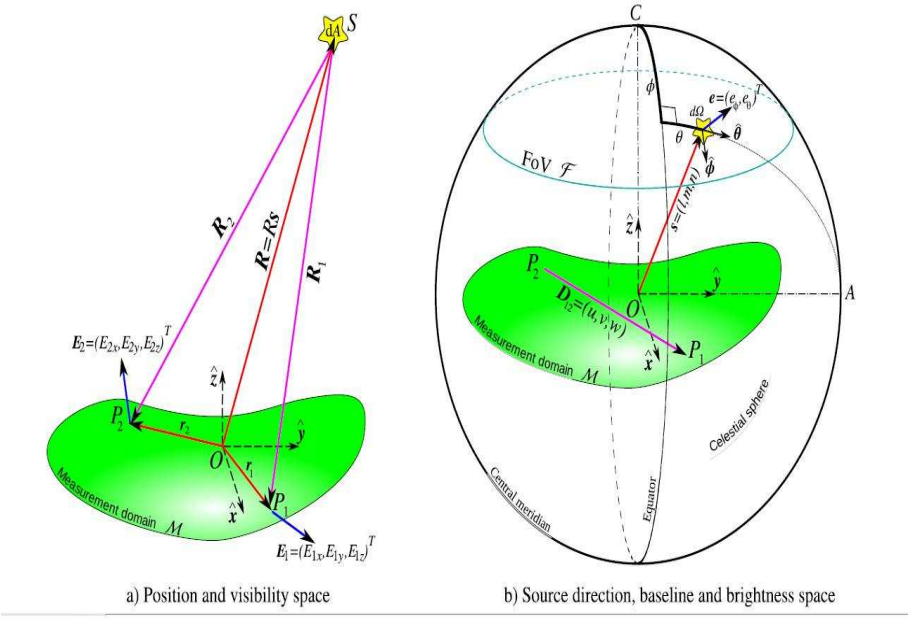

Figure 2.1: The Radio Interferometry Problem Illustrated. a) Illustrates the basic problem, whereby an astronomical source emits radiation, and a time variable electric field **E**(**R**,t) is measured at two different points in domain M. O denotes the origin of the coordinate system used. b) Denotes the common coordinate system used in interferometric measurements. Figure reproduced from Carozzi and Woan [2009].

Figure 2.1 a) illustrates the basic problem we want to solve. All we can learn about a source comes solely from the distribution of its electric field on the sky. Detailed coverage of the underlying physics is given in many widely available texts, for example Thompson [1986], G.B. Taylor [1999], and K. Rohlfs [2000] and I utilise these to compile an introduction of the principles of radio interferometry relevant to my work presented in this Chapter[1]. In order to simplify the theoretical background and give a more concise introduction, I introduce some simplifying assumptions as follows, assuming a similar approach to Chapter 1, of G.B. Taylor [1999].

[1]I would also like to acknowledge here the presentations and notes obtained from a summer school in Synthesis Imaging, held at ATNF Narrabri in October 2009, which were very helpful in aiding my understanding of radio interferometry and were invaluable in explaining some of the key concepts presented in this Chapter.

- That the Electric field E is non time varying over short intervals. This will be generally true for most astrophysical sources of interest, e.g supernova remnants, radio galaxies in which the signal does not vary over observational timescales of hours, but obviously not so for highly variable sources such as pulsars. However it allows the basic physical concepts to be illustrated.
- Polarisation is ignored, and therefore the measured electric field is treated as a scalar quantity, again for simplification.
- That the sources of interest are so far away as to be only measurable in two dimensions, or their 'surface brightness'.
- Finally, that the space in between the source and the observer is empty, and that therefore the propagation of the Electric field through the vacuum is linear and can be described by Maxwell's equations in a vacuum.

Classic electromagnetism theory gives the form of an electric field in a vacuum as

$$E(t) = \int_0^\infty E(\nu) e^{i[\phi(\nu) - 2\pi\nu t]} d\nu \tag{2.2}$$

If the coefficient E(ν) has a form which limits the range of frequency to an interval $\delta\nu$ such that

$$\delta\nu/\bar{\nu} << 1 \tag{2.3}$$

where $\bar{\nu}$ is the mean frequency then the signal is said to be quasi-monochromatic [K. Rohlfs, 2000], which is what is measured in reality: a signal over some small but finite bandwidth. So, applying the no-short-term-time-variability assumption to the quasi-monochromatic measurement of the electric field emitted by our source, $\mathbf{E}(\mathbf{R},t)$, it is possible to express the electric field as Fourier series and utilise only the Fourier coefficients, rather than the full time varying wavefunction, as representative of the electric field at $\mathbf{R}$, $\mathbf{E}_\nu(\mathbf{R})$.

Maxwell's equations for radiation propagating in a vacuum allow the determination of the electric field at location $\mathbf{r}$, in the form of a Green's function solution

$$\mathbf{E}_\nu(\mathbf{r}) = \int\int\int P_\nu(\mathbf{R},\mathbf{r}) \mathbf{E}_\nu(\mathbf{R}) dx dy dz \tag{2.4}$$

where $\mathrm{P}_\nu(\mathbf{R},\mathbf{r})$ is the propagator function which indicates how the source electric field affects the electric field measured at $\mathbf{r}$. By considering the electric field as a scalar, or in only one direction, this equation is simplified, and the assumption that the space between the observer and source is empty is also applied. We also need to consider that the sources observed are so far away, that we can only make surface brightness measurements. For this reason, G.B. Taylor [1999] define a third electric field, $\varepsilon_\nu(\mathbf{R})$, as the electric field distribution on a giant celestial sphere of radius the absolute magnitude of $\mathbf{R}$. This gives us that the electric field measured at $\mathbf{r}$ is,

$$E_\nu(\mathbf{r}) = \int \varepsilon_\nu(\mathbf{R}) \frac{e^{2\pi i\nu|\mathbf{R}-\mathbf{r}|/c}}{|\mathbf{R}-\mathbf{r}|} dS \tag{2.5}$$

where dS is an element of surface area on the celestial sphere. This is then the electric field measured by the observer at $\mathbf{r}$ due to all sources of cosmic electromagnetic radiation.

2.1.2 Spatial Coherence

The very simplest two element interferometer, measures the voltage induced by the electric field at two points, $\mathbf{r}_1$ and $\mathbf{r}_2$, and then proceeds to correlate the signals. The correlation is defined as the expectation value of the product of the two electric fields:

$$V_\nu(\mathbf{r_1}, \mathbf{r_2}) = \langle \mathbf{E}_\nu(\mathbf{r_1}) \mathbf{E}^*_\nu(\mathbf{r_2}) \rangle \tag{2.6}$$

Substituting in equation 2.5, writing $\mathbf{s} = \mathbf{R}/\mathbf{R}_{modulus}$, and $\mathrm{I}_\nu(\mathbf{s})$ for the observed intensity and finally making the assumption that the radiation from two different points of the source is uncorrelated, the following expression, the spatial coherence function, is obtained:

$$V_\nu(\mathbf{r_1}, \mathbf{r_2}) \sim \int \mathbf{I}_\nu(\mathbf{s}) \mathbf{e}^{-\mathbf{2\pi i \nu s}.(\mathbf{r_1}-\mathbf{r_2})/\mathbf{c}} \mathbf{d\Omega} \tag{2.7}$$

This quantity is what a single baseline of an interferometer measures (via induced voltages), and is invertible, in other words, given the spatial coherence function, we can obtain the observed intensity.

Choosing a set of coordinates wisely means that the spatial coherence function may be written in the form of a Fourier transform. If the coordinate system is chosen to be in a plane, we can write the separation vector in terms of the wavelength, $\mathbf{r}_1$-$\mathbf{r}_2$= λ(u,v,w), with the components of $\mathbf{s}$ as (l,m,$\sqrt{1-l^2-m^2}$). Re-writing the coherence function in this coordinate system shows that the coherence function V_ν(u,v,w=0) and the modified intensity $\mathrm{I}_\nu(\mathrm{l,m})/\sqrt{1-l^2-m^2}$ are a Fourier transform pair.

If we then assume that we are looking at a small portion of the sky, in other words, a particular source, we can write $\mathbf{s}$=$\mathbf{s}_0$+σ, where $\mathbf{s}_0$ points from the antenna to the 'phase tracking centre', with the vector σ describing all nearby points on the sky, perpendicular to $\mathbf{s}_0$. This assumption means the w term may be neglected, and equation 2.7 can be reduced to a two dimensional Fourier transform as follows:

$$V_\nu(u, v) = \int \int I_\nu(l, m) e^{-2\pi i(ul+vm)} dl dm \tag{2.8}$$

If geometrical delays are accounted for, then any phase difference relative to the phase tracking centre measured by the interferometer will be due to light from different parts of the source reaching the antennas at different times, giving a fringe pattern, and allowing source positions to be measured.

In practice, two other effects must be accounted for when measuring the spatial coherence function V. Firstly the antenna reception pattern, or 'primary beam'. This is a factor $\mathrm{A}_\nu(\mathbf{s})$ which effectively describes the sensitivity of the interferometer element with radius from the

centre of the dish beam. The expression for spatial coherence then becomes;

$$V_\nu(u,v) = \int\int A_\nu(l,m) I_\nu(l,m) e^{-2\pi i(ul+vm)} dldm \tag{2.9}$$

V_ν(u,v) defined in this way is referred to as a *visibility*. It is then straightforward to correct for this effect at later stages of data processing, when deriving the intensities, if all the interferometer elements have the same reception pattern. It is simply a case of dividing the measured intensities by a primary beam factor, approximately 1 at the phase tracking centre, and falling to smaller factors towards the outer edges of the beam.

Secondly, in practice V_ν(u,v) cannot be sampled everywhere in the uv plane. This is described by a sampling function, S_ν(u,v), which is zero at the points in the plane where no measurements have been taken. Including this and Fourier inverting the visibility measured by the interferometer gives;

$$I^D_\nu(l,m) = \int\int V_\nu(u,v) S(u,v) e^{-2\pi i(ul+vm)} dudv \tag{2.10}$$

The set of fourier inverted visibilities $I^D_\nu(l,m)$ is referred to as the *dirty image*. To obtain the true set of intensity values I_ν(l,m), the synthesised beam B corresponding to the sampling function must be deconvolved from the true intensity distribution.

$$I^D_\nu(l,m) = I_\nu * B \tag{2.11}$$

where B is the synthesised beam, related to the sampling function by;

$$B(l,m) = \int\int S(u,v) e^{2\pi i(ul+vm)} dudv \tag{2.12}$$

Thus in order to make an image of the true intensities, the spatial coherence function must be measured with good coverage in the uv plane by the interferometer and these visibilities then fourier inverted, and the synthesised beam deconvolved. The process of deconvolution usually takes place during several rounds of 'self-calibration'. Instrumental errors and ionospheric disturbances can give rise to errors in the measured visibilities at each antenna. Self-calibration describes a process which reduces these errors, by using a model of the target field (containing bright sources) to solve for the complex gains measured by the individual antennas. Self-calibration works as it preserves the closure phase, which is a combination of the phases measured at three different antennas, the result of which is independent of individual antenna phase errors.

In practical terms, the starting model is usually the first deconvolved 'dirty' image of the target field. Phase-only self-calibration is generally started with, followed by amplitude and phase. A cycle of self-calibration is set up by solving for these complex gains, imaging the self-calibrated dataset, and then using this image as an improved model for the next round, until the final image appears of good quality with expected noise levels, and no deconvolution artifacts.

2.1.3 The Measurement Equation

The basic concepts which I have presented so far are standard as an introduction to radio astronomy, and are described in far greater detail in the classic texts of Thompson [1986] and G.B. Taylor [1999]. This is the standard layout which underpins many of the major existing software packages such as AIPS, MIRIAD etc. Do we need to do better?

- we do not have a full mathematical description of the polarisation.
- the assumptions above are much more difficult to implement for an array of dipoles, with a field of view covering a much larger fraction of the sky.
- existing calibration corrects uv-plane effects: there is no allowance for correction of image plane effects, such as ionospheric variations.
- existing packages are difficult to add to/modify, and are no longer being actively maintained.

In the early 1990s Hamaker *et al.* [1996] derived a mathematically complete description of what is measured by any interferometer.[2] The measurement equation effectively describes the path of the radio signal through the various propagation mediums, such as the ionosphere, antenna feeds etc up until reception by the correlator, by a series of matrices, the Jones matrices.

The field of optical polarimetry has a wide range of formalisms available to describe polarisation. The Stokes parameters describe the state of polarisation of light, and the Jones and Mueller matrices describe the transformation of the polarisation state as the wave propagates through various mediums. As a reminder Mueller matrices are a generalisation of the Jones matrices. Jones matrices are only applicable to fully polarised light.

The Measurement Equation provides a transparent and compact description of radio interferometric measurements at all polarisations, and is being adopted as the formalism in new interferometric reduction packages intended for telescopes such as LOFAR and the SKA (see for example the guide to Meqtrees [see Noordam, 2009], a calibration and simulation package for LOFAR).

Beginning with the assumption that all the radiation arrives from a single point, the propagation of the 'source' electric field is defined as

$$\mathbf{e} = \begin{pmatrix} e_x \\ e_y \end{pmatrix} \tag{2.13}$$

in the xy plane, with z the direction of propagation.

The Measurement Equation formulation makes only one main assumption, that the propagation of the wave is *linear*. Therefore this propagation can be described by a 2x2 matrix, and the voltages measured by each antenna, or station are also linear with respect to $\mathbf{e}$.

$$\mathbf{v} = \mathbf{J}\mathbf{e} \tag{2.14}$$

[2] See G.B. Taylor [1999], Chapter 32, and Smirnov [2011a,d,b,c] for a detailed introduction. The simple derivation I give here is based on the lectures by Oleg Smirnov & Jan Noordam at MCCT SKADS 2009

Returning to the simplest two element interferometer, antennas/stations p and q measure voltages described by

$$\mathbf{v}_p = \mathbf{J}_p\mathbf{e} \tag{2.15}$$

$$\mathbf{v}_q = \mathbf{J}_q\mathbf{e} \tag{2.16}$$

The interferometer measures the cross correlations between the two voltages.

$$v_{xx} = \langle v_{px}v_{qx}^* \rangle \tag{2.17}$$

$$v_{xy} = \langle v_{px}v_{qy}^* \rangle \tag{2.18}$$

$$v_{yx} = \langle v_{py}v_{qx}^* \rangle \tag{2.19}$$

$$v_{yy} = \langle v_{py}v_{qy}^* \rangle \tag{2.20}$$

Writing these as a matrix product

$$\mathbf{V}_{pq} = \left\langle \begin{pmatrix} v_{px} \\ v_{py} \end{pmatrix} (v_{qx}^* v_{qy}^*) \right\rangle = \begin{pmatrix} v_{xx} & v_{xy} \\ v_{yx} & v_{yy} \end{pmatrix} \tag{2.21}$$

This is known as the *visibility* matrix. Substituting in the expressions above

$$\mathbf{V}_{pq} = \langle (\mathbf{J}_p\mathbf{e})(\mathbf{J}_q\mathbf{e})^T \rangle = \langle \mathbf{J}_p(\mathbf{e}\mathbf{e}^T)\mathbf{J}_q^T \rangle = \mathbf{J}_p\langle \mathbf{e}\mathbf{e}^T \rangle \mathbf{J}_q^T \tag{2.22}$$

The inner quantity is known as the source coherency, or source brightness, and can be written in the more familiar terms of the Stokes parameters as

$$\mathbf{B} = \langle \mathbf{e}\mathbf{e}^T \rangle = 0.5 \begin{pmatrix} I+Q & U \pm iV \\ U \pm iV & I-Q \end{pmatrix} \tag{2.23}$$

Finally we can write

$$\mathbf{V}_{pq} = \mathbf{J}_p\mathbf{B}\mathbf{J}_q^T \tag{2.24}$$

which is the measurement equation. The **J**s are known as Jones matrices, and they are a product of individual Jones terms, describing the full signal path. The order of the **J**s is important, it follows the physical order of effects in the signal path, reading right to left in the equation. Note, in what follows, Jan Noordam's latex file of Measurement Equation notation is used in describing the individual terms[3] [Noordam, 1996].

The majority of physical effects on the signal path have a simple Jones matrix representation, for example a Faraday Rotation term would appear as

$$\mathbf{F} = (RM/\nu^2) \begin{pmatrix} cos\theta & -sin\theta \\ sin\theta & cos\theta \end{pmatrix} \tag{2.25}$$

[3] available online at `http://www.astron.nl/~noordam/`.

The generic Jones terms can be listed as

$$\mathsf{J_i} \;=\; \mathsf{G_i}\;[\mathsf{H_i}]\;[\mathsf{Y_i}]\;\mathsf{B_i}\;\mathsf{K_i}\;\mathsf{T_i}\;\mathsf{F_i} \;=\; \mathsf{G_i}\;[\mathsf{H_i}]\;[\mathsf{Y_i}]\;(\mathsf{D_i}\;\mathsf{E_i}\;\mathsf{P_i})\;\mathsf{K_i}\;\mathsf{T_i}\;\mathsf{F_i} \tag{2.26}$$

in which

$\mathsf{F_i}(\vec{\rho},\vec{r_i})$	ionospheric Faraday rotation - the polarisation plane of the wave is rotated after passing through ionosphere.
$\mathsf{T_i}(\vec{\rho},\vec{r_i})$	atmospheric complex gain - refraction/exinction by atmosphere.
$\mathsf{K_i}(\vec{\rho}.\vec{r_i})$	factored Fourier Transform kernel - needed for modelling a tied array.
$\mathsf{P_i}$	projected receptor orientation(s) w.r.t. the sky, or parallactic angle term
$\mathsf{E_i}(\vec{\rho})$	voltage primary beam
$\mathsf{D_i}$	position-independent receptor cross-leakage - how much radiation is picked up by one receptor that should be picked up by the other.
$[\mathsf{Y_i}]$	commutation of IF-channels
$[\mathsf{H_i}]$	hybrid (conversion to circular polarisation coordinates)
$\mathsf{G_i}$	electronic complex gain (feed-based contributions only)

Matrices between brackets ([ ]) are not present in all systems. $\mathsf{B_i}$ is the 'Total Voltage Pattern' of an arbitrary feed, which is usually split up into three sub-matrices: $\mathsf{D_i}\;\mathsf{E_i}\;\mathsf{P_i}$. Jones matrices that model 'image-plane' effects depend on the source position (direction) $\vec{\rho}$. Some also depend on the antenna position $\vec{r_i}$, and most on time and frequency as well.

In general, these matrices do not commute, so the order is key. This is an important point, as in many of the older packages, several effects are often grouped together, when they do not necessarily commute.

For example parallactic angle and ionospheric Faraday rotation come after primary beam, as they do not commute with the primary beam matrix, yet the Faraday rotation matrix is often combined with the reciever gain term. This is also the case for tropospheric effects, which are also often included as part of the receiver gain term. Conversely, grouping several effects together can give substantial gains in computational efficiency. This leads to the obvious question, why does existing calibration apparently work so well?

The answer lies in the fact that several of these effects can be approximated by matrices that do commute with some others whilst in the wrong order. These approximations are good enough for existing arrays, but will not in general apply to newer ones.

Taking the ionosphere as an example, often Faraday rotation and atmospheric complex gain are included as part of the receiver gain. This is an acceptable approximation for most existing arrays where the ionosphere TEC (total electron content) does not change noticeably over the primary beam (field of view of antenna), and there is no appreciable cross-leakage. This however will be a significant effect for new dipole arrays (see Figure 2.2) as the field of view of each dipole is so large as to see a changing ionosphere across the field of view.

This seems very intuitive, so why has the full measurement equation not been implemented until now? Most older existing packages use some implicit, specific to the instrument, form of the measurement equation, and work well for current, well understood instruments such as

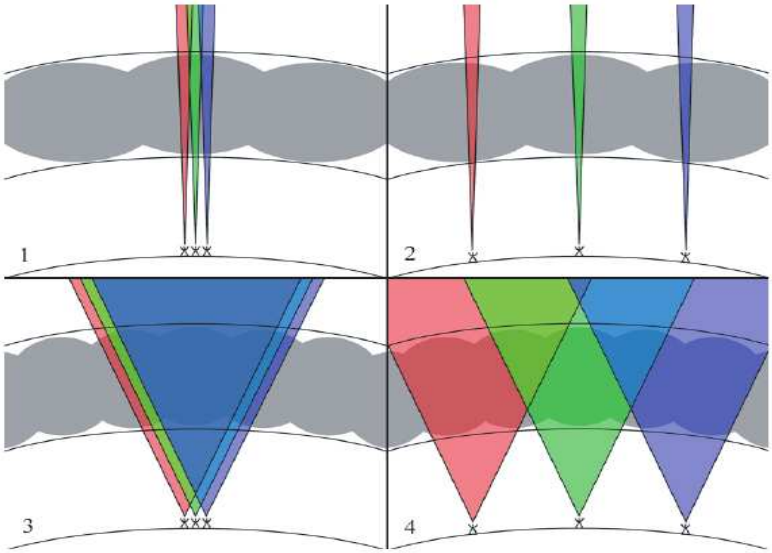

Figure 2.2: Effect of the Ionospheric TEC on Different Arrays. Panels one and two show array elements with narrow fields of view - each element will see an approximately constant TEC. In panels three and four, the wide field of view of the elements imply that each element will see a changing TEC across the field of view. For the compact array illustrated in panels one and three, the variation in the ionospheric TEC for a particular viewing direction in the field of view will be a gradient, however for the extended arrays in two and four, this will not be the case. For panels one and two, traditional self calibration is sufficient to correct the ionospheric effects. However in panels three and four, the ionosphere changes with both time and viewing direction, and more advanced calibration methods are required, such as SPAM, [Intema *et al.*, 2009]. Figure reproduced from Intema *et al.* [2009].

the (E)VLA and WSRT. However even the most widely used packages such as AIPS are no longer being actively developed, and are difficult to modify. Re-writing AIPS is not practical (or indeed necessary for existing instrument data analysis). In the context of this work, the new GMRT radio data that is presented later in this Chapter is reduced in AIPS, but the LOFAR data presented in Chapter 7 requires a Measurement Equation based approach. For the next generation of radio telescopes, the Measurement Equation is not just an elegant formalism, but a requirement, to enable good calibration of polarisation and ionospheric effects.

2.2 The CENSORS Radio Galaxy Sample

The CENSORS sample [Best *et al.*, 2003], is a set of 154 radio sources, defined from combining data from the ESO Imaging Survey Patch D, a 3x2 degree area of sky centred at 09 51 36.0, -21 00 00 (J2000), with the NRAO VLA Sky Survey (NVSS, Condon *et al.* [1998]) at 1.4GHz. There are 135 sources in total forming a complete sample with all sources having a flux at 1.4 GHz greater or equal to 7.2 mJy. The investigation of radio sources with matched counterparts at many other wavelengths and at different flux density levels provide key statistics on the evolution of physical properties of the radio sources with cosmic time. The central aim of the

CENSORS project was to ascertain the high redshift evolution of the radio luminosity function, along with studying dual-population unification schemes for radio sources, and investigating the radio power dependence of the K-z relation for radio galaxies.

The infra-red and spectroscopic follow-up of the CENSORS sample, along with its subsequent use in modelling studies of the high redshift radio luminosity function, constituted the PhD thesis of Mairi Brookes [Brookes, 2005]. The CENSORS survey forms one of the key components in initial modelling work of the radio luminosity function carried out by Brookes *et al.* [2008], and more recently substantially extended by Rigby *et al.* [2011]. However the CENSORS sample lacks information at other, lower radio frequencies, which would allow more detailed imaging of the extended radio sources and accurate spectral index and spectral curvature measurements to be made. These spectral index measurements are an essential ingredient for any radio samples being utilised in RLF modelling studies, as they prevent systematic errors in k-correcting the radio luminosities of the sources. In modelling the radio luminosity function with the CENSORS sample, Brookes et al made the assumption that the sample had an average spectral index $\alpha\sim$-0.7, and applied k-corrections accordingly. This is a standard method when only one radio frequency is available, however many more recent studies looking at spectral indices of individual sources in various radio samples have shown that there is often considerable scatter about this mean value [see for example Garn *et al.*, 2008]. This implies that some sources may be k-corrected to under the flux density limit required for the modelling, which can be very important towards the most uncertain, high redshift end of the RLF.

To address this, the CENSORS sample was observed at the VLA and GMRT at 325MHz and 610MHz respectively in 2004, with observation strategies designed specifically to provide a resolution comparable to that of the NVSS at 1.4GHz, in addition to higher resolution reductions at 610MHz. In addition to providing spectral indices and spectral curvature measurements, the high resolution 610MHz may also give additional information on several sources with ambiguous radio data, and identify for example, radio cores/lobes of multiple sources.

2.3 GMRT 610MHz

The Giant Metrewave Radio Telescope, or GMRT is currently the world's largest low frequency antenna array, operated by the Tata Institute of Fundamental Research, located in Pune, India. It consists of thirty 45m diameter wire mesh antennas in a curved Y shaped configuration and has a frequency range of 150MHz to 1.4GHz.

The CENSORS sample was observed at 610MHz in 18 pointings by the GMRT, over two nights in April 2004. The observational set up of the GMRT for these observations can be seen in Table 2.1. The 18 pointings were observed in a hexagonal pattern, typically separated by 0.5 degrees. The 18 pointings were grouped as four batches, with batch A including pointings 1 to 5, B 6-9, C 10-14 and D 15-18. Batches A and B were observed on the 23rd April, and C and D on the 24th April 2004. There were two circular polarisations and two IFs for every group except A, which contained only one IF due to a corrupted data file at the end of the data tape.

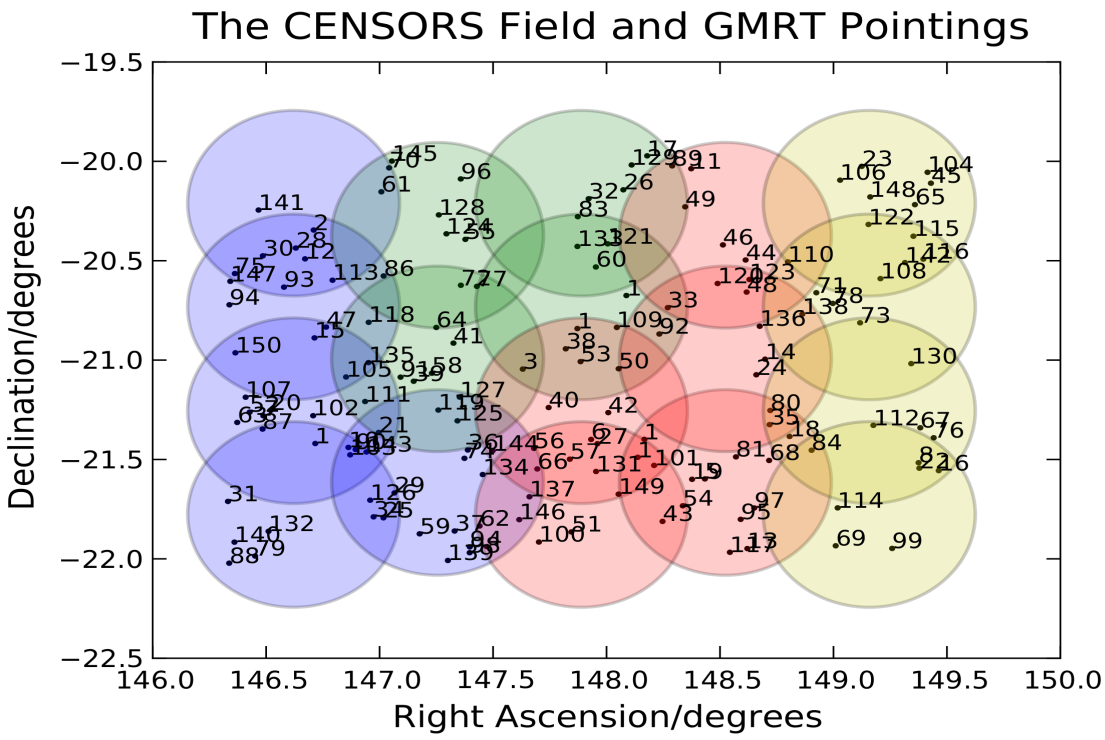

Figure 2.3: The distribution of the CENSORS sample on the sky. The GMRT pointings are indicated by the circles (1 degree in diameter, out to where the primary beam correction falls to 20% of its central value), with blue circles denoting group A observed on the first half of Night 1, green circles group B on the 2nd half of Night 1, red circles group C on the first half of Night 2, and finally yellow circles for group D on the latter half of Night 2.

The two IFs, upper side band (USB) and lower sideband (LSB), were centred on 602MHz and 618MHz respectively, each having a bandwidth of 16MHz, split into 128 spectral channels of 125kHz each. The integration time was 8s, less than the standard 16s, to avoid time smearing effects. The observing strategy was to observe each batch in a sequence of three pointings (each pointing observed for ten minutes for batches A,B,D and for nine minutes for C), the phase calibrator, three CENSORS pointings, then phase calibrator, until each CENSORS pointing had been observed three times. This observing pattern maximises uv coverage by maximising the time between observations of the same pointing, within the allotted time. A flux calibrator

was imaged once per half night.

Primary flux calibrators must be non-variable and are usually unresolved with a very well known flux to provide an accurate amplitude calibration, and 3C147 and 3C286 were used for this purpose. 0837-198 and 1154-350 were used as secondary phase calibrators, as they have very accurately known positions, are compact, bright and relatively close to the target pointings to minimise atmospheric phase errors. The 610MHz GMRT data were fully calibrated and imaged using AIPS [Greison, 2007], the Astronomical Image Processing System developed and maintained by NRAO, and I give a brief summary of the reduction process as follows [4].

Processing of the raw uv data consisted of essentially six stages. Firstly the visibilities must first be 'flagged', manual removal of man-made interference, and then the data calibrated, using observations of sources whose fluxes are already well determined. The resulting flagged and calibrated visibilities are then imaged, by performing an inverse Fourier transform of the visibilities. This produces a 'dirty' image. The 'dirty beam' is then deconvolved from the image via application of the CLEAN algorithm and the technique of self-calibration applied to improve the dynamic range of the obtained images. These steps are described in more detail below.

Table 2.1: GMRT and VLA Observation parameters for the CENSORS Sample.

Telescope	Frequency	Obs Time	Bandwidth	Primary Beam	Synthesised Beam
GMRT	610MHz	30min	16MHz	0.73deg	6"
VLA BnA	325MHz	2.6hr	12.5MHz	2.5deg	12"
VLA CnB	325MHz	5.2hr	12.5MHz	2.5deg	60"

The raw UV files were read from magnetic tape, and the two sidebands from each batch (excepting batch A, with one sideband) were loaded into AIPS uncompressed with FITLD [5], and indexed using INDXR. AIPS stores any reduction carried out as a series of tables associated with the uv datafile: this ensures that that any editing/calibration can be undone, and the original data file remains unaltered. An error in the frequency tables, most prevalent in datasets taken before 2006, where the keyword 'SIDE BAND' appeared instead of 'SIDEBAND' was corrected by editing the associated frequency tables of each sideband. The values of SIDEBAND, -1 for LSB, and 1 for USB were also checked and edited as necessary. Each pair of sidebands, USB and LSB were joined together using VBGLU, a task originally intended for joining differing IFs from VLBI datasets, but which works equally as well here. Batches C and D, each having two IFs and observed on the same night were joined using DBCON and indexed. This gave three files, one containing batch A, one with batch B and one with batches C and D. Each was reduced in a similar manner as follows. SETJY was run on the primary flux calibrator sources, which were either 3C147, 3C286 or both. SETJY calculates the expected flux density of these calibrators from formulae given by Baars *et al.* [1977] and extended to low frequency by Perley & Taylor (the 1999.2 VLA flux scale) and enters the values in the SU table.

[4] The reduction process broadly followed the recipes in Appendix A of Ibar [2008] and also utilised a combination of suggested procedures from GMRT 610MHz reduction notes kindly provided by Edo Ibar and Rob Ivison, and "The VLA Low Frequency Reduction Tutorial [Lazio *et al.*, 2005], available online at `http://lwa.nrl.navy.mil/tutorial/`

[5] I denote AIPS tasks in capitals.

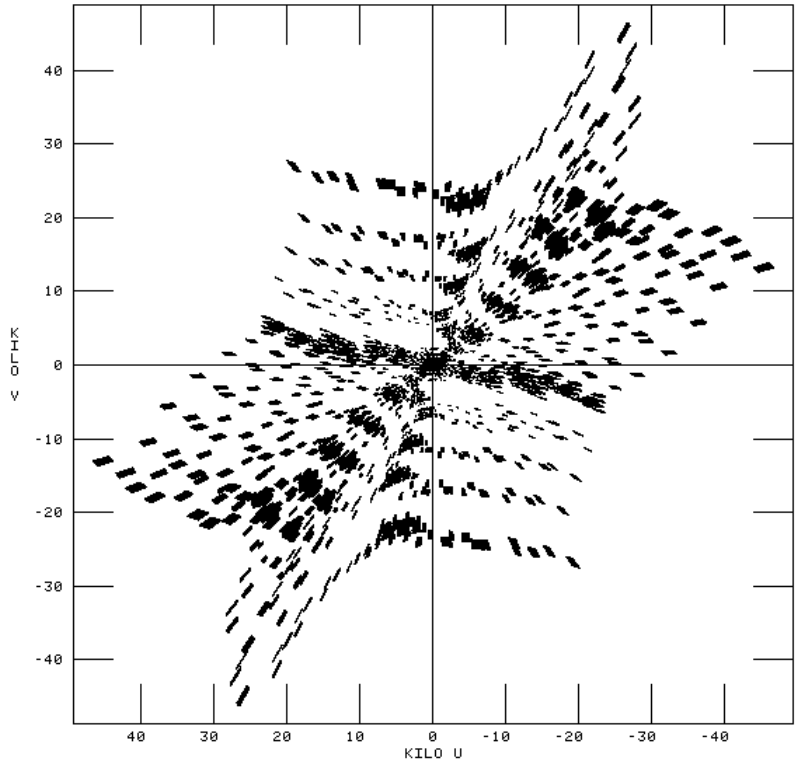

Figure 2.4: Figure illustrating the uv coverage of one pointing (pointing 7) of the GMRT CENSORS observations.

2.3.1 RFI Excision and Calibration

By far the most time consuming aspect of interferometric data reduction is identification of RFI (radio frequency interference), in the dataset, or 'flagging'. This manifests itself as anomalously high data points/patterns caused by local man-made sources, and at the time of reduction, there were no automated procedures for RFI identification in radio interferometric data as good as the human eye for pattern recognition. Work in this area is progressing significantly however [see for example Athreya, 2009], and RFI removal will have to be automated for the next generation of software driven radio telescopes such as LOFAR (e.g. Offringa *et al.* [2010]).

Flagging took place using a variety of tasks such as QUACK, TVFLG, SPFLG and UVFND, and utilising plots of amplitude/phase vs time/baseline length in WIPER. Generally the first five and last three channels in every baseline had to be flagged. Typically the RFI is worst on the shortest baselines, and several antennas were offline, the worst case being during the batch C observations where five antennas were down. All flagging commands, which are used by AIPS in later tasks to define data to be ignored, were stored in an FG table attached to

the dataset, and a copy of each final flag table for each uv data file exported out of AIPS, so that the reduction process is easily repeatable. The GMRT observations consist of a maximum of 465 antenna pairs, or baselines, each with two IFs and two polarisations of 128 channels, implying a large amount of data is available, and that a sizable amount of data can safely be flagged without affecting the final data quality.

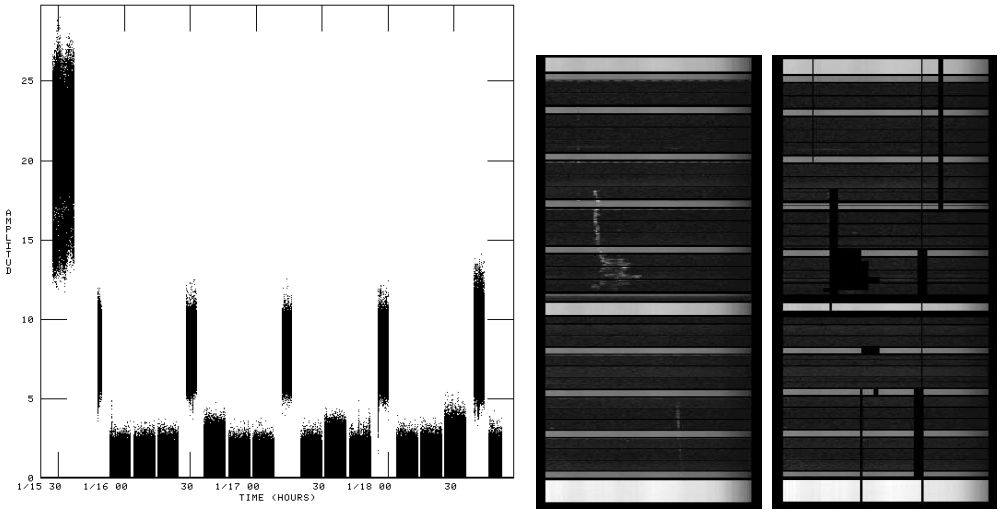

Figure 2.5: a) This figure plots the amplitude versus time of the observations of one half night (batch B) in IF1, LL polarisation, after calibration. b) An illustration of the RFI which must be removed from the 610MHz data before calibration can take place. The figure shows a single baseline one IF (1) and one polarisation (RR), to the left unflagged, and to the right with flagging applied. It also nicely illustrates the sequence of observations in a batch, from the bottom, the primary flux calibrator, followed by interspersed secondary phase calibrator and CENSORS observations and another flux calibrator at the end.

The task BPASS was then run on the primary flux calibrators to correct for antenna gains as a function of channel (frequency), calculated with respect to a reference composed of only a few RFI free channels, in order to avoid phase discontinuities. The bandpass solutions, amplitude and phase, were plotted as a function of channel for each antenna using POSSM, and examined for further RFI. One or two spikes were present, so the BP table was deleted, the spikes were then removed using SPFLG and BPASS rerun. An iterative process of running BPASS and flagging then took place until relatively smooth bandpasses appeared in POSSM. An initial calibration of the data was then carried out using CALIB in amplitude and phase solution mode on the primary calibrators, and then the secondary calibrators, with flagging and the bandpass correction applied. The number of good solutions should be greater than 95%, and gains over each IF/polarisation should be close to one. The solutions were plotted in SNPLT to isolate antennas/timeranges with high gains, and further flagging took place, again in an iterative manner, until the calibration was consistent with the requirements described.

The secondary calibrator fluxes were then entered in the SU table using GETJY, which bootstraps the secondary calibrator fluxes from the calibrated primary calibrator fluxes.

CLCAL was used to interpolate the calibration solutions to the target pointings, and the CL table was again checked visually using SNPLT.

FLGIT is an AIPS task which allows automatic flagging of discrepant data, via amplitude and multiples of the rms limits. However, in order to work, it requires a batch of as RFI-free-as-possible channels from which to make a model, so by definition initial flagging by hand needs to take place first. It is particularly useful for flagging low level RFI missed in the previous flagging sessions by hand, and some experimentation took place with the various parameters to determine the best parameters, aiming for approximately 15-30% of the data to be flagged (as found in previous work, see e.g. Lazio *et al.* [2005]). A small bug was discovered in that running both IFs through FLGIT at once resulted in almost all of one IF being flagged. It is assumed that some small offset between the calibrated amplitudes in each IF is responsible for this, although there is nothing obvious visually when plotting the amplitudes. However passing each IF separately through FLGIT gave between 18-25% data flagged for each data set. The two IFs were then glued back together and indexed using VBGLU and INDXR.

A second iteration of the tasks BPASS and CALIB was then performed on the output by FLGIT; see Figure 2.5 for an example of the calibrated amplitudes obtained for one half night's observations. The second calibration utilised a slightly longer method, running a phase only calibration, one minute intervals on the calibrators, interpolating the solutions to the targets using CLCAL, and then running a final amplitude and phase calibration, with the previous phase only calibration applied. The first phase only calibration allows correction of atmospheric distortions, which occur over timescales of minutes, and produced a marked improvement in the variation of the phases of the calibrator sources. CLCAL was run for a final time, and the CL table created applied in SPLIT, when separating each individual calibrator/pointing into a separate file, ready for imaging. Every four channels of the 128 were averaged in SPLIT, as this can significantly decrease the later imaging process time. It is however important not to average too many channels at this stage as this can introduce bandwidth smearing effects to the images (see later section on imaging quality).

Imaging and Self-Calibration

Radio interferometric observing requires a polyhedron approach to wide field imaging as it produces non-coplanar aberrations. This requires splitting the primary beam into many facets, and was completed using SETFC. The uv visibilities were imaged using the IMAGR, with application of several thousand iterations of the Clark CLEAN algorithm to deconvolve the sampling function, or 'dirty beam' from the observed brightness distribution (the 'dirty map' obtained by a fourier inversion of the visibilities). Self-calibration of the data was then performed, whereby the initial CLEAN'd maps are used as a model for the true brightness distribution, and the data calibrated to this. Four cycles of self-calibration were then performed, three in phase, with solution intervals 10, 3 and 1 minutes, then followed by one cycle of amplitude and phase calibration.

There is a somewhat controversial issue in deciding the number of clean components to use for the self-calibration model. Traditional self calibration methods, and indeed most beginners

guides to data reduction with AIPS[6] advise using only the clean components up to the first negative, and I applied this method in the imaging process. However the opposing argument is that we want the very best, scientifically robust model for the data; which includes all components, this is applied in recent very deep GMRT surveys [see for example Garn, 2008; Ibar, 2008]. The current AIPS documentation itself is contradictory on this matter, with the IMAGR help file advising the use of all clean components, describing the practice of truncating the model at the first negative as having 'little if any scientific validity'. The 2007 AIPS Cookbook section 5.4.3 on Self-Calibration however, states 'When calibrating Stokes I images, do not set NCOMP in CALIB so high that any negative Clean components are included'. The difficulty lies in separating the negative components which are truly representative of the distribution, for example, a source lying exactly between two cells is precisely represented by an infinite series of positive and negative clean components, and those negative components arising from bad calibration solutions, which the self-calibration process is trying to remove. If these are included, the bad calibration solutions will be enmeshed in the model, possibly giving rise to artifacts in the final images. It is also worth pointing out that the true model will be composed of an infinite number of clean components, and must necessarily be truncated somewhere.

G.B. Taylor [1999] address this problem of how many clean components are sufficient for an acceptable model in chapter 13, by generating a 12 hour VLA observation of a 1Jy source, and applying self calibration with varying numbers of components with various cell sizes. They find that maximum amplitude errors are reduced by two methods. (i) use both positive and negative components, or (ii) over sample the beam by at least a factor of two (i.e, at least five points per beam). Of these the latter seems to return better solutions.

There is a sufficient enough divide in the literature to make this worth investigating. I selected one of the pointings, pointing 10 as an example, and redid exactly the same self-calibration process, this time including all clean components in the model. In general the obtained dynamic range and average r.m.s noise on each facet was worse in the images produced from models containing all clean components.

The best compromise would be to access each model individually, and cut off the clean components used when substantial numbers of negative components appear in succession, and/or the flux values are close to the noise levels. However this was not practical for the GMRT pointings where each one can contain up to fifty facets, and so the method of only including clean components up the first negative in the self calibration models was adhered to.

2.3.2 Imaging Quality

Having taken the raw visibilities through the above reduction process, it is necessary to assess the quality of the resultant images. As a first initial check, the calibrator sources were imaged as above, and the fluxes and positions checked. All were found to be as listed in the VLA calibrator

[6]See for example, the lecture on Self-Calibration in the 2008 NRAO Synthesis Imaging school, available at `http://www.aoc.nrao.edu/events/synthesis/2008/lectures/claussen.final.pdf`, or An introductory AIPS guide by Hans Klockner at the University of Oxford available at `http://www-astro.physics.ox.ac.uk/~hrk/AIPS_TUTORIAL/HRK_AIPS_1.html`

manual, and there were no artifacts in the images suggestive of calibration errors/missed RFI, implying that the applied calibration was good.

Bandwidth Smearing

A problem which can potentially degrade the image quality significantly is that of bandwidth smearing. This arises because the theory of synthesis imaging (see Chapter 3) is only strictly true for monochromatic radiation. If radiation of some finite bandwidth is analysed as monochromatic radiation, aberration effects in the image will result, whereby sources towards the edge of the beam will be more 'smeared out'. This leads to a reduction in both resolution and sensitivity. When the product given by;

$$(\frac{\delta\nu}{\nu}) * (N) \sim 1 \tag{2.27}$$

reaches 1, where $\delta\nu$ is the channel size, ν is the total bandwidth and N is the number of beams from the image centre, then bandwidth smearing effects become significant. Bandwidth smearing can be lowered to an acceptable level by splitting the observing bandwidth into many channels, and taking into account the above relation when doing any subsequent averaging of the channels. For the GMRT observations, 128 channels over the 16MHz bandwidth were observed. These were averaged in blocks of 4 channels during calibration, to speed up the processing time, but not introduce any significant bandwidth smearing effects, as per the above relation. The 325 MHz VLA observations were planned similarly to mitigate the effects of bandwidth smearing by observing 16 channels over the bandwidth, and no averaging of these channels prior to the imaging step took place.

Sensitivity

Given the instrument parameters such as system temperature and antenna gain, it is possible to calculate the expected thermal rms noise level for a particular observation. For the GMRT this is;

$$\sigma = \frac{\sqrt{2}T_s}{G\sqrt{n(n-1) \quad N_{IF} \quad \delta\nu \quad \tau}} \tag{2.28}$$

where T_s ~92K is the system temperature, G=0.32K Jy^{-1} is the antenna gain, n is the number of working antennas, which varied from 26 to 28 in the observations, N_{IF} =2 is the number of sidebands, $\delta\nu$ =13.75MHz is the frequency bandwidth of each of the sidebands and τ is the integration time of each pointing. This gives an expected rms noise of ~1x10^{-4}Jy $beam^{-1}$. Several pointings had an rms of approximately this level before primary beam correction, but some were as much as 2-3 times higher. Five of the pointings have a higher rms as they have only one sideband, however why some of the other pointings have a slightly higher rms than predicted is not immediately obvious. Checking a very wide field image of each of the high rms pointings shows no bright sources which have been missed in the cleaning, and the images themselves look very good, with no obvious artifacts.

2.3.3 High and Low Resolution Maps

A balance exists in interferometric imaging between the highest resolution, and the highest signal to noise achievable. Various weighting options of the visibilities need to be considered to achieve one or the other, or the optimal balance of both depending on the science desired. Both GMRT and VLA datasets generally consist of a range of baseline lengths, with a larger concentration of shorter baselines, due to the central cluster of antennas.

Most current imaging software, eg. AIPS, MIRIAD, contain options for two different ways of weighting the visibilities; see Chapter 7 on imaging in G.B. Taylor [1999]. The first is the weighting function. For the high resolution map, the aim is to achieve the very best possible resolution, whilst also maximising signal to noise. This is done by setting the ROBUST parameter to 0 in IMAGR, which achieves an optimal compromise between uniform and natural weighting. The central baselines with (u,v) $< 1.5\text{k}\lambda$ are also excluded, as the GMRT has a central cluster of antennas, 14 in one square kilometer, giving rise to many short baselines which dominate the uv coverage, and affect the restoring beam shape, worsening the resolution. RFI also tended to be most prevalent in these baselines, increasing the rms noise on the images when they were included in the imaging process. The highest resolution maps had a restoring beam of approximately 6 arcsec.

The GMRT data were first imaged at high resolution, firstly to provide the very best amplitude and phase self calibration, and secondly to investigate whether these new radio observations could give any new information on several CENSORS sources which lack infrared identifications/or have existing radio observations which are ambiguous.

Low resolution maps were then made, matched to the resolution of the NVSS by including all short baselines, using fully natural weighting, and adjusting the **uvtaper** and **uvrange** parameters for each pointing, until a restoring beam close to 45"x45" was obtained. The **bmaj** and **bmin** parameters were then set to 45, to deconvolve with a perfect 45" beam.

The GMRT observations were imaged out to where the primary beam correction fell to 10% of its central value, as recommended by the GMRT. Source extraction and flux density measurement was completed using the AIPS tasks JMFIT and TVSTAT (in the case of extended sources), and during this process it was discovered that a primary beam offset error was present in the data. The fluxes of sources measured with JMFIT gave different values dependent on the pointing measured in. In other words, the same source measured in two different pointings generally had a significant difference in measured flux, and these measured flux differences were strongly related to the distance of the source from the pointing centre (see Figure 2.7). This is a relatively recently discovered problem with the GMRT, first reported by Garn *et al.* [2007]. The presence of this varying primary beam offset is a possible cause of the higher than expected background rms.

2.3.4 Primary Beam Pointing Errors

A primary beam offset, where the telescope is actually pointing in a slightly different position to that reported by the software, is a well known problem at the GMRT. Most antennas at

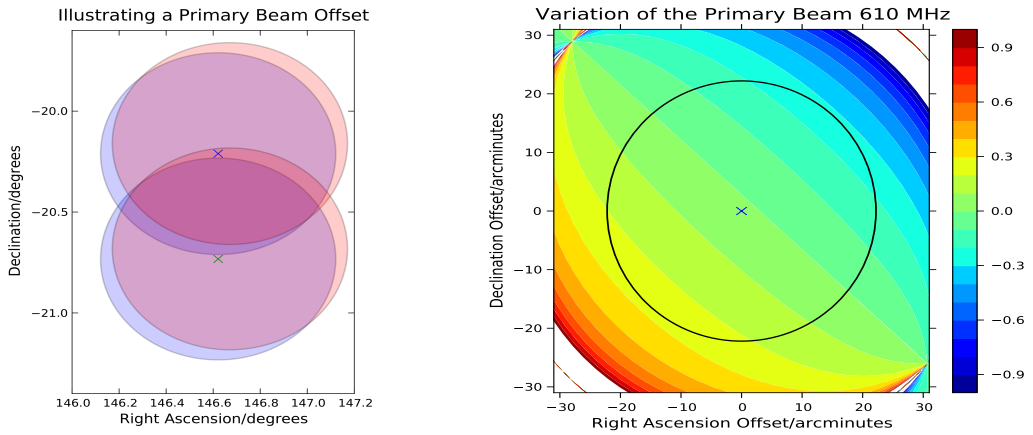

Figure 2.6: Illustrating the effect of a Primary Beam Offset. The left figure shows two pointings of an observation in blue, and where the telescope has truly been pointing in red, for an offset of 3 arcminutes in both RA and DEC. The figure on the right shows the subsequent fractional error in the Primary Beam correction (defined as the ((true correction - measured correction)/true correction)) for a pointing with this offset. The black circle indicates where the primary beam response falls to 50% of its central value.

the GMRT show a systematic variation of 3-4 arcminutes from rise to transit to set. Garn *et al.* [2007], and the Primary Beam Modelling team[7] at the GMRT [Kantharia, 2005] have shown this can be larger, with variations of 4-6 arcminutes in many antennas. Most recently an investigation by de Gasperin *et al.* [2011] show that pointing errors in individual antennas are present in at least eight of the antennae investigated, and some of these can be of order 5-10'. They emphasize the need for further investigation of this issue, given these offsets are much larger than the expected values for the instrument. Figure 2.6 illustrates the effect of a primary beam offset of 3 arcminutes in both RA and DEC for a 610 MHz pointing. The presence of a pointing offset is more problematic at higher frequencies, due to the smaller area covered by the primary beam, and increased resolution (cf. Figure 2.8).

The problem is as follows; normally, each measured flux is corrected for the beamshape by dividing each pixel by a Primary Beam correction factor. In the case of the GMRT at 610MHz, this is;

$$F(x) = 1 + (\frac{a}{10^3})x^2 + (\frac{b}{10^7})x^4 + (\frac{c}{10^{10}})x^6 + (\frac{d}{10^{13}})x^8 \tag{2.29}$$

where a,b,c and d are constants, and x is defined as the separation between the source position and pointing centre in arcminutes, multiplied by the frequency in GHz, 0.61 in the case of these observations[8].

$$a = -3.486 \tag{2.30}$$

$$b = 47.749 \tag{2.31}$$

$$c = -35.203 \tag{2.32}$$

[7] `http://ncra.tifr.res.in/~ngk/`

[8] This is true for all but group A. In group A, only one IF is available as the other was corrupted on disk. Hence the frequency for group A is 0.618

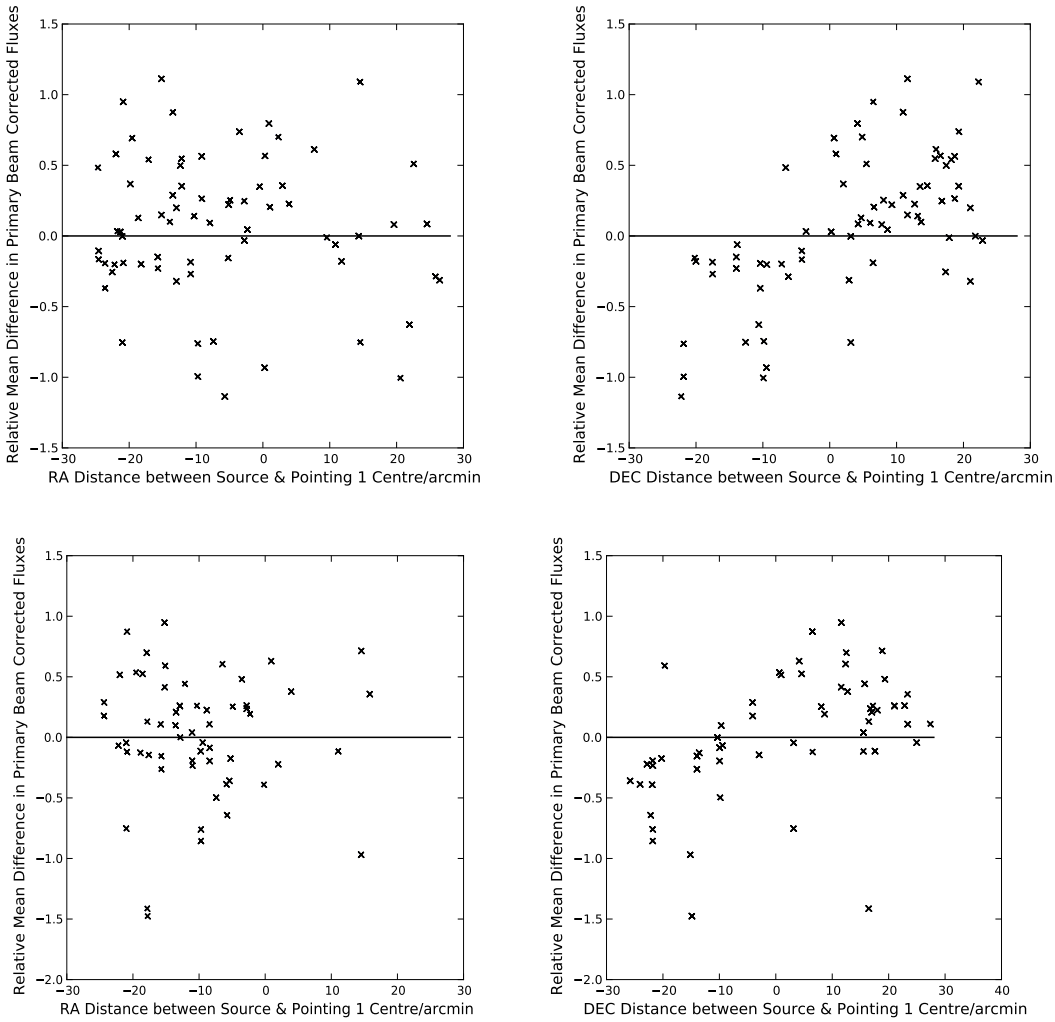

Figure 2.7: The difference in peak primary beam corrected fluxes measured in two different pointings, as a function of the difference in Right Ascension and Declination of the source from the pointing centre. The top figures show this for the low resolution catalogue, and the bottom for the high resolution catalogue. The Relative Mean Difference (RMD) is calculated as $(S_1\text{-}S_2)/0.5(S_1+S_2)$ where S_1 and S_2 are the fluxes of each source measured in the first pointing and second pointing that they are detected in respectively.

$$d = 10.399 \tag{2.33}$$

$$x = 0.61\sqrt{((\alpha_C - \alpha_S)cos(\delta_C))^2 + (\delta_C - \delta_S)^2} \tag{2.34}$$

Define I as the measured flux in one pointing, NOT corrected for primary beam. This value is constant, regardless of where the pointing centre is assumed to be for the subsequent primary beam correction. Therefore we can write

$$I_{PBT} = \frac{I}{F(x_T)} \tag{2.35}$$

$$I_{PBM} = \frac{I}{F(x_M)} \tag{2.36}$$

where I_{PBT} and $\mathrm{F}(x_T)$ are the true flux and primary beam correction, and I_{PBM} and $\mathrm{F}(x_M)$ are the measured flux and primary beam correction with a primary beam offset present. Equating the two gives

$$I_{PBT} = I_{PBM}\frac{F(x_M)}{F(x_T)} \tag{2.37}$$

If one source is measured in two pointings, ideally after primary beam correction, the difference between the two measurements should be close to zero.

$$I_{PBT1} - I_{PBT2} = 0 \tag{2.38}$$

This leads to

$$I_{PBM1}\frac{F(x_{M1})}{F(x_{T1})} - I_{PBM2}\frac{F(x_{M2})}{F(x_{T2})} = 0 \tag{2.39}$$

$$\frac{I_{PBM2}}{I_{PBM1}} = \frac{F(x_{M1})}{F(x_{T1})}\frac{F(x_{T2})}{F(x_{M2})} \tag{2.40}$$

$\mathrm{F}(\mathrm{x}_M)$ is defined in equations 2.29 and 2.30 above, and

$$F(x_T) = 1 + (\frac{a}{10^3})x_T^2 + (\frac{b}{10^7})x_T^4 + (\frac{c}{10^{10}})x_T^6 + (\frac{d}{10^{13}})x_T^8 \tag{2.41}$$

and

$$x_T = 0.61\sqrt{((\alpha_C - \alpha_S - o\alpha)cos(\delta_C - o\delta))^2 + (\delta_C - \delta_S - o\delta)^2} \tag{2.42}$$

where $o\alpha$ and $o\delta$ are the primary beam offsets present in the observation. This assumes that the true primary beam centre is equal to the measured pointing centre minus some unknown offset in RA and/or DEC. Equation 2.40 can now be solved via a least squares method.

It should be clearly emphasised, however, that the offsets obtained from the least squares fitting will be an average of all the antenna movements over a period of six hours, so are an approximate correction at best.

A catalogue of peak fluxes of CENSORS sources detected in more than one pointing was compiled for both the high and low resolution 610MHz data, and a non linear least squares

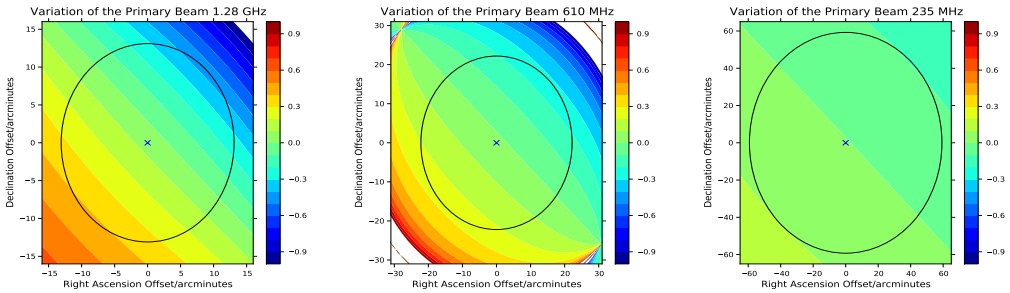

Figure 2.8: The figures here show the subsequent error in the Primary Beam correction (defined as the (true correction - measured correction)/true correction) for a pointing with a 3 arcminute primary beam offset in both RA and DEC, at three different frequencies. In each figure the black circle indicates where the primary beam response falls to 50% of its central value. The effect of an offset being present is most severe at the highest frequencies, and is almost negligible at low $\leq$235 MHz frequencies.

Table 2.2: The Final Calculated Primary Beam Offsets. The Relative Mean Difference (RMD) is calculated as $(S_1\text{-}S_2)/0.5(S_1+S_2)$ where S_1 and S_2 are the fluxes of each source measured in the first pointing and second pointing that they are detected in respectively.

Cat	Group	Offset RA	Offset DEC	No. Sources	Mean Flux RMD Before Correction	Std Dev. Flux RMD	Mean Flux RMD After Correction	Std Dev. Flux RMD
LR	A	-6.56(0.52)	3.65(0.52)	71	0.064(0.059)	0.5	-0.088	0.228
LR	B	3.32(0.7)	7.94(0.64)	71				
LR	C	-3.02(0.75)	1.30(0.49)	71				
LR	D	4.15(1.87)	5.42(0.74)	71				
HR	A	-6.58(0.6)	3.20(0.55)	59	0.0176(0.065)	0.502	-0.045	0.153
HR	B	3.75(0.79)	6.10(0.55)	59				
HR	C	0.81(2.16)	2.04(0.54)	59				
HR	D	-0.14(1.52)	3.22(0.82)	59				

minimisation was run to determine the offsets. As detailed previously, work at the GMRT has shown that these offsets vary strongly with elevation and hour angle, and the results concur with this conclusion. A least squares minimisation using custom python scripts and pyminuit[9] was run on both the low and high resolution double detection catalogue, selecting all sources with a signal to noise of at least 5 in both pointings, and at least 10 in one pointing, and a radius from the measured centre less than 30 arcminutes.

It should be noted that as a non linear model is being fitted, the reduced $\chi^2 = 1$ criterion obtained cannot be used as an indication of the goodness of fit, as the derivation of this criterion explicitly assumes linearity in all parameters. Instead, all that can be done is to search for the minimum value of χ^2 possible [Andrae *et al.*, 2010].

This procedure also allows an estimation of the error remaining in the fluxes, to be incorporated into the fitting procedure, as is detailed below. The results of the fitting may be seen in Table 2.2. The new pointing centre positions were used to calculate the corrected primary beam corrections, and improved the fluxes. For sources detected in more than one pointing, the detection closest to a pointing centre (and therefore requiring the smallest primary beam correction) was used.

[9]available at `http://code.google.com/p/pyminuit/`

As these calculated primary beam offsets are large, and with approximate errors in fitting of order 1 arcminute for all, the original, approximately Gaussian distributed flux density errors estimated by JMFIT will significantly underestimate the true uncertainty in the data, for sources at significant distances from the pointing centre, where the primary beam correction error will dominate (cf. Figure 2.6). In order to utilise these data in later radio spectra fits, some empirical method is needed to estimate these errors in flux, and any calibration error which may also be present in the data. Firstly, there is still a 1 arcmin primary beam pointing centre error present, as the GMRT documentation suggests a maximum pointing accuracy of +/-0.5', and the error in the fitted parameters was approximately 1 arcmin. For majority of sources between 10 and 20 arcmin this is roughly equal to a 5% error in flux.

Observing the relative mean difference between the source flux in two pointings, for sources lying within a 25 arcmin radius, the majority of the points lie within 0.1-0.2. Assuming that 5% of this comes from PB error decided previously, then that implies an $\sim$10% calibration error remaining. Previous studies have found fluxes measured with the GMRT generally suffer from calibration errors of order 5-10% [Garn *et al.*, 2007; Mohan *et al.*, 2001], and so this result is consistent with previous work.

A 10% calibration error and 1 arcmin primary beam centre offset error are henceforth added appropriately into the data flux errors. If the fits are then run incorporating these errors, smaller χ^2 values are obtained. The best fitting primary beam offsets are listed in Table 2.2. Note that the offsets obtained are broadly consistent between the high and low resolution catalogues, but for pointing groups C and D in particular there are less sources in the high resolution than low resolution catalogue, and hence the fits are not so well constrained. Therefore the offsets from the Low Resolution catalogue are utilised, as this contains a higher number of sources.

The correction was first applied to the two catalogues of sources in more than one pointing (high and low resolution) to verify that the derived correction did remove the correlation of gain with radius. It can be clearly seen in Figure 2.9 that corrections remove the correlation between flux difference and radius, in addition to almost halving the range of scatter, with similar results obtained for the High Resolution catalogue.

These standard deviations are broadly in line with a 10% calibration error and an additional small primary beam offset error still present (a 1' error will give an 5% additional error for most sources), verifying the approach taken above to estimating the errors. This correction was then applied to the final low resolution and high resolution integrated flux 610MHz catalogues of the CENSORS sample using a custom Python script. Note that the correction was applied using a python script to the integrated fluxes of each source, and not each individual pixel. This will be correct for the vast majority of sources, but may introduce a small error for very extended sources (of which there are only two greater than 2 arcminutes in extent in CENSORS).

2.4 VLA 325MHz

The CENSORS field was observed in two pointings with the VLA in two configurations, BnA for 10 hours, and CnB for 6 hours in September 2003 and February 2004 respectively. The

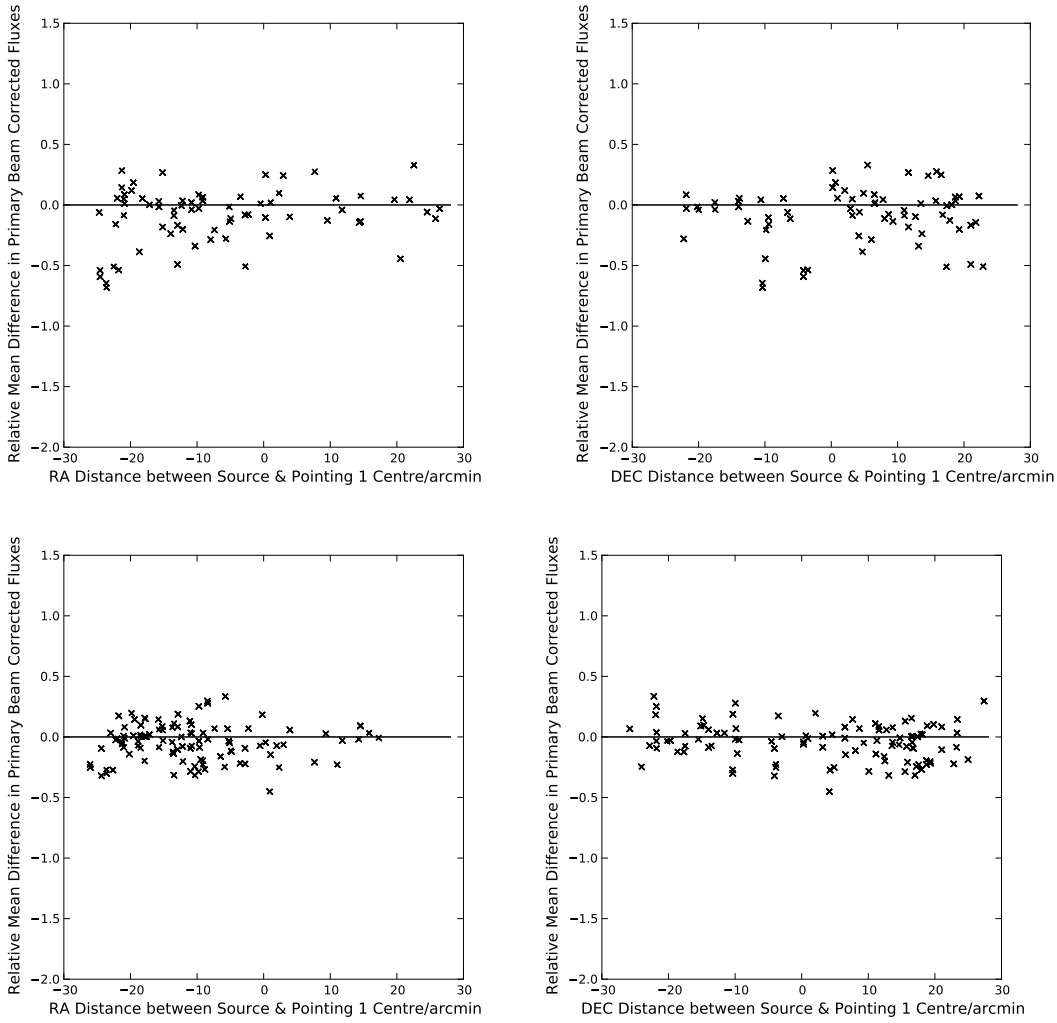

Figure 2.9: The new difference in peak primary beam corrected fluxes measured in two different pointings, with the offset correction applied, as a function of the difference in Right Ascension and Declination of the source from the pointing centre. The top figures show this for the low resolution catalogue, and the bottom for the high resolution catalogue. Again, the Relative Mean Difference (RMD) is calculated as $(S_1\text{-}S_2)/0.5(S_1+S_2)$ where S_1 and S_2 are the fluxes of each source measured in the first pointing and second pointing that they are detected in respectively, after the new primary beam correction is applied.

combination of these datasets will give a resolution comparable to that of the NVSS at 45" and a theoretical noise limit of 0.2mJy beam^{-1}.

The dataset was reduced following a similar reduction procedure in AIPS as was outlined for the 610MHz data in the previous section. The reduction was carried out in AIPS, using a method recommended for P-band observations, as given on the VLA website[10]. This broadly follows the same steps as detailed for the GMRT, albeit with slightly different tasks/appropriate parameters.

After imaging and self calibration, the resulting images from both the BnA and CnB array data had much higher than expected rms levels, of order 1mJy/beam when the theoretical noise level should be close to 0.2mJy/beam, a factor of 5 higher. After combining the BnA and CnB array data, and despite several repetitions of the reduction process, no improvement was able to be made. However as flux density measures were able to be obtained for 90% of the sample at 325MHz with a S/N greater than 5, this did not represent a large loss. It is possible that the ionosphere was particularly active during these observations, and as ionospheric scintillation scales with frequency, this is much worse for low frequency observations. It should also be noted that other authors have seen this problem with no clear explanation, e.g. Orrú *et al.* [2007].

2.5 Results

The final measured integrated fluxes for CENSORS at both 610 MHz and 325 MHz can be seen in Table 2.3. It is important to test the quality of the fluxes obtained, and whether they are consistent with existing datasets in the literature, in order to utilise these data for investigating the radio spectra of the sample.

Best *et al.* [2003] presented new high resolution 1.425 GHz data for the sample, and compared this with the NVSS values for the sample. They found there was a tendency for the new high resolution data to underestimate the flux densities as compared with the NVSS. This is plotted in Figure 2.10. Also in Figure 2.10 a similar plot is presented for the high resolution and low resolution 610 MHz. Ideally, for an unresolved source, the fluxes in both the high and low resolution data should be the same. For sources with lots of diffuse, extended emission, the low resolution fluxes are expected to be or greater than those at the high resolution, since the high resolution data will resolve out some of the emission. The 610 MHz plot appears very similar to that of the 1.4 GHz, with the greatest scatter below ∼20mJy. The 610 MHz low resolution fluxes do appear slightly underestimated relative to the high resolution data, particularly towards the lowest fluxes, however most of the errorbars are within reach of unity, suggesting the error estimate of 10-15% estimated in the previous section is representative of the sample. As noted previously, the presence of a non-negligible varying primary beam offset in the 610MHz observations introduces unavoidable uncertainty into the flux determinations, particularly for sources far from the pointing centre.

[10] http://www.vla.nrao.edu/astro/guides/p-band/p-reduction/index.shtml

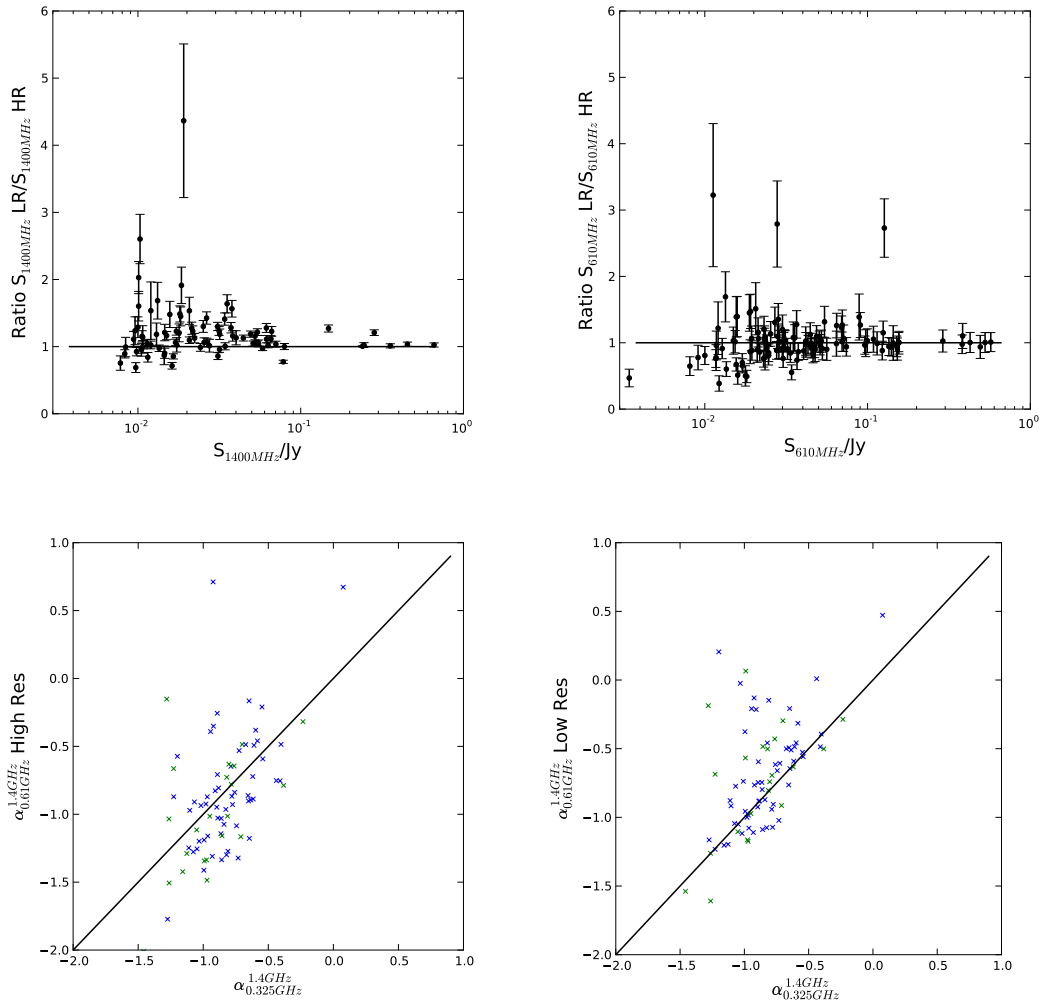

Figure 2.10: Assessing the flux calibration of the 610 MHz data. The top two panels display the ratio of high resolution to low resolution flux at 1.4 GHz (left) and 610 MHz (right) for all CENSORS sources but those with upper limit flux measurements. Note the high resolution 1.4GHz has been corrected from 1.425 GHz to 1.4 GHz assuming the spectral indices listed in Table 2.3. The bottom two panels display the high and low resolution spectral index between 1400 MHz and 610 MHz, against the 1400 MHz-325 MHz spectral index.

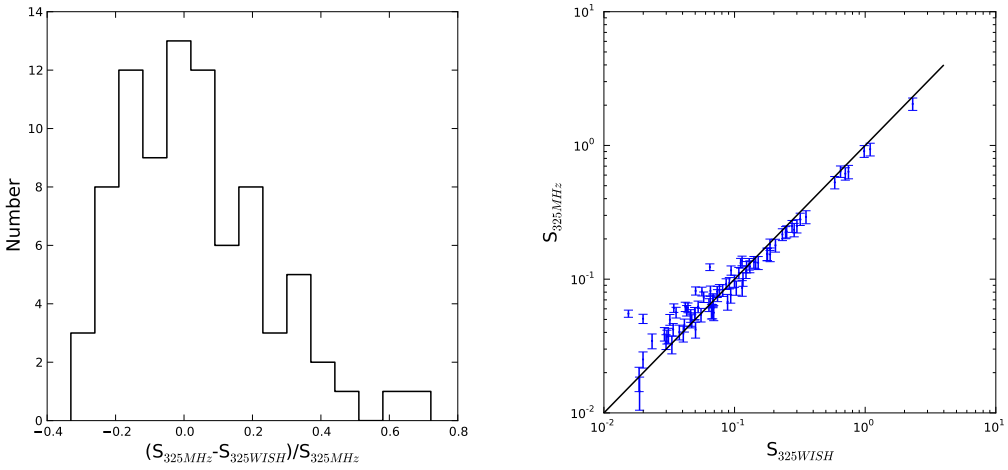

Figure 2.11: Demonstrating the good quality flux calibration of the 325 MHz data.

At 325 MHz, testing the radio data calibration is much more straightforward, as for approximately half (82) of the sources in the complete sample, 352 MHz data from the WISH survey is available for direct comparison. The WISH 352 MHz data was converted to 325 MHz, assuming the spectral indices between 1.4 GHz and 325 MHz as given in Table 2.3. As can be seen in Figure 2.11, the WISH fluxes and the 325 MHz fluxes generally agree well at all but the faintest levels, where WISH approaches its survey limit, to within 10% (a 10% calibration error has been added into the 325 MHz data points to illustrate this). It is also important to note that the WISH survey has a non-standard flux calibration strategy applied, as is detailed in De Breuck et al. The WISH flux densities appeared overestimated by ∼13%, thought to be due to the low elevation at which the survey was observed, and a comparison between the NVSS and WENSS 325 MHz surveys was used to apply a statistical correction.

Table 2.3: Integrated radio fluxes for the CENSORS sample at 610 MHz and 325 MHz. Col1: CENSORS Name, Col2: 325 MHz integrated flux, Col3: 610 MHz integrated flux (low resolution), Col4: 610 MHz integrated flux (high resolution), Col5: NVSS 1.4 GHz integrated flux, Col6: Spectral index α measured between 1.4 GHz and 325 MHz. A † denotes that the flux is an upper limit, generally calculated by measuring the flux at the source position plus 5 x the rms noise. A * indicates that the flux has been measured at 618 MHz, rather than 610 MHz (Group A pointings, as described in Section 2.3).

CEN	S_{325MHz} Jy	S_{610MHz}lr Jy	S_{610MHz}hr Jy	$S_{1.4GHz}$ Jy	α
1	2.045(0.2045)	1.3988(0.14)	1.3921(0.1394)	0.6595(0.0198)	-0.77
2	0.6361(0.0637)	0.5717(0.0573)*	0.5661(0.0567)*	0.4523(0.0136)	-0.23
3	0.6394(0.064)	0.4927(0.061)	0.5256(0.0725)	0.3553(0.0107)	-0.4
4	0.9366(0.0938)	0.4265(0.0454)*	0.4248(0.0454)*	0.283(0.0095)	-0.82
5	0.9056(0.0906)	0.5274(0.0558)	0.5254(0.0556)	0.2447(0.0082)	-0.9
6	0.5294(0.053)	0.3812(0.0386)	0.3901(0.0395)	0.2397(0.0013)	-0.54
7	0.6156(0.0617)	0.3838(0.0465)*	0.348(0.0422)*	0.1482(0.0051)	-0.98
8	0.3215(0.0323)	0.2901(0.0332)	0.2826(0.0324)	0.1263(0.0038)	-0.64
9	0.0384(0.0056)	0.0472(0.0053)*	0.0513(0.0055)*	0.1182(0.0036)	0.77
10	0.25(0.0252)	0.14(0.0143)*	0.1499(0.0154)*	0.0794(0.0029)	-0.79
11	0.07(0.0078)	0.0528(0.007)	0.0578(0.0076)	0.0781(0.0024)	0.07
12	0.2817(0.0283)	0.1559(0.0189)*	0.1557(0.0188)*	0.0704(0.0026)	-0.95
13	0.2342(0.0238)	0.1232(0.0139)	0.1396(0.0158)	0.0663(0.0027)	-0.86
14	0.2238(0.0225)	0.1353(0.0136)	0.1434(0.0145)	0.0656(0.0024)	-0.84
15	0.2922(0.0293)	0.1554(0.0157)*	0.1539(0.0155)*	0.063(0.0019)	-1.05
16	0.2162(0.022)	0.1524(0.0199)	0.1684(0.022)	0.0617(0.0023)	-0.86
17	0.1791(0.0182)	0.1438(0.0267)	0.1443(0.0266)	0.0615(0.0023)	-0.73
18	0.1299(0.0133)	0.0903(0.0095)	0.0713(0.0075)	0.0583(0.0018)	-0.55
19	0.2269(0.0229)	0.1247(0.0135)	0.1085(0.0119)	0.0551(0.0021)	-0.97
20	0.1531(0.0156)	0.1144(0.0143)*	0.1156(0.0144)*	0.0542(0.0021)	-0.71
21	0.1334(0.0137)	0.0906(0.0096)*	0.0936(0.0099)*	0.054(0.0017)	-0.62
22	0.2125(0.0215)	0.1511(0.0176)	0.1599(0.0186)	0.0529(0.0017)	-0.95
23	0.2493(0.0252)	0.0996(0.0122)	0.0965(0.0118)	0.0524(0.002)	-1.07
24	0.1328(0.0135)	0.0962(0.0097)	0.0998(0.01)	0.051(0.0016)	-0.66
25	0.086(0.0092)	0.0741(0.0078)*	0.079(0.0083)*	0.0492(0.0019)	-0.38
26	0.1818(0.0184)	0.1087(0.0144)	0.1032(0.0136)	0.0444(0.0014)	-0.97
27	0.1486(0.0169)	0.0796(0.0091)	0.0326(0.0048)†	0.0404(0.0023)	-0.89
28	0.1115(0.0116)	0.0511(0.0058)*	0.0527(0.0058)*	0.0401(0.0019)	-0.7
29	0.1234(0.0129)	0.07(0.0088)*	0.0552(0.007)*	0.0382(0.0016)	-0.8

Continued on next page

Table 2.3 – continued from previous page

CEN	S_{325MHz} Jy	S_{610MHz}lr Jy	S_{610MHz}hr Jy	$S_{1.4GHz}$ Jy	α
30	0.132(0.0139)	0.0562(0.0076)*	0.0623(0.0079)*	0.0378(0.002)	-0.86
31	0.154(0.0162)	0.0974(0.014)*	0.0981(0.0142)*	0.0373(0.0015)	-0.97
32	0.1373(0.0142)	0.0888(0.0157)	0.064(0.0113)	0.0353(0.0015)	-0.93
33	0.1244(0.0128)	0.0713(0.0094)	0.0667(0.0088)	0.0343(0.0011)	-0.88
34	0.0419(0.0054)	0.0276(0.003)*	0.0313(0.0033)*	0.0342(0.0011)	-0.14
35	0.0863(0.009)	0.0521(0.0061)	0.0508(0.0057)	0.0341(0.0014)	-0.64
36	0.0619(0.0068)	0.0285(0.0034)*	0.0419(0.0049)*	0.0323(0.0011)	-0.45
37	0.097(0.0103)	0.0452(0.0048)*	0.0455(0.0049)*	0.0318(0.0014)	-0.76
38	0.1001(0.0104)	0.0693(0.0072)	0.0566(0.0058)	0.0317(0.0011)	-0.79
39	0.1343(0.0137)	0.0697(0.0071)	0.0686(0.007)	0.0315(0.0011)	-0.99
40	0.076(0.008)	0.0505(0.0057)	0.0497(0.0055)	0.0309(0.0013)	-0.62
41	0.0736(0.0084)	0.0417(0.0062)	0.0406(0.006)	0.0275(0.0017)	-0.67
42	0.0828(0.0087)	0.0646(0.0066)	0.0513(0.0054)	0.0265(0.0009)	-0.78
43	0.0678(0.0073)	0.0451(0.0051)	0.0492(0.0055)	0.0264(0.0009)	-0.65
44	0.0125(0.0024)	0.0236(0.0025)	0.0229(0.0024)	0.0261(0.0009)	0.5
45	0.0937(0.0102)	0.0418(0.0057)	0.0432(0.0058)	0.0255(0.0012)	-0.89
46	0.0261(0.0039)	0.0156(0.0017)	0.0232(0.0024)	0.0252(0.0009)	-0.02
47	0.0826(0.0086)	0.0486(0.0052)*	0.0444(0.0046)*	0.0252(0.0009)	-0.81
48	0.0623(0.0067)	0.0288(0.0033)	0.0281(0.0031)	0.0242(0.0009)	-0.65
49	0.0558(0.0065)	0.023(0.0028)	0.0302(0.0035)	0.0238(0.0009)	-0.58
50	0.113(0.0115)	0.0462(0.0052)	0.0558(0.0062)	0.0223(0.0008)	-1.11
51	0.0643(0.0071)	0.0375(0.004)	0.0434(0.0045)	0.0217(0.0008)	-0.74
52	0.0152(0.0023)†	0.0045(0.001)*†	0.0111(0.0016)*	0.0217(0.0008)	0.24
53	0.0588(0.0065)	0.0445(0.005)	0.0396(0.0044)	0.0216(0.0011)	-0.69
54	0.0517(0.0062)	0.028(0.0034)	0.0255(0.003)	0.0214(0.0008)	-0.6
55	0.0555(0.0064)	0.0322(0.0041)	0.0355(0.0043)	0.0214(0.0008)	-0.65
56	0.0708(0.0077)	0.0357(0.0047)	0.0333(0.0044)	0.0208(0.0011)	-0.84
57	0.0687(0.0075)	0.0303(0.0038)	0.0397(0.005)	0.0207(0.0011)	-0.82
58	0.0757(0.0081)	0.0431(0.0045)	0.0444(0.0045)	0.0207(0.0008)	-0.89
59	0.081(0.0093)	0.0181(0.0026)*	0.0368(0.0046)*	0.0191(0.0011)	-0.99
60	0.0449(0.0052)	0.0312(0.0036)	0.0305(0.0032)	0.0189(0.0007)	-0.59
61	0.0806(0.0089)	0.0341(0.0052)	0.0616(0.0083)	0.0185(0.0007)	-1.01
62	0.046(0.0058)	0.0239(0.0028)*	0.025(0.0031)*	0.0184(0.0007)	-0.63
63	0.1539(0.016)	0.0644(0.0088)*	0.0653(0.0088)*	0.0183(0.0007)	-1.46
64	0.1164(0.012)	0.0476(0.0068)	0.0531(0.0075)	0.0181(0.001)	-1.27
65	0.042(0.0057)	0.0233(0.0029)	0.0217(0.0026)	0.0179(0.001)	-0.58
66.82	0.123(0.013)	0.0369(0.0052)	0.05(0.0065)	0.031(0.0011)	-0.94

Continued on next page

Table 2.3 – continued from previous page

CEN	S_{325MHz} Jy	S_{610MHz}lr Jy	S_{610MHz}hr Jy	$S_{1.4GHz}$ Jy	α
67	0.0609(0.0072)	0.0336(0.004)	0.0397(0.0047)	0.0173(0.0007)	-0.86
68	0.0326(0.0042)	0.0171(0.0021)	0.0262(0.0028)	0.0172(0.0007)	-0.44
69	0.0819(0.0094)	0.0405(0.0044)	0.0462(0.0047)	0.017(0.0007)	-1.08
70	0.0676(0.0079)	0.0476(0.0092)†	0.0804(0.015)	0.017(0.002)	-0.94
71	0.0533(0.0059)	0.0307(0.0034)	0.0297(0.0032)	0.0167(0.0007)	-0.79
72	0.0402(0.0049)	0.0247(0.0029)	0.0291(0.003)	0.0165(0.0007)	-0.61
73	0.0623(0.007)	0.0306(0.0031)	0.0304(0.0031)	0.0162(0.0007)	-0.92
74	0.0616(0.0068)	0.0232(0.0028)*	0.0221(0.0024)*	0.016(0.0007)	-0.92
75	0.0818(0.0096)	0.0279(0.0052)*†	0.0187(0.0038)*	0.0157(0.001)	-1.13
76	0.0486(0.0065)	0.0299(0.0038)	0.0326(0.0042)	0.0153(0.0007)	-0.79
77	0.0501(0.0058)	0.0367(0.0044)	0.0287(0.0032)	0.015(0.0007)	-0.83
78	0.042(0.0052)	0.0242(0.0026)	0.0252(0.0027)	0.0146(0.0007)	-0.72
79	0.0922(0.0109)	0.0544(0.0067)*	0.0414(0.0053)*	0.0146(0.0011)	-1.26
80	0.0422(0.0052)	0.0283(0.0036)	0.0209(0.0025)	0.0145(0.0006)	-0.73
81	0.0534(0.0068)	0.027(0.0033)	0.0206(0.0026)	0.0145(0.0014)	-0.89
83	0.0564(0.0064)	0.031(0.0034)	0.0298(0.003)	0.0135(0.0006)	-0.98
84.85	0.3732(0.0389)	0.1268(0.0133)	0.0465(0.0057)	0.0924(0.0038)	-0.96
86	0.0324(0.0041)	0.0218(0.0026)	0.0253(0.0026)	0.0132(0.0006)	-0.62
87	0.0562(0.0067)	0.021(0.0034)*	0.0235(0.0032)*	0.0132(0.0006)	-0.99
88	0.0304(0.0053)	0.035(0.0057)*	0.0324(0.0047)*	0.0131(0.0006)	-0.58
89	0.0556(0.0066)	0.0178(0.0032)	0.0355(0.0088)	0.013(0.001)	-1.0
90	0.0389(0.0048)	0.0254(0.0032)*	0.0224(0.0024)*	0.0128(0.0006)	-0.76
91	0.0079(0.0018)†	0.003(0.0006)†	0.0047(0.0007)	0.0127(0.0006)	0.33
92	0.0804(0.0089)	0.0159(0.0031)	0.0311(0.0058)	0.0126(0.0011)	-1.27
93	0.0339(0.0044)	0.0265(0.0048)*†	0.0365(0.0054)*	0.0122(0.0006)	-0.7
94	0.06(0.0067)	0.0285(0.0055)*	0.0283(0.0042)*	0.0122(0.0006)	-1.09
95	0.045(0.0068)	0.0191(0.0025)	0.013(0.0015)	0.0122(0.0012)	-0.89
96	0.0541(0.0069)	0.0122(0.003)	0.0317(0.0054)	0.012(0.0006)	-1.03
97	0.0392(0.0053)	0.0136(0.0018)	0.0225(0.0028)	0.012(0.0012)	-0.81
98	0.0142(0.0045)	0.0108(0.0017)*†	0.0125(0.0016)*	0.0118(0.0006)	-0.13
99	0.0229(0.0042)	0.0214(0.003)	0.0201(0.0022)	0.0116(0.0006)	-0.47
100	0.0576(0.0065)	0.0246(0.0032)	0.0306(0.0035)	0.0115(0.0006)	-1.1
101	0.0345(0.0047)	0.019(0.0032)	0.022(0.0027)	0.0114(0.0006)	-0.76
102	0.0276(0.0044)	0.0107(0.0016)*†	0.0213(0.0029)*	0.0111(0.0011)	-0.62
103	0.0677(0.0078)	0.03(0.0042)*	0.025(0.0029)*	0.0107(0.0006)	-1.26
104	0.0612(0.0081)	0.0184(0.0031)†	0.0142(0.0026)	0.0107(0.0006)	-1.19
105	0.0575(0.0063)	0.0288(0.0037)	0.0294(0.0033)	0.0106(0.0006)	-1.16

Continued on next page

Table 2.3 – continued from previous page

CEN	S_{325MHz} Jy	S_{610MHz}lr Jy	S_{610MHz}hr Jy	$S_{1.4GHz}$ Jy	α
106	0.0251(0.0043)	0.0154(0.0018)	0.0151(0.0017)	0.0105(0.0006)	-0.6
107	0.0341(0.0058)	0.0057(0.0011)*†	0.0124(0.0023)*	0.0103(0.001)	-0.82
108	0.0121(0.0039)	0.0034(0.0009)	0.0073(0.001)	0.0102(0.0006)	-0.12
109	0.038(0.0052)	0.0121(0.0034)	0.0099(0.0016)	0.0101(0.0006)	-0.91
110	0.039(0.0053)	0.0113(0.002)	0.0035(0.001)	0.0101(0.0013)	-0.92
111	0.0182(0.0032)	0.015(0.0023)	0.0145(0.0018)	0.01(0.0006)	-0.41
112	0.0453(0.0056)	0.0234(0.0025)	0.0301(0.0066)	0.0098(0.0006)	-1.05
113	0.0583(0.0067)	0.017(0.0025)*	0.0243(0.003)*	0.0097(0.0006)	-1.23
114	0.0169(0.0038)	0.0194(0.0027)	0.0182(0.0019)	0.0096(0.0006)	-0.39
115	0.0553(0.0108)	0.0081(0.0014)	0.0125(0.0017)	0.0096(0.001)	-1.2
116	0.0186(0.0028)†	0.0075(0.0015)†	0.0074(0.001)	0.0096(0.0006)	-0.45
117	0.0201(0.0033)	0.0046(0.001)†	0.0154(0.0022)	0.0095(0.0006)	-0.51
118	0.0487(0.0055)	0.0254(0.0043)	0.0243(0.0026)	0.0094(0.0006)	-1.13
119	0.0336(0.0044)	0.0195(0.0024)	0.0221(0.0024)	0.0094(0.0006)	-0.87
120	0.0116(0.0018)†	0.003(0.0007)†	0.0079(0.0011)	0.0091(0.0006)	-0.17
121	0.0154(0.0032)	0.0118(0.0023)	0.0123(0.0014)	0.009(0.0005)	-0.37
122	0.0181(0.0039)	0.01(0.0012)	0.0124(0.0014)	0.009(0.0006)	-0.48
123	0.0165(0.0029)	0.0117(0.0016)	0.0153(0.0017)	0.0087(0.0005)	-0.44
124	0.0359(0.0058)	0.0137(0.0028)	-	0.0087(0.0006)	-0.97
125	0.0371(0.0051)	0.0213(0.0031)	0.0184(0.0022)	0.0084(0.0005)	-1.02
126	0.0395(0.0075)	0.0278(0.0044)*	0.01(0.0017)*	0.0084(0.0013)	-1.06
127	0.0498(0.0062)	0.0231(0.0028)	0.0192(0.002)	0.0083(0.0005)	-1.23
128	0.0222(0.0038)	0.0117(0.0024)	0.0151(0.0022)	0.0083(0.0005)	-0.67
129	0.0265(0.0046)	0.0102(0.0022)†	0.0189(0.0032)	0.0083(0.0006)	-0.79
130	0.0178(0.0034)†	0.011(0.0021)†	0.0043(0.0006)	0.0082(0.0005)	-0.53
131	0.0181(0.0033)	0.0059(0.0016)†	0.0075(0.0015)	0.0082(0.0006)	-0.54
132	0.0169(0.0029)†	0.0062(0.0011)*†	0.0075(0.001)*	0.0079(0.0006)	-0.52
133	0.0286(0.0046)	0.0134(0.0022)	0.0079(0.0012)	0.0078(0.0012)	-0.89
134	0.0506(0.007)	0.0091(0.0017)*	0.0117(0.0018)*	0.0078(0.0006)	-1.28
135	0.0163(0.0029)	0.0158(0.0028)	0.0113(0.0015)	0.0078(0.0006)	-0.51
136	0.0362(0.0049)	0.0128(0.0016)	0.014(0.0016)	0.0075(0.0006)	-1.08
137	0.0289(0.0062)	0.0092(0.0016)†	0.0187(0.003)†	0.0074(0.0012)	-0.93
138	0.0414(0.0054)	0.0188(0.0023)	0.013(0.0019)	0.0147(0.0005)	-0.71
139	0.0145(0.0022)†	0.0162(0.0026)*†	0.0068(0.0014)*	0.0069(0.0005)	-0.51
140	0.0153(0.0022)†	0.0062(0.0012)*†	0.0079(0.0013)*	0.0068(0.0005)	-0.55
141	0.014(0.0035)	0.0065(0.0015)*†	0.0142(0.002)*	0.0066(0.0006)	-0.52
142	0.0126(0.002)†	0.0064(0.0018)	0.0068(0.0008)	0.0063(0.0006)	-0.47

Continued on next page

Table 2.3 – continued from previous page

CEN	S_{325MHz} Jy	S_{610MHz}lr Jy	S_{610MHz}hr Jy	$S_{1.4GHz}$ Jy	α
143	0.0127(0.003)	0.0106(0.0022)*†	0.0086(0.001)*	0.0061(0.0006)	-0.5
144	0.0158(0.0024)†	0.0064(0.0011)*†	0.0039(0.0009)*	0.006(0.0006)	-0.66
145	0.0071(0.0016)	0.0106(0.0026)†	0.0116(0.0026)	0.0058(0.0003)	-0.14
146	0.0312(0.0047)†	0.0101(0.0016)*†	0.0017(0.0007)*	0.0054(0.0006)	-1.2
147	0.0276(0.0065)	0.0121(0.0027)*†	0.008(0.0017)*	0.0042(0.0007)	-1.29
148	0.0223(0.0033)†	0.0059(0.001)†	0.002(0.0004)	0.0041(0.0008)	-1.16
149	0.0168(0.0028)†	0.0021(0.0004)†	0.0038(0.0007)	0.004(0.0007)	-0.98
150	0.019(0.0028)†	0.0164(0.0029)*†	0.011(0.0019)*†	0.0038(0.0007)	-1.1
1.1	0.0254(0.0044)	0.0029(0.0007)*†	0.0117(0.0013)*	0.0072(0.0005)	-0.86
1.2	0.0266(0.0047)	0.0206(0.0044)	0.0136(0.002)	0.0068(0.0005)	-0.93
1.3	0.0582(0.0135)	0.0156(0.0026)	0.0112(0.0016)	0.0067(0.0005)	-1.48
1.4	0.2645(0.0304)	0.0464(0.0086)†	0.0474(0.0092)	0.0074(0.0007)	-2.45

2.5.1 CENSORS New Host Galaxy Identifications

Finally, these new low frequency radio observations have allowed several new host galaxy identifications to be made for CENSORS, in addition to unveiling additional lobes/structure for several other sources. These are detailed individually in this section.

CENSORS 84+85: A New Giant X Shaped Radio Galaxy

CENSORS 84 and 85 are the lobes of an extended double radio source, approximately five arcminutes in extent, with the host galaxy clearly located at 09 55 36.87, -21 27 12.5. These lobes are listed as several sources in the NVSS, and were originally thought to be correlated noise. In Best *et al.* [2003] the lobes are classed as two separate sources, CENSORS 84 and CENSORS 85. However the radio data at 325MHz and 610MHz has shown the structure to be consistent with the structure visible in the NVSS. The K band aperture corrected (to a standard 63.9 kpc aperture) magnitude for the host is 13.1 +/- 0.2, giving a corresponding K-z redshift of 0.15, following the Willott *et al.* [2003] relation. The radio structure clearly places the source in the relatively rare 'X-shaped' radio galaxy category, having a pair of low surface brightness wings orientated at an angle to the active lobes (cf. Figure 2.12). Cheung and Springmann [2007] carried out a search of the FIRST survey for such objects, building a list of 100 candidate X-shaped sources, where previously there were only approximately 17 known in the literature. These sources are of interest, as the mechanisms which give rise to 'X' structures are not clear. Several mechanisms have been proposed, the most popular of which are that the two sets of lobes are a product of a supermassive black hole merger event, or that they are a result of backflowing plasma from the active lobes into a surrounding asymmetric medium. Recent studies of spectral index have shown conflicting results, with some sources showing steeper spectrum wings, and flatter spectrum active lobes, and vice versa [Lal and Rao, 2004]. It is worth noting that the

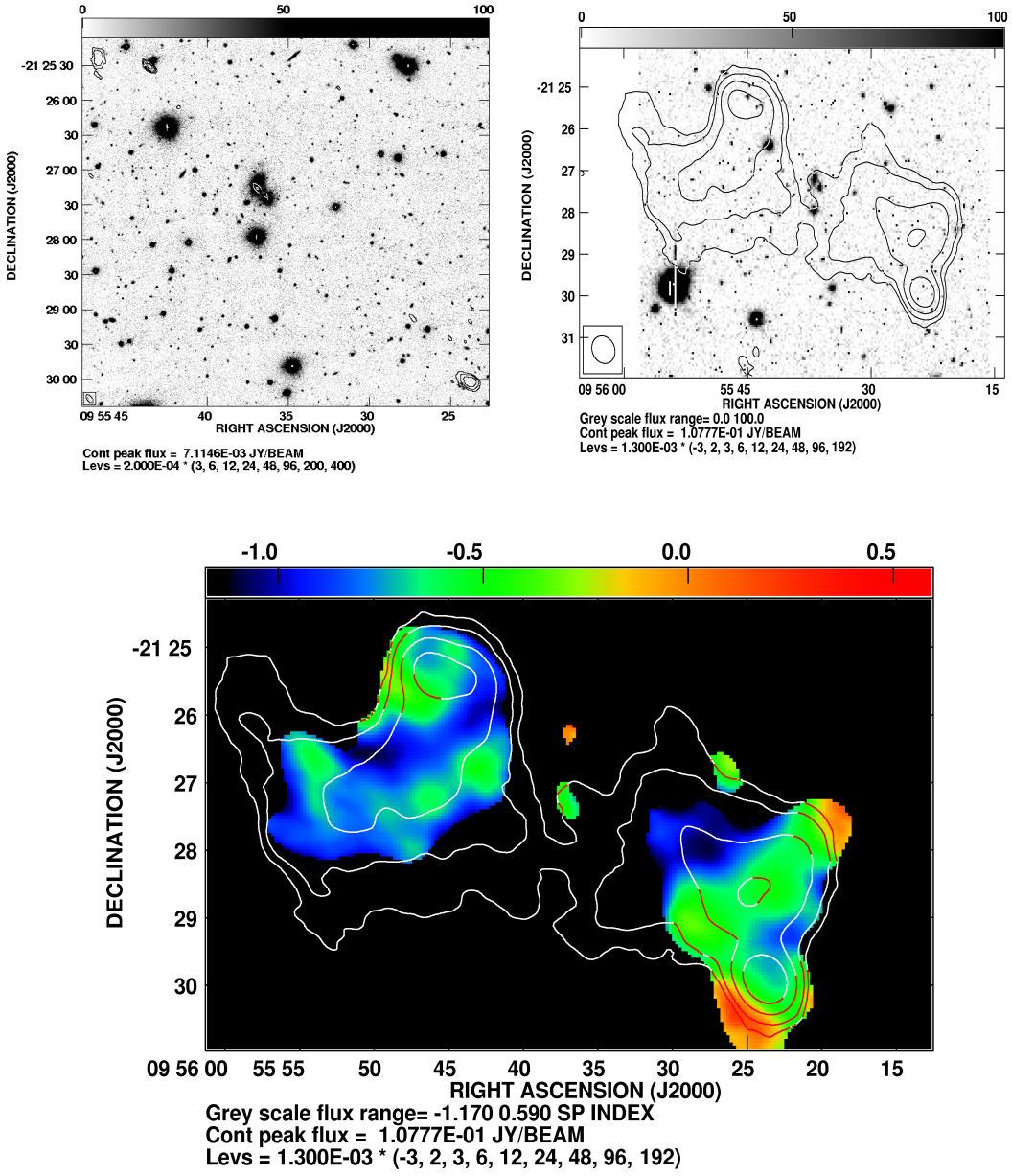

Figure 2.12: CENSORS 84+85. The top left figure shows the EISD I band image overlaid with the new high resolution 610 MHz radio data. These reveal a core detection (not detected at high resolution 1.4 GHz) on top of a bright galaxy, located in the middle of a small group/cluster. The figure on the top right shows the same I band image, this time overlaid with the 325 MHz data, with the extended emission seen in the NVSS confirmed as real. The bottom panel shows a spectral index map for the source, between 1.4 GHz (NVSS) and 325 MHz, revealing a flat core and hotspots in the active lobes, and diffuse steep emission from older electrons.

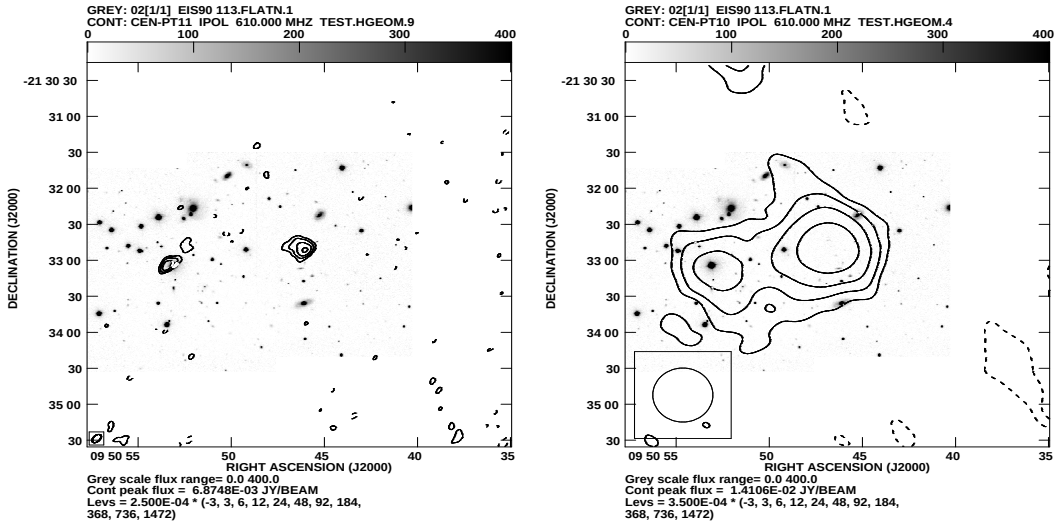

Figure 2.13: An 610 MHz - optical high resolution overlay on the left, and a 325 MHz - optical overlay on the right, showing the extended emission between the two components of CENSORS 66+82.

X-shaped structure visible for this source would not have been identified from high resolution data alone - the second diffuse set of lobes are not visible in either the VLA 1.4 GHz or GMRT 610 MHz at high resolution. This new identification removes two unidentified sources from the sample, and is confirmed spectroscopically in Chapter 3.

CENSORS 66+82

In Brookes et al. (2003), CENSORS 66 was identified with a z = 0.355 galaxy, offset slightly from the centre of the radio source. CENSORS 82 had no host candidate detected in either the I or K band. CENSORS 66 and 82 are separated by $\sim$ 1.7 arcminutes. Gendre (priv communication) identified these two sources as individual components of a large radio galaxy, and this is confirmed with the new radio observations presented in this Chapter. In Figure 2.13, the 325 MHz BnA data shows clear extended emission between the two components. There is a galaxy located on the axis between these two sources with K-band magnitude K=17.8, which is expected to be the host. This identification is confirmed spectroscopically in Chapter 3.

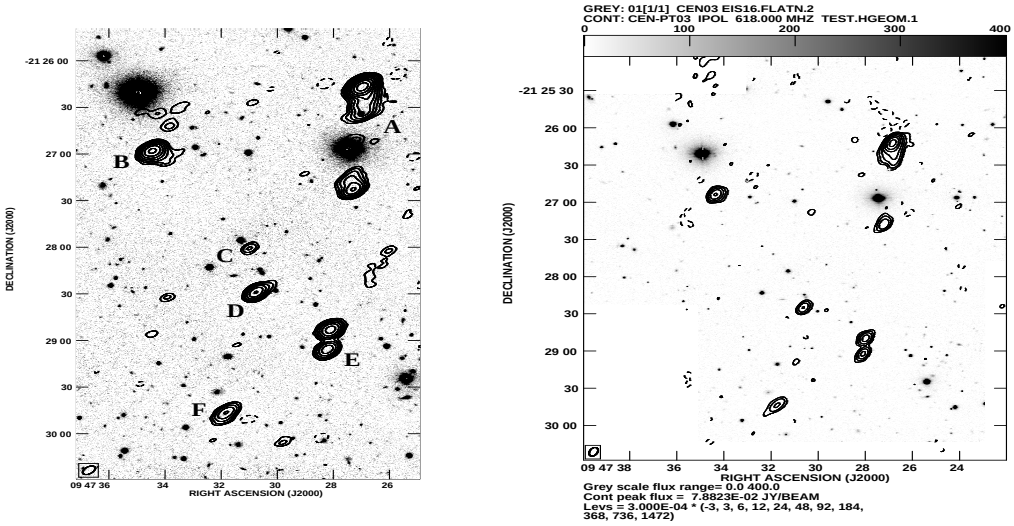

Figure 2.14: On the left, a 1.4 GHz -optical overlay of CENSORS 90+103, reproduced from Best et al. (2003). Components B, E and C are possibly components of one giant radio source. Source C is not detected at 610 MHz (right), adding weight to the possiblity that it is the radio core, with components B and E the lobes.

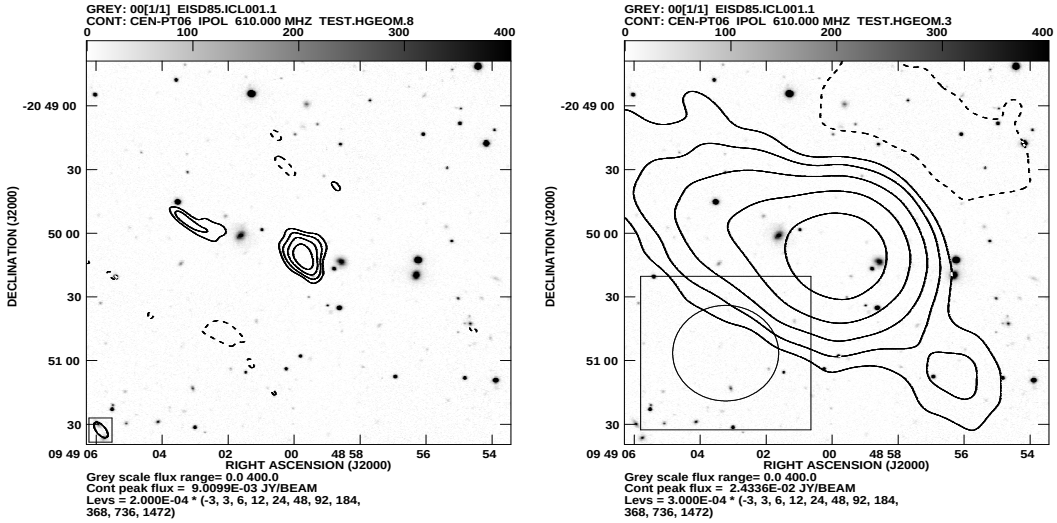

Figure 2.15: On the left, a 610 MHz-optical overlay for CENSORS 64, showing the previously undetected steep spectrum lobe. There is a host galaxy located directly in the middle of the axis between the two lobes. The right figure shows a 325 MHz BnA-optical overlay, showing clearly the extended emission.

CENSORS 90+103

The new radio data for CENSORS 90 and 103 are inconclusive as to whether these are two individual sources, or components of a single much larger radio galaxy, due to their proximity to several other, unrelated radio sources [see Best *et al.*, 2003]. Figure 2.14 shows the original 1.4 GHz radio-optical overlay, and the new 610 MHz optical overlay. Best *et al.* [2003] queried

whether sources B and E were part of the same giant radio galaxy, with component C being the core. Component C is not detected in the 610 MHz, suggesting an inverted radio spectrum (which would be typical of a radio core). There are also no detected host candidates in deep K-band observations around either of the radio sources B and E. Blind spectra have been previously taken by Brookes *et al.* [2008] at the radio position of both sources, with no detections, so the explanation of B, E and C being one large radio source remains the most likely.

CENSORS 64

CENSORS 64 was originally thought to be a single radio source, with an undetected host. The new radio data at 610 MHz and 325 MHz (Figure 2.15) reveals an additional steep spectrum lobe undetected at 1.4 GHz, providing a new host galaxy identification for this source.

Chapter 3

Optical and Near-IR Spectroscopy of CENSORS Sources

3.1 Introduction

Complete and precise spectroscopic redshifts are essential for CENSORS, to allow observational properties of the highest redshift sources in the sample to be determined. Spectroscopic redshifts for ∼70% of the sample were determined through several observational campaigns by Brookes *et al.* [2008]. The remainder were either not targeted due to a lack of observing time or an uncertain host position (now resolved through the new low frequency GMRT and VLA data presented in Chapter 2), or for which optical spectroscopy had failed to produce a redshift. In many cases these sources had photometric[1] redshifts placing them within the 'redshift desert', $1.2 \leq z \leq 2.5$, where O[II]3727 is shifted outwith the observed optical range, but Lyα has not yet entered it.

3.2 Strategy

Observations of the 38 CENSORS sources without a spectroscopic redshift were made using 3 telescopes over a course of 4 observing runs (see Table 3.1). Those sources previously unobserved, or with a new host galaxy identification, or whose photometric redshift suggested $z \leq 1.2$ (placing O[II] within the optical range) were targeted using optical long-slit spectroscopy, with the WHT(ISIS) in service mode and with the NTT(EFOSC2) in visitor mode. The latter run with EFOSC2 used Grism 5, which provides increased wavelength coverage to 9000Å. This was important as previous runs had in many cases only targeted a wavelength range up to $\sim 8000\mathring{A}$ - the increased wavelength coverage at the red end enabled the [OII]3727 emission

[1] unless otherwise stated, photometric redshifts for CENSORS sources are estimated from the K-z relation

Table 3.1: The Four Spectroscopy Observing Runs for CENSORS.

Run No.(Obs ID.)	Date	Telescope (Instru.)	Grism/Grating	λ Coverage $\AA$	Resolution $\AA$	Slit/F.O.V. arcsec
1(1419717)	22/04/2010	WHT(ISIS:RED)	R158R	5294:9706	12	1.5
		WHT(ISIS:BLUE)	R300B	3282:5718	13	1.5
2(086.A-0070(A))	7-10/02/2011	NTT(EFOSC2)	Grism 5	5200-9350	13	1.5
3(086.A-0070(B))	Jan-Feb 2011	VLT(SINFONI)	H+K	14380:18000 20000:24620	12	8x8
4(088.A-0389(A))	Jan-Feb 2012	VLT(SINFONI)	H+K	14380:18000 20000:24620	12	8x8

line to be detected if present, out to higher redshift (z$\sim$1.4). The remainder with either an uncertain host position, or a photometric redshift in the range 1.2$\leq$z$\leq$2.5 were targeted with the near-IR integral field unit SINFONI on the VLT. Note that several Infra-red Faint Radio Source candidates were also observed during the EFOSC2 run in addition to CENSORS, details of which are presented in Chapter 6.

3.3 Long Slit EFOSC2 and ISIS Spectroscopy

Long slit spectroscopy observations of CENSORS were completed with EFOSC2 on the NTT at La Silla in visitor mode, and with ISIS (blue and red arm) on the WHT at La Palma in service mode. Each target was observed for a series of 20 minute exposures up to a maximum of 1.3 hours per target, with the observation aborted as soon as emission lines/absorption features became clearly apparent, in order to maximise observing efficiency. The same reduction procedure was followed for all sources observed with EFOSC2 on the NTT and ISIS on the WHT (runs 1 and 2) using the **IRAF** astronomical data reduction package, as follows:

- A minimum of 10 bias frames were observed at the beginning of each night of the observations. These were then median combined to make a master bias frame.

- A minimum of 10 spectrocopic dome flats were taken each night, the required lamp and exposure settings being determined automatically from a table of values appropriate for the instrument set-up. These were median combined to make a master flat.

- One or two ARC frames were taken using the Helium-Argon lamp for EFOSC2 and the Copper-Neon+Copper-Argon lamps in the case of ISIS.

- The master bias and master flat frames were trimmed, and the master flat bias-subtracted. This was then used to create a response curve of illumination vs wavelength for the master flat frame. The master flat is then divided by the response curve to give a final flat that solely reflects the pixel to pixel sensitivity differences across the CCD. This response-corrected flat is then used to flat-field the subsequent target, standard star and ARC frames.

- All target, standard star, and ARC frames were bias-subtracted, flat-fielded, and combined as necessary.

- Standard Star and target frames were carefully background-subtracted to remove sky lines using **background**.

- A spectrum was extracted from the ARC frames using the **Apall** task. This was used to create a wavelength reference by identifying the lines with the **Identify** task.

- Spectra were then extracted from the target and standard star frames, and wavelength calibrated using **refspec** and **dispcor**. The apertures used for extraction varied in order to maximise the signal to noise achievable for each individual target.

- Standard star spectra were flux calibrated using **standard** and **sensfunc**, and using extinction files appropriate to La Silla and the WHT. This flux calibration was then applied to the target spectra.

3.4 IFU SINFONI Spectroscopy

SINFONI (Spectrograph for INtegral Field Observations in the Near Infrared) is an integral field spectrograph which operates in the mid-infrared, covering a wavelength range of 1.1-2.45μm. 28 CENSORS sources were observed in two runs with SINFONI using the H+K grating, with the aim of capturing Hα from z$\geq$1.2. Both of these runs were bad-weather backup projects, since good seeing was relatively unimportant - obtaining deep observations of any extended emission structure, for which good seeing would be necessary, was not a primary goal. The large field of view (8"x8") afforded by SINFONI gives the added benefit of picking up any extended emission which radio galaxies often have, and essentially eliminates any concerns about positional uncertainties in the host galaxy detection.

Each target was observed for one hour (including overheads) in service mode. As any emission line structure was expected to be small-scale ($<$ 2-3 arcsec), the targets were dithered on-source for sky subtraction, to maximise observing efficiency within each one hour observing block (OB). Each OB was comprised of eight or nine exposures of 300s each, jittered around the target position (offsets of order 1-2 arcsec). The jitter pattern was chosen individually for each target to maximise available sky area, whilst minimising observations of any bright nearby sources that may have contaminated the sky areas.

The SINFONI observations from run 3 were automatically pipeline reduced by ESO. For run 4, an archive policy change by ESO meant that only the raw data products were available, and the pipeline had to be run manually, using version 2.2.9 and following the recipes detailed in the SINFONI Pipeline v2.2.9 Manual. The pipeline consists of six recipes.

- **sinfo_rec_detlin**: To reduce the set of 24 linearity frames taken as part of the calibration plan. These are used to determine a map of 'bad' pixels with a non-linear response on the detector.

- **sinfo_rec_mdark**: To reduce the set of dark frames, and produce a Master dark frame for use in subsequent reduction steps.

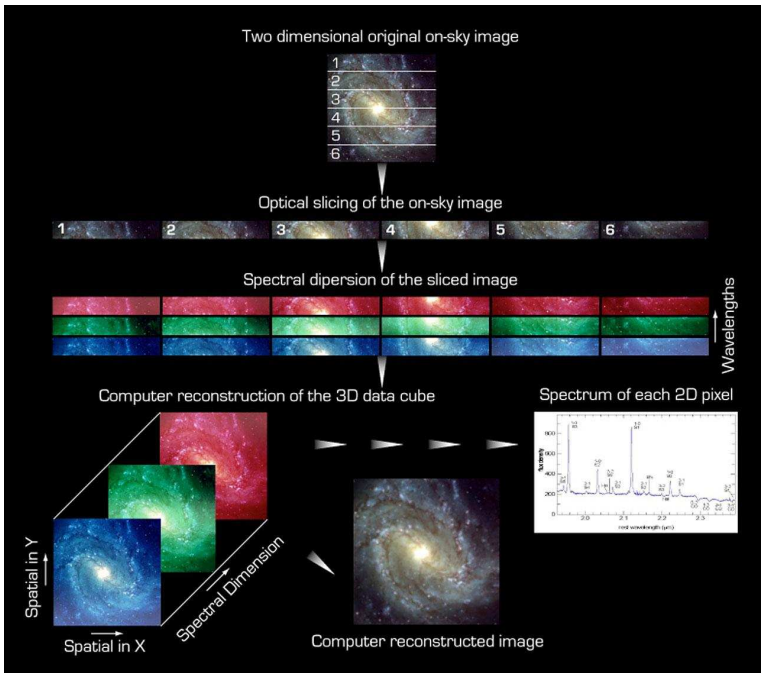

Figure 3.1: Figure illustrating the principles of IFU spectroscopy, which allows the spectra from every part of the target to be recorded simultaneously. Image credit: eso.org

- **sinfo_rec_mflat**: Reduces and combines flat images into a Master flat frame, to correct for differences in the pixel to pixel gain.
- **sinfo_rec_distortion**: Reduces the 80 Fibre frames to calculate optical distortions and slitlet distances (necessary for successful cube reconstruction) .
- **sinfo_rec_wavecal**: Computes the wavelength calibration for the cube.
- **sinfo_rec_jitter**: Used to reduce both the standard star frames (if required) and the science frames. Applies the previously obtained calibrations, wavelength calibration, and combines the jittered frames to produce a final reduced cube of the science target.

The package QFitsView was used to visually inspect the observations and to extract the 1D spectra. Note that no flux calibration was performed on these spectra. As any line detections were expected to be faint, an independent reduction of some of the SINFONI data from run 3 was also made by Nicole Nesvadba, using a privately-developed pipeline, which confirmed the detections presented here.

3.5 Results

Once the final spectra were obtained, the following procedure was adopted for determining the redshift:

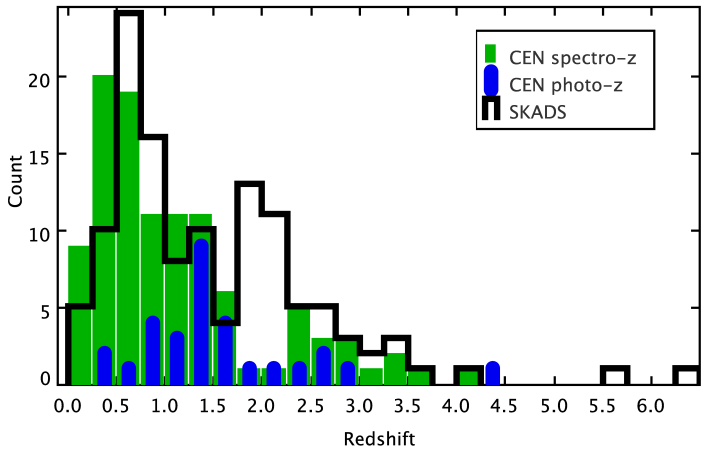

Figure 3.2: The final CENSORS redshift distribution, with the total split into two histograms. Sources with spectroscopic redshifts constitute the green histogram, and sources without a spectroscopic redshift, and only a photometric estimate (K-z or K-z limit) overplotted in the blue histogram. Also plotted in black is the output from a sample of $S_{1.4GHz}$ >7.2mJy sources from a randomly selected six square degree area (the same selection criteria as CENSORS) from the SKADS S^3-SEX simulation, showing relatively good agreement between observation and simulation.

- If the spectrum displayed multiple emission lines, the ratio of line wavelengths was used to identify these and derive an approximate redshift.

- If there was only one emission line present, in the optical this was assumed to be one of either Lyα, MgII, or [OII], the only lines which could be expected to appear alone in an optical spectrum. In the infrared SINFONI observations, Hα is the only realistic single line candidate. MgII can be distinguished by its distinctive broad shape. Lyα displays a characteristic line shape, and no continuum blueward of the line. [OII] and Hα can be distinguished by taking into consideration the estimated redshift from the K-z relation (K-band data exists for all CENSORS sources, and the K-z relation has been shown to be reasonably tight, e.g. Brookes *et al.* 2006, Willott *et al.* 2003). Additionally, in Figure 3.3, the [OII] emission line - radio flux, radio linear size diagnostic diagrams for all CENSORS sources with a measured [OII] line are plotted in order to aid line identification for sources with only a single line spectrum, or those with an uncertain host. Willott *et al.* [1999] showed that a correlation exists between [OII] emission line flux and radio flux as follows [cf. Rigby, 2007].

$$\frac{S_{1.4GHz}}{\mu Jy} = 4.7 \times 10^4 \left(\frac{f[OII]}{10^{-16} ergs^{-1} cm^{-2}} \right)^{1.45} \tag{3.1}$$

- Spectra with emission line(s) were then smoothed if necessary by a factor up to 5, and

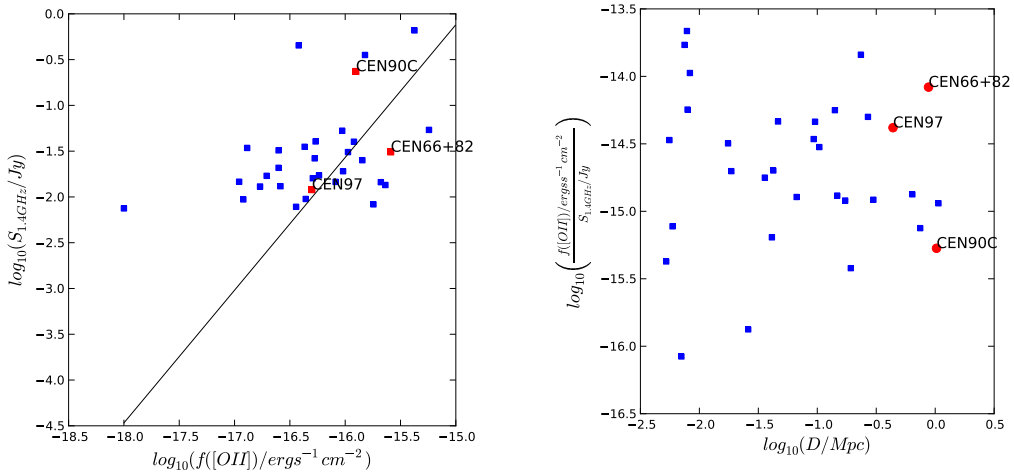

Figure 3.3: On the left, the [OII] flux versus radio flux, with the relation of Rigby [2007] overplotted, showing a reasonably good fit to the sources which have measured [OII] (noting that CENSORS is a single flux-limited sample, so any relation derived using CENSORS alone will be highly biased by this). On the right, the [OII]/radio flux versus radio size for CENSORS sources with a measured [OII] line. Note that this subset of CENSORS sources is by no means complete - most of the sources are those with [OII] lying in the easily accessable 5000-8000$\mathring{A}$ range, and some brighter CENSORS sources are excluded as there are only AAT spectra available for these, which are not flux calibrated. Three CENSORS sources with uncertain hosts and only single emission lines, tentatively identified as [OII] are plotted, showing that all are consistent with other other sources in the sample with confirmed [OII].

analysed using an IDL script kindly provided by Philip Best, which takes the estimated redshift and line positions, and measures the FWHM, equivalent width, emission line fluxes, and provides a more accurate redshift. These are the parameters given in Table 3.2.

- Spectra without emission lines, but with clear absorption features had their redshifts measured by hand using the **splot** task in **IRAF**

Notes on individual sources are given below, with spectral parameters (if any) listed in Table 3.2, and spectra plotted in Figures 3.4-3.15. Spectroscopic redshifts are obtained for 10 sources (CENSORS 21, 22, 51, 69, 66+82, 64, 84+85, 90+103C, 112, 128), with a further six (CENSORS 14, 86, 94, 113, 123 and 97) more uncertain identifications. The updated redshift distribution of CENSORS as a result of these 10 new firm spectroscopic identifications may be seen in Figure 3.2.

A list of sources with no identifiable redshift, and with both optical and SINFONI spectra is given in Table 3.1. These sources have both SINFONI infrared spectroscopy, and optical spectroscopy over the ranges 0.4-0.9, 1.4-1.8 and 2.0-2.4μm, with no emission lines or distinguishing features. CENSORS 26 is the only remaining unconfirmed z>4 candidate in

the sample (see note below), being undetected in both I and K bands. CENSORS 31 and 87 have an uncertain host position and CENSORS 126 is very close to a bright star. CENSORS 25, 34, 60, 86, 91, 98, 130 and 132 have radio linear sizes and spectra consistent with being young GPS/CSS radio sources at z>1 - more likely to be enshrouded in a dusty environment and hence to display attenuation of any emission lines, or with low luminosity LERGs, such as those found in the SDSS [Best and Heckman, 2012]. The remaining 9, CENSORS 15, 19, 23, 57, 61, 73, 94, 100, 106 and 109, are all extended, steep spectrum sources with photometric redshifts in the range z=1.2-2, and are likely to be low excitation radio galaxies in the redshift desert (cf Chapter 6).

3.5.1 Notes on Individual Sources

CENSORS 14 displays a featureless continuum in previously taken optical spectra. The K-z estimated redshift is z∼1.445. The SINFONI spectrum (Figure 3.7) shows faint continuum, and a possible line feature at ∼1.5-2σ significance at 15789$\mathring{A}$. This feature falls very close to where Hα would be expected to be from the K-z estimate, with a z=1.41. Whilst this feature is not strong enough to make a firm identification, it does add weight to the K-z estimated redshift.

CENSORS 21 Strong continuum and one single line is detected (cf. Figure 3.4), which is identified as [OII], with z=1.26. This is consistent with the K-z estimate of z=1.21.

CENSORS 22 Weak continuum and one single line is detected as shown in Figure 3.4. The line shape is not consistent with the broad profile of MgII, and the line is unlikely to be Lyα, given that faint continuum is seen blueward of the line. Assuming it is [OII], the redshift is consistent with K-z redshift estimate of z=0.91.

CENSORS 26 CENSORS 26 is a single bright 2.1" radio source with no detection in either the I or K band (to a limiting magnitude of K∼20.9). 1.5 hrs on source revealed no firm detection of any continuum or emission lines with EFOSC2 (there is a very faint feature at 9000$\mathring{A}$, highlighted in Figure 3.8, but this is too faint to draw any definitive conclusions). A 45 minute integration with SINFONI shows only a very low significance possible feature at 14638$\mathring{A}$, approximately 2 arcseconds away from the radio position (see Figure 3.8). CENSORS 26 is now one of only three sources in the sample to have no continuum or emission lines detected in the optical, and without strong lines in the infrared (implying that it is not simply a 'redshift desert' source). This leaves only two likely options, that CENSORS 26 is either very high redshift and the Lyα emission line is either very faint or falls in between the ranges of the optical and infrared observations, or that it is a highly obscured AGN at more moderate redshift. CENSORS 26 displays a negatively curved radio spectrum, with an ultra-steep spectral index $\alpha^{8GHz_z}_{1.4GHz}$=−1.2, and a $\alpha^{1.4GHz_z}_{325MHz}$=−0.9. It is undetected at 74 MHz, suggesting that there is likely to be a turnover in the spectrum around 100-200 MHz. This is very similar to the radio spectrum displayed by TNJ029, the currently highest redshift radio source known at z=5.2. TNJ029 also has a very faint K-band magnitude of K∼21.3, a detection fainter than the limit of

the available K-band data for CENSORS 26. If Lyα does indeed fall outside of the optical window, this suggests a z$\geq$6.4. Further imaging observations in the far-infrared and/or sub-mm, or wide range spectroscopy (e.g. XSHOOTER) will be required to constrain the redshift for CENSORS 26. The K-z limit estimate of z=4.45 is hence retained for this source.

CENSORS 31 CENSORS 31 is a double source with an uncertain host position, having no detections in the optical or the K-band between the two lobes. SINFONI observations failed to detect the host, so the K-z limit estimate of z=2.47 is retained.

CENSORS 51 Optical spectra gave no detection for this source, however a 40 min integration with SINFONI revealed a clear [OIII] doublet and Hα detection, placing this source at z=2.27.

CENSORS 64 CENSORS 64 has a host galaxy identification given by the new radio data presented in Chapter 2. The spectrum in Figure 3.5 is smoothed by a factor 9 over a range 3500-9000$\mathring{A}$ and shows no emission lines, but strong continuum and a clear 4000A break, giving z=0.23, which is consistent with its estimated K-z redshift of 0.33.

CENSORS 66+82 In Brookes *et al.* [2008], CENSORS 66 was identified with a z = 0.355 galaxy, offset slightly from the centre of the radio source. CENSORS 82 had no host candidate detected in either the I or K band. CENSORS 66 and 82 are separated by $\sim$ 1.7 arcminutes. As discussed in Chapter 3 these two sources are identified as individual components of a large radio galaxy, with new radio observations. There is a galaxy located on the axis between these two sources with K-band magnitude K=17.8, and this was targetted with EFOSC2. The spectrum in Figure 3.4 shows faint continuum and only one strong emission line, which is identified as [OII], given that the [OII] flux, radio flux and radio size measured is also consistent with other extended sources in the sample (cf. Figure 3.3). The redshift for CENSORS 66+82 is hence z=1.034.

CENSORS 69 The spectrum of CENSORS 69 in Figure 3.5 shows a strong Lyα line and a weak confirming CIV line, along with very faint continuum redwards of Lyα. This places it at z=4.11, the highest redshift radio galaxy in the CENSORS sample, and the sixth highest redshift radio galaxy known at the time of writing.

CENSORS 84+85 CENSORS 84 and 85 are confirmed as components of a single giant radio galaxy in Chapter 2. K band imaging shows the host to be a bright K=13.1 galaxy, located within a small group. Multiple bright emission lines (cf. Figure 3.4) place this source at z=0.107.

CENSORS 86 A previous VLT spectrum shows that the identified central K-band host of CENSORS 86 in the optical shows a featureless continuum, with no clear emission lines or absorption features [Brookes *et al.*, 2008]. The EFOSC2 spectra (Figure 3.10), covering a longer wavelength range than the original VLT spectrum, gave a similar result, but of poorer resolution as the seeing was poor during the observation. However, there is also

another galaxy about 1.5" away, with an equivalent K-band magnitude. Spectra of this galaxy shows a clear 4000A break, placing the galaxy at z=0.81. The SINFONI spectra show featureless continuum for both galaxies. Radio data shows an unresolved source, with an inverted spectrum, giving rise to the possibility that CENSORS 86 is a compact unresolved core-jet source, possibly triggered by an ongoing interaction between the two galaxies. As the K-band magnitudes of both galaxies suggest that they are at a similar redshift (z=0.82), and their close proximity to one another is suggestive of a relation-possibly even a merging system, and this adds significant weight to the K-z estimate of z=0.82 for this source.

CENSORS 87 This is an extended, radio source with no identifiable host in either the optical or K-band (the host position is highly uncertain due to the odd shape of the radio source). The SINFONI spectrum shows no detection, and so the K-z limit estimate of z=2.72 is retained.

CENSORS 90+103C The radio data for CENSORS 90 and 103 are inconclusive as to whether these are two individual sources, or components of a single much larger radio galaxy, due to their proximity to several other, unrelated radio sources (see Chapter 2). There are no detected host candidates in deep K-band observations around either of the radio sources. Blind spectra have been previously taken by Brookes *et al.* [2008] at the radio position of both sources, with no detections. There is, however, a faint unresolved possible radio core candidate directly in the middle of the axis defined by the two radio sources, associated with a faint K=17.8 source. This source was targetted, and continuum and a single line detected, which is identified as [OII] given the consistency with the K-z estimated redshift. The [OII] flux, radio flux and radio size measured are also consistent with other extended sources in the sample (cf. Figure 3.3). The [OII] flux would be unusually bright for the radio flux of just the radio central component alone . This gives a redshift for the source of z=0.62. Whilst the possibility of these two sources being unrelated cannot be ruled out, the spectroscopic detection of the radio core candidate, with an emission line of appropriate flux density at an appropriate redshift, combined with the lack of any host detection at the two 'lobes' argues in favour of the single source identification, and the redshift of z=0.62 is adopted for CENSORS 90+103.

CENSORS 91 CENSORS 91 has a faint featureless continuum in the optical, as presented by Brookes et al. (2008). There is a possible line feature at 8421$\mathring{A}$, which if [OII] would be consistent with the K-z estimate of 1.24, however this is highly uncertain as it lies directly on a sky line. Strong continuum is detected in the SINFONI observation, but no lines. Hence the K-z redshift estimate of z=1.24 is retained.

CENSORS 94 CENSORS 94 has only a very faint continuum detection in the optical. The SINFONI integration reveals faint continuum emission, and a very faint ($\sim 2\sigma$) possible line detection, which if Hα, would place the source at z=1.716 (see Figure 3.11). As this is too faint to be a firm detection, the K-z estimate of z=1.648 is retained for this source.

CENSORS 97 CENSORS 97 has a very faint optical spectrum, and a low significance line at 7092$\AA$ (Figure 3.6). It has not yet been targetted with SINFONI. Although this potential line is very weak, it is not a cosmic ray or residual skyline, and is a genuine feature in all three 30 minute exposures. It is not possible to determine the line shape due to the low signal to noise. The K-z estimate for this source is z=1.63: if the line was [OII] this gives a z=0.898, and if the line was MgII, this gives z=1.534, both of which are within the scatter observed in the K-z relation. If the line is assumed to be [OII], this in addition to the other observed properties of the source is consistent with other confirmed [OII] emitters in the CENSORS sample (see Figure 3.3). Given the ambiguity in the line identification, the K-z estimate for this source is retained.

CENSORS 112 Optical spectra gave no detection for this source, however a 40 min integration with SINFONI revealed a clear single line, and one lower significance line, consistent with the [OIII] doublet, placing this source at z=1.99, firmly in line with the K-z estimate for this source.

CENSORS 113 CENSORS 113 in the optical shows faint continuum (Figure 3.6), with a possible faint line detection, although this is next to a sky line, and therefore not possible to distinguish definitively. The SINFONI spectrum shows only featureless continuum. If the line was [OII], this would place the source at z=1.048, adding weight to the K-z estimate for this source of z=0.94.

CENSORS 123 CENSORS 123 has only one 30 min exposure due to a power failure at La Silla whilst observing with the NTT. From the single exposure, faint continuum is visible (Figure 3.6), with no clear emission lines, but a possible 4000A break present at z=0.86. This would be consistent with the estimate from the K-z relation, at z=0.825. However, because this spectrum has very low signal to noise, and hence is very uncertain, the K-z estimate is retained.

CENSORS 126 Brookes *et al.* [2006] presented two possible hosts for this source. The first, brighter candidate they ruled out as a host, as subsequent spectroscopy identified it as a star. The second candidate was noted as the probable host galaxy, albeit with considerable uncertainty as it lies a little off the axis between the two radio components. This second host candidate has never been followed up spectroscopically. The SINFONI spectra shown in Figure 3.14 confirm that the second host candidate is also a star, and show no evidence for any other candidates in the vicinity. It is therefore likely that the true host lies behind one of these stars. The radio size of 38 arcseconds would suggest that the source is not at very high redshift - 90% of the CENSORS complete sample with radio sizes greater than 30 arcseconds have z$\leq$1.5. The large size in combination with the steep spectral index α=-1.05 also adds weight to this - large radio sources with steep spectra tend to be located at z$\leq$1.0 (cf Chapter 4). CENSORS 126 is most likely an old radio source associated with a low redshift cluster. As the SINFONI data are very recent, the K-z estimate of 0.38 was retained for this source in subsequent studies in this thesis, but for future work, it should be removed from the sample.

CENSORS 128 CENSORS 128 was misidentified in Brookes *et al.* [2006], and is in fact associated with a K=17.81 host. Strong Lyα, Si & [OIV], and CIV lines place this source at z=3.71. The Lyα and CIV lines are broad, and this in conjunction with the very bright K-band magnitude means that this source is a quasar.

Table 3.2: Optical and Infrared Spectroscopy Results for CENSORS. Col1: Source Name, Col2: Photometric redshift, Col3: Observing run identification (as in Table 3.1) Col4: Exposure time, Col5: Emission line, Col6: Emission line observed wavelength, Col7: Observed emission line flux, Col8: δv_{FWHM} (observed frame), Col9: Equivalent Width (observed frame), Col10: Spectroscopic redshift - a ? indicates that the redshift is uncertain, and is discussed further in the text.

CEN	z(K)	Run	Exp. Time s	Line	λ Obs $\AA$	Flux x 10^{-16} ergs s^{-1} cm^{-2}	δv_{FWHM} km s^{-1}	EW $\AA$	z(δz)
14	1.445	3	2700	Hα	15789	-	-	-	1.41(0.01)?
15	1.417	3	2700	-	-	-	-	-	-
19	1.205	2	3600	-	-	-	-	-	-
		3	2700	-	-	-	-	-	-
21	1.219	2	3600	[OII]	8424.4	5.72(0.66)	1139(262)	80(14)	1.2604(0.0008)
22	0.907	2	3600	[OII]	7182.9	0.94(0.15)	592(213)	86(27)	0.9272(0.0005)
23	1.929	3	2700	-	-	-	-	-	-
25	2.022	3	2700	-	-	-	-	-	-
26	4.45	2	3600	-	-	-	-	-	-
		3	2700	-	-	-	-	-	-
31	2.47	3	2700	-	-	-	-	-	-
34	1.319	3	2700	-	-	-	-	-	-
51	2.955	3	2700	[OIII]4959	16224.2				2.271(0.0004)
				[OIII]5007	16378.4				
				Hα	21470.8				
69	4.03	1	3600	Lyα	6215.2	3.43(0.35)	476(200)	84(27)	4.1108(0.0009)
				CIV	7913.3	2.39(0.27)	864(301)		
66.82	1.4	2	3600	[OII]	7580.0	2.58(0.28)	885(184)	55(7)	1.034(0.0004)

Continued on next page

Table 3.2 – continued from previous page

CEN	z(K)	Run	Exp. Time s	Line	λ Obs $\AA$	Flux x 10^{-16} ergs s^{-1} cm^{-2}	δv_{FWHM} km s^{-1}	EW $\AA$	z(δz)
57	1.196	3	2700	-	-	-	-	-	-
60	1.622	3	2700	-	-	-	-	-	-
61	1.452	3	2700	-	-	-	-	-	-
64	0.33	1	3600	K,H					0.2335(0.0084)
				G-band					
				Mg b					
73	1.364	3	2700	-	-	-	-	-	-
84.85	0.15	2	1200	[OIII]4959	5489.4	105.90(10.73)	797(224)	41(4)	0.1070(0.0011)
				[OIII]5007	5542.7	278.54(27.92)	956(215)	109(11)	
				[OI]	6981.8	9.71(1.39)	1253(357)	4(1)	
				Hα	7274.7	111.57(11.23)	1549(176)	43(4)	
				[SII]	7440.1	66.13(6.76)	1060(200)	27(3)	
86	0.82	2	3600	K,H					0.81?
		3	2700	-	-	-	-	-	-
87	2.72	3	2700	-	-	-	-	-	-
90.103	-	2	3600	[OII]	6051.9	1.25(0.14)	1065(259)	63(9)	0.624(0.0004)
91	1.242	2	3600	-	-	-	-	-	-
		3	2700	-	-	-	-	-	-
94	1.648	3	2700	Hα	17821.8	-	-	-	1.716(0.0028)?
97	1.635	2	3600	[OII]	7080.3	0.5(0.13)	1491(592)	55(22)	0.898(0.0035)?
98	1.635	3	2700	-	-	-	-	-	-
100	1.288	2	3600	-	-	-	-	-	-
		3	2700	-	-	-	-	-	-

Continued on next page

Table 3.2 – continued from previous page

CEN	z(K)	Run	Exp. Time s	Line	λ Obs $\AA$	Flux x 10^{-16} ergs s^{-1} cm^{-2}	δv_{FWHM} km s^{-1}	EW $\AA$	z(δz)
104	0.884	3	2700	-	-	-	-	-	-
106	1.285	3	2700	-	-	-	-	-	-
109	0.719	2	3600	-	-	-	-	-	-
		3	2700	-	-	-	-	-	-
112	1.75	3	2700	[OIII]5007	14947.4				1.985(0.0006)
				Hα	19595.5	-	-	-	-
113	0.942	2	3600	[OII]	7633.2	-	-	-	1.048(0.001)?
		3	2700	-	-	-	-	-	-
123	0.825	2	3600	-	-	-	-	-	0.86?
		3	2700	-	-	-	-	-	-
126	0.382	3	2700	-	-	-	-	-	-
128		2	3600	Lyα	5754.2	16.35(1.66)	5285(593)	121(15)	3.719(0.005)
				NV	5849	4.21(0.44)	1548(477)	28(3)	
				SiV/OIV	6608.2	1.93(0.25)	2529(1613)	14(2)	
				CIV	7309.5	5.07(0.59)	5581(1922)	44(6)	
				HeII	7751.9				
				CIII	9018.9				
130	2.878	3	2700	-	-	-	-	-	
132	2.545	3	2700	-	-	-	-	-	

Table 3.1: CENSORS Sources with both SINFONI and Optical Spectra, but no Redshift.

CEN	I	K	z(K)	α	θ/arcsec	Notes
15	20.57	18.2	1.417	-1.05	6.1	
19	-	17.94	1.205	-0.97	23.9	
23	-	18.66	1.929	-1.07	21.7	
25	-	18.73	2.022	-0.38	0.7	GPS/CSS source
26	-	>20.6	>4.45	-0.97	2.1	uncertain host
31	-	>19.4	>2.47	-0.97	28.5	uncertain host
34	24.95	18.09	1.319	-0.14	0.9	GPS/CSS source
57	22.19	17.93	1.196	-0.82	22.5	
60	23.48	18.41	1.622	-0.59	0.8	GPS/CSS source?
61	-	18.24	1.452	-1.00	21.3	
73	-	18.14	1.364	-0.92	15.8	
86	23.0	17.26	0.82	-0.62	1.3	GPS/CSS source?
87	-	>19.6	>2.72	-0.99	9.4	uncertain host
91	22.43	17.99	1.242	0.32	1.3	GPS/CSS source
98	-	18.42	1.635	-0.13	1.1	GPS/CSS source
100	23.77	18.62	1.288	-1.10	4.7	
106	21.96	18.05	1.285	-0.60	5.6	
109	-	17.01	0.719	-0.91	3.9	
126	-	-	-	-1.06	38.3	Next to bright star
130	-	19.19	2.878	-0.53	1.2	GPS source
132	-	19.03	2.545	-0.52	2.7	GPS source

3.6 Summary

All 38 sources without a spectroscopic redshift in the CENSORS sample have been targetted with either optical or near-infrared spectroscopy, and in some cases both. Secure spectroscopic redshifts have been obtained for 10 of these sources, with a further 6 with a more uncertain redshift. After analysis of this new spectroscopy in conjunction with existing radio data, two sources CENSORS 90 and 103 are now thought to be components of a single larger source. CENSORS 128 and CENSORS 69 are shown to be the two highest redshift objects in the sample, at z=3.72 and z=4.11 respectively. CENSORS 69 is particularly interesting, as it is only the third of the nine now known z>4 radio galaxies to have been located through anything other than an ultra-steep spectrum radio sample. 21 sources have both SINFONI infrared spectroscopy, and optical spectroscopy over the ranges 0.4-0.9, 1.4-1.8 and 2.0-2.4μm, with no emission lines or distinguishing features.

These observations bring the spectroscopic completeness of the CENSORS sample up to 80%, and gives CENSORS one of the largest redshift ranges of any complete radio sample currently in existence[2]. Of the ten secure spectroscopic redshifts, six have spectroscopic redshifts generally consistent with the K-z estimate calculated by Brookes *et al.* [2008]. This suggests

[2]Note that in the subsequent analyses presented in this thesis, only spectroscopic redshifts for CENSORS 21, 22, 51, 69, 66+82, 84+85, 112 and 128 are updated in the sample (78% spectroscopic completeness) due to variations in data collection times.

that the main conclusions of that study; that the established K-z relation for CENSORS is fainter than 3CRR, and agrees well with that measured for the 7C sample, remains valid. In more recent work, Rigby *et al.* [2011] measure the evolution of the steep spectrum radio luminosity function from a combination of complete samples. Several of the new host galaxy identifications presented here are already included in the study, and given the consistency with the K-z relation for the majority, these new updated redshifts will have a negligible effect on the conclusions of this work also.

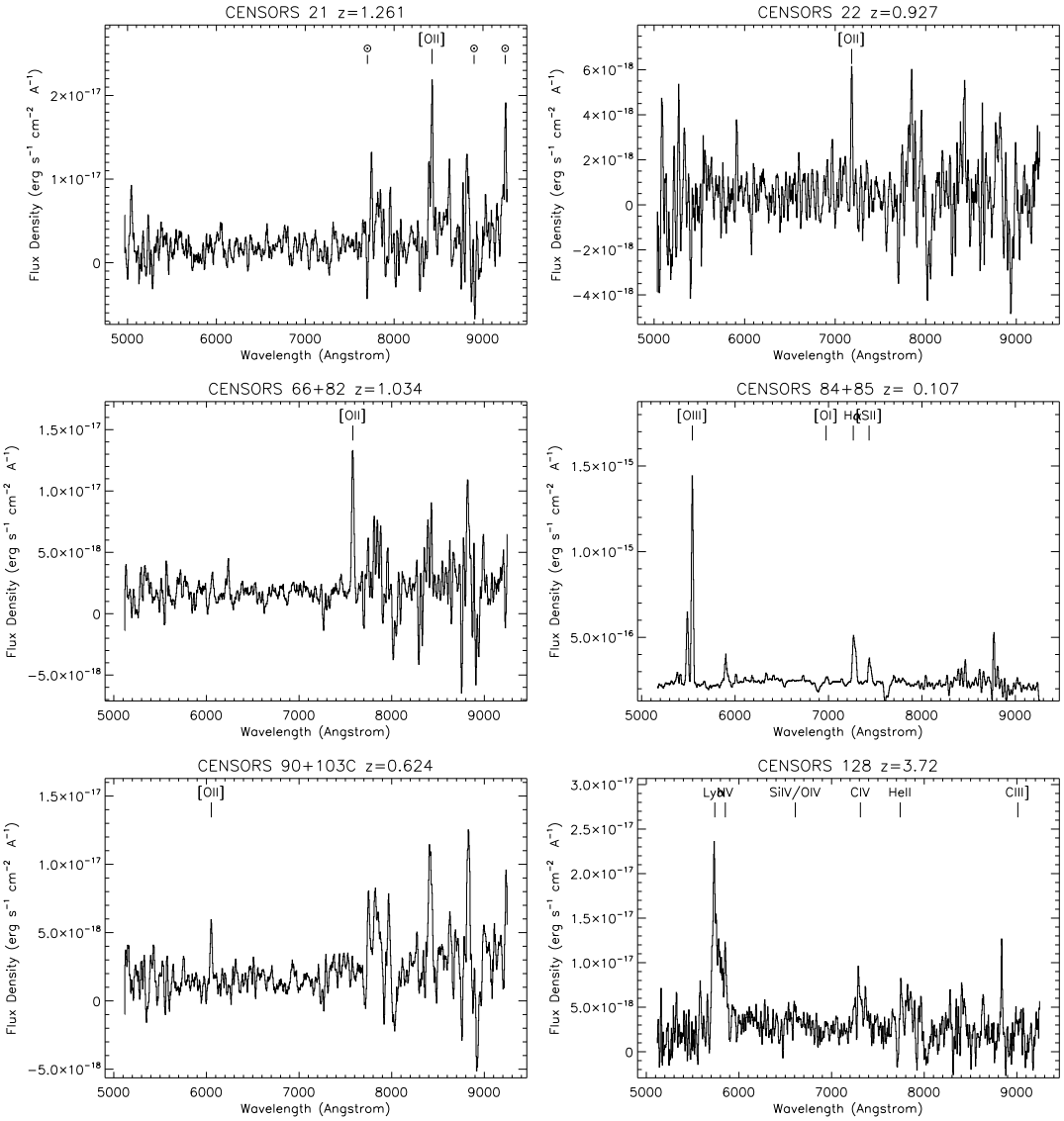

Figure 3.4: EFOSC2 CENSORS Spectra with confirmed redshifts.

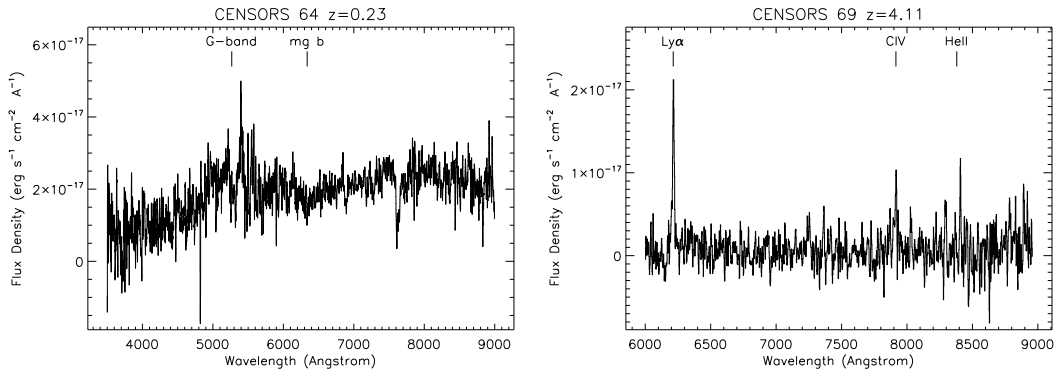

Figure 3.5: WHT CENSORS Spectra with confirmed redshifts, including the highest redshift radio galaxy in the sample, CENSORS 69, at z=4.11.

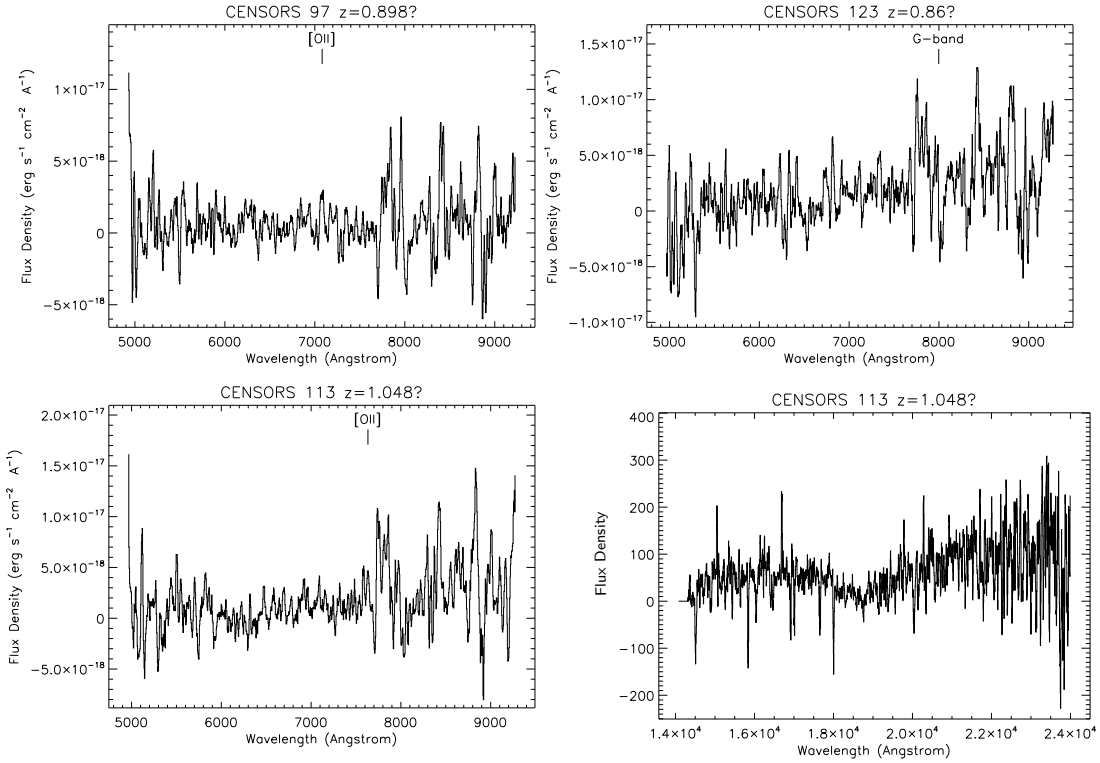

Figure 3.6: CENSORS Spectra with less certain redshifts. Plotted are EFOSC2 spectra for CENSORS 97 and 123 on the top, and the EFOSC2 (bottom left) and SINFONI (bottom right) spectra for CENSORS 113.

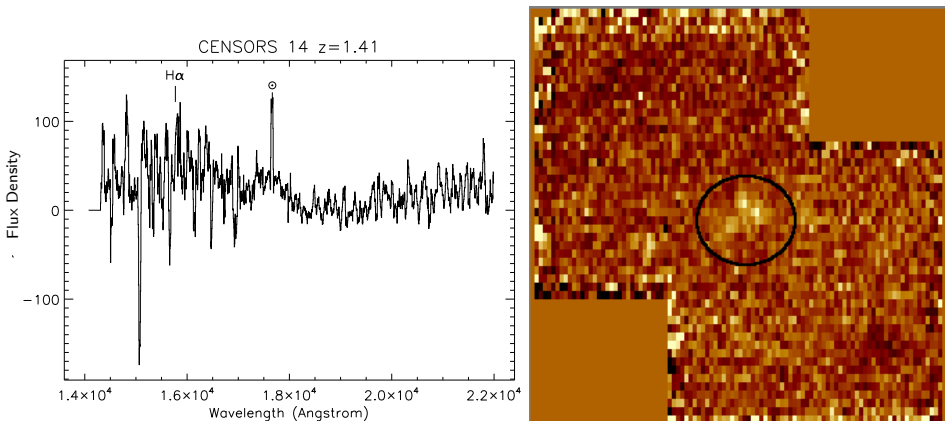

Figure 3.7: A very tentative identification of the Hα in a 2700s SINFONI observation of CENSORS 14. Note that the SINFONI spectrum is not flux-calibrated.

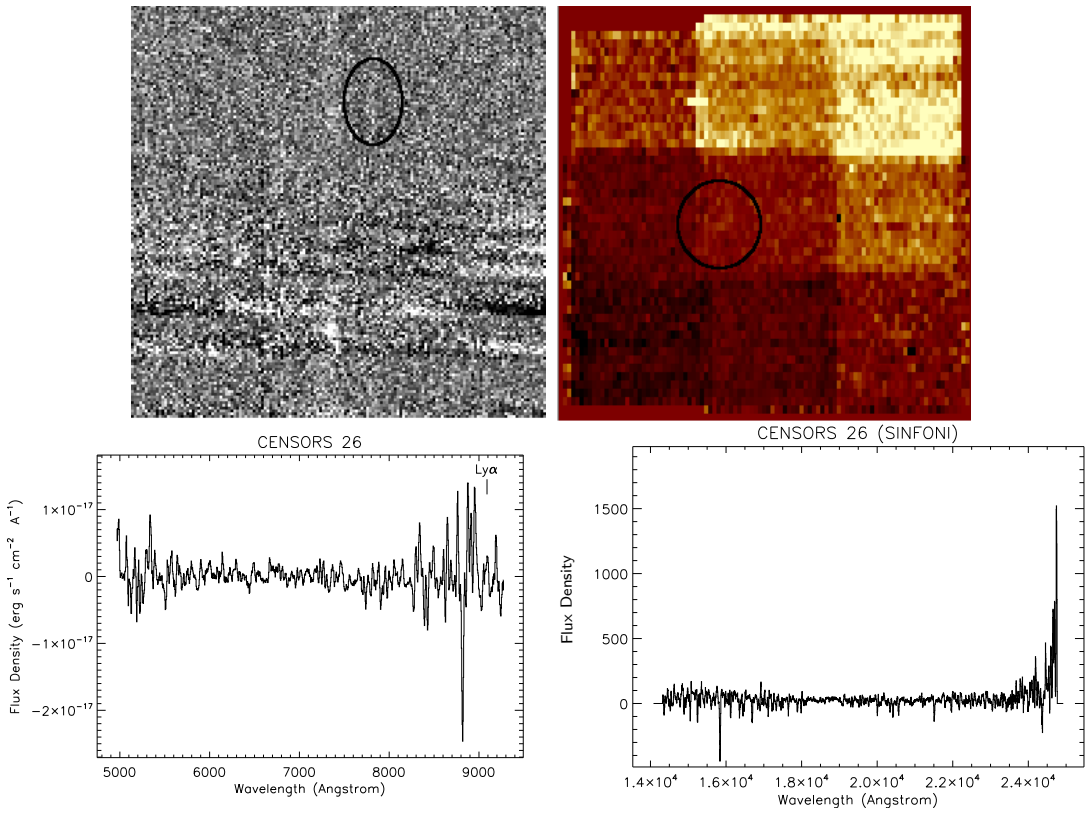

Figure 3.8: The EFOSC2 spectrum for CENSORS 26 (left) shows a faint feature at around 9000$\mathring{A}$. There is a further possible very low significance SINFONI line detection (right), approximately 2 arcseconds away from the radio position in CENSORS 26, at 14638$\mathring{A}$. Note that the SINFONI spectrum is not flux-calibrated.

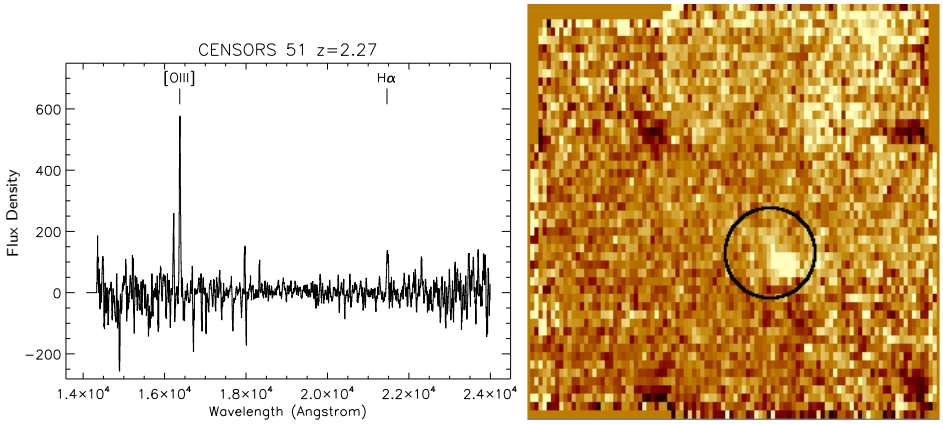

Figure 3.9: Strong SINFONI detection of two lines in CENSORS 51, consistent with [OIII]. Note that the SINFONI spectrum is not flux-calibrated.

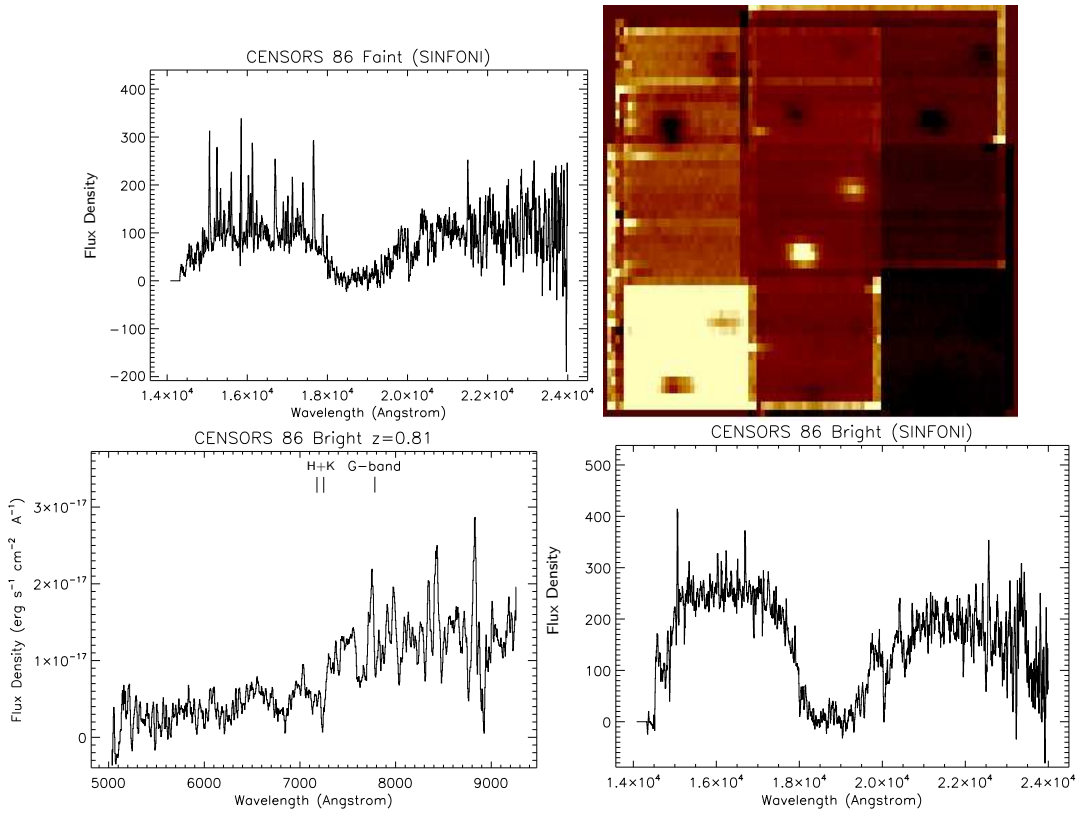

Figure 3.10: EFOSC2 and SINFONI spectra for CENSORS 86. CENSORS 86 is identified with a faint host, seen in the top right of the SINFONI median image. There is a brighter source less than two arcseconds away. The faint host candidate shows featureless optical continuum, and also featureless continuum in the SINFONI spectrum (top left), with no redshift determination possible. The brighter source shows a clear break in the optical (bottom left) giving z=0.81.

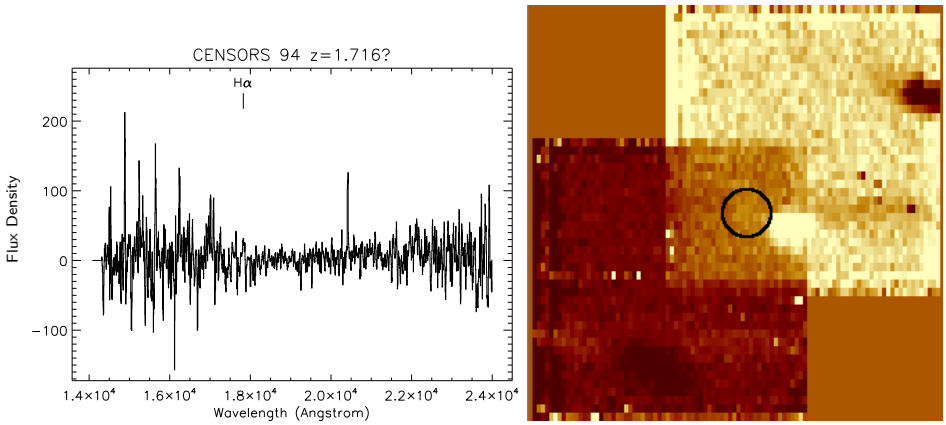

Figure 3.11: There is one possible low significance SINFONI line detected at 17828$\mathring{A}$, which would be consistent with Hα. Note that the SINFONI spectrum is not flux-calibrated.

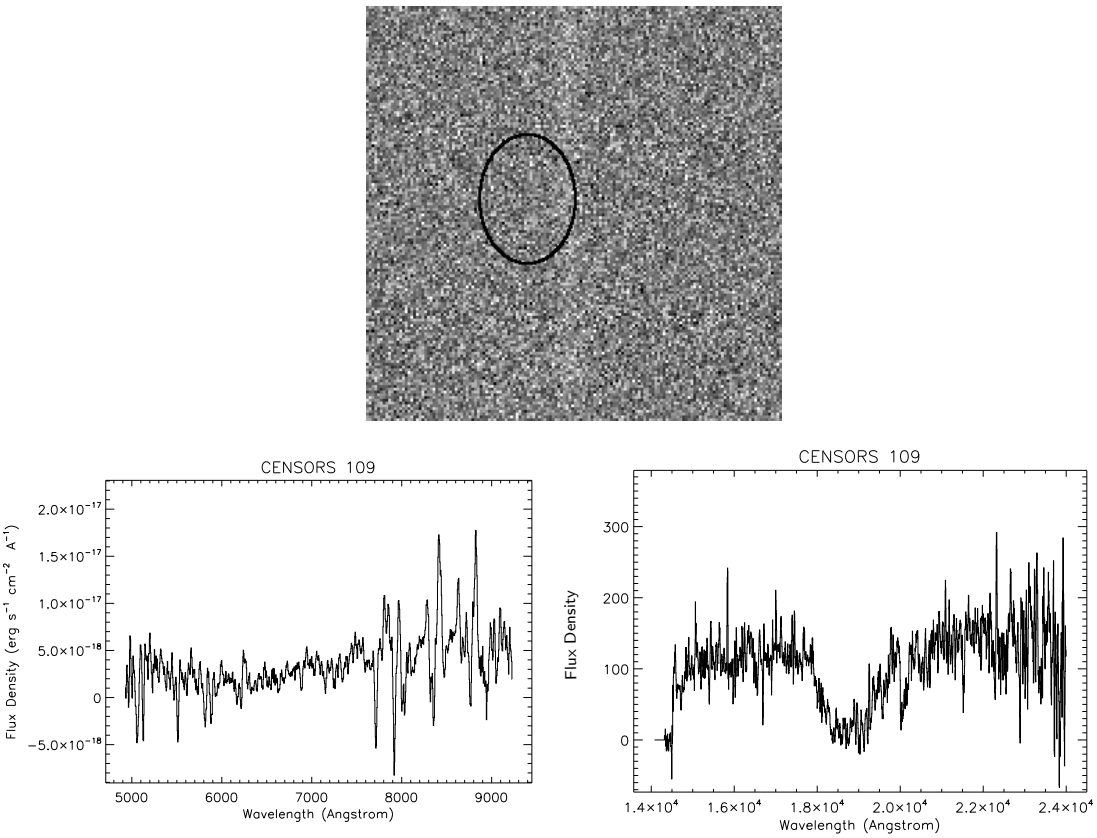

Figure 3.12: CENSORS 109 shows featureless continuum in both the optical (top) and SINFONI spectra (bottom). It is worthwhile noting that there is a faint, but genuine line detection approximately three arcseconds away from the K-band position seen on the EFOSC2 spectrum (circled above).

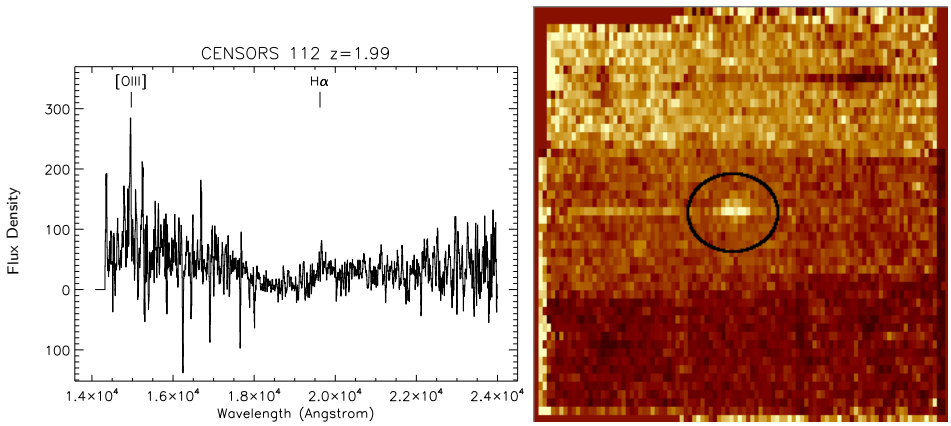

Figure 3.13: Firm detection of the [OIII] doublet and Hα emission lines place CENSORS 112 at a redshift of 1.99. Note that the SINFONI spectrum is not flux calibrated.

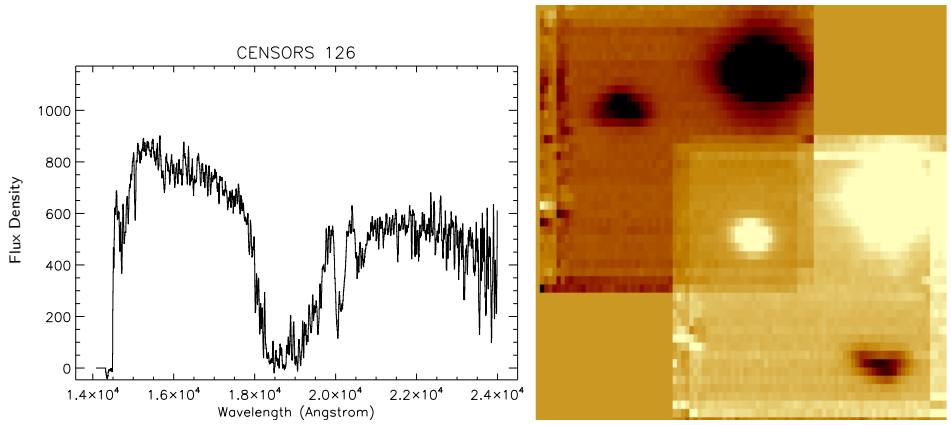

Figure 3.14: The second host candidate for CENSORS 126 is likely to be a star. There are no other host candidates in the vicinity visible in the SINFONI observations.

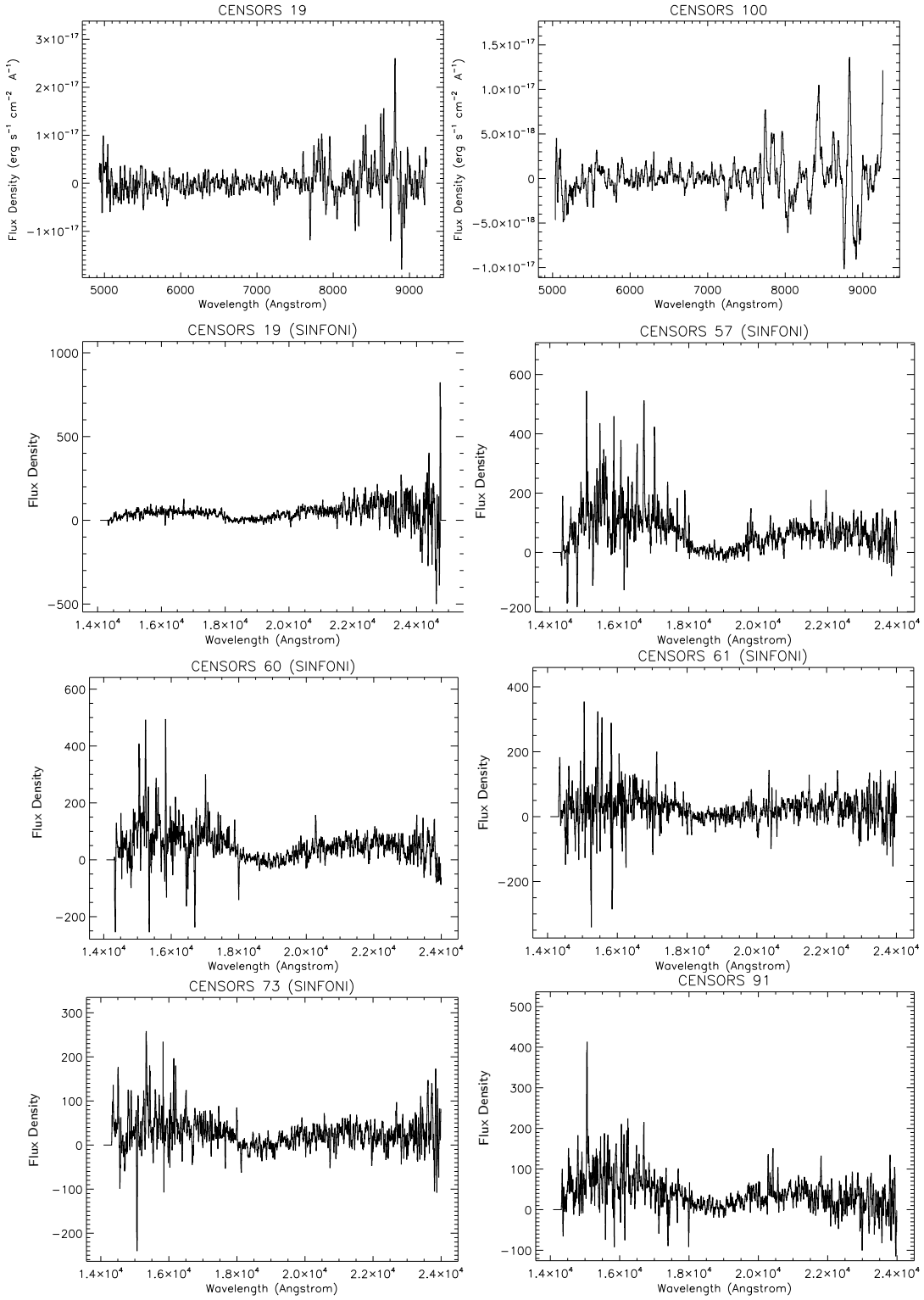

Figure 3.15: EFOSC2 and/or SINFONI CENSORS Spectra showing faint continuum, but with no confirmed redshifts.

Chapter 4

New Insights on the z-α Correlation from Complete Radio Samples

The content from this chapter has been published in the journal Monthly Notices of the Royal Astronomical Society.

L.M. Ker, P.N. Best, E.E. Rigby, H.J.A. Röttgering, M. Gendre. "New Insights on the z-α Correlation from Complete Radio Samples", MNRAS, 420, 2644-2661, 2012.

4.1 Introduction

Vast amounts of multi-frequency radio data at long wavelengths will soon begin to flow from next generation radio instruments such as the LOw Frequency ARray (LOFAR) and eventually the Square Kilometre Array (SKA). With this, opportunities will arise for studying some of the earliest radio sources in the universe, their environments and their evolution over cosmic time. There is also the tantalizing possibility of studying conditions within the Epoch of Reionisation itself through high-z radio sources: if sufficiently bright radio sources can be found at redshifts greater than 6.5, it should be possible to measure absorption signatures of neutral hydrogen, and hence trace changes in the ionisation state of the Universe with cosmic time [e.g. Carilli *et al.*, 2007; Meiksin, 2011].

The existence of a correlation between redshift and observed spectral index α[1] for powerful radio sources was first suggested by Tielens *et al.* [1979] who found that the introduction of a steep spectral index cut led to an increasing fraction of sources without optical counterparts identified on POSS-I ($R < 20$) plates. Blundell *et al.* [1999] used the combination of complete samples from the 3CRR [Laing *et al.*, 1983], 6CE [Rawlings *et al.*, 2001] and 7CRS [Willott

[1] where $S_\nu \propto \nu^\alpha$

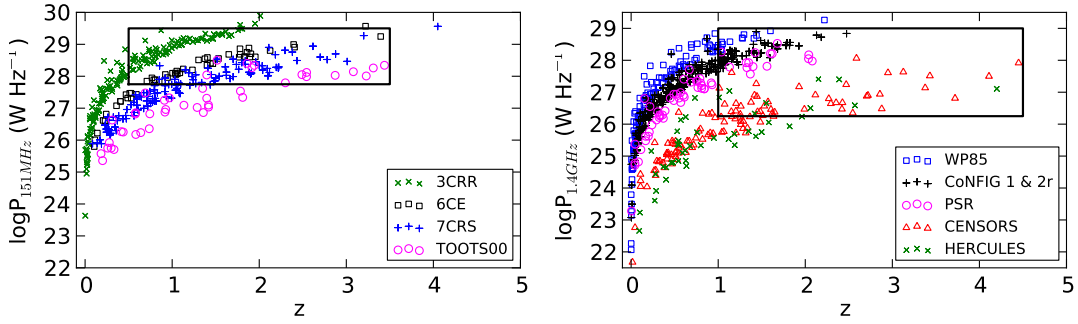

Figure 4.1: Radio luminosity vs redshift plane coverage for the low frequency selected samples 3CRR, 6CE, 7CRS and TOOTS (left) and for the high frequency selected samples WP85r, PSRr, CoNFIG 1 & 2r, CENSORS and Hercules (right). Only sources with $\alpha < -0.5$, as used in this study are shown. The boxes indicate the Malmquist-bias-free sections of the P-z plane at high and low frequency, whichIuse in later analysis, for 151 MHz samples: logP=27.75-29.5, z=0.5-3.5, and for 1.4 GHz samples: logP=26.25-29.0, z=1.0-4.5.

et al., 2003; Lacy *et al.*, 1999] surveys to confirm that the high frequency (5 GHz) rest-frame spectral index correlates with redshift, but showed that this correlation is weaker for spectral index measured at lower rest-frame frequencies. Since then, there have been many surveys designed to pick out only Ultra Steep Spectrum (USS) sources for further infra-red imaging and spectroscopic follow-up [e.g. Röttgering *et al.*, 1996; de Breuck *et al.*, 2000], having varying degrees of success selecting high-z sources. Many of these have additional selection criteria such as small angular size and faint infrared magnitude applied after the USS cut, which makes it difficult to determine the extent to which the USS cut is responsible for selecting high-z sources.

Klamer *et al.* [2006] present a sample of USS selected galaxies selected from the Sydney University Molonglo Sky Survey (SUMSS), and discuss the apparent mechanisms for the z-α correlation in detail. They dismiss the possibility of k-corrections being the cause of the observed steepening radio spectra, given that the majority of their radio spectra show no evidence for curvature. They suggest that enhanced spectral aging due to inverse Compton losses against the Cosmic Microwave Background (CMB) at high redshift is the most likely origin for the observed z-α correlation, or that it may arise due to an intrinsic relation between low frequency α and radio luminosity coupled to a Malmquist bias. Following on from this work, Bryant *et al.* [2009] compare the median redshift of several complete samples with the median redshift obtained from USS selected samples. They find it to be lower in complete samples, and argue that this is strong evidence for the efficiency of the USS technique. However whilst USS samples clearly do select higher redshift sources, sample comparisons between USS and complete samples are not ideal for either optimising or quantifying the efficiency of the technique. The most rigorous approach would be to apply a selection criterion to complete samples with significant numbers of sources at the highest redshifts currently known, and quantify the number of high redshift sources included/missed.

Despite the wide use of the z-α technique to select high redshift galaxies, there has been very little work on quantifying the efficiency. Pedani [2003] states that, for the first time,

Table 4.1: Details of the complete samples used in this study. Note that the spectral indices for CoNFIG are taken from Gendre et al. (2010), from a linear fit to flux densities between 1.4 GHz and 178 MHz, rather than a two point spectral index.

Survey	Selection ν	no. of Sources	Sky Area (sr)	Flux Limit (Jy)	% z_{spect}	% no z	α range (GHz)
3CRR	178 MHz	173	4.239	S_{178} >10.9	100	0.0	0.75-0.151
6CE	151 MHz	58	0.102	2.00<S_{151} <3.93	97	3.0	1.4-0.151
7CI	151 MHz	37	0.0061	S_{151} >0.51	90	0.0	1.4-0.151
7CII	151 MHz	37	0.0069	S_{151} >0.48	90	0.0	1.4-0.151
7CIII	151 MHz	54	0.009	S_{151} >0.50	95	0.0	1.4-0.151
TOOTS-00	151 MHz	47	0.0015	S_{151} >0.10	85	2.0	1.4-0.151
WP85r	1.4 GHz	138	9.81	S_{1400} >4	95	0.0	5.0-1.4
CoNFIG1	1.4 GHz	273	1.5	S_{1400} >1.3	83	3.6	1.4-0.178
CoNFIG2r	1.4 GHz	61	0.89	1.0<S_{1400} <1.3	52	4.9	1.4-0.178
PSRr	1.4 GHz	59	0.075	S_{1400} >0.36	61	0.0	2.7-1.4
CENSORS	1.4 GHz	135	0.0018	S_{1400} >0.0072	78	3.7	1.4-0.325
Hercules	1.4 GHz	64	0.00038	S_{1400} >0.002	66	3.0	1.4-0.61

they present the true quantitative searching efficiency for high-z radio galaxies using a sample selected from the Molonglo Reference Catalogue (MRC). They utilise 225 sources with full redshift information from this sample to measure the efficiency of optical, USS and size selection. They find that the efficiency (defined as the fraction of z>2 sources in the recovered sample) of the USS criterion alone is 0.33, increasing to a maximum of ∼0.59 in combination with an optical cut. However, their 225 source sample is not complete, being composed of only objects with redshift information amongst the complete MRC 1 Jy radio sample of 446 sources. They argue that the redshift-complete subsample is representative of the full sample, as both contain similar proportions of USS sources. However they also note that the median magnitude of the subset of galaxies without redshifts is fainter than that for those included. This means firstly, that there is an optical magnitude bias towards brighter magnitudes in the analysed sample, and secondly, that the work is based on the implicit assumption that the USS criterion is more important than optical magnitude in selecting high redshift candidates. With 50% of the sample not analysed, and at fainter optical magnitudes, the redshift incompleteness towards higher redshift cannot be quantified, and this could be substantial.

Potential biases such as these are common in the literature, due to the difficulty and expense of building spectroscopically complete radio samples. As such, any attempt to use large collections of radio data available in the literature to investigate evolution of basic radio properties is not valid, despite the large number statistics, without clearly defined and well understood selection criteria. For example, recent work by Khabibullina and Verkhodanov [2009] uses a large sample of 2442 radio galaxies with measured redshifts selected from large publicly available radio source catalogues. They determine the dependence of α on z, and select a sample of distant objects using this relation. Crucially however, as they note, the samples they use are not complete in any sense, and some of the largest high-z radio source samples with radio spectra publicly available are ones with an USS criterion applied [e.g. de Breuck *et al.*, 2000] which will irrevocably bias spectral index studies of any sample contructed from them.

In summary, although the existence of the so-called z-α correlation has been known for some time, there has been little attempt to quantify the strength of this consistently across a wide

range of spectroscopically complete samples at different selection frequencies, and measure the resultant efficiency of using an USS α cut-off in order to isolate high-z candidates. In this study, these shortcomings are addressed, thus providing a vital tool for the design of further high-z source searches from upcoming radio surveys by new survey instruments, e.g. LOFAR. This work builds significantly on current knowledge in five ways:

- Nine highly spectroscopically complete and unbiased radio source samples are used. Most have a spectroscopic completeness in the range 80-100%, and robust redshift estimates (e.g. photometric or based on the K-z relation) are available for the vast majority of the remaining sources, such that all samples are at least 95% redshift-complete.
- New radio data from the CENSORS radio sample [Best *et al.*, 2003] is utilised, which contains a large number of sources with z $>$ 2, improving high redshift statistics.
- Selection frequency effects are fully explored - four samples are selected at frequencies below 200 MHz, and five at 1.4 GHz.
- The samples have a wide range of flux density limits, so that correlations such as the P-α and z-α relations may be safely disentangled.
- Radio linear size (D) is also considered in order to investigate its role in selecting high redshift sources.

The layout of this Chapter is as follows. In Section 4.2 the complete radio samples used in this study are described in detail. In Section 4.3 a brief summary of radio source properties and sample selection effects is given. In Section 4.4 observable trends are investigated and principal component analysis employed to identify fundamental correlations in the PDαz parameter space for various collections of samples. In Section 4.5 an attempt is made to fit various functional forms for α to the observed data, which identifies a large intrinsic scatter in α, not dependent on P, z or D. In Section 5.6 the physical origins of the observed z-α correlation are discussed, and finally in Section 5.7 the implications of these findings in the search for the highest redshift radio galaxies are outlined, and complete samples are then used to explore the efficiency of often used techniques in the literature to find these.

4.2 Complete Radio Samples Selection

A quantification of the z-α correlation at a wide range of frequencies and flux density limits is required, as is an investigation into the extent to which this is an intrinsic property of sources (rather than being driven by, for example, a P-α correlation), in addition to understanding any selection effects present. In order to do this, data is collated from several complete samples already available in the literature: the 3CRR, 6CE, 7CRS and TOOTS-00 selected at low frequency, and the WP85r, CoNFIG1&2, PSRr, CENSORS, and Hercules samples selected at high frequencies. These samples are described below, summarised in Table 4.1, and displayed on the P-z plane in Figure 4.1. A full listing of the samples used is included at the end of this Chapter.

4.2.1 The 3CRR Sample

The 3CRR, or Third Cambridge Revised Revised sample of extragalactic radio sources [Laing *et al.*, 1983], is a complete sample containing all radio sources above 10.9 Jy at 178 MHz in an area of sky covering 4.239 sr. The sample comprises 173 objects in total, and is 100% spectroscopically complete. The data were obtained from the 3CRR catalogue webpage maintained online[2]. As this sample is the only low frequency selected sample observed at 178 MHz as opposed to 151 MHz, the flux densities are converted to 151 MHz fluxes assuming the spectral indices given in the catalogue. The observed spectral index α is measured between 750 MHz and 178 MHz for this sample.

4.2.2 The 6CE Sample

The 6CE sample is based on a original sample selected by Eales [1985] from the Sixth Cambridge radio survey (6C) comprising of 67 radio sources between 2.2 Jy and 4 Jy selected at 151 MHz, over a sky area of 0.102 sr. For this study, I use a reselected, updated version, available online[3], the 6CE sample of Rawlings *et al.* [2001]. This consists of all sources with a 151 MHz flux density in the range $2.00 \geq S_{151} \geq 3.93$ Jy in the same 0.102 sr patch of sky. There are 59 sources in total, with all but one having a firm identification, and 56 of the 59 having spectroscopic redshifts. Of the three sources without spectroscopic redshifts, one is obscured by a bright star and so is excluded from the sample, and the other two have a redshift estimate from the K-z relation. Observed spectral indices have been calculated between 1.4 GHz and 151 MHz using 1.4 GHz fluxes obtained from the NVSS.

4.2.3 The 7CRS Sample

The 7CRS, or Seventh Cambridge Redshift Survey is composed of three subsamples, 7CI, 7CII and 7CIII. 7CI and 7CII are each composed of 37 sources with flux density limits of $S_{151} \geq 0.51$ Jy and $S_{151} \geq 0.48$ Jy respectively in the 7C survey and are defined in Willott *et al.* [2003]. The redshifts and linear sizes for the 7CI & 7CII samples are available online from the data of Grimes *et al.* [2004][4]. The 7C-III sample contains 54 objects with a flux limit of $S_{151} > 0.50$ Jy, detailed in Lacy *et al.* [1999]. The 7CIII data from Table 8 in Lacy *et al.* [1999] is utilised to get the redshifts and linear sizes of the sample.

The spectral indices for this sample are not yet available in a collective form in the literature. The observed spectral index is estimated by cross-matching 151 MHz fluxes for each source from the 7C 151 MHz catalogue of Hales *et al.* [2007] with the NRAO VLA Sky Survey [NVSS; Condon *et al.*, 1998], at 1.4 GHz. All extended sources listed in the 7C Hales catalogue as having separate components were checked, and maps at 151 MHz were cross-checked with NVSS maps in order to correctly identify components and catalogue the correct integrated flux for each source. The source list was also matched with the TEXAS 365 MHz/WENSS 327 MHz surveys, the 5C 408 MHz survey, and finally the VLA Low Frequency Sky Survey at 74 MHz

[2] `http://3crr.extragalactic.info/`
[3] `http://www-astro.physics.ox.ac.uk/~sr/6ce.html`
[4] `http://www-astro.physics.ox.ac.uk/~sr/grimes.html`

[VLSS; Cohen *et al.*, 2007] with the addition of the 38 MHz 8C survey for 7CIII [Lacy *et al.*, 1999], all of which are of comparable resolution, for later curvature analysis (see Section 6, and Chapter 5). Note that it is possible that very extended sources may not have correct fluxes in these catalogues.

7CI and 7CII both have 90% spectroscopic redshift completeness, and 7CIII is 95% complete. The remaining sources in all three subsamples have photometric redshifts estimated from the K-z relation.

4.2.4 The TOOTS-00 Sample

The TOOT00 region, [Vardoulaki *et al.*, 2010], is the first complete region of the Tex-Ox-1000 redshift survey of radio sources. This survey selects all sources above 100 mJy in the Cambridge 7C 151 MHz survey, and is designed to be approximately 5 times fainter than the 7CRS, with much greater numbers. Vardoulaki *et al.* [2010] present complete radio, near-infrared and spectroscopic data or redshift estimates for the first region of the survey, comprising 47 sources. 40 of the radio sources have spectroscopic redshifts, with a further six using a redshift estimated from the K-z relation. The final source has a K-limit only and I adopt the lower redshift limit as the redshift estimate for this source (the K-band data reaches sufficient depth to place the source at high-z, and hence for the lower redshift limit to be adopted as the redshift estimate with little loss of accuracy). The observed spectral index was calculated for each source using flux data at 151 MHz and 1.4 GHz (NVSS) from Vardoulaki *et al.* [2010].

4.2.5 The Wall and Peacock 2.7 GHz Sample

The original Wall and Peacock [1985] 2.7 GHz 233 source sample covers 9.81 sr of sky, and includes all radio sources brighter than 2 Jy. The sample now stands at 98% spectroscopically complete [Rigby *et al.*, 2011]. In this study, the 138 source sample is used, reselected by Rigby *et al.* [2011] to be complete at 1.4 GHz to a flux limit of 4 Jy with a spectral index between 5 and 1.4 GHz steeper than -0.5. This re-selected sample is 97% spectroscopically complete, and the remaining three sources have photometric redshift estimates. This sample is henceforth referred to as WP85r.

4.2.6 The CoNFIG Samples

Two complete samples from the Combined NVSS-FIRST Galaxy catalogue (CoNFIG), ConFIG regions 1 and 2 [Gendre *et al.*, 2010] are utilised in this study.

CoNFIG1 contains 273 sources complete to 1.4 GHz $\geq$ 1.3 Jy, and is 83% spectroscopically complete. In CoNFIG 1, 226 sources have spectroscopic redshifts, 37 have photometric redshift estimates and 10 sources (4%) have only lower redshift limits from SDSS I-band non-detections. These non-detections are not sufficently deep to provide a useful constraint on the redshift (the SDSS limiting I-band magnitude only constrains each source to z$\geq$1). However of these 10 sources, only four have an observed spectral index steeper than -0.5, and hence should be included in the analysis (see Section 3). These four sources are chosen not to be included, as

the redshift estimate is not reliably constrained, and such a small fraction will have a statistically insignificant effect on the results. All four sources have very different morphological types and spectral indices, so are unlikely to be biased toward any one redshift range.

CoNFIG2 contains 132 sources and is complete between 1.3 Jy and 0.8 Jy at 1.4 GHz (only sources with 1.4 GHz fluxes less than 1.3 Jy were used from CoNFIG2, to ensure no duplication with sources also in CoNFIG1[5]). At fainter flux densities the redshift completion of CoNFIG2 is relatively low, so the sample is reselected to above 1 Jy at 1.4 GHz, creating a new sample of 61 sources which is referred to henceforth as CoNFIG2r. For this revised sample, reselecting to above 1 Jy at 1.4 GHz reduces the proportion of unidentified redshift sources to a negligible number of 3. Of these three sources, only two have a spectral index steeper than -0.5, and hence should be included in the analysis. As these two have greatly differing spectral indices and morphologies, again they are unlikely to be limited to any one redshift range, and similarly to CoNFIG1, these two sources are not included in the subsequent analysis.

The observed spectral index is taken from Gendre *et al.* [2010], calculated using a linear fit to flux data points between 1.4 GHz and 151 MHz. The CoNFIG catalogues were cross-matched with the VLSS and 7C 151 MHz [Hales *et al.*, 2007] catalogue, giving flux data at 74, 151, 365, 408, 1400, 2700 and 5000 MHz for both samples to allow curvature analysis (see Section 6, and Chapter 5). Frequency coverage for this dataset is very good: only 28 sources have no data at 74/151 MHz, and only 15 have no 2.7/5 GHz data.

4.2.7 Parkes Selected Regions

The original Parkes Selected Regions [Wall *et al.*, 1968; Downes *et al.*, 1986; Dunlop *et al.*, 1989] is a complete 178 object sample containing all radio sources brighter than 0.1 Jy over a 0.075 sr sky area at 2.7 GHz. The sample has been reselected at 1.4 GHz > 0.36 Jy as PSRr, to which flux limit there are 59 sources with an observed spectral index between 2.7 GHz and 1.4 GHz steeper than -0.5. 36 of these sources have spectroscopic redshifts, with the remaining 23 having redshift estimates from the K-z relation or photometric spectral fitting.

4.2.8 The CENSORS Sample

The Combined EIS-NVSS Survey of Radio Sources, or CENSORS sample is a 135 source sample of all radio sources with an NVSS 1.4 GHz flux density greater than 7.2 mJy in a six square degree patch of the sky centred on the ESO Imaging Survey (EIS) Patch D [Best *et al.*, 2003]. The sample currently stands at 96% identified and 78% spectroscopically complete, and is currently one of the largest highly spectroscopically complete faint 1.4 GHz selected samples in existence [Brookes *et al.*, 2006, 2008; Rigby *et al.*, 2011, Chapter 3]. 105 sources have spectroscopic redshifts, and of the remaining 30, 25 have redshift estimates based on the K-z relation, and 5 have only a lower limit redshift estimate from a K-band non-detection. At K-

[5]After publication of this Chapter in Ker et al. (2012) it was discovered that there was also some overlap between CoNFIG 1 and 2r and WP85r and PSRr. In total there are 17 sources present in both ConFIG1&2r and WP85r, and 6 sources present in both CoNFIG1&2r and PSRr which have been included twice. However as this number is very small in comparison with the total sample size (>400), the effects of this will be negligible.

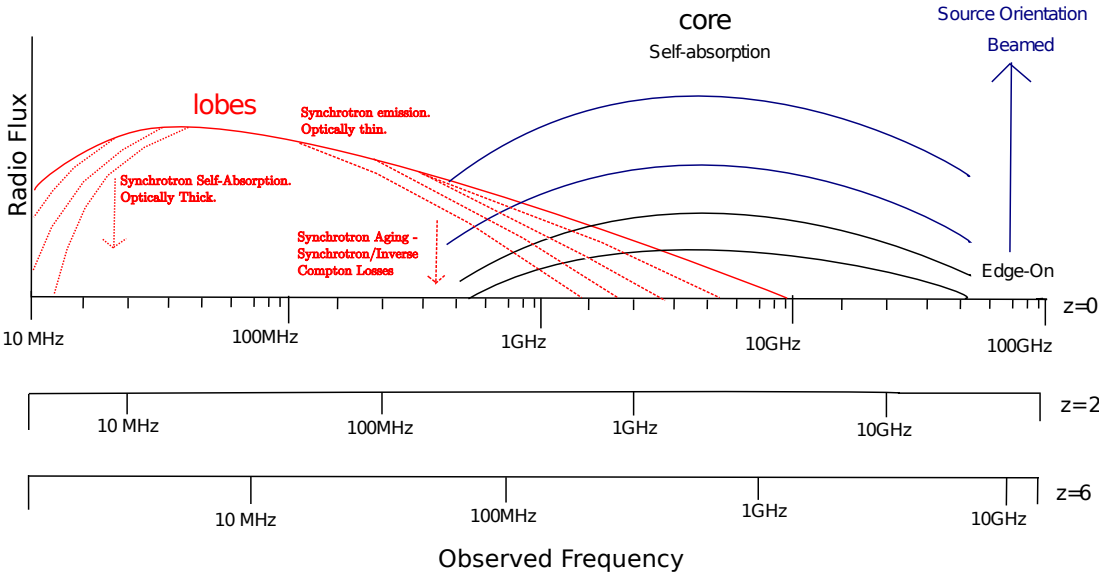

Figure 4.2: A sketch of the contributions of the various components of a typical double radio galaxy to the rest-frame radio regime, and the effects of synchrotron self-absorption, losses and beaming on the observed radio spectrum. Also shown are the observed frequencies at which these features would be observed at redshifts two and six for comparison.

band limits of ∼19 and above, the non-detections are sufficiently deep that the sources must be at high redshift, and the lower redshift limit can be adopted as the estimated redshift without great loss of accuracy. The observed spectral index is measured between 1.4 GHz and 325 MHz (see Chapter 2).

4.2.9 The Hercules Sample

The Hercules sample is taken from a field in the Leiden-Berkeley Deep Survey, and consists of 64 sources selected to have a flux density greater than 2 mJy at 1.4 GHz [Waddington *et al.*, 2001]. The spectroscopic completeness stands at 66%, with 20 sources having photometric redshifts based on the K-z relation, and the final two having a redshift limit estimated from K-band limits. Again, at K-band limits of 20.7 and 19.85 mag respectively, the non-detections are sufficiently deep that the sources must be at high redshift, and the lower redshift limit can be adopted as the estimated redshift. Observed spectral indices are calculated between 1.4 GHz and 610 MHz.

4.3 Radio Source Properties and Sample Selections

Complete radio samples will select very different populations, depending on the frequency at which they are selected, and their flux density limit, as different physical contributions dominate at differing rest-frame frequencies. In this study, samples selected in both the MHz and GHz regimes are used, representative of existing spectral index studies.

Figure 4.2 illustrates the contributing components of a typical extended radio galaxy. If the source is not highly beamed, i.e. not viewed along the jet axis, the emission is dominated at low frequency by synchrotron emission in the radio lobes. Radio lobes typically display a steep-spectrum power law slope, which can steepen further at higher frequency due to both synchrotron and inverse Compton losses (see for example Carilli *et al.* [1991] who analyse the radio spectrum of the well-studied local radio galaxy Cygnus A in depth). At low frequencies, the lobe spectrum can turn over due to synchrotron self-absorption. The frequency at which this happens depends on both the size and intensity of the emitting component: it occurs at higher frequencies for smaller emitters, leading to the smallest radio sources at sub-kpc size being GHz Peaked Sources (GPS).

At higher frequencies (above a few GHz), the contribution to the spectrum from the core is often important. Emission from the core is typically flat spectrum, due to the superposition of self-absorbed components of different sizes at the base of the radio jet. If the jet is orientated towards us, it can be Doppler-boosted by beaming, and can become dominant at lower frequencies. As can be seen from Figure 4.2, if a sample is selected at a few hundred MHz, up to high redshifts the radio emission will still be probing the lobe-dominated regime, giving a sample of similar, directly comparable sources. However, if a sample is selected at GHz frequencies or above, sources with a significant core component that are orientated such that the jet is aligned along the line of sight towards us (beamed) will be preferentially included, especially at higher redshifts.

It is thought that the observed z-α relation may arise because sources at higher redshift have lobes doing work against a denser medium. Working against a denser medium means there will be less adiabatic expansion losses, and therefore greater synchrotron losses, with the result that the source is brighter but the radio spectrum steepens faster. However, as shown, in GHz selected samples, the observed spectral index may alternatively be flattened at the highest redshifts by an increasing contribution of a core component, and be less affected by environment. Although only rest-frame spectral indices should have any direct physical correlation with other observables (observed spectral indices being a good approximation), as far as possible, a traditional two point observed spectral index is used for the analysis in this Chapter, so as to match the situation most widely encountered in the literature and most simply provided by the observations, e.g. for the selection of USS sources.

There is a strong argument to exclude as far as possible all significantly beamed sources identified in the samples, as not only will their spectral index estimates be distorted (the beamed component generally being flatter spectrum), they will also be heavily foreshortened in size. However, as our primary motivation is measuring the efficiency of radio-based correlations in selecting high redshift radio sources from radio surveys, a simple approach must be adopted to removing these that can be widely applied to blind radio surveys. In most comparible observational studies, a cut of α=-0.5 is used as a division, to separate out flat and steep spectrum sources (and indeed such a cut has already been applied in the definition of some of the samples used). Hence, in order to analyse comparable parts of the radio spectrum, analysis is restricted in this study only sources with an observed spectral index less than -0.5; these will

Table 4.2: Spearman Rank Correlation Coefficients and the associated 2-tailed p-value for various combinations of PDαz. A * denotes that only the CENSORS and Hercules samples were used in measuring the correlation, as these are the only two high frequency selected samples with size information readily available.

Combination	151 MHz(All)	151 MHz(P-z)	1.4 GHz(All)	1.4 GHz(P-z)
logP-log(1+z)	r= 0.72, p=0.000	r= 0.02, p=0.780	r = 0.61, p=0.000	r =−0.19, p=0.030
logP-logD	r=−0.14, p=0.010	r= 0.07, p=0.350	r*= 0.01, p=0.860	r*= 0.04, p=0.790
logP-α	r=−0.36, p=0.000	r=−0.10, p=0.180	r =−0.11, p=0.010	r = 0.01, p=0.890
log(1+z)-α	r=−0.34, p=0.000	r=−0.15, p=0.050	r =−0.19, p=0.000	r =−0.14, p=0.100
log(1+z)-logD	r=−0.25, p=0.000	r=−0.15, p=0.050	r*=−0.10, p=0.213	r*=−0.50, p=0.000
logD-α	r=−0.16, p=0.001	r=−0.26, p=0.000	r*=−0.18, p=0.027	r*=−0.24, p=0.090

largely be of a similar type (lobe dominated). Sources with a flatter spectral index represent a composite population: as well as quasars and core-dominated sources, they may also include for example young peaked radio sources (see Chapter 5). Starburst galaxies are not removed, as their numbers are negligibly low in all samples.

Luminosities were calculated for each sample using $\mathrm{P}_\nu = 4\pi \mathrm{S}_\nu (1+\mathrm{z})^{-1-\alpha} \mathrm{D}_L^2$, where α is the observed spectral index, defined as $S_\nu \propto \nu^\alpha$ and D_L is the luminosity distance. The transverse linear size in Mpc of each radio source was calculated using $D = \theta D_A$ where θ is the maximum measured angular extent of the radio source on the sky in radians, and D_A is the angular diameter distance ($D_A = D_L/(1+z)^2$). For Hercules, CENSORS, TOOTS, 7CRS, 6CE and 3CRR θ is determined at 1.4 GHz. There are no readily available angular size measurements in the literature for WP85r, PSRr and CoNFIG 1 & 2r.

4.4 Observable Trends

The complete samples detailed previously provide excellent coverage of the PzαD parameter space. In Figure 4.3, the logP, logD, α and log(1+z) planes are plotted, along with best fitting straight lines to the data (with all data points weighted equally). By eye, the data appear to display similar dependencies of spectral index to those reported by Blundell *et al.* [1999] for the 3CRR, 6CE and 7CRS combined complete radio samples, namely that observed spectral indices steepen with linear size, redshift and radio power (upper panels). Equations of the linear dependencies fitted for spectral index on luminosity, linear size and redshift are given in Tables 5 and 6.

As can be clearly seen from the P-z panels in Figure 4.3, the use of only one complete sample means that a strong, dominating, P-z correlation due to Malmquist bias is present, and this makes disentangling the various dependancies between P, z, α and D very difficult. The addition of several complete samples mitigates this correlation somewhat, and indeed many previous studies, e.g. Blundell *et al.* [1999], argue that the combination of several complete samples essentially removes the Malmquist bias.

The excellent coverage of the P-z plane afforded by our nine complete samples, allows this to be tested. A Malmquist-bias-free section of the P-z plane is selected for both the high and

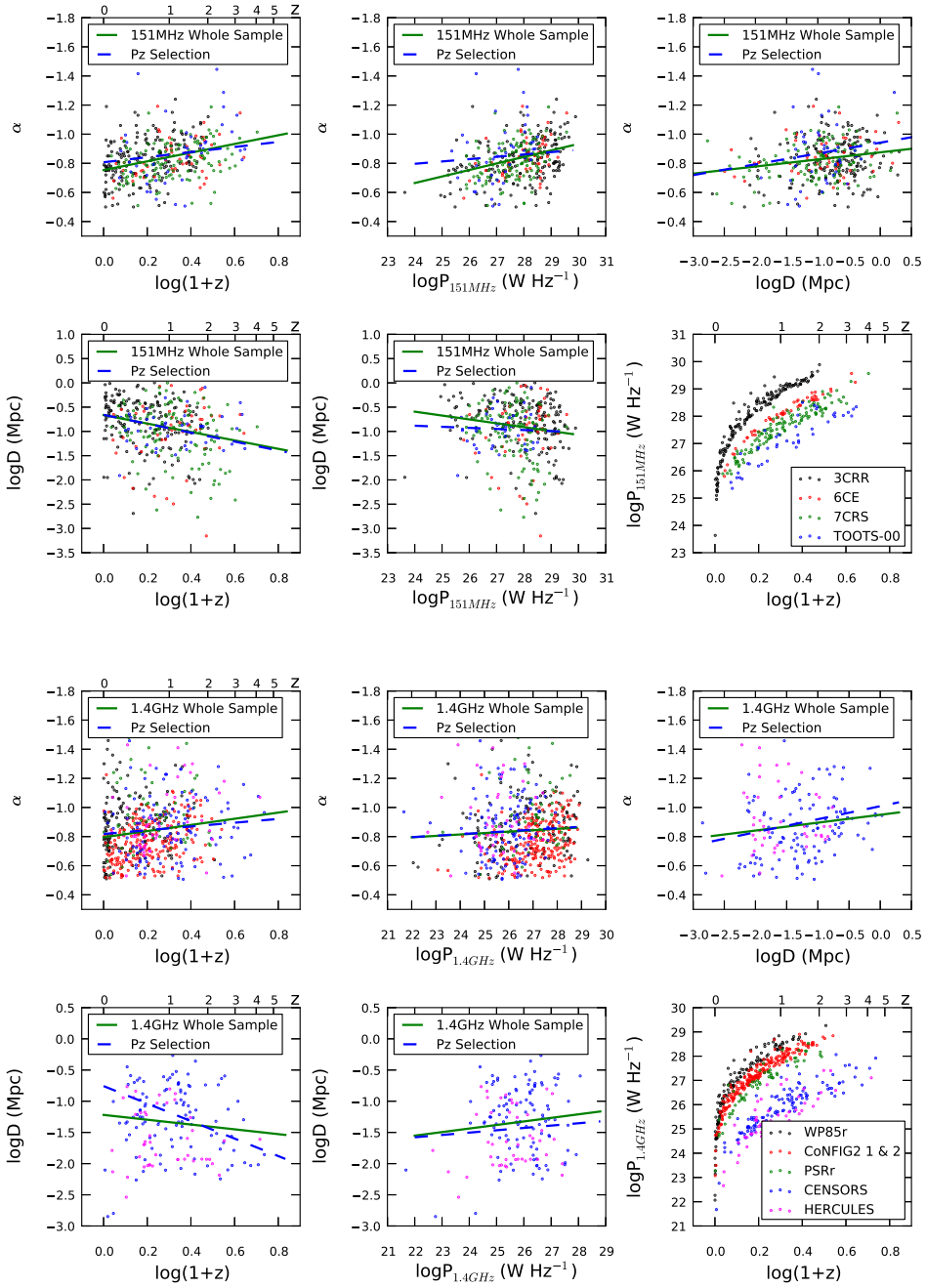

Figure 4.3: The zαPD planes for the 151 MHz (upper 6 panels) and 1.4 GHz (lower 6 panels) selected samples. Spectral indices are measured between 1400-151 MHz for 6CE, 7CRS, TOOTS-00 and CoNFIG1&2r, 750-151 MHz for 3CRR, 5-2.7 GHz for WP85r, 2-1.4 GHz for PSRr, 1400-325 MHz for CENSORS and between 1400 MHz and 610 MHz for Hercules. Only sources with α steeper than -0.5 are utilised. The solid green lines indicate the best fitting straight line to the data. The blue dashed lines indicate the linear fit repeated for a Malmquist-bias-free section of the P-z plane, as defined in Figure 4.1. Note that only CENSORS and Hercules are included in the linear size figures for the 1.4 GHz samples (see text).

low frequency selected samples, covering a large range in both redshift and radio power (see Figure 4.1 for the area definition), and the linear fits are repeated (plotted as blue dashed lines in Figure 4.3). This utilises 186 sources in 151 MHz samples, and 133 sources in the 1.4 GHz samples (reduced to 56 sources when investigating linear size, as for the 1.4 GHz samples only CENSORS and Hercules have readily available size information). The D-α relation appears to increase in strength when the residual P-z correlation is removed, whilst the z-α and P-α decrease in strength.

In Table 4.2 the Spearman rank correlation coefficients are presented for the relations plotted in Figure 4.3. Also listed is the 2-tailed p-value, which gives an approximate indication of the probability of an uncorrelated system having a Spearman correlation at least as strong as the one calculated from the observed data. The table illustrates several important points. Firstly it shows that the P-z correlation dominates, even when several complete samples are coadded and analysed together, in other words, *simply adding several complete samples does not provide sufficient coverage of the P-z plane to fully remove the dominant P-z correlation.* Secondly it reveals that the D-α, D-z and z-α correlations are the strongest observed in both high and low frequency selected samples. The z-α correlation is stronger than the P-α correlation (correlations between P, α and D more or less disappear once the P-z correlation is removed). Of particular relevance to this study is the fact that the variation of observed α with size and redshift is relatively weak for both samples.

4.4.1 Principal Component Analysis

Analysing fully covered sections of the P-z plane has shown that relations between P, z, α and D are strongly coupled to the Malmquist bias. With this in mind, another statistical test is utilised, Principal Component Analysis (PCA), which is a technique designed to pick out the intrinsic, dominant linear correlations existing in a multi-variable dataset, as opposed to secondary correlations arising due to combinations of others (in this case, particularly the Malmquist bias). The method of PCA involves calculating the eigenvalues and eigenvectors, composed of linear combinations of the normalised input parameters, which span the directions of maximum variance in the input dataset. These eigenvectors and eigenvalues describe the intrinsic correlations present in the dataset (principal components), along with the percentage of the variance in the data that each explain.The results of PCA are most commonly presented in table form, listing each of the principal components, the percentage of the data variance that they explain, and the composition of each principal component. Each principal component is composed of a normalised combination of the entered variables, in this case α, log(1+z), logP and logD, as PC = $x_1\alpha$ +$x_2$log(1+z) + $x_3$logP + $x_4$logD, and the final four columns in the table present x_1, x_2, x_3,and x_4, showing the relative contributions of each variable for each principal component.

A low frequency selected sample is selected first, composed of the 3CRR, 6CE, 7CRS and TOOTS samples, and a PCA analysis performed (see Table 4.3, upper). The P-z correlation dominates (i.e. the first principal component is along an axis primarily composed of P and z), contributing roughly half of the observed variance. A further $\sim$30% variance is contributed

by a D-α anticorrelation, whereby sources of larger size have steeper spectra. The final two components largely just account for scatter around the two dominating independent relations between P-z and D-α. This is an important finding, which is consistent with that demonstrated by the previous section, that the P-z correlation remains dominant even when a large collection of complete samples is used.

Although PCA should successfully identify all underlying independent correlations in the data, the analysis was run again on just the subsamples in a well-covered region of the P-z plane, thereby removing the selection effect (see Figure 4.1). A second motivation for doing this is to restrict analysis to only high-power radio sources, thus studying a relatively uniform population (extended double radio sources), with little contamination from low power sources which are often unresolved [see for example, Baldi and Capetti, 2009]. In this case, the observed variance can be attributed to two independent relations, each giving an almost equal contribution to the variance (see Table 4.3, lower). The largest contributor, at 33%, is an anticorrelation between α and D as found for the whole sample, followed by 28% contribution between D and z. The third 24% contribution arises almost solely along the logP axis, uncorrelated with the other parameters. This confirms the earlier findings, that D-α and D-z relations are intrinsic to the dataset, irrespective of the presence of Malmquist bias.

The results for a high frequency selected collection of samples (composed of CENSORS and Hercules) show broadly similar results, albeit with some difference in the detail (see Table 4.4). For the entire sample, the results are very similar, again with approximately half the variance being acounted for by the P-z correlation, and a further 30% by a D-α correlation. The main difference is that this latter correlation is weakened somewhat by the third component. If a well covered section of the P-z plane is then selected (see Figure 4.1), then similarly to the low frequency data, approximately 40% of the variance is accounted for by a D-z anticorrelation, followed by a 32% α-D, P anticorrelation (see Table 4.4, lower). A weaker P-α correlation accounts for the large remainder of the variance, which removes the weak P-α anticorrelation contribution of the second component.

From this analysis it can be tentatively concluded that there are two firm independent relations present in both datasets, between D and α, and between P and z. By utilising the full P-z coverage subsamples, the D-α correlation is confirmed to be fully independent of Malmquist bias. In the subsamples restricted to be high power sources with good P-z coverage, a strong D-z anticorrelation is also seen. That the D-α correlation is slightly stronger in the low frequency dataset, and the D-z anticorrelation stronger in the high frequency sample is most likely down to the differing types of sources which low and high frequency selected samples collect. Low frequency samples will primarily be composed of lobe dominated sources, suffering little in the way of orientation bias, and hence a large proportion of large, steep spectrum sources. High frequency selected samples will include many more beamed, core dominated and young GPS/CSS sources, and less classical lobed dominated sources.

The correlation between D and α arises due to aging of the radio sources. As a source gets older, it increases in size and the spectrum steepens with age. The physical cause of the anticorrelation between D and z is subject to more debate. It could arise as the result of the

Table 4.3: Upper Table: Principal Component Analysis for the low frequency selected samples, comprising 375 sources with $\alpha < -0.5$. Lower Table: The same analysis repeated for a well covered section of the P-z plane: logP(W Hz^{-1})=27.75-29.5 z=0.5-3.5, using 186 sources.

PC	%	α_{obs}	log(1+z)	logP_{151MHz}	logD(Mpc)
1	49	0.38	−0.65	−0.64	0.19
2	29	−0.60	−0.10	−0.02	0.79
3	15	0.70	0.20	0.38	0.57
4	7.0	0.06	0.72	−0.67	0.12
1	33	0.71	−0.15	−0.30	−0.62
2	28	−0.20	0.85	0.10	−0.48
3	24	0.25	−0.13	0.95	−0.15
4	15	−0.63	−0.48	0.003	−0.61

Table 4.4: Upper Table: Principal Components Analysis on the GHz frequency selected samples of CENSORS and Hercules, comprising 158 sources with $\alpha < -0.5$. Lower Table: Repeated for a well covered selection of the P-z plane: logP(W Hz^{-1})=26.25-29 z=1-4.5, using 56 sources.

PC	%	α_{obs}	log(1+z)	log$P_{1.4GHz}$	logD(Mpc)
1	47	−0.13	0.70	0.70	0.02
2	29	0.66	0.12	0.02	−0.74
3	22	−0.74	0.08	−0.19	−0.64
4	3.0	−0.10	−0.70	0.69	−0.18
1	42	0.007	0.71	0.48	−0.52
2	32	0.71	−0.08	−0.46	−0.52
3	19	−0.67	0.15	−0.62	−0.39
4	7.0	−0.22	−0.69	0.42	−0.56

environment at high redshift, or as a result of sources at high redshift being more likely to be younger, and hence smaller [cf. Blundell and Rawlings, 1999]. It is interesting to note that despite a Spearman rank test (see Table 4.2) suggesting the presence of a correlation between z and α almost as strong as that between D and z, the Principal Component Analysis does not clearly identify an independent z-α relation in either the high or low frequency selected samples, suggesting that the correlation observed may be largely a result of selection effects. One which may be present is that between radio power and linear size. It is thought that radio sources follow tracks on the P-D plane, beginning with high power, small sources, and evolving into lower power, larger sources in time [see for example Kaiser and Best, 2007]. Individual low frequency samples, which are more sensitive to extended radio lobes, show a trend for radio power to increase as linear size decreases, which could arise from the combination of Malmquist bias and the D-z correlation (and indeed, this correlation weakens substantially once Malmquist bias is removed). In a collection of low frequency selected samples, this trend in conjunction with any remaining Malmquist bias and the D-α correlation would naturally lead to an extrinsic contribution to the z-α correlation.

4.5 A Large Intrinsic Scatter in α

Given the independent trends between spectral index, linear size and redshift, identified both visually and by the PCA analysis, an attempt was made to fit an analytical form to the spectral

Table 4.5: The results of fitting functions of α dependent on z, P and D for the low frequency selected samples. A measurement error of 0.1 is assumed in α for all fits, for the determination of the reduced χ^2 and σ.

Model	Sample	rχ^2	σ	a_1	a_2	a_3	a_4
α=-0.8	whole	2.47	0.15	-	-	-	-
	Pz	2.53	0.14	-	-	-	-
$\alpha=a_1\log(1+z)+a_2$	whole	1.98	0.15	-0.30(0.03)	-0.75(0.01)	-	-
	Pz	1.01	0.14	-0.17(0.06)	-0.80(0.02)	-	-
$\alpha=a_1\log P+a_2$	whole	1.99	0.15	-0.04(0.01)	0.40(0.14)	-	-
	Pz	1.02	0.14	-0.02(0.02)	-0.41(0.43)	-	-
$\alpha=a_1\log D+a_2$	whole	2.12	0.15	-0.05(0.01)	-0.88(0.01)	-	-
	Pz	0.92	0.14	-0.07(0.01)	-0.94(0.01)	-	-
$\alpha=a_1\log(1+z)+a_2\log P+a_3$	whole	1.95	0.15	-0.17(0.05)	-0.03(0.01)	-0.09(0.18)	-
	Pz	1.00	0.14	-0.17(0.06)	-0.01(0.02)	-0.59(0.44)	-
$\alpha=a_1\log P+a_2\log D+a_3$	whole	1.87	0.14	-0.05(0.01)	-0.06(0.01)	0.49(0.14)	-
	Pz	0.92	0.14	-0.02(0.02)	-0.07(0.01)	-0.44(0.44)	-
$\alpha=a_1\log(1+z)+a_2\log D+a_3$	whole	1.83	0.14	-0.36(0.03)	-0.07(0.01)	-0.80(0.01)	-
	Pz	0.88	0.13	-0.25(0.06)	-0.08(0.01)	-0.86(0.02)	-
$\alpha=a_1\log(1+z)+a_2\log P+a_3\log D+a_4$	whole	1.80	0.14	-0.25(0.05)	-0.02(0.01)	-0.07(0.01)	-0.18(0.19)
	Pz	0.88	0.13	-0.25(0.06)	-0.01(0.02)	-0.08(0.01)	-0.70(0.44)

Table 4.6: The results of fitting functions of α dependent on z, P and D for the high frequency selected samples. A measurement error of 0.1 is assumed in α for all fits, for the determination of the reduced χ^2 and σ. Models marked with a * use only CENSORS and Hercules, the only two high frequency selected samples for which there is size data readily available.

Model	Sample	rχ^2	σ	a_1	a_2	a_3	a_4
α=-0.8	whole	4.10	0.20	-	-	-	-
	Pz	3.70	0.19	-	-	-	-
$\alpha=a_1\log(1+z)+a_2$	whole	2.75	0.20	-0.21(0.03)	-0.80(0.01)	-	-
	Pz	1.56	0.18	-0.13(0.04)	-0.81(0.01)	-	-
$\alpha=a_1\log P+a_2$	whole	2.81	0.20	-0.01(0.003)	-0.58(0.09)	-	-
	Pz	1.57	0.19	-0.01(0.01)	-0.57(0.20)	-	-
$\alpha^*=a_1\log D+a_2$	whole	3.20	0.21	-0.054(0.01)	-0.95(0.02)	-	-
	Pz	0.81	0.18	-0.09(0.02)	-1.01(0.04)	-	-
$\alpha=a_1\log(1+z)+a_2\log P+a_3$	whole	2.74	0.20	-0.24(0.03)	0.006(0.003)	-0.95(0.10)	-
	Pz	1.56	0.18	-0.13(0.04)	-0.0001(0.01)	-0.81(0.22)	-
$\alpha^*=a_1\log P+a_2\log D+a_3$	whole	3.20	0.21	-0.004(0.01)	-0.05(0.01)	-0.85(0.20)	-
	Pz	0.79	0.18	-0.06(0.03)	-0.09(0.03)	0.58(0.80)	-
$\alpha^*=a_1\log(1+z)+a_2\log D+a_3$	whole	3.14	0.21	-0.18(0.05)	-0.06(0.01)	-0.90(0.02)	-
	Pz	0.75	0.17	-0.41(0.11)	-0.12(0.01)	-0.87(0.05)	-
$\alpha^*=a_1\log(1+z)+a_2\log P+a_3\log D+a_4$	whole	3.02	0.20	-0.63(0.1)	0.08(0.02)	-0.09(0.01)	-2.90(0.38)
	Pz	0.74	0.17	-0.42(0.13)	0.01(0.04)	-0.12(0.03)	-0.99(0.94)

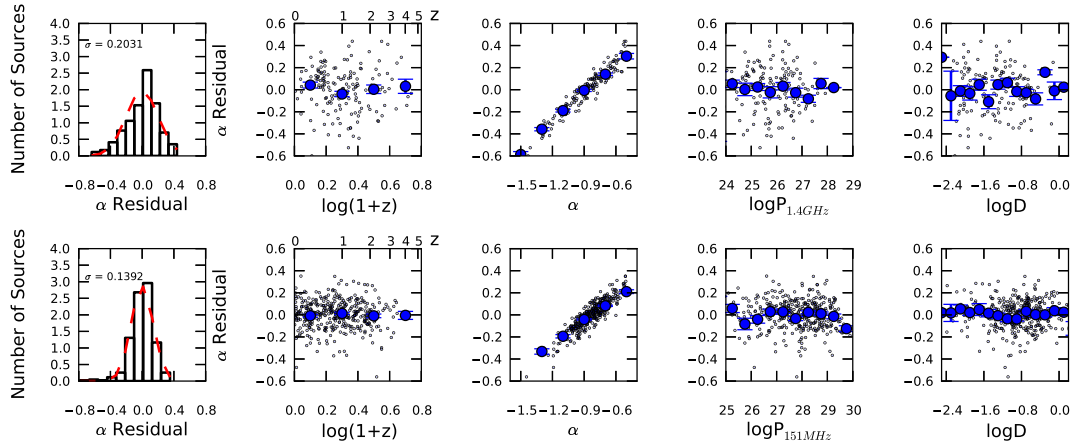

Figure 4.4: Fitting the function α=a$_1$log(1+z) + a$_2$logP + a$_3$logD + a$_4$ to the CENSORS and Hercules combined samples (upper five panels), and to the 3CRR, 6CE, 7CRS and TOOTS combined samples (lower five panels).The panels on the extreme left show the distributions of the spectral index α residuals (observed α minus the model predicted α), and the next four panels on each line show how the α residual depends on z, α, P, and D. Small points are the raw data, large points are the binned means. Fitting the functions clearly removes trends in z,D, and P but large scatter remains, as indicated in the α plot.

index using linear size, luminosity and redshift. Again, as detailed in Section 4.3, only sources with an observed spectral index steeper than -0.5 were used.

Table 4.5 and Table 4.6 list the best fitting coefficients for each relation modelled. To begin with, only very simple linear fits were used, and this progressed to fitting planes modeling all four variables. It can clearly be seen that both the reduced χ^2 and the residual standard deviation decrease, albeit by a small amount, with the inclusion of additional variables in the model for both the high and low frequency selected samples. A plane fit of all four variables gives the best fit, and the smallest deviation in α residuals for both low and high frequency selected samples. The best fitting model is illustrated in Figure 4.4. Although the plane model manages to successfully remove the trends between spectral index and linear size, radio power and redshift, the key finding is that it is unable to predict the observed α. The intrinsic scatter in α is much greater than that arising from any physical trends with other observables present in the datasets.

Whilst this was a simplistic approach designed to see if it was possible to predict the observed spectral index with any success from other properties, it should be noted that much more complex models, incorporating the physics of radio sources can reproduce the observed luminosity, linear size and redshift distributions with some success, but struggle to reproduce α [see for example Barai and Wiita, 2007].

It is very clear that the correlations between α and size, luminosity and redshift are weak. The results of this suggest that the use of spectral index alone is unlikely to be efficient in selecting high redshift radio sources. The equally strong D-z correlation indicates that inclusion of radio size information may increase the efficiency of selection based solely on radio

observables.

4.6 The Origin of the α-z Correlation in Flux Limited Samples

The tendency for observed spectral indices to steepen with redshift has been attributed to a k-correction, where as the source spectrum is redshifted, a steeper part of the spectrum is sampled. How much of an effect this is has been a source of much debate in the literature. It has also been suggested that the strength of the z-α correlation increases with frequency, as high frequency parts of the radio spectrum undergo more significant synchrotron losses.

Klamer *et al.* [2006] find the majority of their USS sample display no curvature, and also cite the well studied high redshift source 4C41.17, at z=3.8, as having a straight radio spectrum from 26 MHz to GHz frequencies. They therefore infer that the k-correction is irrelevant for high-z USS sources. However, based on this, it cannot be simply concluded that the contribution to any z-α correlation from the k-correction is negligible. In fact, Figure 4.6 shows the radio spectra of all currently known z>4 radio galaxies - the majority of which show some evidence of curvature in the observed radio spectrum. Most of the currently known radio galaxies at z>4, display a compact steep radio spectrum, with curvature occurring at low observed frequencies ($\sim$100 MHz), data which Klamer et al did not have for their sample. Bornancini *et al.* [2007] also confirm the presence of curvature at low MHz frequencies for their USS sample.

To quantify the potential effect of the k-corrections, two samples, CoNFIG and 7CRS were used. These two samples have the best multi-frequency coverage, and hence most accurately determined radio spectra. Rest frame spectral indices are calculated from fitting a 2nd-order polynomial ($\log S_\nu = a_1 + a_2 \log\nu + a_3 \log^2\nu$) to the radio spectrum for each source, and measuring the gradient ($\alpha = a_2 + 2a_3 \log\nu$) at the desired frequency; details of this will be presented in Chapter 5. A 2nd order polynomial fit provides a good fit to the radio spectra of the vast majority of sources in each sample.

A simple linear fit was performed on the observed and rest-frame spectral index measured at three frequencies as a function of log(1+z) for both CoNFIG and 7CRS (see Figure 4.5). The fit was performed only on sources with an observed spectral index between 1.4 GHz and 151 MHz less than -0.5 and with a well determined radio spectrum. The gradients of these fits then reflect the strength of the z-α correlation present (if any). The results obtained are striking. For 7CRS it is confirmed that the gradient of both the observed and the rest-frame z-α correlation increases with the frequency at which α is measured, as first reported by Blundell *et al.* [1999]. It can also be seen that the measured z-α correlation is approximately twice as steep in the observed-frame than in the rest-frame (dependent on frequency). It is also worthwhile noting that for 7CRS, contrary to the z-α correlation, the D-α correlation strengthens in the rest-frame.

Similarly, for CoNFIG the observed-frame correlation can be 50% steeper, or more at all frequencies than that measured in the rest-frame. However the increase in gradient with frequency is not seen. This may be because GHz selected samples pick out very different

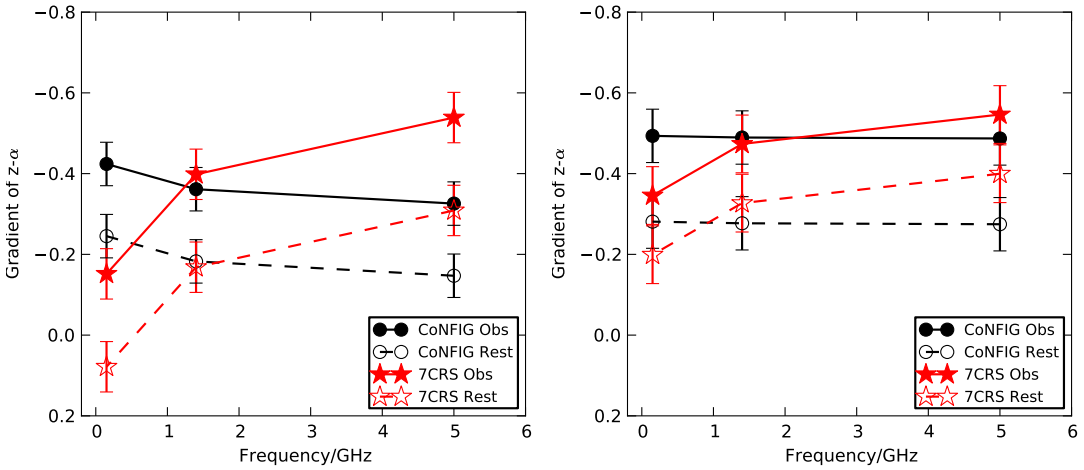

Figure 4.5: The upper panel shows the gradient 'a' from fitting α=a*log(1+z)+b to rest-frame and observed spectral indices for CoNFIG and 7CRS, again assuming an error of 0.1 in α. Whilst both samples show a clear decrease in the gradient of the z-α correlation when k-corrections are applied, only 7CRS shows a marked increase in strength with the frequency at which α is measured. The lower figure shows the same fit again for CoNFIG and 7CRS, but this time with all known quasars and compact objects (classifed as compact in CoNFIG, or less than 30kpc in size in 7CRS) removed. The gradients become very similar at all frequencies and for both samples when only extended sources are considered. These figures clearly show that the k-correction can be responsible for up to 50% of the z-α gradient observed in flux limited radio samples.

proportions of various types of radio source, favouring young GPS/CSS, core and beamed sources (much higher orientation bias).

To test this, the fits were re-run, this time excluding all known quasars, and objects classified as compact in CoNFIG, and sources with a size less than 30kpc in 7CRS. This ensured that the vast majority of sources included in both samples would be lobe dominated and working against the IGM, and are not heavily contaminated by beamed sources or are sources so small that they are still propagating through the medium of their host galaxy rather than the IGM. The results are plotted in the bottom panel of Figure 4.5, and the difference is clear to see. Both CoNFIG and 7CRS now follow very similar relations, both displaying observed gradients which are approximately twice as strong as the rest-frame gradients, but which are now largely independent of the frequency at which α is measured. It is interesting to note that the strength of the gradient for observed α for both samples is very similar to that determined by Ubachukwu et al. (1995) for a sample of radio galaxies compiled from the 3CRR and WP85 samples, again excluding compact sources.

The results confirm that once the k-correction is removed, a weak correlation between z and α remains for extended radio galaxies, which would fit in with a scenario where lobes are working against a denser environment at higher redshift, and hence high frequency losses are greater. Miley and De Breuck [2008] note, however, that it is very difficult to reproduce the observed z-α relation from this somewhat simplistic density-dependent effect. They suggest that as the

density of gas around high redshift sources has been observed to be highly inhomogeneous, and denser close to the nucleus of the galaxy, that the ultra-steep radio spectra are produced by some as yet unknown mechanism within the host galaxy, rather than by the IGM conditions through which the radio lobes are propagating.

It is also concluded that GHz selected samples have a much greater orientation bias present, which can disguise the presence of the z-α correlation displayed by extended radio galaxies. Finally it has been successfully demonstrated that the k-correction is not negligible when measuring the strength of any z-α correlation, and can be responsible for more than 50% of the strength of the observed gradient in a flux-limited sample.

4.7 Implications for High Redshift Searches

The data collected for the nine complete samples allows a measurement to be made, for the first time, of the efficiency of the three most commonly used methods in the literature for searching for high redshift radio galaxies, namely radio spectral index, angular size and K-band magnitude. The ideal search criteria would minimise the size of the selected subsamples that would require follow up observations, whilst maximising the number of high-z galaxies retained in this sample. A definition of highest efficiency is assumed as maximising the difference between the total fraction of the sample recovered, and the total fraction of high-z sources recovered, with each increasing cut in the selection parameter under study. 'z>2' radio galaxies are chosen to be considered as high-z sources, as for the datasets under consideration this provides the optimal compromise between maximising the redshift whilst still maintaining sufficient high-z sources to allow a robust analysis. For comparison, also shown is the analysis repeated for z>3 where possible, albeit with much lower number statistics (there are 10 z>3 radio galaxies with spectroscopic redshifts - see Table 4.7 - and 6 with photometric redshifts in the samples). As there are only approximately 50 radio galaxies with z>3 known [Ishwara-Chandra *et al.*, 2010], the samples are hence representative of the highest known redshift radio galaxy parameter space.

4.7.1 Spectral Index Selection

As discussed above, an initial steep radio spectral index cut is an extremely popular method of reducing very large radio samples down to managable sizes for imaging and spectroscopic follow-up, in order to locate high redshift sources. It is important to determine whether a first spectral index cut does indeed recover a significant proportion of high-z sources present in the samples. Many recent studies in the literature base searches for high-z radio galaxies on the assumption that they may be distinguished by a steep spectrum. Ishwara-Chandra *et al.* [2010] provide a list of the highest redshift, z>3, known radio galaxies, 47 in number, the vast majority of which have been selected from an USS sample. However Jarvis *et al.* [2009], also recently reported the discovery of the second highest redshift radio galaxy known, a source which they noted clearly does not have a ultra steep spectral index (see Figure 4.6). Work with the DRaGONS study [Schmidt *et al.*, 2006], which uses a large, bright radio sample from the

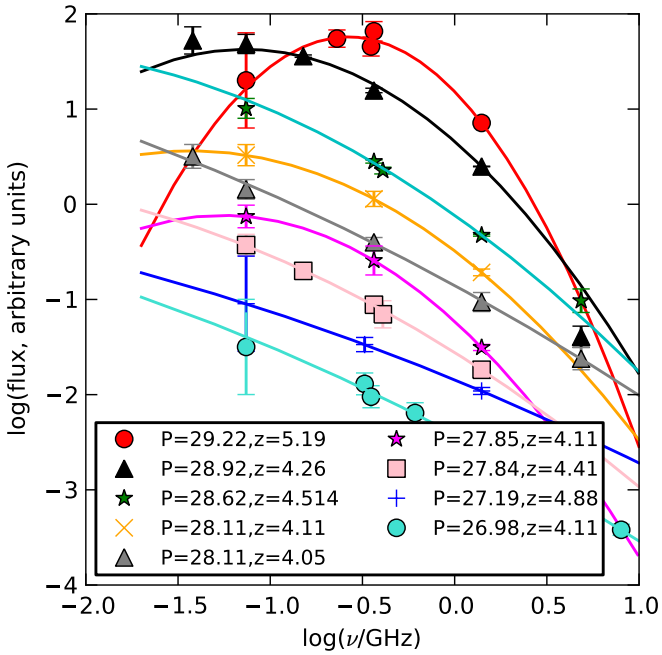

Figure 4.6: Radio spectra for the nine highest redshift z>4 radio galaxies known. Fluxes were obtained from the NASA Extragalactic Database (NED), at frequencies ranging from 38 MHz to 8 GHz. These were not corrected for differences in flux scale, which will be of order the size in the error bars, or less (Chapter 5). The flux scale is offset by a small arbitrary amount for each source to allow the shapes of the radio spectra to be compared. TN J0924 (z=5.19), J1639 (z=4.88) and CEN69 (z=4.11) have spectral indices which imply that they should be detected in the VLSS [Cohen *et al.*, 2007] assuming a straight spectrum, however all three are not. The noise (σ) is measured at each source position in the VLSS maps, and the 2σ value is taken as the upper limit 74 MHz flux, assuming a one σ error. Note that interestingly, the two highest redshift known sources are easily detectable at 1.4 GHz in the NVSS, at 71.5 mJy and 21.8 mJy respectively, but would not be detected in any currently existing 150 MHz or 74 MHz surveys. The vast majority of the spectra are classified as compact steep spectrum, most flattening towards lower frequencies (four of these are potentially peaked). Only one (7C1814, at the lowest redshift) is confirmed as straight over the frequency range 74 MHz to 5 GHz. This negates the common assumption that high redshift, USS sources display no curvature over a large frequency range. The sources are ordered in $P_{1.4GHz}$ (calculated with full curvature information), and it can be clearly seen that the most powerful sources are more likely to display significant curvature. It is also worth noting that all but one of these sources (7C1814) are compact, and have θ<6".

1.4 GHz FIRST survey with redshifts estimated from the K-z relation, also suggests that even with a relatively flat spectral index selection criterion of $\alpha < -0.8$, one third of the z>2 sources are missed. In Table 4.7, I present a list of the 10 radio galaxies with a confirmed spectroscopic redshift of z>3 from all of the samples used in this study. Five of these do have a steep $\alpha < -1.0$, however the remainder display a wide variety of spectral indices.

In studies utilising an ultra steep selection criterion, an often used argument to justify the use of steep spectral index cut-offs is the apparent strong shift in redshift distribution to high redshift. However, in the majority of these studies [e.g. de Breuck *et al.*, 2000; Bryant *et al.*, 2009], the samples are very large (numbering in the hundreds), and spectroscopic follow up is expensive, and so often faint K or I/R band detections or limits are used as additional selection criteria when deciding which targets to pursue with spectroscopy. This makes it very difficult to disentangle the extent to which the ultra steep spectrum, or the optical/near-infrared selection criterion are responsible for preferentially selecting high redshift sources.

Armed with spectroscopically complete samples at a variety of flux density limits and finding frequencies, it is possible to determine the efficiency of the USS selection technique in an unbiased way, for an observed $\alpha \geq$-1.2 (there are too few sources steeper than this to study robustly). In Figure 4.7, each sample is taken in its entirety, a decreasing spectral index limit cut is applied blindly, and the median redshift of the resulting sample of sources steeper than that limit is calculated. Considering first the results with no cuts applied, Figure 4.7 offers a clear observational confirmation that the redshift distributions of complete samples are dependent on the corresponding flux density limits of each sample and selection frequency. It is immediately apparent that low-frequency selected samples, even at relatively bright flux density limits, select on average higher redshift sources. For both low and high frequency selected samples applying a cut of -0.9 generally increases the median redshift of the obtained sample. That the median redshift decreases at very steep spectral index cuts is most likely due to the inclusion of very steep spectrum, low redshift sources [e.g. de Breuck *et al.*, 2000]. The samples selected at increasingly faint flux density limits for both high and low frequency selected samples also display higher median redshifts, except for the faint Hercules sample at high frequency. As described in Best *et al.* [2003], the CENSORS flux limit was chosen because, according to the models of Dunlop and Peacock [1990], a survey with a flux density limit of approximately 10 mJy at 1.4 GHz is optimal for detecting sources at redshifts greater than 2.5, with the percentage of high-z sources detected decreasing at lower and higher flux densities. Our results for the GHz selected samples are consistent with this. Most recently, Afonso *et al.* [2011] have extended the search for ultra-steep spectrum, high redshift sources to the sub-mJy level, and their sample appears to be broadly consistent in expected content with the much brighter samples studied here. Also illustrated clearly by Figure 4.7, is the fact that the median values of redshift obtained from existing USS selected samples are very similar to those I obtain for USS selection of the complete samples used in this study (excepting the de Breuck *et al.* [2000] USS sample, which includes a very strong additional selection criteria of targetting only those sources with the faintest K-band magnitudes).

In Figure 4.8 the efficiency and completeness of an ultra-steep spectrum criterion in selecting

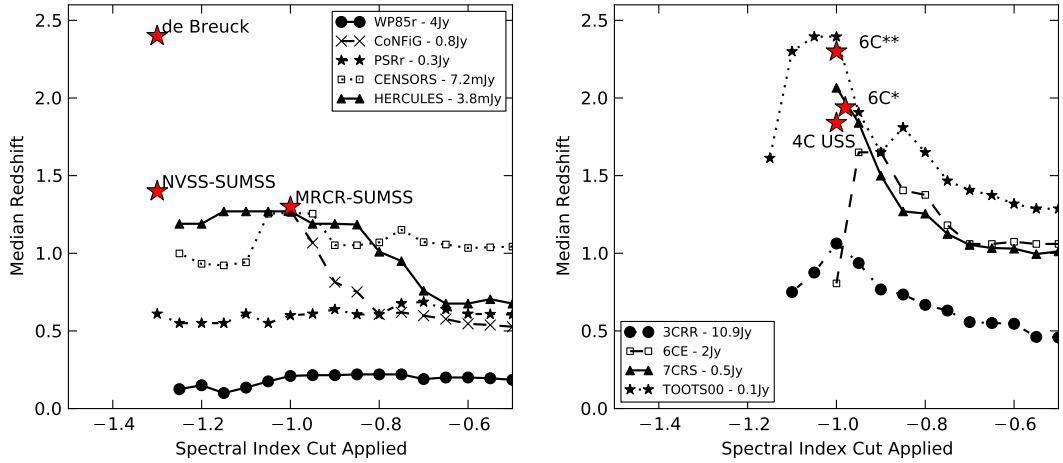

Figure 4.7: The median redshift of all sources in a given sample which have spectral index steeper than a given spectral index, as a function of the spectral index limit. Data points are only plotted if the remaining sample size is at least five sources. The left panel displays the 1.4 GHz-selected samples, and the right panel shows the 150 MHz-selected samples. Highlighted in stars are the de Breuck *et al.* [2000] 1.4 GHz USS sample median redshift and the median redshifts of the MRCR-SUMSS [Bryant *et al.*, 2009], NVSS-SUMSS [Klamer *et al.*, 2006], 4C USS [Chambers *et al.*, 1996] 6C* [Jarvis *et al.*, 2001] and 6C** [Cruz *et al.*, 2007] USS samples. These samples have additional biases due to K-band selection and incomplete spectroscopic redshifts, and hence a direct comparison is not possible, but it is interesting to note that their median redshifts are broadly consistent with what I see in spectral index cut, spectroscopically complete samples.

Table 4.7: Observable Parameters for all spectroscopically confirmed radio galaxies at redshift z >3 in all of the samples studied. A CSS radio spectrum indicates that the source is compact, steep and peaks at low frequencies. A C- spectrum displays negative curvature, but no peak within the observed frequency range.

Name	Sample	z	K	α	D/kpc	Radio Spectrum
7C1745+6624	7CRS	3.01	20.25	-0.78	3.85	CSS
TOOT0-1214	TOOTS	3.081	18.6	-1.13	115	C-
CEN 16	CENSORS	3.126	19.32	-0.86	99.6	C-
7C1748+6703	7CRS	3.2	18.27	-0.97	106	C-
6C1232+3942	6CE	3.22	17.82	-1.14	228	C-
CEN 105	CENSORS	3.38	20.16	-1.16	50	straight
6C 0902+3419	6CE	3.4	19.70	-0.84	91.3	straight
CEN 24	CENSORS	3.43	19.30	-0.66	10	CSS
7C1814+6702	7CRS	4.05	19.16	-1.01	124	straight
CEN 69	CENSORS	4.11	19.60	-1.08	9.6	C-

high-z radio galaxies is considered. The figure shows the proportion of high-z sources recovered in each sample as steeper spectral index cuts are applied, along with the proportion of the entire sample that is returned, and the overall high-z content of the reduced subsample. This analysis is carried out using 7CRS and TOOT-00 samples at low frequency, and CENSORS and Hercules at high frequency. The brighter samples are not included as they have very few z>2 sources, and the combination of CENSORS and Hercules, 7CRS and TOOTS-00 provides two large samples of approximately 150 sources each. The results of this are very interesting: for the low frequency selected sample, the baseline 15% fraction of high-z sources in the recovered subsample nearly doubles to 30% with a spectral index cut α=-1, but at a cost of removing 60-70% of the known high-z sources from the recovered subsample. For the high frequency selected samples there is hardly any difference, regardless of the spectral index cut applied. In other words for the high-frequency selected sample, by excluding sources flatter than the cut, there is not a substantial gain in the proportion of high z sources above that which would be expected if there was no correlation, and the data were distributed evenly across the alpha-z plane.

In utilising complete samples to address the question of high-z selection efficiency using USS samples, the main limitation is the low number of extreme spectral index sources included in the collection of complete samples studied. Any radio sample will include $\sim$5% $\alpha < -1$, and $\sim$1% $\alpha < -1.3$ [e.g. de Breuck *et al.*, 2000], and indeed these proportions hold for the samples presented here: there are too few sources to study the $\alpha<-1.2$ range. What is needed is complete spectroscopic follow up of USS samples encompassing these extreme spectra sources, in order to determine the high-z fraction. However very few USS samples available in the literature have substantial spectroscopic completeness. Most have additional optical or angular size biases applied [e.g. Röttgering *et al.*, 1996; de Breuck *et al.*, 2000] when selecting candidates for spectroscopy. Chambers *et al.* [1996] present one of the most complete USS samples available. They study a small sample of 4C USS sources ($\alpha < -1.0$), selected from Tielens *et al.* [1979] which is 50% spectroscopically complete, with 15 having R or I band magnitudes, one with an I band limit, and one with no magnitude data. There are eight sources with spectroscopic redshift z>2. From the magnitude distribution, it is likely that those without spectroscopic redshifts are in the range 1.0<z<1.6. This gives the fraction of the USS sample with z>2 = 24% which is very much in line with our findings for low frequency samples with this spectral index limit (see Figures 7 and 8).

We can conclude from this that a USS selection criterion does work at low frequency, but is not a strong effect, whilst it is inefficient for high frequency selected samples.

4.7.2 Angular Size Selection

Another often used criterion for maximising the high-z content of radio source samples is that of angular size. In Figure 4.9, a similar diagram is plotted to that of the spectral index cuts. In this, it is clear that moderate cuts can be made to the sample based on angular size, whilst still ensuring the large majority of high redshift sources remain.

The fraction of high-z sources in the recovered sample is similar for both samples, remaining

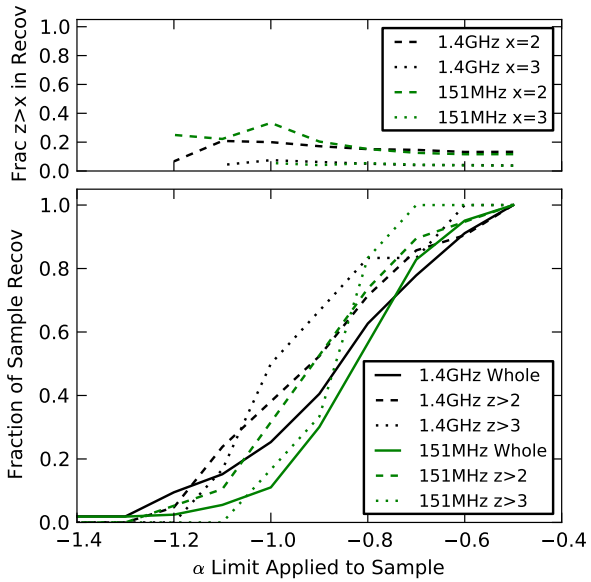

Figure 4.8: The bottom panel shows the fraction of all sources (solid lines) and the fraction of z>2 (dashed) and z>3 (dotted) radio galaxies that have steeper spectral indices than the given limit, as a function of that limit, for both the high (black) and low (green) frequency selected samples. The top panel displays the fraction of high-z radio galaxies in the sample recovered by these cuts. Note that the z>3 lines are much more uncertain, due to the relatively low numbers of these (see text).

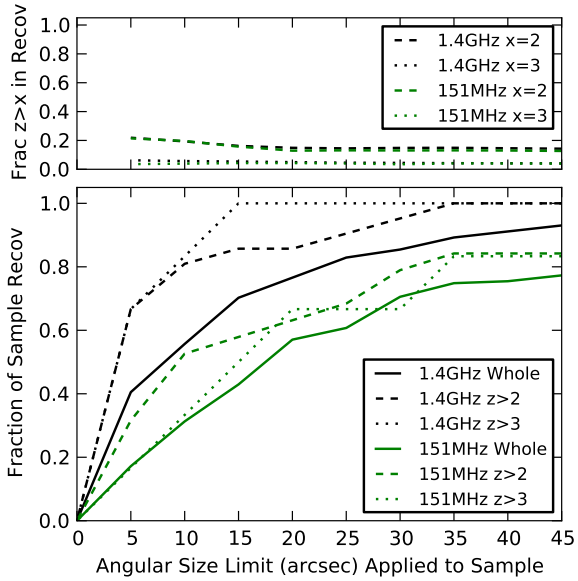

Figure 4.9: The bottom panel shows the fraction of all sources (solid lines) and the fraction of z>2 (dashed) and z>3 (dotted) radio galaxies that have smaller angular sizes than the given limit, as a function of that limit, for both the high (black) and low (green) frequency selected samples. The top panel displays the fraction of high-z radio galaxies in the sample recovered by these cuts. Note that the z>3 lines are much more uncertain, due to the relatively low numbers of these.

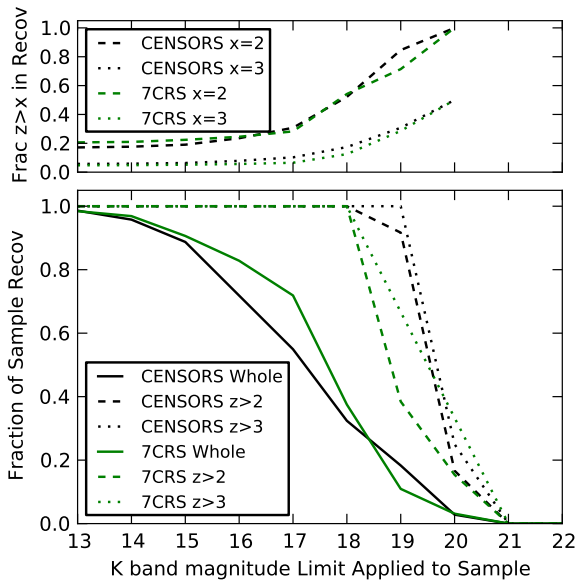

Figure 4.10: The bottom panel shows the fraction of all radio galaxies (solid lines), and the fraction of z>2 (dashed), z>3 (dotted) radio galaxies that have fainter K-band magnitudes than the given limit (bins of one magnitude), as a function of that limit, for both CENSORS (black) and 7CRS (green) samples. The top panel displays the fraction of z>2, z>3 radio galaxies in the two samples recovered by these cuts. Note that the z>3 lines are much more uncertain, due to the relatively low numbers of these.

constant at ∼15% for the majority of angular size cuts, and increasing up to ∼25% for angular size cuts less than 10 arcsec. Contrary to a spectral index cut, angular size cuts prove to be generally more effective for high frequency selected samples. For example, applying a cut of 5 arcsec retains 70% of known high-z sources in the sample, whilst reducing the total sample to 40% of its original size. However, a similar cut for the low frequency sample retains less than 40% of the known high-z sources in the sample. Despite the high-z fraction in the remaining subsample having nearly the same dependence on the θ cut for both high and low frequency selected samples, at low frequency a much smaller proportion of the total high-z galaxies is recovered.

It can therefore be concluded that angular size cuts can successfully retain the majority of high-z sources, whilst almost halving the original sample size for high-frequency selected samples. A larger angular size cut must be applied to low frequency samples in order to retain the same efficiency as seen for high frequency samples with a smaller cut applied. However, once again this is not a particularly efficient technique.

4.7.3 *K*-band Selection

Selecting high redshift galaxies from near infrared imaging is possible, thanks to the very tight relation observed between K-band magnitudes and redshift [e.g. Lilly and Longair, 1982; Willott *et al.*, 2003]. It is worth noting too here that developments in recent years have identified a

new population of radio sources without optical or infrared detections, Infra-Red faint Radio Sources (IFRS). These are potentially excellent very high redshift candidates; see for example Middelberg *et al.* [2011], Garn and Alexander [2008]. The second highest redshift known radio galaxy identified by [Jarvis *et al.*, 2009] is an IFRS, and was selected for follow-up based purely on its lack of optical or K-band detection (it has a spectral index which is not USS, $\alpha = -0.75$).

The main drawback with this method however, is that very deep K-band imaging is required over the radio survey area. To illustrate the efficiency of K-band imaging in selecting high redshift radio sources, a similar analysis is completed to that performed for spectral index and angular size. Only CENSORS and 7CRS are used for this analysis, as both samples are highly spectroscopically complete, and have readily available K-band data. For both of these samples, in addition to the -0.5 spectral index cut as detailed in Section 4, all known radio quasars are excluded in both samples, as these do not follow the K-z relation of radio galaxies. The high spectroscopic completeness is necessary, as only sources with spectroscopic redshifts can be used (not those with redshifts estimated from the K-z relation). The aperture corrected K-band data for CENSORS is taken from Brookes *et al.* [2006], and Rigby *et al.* [2011], and for 7CRS, aperture corrected K-band data was obtained from publicly available online catalogues[6]. It should be noted that 7CRS does not have complete K-band data for the sample, with 26 of the 92 radio galaxies having no K magnitude. However, all but one of these sources without a K measurement are at redshift one or below, and given the very tight K-z relation, all of these are expected to be bright, $K<17$ sources, and should not significantly affect the analysis of high-z sources in this sample.

In Figure 4.10 the fraction of high-z sources recovered with an increasing K-band magnitude cut for CENSORS and 7CRS is plotted. It is immediately clear that a cut of 18.5 in K-band magnitude recovers almost all high-z sources for both samples, with very few low redshift sources included. In previous years, applying this technique required dedicated deep K-band surveys and high resolution, wide and deep radio surveys (limited to GHz frequencies). This was expensive in telescope time: cross-matching with existing wide area K-band surveys such as 2MASS would potentially reduce the sample size by 10-20%, but this is limited by the bright K-band magnitude limits. The release of UKIDSS [Lawrence *et al.*, 2007] Large Area Survey data mitigates this somewhat, as the K-limit reaches 18^{th} magnitude (Vega), and covers many thousands of square degrees in sky area. If an 18^{th} magnitude limit is applied to our samples, then all the high-z sources are recovered, whilst the sample is reduced to $\sim$30% of its original size. This is a far more successful selection method than any based on radio properties alone, and is now feasible over large sky areas. Note that in order for this technique to be successful, the radio data need to be of sufficiently high angular resolution to allow robust matching of radio sources to host galaxies: in the next few years, LOFAR will produce such wide-area, sensitive, high-angular resolution radio surveys. K-band imaging to depths of 19 and below would be still more efficient (especially for even higher redshift cuts) but is extremely expensive in telescope time, and is impractical to be carried out over the large areas necessary to locate significant numbers of high redshift radio AGN.

[6] `https://www.astrosci.ca/users/willottc/kz/kz.html`

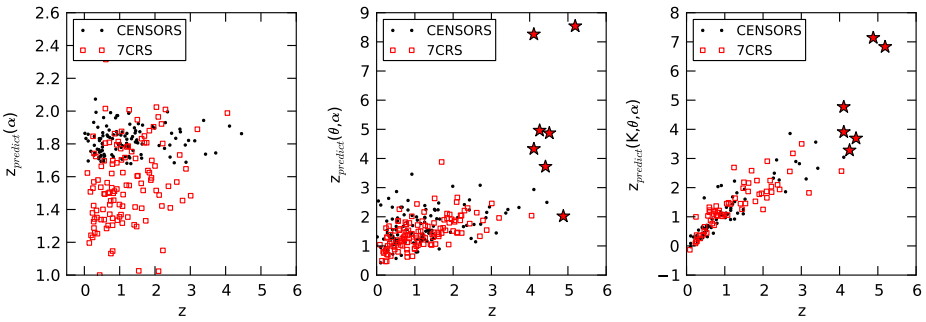

Figure 4.11: Each panel plots the predicted redshift versus the actual redshift for CENSORS (dots) and 7CRS (squares), for three different relations. The left panel plots the predicted redshift from a simple linear fit to spectral index, and the middle the predicted redshift from fitting z as a function of θ and α as described in the text. It is immediately clear that the combination of both radio observables is much more effective in predicting the source redshift. The panel on the right displays the predicted redshift from fitting z as a function of K, θ and α, a relation which offers little improvement over a simple fit to K magnitude alone. Plotted in red stars are the highest redshift radio galaxies known with K, θ and α data available, all of which would be successfully singled out using a $z_{predict}$(K,θ,α)

4.7.4 Optimal Search Criteria for High-z Radio Galaxies

Many combinations of cuts using the K-band magnitude, angular size and spectral index have been utilised in the literature, but as yet there have been no investigations into the most efficient combination of these for selecting high-z radio galaxies. As has been shown previously, there are some correlations present between D, α and z in flux limited samples, in addition to the well known K-z relation.

It is therefore useful to test whether fitting a simple relation to these observed parameters would enable a more efficient selection to be made. A function was first fitted to angular size and observed spectral index (i.e. a radio-only selection method), and then to angular size, spectral index and K-band magnitude (just for the radio galaxies, c.f. previous section) as follows:

$$log(1+z) = a_1 log\theta + a_2\alpha + a_3 \tag{4.1}$$

$$log(1+z) = a_1(K-18)^2 + a_2(K-18) + a_3 log\theta + a_4\alpha + a_5 \tag{4.2}$$

A measurement error of 0.01 in z was assumed for each source, and this error propagated appropriately in log(1+z). Having obtained best-fit parameters, these two relations were used to derive a predicted redshift, z_p, for each source (see Table 4.8). The results of this can be seen in Figure 4.11. The combination of radio observables does far better than fitting only one single radio parameter (spectral index) alone, whereas in contrast, the addition of radio variables to the K-band function provides little discernable improvement over fitting K-band magnitudes alone. Applying these findings, the analysis of the previous subsections was then repeated by applying increasing predicted redshift cuts from these two relations. The results

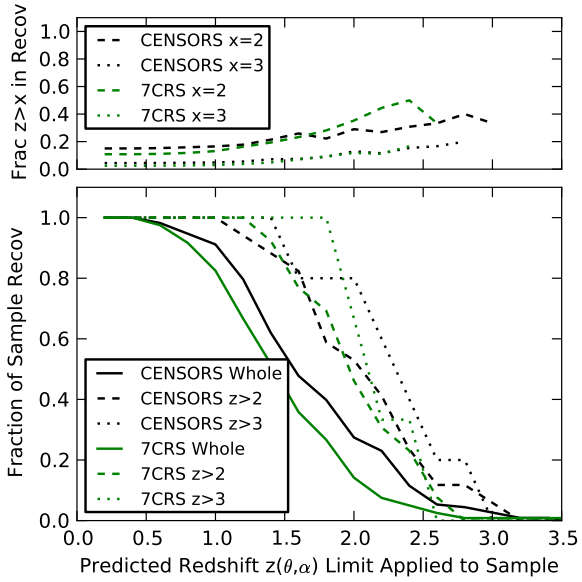

Figure 4.12: The bottom panel shows the fraction of all sources (solid lines), and the fraction of z>2 (dashed) and z>3 (dotted) radio galaxies that have larger predicted redshifts z(θ, α) than the given limit, as a function of that limit, for both CENSORS (black) and 7CRS (green) samples. The top panel displays the fraction of high-z radio galaxies in the sample recovered by these cuts. Note that the z>3 lines are much more uncertain, due to the relatively low numbers of these.

are shown in Figures 4.12 and 4.13. Whilst the z(θ,α) relation does not give a perfect fit to the data (see Table 4.8), applying cuts based on the predicted redshifts results in a substantially higher efficiency than any one radio variable cut alone (see Figure 4.12). The z(θ, α) fit is less efficient for the high frequency sample CENSORS than for the low frequency selected 7CRS, as I would expect from the findings of the preceding subsections. The z(K,θ, α) fit appears equally efficient for both (note that 7CRS falls off more quickly in Figure 4.13, as it contains far less sources above z=3 than CENSORS), but on comparison with a simple K magnitude fit (see Figure 4.10), any improvement is very marginal.

As a final test, z(θ, α) and z(K,θ, α) were also calculated for the nine highest redshift radio sources known (see Figure 4.11). For all of these sources, the z(K,θ,α) and z(θ,α) relations predict high redshifts, z>2, which if applied as cuts to a complete sample of radio galaxies, would leave only a very small proportion of the original sample.

4.8 Conclusions

The main conclusions of this Chapter are:

- The strongest independent relation measured in both high and low frequency selected samples, excluding the P-z correlation (which is a selection effect) is between D and α
- The observed z-α correlation reaches maximum strength for an observed α measured at

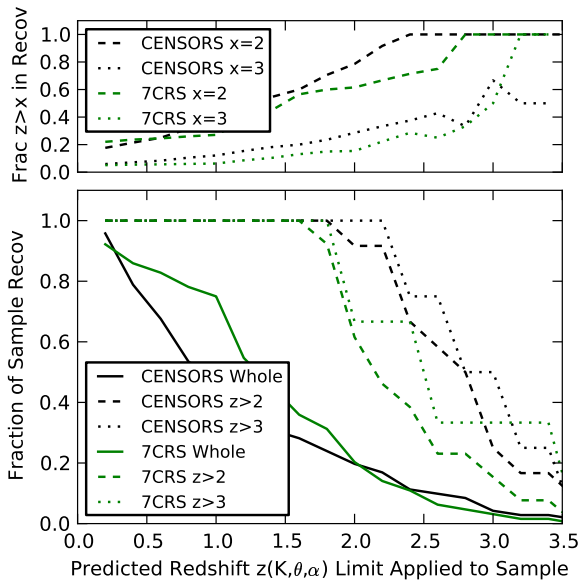

Figure 4.13: The bottom panel shows the fraction of all radio galaxies (dashed lines), and the fraction of z>2 (dashed) and z>3 (dotted) radio galaxies that have larger predicted redshifts z(K,θ,α) than the given limit, as a function of that limit, for both CENSORS (black) and 7CRS (green) samples. The top panel displays the fraction of high-z radio galaxies in the sample recovered by these cuts. Note that the z>3 lines are much more uncertain, due to the relatively low numbers of these.

high frequencies, in a low frequency selected sample. However this correlation is weak in comparison to the other observed correlations between α-D and D-z.

- Up to 50% of the measured z-α gradient can be contributed by a k-correction, in both high and low frequency selected samples. This is important as almost all known z>4 galaxies display curvature in their spectrum.

- Selecting high redshift (z>2) sources based only on their observed α provides only a small increase in searching efficiency for low frequency selected samples, and almost none for high frequency selected samples. Table 4.9 displays the fraction of the samples that have z>2 and z>3 for a selection of the observational cuts studied.

- Whilst the presence of a z-α correlation is confirmed for extended classical radio galaxies, if it arises as a result of radio lobes working against an increasingly denser IGM, giving a steeper spectrum, it is cautioned that this may not be as useful at the very highest redshifts.The very highest z>4 known radio sources present observational characteristics which are more consistent with being young radio sources, still confined within their host galaxies.

- K-band selection is very much more efficient than radio-based selection to maximise the number of high-z galaxies selected whilst minimising the total sample size. Recent existing

surveys such as UKIDSS Large Area Survey are just deep enough to enable efficient searches.

- Searching based on a combination of criteria, such as near-infrared magnitude, radio spectrum, and θ provides optimal searching efficiency for all types of radio source at high redshift.

The key finding of this Chapter is that the efficiency of the Ultra Steep Spectrum criterion *alone* in selecting the highest redshift radio galaxies is not as robust as has sometimes been implied in the literature. There is a z-α correlation observed, but it is weak, and the intrinsic scatter in α dominates. The z-α correlation is strongest for extended sources, which is consistent with the interpretation of radio lobes growing into a denser IGM as redshift increases.

The strongest correlation which is observed in the data, between D and α can be easily understood: as the sources grow, they age and the spectrum grows steeper. In addition to this, as a result of synchrotron self-absorption, young sources generally have a turn-over in their spectra (e.g. GPS, CSS sources) which gives rise to a flatter spectrum. These sources are usually small, being recently triggered, and often still propagating through the host galaxy. These small, flat sources again contribute to the strong observed correlation between D and α.

These young sources also contribute to the strong correlation observed between z and D, where sources are on average smaller at higher redshifts. This may be understood in the context of the 'youth-redshift degeneracy' outlined by Blundell and Rawlings [1999]. Their argument is that sources at high redshifts are increasingly likely to be young, and hence smaller, because radio sources fade as they grow in size due to the decreasing ambient density, and any flux-limited sample selects only the most luminous sources at high redshift. The degeneracy is most pronounced over a luminosity range where the luminosity function is steep (i.e. above the break) and hence is typically stronger at high redshift than low redshift for current flux limits. In higher frequency samples, the degeneracy may be enhanced further, as synchrotron losses lead to a faster drop in the luminosity with age. Identifying high redshift candidates in the radio regime requires a sufficiently young source that synchrotron and inverse compton losses have not yet had time to deplete the rest-frame GHz part of the spectrum, making the source too faint to be included.

This D-z relation has implications for the z-α correlation, in that as we move out to higher and higher redshifts, we will eventually reach a regime where radio sources are mostly ∼host galaxy sizes. The association of a significant fraction of Infrared Faint Radio Sources (which are radio sources without an optical or infrared identification, and hence potentially high redshift candidates, but often not with an Ultra-Steep Spectrum; e.g. Jarvis *et al.* [2009]), as CSS sources [Middelberg *et al.*, 2011] offers further support for this. Some CSS sources are very luminous, and can display observed spectral indexes of a steepness comparable to Ultra Steep Spectrum sources [cf. O'Dea, 1998], which would be expected as the source is expanding through the dense medium of its host. If sources are still propagating through the host galaxies, as opposed to the IGM, this may change the nature of the z-α correlation at high redshifts, as CSS/GPS sources have a self-absorbed (peaked) radio spectrum. Such sources may be selected on an USS

spectral index in the GHz regime, but not at lower frequencies. Table 4.7, and Figure 4.9 both suggest that the fraction of young CSS sources gets higher at high redshifts.

Radio-based techniques could be expanded to compare candidate source sizes with the location of the spectral peak [e.g. Falcke *et al.*, 2004], as well as the radio spectral shape. Especially in combination with existing and up-coming deep, widefield optical and near-infrared data, next generation instruments such as LOFAR and the SKA will provide the crucial high resolution and sensitivity across a wide spectral range necessary to do this, and in conjunction with upcoming high frequency wide area surveys such as WODAN [Röttgering *et al.*, 2011], will enable very good high redshift radio source candidates to be successfully located.

Table 4.8: The fits to z(θ,α) and z(K,θ,α) for 7CRS and CENSORS as described in the text.

Sample	Function	$\mu(z_{obs}\text{-}z_p)$	$\sigma(z_{obs}\text{-}z_p)$	a_1	a_2	a_3	a_4	a_5
7CRS	$\log(1+z)=a_1\log\theta+a_2\alpha+a_3$	-0.26	0.64	-0.1213	-0.5840	0.045	-	-
CEN	$\log(1+z)=a_1\log\theta+a_2\alpha+a_3$	-0.45	0.88	-0.1687	-0.1973	0.40725	-	-
CEN	$\log(1+z)=a_1(K\text{-}18)^2+a_2(K\text{-}18)+a_3\log\theta+a_4\alpha+a_5$	-0.08	0.40	0.011	0.11287	-0.0497	0.0024	0.4074
7CRS	$\log(1+z)=a_1(K\text{-}18)^2+a_2(K\text{-}18)+a_3\log\theta+a_4\alpha+a_5$	-0.12	0.47	0.004	0.1025	-0.003	-0.1327	0.2963

Table 4.9: The fraction of high-z sources in samples with various observational cuts applied. Column 1 displays the samples used, the second and third columns display the fractions of z>2, z>3 radio galaxies in the whole sample, and the fourth column the observational cut (in spectral index, size, K-band, or predicted redshift from a combination of these) applied to the sample(s) used. Column 5 displays the total fraction of the sample(s) that is returned by applying the observational cut, and the final two columns display the fractions of z>2, z>3 radio galaxies in the returned sample.

Samples used	% of Whole Sample at z>2	% of Whole Sample at z>3	Cut Applied	% of Whole Sample Retained	% of Retained Sample at z>2	% of Retained Sample at z>3	% of Sources at z>2 Lost by Cut	% of Sources at z>3 Lost by Cut
CEN,Her	13%	4%	α<-1.0	10%	20%	8%	62%	50%
7C,TOOT	12%	4%	α<-1.0	20%	33%	6%	68%	83%
CEN,Her	13%	4%	θ<10	55%	20%	6%	19%	17%
7C,TOOT	12%	4%	θ<10	30%	20%	4%	47%	67%
CEN	15%	5%	$z_p(\alpha,\theta)$>2	25%	30%	13%	47%	20%
7C	11%	3%	$z_p(\alpha,\theta)$>2	15%	35%	12%	54%	33%
CEN	18%	6%	K>19	20%	83%	30%	8%	0%
7C	21%	5%	K>19	10%	70%	29%	62%	33%
CEN	18%	6%	$z_p(K,\alpha,\theta)$>2	20%	80%	28%	8%	0%
7C	21%	5%	$z_p(K,\alpha,\theta)$>2	20%	62%	16%	38%	33%

Table 4.10: The Wall & Peacock 1985 [Wall and Peacock, 1985] sample at α<-0.5. Col1: Source name, Col2: redshift, Col3: Redshift type S = spectroscopic, P = photometric, Col4: Flux at 1.4 GHz, Col5: Spectral index α measured between 2.7 GHz and 1.4 GHz, Col6: Radio luminosity at 1.4 GHz.

Name	z	ztype	$S_{1.4GHz}$ Jy	α	$\log P_{1.4GHz}$ W Hz^{-1}
1322-42	0.0010	S	281.51	-1.2	23.79
1228+12	0.0040	S	221.03	-0.93	24.89
0320-37	0.01	S	137.9	-0.52	25.49
1717-00	0.03	S	58.68	-0.84	26.08
0518-45	0.04	S	58.56	-1.07	26.34
1648+05	0.15	S	51.0	-1.11	27.5
0433+29	0.22	S	48.5	-0.86	27.83
0915-11	0.05	S	42.44	-0.9	26.4
2152-69	0.03	S	30.72	-0.71	25.8
2356-61	0.1	S	24.97	-1.36	26.82
1409+52	0.46	S	22.88	-0.99	28.25
0538+49	0.55	S	21.79	-0.77	28.38
1934-63	0.18	S	19.78	-0.88	27.25
1216+06	0.01	S	18.49	-0.56	24.61
1333-33	0.01	S	16.9	-0.79	24.58
1828+48	0.69	S	16.69	-0.78	28.49
0134+32	0.37	S	15.87	-0.85	27.85
1328+30	0.85	S	14.7	-0.53	28.59
0809+48	0.87	S	14.37	-0.94	28.71
2121+24	0.1	S	14.14	-1.07	26.56
1814-63	0.06	S	13.63	-0.91	26.07
0407-65	0.962	S	13.47	-1.11	28.84
0106+13	0.06	S	13.21	-0.76	26.05
2104-25	0.04	S	13.1	-0.89	25.69
0518+16	0.76	S	12.99	-0.92	28.52
1932-46	0.231	S	12.86	-1.03	27.31
0409-75	0.693	S	12.72	-0.86	28.4
2243+39	0.08	S	11.23	-0.97	26.25
0356+10	0.03	S	10.61	-0.92	25.34
1845+79	0.06	S	10.52	-0.7	25.95
0040+51	0.17	S	10.45	-0.72	26.9
2211-17	0.15	S	10.34	-1.26	26.81
1559+02	0.1	S	9.41	-0.95	26.38
0023-26	0.322	S	9.19	-0.7	27.46
0210+86	0.19	S	8.91	-1.31	26.98
1458+71	0.9	S	8.89	-0.77	28.49
0043-42	0.05	S	8.85	-0.87	25.72
0917+45	0.17	S	8.83	-1.06	26.85
1733-56	0.098	S	8.4	-0.73	26.3
0951+69	0.0010	S	8.34	-0.59	22.26
1251-12	0.01	S	8.29	-0.93	24.27
2230+11	1.04	S	8.23	-0.67	28.57
0305+03	0.03	S	8.13	-0.64	25.22
1502+26	0.05	S	8.09	-1.46	25.69
0316+16	0.907	S	8.01	-0.79	28.46
0625-53	0.05	S	7.98	-1.17	25.68
2335+26	0.03	S	7.87	-1.03	25.21
0131-36	0.03	S	7.83	-0.51	25.2
2032-35	0.631	S	7.62	-1.1	28.13
0237-23	2.22	S	7.46	-0.64	29.26
0220+42	0.02	S	7.46	-0.54	24.83
1740-51	0.35	P	7.38	-0.72	27.45
0945+07	0.09	S	7.37	-0.82	26.17
2153+37	0.29	S	7.26	-1.22	27.31
0442-28	0.147	S	7.07	-0.93	26.61

Continued on next page

Table 4.10 – continued from previous page

Name	z	ztype	$S_{1.4GHz}$ Jy	α	$\log P_{1.4GHz}$ W Hz^{-1}
1328+25	1.05	S	7.05	-0.65	28.51
0314+41	0.03	S	7.01	-0.54	25.16
1222+13	0.0030	S	6.99	-0.74	23.14
0859-25	0.305	S	6.71	-1.08	27.31
1005+07	0.88	S	6.62	-0.97	28.39
1151-34	0.26	S	6.58	-0.69	27.1
0252-71	0.568	S	6.55	-1.14	27.96
1938-15	0.452	S	6.51	-0.82	27.66
1827-360	0.12	P	6.49	-1.12	26.39
1245-19	1.275	S	6.49	-0.76	28.71
0035-02	0.22	S	6.48	-0.72	26.94
1157+73	0.97	S	6.41	-0.7	28.4
1954-55	0.06	S	6.24	-0.78	25.73
1609+66	0.55	S	6.19	-0.76	27.83
1607+26	0.473	S	6.18	-1.08	27.73
0104+32	0.02	S	6.13	-0.84	24.74
0404+76	0.599	S	6.01	-0.6	27.87
0123-01	0.02	S	5.98	-0.91	24.73
1949+02	0.06	S	5.94	-0.73	25.7
0958+29	0.18	S	5.94	-1.06	26.74
1842+45	0.09	S	5.84	-0.94	26.07
0255+05	0.02	S	5.81	-0.86	24.72
1318-43	0.01	S	5.8	-0.96	24.11
0038+09	0.19	S	5.79	-1.0	26.77
1308-22	0.0050	S	5.71	-1.3	23.5
0055-01	0.05	S	5.7	-0.76	25.52
1637-77	0.02	S	5.66	-0.62	24.71
1254+47	1.0	S	5.59	-1.02	28.47
1514+07	0.04	S	5.52	-1.4	25.32
2221-02	0.06	S	5.48	-0.7	25.67
0404+03	0.09	S	5.39	-0.64	26.02
1939+60	0.2	S	5.35	-0.99	26.79
0325+02	0.03	S	5.34	-0.79	25.04
0045-25	0.0010	S	5.29	-0.62	22.07
0802+24	0.06	S	5.26	-0.71	25.65
0240-00	0.0040	S	5.22	-0.78	23.27
0743-67	0.4	S	5.18	-0.97	27.46
1518+04	1.296	S	5.1	-1.28	28.81
1634+62	0.99	S	5.09	-0.96	28.4
1526-423	0.5	P	5.08	-1.02	27.69
2058-28	0.04	S	5.04	-0.74	25.27
1416+06	1.44	S	4.97	-0.93	28.78
1323+32	0.36	S	4.97	-0.6	27.29
0117-15	0.565	S	4.91	-0.9	27.78
0008-42	1.6	P	4.86	-1.03	28.92
2331-41	0.907	S	4.84	-0.91	28.27
2128+04	0.99	S	4.84	-0.67	28.29
1017-42	1.28	S	4.74	-1.08	28.69
0744+55	0.04	S	4.74	-0.78	25.24
1350+31	0.05	S	4.73	-0.73	25.44
0022-42	0.937	S	4.71	-0.77	28.26
2229+39	0.02	S	4.67	-0.95	24.63
1529+24	0.1	S	4.65	-1.14	26.08
1142+19	0.02	S	4.63	-0.53	24.62
0105-16	0.4	S	4.63	-1.1	27.43
1453-10	0.94	S	4.6	-0.93	28.29
0307+16	0.26	S	4.6	-0.93	26.97
1355-41	0.31	S	4.59	-0.93	27.15

Continued on next page

Table 4.10 – continued from previous page

Name	z	ztype	$S_{1.4GHz}$ Jy	α	$logP_{1.4GHz}$ W Hz^{-1}
0213-13	0.14	S	4.54	-0.74	26.36
0453-20	0.04	S	4.51	-0.73	25.22
1414+11	0.02	S	4.5	-0.76	24.61
0428+20	0.22	S	4.5	-0.53	26.77
2250-41	0.31	S	4.48	-0.99	27.14
2314+03	0.22	S	4.46	-0.97	26.8
1637+62	0.75	S	4.45	-1.03	28.07
1832+47	0.16	S	4.38	-0.96	26.48
2342+82	0.73	S	4.35	-0.95	28.01
1602+01	0.46	S	4.32	-1.07	27.54
0034-01	0.07	S	4.3	-0.79	25.7
3c325	1.135	S	4.29	-1.29	28.58
1306-09	0.464	S	4.29	-0.65	27.48
1136-13	0.55	S	4.29	-0.65	27.65
0834-19	1.032	S	4.28	-0.82	28.33
2135-20	0.635	S	4.27	-0.82	27.83
0235-19	0.62	S	4.27	-0.87	27.81
0349-27	0.07	S	4.26	-0.59	25.69
0003-00	1.04	S	4.22	-0.86	28.34
1358+62	0.43	S	4.2	-0.68	27.4
0605+48	0.28	S	4.18	-0.89	27.0
0114-21	1.41	S	4.16	-0.95	28.69
0625-35	0.06	S	4.11	-0.53	25.54
0453+22	0.21	S	4.08	-1.01	26.72
0157-31	0.68	S	4.03	-0.81	27.87

Table 4.11: The CoNFIG 1 & 2r Samples [Gendre *et al.*, 2010] at α<-0.5. Col1: Source name, Col2: redshift, Col3: Redshift type S- spectroscopic, P = photometric, Col4: Flux at 1.4 GHz, Col5: Spectral index α measured from a fit to flux data points between 1.4 GHz and 151 MHz, Col6: Radio luminosity at 1.4 GHz, Col7: Radio morphological type as defined in Gendre *et al.* [2010], C = compact, C* = confirmed compact, S = compact steep spectrum, I = FRI, II = FRII, U = uncertain, Col8: SDSS Spectral Type - 2 = galaxy, 3 = quasar, 4 = high-z quasar, 0 =unknown.

Name	z	ztype	$S_{1.4GHz}$ Jy	α	$\log P_{1.4GHz}$ W Hz^{-1}	Radio Morph	SDSS Type
M87	0.0042	S	141.95	-0.98	24.74	I	2
3C295	0.4614	S	22.72	-0.63	28.19	II	2
3C196	0.871	S	15.01	-0.75	28.68	II	2
3C270	0.0073	S	10.44	-0.8	24.09	I	2
3C327	0.1041	S	8.3	-0.69	26.35	II	2
3C219	0.1744	S	8.1	-0.79	26.82	II	2
3C227	0.0865	S	7.62	-0.64	26.14	II	2
3C310	0.0535	S	7.61	-0.97	25.71	I	2
3C237	0.88	S	6.52	-0.59	28.28	C	2
3C298	1.4374	S	6.1	-1.02	28.9	S*	3
M84	0.0030	S	6.01	-0.57	23.08	I	2
3C264	0.0214	S	5.69	-0.76	24.77	I	2
3C234	0.1849	S	5.6	-0.83	26.72	II	2
3C192	0.06	S	5.33	-0.67	25.65	II	2
3C280	0.996	S	5.1	-0.75	28.35	II	2
NGC5532	0.024	S	4.45	-0.52	24.76	I	2
3C315	0.108	S	4.33	-0.71	26.1	I	2
3C216	0.67	S	4.23	-0.77	27.87	S*	3
3C244.1	0.43	S	4.19	-0.78	27.41	II	2
3C313	0.461	S	3.8	-0.85	27.45	II	2
3C300	0.272	S	3.74	-0.76	26.91	II	2
3C223	0.1368	S	3.72	-0.65	26.25	II	2
3C228	0.552	S	3.71	-0.84	27.63	II	2
3C338	0.0298	S	3.68	-1.23	24.88	I	2
3C275	0.48	S	3.67	-0.68	27.45	II	2
3C346	0.1617	S	3.67	-0.55	26.39	I	2
3C321	0.0962	S	3.58	-0.64	25.91	II	2
4C-05.64	1.191	S	3.57	-0.53	28.3	C	0
3C325	1.135	S	3.56	-0.74	28.32	II	2
3C288	0.246	S	3.36	-0.85	26.77	I	2
3C349	0.205	S	3.36	-0.69	26.59	II	2
3C225	0.58	S	3.34	-1.01	27.66	II	2
3C245	1.0293	S	3.31	-0.73	28.18	S*	3
3C351	0.3715	S	3.26	-0.7	27.15	II	3
3C236	0.0992	S	3.24	-0.61	25.89	II	3
3C326	0.09	S	3.21	-0.64	25.8	II	2
3C300.1	1.159	S	3.16	-0.73	28.28	II	2
3C337	0.63	S	3.16	-0.67	27.65	II	2
3C230	1.487	S	3.15	-0.94	28.62	II	2
3C299	0.367	S	3.15	-0.65	27.11	II	2
3C254	0.7361	S	3.13	-0.92	27.87	II	3
3C263.1	0.366	S	3.13	-0.91	27.14	II	2
3C305	0.0416	S	3.01	-0.81	25.08	I	2
3C238	1.405	S	2.96	-0.85	28.5	II	0
4C-06.35	0.625	S	2.96	-0.88	27.66	II	0
3C274.1	0.422	S	2.92	-0.84	27.25	II	2
3C277.3	0.0858	S	2.92	-0.68	25.72	II	2
3C275.1	0.557	S	2.9	-0.91	27.54	II	3
3C265	0.8105	S	2.89	-0.94	27.94	II	2
3C247	0.749	S	2.88	-0.84	27.83	II	2
3C270.1	1.5328	S	2.85	-0.78	28.54	II	3
3C249	0.311	S	2.8	-0.88	26.93	II	0

Continued on next page

Table 4.11 – continued from previous page

Name	z	ztype	$S_{1.4GHz}$ Jy	α	$\log P_{1.4GHz}$ W Hz^{-1}	Radio Morph	SDSS Type
4C53.24	1.065	S	2.76	-0.59	28.1	II	3
NGC2484	0.0408	S	2.72	-0.68	25.02	I	2
4C03.18	0.535	S	2.71	-0.52	27.4	II	2
3C318	1.574	S	2.69	-0.76	28.54	S*	2
4C01.32	0.443	S	2.69	-0.6	27.22	II	2
3C287.1	0.2157	S	2.65	-0.54	26.52	II	3
3C319	0.192	S	2.62	-0.85	26.43	II	2
3C336	0.927	S	2.61	-0.73	27.98	II	3
3C207	0.6804	S	2.61	-0.81	27.68	II	3
3C340	0.775	S	2.6	-0.68	27.78	II	2
3C332	0.1517	S	2.6	-0.63	26.19	II	2
4C19.44	0.72	S	2.59	-0.53	27.67	II	2
3C303	0.141	S	2.54	-0.73	26.12	II	2
3C324	1.2061	S	2.52	-0.9	28.29	II	2
3C267	1.144	S	2.52	-0.86	28.22	II	2
4C33.21	0.701	P	2.47	-0.56	27.63	C	2
4C04.41	0.0772	S	2.41	-0.76	25.54	II	2
3C289	0.967	S	2.4	-0.79	28.0	II	2
4C01.39	0.819	S	2.4	-0.7	27.81	II	2
3C323.1	0.264	S	2.4	-0.66	26.68	II	3
3C226	0.8178	S	2.39	-0.93	27.86	II	2
3C212	1.043	S	2.37	-0.87	28.1	II	2
3C208	1.1115	S	2.36	-0.97	28.2	II	3
3C326.1	1.825	S	2.31	-0.63	28.56	II	0
3C277.1	0.3201	S	2.29	-0.69	26.85	S*	3
3C205	1.536	S	2.26	-0.86	28.48	II	2
4C37.24	0.9188	S	2.26	-0.65	27.88	C	3
4C01.42	0.792	S	2.26	-0.66	27.74	II	2
4C11.45	2.1832	S	2.24	-0.65	28.73	II	3
4C37.29	0.3456	S	2.21	-0.61	26.9	II	2
4C59.16	0.8162	P	2.18	-0.56	27.72	C	2
3C208.1	1.02	S	2.16	-0.71	27.98	II	2
4C20.24	1.11	S	2.14	-0.72	28.07	II	2
4C-04.40	0.1612	P	2.14	-0.64	26.16	II	0
4C-04.53	0.4403	S	2.1	-0.81	27.14	II	0
4C52.18	0.189	S	2.1	-0.62	26.3	II	2
3C217	0.898	S	2.09	-0.95	27.91	II	2
4C21.35	0.435	S	2.09	-0.53	27.09	C*	2
3C285	0.0794	S	2.08	-0.81	25.5	II	2
4C37.32	0.1148	S	2.07	-0.56	25.83	II	2
3C194	1.184	S	2.06	-0.78	28.14	II	0
1128+455	0.404	S	2.05	-0.65	27.02	II	2
3C200	0.458	S	2.04	-0.92	27.19	II	2
3C284	0.24	S	2.04	-0.85	26.53	II	2
3C329	1.781	S	2.03	-0.65	28.49	II	2
3C341	0.448	S	2.0	-0.82	27.14	II	2
3C213.1	0.194	S	2.0	-0.58	26.3	II	2
4C12.39	2.1293	S	1.99	-0.92	28.79	S*	3
3C334	0.555	S	1.99	-0.84	27.36	II	2
3C268.4	1.3971	S	1.98	-0.81	28.3	II	3
3C223.1	0.1075	S	1.98	-0.54	25.75	II	2
3C277.2	0.766	S	1.95	-0.89	27.7	II	2
1355+01	0.6606	P	1.92	-0.7	27.49	S	2
3C220.2	1.157	S	1.88	-0.68	28.04	II	3
3C202	0.6237	P	1.88	-0.72	27.43	II	2
4C17.44	0.296	S	1.88	-0.57	26.67	C	2
3C352	0.806	S	1.87	-0.9	27.73	II	0
3C322	1.681	S	1.85	-0.85	28.48	II	0

Continued on next page

Table 4.11 – continued from previous page

Name	z	ztype	$S_{1.4GHz}$ Jy	α	$\log P_{1.4GHz}$ W Hz^{-1}	Radio Morph	SDSS Type
3C320	0.342	S	1.82	-0.8	26.83	II	2
3C210	1.169	S	1.81	-0.83	28.08	II	2
4C20.33	0.871	S	1.81	-0.7	27.75	II	0
4C13.56	0.672	P	1.81	-0.65	27.47	S	2
3C211	0.4789	P	1.8	-0.77	27.15	II	2
3C229	0.2739	P	1.79	-0.64	26.58	II	0
3C197.1	0.128	S	1.79	-0.75	25.87	II	3
3C333	1.324	P	1.75	-0.69	28.15	II	2
4C54.25	0.7744	P	1.74	-0.56	27.58	C	2
3C255	1.355	S	1.73	-1.0	28.28	S	0
3C257	2.474	S	1.72	-0.85	28.84	S	0
4C43.21	1.6819	S	1.72	-0.64	28.36	II	0
3C241	1.617	S	1.69	-0.94	28.43	II	2
3C297	1.406	S	1.69	-0.86	28.26	S	0
4C09.44	0.2364	P	1.68	-0.62	26.42	II	2
4C-02.55	1.0433	S	1.65	-0.72	27.89	C*	3
4C00.52	0.4381	S	1.65	-0.65	27.01	S	2
4C00.46	0.419	S	1.64	-0.85	26.99	II	2
4C29.44	0.3292	S	1.62	-0.71	26.73	II	2
4C59.13	0.2398	P	1.61	-0.81	26.43	II	2
4C34.47	0.206	S	1.61	-0.52	26.26	II	2
4C53.18	0.5974	P	1.6	-0.77	27.33	II	2
4C02.34	0.2126	P	1.6	-0.59	26.29	II	2
4C05.57	0.1362	S	1.6	-0.61	25.88	I	3
3C253	0.1251	S	1.6	-0.77	25.8	II	0
3C215	0.4115	S	1.59	-0.95	26.97	II	2
4C59.17	0.2601	P	1.59	-0.75	26.49	S	2
4C17.56	0.611	P	1.57	-0.62	27.31	II	2
4C43.22	0.5724	S	1.57	-0.7	27.26	II	2
4C49.22	0.334	S	1.57	-0.62	26.72	S*	3
3C239	1.79	S	1.56	-1.05	28.56	II	2
4C24.31	0.6532	S	1.56	-0.77	27.41	II	3
3C311	1.022	S	1.55	-0.78	27.86	C	2
4C50.30	0.481	P	1.55	-0.72	27.08	S	2
NGC2656	0.0453	S	1.54	-0.58	24.86	I	2
4C17.48	0.5395	P	1.53	-0.74	27.2	II	2
4C45.17	0.2072	S	1.53	-0.6	26.25	II	2
4C12.42	0.0812	S	1.53	-0.62	25.38	I	2
4C-05.60	1.094	S	1.52	-0.9	27.97	II	0
4C32.24	0.4306	P	1.52	-0.68	26.96	II	2
1227+119	0.083	S	1.52	-0.85	25.41	I	2
3C356	1.079	S	1.51	-0.99	27.97	II	0
4C04.40	0.5267	P	1.5	-0.83	27.18	II	2
4C53.16	0.0643	S	1.5	-0.63	25.17	II	0
3C288.1	0.9642	S	1.49	-0.88	27.82	II	3
4C39.23	1.216	S	1.48	-0.56	27.95	C*	3
4C31.32	0.0673	S	1.48	-0.52	25.2	II	2
4C-00.50	0.8916	S	1.47	-0.56	27.64	C*	3
0757+503	0.4855	P	1.47	-1.02	27.12	II	2
4C09.45	1.409	S	1.46	-0.94	28.23	II	2
4C46.21	0.5367	P	1.44	-0.72	27.16	II	2
3C266	1.275	S	1.42	-1.02	28.14	II	2
3C344	0.52	S	1.42	-0.88	27.15	II	2
4C20.27	0.3326	P	1.42	-0.76	26.69	S	2
4C32.44B	0.2272	P	1.42	-0.64	26.3	S	2
4C29.50	1.927	S	1.41	-0.74	28.45	C	2
3C331	0.3962	P	1.4	-0.81	26.86	S	2
4C41.19	0.4783	P	1.39	-0.7	27.03	II	2

Continued on next page

Table 4.11 – continued from previous page

Name	z	ztype	$S_{1.4GHz}$ Jy	α	$\log P_{1.4GHz}$ W Hz^{-1}	Radio Morph	SDSS Type
4C03.27	0.269	S	1.39	-0.68	26.46	I	2
4C39.29	0.206	S	1.39	-0.72	26.21	II	2
4C16.33	0.0684	S	1.38	-0.72	25.19	I	2
3C280.1	1.667	S	1.37	-1.05	28.42	II	2
4C16.27	0.9182	P	1.37	-0.77	27.7	II	2
3C256	1.819	S	1.36	-0.94	28.47	S	2
4C31.30	0.4608	S	1.36	-0.55	26.96	II	3
3C272	0.944	S	1.35	-0.98	27.78	II	0
4C61.34	0.523	S	1.35	-0.67	27.1	II	2
3C252	1.105	S	1.34	-1.03	27.96	II	0
4C38.21	1.0665	S	1.34	-1.11	27.95	C	3
3C323	0.679	S	1.34	-0.91	27.41	II	2
3C342	0.561	S	1.34	-0.81	27.19	II	3
3C316	0.42	P	1.34	-0.73	26.89	S	2
4C20.29	0.68	S	1.33	-0.57	27.34	II	3
3C294	1.779	S	1.32	-1.02	28.46	II	0
4C06.32	0.2206	P	1.32	-0.53	26.24	II	2
4C51.25	0.5621	P	1.31	-0.81	27.19	II	2
4C61.23	0.111	S	1.31	-0.55	25.6	II	2
3C268.2	0.362	S	1.3	-0.93	26.75	II	2
3C350	0.346	P	1.3	-0.86	26.7	II	2
4C20.29	0.68	S	1.27	-0.66	27.33	II	3
3C240	0.4678	S	1.27	-0.75	26.98	II	3
4C-00.45	0.16	S	1.27	-0.61	25.92	C	2
4C32.34	0.6793	P	1.26	-0.98	27.4	II	2
3C232	0.5306	S	1.25	-0.79	27.1	S*	3
3C242	0.4542	P	1.25	-0.89	26.96	II	2
4C29.46	0.8608	P	1.23	-0.77	27.58	II	2
1152+551	0.7414	P	1.23	-0.82	27.44	II	2
4C20.20	0.1677	S	1.23	-0.65	25.96	I	2
4C-00.37	1.4956	P	1.22	-0.99	28.23	II	2
4C56.18	0.4059	P	1.21	-0.93	26.84	S	2
4C49.25	0.2067	S	1.2	-0.54	26.14	C	3
4C00.30	0.4785	P	1.19	-0.72	26.96	C	2
4C14.35	1.0264	P	1.17	-0.8	27.75	II	2
4C46.25	0.7428	S	1.16	-0.71	27.39	C	2
3C277	0.414	S	1.16	-0.99	26.85	II	3
3C261	0.6133	S	1.15	-1.0	27.26	II	3
4C05.50	0.2828	S	1.15	-0.92	26.45	II	2
4C17.52	0.0111	S	1.14	-0.57	23.5	I	2
3C281	0.599	S	1.12	-0.87	27.2	II	2
4C22.25	0.419	S	1.12	-0.76	26.81	II	3
4C12.41	0.6763	P	1.11	-0.89	27.32	II	3
4C20.31	1.2332	P	1.1	-0.66	27.87	II	2
3C250	1.4836	P	1.09	-1.1	28.22	II	2
4C-00.48	1.4449	P	1.09	-0.84	28.09	II	2
4C52.27	1.0574	S	1.09	-0.78	27.75	II	3
4C00.35	0.6108	P	1.08	-0.71	27.17	II	2
4C59.11	0.5614	P	1.08	-0.88	27.11	II	2
4C59.10	0.5128	P	1.08	-0.91	27.03	S	2
4C15.34	0.9748	P	1.07	-0.72	27.64	S	2
4C-00.43	0.426	S	1.07	-0.67	26.79	II	2
4C18.29	0.4155	P	1.07	-0.88	26.8	C	2
4C09.41	1.0822	S	1.06	-1.1	27.86	II	3
4C17.49	0.5077	P	1.06	-0.9	27.01	II	2
4C01.31	0.43	S	1.06	-0.89	26.83	C	2
4C20.28	0.5687	P	1.05	-0.75	27.09	II	2
4C08.31	0.3578	P	1.04	-0.74	26.62	II	2

Continued on next page

Table 4.11 – continued from previous page

Name	z	ztype	$S_{1.4GHz}$ Jy	α	$\log P_{1.4GHz}$ W Hz^{-1}	Radio Morph	SDSS Type
4C35.23	1.594	S	1.03	-0.64	28.08	C	2
3C221	0.4957	P	1.03	-0.93	26.97	II	0
4C55.21	0.3694	P	1.03	-0.96	26.68	II	2
4C17.54	0.5831	P	1.01	-0.68	27.08	S*	2
1223+099	0.3093	P	1.01	-0.63	26.45	I	2

Table 4.12: The Parkes Selected Regions sample [Dunlop *et al.*, 1989] sample at α<-0.5. Col1: Source name, Col2: redshift, Col3: Redshift type S = spectroscopic, P = photometric, Col4: Flux at 1.4 GHz, Col5: Spectral index α measured between 2.7 GHz and 1.4 GHz, Col6: Radio luminosity at 1.4 GHz.

Name	z	ztype	$S_{1.4GHz}$ Jy	α	$\log P_{1.4GHz}$ W Hz^{-1}
2211-172	0.153	S	9.74	-1.17	26.8
0240-002	0.0040	S	5.4	-0.83	23.28
0055-016	0.045	S	5.08	-0.63	25.38
0003-003	1.037	S	3.87	-0.72	28.26
1330+022	0.216	S	2.82	-0.59	26.55
2154-184	0.668	S	2.39	-1.17	27.7
0010+005	0.606	S	1.74	-0.92	27.41
2154-183	1.423	S	1.68	-0.79	28.24
0038-019	1.679	S	1.45	-1.22	28.53
0053-015	0.044	S	1.33	-0.81	24.78
0053-016	0.044	S	1.15	-0.74	24.71
0222-008	0.687	S	1.11	-0.79	27.31
1337-033	0.79	P	1.01	-0.84	27.43
1343-007	0.45	P	0.98	-0.69	26.81
1340+022	0.49	P	0.98	-0.91	26.94
1212-007	1.6	S	0.98	-1.0	28.21
0233-025	1.321	S	0.97	-0.78	27.92
1159-023	1.13	P	0.85	-1.03	27.79
2355-010	0.76	P	0.83	-1.02	27.35
0059+017	0.52	P	0.8	-1.06	26.94
2204-203	1.62	S	0.77	-1.2	28.21
1336+020	0.567	S	0.74	-1.02	26.99
2152-218	0.306	S	0.71	-1.48	26.39
2202-179	1.35	S	0.7	-1.11	27.93
1352+008	0.8	P	0.7	-0.85	27.29
2159-201	0.75	P	0.6	-1.66	27.35
2204-182	2.04	P	0.59	-0.83	28.17
1207-013	0.33	P	0.59	-0.7	26.29
2150-202	1.33	S	0.58	-0.95	27.77
0230-027	0.239	S	0.57	-0.83	25.97
1349-017	0.167	S	0.55	-0.88	25.62
2215-179	0.49	P	0.54	-1.26	26.74
2158-177	0.81	P	0.54	-0.93	27.21
0242+028	0.767	S	0.53	-0.95	27.15
0043+000	0.6	P	0.53	-1.03	26.9
1212+005	0.39	P	0.51	-0.89	26.42
0054+018	0.291	S	0.51	-0.95	26.13
2155-202	0.55	P	0.49	-1.24	26.82
0225-014	2.037	S	0.49	-0.75	28.05
2213-156	0.81	P	0.48	-0.8	27.12
0041+007	0.112	S	0.48	-1.24	25.2
1211+000	0.321	S	0.47	-1.08	26.21
0235+023	0.209	S	0.47	-0.72	25.75
0003+006	0.92	P	0.47	-0.97	27.29
1343-026	0.36	P	0.45	-0.93	26.29
2159-187	0.334	S	0.44	-1.33	26.25
0223-023	0.93	P	0.41	-0.93	27.23
1342-016	0.167	S	0.4	-0.87	25.48
0235-019	0.84	S	0.4	-0.89	27.1
0223+012	1.369	S	0.4	-0.76	27.57
0011-023	2.08	S	0.4	-0.74	27.98
2357+004	0.084	S	0.39	-0.54	24.82
1329+012	0.84	P	0.39	-0.95	27.11
2356+033	0.57	P	0.38	-0.9	26.68
2158-170	1.56	P	0.37	-1.12	27.81

Continued on next page

Table 4.12 – continued from previous page

Name	z	ztype	$S_{1.4GHz}$ Jy	α	$\log P_{1.4GHz}$ W Hz^{-1}
0000+035	0.61	P	0.37	-1.41	26.84
2353-003	0.198	S	0.36	-1.2	25.62
2158-206	0.37	S	0.36	-0.67	26.18
1331+004	1.4	S	0.36	-1.44	27.8

Table 4.13: The CENSORS sample [Best *et al.*, 2003] sample at α<-0.5. Col1: Source name, Col2: redshift, Col3: Redshift type S- spectroscopic, P = photometric, Col4: Flux at 1.4 GHz, Col5: Spectral index α measured between 1.4 GHz and 325 MHz, Col6: Radio luminosity at 1.4 GHz., Col7: Angular size, Col8: Linear size, Col9: Type RG = Radio galaxy, Q = quasar, Col10: aperture corrected K band magnitude.

Name	z	ztype	$S_{1.4GHz}$ Jy	α	$\log P_{1.4GHz}$ W Hz^{-1}	size arcsec	D Mpc	Type	Kmag mag
1	1.155	S	0.6595	-0.77	27.62	5.0	0.0412	RG	17.78
4	1.013	S	0.283	-0.82	27.13	29.5	0.237	RG	17.65
5	2.588	S	0.2447	-0.9	28.06	31.7	0.2539	RG	19.01
6	0.547	S	0.2397	-0.54	26.37	1.8	0.0115	Q	16.18
7	1.437	S	0.1482	-0.98	27.27	32.2	0.2719	Q	17.79
8	0.271	S	0.1263	-0.64	25.42	5.8	0.024	RG	15.1
84.85	0.107	S	0.0924	-0.96	24.43	426.04	0.834	RG	13.1
10	1.074	S	0.0794	-0.79	26.63	66.5	0.5409	Q	15.98
12	0.821	S	0.0704	-0.95	26.34	1.8	0.0136	RG	18.74
13	2.95	S	0.0663	-0.86	27.61	2.1	0.0163	RG	19.49
14	1.445	P	0.0656	-0.84	26.87	10.0	0.0845	RG	18.23
15	1.417	P	0.063	-1.05	26.91	6.1	0.0515	RG	18.2
16	3.126	S	0.0617	-0.86	27.63	13.1	0.0996	RG	19.32
17	0.893	S	0.0615	-0.73	26.31	11.2	0.0871	RG	17.84
18	0.109	S	0.0583	-0.55	24.23	0.8	0.0016	RG	12.45
19	1.205	P	0.0551	-0.97	26.65	23.9	0.1983	RG	17.94
20	1.377	S	0.0542	-0.71	26.69	7.1	0.0598	RG	19.6
21	1.26	S	0.054	-0.62	26.56	1.0	0.0084	RG	17.96
22	0.928	S	0.0529	-0.95	26.35	4.6	0.0361	RG	17.45
23	1.929	P	0.0524	-1.07	27.17	21.7	0.1823	RG	18.66
24	3.431	S	0.051	-0.66	27.51	1.4	0.0103	RG	19.3
26	4.45	P	0.0444	-0.97	27.92	2.1	0.0139	RG	20.6
27	0.423	S	0.0404	-0.89	25.4	115.2	0.6401	RG	15.78
28	0.472	S	0.0401	-0.7	25.48	17.6	0.1041	RG	15.91
29	0.965	S	0.0382	-0.8	26.2	27.6	0.2191	Q	17.29
30	0.108	S	0.0378	-0.86	24.05	50.1	0.0989	RG	13.2
31	2.47	P	0.0373	-0.97	27.24	28.5	0.2306	RG	19.4
32	1.151	S	0.0353	-0.93	26.39	36.3	0.2991	RG	17.56
33	1.203	S	0.0343	-0.88	26.41	23.2	0.1925	RG	18.75
35	0.473	S	0.0341	-0.64	25.4	12.2	0.0723	RG	16.46
37	0.511	S	0.0318	-0.76	25.47	21.3	0.1315	Q	19.45
38	2.116	S	0.0317	-0.79	26.92	3.4	0.0283	Q	17.25
39	1.572	S	0.0315	-0.99	26.7	6.4	0.0542	Q	17.63
66.82	1.034	S	0.031	-0.94	26.23	104.12	0.8402	RG	18.2
40	1.158	S	0.0309	-0.62	26.24	11.3	0.0932	RG	18.06
41	0.295	S	0.0275	-0.67	24.85	42.2	0.1858	RG	14.89
42	1.254	S	0.0265	-0.78	26.31	18.2	0.1518	RG	19.3
43	0.778	S	0.0264	-0.65	25.78	5.7	0.0424	RG	17.15
45	0.796	S	0.0255	-0.89	25.85	6.2	0.0465	RG	16.84
47	0.508	S	0.0252	-0.81	25.37	9.0	0.0554	RG	16.45
48	1.606	S	0.0242	-0.65	26.46	1.4	0.0119	Q	17.52
49	0.41	S	0.0238	-0.58	25.09	1.0	0.0055	RG	15.78
50	1.529	S	0.0223	-1.11	26.57	5.0	0.0423	RG	18.39
51	2.27	S	0.0217	-0.74	26.8	5.8	0.0477	RG	19.22
53	0.426	S	0.0216	-0.69	25.1	10.9	0.0608	RG	15.24
55	0.557	S	0.0214	-0.65	25.36	14.0	0.0903	RG	16.64
54	0.41	S	0.0214	-0.6	25.05	2.3	0.0125	RG	14.15
56	1.483	S	0.0208	-0.84	26.4	20.4	0.1725	RG	17.84
57	1.196	P	0.0207	-0.82	26.17	22.5	0.1865	RG	17.93
59	1.07	S	0.0191	-0.99	26.07	33.1	0.269	RG	17.91
60	1.622	P	0.0189	-0.59	26.34	0.8	0.0068	RG	18.41
61	1.452	P	0.0185	-1.01	26.39	21.3	0.18	RG	18.24
62	0.574	S	0.0184	-0.63	25.32	17.7	0.1159	RG	16.81
63	0.314	S	0.0183	-1.46	24.82	6.3	0.029	RG	16.08

Continued on next page

Table 4.13 – continued from previous page

Name	z	ztype	$S_{1.4GHz}$ Jy	α	$\log P_{1.4GHz}$ W Hz^{-1}	size arcsec	D Mpc	Type	Kmag mag
64	0.33	P	0.0181	-1.27	24.85	54.08	0.257	RG	15.04
65	0.549	S	0.0179	-0.58	25.25	7.3	0.0468	RG	16.65
67	0.428	S	0.0173	-0.86	25.04	38.8	0.2171	RG	15.96
70	0.645	S	0.017	-0.94	25.47	154.3	1.0656	RG	17.19
69	4.11	S	0.017	-1.08	27.5	1.4	0.0096	RG	19.6
71	2.857	S	0.0167	-0.79	26.94	3.5	0.0273	RG	19.62
72	2.427	S	0.0165	-0.61	26.67	0.7	0.0057	Q	17.88
73	1.364	P	0.0162	-0.92	26.23	15.8	0.133	RG	18.14
74	0.667	S	0.016	-0.92	25.47	2.5	0.0175	RG	17.0
75	0.265	S	0.0157	-1.13	24.55	10.9	0.0445	RG	14.8
76	0.282	S	0.0153	-0.79	24.56	10.9	0.0465	RG	15.09
77	1.512	S	0.015	-0.83	26.27	2.2	0.0186	RG	18.67
138	0.508	S	0.0147	-0.71	25.11	121.25	0.7464	RG	17.03
79	1.255	S	0.0146	-1.26	26.22	16.91	0.1411	RG	17.44
78	0.413	S	0.0146	-0.72	24.91	6.9	0.0378	RG	16.48
81	0.462	S	0.0145	-0.89	25.04	40.1	0.2344	RG	18.8
80	0.366	S	0.0145	-0.73	24.79	10.9	0.0554	RG	14.65
83	0.521	S	0.0135	-0.98	25.15	1.2	0.0075	RG	16.17
87	2.72	P	0.0132	-0.99	26.9	9.4	0.0744	RG	19.6
86	0.82	P	0.0132	-0.62	25.53	1.3	0.0098	RG	17.26
88	1.064	S	0.0131	-0.58	25.77	2.3	0.0187	RG	-99.0
89	0.909	S	0.013	-1.0	25.73	18.9	0.1477	RG	19.16
90	1.26	P	0.0128	-0.76	25.99	3.1	0.0259	RG	19.5
92	0.743	S	0.0126	-1.27	25.57	94.1	0.6881	Q	16.47
95	0.045	S	0.0122	-0.89	22.76	1.6	0.0014	S	12.08
94	1.648	P	0.0122	-1.09	26.38	8.5	0.072	RG	18.43
93	0.183	S	0.0122	-0.7	24.04	14.5	0.0446	RG	15.13
97	1.635	P	0.012	-0.81	26.25	51.8	0.4388	RG	18.42
96	2.706	S	0.012	-1.03	26.88	1.0	0.0079	RG	20.07
100	1.288	P	0.0115	-1.1	26.09	4.7	0.0393	RG	18.62
101	1.043	S	0.0114	-0.76	25.75	3.0	0.0243	RG	17.86
102	0.468	S	0.0111	-0.62	24.9	12.0	0.0707	RG	15.63
104	0.884	P	0.0107	-1.19	25.67	31.8	0.2465	RG	17.4
103	1.26	P	0.0107	-1.26	26.09	12.6	0.1052	RG	19.4
105	3.377	S	0.0106	-1.16	27.14	6.8	0.0504	RG	20.16
106	1.285	P	0.0105	-0.6	25.86	5.6	0.0469	RG	18.05
107	0.512	S	0.0103	-0.82	24.99	7.0	0.0433	RG	16.01
110	0.282	S	0.0101	-0.92	24.39	83.4	0.3557	RG	14.6
109	0.719	P	0.0101	-0.91	25.35	3.9	0.0282	RG	17.01
112	1.99	S	0.0098	-1.05	26.47	1.1	0.0092	RG	-99.0
113	0.942	P	0.0097	-1.23	25.71	19.7	0.1554	RG	17.52
115	0.545	S	0.0096	-1.2	25.09	13.1	0.0836	RG	15.18
117	1.204	S	0.0095	-0.51	25.73	5.6	0.0465	RG	18.15
119	1.484	S	0.0094	-0.87	26.06	7.9	0.0668	RG	17.92
118	2.294	S	0.0094	-1.13	26.64	3.7	0.0304	RG	19.31
124	0.0156	S	0.0087	-0.97	21.68	24.8	0.0079	S	-99.0
126	0.382	P	0.0084	-1.06	24.64	38.3	0.2	RG	15.69
125	0.701	S	0.0084	-1.02	25.27	11.8	0.0844	RG	15.8
129	2.421	S	0.0083	-0.79	26.47	2.1	0.0171	RG	19.0
128	3.72	S	0.0083	-0.67	26.81	1.3	0.0093	Q	17.81
127	0.922	S	0.0083	-1.23	25.61	1.0	0.0078	RG	17.1
131	0.47	S	0.0082	-0.54	24.76	9.5	0.0561	RG	15.87
130	2.878	P	0.0082	-0.53	26.48	1.2	0.0094	RG	19.19
132	2.545	P	0.0079	-0.52	26.35	2.7	0.0217	RG	19.03
135	1.316	S	0.0078	-0.51	25.73	10.4	0.0872	RG	18.78
134	2.354	S	0.0078	-1.28	26.67	22.4	0.183	RG	19.93
133	1.335	S	0.0078	-0.89	25.88	11.4	0.0958	RG	17.77
136	0.629	S	0.0075	-1.08	25.11	3.8	0.026	RG	19.4

Continued on next page

Table 4.13 – continued from previous page

Name	z	ztype	$S_{1.4GHz}$ Jy	α	$\log P_{1.4GHz}$ W Hz^{-1}	size arcsec	D Mpc	Type	Kmag mag
137	0.526	S	0.0074	-0.93	24.89	33.0	0.2069	RG	16.53

Table 4.14: The Hercules sample [Waddington *et al.*, 2001] at α<-0.5. Col1: Source name, Col2: redshift, Col3: Redshift type S- spectroscopic, P = photometric, Col4: Flux at 1.4 GHz, Col5: Spectral index α measured between 1.4 GHz and 610 MHz, Col6: Radio luminosity at 1.4 GHz, Col7: Angular size, Col8: Linear size, Col9: Type RG = Radio galaxy, Q = quasar.

Name	z	ztype	$S_{1.4GHz}$ Jy	α	$\log P_{1.4GHz}$ W Hz^{-1}	size arcsec	D Mpc	Type
53W008	0.733	S	0.3066	-0.79	26.82	1.9	0.0138	Q
53W015	1.129	S	0.1846	-0.78	27.04	16.1	0.1322	Q
53W051	1.01	P	0.1416	-0.87	26.84	19.6	0.1573	RG
53W031	0.628	S	0.1165	-0.7	26.22	4.1	0.028	RG
53W023	0.57	S	0.1099	-0.87	26.14	9.3	0.0607	RG
53W075	2.15	S	0.0961	-0.78	27.41	1.2	0.01	Q
53W049	0.23	S	0.0951	-0.81	25.16	30.9	0.1135	RG
53W046	0.528	S	0.0631	-0.69	25.78	3.2	0.0201	RG
53W002	2.39	S	0.0501	-1.1	27.4	0.8	0.0065	RG
53W080	0.546	S	0.0276	-0.8	25.48	10.4	0.0664	Q
53W047	0.534	S	0.0239	-0.67	25.37	1.4	0.0088	RG
53W067	0.759	S	0.0232	-0.81	25.74	12.6	0.0929	RG
53W091	1.552	S	0.0221	-1.3	26.66	4.0	0.0339	RG
53W026	0.55	S	0.0211	-0.74	25.36	3.5	0.0224	RG
53W059	1.42	P	0.0187	-0.9	26.33	3.0	0.0253	RG
53W081	2.06	S	0.0122	-0.84	26.5	1.4	0.0117	RG
53W048	0.676	S	0.0115	-0.81	25.32	1.3	0.0092	RG
53W034	0.281	S	0.0109	-1.0	24.43	40.2	0.171	RG
53W032	0.37	S	0.0105	-0.8	24.67	22.4	0.1147	RG
53W024	1.961	S	0.0103	-0.55	26.24	1.4	0.0117	Q
53W060	0.62	P	0.0097	-0.93	25.18	1.4	0.0095	RG
53W041	0.59	P	0.0094	-0.88	25.1	1.4	0.0093	RG
53W052	0.46	S	0.0086	-0.74	24.79	2.2	0.0128	RG
53W027	0.403	S	0.0083	-0.8	24.65	26.8	0.1446	RG
53W010	0.48	S	0.0081	-0.73	24.8	11.0	0.0657	RG
53W077	0.8	S	0.0078	-0.87	25.34	16.8	0.1261	RG
53W005	0.95	S	0.0076	-1.09	25.57	11.9	0.0941	RG
53W019	0.542	S	0.0068	-0.72	24.85	3.2	0.0204	Q
53W020	0.1	S	0.0067	-1.07	23.23	4.0	0.0074	RG
53W042	1.58	P	0.0066	-1.07	26.06	1.3	0.011	RG
53W037	4.2	P	0.0066	-1.07	27.11	3.6	0.0245	RG
53W087	2.57	P	0.0058	-1.18	26.59	2.9	0.0233	RG
53W065	1.185	S	0.0053	-1.21	25.7	1.4	0.0116	RG
53W083	0.628	S	0.0050	-0.7	24.86	1.4	0.0096	RG
53W021	1.12	P	0.0047	-1.07	25.53	12.9	0.1058	RG
53W085	1.35	S	0.0043	-1.29	25.78	1.4	0.0118	Q
53W066	1.82	P	0.0041	-0.91	25.93	1.4	0.0118	RG
53W069	1.432	S	0.0037	-0.87	25.62	1.6	0.0135	RG
53W039	0.402	S	0.0034	-0.82	24.26	11.4	0.0614	RG
53W036	1.5	P	0.0032	-1.24	25.75	6.5	0.055	Q
53W071	0.287	S	0.0028	-1.43	23.91	1.4	0.0060	RG
53W089	0.635	S	0.0025	-1.29	24.69	3.2	0.0219	RG
53W090	0.094	S	0.0021	-0.83	22.66	9.3	0.0162	RG
53W082	1.19	P	0.0020	-1.41	25.35	1.4	0.0116	RG
53W078	0.27	S	0.0020	-0.53	23.61	0.7	0.0029	RG

Table 4.15: The 3CRR sample [Laing *et al.*, 1983] at α<-0.5. Col1: Source name, Col2: redshift, Col3: Flux at 151 MHz, Col4: Spectral index α measured between 750 MHz and 151 MHz, Col5: Radio luminosity at 151 MHz, Col6: Linear size, Col7: Type - 0 = low excitation radio galaxy, 1 = narrow line radio galaxy, 2 = broad line radio galaxy, 3 = quasar. Values obtained from the online 3CRR catalogue maintained by Martin Hardcastle, as described in Section 4.2.1

Name	z	S_{151MHz} Jy	α	$\log P_{151MHz}$ W Hz^{-1}	D Mpc	Type
3C274	0.0041	1303.33	-0.79	25.68	0.0708	1
3C123	0.2177	231.14	-0.7	28.48	0.1332	0
3C295	0.4614	100.94	-0.63	28.84	0.035	1
3C196	0.871	84.61	-0.79	29.44	0.0463	3
3C84	0.0177	75.95	-0.78	25.73	0.4856	1
3C380	0.691	72.72	-0.71	29.12	0.0107	3
3C310	0.054	69.92	-0.92	26.68	0.3205	0
3C433	0.1016	69.35	-0.75	27.25	0.1272	1
3C452	0.0811	67.42	-0.78	27.03	0.428	1
3C33	0.0595	67.2	-0.76	26.75	0.2929	1
3C48	0.367	66.12	-0.59	28.43	0.0020	3
3C338	0.0303	62.15	-1.19	26.12	0.071	1
3C390.3	0.0569	58.6	-0.75	26.65	0.2527	2
3C98	0.0306	58.44	-0.78	26.1	0.1898	1
3C438	0.29	56.29	-0.88	28.16	0.0983	0
3C20	0.174	52.17	-0.66	27.62	0.1583	1
3C219	0.1744	51.3	-0.81	27.63	0.5622	2
3C465	0.0293	46.61	-0.75	25.96	0.354	0
3C234	0.1848	39.4	-0.86	27.57	0.3472	1
3C79	0.2559	38.62	-0.92	27.88	0.354	1
3C61.1	0.186	38.59	-0.77	27.56	0.5795	1
3C330	0.549	34.05	-0.71	28.56	0.3843	1
3C427.1	0.572	34.02	-0.97	28.65	0.1765	0
3C47	0.425	33.84	-0.98	28.34	0.429	3
3C83.1B	0.0255	32.11	-0.62	25.67	0.6242	0
3C264	0.0208	32.02	-0.75	25.49	0.1726	0
3C388	0.0908	30.07	-0.7	26.78	0.0846	0
3C280	0.996	29.48	-0.81	29.13	0.1096	1
3C386	0.0177	28.76	-0.59	25.3	0.105	0
3C228	0.5524	28.06	-1.0	28.53	0.2956	1
3C55	0.735	27.77	-1.04	28.84	0.5243	1
3C225B	0.58	27.08	-0.94	28.56	0.0329	1
3C109	0.3056	27.03	-0.85	27.89	0.4647	2
3C309.1	0.904	26.95	-0.53	28.91	0.0234	3
DA240	0.0356	26.33	-0.77	25.88	1.4932	0
3C192	0.0598	26.19	-0.79	26.35	0.2311	1
3C268.1	0.9731	25.67	-0.59	28.98	0.3659	1
3C326	0.0895	25.66	-0.88	26.71	2.0149	1
3C401	0.201	25.62	-0.71	27.45	0.0782	0
3C254	0.734	25.41	-0.96	28.78	0.1092	3
3C244.1	0.428	25.29	-0.82	28.2	0.2853	1
3C216	0.668	25.26	-0.84	28.65	0.0372	3
3C265	0.8108	24.94	-0.96	28.88	0.5958	1
3C171	0.2384	24.58	-0.87	27.61	0.1227	1
3C382	0.0578	23.91	-0.59	26.27	0.2071	2
3C288	0.246	23.69	-0.85	27.62	0.1399	0
3C9	2.012	23.32	-1.12	29.89	0.1171	3
3C275.1	0.557	23.3	-0.96	28.46	0.1	3
3C272.1	0.0029	23.29	-0.6	23.63	0.0113	0
3C263.1	0.824	22.85	-0.87	28.84	0.0682	1
3C175	0.768	22.56	-0.98	28.78	0.3849	3
3C436	0.2145	22.35	-0.86	27.47	0.3801	1
3C300	0.272	22.17	-0.78	27.69	0.4195	1

Continued on next page

Table 4.15 – continued from previous page

Name	z	S_{151MHz} Jy	α	$\log P_{151MHz}$ W Hz^{-1}	D Mpc	Type
3C315	0.1083	21.84	-0.72	26.8	0.3985	1
3C208	1.109	21.43	-0.96	29.15	0.1146	3
3C28	0.1952	21.19	-1.06	27.37	0.1476	0
3C274.1	0.422	20.77	-0.87	28.1	0.8322	1
3C381	0.1605	20.68	-0.81	27.15	0.2024	2
3C442A	0.027	20.49	-0.96	25.53	0.3239	0
3C31	0.0167	20.1	-0.57	25.1	0.9174	0
3C220.1	0.61	20.04	-0.93	28.48	0.2358	1
3C324	1.2063	19.94	-0.9	29.18	0.0938	1
3C305	0.0417	19.67	-0.85	25.9	0.0112	1
3C173.1	0.292	19.42	-0.88	27.71	0.2645	0
3C319	0.192	19.36	-0.9	27.3	0.3361	0
3C220.3	0.685	19.35	-0.75	28.54	0.0708	1
3C212	1.049	19.2	-0.92	29.03	0.0866	3
3C190	1.197	19.11	-0.93	29.17	0.0249	3
3C325	0.86	19.07	-0.7	28.76	0.1345	3
3C172	0.5191	19.01	-0.86	28.27	0.7533	1
3C263	0.652	19.0	-0.82	28.5	0.3538	3
3C226	0.82	18.95	-0.88	28.75	0.246	1
3C65	1.176	18.78	-0.75	29.08	0.1596	1
3C181	1.382	18.63	-1.0	29.34	0.0615	3
3C153	0.2769	18.62	-0.66	27.61	0.0383	1
3C186	1.063	18.61	-1.15	29.1	0.0203	3
3C267	1.144	18.53	-0.93	29.11	0.3127	1
3C368	1.132	18.39	-1.24	29.19	0.0945	1
3C437	1.48	18.11	-0.79	29.31	0.3383	1
3C223	0.1368	18.07	-0.74	26.94	0.7405	1
4C73.08	0.0581	17.94	-0.85	26.16	1.1295	1
3C245	1.029	17.85	-0.78	28.93	0.0435	3
3C239	1.781	17.2	-1.08	29.61	0.1141	1
3C207	0.684	17.16	-0.9	28.52	0.092	3
3C236	0.0989	17.07	-0.51	26.61	4.5256	0
3C457	0.428	16.88	-1.01	28.05	1.1749	1
3C351	0.371	16.8	-0.73	27.86	0.3794	3
3C270.1	1.519	16.74	-0.75	29.29	0.0931	3
3C191	1.9523	16.68	-0.98	29.65	0.0445	3
3C6.1	0.8404	16.66	-0.68	28.67	0.206	1
3C132	0.214	16.66	-0.68	27.32	0.0779	1
3C184	0.994	16.59	-0.86	28.89	0.0456	1
3C349	0.205	16.38	-0.74	27.28	0.289	1
3C321	0.096	16.22	-0.6	26.56	0.5461	1
3C68.1	1.238	15.97	-0.8	29.08	0.4414	3
3C184.1	0.1187	15.88	-0.68	26.75	0.39	1
3C296	0.0237	15.85	-0.67	25.3	0.2089	0
3C205	1.534	15.83	-0.88	29.33	0.1609	3
3C455	0.5427	15.73	-0.71	28.21	0.0248	3
3C33.1	0.181	15.72	-0.62	27.13	0.692	2
3C441	0.708	15.7	-0.83	28.51	0.262	1
3C277.2	0.766	15.49	-1.02	28.63	0.4067	1
3C34	0.689	15.48	-1.06	28.52	0.3479	1
3C13	1.351	15.27	-0.93	29.2	0.2522	1
3C318	1.574	15.23	-0.78	29.3	0.0102	0
3C76.1	0.0324	15.1	-0.77	25.56	0.1294	0
3C22	0.938	15.01	-0.78	28.76	0.2049	2
3C289	0.9674	14.97	-0.81	28.8	0.0937	1
3C241	1.617	14.78	-0.97	29.39	0.0085	1
4C74.16	0.81	14.77	-0.87	28.63	0.3393	-1
3C42	0.395	14.77	-0.73	27.87	0.1546	1

Continued on next page

Table 4.15 – continued from previous page

Name	z	S_{151MHz} Jy	α	$\log P_{151MHz}$ W Hz^{-1}	D Mpc	Type
3C215	0.411	14.76	-1.06	27.96	0.3059	3
3C19	0.482	14.64	-0.63	28.05	0.0371	1
3C454	1.757	14.61	-0.9	29.44	0.0101	3
A1552	0.0837	14.59	-0.94	26.4	0.2643	0
3C356	1.079	14.55	-1.02	28.97	0.6106	1
3C175.1	0.92	14.4	-0.91	28.76	0.0705	1
3C285	0.0794	14.38	-0.95	26.35	0.2699	1
3C284	0.2394	14.38	-0.95	27.39	0.6744	1
3C299	0.367	14.36	-0.65	27.77	0.0575	1
3C337	0.635	14.31	-0.63	28.31	0.3121	1
3C266	1.272	14.29	-1.01	29.13	0.046	1
3C43	1.47	14.25	-0.75	29.19	0.011	3
3C16	0.405	14.24	-0.94	27.91	0.3952	0
3C352	0.806	14.22	-0.88	28.61	0.1129	1
3C252	1.105	14.22	-1.03	28.99	0.4662	1
3C469.1	1.336	14.17	-0.96	29.17	0.651	0
3C200	0.458	14.12	-0.84	28.01	0.1425	0
3C432	1.805	14.1	-0.98	29.49	0.1266	3
3C336	0.927	14.09	-0.73	28.71	0.2199	3
4C13.66	1.45	14.05	-0.81	29.19	0.0118	1
3C217	0.8975	13.96	-0.77	28.68	0.109	1
4C14.11	0.206	13.89	-0.84	27.22	0.3917	0
3C303	0.141	13.82	-0.76	26.85	0.1167	2
3C449	0.0171	13.75	-0.58	24.95	0.5216	0
3C334	0.555	13.71	-0.86	28.2	0.3735	3
3C204	1.112	13.62	-1.08	28.99	0.303	3
3C341	0.448	13.57	-0.85	27.98	0.4251	1
3C314.1	0.1197	13.56	-0.95	26.7	0.4339	0
4C14.27	0.392	13.53	-1.15	27.88	0.19	1
4C16.49	1.296	13.44	-1.0	29.12	0.1507	3
3C46	0.4373	13.37	-1.13	27.99	0.8951	1
3C249.1	0.311	13.37	-0.81	27.6	0.2128	3
3C294	1.786	13.36	-1.07	29.5	0.1368	1
NGC6109	0.0296	13.26	-0.76	25.42	0.5277	0
NGC7385	0.0243	13.24	-0.75	25.25	0.437	0
NGC6251	0.024	13.06	-0.72	25.23	1.907	0
3C68.2	1.575	12.96	-1.05	29.34	0.2541	0
3C346	0.162	12.96	-0.52	26.94	0.0474	1
3C35	0.0677	12.94	-0.77	26.15	0.9722	0
3C14	1.469	12.91	-0.81	29.17	0.2198	3
3C247	0.7489	12.82	-0.61	28.42	0.1071	1
3C268.4	1.4	12.78	-0.8	29.11	0.0877	3
3C41	0.795	12.62	-0.51	28.45	0.1873	1
4C12.03	0.156	12.58	-0.87	26.91	0.5807	0
3C322	1.681	12.57	-0.81	29.29	0.3133	1
3C292	0.71	12.55	-0.8	28.4	1.006	1
3C470	1.653	12.49	-0.77	29.26	0.2202	1
3C49	0.6207	12.46	-0.65	28.23	0.0081	1
3C340	0.7754	12.4	-0.73	28.47	0.3416	1
3C67	0.3102	11.99	-0.58	27.52	0.0137	2

Table 4.16: The 6CE sample [Rawlings *et al.*, 2001] at α<-0.5. Col1: Source name, Col2: redshift, Col3: Flux at 151 MHz, Col4: Spectral index α measured between 1.4 GHz and 151 MHz, Col5: radio luminosity at 151 MHz, Col6: Linear size, Col7: Type: LEG = low excitation radio galaxy, HEG = high excitation radio galaxy, Q = quasar.

Name	z	S_{151MHz} Jy	α W Hz^{-1}	$logP_{151MHz}$ Mpc	D	Type
6C1204+3708	1.779	3.92	-0.85	28.86	0.7242	HEG
6C1205+3912	0.243	3.83	-0.81	26.82	0.0112	LEG
6C1148+3842	1.303	3.83	-0.8	28.51	0.0985	Q
6C1255+3700	0.71	3.66	-0.71	27.85	0.0046	Q
6C1301+3812	0.47	3.46	-0.81	27.42	0.1519	HEG
6C0955+3844	1.405	3.45	-0.92	28.59	0.3327	Q
6C1204+3519	1.376	3.43	-0.87	28.55	0.2625	HEG
6C0823+3758	0.207	3.35	-0.97	26.62	0.2823	LEG
6C1232+3942	3.221	3.27	-1.15	29.57	0.2228	HEG
6C0922+3640	0.112	3.27	-0.68	26.01	0.2224	LEG
6C1148+3638	0.141	3.21	-0.8	26.22	0.0357	LEG
6C1130+3456	0.512	3.2	-0.75	27.47	0.3279	LEG
6C0847+3758	0.407	3.07	-0.72	27.21	0.2329	HEG
6C0822+3417	0.406	3.06	-0.73	27.21	0.0486	LEG
6C1019+3924	0.922	2.99	-0.82	28.06	0.0677	LEG
6C1025+3900	0.361	2.97	-0.68	27.08	0.0067	LEG
6C0822+3434	0.768	2.93	-1.19	27.95	0.0848	LEG
6C0854+3956	0.528	2.92	-0.8	27.47	1.574	HEG
6C1230+3459	1.533	2.9	-0.8	28.56	0.2083	HEG
6C1256+3648	1.128	2.88	-0.76	28.23	0.1111	HEG
6C0905+3955	1.882	2.82	-1.08	28.88	1.9702	HEG
6C0919+3806	1.65	2.72	-0.99	28.69	0.1073	LEG
6C0857+3907	0.229	2.71	-0.75	26.6	0.0742	HEG
6C1042+3912	1.77	2.68	-0.63	28.6	0.1776	HEG
6C1017+3712	1.053	2.68	-0.88	28.16	0.1061	HEG
6C1043+3714	0.789	2.62	-1.03	27.89	0.031	LEG
6C1018+3729	0.806	2.52	-1.02	27.89	0.8483	HEG
6C1220+3723	0.489	2.52	-0.75	27.32	0.0382	Q
6C1141+3525	1.781	2.4	-0.93	28.69	0.1147	HEG
6C1217+3645	1.088	2.4	-0.74	28.11	0.0032	HEG
6C1257+3633	1.004	2.4	-0.98	28.1	0.2576	HEG
6C0820+3642	1.86	2.39	-0.98	28.75	0.4795	HEG
6C1129+3710	1.06	2.36	-0.76	28.08	0.195	HEG
6C1113+3458	2.406	2.33	-0.79	28.91	0.2081	HEG
6C1031+3405	1.832	2.33	-0.75	28.62	0.7719	HEG
6C0908+3736	0.105	2.33	-0.56	25.8	0.0663	LEG
6C0943+3958	1.035	2.31	-0.94	28.1	0.1363	LEG
6C1016+3637	1.892	2.28	-0.66	28.6	0.3077	HEG
6C1100+3505	1.44	2.26	-0.86	28.41	0.1319	HEG
6C0930+3855	2.395	2.21	-1.0	29.0	0.0457	LEG
6C1159+3651	1.4	2.2	-0.8	28.35	0.0096	LEG
6C0902+3419	3.395	2.14	-0.84	29.25	0.0913	HEG
6C1212+3805	0.947	2.14	-0.89	27.96	0.0041	LEG
6C1158+3433	0.53	2.12	-0.7	27.31	0.26	LEG
6C0825+3452	1.467	2.1	-0.85	28.39	0.1359	HEG
6C1011+3632	1.042	2.1	-0.9	28.05	0.8812	HEG
6C1108+3956	0.59	2.1	-0.78	27.43	0.1427	LEG
6C1134+3656	2.125	2.07	-0.93	28.8	0.2081	HEG
6C0901+3551	1.904	2.07	-0.96	28.7	0.0442	HEG
6C1125+3745	1.233	2.07	-0.83	28.2	0.151	Q
6C1045+3553	0.851	2.07	-0.85	27.82	0.0672	LEG
6C1143+3703	1.955	2.06	-0.7	28.61	7.0E-4	LEG
6C1045+3403	1.827	2.0	-0.84	28.59	0.1752	HEG

Table 4.17: The 7CRS sample at α<-0.5. Col1: Source name, Col2: redshift, Col3: Flux at 151 MHz, Col4: Spectral index α measured between 1.4 GHz and 151 MHz, Col5: Linear size, Col6: Type G = galaxy, Q = quasar, HEG = high excitation radio galaxy, LEG = low excitation radio galaxy, WQ = weak quasar, NLG = narrow line galaxy. Data aquired from several sources, see Section 4.2.3.

Name	z	ztype	S_{151MHz} Jy	α	$\log P_{151MHz}$ W Hz^{-1}	θ arcsec	D Mpc	Class	Kmag Mags
1732+6535	0.856	S	6.17	-0.96	28.33	20.0	0.1535	Q	-
7C0825+2446	0.086	S	4.299	-0.85	25.89	75.75	0.1221	G	11.9
1747+6533	1.516	S	2.72	-0.84	28.54	0.65	0.0055	WQ	-
5C6.78	0.263	S	2.623	-0.75	26.72	359.75	1.4597	G	15.22
7C0221+3417	0.852	S	2.565	-0.8	27.9	18.37	0.1408	G	17.47
1816+6710	0.92	S	2.36	-0.8	27.95	1.9	0.0149	NLG	-
5C7.78	1.151	S	2.327	-0.89	28.2	22.77	0.1876	G	17.76
1814+6702	4.05	S	2.26	-1.01	29.56	18.0	0.1245	NLG	19.16
1748+6703	3.2	-	2.17	-0.97	29.27	14.0	0.1057	-	18.27
1807+6831	0.58	S	2.12	-0.79	27.42	29.0	0.1908	HEG	-
5C7.9	0.233	S	2.042	-0.65	26.49	118.8	0.4408	G	14.01
5C6.19	0.799	S	2.035	-0.69	27.71	9.1	0.0683	G	17.21
5C7.70	2.617	S	1.981	-0.82	28.94	1.72	0.0137	Q	17.48
1802+6456	2.11	S	1.97	-1.19	28.9	26.0	0.2162	NLG	19.31
1743+6639	0.272	S	1.97	-0.68	26.62	50.0	0.2079	LEG	-
1815+6805	0.23	S	1.96	-0.73	26.46	50.0	0.1837	WQ	-
5C6.217	1.41	S	1.921	-0.69	28.25	12.22	0.1031	G	18.04
1743+6431	1.7	-	1.89	-0.94	28.54	45.0	0.3809	-	-
1758+6307	1.19	S	1.86	-0.81	28.11	3.4	0.0282	WQ	-
5C7.8	0.673	S	1.737	-0.79	27.49	45.55	0.3203	G	16.44
5C7.111	0.628	S	1.664	-0.68	27.37	11.78	0.0804	G	16.86
1825+6602	2.38	S	1.63	-0.81	28.76	1.0	0.0082	NLG	18.82
1753+6543	0.14	S	1.62	-0.63	25.91	84.0	0.2073	WQ	-
1743+6344	0.324	S	1.59	-0.9	26.73	14.0	0.0657	LEG	-
5C6.287	2.296	S	1.575	-1.02	28.82	12.66	0.1039	Q	16.11
1733+6719	1.84	S	1.55	-0.85	28.49	2.5	0.0211	WQ	18.14
5C7.194	1.738	S	1.546	-0.7	28.37	1.98	0.0168	Q	15.91
5C7.205	0.71	S	1.536	-0.79	27.49	14.93	0.1073	G	17.22
1755+6830	0.744	S	1.52	-0.77	27.53	8.9	0.0651	NLG	-
1813+6846	1.03	S	1.51	-0.92	27.9	52.0	0.4193	Q	-
1745+6422	1.23	S	1.41	-0.71	27.99	16.0	0.1331	WQ	-
5C6.83	1.8	P	1.396	-0.86	28.43	14.09	0.119	G	17.96
1826+6510	0.646	S	1.39	-0.82	27.36	34.0	0.235	LEG	-
5C7.245	1.61	P	1.381	-0.82	28.29	11.83	0.1002	G	18.53
1815+6815	0.794	S	1.37	-0.88	27.58	200.0	1.4977	NLG	-
1801+6902	1.27	S	1.37	-0.81	28.04	21.0	0.1755	Q	-
5C7.10	2.185	S	1.35	-0.99	28.68	20.58	0.1703	G	18.82
5C7.85	0.995	S	1.334	-0.71	27.75	28.43	0.2274	Q	16.24
5C7.118	0.527	S	1.32	-0.74	27.11	12.16	0.0763	B	15.48
5C6.201	0.595	S	1.304	-1.03	27.29	11.55	0.0769	G	17.37
7C0825+2443	0.243	S	1.302	-0.81	26.35	98.15	0.3758	G	13.99
1758+6553	0.171	S	1.3	-0.79	26.01	115.0	0.3349	LEG	-
1816+6605	0.92	S	1.29	-0.88	27.7	27.0	0.2116	NLG	-
5C6.24	1.073	S	1.282	-0.69	27.8	1.36	0.0111	G	17.25
5C6.233	0.56	S	1.266	-0.89	27.18	7.45	0.0483	G	16.94
1814+6529	0.96	S	1.22	-0.94	27.74	126.0	0.9989	NLG	-
1755+6314	0.386	S	1.19	-0.83	26.77	40.21	0.211	LEG	-
1819+6550	0.72	S	1.17	-0.72	27.37	8.5	0.0614	Q	-
5C7.106	0.264	S	1.138	-0.7	26.36	25.75	0.1048	G	14.3
1758+6535	0.8	S	1.13	-0.71	27.46	106.0	0.7958	NLG	-
1827+6709	0.48	S	1.1	-0.87	26.96	17.0	0.1015	LEG	-
1753+6311	1.96	S	1.06	-0.98	28.45	17.0	0.1426	NLG	18.24
5C6.264	0.831	S	1.047	-0.77	27.48	5.34	0.0406	Q	16.16
1805+6332	1.84	S	1.04	-0.97	28.37	14.0	0.118	NLG	18.84

Continued on next page

Table 4.17 – continued from previous page

Name	z	ztype	S_{151MHz} Jy	α	$\log P_{151MHz}$ W Hz^{-1}	θ arcsec	D Mpc	Class	Kmag Mags
5C7.23	1.098	S	1.032	-0.79	27.76	28.79	0.2352	G	17.98
1751+6809	1.54	S	1.03	-0.53	28.0	2.0	0.0169	-	18.24
5C6.160	1.624	S	0.998	-0.74	28.13	6.32	0.0535	Q	17.95
5C7.178	0.246	S	0.98	-0.95	26.25	31.47	0.1216	G	16.78
5C6.17	1.05	P	0.973	-0.89	27.72	48.92	0.3961	G	17.8
1822+6601	0.37	S	0.97	-0.66	26.61	52.0	0.2662	LEG	-
5C6.62	1.45	P	0.953	-0.89	28.05	32.07	0.271	G	17.43
1811+6321	0.273	S	0.95	-0.91	26.33	52.0	0.2167	LEG	-
5C6.292	1.241	S	0.928	-0.93	27.89	4.97	0.0414	G	19.38
5C7.15	2.433	S	0.918	-0.74	28.49	2.02	0.0164	G	18.7
5C7.170	0.268	S	0.906	-0.82	26.29	23.6	0.0971	G	14.05
5C7.195	2.034	S	0.889	-0.8	28.33	2.64	0.0221	Q	17.71
5C6.214	0.595	S	0.877	-0.93	27.09	32.5	0.2164	G	17.17
5C7.208	2.0	P	0.873	-0.87	28.34	17.53	0.1467	G	17.44
5C6.95	2.877	S	0.865	-0.86	28.7	14.5	0.113	Q	16.04
5C7.271	2.224	S	0.835	-0.6	28.29	1.16	0.0096	G	18.74
5C7.87	1.764	S	0.834	-0.94	28.22	11.21	0.0948	Q	18.74
5C7.82	0.918	S	0.822	-0.93	27.52	45.73	0.3583	G	17.0
1736+6710	0.188	S	0.82	-0.65	25.89	29.96	0.094	LEG	-
5C7.7	0.435	S	0.804	-0.51	26.67	2.37	0.0134	G	15.59
5C6.43	0.775	S	0.792	-0.81	27.3	4.255	0.0316	G	17.73
5C6.25	0.706	S	0.79	-0.94	27.23	27.64	0.1982	G	17.21
5C6.63	0.465	S	0.787	-0.81	26.77	63.17	0.3706	G	15.59
5C6.5	1.038	S	0.782	-0.72	27.57	23.08	0.1864	Q	16.26
1758+6719	2.7	S	0.76	-0.9	28.6	45.0	0.3567	NLG	19.29
1741+6704	1.054	S	0.72	-0.97	27.62	3.9	0.0316	NLG	-
1807+6719	2.78	S	0.71	-0.77	28.53	1.9	0.0149	NLG	20.01
5C6.239	0.805	S	0.707	-0.89	27.31	81.93	0.6164	G	17.22
5C6.282	2.195	S	0.707	-0.75	28.28	0.97	0.0080	Q	18.2
5C7.145	0.343	S	0.705	-0.74	26.41	19.12	0.0932	G	15.15
5C7.125	0.801	S	0.702	-0.6	27.22	16.0	0.1202	G	17.38
5C6.258	0.752	S	0.693	-0.59	27.15	0.326	0.0024	G	17.66
5C7.95	1.203	S	0.672	-0.92	27.72	58.68	0.4868	Q	16.61
1756+6520	1.48	S	0.67	-0.68	27.84	4.6	0.0389	NLG	18.84
1751+6455	0.294	S	0.65	-0.66	26.21	43.0	0.1889	LEG	-
5C7.57	1.622	S	0.648	-0.95	28.03	74.92	0.6347	G	18.78
7C0808+2854	1.883	S	0.646	-0.83	28.13	58.43	0.4919	Q	16.06
5C6.286	1.339	S	0.643	-0.91	27.81	16.7	0.1403	Q	17.62
1748+6731	0.56	S	0.64	-0.79	26.87	108.0	0.6986	HEG	-
5C6.279	0.473	S	0.63	-0.71	26.67	30.99	0.1836	G	16.24
1804+6313	1.5	-	0.62	-1.0	27.94	30.0	0.2538	-	18.74
1742+6346	1.27	S	0.62	-1.02	27.78	51.0	0.4261	NLG	17.94
5C7.17	0.936	S	0.62	-0.7	27.35	87.8	0.6915	B	17.19
5C6.75	0.775	S	0.611	-0.85	27.19	15.08	0.112	G	17.04
1826+6704	0.287	S	0.6	-0.71	26.16	19.0	0.0821	WQ	-
1807+6841	0.816	S	0.6	-0.79	27.22	12.0	0.0907	NLG	-
1812+6814	1.08	S	0.59	-0.75	27.49	27.0	0.2199	NLG	-
1745+6415	0.673	S	0.59	-0.69	27.0	5.6	0.0394	HEG	-
5C6.33	1.496	S	0.589	-0.84	27.86	14.66	0.124	Q	18.23
5C6.29	0.72	S	0.571	-0.75	27.07	12.79	0.0924	G	16.31
5C6.251	1.665	S	0.565	-0.8	27.93	5.99	0.0507	Q	17.66
1804+6625	1.91	S	0.55	-0.89	28.1	4.0	0.0336	Q	-
5C6.242	1.9	P	0.548	-0.84	28.07	5.06	0.0426	G	18.36
5C7.223	2.092	S	0.543	-1.0	28.25	5.07	0.0422	G	18.29
1740+6640	2.1	S	0.54	-0.52	28.01	0.5	0.0042	NLG	18.54
5C7.79	0.608	S	0.535	-1.14	26.95	277.11	1.8639	G	17.05
5C7.269	2.218	S	0.535	-0.93	28.27	7.46	0.0616	G	18.61
5C6.39	1.437	S	0.532	-0.75	27.74	25.4	0.2145	Q	17.87

Continued on next page

Table 4.17 – continued from previous page

Name	z	ztype	S_{151MHz} Jy	α	$\log P_{151MHz}$ W Hz^{-1}	θ arcsec	D Mpc	Class	Kmag Mags
5C7.47	1.7	P	0.529	-0.95	27.99	0.2	0.0017	G	19.2
1731+6641	0.562	S	0.52	-0.71	26.76	1.0	0.0065	HEG	-
1745+6624	3.01	S	0.51	-0.78	28.47	0.5	0.0038	NLG	20.25
5C6.34	2.118	S	0.505	-0.78	28.12	7.99	0.0664	Q	15.94
5C6.267	0.357	S	0.504	-0.71	26.3	4.74	0.0237	G	14.73
1813+6439	2.04	S	0.5	-1.03	28.19	38.0	0.3173	WQ	-
1754+6420	1.09	S	0.5	-0.85	27.46	15.0	0.1224	NLG	-
5C7.242	0.992	S	0.477	-0.75	27.31	48.78	0.3899	G	17.24

Table 4.18: The TOOTS-00 sample [Vardoulaki *et al.*, 2010] at α<-0.5. Col1: Source name, Col2: redshift, Col3: redshift type S = spectroscopic, P = photometric, Col4: Flux at 151 MHz, Col5: Spectral index α measured between 1.4 GHz and 151 MHz, Col6: Radio luminosity at 151 MHz, Col7: Angular size, Col8: Linear size, Col9: Type, G = galaxy, Q = quasar, Col10: Radio Morphology - FRII, FRI or CSS (compact steep spectrum).

Name	z	ztype	S_{151MHz} Jy	α	$\log P_{151MHz}$ W Hz^{-1}	θ arcsec	D Mpc	Class	Kmag Mags
TOOT00_1094	1.516	S	2.21	-0.98	28.5	7	0.0593	G	CSS
TOOT00_1200	0.691	S	1.59	-0.79	27.48	27	0.1919	G	FRII
TOOT00_1134	0.311	S	1.43	-0.81	26.63	50	0.2283	G	FRI
TOOT00_1129	1.86	S	1.16	-0.9	28.4	15	0.1264	Q	FRII-Q
TOOT00_1203	1.397	S	1.06	-0.84	28.04	5	0.0422	G	FRII
TOOT00_1048	1.943	S	0.86	-0.95	28.34	7	0.0588	G	FRII
TOOT00_1125	1.916	S	0.76	-0.94	28.27	96	0.8069	Q	FRII-Q
TOOT00_1034	0.58	S	0.61	-0.66	26.86	45	0.2961	G	FRI
TOOT00_1072	0.577	S	0.55	-0.72	26.82	27	0.1772	G	FRII
TOOT00_1140	0.911	S	0.53	-0.66	27.25	18	0.1407	G	FRI
TOOT00_1267	0.968	S	0.52	-0.74	27.32	10	0.0794	G	FRII
TOOT00_1132	0.183	S	0.42	-0.7	25.58	4	0.0123	G	FRI
TOOT00_1250	1.35	S	0.41	-0.91	27.62	25	0.2102	Q	FRII
TOOT00_1215	0.278	S	0.35	-0.94	25.92	15	0.0633	G	FRI
TOOT00_1235	0.743	S	0.34	-0.55	26.82	6	0.0439	Q	Q-F
TOOT00_1115	0.416	S	0.32	-0.78	26.26	8	0.044	G	FRI
TOOT00_1149	0.26	S	0.27	-0.99	25.75	26	0.1046	G	FRI
TOOT00_1228	1.135	S	0.25	-0.52	27.09	4	0.0329	G	CSS
TOOT00_1224	3.438	P	0.24	-0.9	28.34	6	0.0442	G	CSS
TOOT00_1152	3.31	P	0.24	-0.82	28.26	30	0.2239	G	FRII
TOOT00_1143	0.438	S	0.22	-1.42	26.25	18	0.1021	G	FRI
TOOT00_1251	2.49	S	0.21	-1.06	28.05	25	0.2019	G	FRII
TOOT00_1291	0.917	P	0.2	-0.83	26.88	63	0.4934	G	FRII
TOOT00_1261	2.544	S	0.2	-1.19	28.12	5	0.0402	Q	FRII-Q
TOOT00_1090	0.201	S	0.2	-0.88	25.36	59	0.1954	G	FRI
TOOT00_1066	0.926	S	0.19	-1.16	26.96	19	0.1492	G	FRII
TOOT00_1099	1.397	S	0.17	-1.01	27.31	12	0.1012	G	FRI
TOOT00_1107	0.3	S	0.17	-1.52	25.75	25	0.1114	G	FRI
TOOT00_1289	1.784	S	0.17	-0.92	27.53	15	0.1267	G	FRII
TOOT00_1022	2.872	P	0.15	-1.02	28.03	7	0.0546	G	CSS
TOOT00_1173	0.332	S	0.15	-0.74	25.71	41	0.1956	G	FRI
TOOT00_1298	1.287	S	0.14	-0.69	27.02	16	0.1339	G	FRI
TOOT00_1214	3.081	S	0.14	-1.13	28.14	15	0.1146	Q	FRII-Q
TOOT00_1240	2.543	S	0.13	-1.29	27.99	209	1.6805	G	FRII
TOOT00_1252	3.229	P	0.13	-0.89	28.01	52	0.3914	G	FRII
TOOT00_1255	0.582	S	0.13	-0.6	26.18	8	0.0527	G	FRII
TOOT00_1204	0.6395	S	0.12	-0.6	26.23	17	0.117	G	FRI
TOOT00_1180	1.81	S	0.11	-0.87	27.34	15	0.1266	G	FRII
TOOT00_1188	1.417	S	0.11	-0.9	27.1	17	0.1435	G	FRII
TOOT00_1196	1.662	P	0.11	-2.16	27.8	-99	-	G	FRII
TOOT00_1029	0.737	S	0.11	-0.68	26.36	5	0.0364	G	CSS
TOOT00_1195	1.418	P	0.1	-0.85	27.04	49	0.4135	G	FRII
TOOT00_1244	1.358	S	0.1	-0.51	26.86	6	0.0505	Q	Q-F
TOOT00_1069	2.3	S	0.09	-1.45	27.79	10	0.082	Q	CSS-Q

Chapter 5

Radio Spectral Curvature & the Radio Luminosity Function

5.1 Introduction

The low frequency radio spectra of radio galaxies open a window into the physical conditions in and surrounding the central engine, and provide a crucial constraint on the evolution of such sources over cosmic time. The traditional view is that radio emission in active galaxies arises from the synchrotron radiation process, giving rise to a predominantly power-law spectrum. This leads to the common usage of a two-point spectral index to describe the radio spectrum for radio sources, as is used in Chapter 4. However, very few radio sources have a spectrum fully consistent with a simple power law across a wide range in frequency [e.g. Kellermann, 1998].

Synchrotron self-absorption and cooling losses allow deviations from the power law shape which can give strong insights into the evolution and orientation of the radio source (see Chapter 4, Figure 4.2). The radio spectrum has also been shown to inform on adiabatic expansion and the environment around the radio source [e.g. Kaiser, 2000], and is essential to determine the intrinsic luminosity of a source at a particular frequency, in addition to providing constraints on age in conjunction with source radio size [as in e.g. Murgia, 2003]. The extent of radio spectral curvature present in radio sources, particularly at high redshift, has been a subject of much debate.

The seminal work in the literature on spectral curvature was a study by Laing and Peacock [1980], who measured the radio spectra of two samples of sources from the 3CRR (165 sources) and the Wall and Peacock 2.7GHz (161 sources) complete samples respectively, using flux data points from 10 MHz to 14900MHz. They found that almost all sources in their sample displayed some degree of curvature. They also found that the shape of the radio spectra, in the low frequency range of a few MHz to a few GHz, were correlated with their luminosities. The lowest luminosity sources were most likely to display positive curvature, an inverted spectrum. Other than these, sources usually had negative curvature, and the degree of this curvature

increases with luminosity. Most recently, Duffy and Blundell [2012] also argue that the vast majority of radio source spectra can be characterised successfully with a polynomial fit, from which key physical parameters may be derived, including the equipartition magnetic field, without the need to fit complex power-law based models.

In early studies of radio spectra, as summarised by Kellermann [1998], sources were often classified simply by their shape into steep, flat, concave, convex or complex spectra. Whilst these radio spectral types are not absolutely tied to a specific type of source, some trends are apparent. The most powerful, classical double radio sources are most commonly associated with steep or concave spectra (see for example, the radio spectrum of Cygnus A, as presented in Duffy and Blundell [2012]). Very flat spectrum sources almost always indicate that the source is a quasar, or a broad-lined radio galaxy with jets aligned very closely to the line of sight (although note that quasars may also be steep or have concave spectra too). Convex, or inverted spectra are usually associated with a radio source dominated by emission from the core at GHz frequencies. As detailed in Chapter 4, core emission is typically flat spectrum, as a result of the superposition of self-absorbed components of different sizes at the origin of the radio jet. When such sources have their jets orientated towards the line of sight, this emission can be Doppler boosted, giving rise to a greater core contribution, and hence a flat or inverted spectrum. More extreme concave spectra, where there is a visible peak in the radio spectrum are associated with young, small, GPS or CSS sources. There is considerable interest in these relatively rare sources, as the general consensus now is that they are recently triggered (or restarted) 'baby' radio sources, which may constitute vital input into the current understanding of the triggering of AGN, and the AGN duty cycle [see e.g. Murgia, 2003; Nesvadba *et al.*, 2007]. Radio spectra, in conjunction with radio size measurements can give an estimate of the age of the source, particularly for very young radio sources (GPS or CSS) which display strong synchrotron self-absorption (a peaked spectrum) due to confinement within the host galaxy [cf. O'Dea, 1998], and very old, giant radio sources with an old electron population [e.g. Orrù *et al.*, 2010].

The most general distinction in radio spectra is that of 'flat' and 'steep' sources, the cut-off between the two generally being an observed two-point spectral index of α<-0.5. This cut is often used in the literature to obtain a sample without heavily beamed sources [cf Chapter 4, Rigby *et al.*, 2011], and primarily composed of comparable, classical double radio sources. However, this two-point spectral index is generally not sensitive to any curvature present in the spectrum, except for the most extreme cases, and gives no information of the relative proportions of spectral types. The exact proportions of radio sources samples which are GPS/CSS, or core-dominated has been called into question by several authors. Blundell *et al.* [1999] argue that radio samples selected at GHz frequencies are not as useful for studying classical radio galaxies as they will include high number densities of GPS/CSS, core-dominated and flat spectrum sources out to high redshift, thus complicating any study looking at evolution of classical double radio galaxies, but give no quantifications. Jarvis and Rawlings [2000] present the only existing measure in the literature, and suggest that it may be necessary to model these populations separately when constructing radio luminosity functions for high frequency (GHz) selected flat and steep spectrum samples. However, the proportions, and evolution of differing radio spectral

types within radio galaxy samples remains in question.

Another important driver for measuring radio spectra within complete radio galaxy samples is to determine whether it influences searches for high redshift radio galaxies, which rely on a two-point observed spectral index as being representative of the spectrum. The concave curvature of the majority radio spectra has often been put forward as the primary source of the observed correlation between redshift and observed spectral index. As the concave spectrum is redshifted, an increasingly steeper part of the spectrum will be observed; a k-correction. In Chapter 4 it is shown that indeed a k-correction can account for up to 50% of the observed z-α correlation. Studies of ultra-steep spectrum samples in the literature remain inconclusive over whether measurable curvature exists in the radio spectra with ultra-steep two-point spectral indices [cf. Ishwara-Chandra *et al.*, 2010; Bornancini *et al.*, 2007].

Work by Klamer *et al.* [2006] suggested that in addition to the correlation arising solely from the k-correction there may be an intrinsic z-α correlation arising from a denser surrounding medium and that the radio spectra of high redshift galaxies may in fact be an important probe of their environment. As high redshift radio galaxies are the only known early galaxies with radio jets, this has important implications for studying the role of feedback, central to controlling galaxy formation and evolution at high redshift, through radio jets either quenching star formation by heating the surrounding gas, or triggering star formation through shocks. Gopal-Krishna *et al.* [2012] however dispute this explanation, showing that there is no evidence for a steeper electron injection spectrum in a sample of CSS sources within dense environments, and instead suggest a much simpler explanation, namely that curvature present at low frequency due to synchrotron losses has simply moved out of the observable range at high redshift, giving ultra-steep measured spectra (Klamer *et al.* [2006] only had radio spectra reaching down to 800 MHz). They also point out that very high redshift radio sources would be expected to have stronger downward curvature than local sources, due to increased inverse Compton losses at high redshift. In Chapter 4 it has already been shown that the highest known redshift radio galaxies almost all display some curvature down to low frequencies, which supports this latter view. Interestingly, as discussed in Chapter 4, Falcke *et al.* [2004] suggest that GPS/CSS type radio sources are most likely to be seen at very high redshift: the highest redshift known radio galaxy is of this spectral type. However, radio spectra for several complete radio samples would be needed to measure how curvature correlates with redshift and observed spectral index, and whether indeed the fraction of GPS/CSS sources does increase at high redshift.

Finally, studying radio spectral curvature is vital in order to measure how the radio source population as a whole evolves with both radio power, and over cosmic time. The numbers of high redshift sources expected to be found in a particular sky area and at a particular finding frequency/flux density limit can be estimated through constructing and modeling radio luminosity functions from complete samples. The radio luminosity function, or RLF, measures the number density of galaxies at a particular luminosity over the redshift range of the sample. In order to measure this precisely, the form of the radio spectrum of each source must be known in order to compute the radio powers at the same rest-frame frequency. Traditionally, a simple power-law approximation is often used, as compiling homogeneous radio data over a

wide range of frequencies is time-consuming, and often radio data of comparable depth and resolution are not readily available for large samples. A power-law approximation is acceptable when the spectrum is close to straight: most luminosity function studies assume a constant spectral index between two fixed observing frequencies when calculating luminosities, or model the entire sample with an average spectral index of -0.7 or -0.8. However, this approximation will not be correct when there is significant spectral curvature present. At high redshift, where the numbers are low, this can have a significant effect on the high redshift end of the RLF, potentially shifting sources between different luminosity bins, or below the flux density limit of the sample.

Early studies have shown that there are some indications of a decline in density in the RLF beyond z=2.5 [see e.g. Dunlop and Peacock, 1990; Jarvis and Rawlings, 2000; Willott *et al.*, 2001], which would be expected, as some time is needed for the galaxies to grow into massive ellipticals, leading to a peak in number density at some point in the cosmic history. However these results failed to provide a definitive answer, as the various samples suffered from problems such as low depth or volume. CENSORS, a radio source sample of all sources above 7mJy at 1.4GHz, over six square degrees was designed to address this. Rigby *et al.* [2011] utilise the the complete CENSORS sample to model the RLF in conjunction with several other complete radio samples to provide comprehensive coverage of the P-z plane, and find shallow declines beyond a luminosity dependent peak redshift. However, one of the largest uncertainties in this study remained the lack of radio spectral information for the CENSORS sample, which can change the luminosities by a non trivial amount compared to luminosities calculated assuming a simple power law spectral index.

This is demonstrated clearly in Jarvis and Rawlings [2000], who investigated the luminosity function of a flat spectrum radio source sample. The sample contained a number of GPS, CSS and variable spectrum sources, and they showed that if these curvatures are taken into account, a substantially different RLF is obtained, refuting previous findings by e.g. Shaver *et al.* [1996] of a very sharp cut-off in the radio-loud quasar RLF. They demonstrated that an RLF with either an abrupt cut-off, or no decline was unlikely, and that the data favoured an RLF with a more gradual decline in space density.

Blundell *et al.* [1999] fit the spectra for the 3CRR, 6CE and 7CRS samples with a first or second order polynomial, and currently the RLF modeling efforts based on these samples are the only ones to incorporate curvature into the luminosity determination for each source. However they do not investigate any further spectral curvature or proportions of spectral types. There has been no further recent comprehensive work in looking at radio spectral curvature of complete samples with different selection frequencies and flux density limits. Leading on from this, there has been significant work over the last few years to accurately model what is currently known of the radio source sky, as part of the SKA Design Studies project, to enable predictions of what the SKA will be able to achieve [Wilman *et al.*, 2008]. However this does not use radio spectral information, due to the difficulties in modelling the observed spectral index, which generally shows only weak trends with other radio source parameters (cf. Chapter 4).

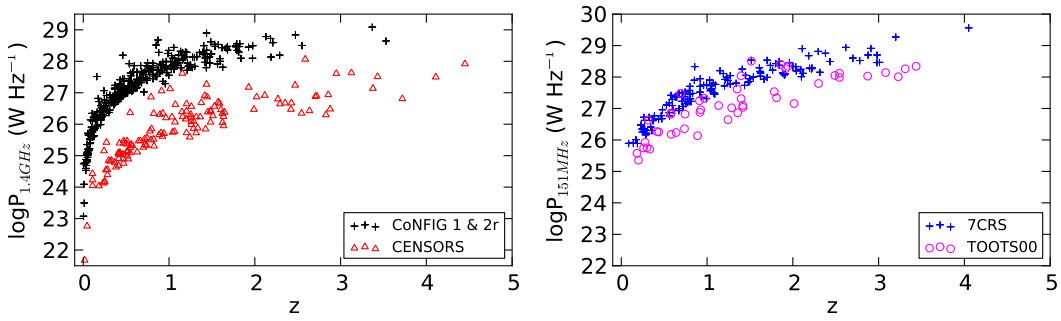

Figure 5.1: Luminosity Redshift plane coverage for 7CRS and TOOTS-00 selected at 151 MHz, and CENSORS and CoNFIG 1 & 2, selected at 1.4 GHz.

With the advent of next-generation radio facilities such as the LOFAR and the SKA, compiling the necessary data over a wide range of radio frequencies will soon become straightforward for large samples of radio sources. Already, early opportunties for addressing this important question are becoming feasible, with the completion of the 74 MHz VLSS survey [Cohen *et al.*, 2007], and deep 151 MHz TGSS (TIFR GMRT Sky Survey) ongoing. In order to provide a fully comprehensive and comparable view of spectral curvature, in this Chapter a quantitative study of how significant spectral curvature is across complete radio samples differing in selection frequency and flux density limits is presented, with the specific aim of quantifying how neglecting curvature affects the radio luminosity function of steep-spectrum sources. The unique contribution of this study is that although the samples utilised don't have the same extensive frequency coverage that previous studies such as Laing and Peacock [1980] or Blundell *et al.* [1999] used, the samples studied have differing flux density limits as well as selection frequencies, and as such can be used to explore spectral curvature over a much higher redshift range, in addition to ensuring that selection effects are minimised.

5.2 Compiling Flux Catalogues

Four complete radio samples, two selected at 1.4 GHz (CoNFIG1&2r, CENSORS), and two at 151 MHz (7CRS and TOOTS-00) were chosen to investigate spectral curvature. These samples are described in detail in Chapter 4, and were chosen to provide relatively good coverage of the P-z plane, and because all have flux data available in the literature over a wide range of frequencies.

5.2.1 CENSORS

The 135 source 1.4 GHz CENSORS sample has new low frequency radio data at 610 MHz and 325 MHz as detailed in Chapter 3, all of which are on the Perley-Taylor 1999 flux scale, in addition to data at 352 MHz from the WISH survey. As detailed in Chapter 3, a 10% error was added in quadrature with the measured errors for both the 325 MHz and 352 MHz data.

There are also 8GHz data for the compact, single component sources in CENSORS, kindly made available by Melanie Gendre, which is also on the Perley-Taylor 1999 scale.

Flux data were also obtained at 150 MHz from the new TIFR GMRT Sky Survey[1], or TGSS via early data release 4. The full fits image of the CENSORS field was downloaded from the TGSS archive, and fluxes for each CENSORS source measured using the AIPS task TVSTAT. For undetected sources, a measure of 5 x the rms noise at their position was taken as an upper limit value at 150 MHz. Note that errors in these measured fluxes and upper limits were calculated as 25% of their measured value, as the TGSS is still in the preliminary release stages, and the current error in the flux density scale is quoted to be around 25%. This value is expected to improve with later releases. The TGSS is on the Baars flux density scale. At 74 MHz, the VLSS image of the CENSORS field at 74 MHz was searched for counterparts for every source, and a detection entered into the catalogue as necessary. Note that for sources with no detection, an upper limit at 74 MHz was determined by taking a value of 2 x the RMS noise at the expected source position in the VLSS map, following Vardoulaki *et al.* [2010], but after the new TGSS data were obtained, these were no longer used in the subsequent fitting process (described below). This is because the TGSS (sensitivity ∼9 mJy) is much more sensitive, and in the case of no detection, provides a better constrained measure at a similar low frequency to the VLSS (sensitivity 100 mJy). The VLSS is also on the Baars flux density scale.

5.2.2 CoNFIG1&2r

ConFIG regions 1 and 2 have flux data from 365MHz to 5GHz, as presented in Gendre *et al.* [2010]. Flux data were added from the 7C 151MHz survey [Hales *et al.*, 2007] for 181 sources, and from the VLSS at 74 MHz for 366 sources. Data at 5 GHz, 2.7 GHz, 408 MHz and 365 MHz from Gendre *et al.* [2010] had no flux density error listed so a 10% error in flux density was assumed as an approximate estimation of the flux density error. A 3% error was assumed in the 1.4 GHz fluxes as these were obtained from the NVSS, and Condon *et al.* [1998] estimate a 3% error in fluxes for these data. For the 1.4GHz selected CoNFIG 1 and 2 datasets, all 406 sources have sufficient flux density data points in the range 365MHz to 5GHz to be fitted. Frequency coverage for this dataset is very good: only 28 sources have no data at 74/151MHz, and only 15 have no 2.7/5GHz data. In the final sample, only sources with 1.4GHz fluxes less than 1.3Jy were used from CoNFIG 2r, to ensure no duplication with sources also in CoNFIG 1 (see Chapter 4) giving a total of 334 sources in the sample.

Note that it is possible that very extended sources or confused sources may have incorrect fluxes measured at frequencies other than at the sample selection frequency of 1.4 GHz. Due to the large number in this sample, it was impractical within the time available to check every source by hand, however those with obviously discrepant flux data points (highlighted by very poor spectral fits) were double checked in the NASA Extragalactic database, and a few small adjustments were made. 4C12.39 was changed from 1.1Jy to 2 Jy [from White and Becker, 1992]. at 1.4 GHz. Several sources (4C07.32, 4C45.17, 4C32.25A, 4C31.32, 4C48.29A, 4C29.47, B2 1502+28, B0953+254, 4C41.22, 3C258) had their 365 MHz flux values removed, and in the

[1]This research work has used the TIFR GMRT Sky Survey (`http://tgss.ncra.tifr.res.in`) data products

case of 4C37.32, the 408 MHz value removed, as these fluxes were clearly underestimated in comparison to the rest of the measured radio spectrum (most of these were close to the flux limit of the TEXAS 365 MHz survey). In the case of B2 1502+28, and 4C29.47, data at 408 MHz from NED was added in replacement. Sources 1152+551, 4C61.23, 4C37.32 and 3C192 had their 151 MHz points removed also.

This process represented a best effort to obtain representative radio spectra for each source in the sample from the literature, but it should be emphasized that the radio fluxes come from a heterogeneous range of observations over several decades in time. Whilst the radio spectra of classical double radio sources are expected to remain relatively stable over time, for highly variable sources, e.g. flat spectrum quasars this will not be the case. In this study, the interest lies primarily in the former, but as a note of caution, catalogued spectra presented for flat spectrum, compact sources in the sample should not be treated as reliable.

5.2.3 7CRS

The 7CRS, or Seventh Cambridge Redshift Survey is composed of three subsamples, 7CI, 7CII and 7CIII. 7CI and 7CII, are each composed of 37 sources with a flux density limit of S_{151} >0.51 and S_{151} >0.48 in the 7C survey respectively (see Chapter 4 for details). For 7CI and 7CII, integrated fluxes were obtained from the literature at 4.85 GHz, 1.4 GHz (NVSS), 408 MHz (5C), 365 MHz (TEXAS), 151 MHz (7C) and 74 MHz (VLSS). Fluxes at 4.85 GHz, 1.4 GHz, and 74 MHz were on the Baars scale. The 408 MHz fluxes were on the KPW scale, which differs from the Baars by only 3%, and the 365 MHz fluxes were on the TEXAS scale, differing from Baars by just 4%. Thus no corrections were made to these data points (see discussion in Section 5.3). As 5C was a much older catalogue, and had no listed flux errors, an error of 10% was assumed for these data.

For 7CIII, integrated fluxes were compiled from cross-matching the 7C 151MHz catalogue of Hales *et al.* [2007], with the WENSS 327MHz survey, the VLSS 74MHz survey, the 8C 38 MHz survey, the NVSS at 1.4GHz, and finally 4.85GHz fluxes from Becker *et al.* [1991], which are all of comparable resolution. The 151 MHz and 38 MHz data were double checked for consistency against the values given by Lacy *et al.* [1999] for the 7CIII sample, and at 38 MHz, 7C1742+6346, and 7C1743+6344 had their 38 MHz values adjusted to those given in Lacy *et al.* [1999], as they are confused in the 8C catalogue. As the 38 MHz data are the least reliable, if a source was undetected, no upper limit was utilised. In order to constrain the very low frequency end of the spectra, an upper limit of 0.2 Jy (twice the average VLSS rms noise) was assumed for sources undetected in the VLSS 74 MHz catalogue, similarly to Vardoulaki *et al.* [2010]. For those catalogues with no flux density error listed a 10% error in flux density was assumed for each source. Fluxes at 4.85 GHz, 1.4 GHz, and 327 MHz are on the Baars scale, and the 151 MHz and 38 MHz data are on the RCB scale.

Note also that for the 7C sample, it is still possible that very extended sources may not have correct fluxes in these catalogues. Complete flux data for the entire sample is referenced several times in the literature [in e.g. Blundell *et al.*, 1999; Lacy *et al.*, 1999], but is as yet unavailable publicly in a collated form. In order to mitigate this, all extended sources listed

in the 7C Hales 151 MHz catalogue as having separate components were checked, and radio maps at 151MHz from the 7C data were cross-checked with NVSS maps in order to identify components and catalogue the correct integrated flux for each source.

5.2.4 TOOTS-00

The TOOT-00 region [Vardoulaki *et al.*, 2010], is the first complete region of the Tex-Ox-1000 redshift survey of radio sources. This survey selects all sources above 100mJy in the Cambridge 7C 151MHz survey, and is designed to be approximately 5 times fainter than the 7CRS, with much greater numbers. Vardoulaki *et al.* [2010] present complete radio, infra-red and spectroscopic data for the first region of the survey, comprising 47 sources. For TOOTS, flux data was obtained at 74MHz, 151MHz, and 1.4GHz (NVSS) from Vardoulaki *et al.* [2010], and at 327MHz from the WENSS catalogue. It should be noted that some of the 74MHz fluxes are upper limits and with only four data points maximum for each spectrum, spectra for this sample are less constrained than the others.

5.3 Flux Scales

With these flux density data, it was then possible to construct radio spectra for all the sources in the samples, and classify the sources according to their radio spectra. Luminosities and sizes were calculated for each sample similarly to Chapter 4, unless otherwise stated in the text. However, before fitting radio spectra, it is important to test whether the individual flux data points, compiled from multiple radio surveys, are consistent, and normalised to the same scale. If they are not, this could lead to erroneous measures of the whole radio spectrum.

For the vast majority of large radio surveys completed, the Baars *et al.* [1977] radio flux density scale is utilised as a common flux density scale. Other scales include the KPW [Kellermann *et al.*, 1969] and RCB [Roger *et al.*, 1973] scales, and at frequencies above $\sim$300 MHz, these agree to less than 10% [Scaife and Heald, 2012]. The RCB scale is used particularly at low frequencies, as the Baars scale has been shown to be less accurate here, as it is based on the flux density of Cassiopeia A, which is fading with time, and the rate at which it fades also varies with frequency, which is overestimated in Baars *et al.* [1977] [see e.g Helmboldt *et al.*, 2008; Rees, 1990]. The history of the usage of these scales is complex, it is not often clear in the literature which derivative scale has been utilised, and there remains some considerable uncertainty over how accurate the scales are at very low frequencies, $<$300 MHz, and at very high frequencies, $>$15 GHz. Converting between scales is not just a case of a simple scaling relation: the frequency dependence of the conversion factor, the usage of different calibrators in surveys, potentially with low frequency variability present, and flux calibration via bootstrapping from older surveys further complicates matters. This is an area that LOFAR will address.

However, until such times as new radio instruments are able to determine the flux scale accurately at low frequencies, it is useful to gain some constraints over how much the various scales produce differing radio spectra at the very lowest frequencies. Helmboldt *et al.* [2008] present spectra of the brightest VLSS sources at 74 MHz, and list correction factors to move

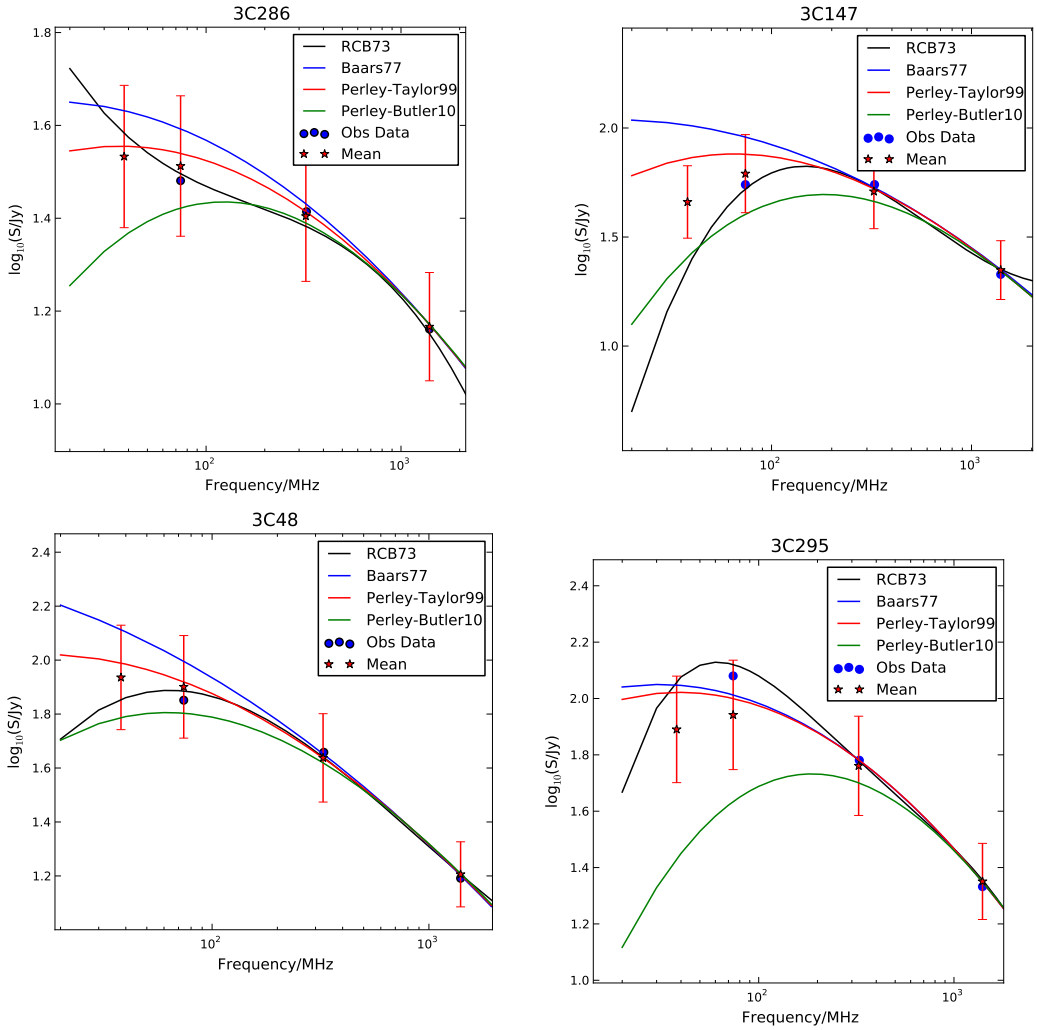

Figure 5.2: The radio spectra of bright unresolved calibrators 3C286, 3C147, 3C48 and 3C295 according to the Baars *et al.* [1977] (blue), Perley-Taylor 1999 (red), Perley-Butler 2010 (green) and Roger *et al.* [1973] (black) flux density scales. The overplotted black points indicate the 2001 VLA values between 327.5 MHz and 43 GHz, and the VLSS 74 MHz value for the source. The red points give the mean of all four scales at 38 MHz, 74 MHz, 325 MHz and 1.4 GHz.

existing radio data in the literature on to the Baars *et al.* [1977] scale, based on comparison of bright 3C fluxes: most of these give a maximum of a 10% correction or less. Most recently Scaife and Heald [2012] published well-determined spectra of several bright unresolved 3C sources commonly used as flux calibrators, tied to the RCB scale, as an initial calibrator catalogue for the LOFAR. There is corresponding data for these sources on the original Baars *et al.* [1977] scale, the Perley-Taylor 1999 scale, and the most recent Perley-Butler 2010 scale available in the VLA calibrator manual.

In Figure 5.2, the spectra for 3C286, 3C147, 3C48 and 3C295 are plotted for the Baars *et al.* [1977] (blue), Perley-Taylor 1999 (red), and Perley-Butler 2010 (green) defined scales, as given in polynomial form in the 2003 VLA Calibrator Manual[2] and AIPS Cookbook. Polynomials from Scaife and Heald [2012] are then plotted (derived from best fits to flux data corrected to the RCB scale) in black to represent the RCB scale. Note that only the frequency range less than 1.4 GHz is plotted for comparison purposes, as the Scaife and Heald [2012] is only valid over this range. Also plotted are VLA data for the calibrators at frequencies from 327 MHz-1.4 GHz[3] from the VLA calibrator manual (2001 values), and the VLSS at 74 MHz as blue circles. Finally, the red data points indicate the mean value of all four scales at 38 MHz, 74 MHz, 325 MHz and 1.4 GHz.

It is immediately clear that the scales agree reasonably well above ∼300 MHz for all four calibrators, to within 5%. The Baars and Perley-Taylor 99 scales appear to overestimate the flux at low frequencies for all but one source relative to the other scales. The Perley-Butler scale underestimates the flux at low frequencies - this is most likely because it has been determined solely between the frequencies of 300 MHz and 43 GHz, and so whilst it is now the default set of flux density calibrator coeeficients in both AIPS and CASA, caution should be used when applying it in low frequency (<300 MHz) data reduction. The main difficulties arise below 100 MHz, where only early data at a few tens of MHz (pre-1990) exists, the only recent data available being a single data point at 74 MHz from the VLSS. In Figure 5.3, the ratio between the Baars-derived scales and the RCB scale for the sources is plotted. Above ∼ 300 MHz, these agree to within +/- 5% for all calibrators. At lower frequencies, down to 40 MHz, the scales agree to within 10% for all calibrators but 3C147, for which the difference is up to 40%. This is most likely because 3C147 has been noted in the past to display low frequency radio variability over the timescale of years (see Ott et al 1994 and refs therein). These differences between flux scales, even at a few tens of MHz, are small (10% being the usual level of precision obtainable for radio data from current instruments), and are hence unlikely to give rise to false features, e.g. a low frequency turnover in the spectrum. New extensive, deep low frequency data would be needed to confirm whether the Baars-based or RCB scales are more accurate at the very lowest frequencies, which awaits the arrival of LOFAR. However, the mean of all four scales is within one 10% errorbar of all the individual scales for all sources for the four representative frequencies measured.

For this reason, it was decided not to correct the data to any one flux scale, as the radio data utilised in this chapter are all tied to one of the RCB, Perley-Taylor 1999 or Baars scales,

[2] http://www.vla.nrao.edu/astro/calib/manual/
[3] http://www.vla.nrao.edu/astro/guides/vlas/current/node31.html

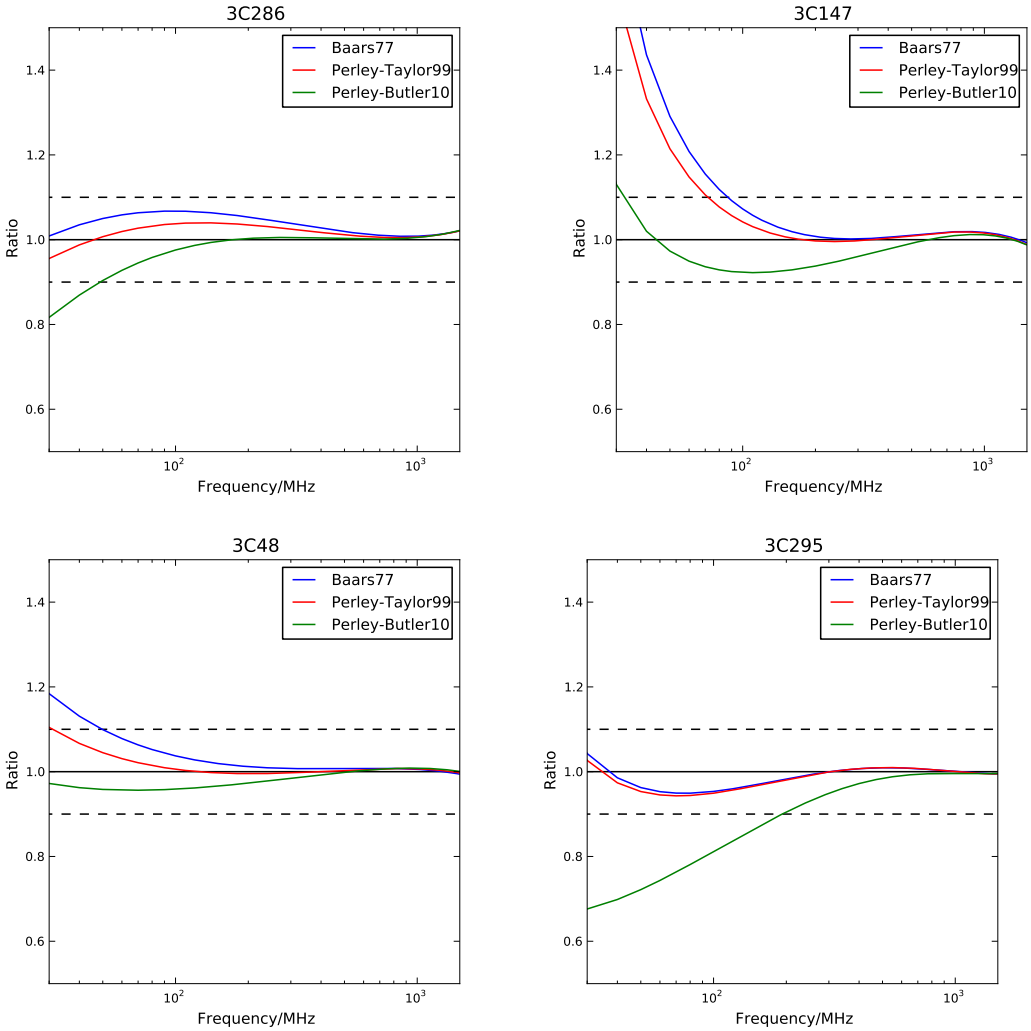

Figure 5.3: The ratio of the three Baars derived scales to the RCB scale for bright unresolved calibrators 3C286, 3C147, 3C48 and 3C295. Baars et al (1977) is in blue, Perley-Taylor 1999 in red, an Perley-Butler 2010 is in green. The black dashed lines indicate a difference from unity greater than 10%.

Table 5.1: Sources for the radio flux data used in this analysis. All data used is on a Baars or Baars-derivative scale, or the RCB scale, as discussed in the text. Scales marked with a * agree with either the Baars or RCB scales to less than 5% at the given frequency, and hence are not corrected.

Sample	Frequency	Scale	Reference
7CIII	38 MHz	RCB	8C,Rees [1990]
All	74 MHz	Baars	VLSS, Cohen *et al.* [2007]
CoNFIG, 7CRS, TOOTS-00	151 MHz	RCB	7C, Hales *et al.* [2007]
CENSORS	151 MHz	Baars	TGSS
CENSORS	325 MHz	Perley-Taylor 1999	Chapter 2, Ker
TOOTS-00, 7CIII	327 MHz	Baars	WENSS, Rengelink *et al.* [1997]
CENSORS	352 MHz	Baars	WISH, de Breuck *et al.* [2002]
CENSORS, CoNFIG, 7CI, 7CII	365 MHz	TEXAS*	Douglas *et al.* [1996]
CENSORS	408 MHz	TEXAS*	Molonglo Reference Catalogue
7CRS	408 MHz	KPW*	5C, Pearson and Kus [1978]
CoNFIG	408 MHz	Parkes*	PKSCAT90/Bologna, Gendre *et al.* [2010]
CENSORS	610 MHz	Perley-Taylor 1999	Chapter 2, Ker
All	1.4 GHz	Perley-Taylor 1999	NVSS, Condon *et al.* [1998]
CoNFIG	2.7 GHz	KPW/Parkes*	3C/PKSCAT90,Gendre *et al.* [2010]
7CRS	4.85 GHz	Baars	Becker *et al.* [1991]
CoNFIG	5GHz	KPW/Parkes/Baars*	3C/PKSCAT90/MIT,Gendre *et al.* [2010]
CENSORS	8 GHz	Perley-Taylor 1999	Section 5.2.1, Gendre

as listed in Table 5.1. Above 300 MHz, the data are tied to one of the Baars-based scales, which all agree to <5% with each other and with the RCB scale. Below 300 MHz, the data are on a mix of Baars-based scales (TGSS 151 MHz, VLSS 74 MHz) and the RCB scale (7C 151 MHz, 8C 38 MHz), which agree to within 10%, and should give a good indication as to how the radio spectra behave at very low frequencies, in addition to avoiding the risk of choosing an outlier flux scale.

5.3.1 Polynomial Fits to Radio Spectra

In order to measure the maximum amount of spectral curvature possible in each source, and to ensure all sources had a directly comparable measure of spectral curvature, a second order polynomial was fitted to all sources with greater than 2 flux data points

$$logS_\nu = \gamma + \alpha log\nu + \beta(log\nu)^2 \tag{5.1}$$

where S_ν is the flux density in Jy at frequency ν in GHz, and γ, α and β are the fitted parameters. α measures the gradient of the spectrum, and β provides a measure of the spectral curvature present.

Having fitted a polynomial of this form to the radio spectrum, it then becomes straightforward to obtain a best estimate of the spectral index at a particular frequency, α_ν

$$\alpha_\nu = \alpha + 2\beta log\nu \tag{5.2}$$

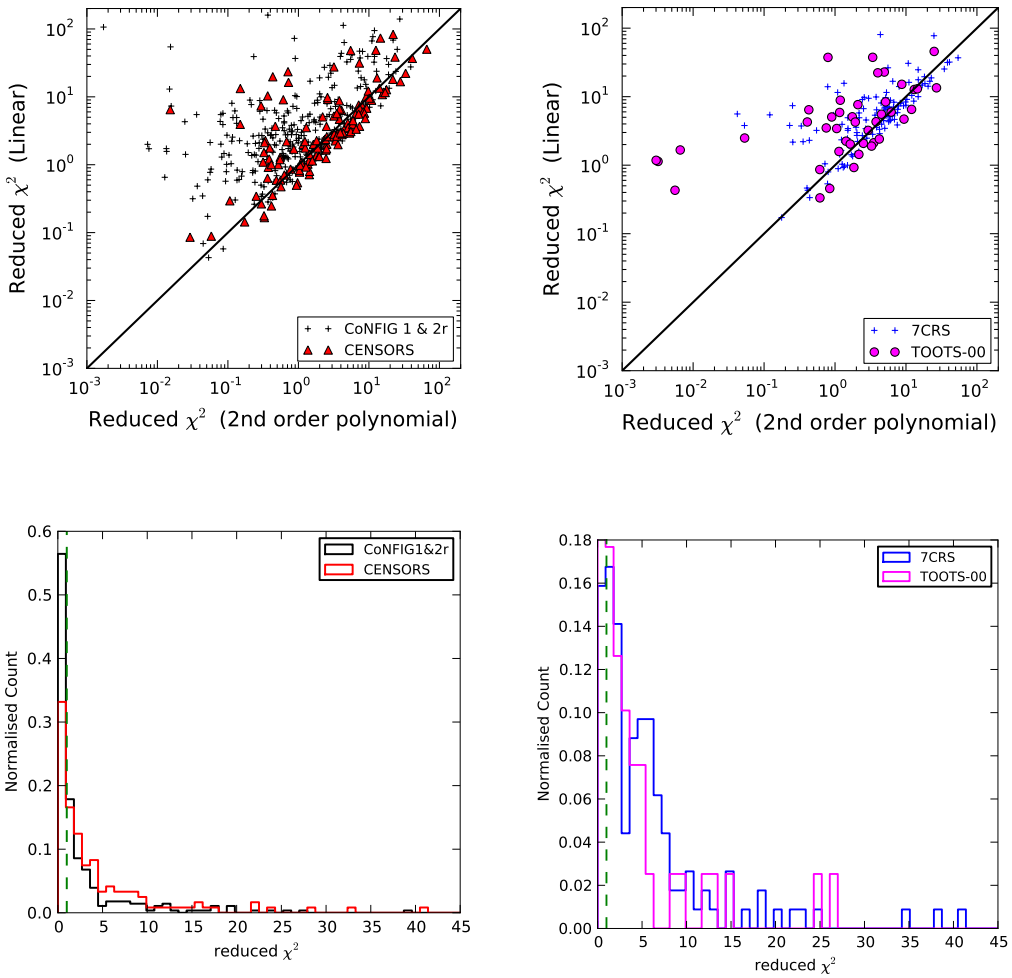

Figure 5.4: The top two panels display the reduced χ^2 values for both linear and polynomial fits to 7CRS and TOOTS, and CENSORS and CoNFIG 1 & 2r. These demonstrate that for many sources, the fit is greatly improved (lower rχ^2) using a 2nd order polynomial model. The lower two panels display histograms of the rχ^2 values for the 2nd order polynomial fits for the samples.

and finally at the rest frame frequency spectral index $\alpha_{\nu_{\rm rf}}$, using

$$\alpha_{\nu_{\rm rf}} = \alpha + 2\beta log(\frac{\nu}{(1+z)}) \tag{5.3}$$

The rest-frame peak frequency of the spectrum (if present) is:

$$\nu_{\rm peak_{rf}} = (1+z)10^{\frac{-\alpha}{2\beta}} \tag{5.4}$$

where β<0. Table 5.3-5.6 located at the end of this Chapter display the fitted parameters γ, α and β, and the errors in α and β, along with the radio fluxes used in the fitting.

Fit Quality

In Figure 5.4, the reduced χ^2 for both a linear and 2nd order polynomial fit is plotted for all the samples. It is immediately apparent that the polynomial provides a better fit to a greater majority of sources than does the linear. For CoNFIG and CENSORS, the majority of sources have a reduced χ^2 value close to one, suggesting the second order polynomial is a good fit. This is also true for 7CRS and TOOTS-00, albeit a slightly lower proportion. The 7CIII subsample of 7CRS has a much higher proportion of poorly fitted spectra, mostly likely due to the inclusion of 38MHz flux densities which have a high associated uncertainty. TOOTS-00 also has a high proportion of poorer fits, but has a low number of flux data points to fit, in addition to having a large number of upper limits at the lowest frequency measured. For those obviously not well fitted, possible explanations include several contributions to the radio spectra, e.g. a large contribution from the radio core, dominating above the lobes at high frequencies, introducing a complex spectra, or radio variability.

It is possible to fit more complex spectral shapes to radio spectra, as in e.g. Machalski *et al.* [2009], Murgia *et al.* [1999]. This has been attempted particularly for giant radio sources, and compact GPS/CSS sources in an attempt to measure spectral ages, magnetic fields etc. However, this is only really practical for sources with radio spectra determined to high precision, measured at multiple frequencies within a similar epoch. The results here demonstrate that a polynomial provides an accurate representation of the radio spectrum in the vast majority of cases for samples selected at both low and high frequency, and at varying flux densities across a range ∼100 MHz - 1 GHz.

The chief uncertainty in the curvature determinations, outside of the general flux data quality, lies in the fact that flux data are utilised from different epochs, giving rise to the possibility that variability is not accounted for in the some of the radio sources. Variability increases with shortening wavelength [Kellermann, 1998] due to the fact the core compact component dominates at higher frequencies, and it is this component that shows the most variability, rather than the radio lobes, which are only weakly variable at most, and follow a power law spectrum. However, variability has been shown to strongly correlate with spectral index, and generally only flat or complex spectra and a small angular size are associated with strong variability. For CoNFIG, this could potentially be quite a substantial effect, as 22% of ConFIG sources are classified as flat and compact, and the proportion of these increases to

almost 50% after redshift 2. For the much lower flux density limit sample CENSORS, only 14% meet the criteria and the possible radio variability candidates constitute a negligible proportion of the sample, particularly at high redshifts. The flux data for CENSORS were also taken closer together in time. 7CRS, and TOOT-00, being low-frequency selected, have a much lower proportion of flat-spectrum sources.

The Fitted Parameters

In Figure 5.5, the histograms for the fitted parameters α and β are shown for CoNFIG 1& 2r and CENSORS, and 7CRS and TOOTS-00, along with the best-fitting Gaussian approximation of the parameter distribution. 7CRS and CoNFIG show very similar distributions, with a clear high peak in both $\alpha \sim$ -0.7, and $\beta \sim$ -0.1. TOOTS-00 and CENSORS also peak around these values, but with a wider distribution, as would be expected from their less-constrained radio spectra.

A basic classification was then performed on the radio data, placing all sources into one of the following categories.

- Steep Straight Spectrum (S) if β was within 1σ of zero (where σ is the error in the fitted parameter β), and the observed spectral index between 1.4GHz and 325MHz was less than -0.5.
- Curved (C-) if β was more than 1σ below zero, with no maximum visible in frequency range 50 MHz- 15 GHz.
- Peaked (P) if β was more than 1σ below zero, with a maximum visible in the rest frame frequency range between 50MHz and 15GHz.
- Inverted (C+)if β was more than 1σ above zero.
- Flat Spectrum (F) if β was within 1σ of zero, and the observed spectral index between 1.4GHz and 325MHz was greater than -0.5.
- Undefined (U) if the spectrum had only three flux data points or less (not enough to obtain a reliable spectrum measurement).

Table 5.1: Radio Spectrum Classifications for the Samples.

Sample	Total Sources	Steep(S)	Curved(C-)	Peaked(P)	Inverted(C+)	Flat(F)	Undefined(U)
7CRS	128	58 (45%)	47 (37%)	13 (10%)	8 (6%)	1 (1%)	1 (1%)
TOOTS	47	13 (28%)	13 (28%)	8 (17%)	9 (19%)	1 (2%)	3 (6%)
CoNFIG	334	41 (12%)	166 (50%)	55 (16%)	36 (12%)	25 (8%)	11 (3%)
CENSORS	135	61 (45%)	20 (15%)	25 (19%)	20 (15%)	9 (7%)	0

The results can be seen in Table 5.1. The proportions of peaked sources are broadly consistent between the high and low frequency selected samples, comprising between 10% and 20% of the total sample sizes. The proportion of flat sources is very low in the low frequency selected samples of 7CRS and TOOTS-00, at only 1-2% of the total samples. In contrast, the high frequency selected samples of CoNFIG and CENSORS contain almost a factor of ten

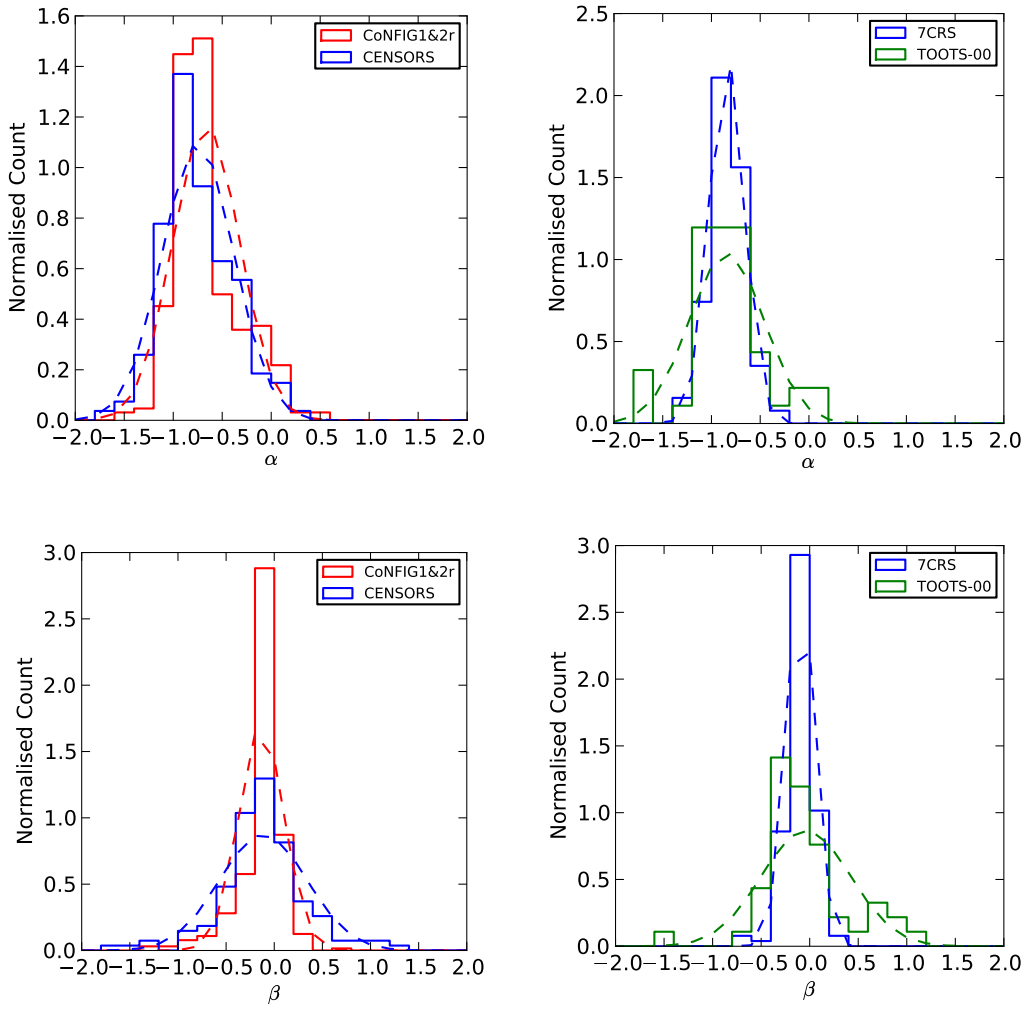

Figure 5.5: Fitted parameters α and β for the GHz and MHz samples, along with the best-fitting Gaussian (dashed lines) for each distribution.

greater proportion of flat spectrum sources. This is in line with the expectation that high frequency selected samples will detect more peaked and flat sources respectively, as they are more sensitive to the core emission, which dominates the total flux from these objects (cf. Figure 4.2, Chapter 4).

By the same argument, high frequency selected samples should be more sensitive to inverted spectrum sources if the inversion is caused by an increasingly important core contribution at high frequencies, and indeed inverted sources compose $\sim$ 12-15% of the high frequency samples, and just 6% of 7CRS. TOOTS-00 has an anomalously high proportion of inverted sources in comparison with 7CRS, and this is most likely due to TOOTS having less well-determined spectra (only four flux data points, and a large proportion of upper limits utilised) and a large associated uncertainty in the fitted parameters.

Where the largest difference lies is in the proportions of steep, and curved (C-) sources for the high frequency selected samples. For the low frequency selected samples, the relative proportions of steep and curved sources are consistent, at 30-40% for the former and 20-30% for the latter. For CENSORS and CoNFIG, the proportions of steep and curved sources are reversed, with CENSORS showing a much higher proportion of steep straight sources than CoNFIG. The reason for this difference is most likely to be the fact that the CENSORS spectra are much less well-constrained (cf. Figure 5.5), due to large uncertainties on the measured flux data points, and many more 74 MHz/151 MHz being upper limits, giving a large uncertainty in β and moving sources between classifications. This is demonstrated clearly in Figure 5.5, where as previously discussed, it can be seen that both samples broadly follow the same distribution in fitted parameters α and β. Hence the CENSORS classification between steep straight and curved should be treated with caution, until further constraining radio data can be obtained. In Figure 5.6, the fractions of the above defined spectral types are plotted, versus other radio observables: redshift, radio luminosity, and linear size (CENSORS, 7CRS and TOOTS-00) only. Some interesting trends are immediately apparent:

- The fraction of steep, curved and inverted sources remains approximately constant with redshift, for both high and low frequency selected samples.
- The fraction of peaked and flat sources shows a weak increase with redshift, again for both high and low frequency selected samples.
- Flat, peaked and inverted sources show no clear correlation with radio luminosity.
- The fraction of inverted, peaked and flat spectrum sources increases with decreasing radio size for all samples. The fraction of curved sources show very little correlation with linear size, but the fraction of steep sources very clearly increases with increasing radio size, again for both samples.

5.4 Radio Spectra and Source Evolution

Radio spectral curvature versus other observed radio parameters for each sample is plotted in Figure 5.7. What is immediately apparent is that both high and low frequency selected

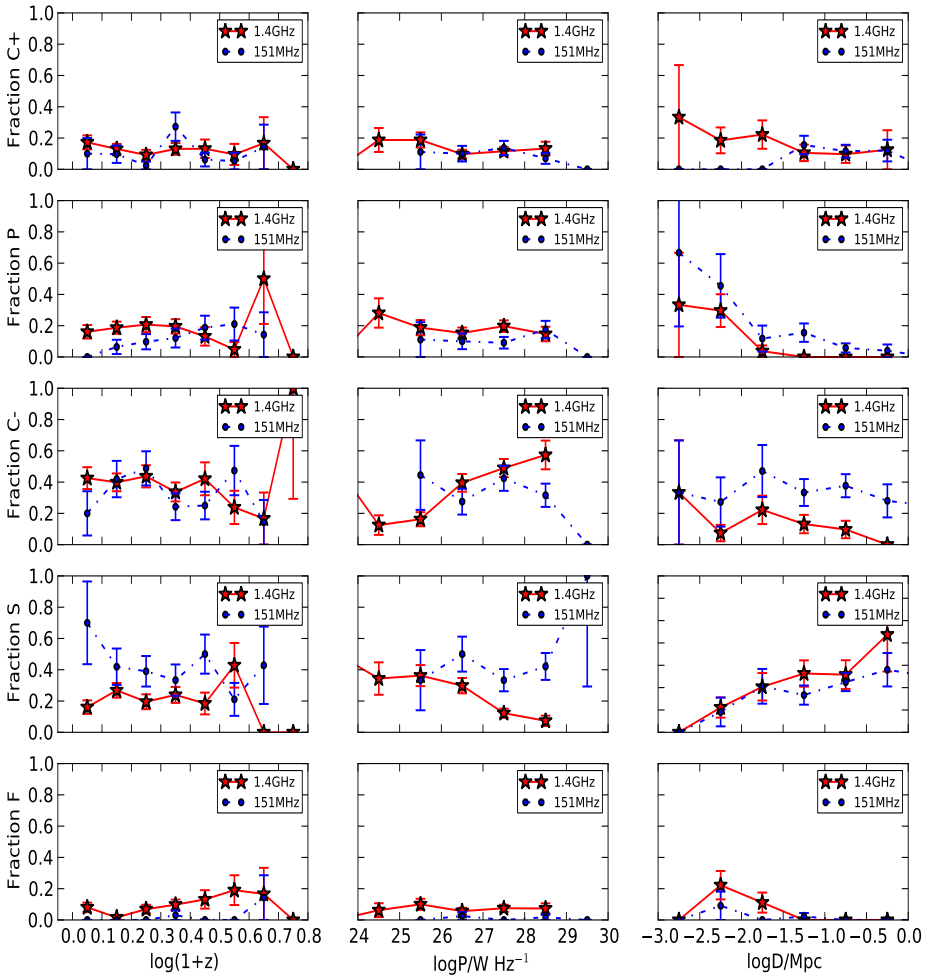

Figure 5.6: The fractions of radio spectral types for CoNFIG 1 & 2r and CENSORS (red) and 7CRS and TOOTS-00 (blue) against observable properties redshift, radio luminosity, and linear size. Note for linear size only CENSORS is used in red, as CoNFIG has no readily available size information.

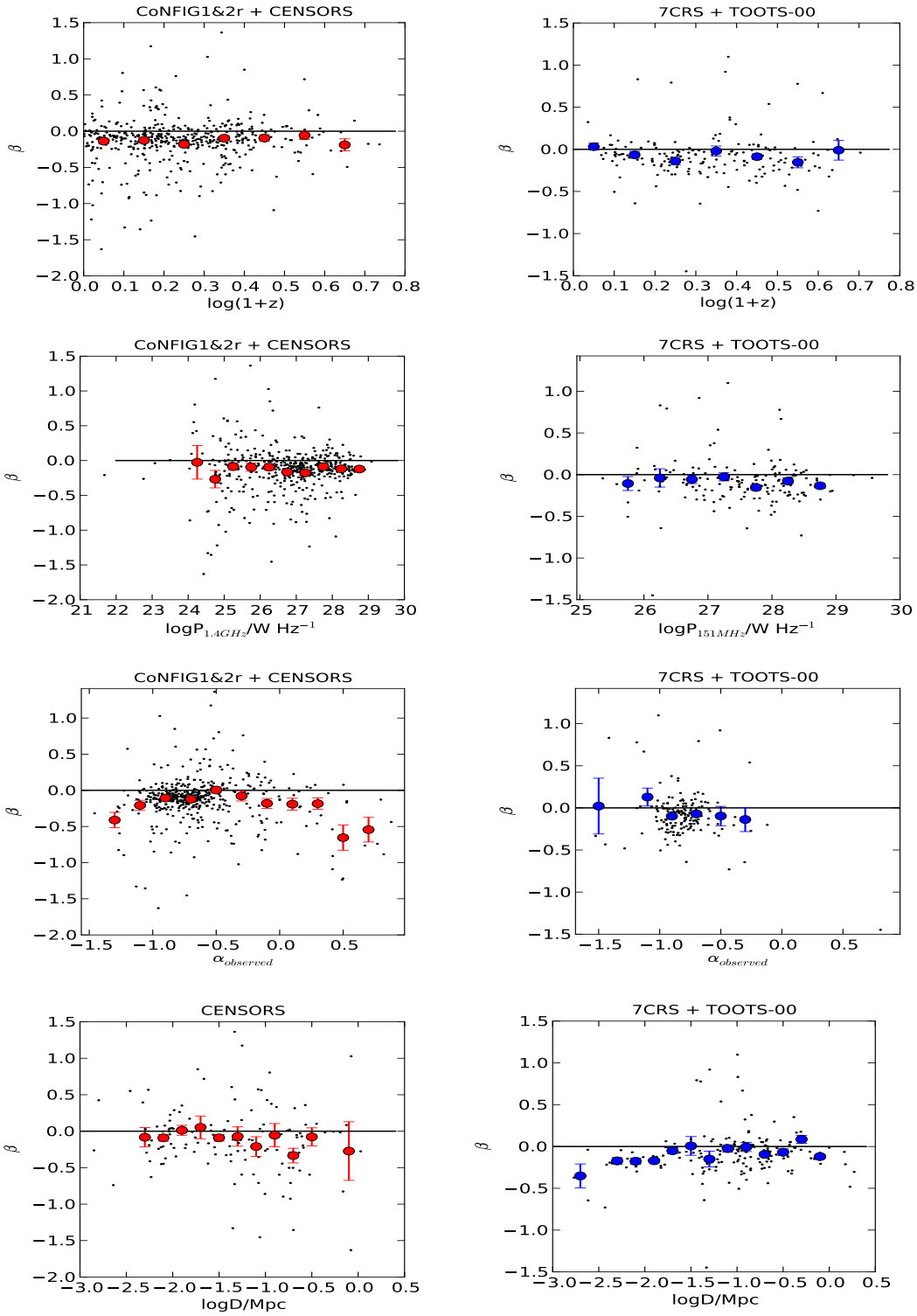

Figure 5.7: The spectral curvature parameter β versus redshift, radio luminosity, measured spectral index and radio size. Spectral index is measured between 1.4 GHz and 151 MHz for 7CRS and TOOTS-00, fitted between 1.4 GHz and 151 MHz for CoNFIG1 & 2r and measured between 1.4 GHz and 325 MHz for CENSORS. Plots on the left are for CoNFIG+CENSORS (red) and on the right 7CRS+TOOTS-00 (blue).

samples follow similar trends with redshift, with curvature for the bulk of the sources remaining approximately constant at -0.1 out to high redshift. There is a tendency for highly inverted sources to be located at lower luminosities, particularly at high frequency - a result which corroborates well with the findings of Laing and Peacock [1980].

Taking next the curvature versus observed spectral index (between 1.4 GHz and either 325 or 151 MHz), both the low and high frequency samples follow broadly the same trend, namely that there is much more curvature present in flat spectrum sources than steep spectrum sources. Bryant *et al.* [2009], studying a 408 MHz selected USS sample add 74MHz data to their high frequency data, find 75% of their source spectra are straight across this large frequency range, and therefore argue that the lack of curvature seen in their sample is evidence for intrinsic environmental effects seen in sources at high redshift - at high redshift there is much more gas around, a much denser environment, causing spectra to be steeper. This is slightly misleading, as a low-frequency selected sample selected by observed steep spectral index between two fixed frequencies will be biased toward low curvature sources, not necessarily at high redshift, as demonstrated by Figure 5.7. As can also be seen from the redshift versus observed spectral index plots in Chapter 4, for these samples, steep spectrum sources are only a little more likely to be at high redshift than low, so great care must be taken when inferring possible environmental effects from a sample with biased spectral index criteria.

This relation may also go some way to reconcile the apparently conflicting results of Klamer *et al.* [2006] who present a sample of 37 USS selected galaxies and show that only 11% of these show any curvature, and the low frequency selected complete samples of Blundell *et al.* [1999], of which $\sim$70% show definite curvature. The Klamer *et al.* [2006] sample had radio data covering only a high frequency range of 843MHz-18GHz. By selecting ultra-steep spectrum sources, again their sample would preferentially pick out low curvature sources over this frequency range. In the low frequency selected complete samples of Blundell et al (151-1400MHz) , there is no such spectral index cut, and a wide range of curvature is seen.

5.4.1 A Typical Radio Galaxy Spectrum

The results of the previous section would suggest that it is possible to define a 'typical' radio galaxy spectrum for a radio galaxy. In Table 5.2, the mean and median fitted values for γ, α, and β are listed, showing a remarkable similarity between all four samples, namely that β is $\sim$-0.1, and $\alpha\sim$-0.7, -0.8 for high and low frequency selected samples respectively. In Figure 5.8, the median radio spectrum for both the high and low frequency selected samples is plotted. This is calculated by calculating the flux at each frequency for each source using the fitted parameters, normalising by the flux at 1.4 GHz, and then finally taking the median flux at each frequency from all the sources in the sample. This median is what is plotted for each sample in Figure 5.8, verifying that the spectra in the high frequency selected samples are generally flatter than those in the low frequency selected samples.

This leads to the next interesting line of investigation. How many sources in a sample are 'atypical' in radio spectrum, and do these atypical sources correlate with any other observable? In Figure 5.6, the fraction of the various radio spectrum classifications is plotted against radio

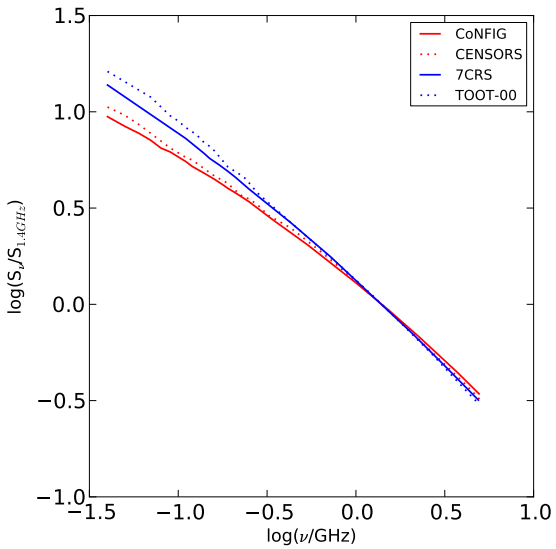

Figure 5.8: The median radio spectrum for both CoNFIG and CENSORS sources (red, solid/dotted), and 7CRS and TOOTS-00 (blue, solid/dotted).

Sample	N	Median			Mean			Std. Dev σ		
		γ	α	β	γ	α	β	γ	α	β
CONFIG	321	0.35	-0.75	-0.10	0.41	-0.66	-0.13	0.27	0.34	0.23
CENSORS	135	-1.65	-0.80	-0.12	-1.55	-0.75	-0.11	0.41	0.36	0.45
7CRS	128	-0.63	-0.86	-0.08	-0.62	-0.84	-0.10	0.27	0.18	0.15
TOOT-00	46	-1.37	-0.84	-0.12	-1.27	-0.84	-0.04	0.48	0.38	0.46

Table 5.2: The Median and Mean values of the spectral fitted parameters for each of the four samples, CoNFIG1&2r, CENSORS, 7CRS and TOOT-00.

luminosity, redshift, and linear size. It has already been shown that the proportion of peaked and flat spectrum sources weakly increases with redshift, and highly inverted sources are preferentially found at low radio luminosity. There have been some arguments presented in the literature [e.g. Blundell *et al.*, 1999] that orientation bias in GHz selected samples may adversely affect the correct determination of the radio luminosity function. Sources with an inverted spectrum are thought to be a result of orientation bias, with a stronger contribution from the flat spectrum core as it is viewed along the line of sight (cf Chapter 4).

5.4.2 The Origin of the C+ Sources

The proportion of inverted sources present in the samples is around 10%. For 7CRS and CoNFIG, the largest samples with the most well-determined spectra, the relative proportions are 6% and 12% respectively, so high frequency selected samples do appear to contain a larger proportion of inverted sources, than do lower frequency samples. At GHz rest frame frequencies, the core of a typical radio source will begin to contribute a substantial amount of the total flux

of the radio spectrum, and so samples selected at these frequencies will preferentially include fainter sources with cores orientated towards our line of sight, and which are hence undergoing Doppler boosting and will be increased above the flux density limit.

Core Contribution

It is important to place some constraints on the number of sources which show a genuinely inverted spectrum. It should then be possible to ascertain by how much contributions from the cores of the radio sources affect the sample. CENSORS has sufficient information to allow an attempt to test and quantify this effect, having 1.4GHz flux density information for all components of the individual sources. Using this, the radio core for each source was defined as being the radio component detected directly on top of the optical or infra-red host, and the ratio of core to total flux was calculated. Note that this will generally overestimate the true core flux, as it will contain the base of the jet, and possibly some lobe emission, but it is good enough to give a reasonable approximation.

Unambiguous cores were identified for 26 multi component radio sources in the sample. The remainder of the sample was classified as either being a double radio source with no unambiguous core (43), a single resolved source (28), or a single unresolved source (38). For the double radio sources, 18 had joined/blended lobes, from which it was not possible to separate a core feature. The other 25 had clearly separated lobes, and a host with no measurable radio emission - for these an upper limit to the core was estimated using 5 times the greatest rms flux measured in the radio maps of Best *et al.* [2003], which equated to 0.325 mJy.

In figure 5.9, the ratio of 1.4 GHz core to total flux vs β (curvature), and vs total 1.4GHz flux density is plotted. A weak correlation is seen in both. Curvature becomes increasingly convex as the core flux begins to dominate - a Spearman rank test on the cores (not including upper limits) gives a weak positive correlation of 0.19 with a p-value = 0.34, which is statistically insignificant. However, the sources with core upper limits are heavily weighted towards more negative curvature values, consistent with being lobe-dominated sources. Plotted versus 1.4GHz flux density, the core contribution increases with decreasing flux density, rising up to 40% of the total source flux at flux densities below 30mJy, a conclusion which remains robust even when the upper limits are considered. This is consistent with unification theories, in that at low flux densities, an increasing number of sources that have been Doppler boosted over the flux density limit due to a decreasing angle with the line of sight will be included.

Also plotted are histograms showing the curvature of 1) sources with a clear core, 2) double radio sources with no measurable core, and 3) single unresolved sources, in comparison to the curvature of the entire sample. Sources with a clear core appear to weighted towards positive curvature, whereas double sources with no measurable core appear to be weighted towards negative curvature, strengthening the results above. A two-sample KS test comparing the distribution of β for the 26 sources with a measurable core to the distribution of β for the 43 double sources with no measurable core shows that the hypothesis that both are drawn from the same distribution can be rejected at the 10% level, suggesting that the cores do indeed contribute to the spectrum shape. Single unresolved sources follow much the same distribution

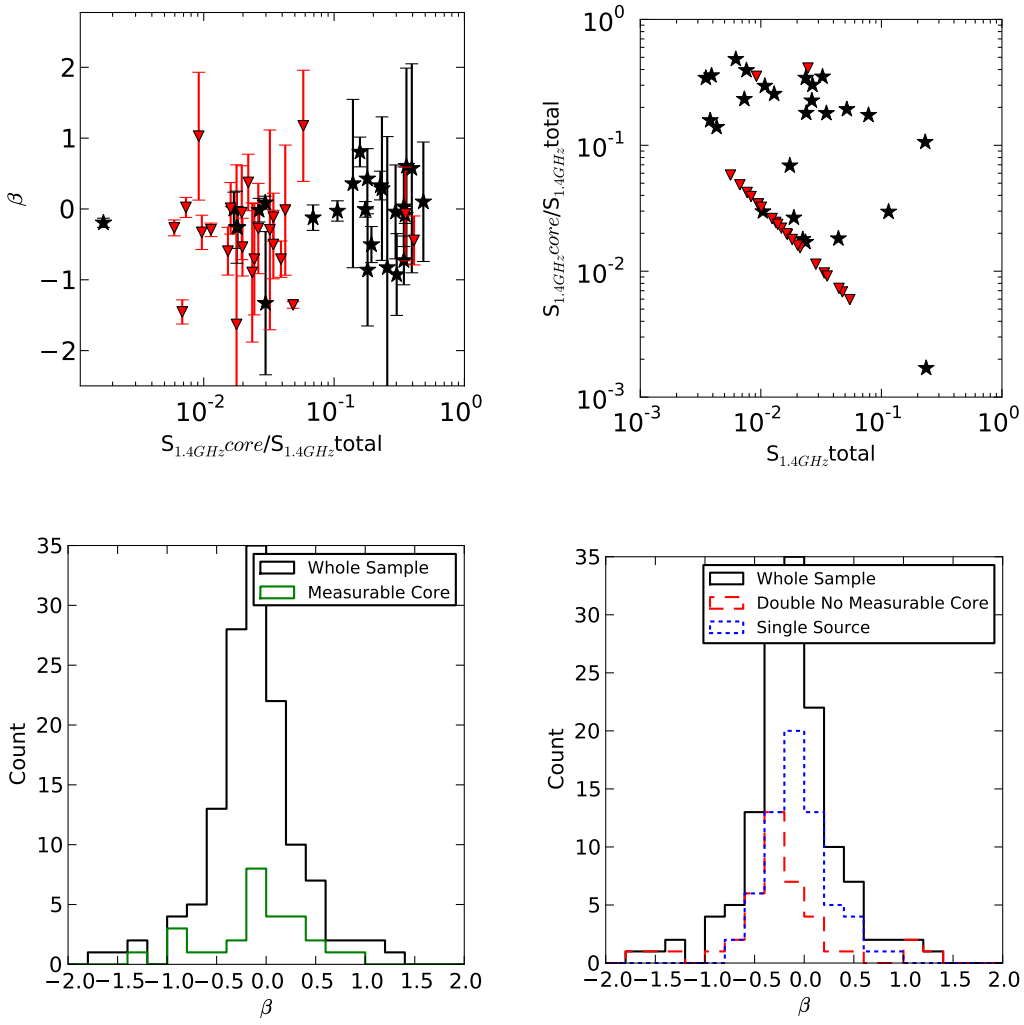

Figure 5.9: The top two figures show the ratio of core to total 1.4 GHz flux for the 26 CENSORS sources with an identifiable core, as described in the text, versus curvature β, and total 1.4 GHz flux (red triangles indicate upper limits in core flux for a further 25 double sources with no detected core). A very weak trend is visible with β, sources with a higher ratio seem to show increased positive curvature, although the data are very noisy. A trend is also apparent with total 1.4 GHz flux, with fainter sources more likely to show more positive curvature. The bottom two figures show histograms of β for the core classified sources, with the total sample plotted also for comparison.

as the entire sample as they dominate this. In the context of unification, unresolved sources may be young radio sources with recently triggered jets and hence too small to be resolved, or sources observed with their jet axis aligned to the line of sight, and hence undergoing Doppler boosting. Radio spectra may distinguish the first two, with the first having a S or C- spectrum and young radio sources having a GPS or CSS spectrum. If it is assumed that at a minimum, a similar proportion of the C+ single sources are core dominated to the already identified core dominated multi component sources, then the conclusion is that a moderate proportion of the sample has measurable core contributions to the radio spectra, up to 30%.

5.4.3 Young Radio Sources

Some of the very youngest radio galaxies known are thought to exhibit a Gigahertz Peaked (GPS), or Compact Steep (CSS) Spectrum. There is no one consistent set of selection criteria for Gigahertz Peaked and Compact Steep Spectrum sources available in the literature. However, what is generally agreed on is that GPS sources have a radio spectrum which peaks somewhere between 500MHz and 10GHz, and CSS have a radio spectrum which peaks around a few 100 MHz or below. Both classes are extremely compact, with GPS sources being less than 1kpc in size, and CSS less than 20kpc (see O'Dea [1998] for a description of the varied selection criteria used in early GPS/CSS sample definitions).

In Section 5.3.1, it was shown that sources with a 'peaked' radio spectrum, accounted for $\sim$10% of low frequency selected samples, and nearer 20% for high frequency selected samples. It can also be seen in Figure 5.6, that the fraction of peaked sources appears to weakly increase with redshift, remains relatively static with radio luminosity, and increases with decreasing source size, for both high and low frequency selected samples. The weak increase in redshift observed, if all the classified 'peaked' sources are true GPS/CSS sources, would be consistent with the 'youth-redshift' degeneracy postulated by Blundell and Rawlings [1999], whereby sources observed at high redshift are expected to be substantially younger than their low redshift counterparts.

A definition of true GPS and CSS in the samples is then adopted by adding a size constraint to the data of less than 30kpc. As there are no VLBI observations for the samples, the only constraints for the linear size come from the 1.4GHz VLA data presented Best *et al.* [2003] for CENSORS, and linear sizes already available in the literature for 7CRS and TOOTS-00. CoNFIG is excluded from this analysis as there is no readily available size data for this sample.

There is an additional complication in that the low frequency end of the spectrum is poorly constrained, with the lowest data point only at 151 MHz or 74 MHz for the majority of sources, some of these being upper limits. Hence a turnover at frequencies below $\sim$ 100 MHz could be missed. Therefore sources classed as curved (C-), but also with sizes less than 20 kpc were included in the definition of GPS/CSS, and an upper limit in observed peak frequency of 74 MHz assumed for these.

Observed and rest-frame peak frequencies were calculated as

$$\nu_{peak} = 10^{\frac{-\alpha}{2\beta}} \tag{5.5}$$

and

$$\nu_{peak_{\rm rf}} = (1+z)10^{\frac{-\alpha}{2\beta}} \tag{5.6}$$

respectively.

In the case of CENSORS, four sources had rest-frame spectral peaks >500 MHz and <15 GHz, and were smaller than 20 kpc (all were in fact smaller than 10 kpc), and could be classed as GPS sources, namely CENSORS 9, 25, 34, and 46. A further 6 sources, CENSORS 2, 3, 21, 24, 68, and 72 had a rest-frame spectral peak <500 MHz and a size less than 20 kpc and were classed as CSS sources. There were six remaining sources with a size less than 20 kpc and a curved spectrum, but no rest-frame spectral peak visible above 50 MHz (note that 4 of these sources were undetected at 74 MHz, making the presence of a peak at low frequency likely). These were CENSORS 12, 26, 69, 83, 88 and 95. Of these, CENSORS 95 is classed as a starbust galaxy, and CENSORS 72 as a quasar. This gives a minimum of 7% of the total sample being composed of young GPS/CSS radio galaxies (not including those with no visible spectral peak), but more likely closer to 10% of the sample in total. In 7CRS, 18 sources meet

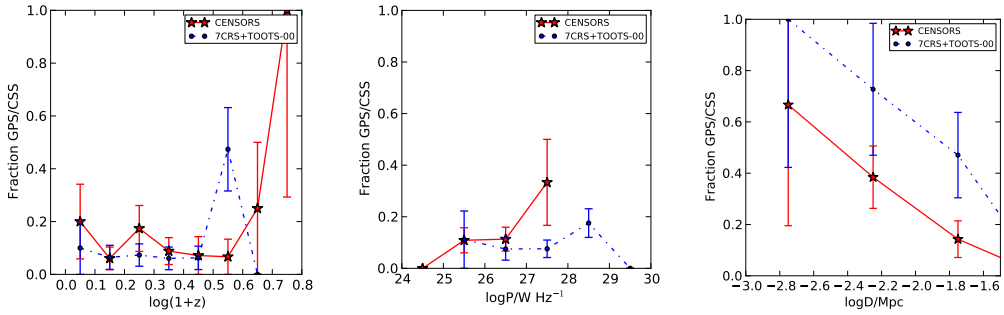

Figure 5.10: The fractions of GPS/CSS radio galaxies for CENSORS (red) and 7CRS/TOOTS-00 (blue)

the above criteria for a GPS/CSS classification. Three sources have rest-frame spectral peaks >500 MHz and <15 GHz and a size less than 20 kpc, and are classed as GPS sources. Of these, one is a quasar. A further 9 sources have a spectral peak in the range 50 MHz to 500 MHz and a size less than 20 kpc. Of these, three sources are quasars. Finally, 5 sources have a size less than 20 kpc, and no visible spectral peak. This gives a total of two GPS and six CSS radio galaxies, with a further five more uncertain CSS sources. This gives a minimum proportion of 6% and a more likely proportion of 10% of the sample in total being genuine GPS/CSS radio galaxies.

Only one source in TOOTS-00 (2% of the total sample) is a possible CSS source. This source is 12 kpc in size, and has no visible spectral peak. Note that Vardoulaki *et al.* [2010] classify six sources as being 'CSS', but this originates from a different criterion based on radio morphology. Most of these sources do show a spectral peak, but have sizes in the range 30-40kpc, just above the cut used here.

It is extremely interesting to note that both CENSORS, at high frequency, and 7CRS, at low

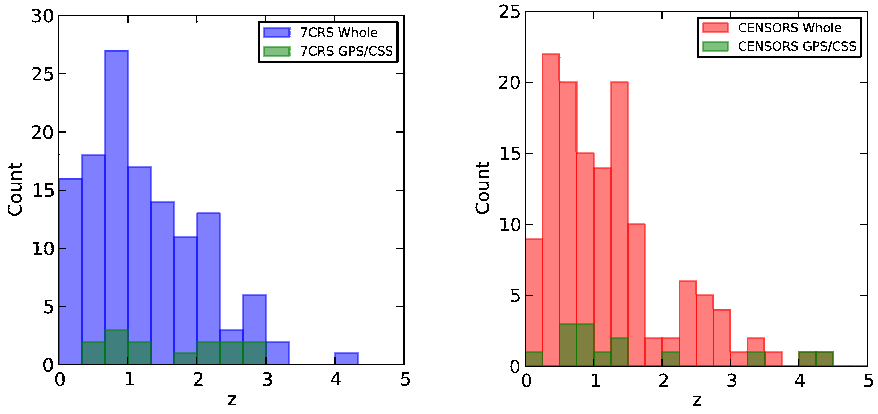

Figure 5.11: The redshift distribution of GPS/CSS radio galaxies in CENSORS (red) and 7CRS (blue), showing the tendancy for GPS/CSS sources to be located at higher redshifts. Note that this excludes known starbursts or quasars fitting the GPS/CSS criteria in the samples.

frequency, have almost exactly the same proportions of young radio galaxies present, of order 10%. The difference lies in the relative proportions of these: the proportion of GPS sources in CENSORS is double that found in 7CRS (although note low number statistics), but 7CRS contains a higher proportion of CSS sources peaking at low frequency. This is exactly as would be expected - the peak frequency in CSS sources is around the selection frequency of 7CRS, which means CSS sources will be included, but GPS sources, peaking at high frequencies will be missed in low frequency selected samples.

Plotted in Figure 5.10 is the fraction of GPS/CSS sources, as a total of the sample, for both CENSORS (red) and 7CRS/TOOTS-00 (blue). The weak increase with redshift remains, and an increase in the fraction of GPS/CSS sources with increasing radio luminosity and decreasing radio size is clearly apparent. This leads to a key question: do GPS/CSS radio galaxies constitute a higher fraction of sources at high redshift, and can they be utilised in future high redshift radio galaxy searches?

High Redshift Searches

Falcke *et al.* [2004] present an interesting hypothesis: that the very first black holes could reasonably be expected to show similar characteristics to more local GPS/CSS sources, growing in a confined environment (see Chapter 4, discussion). GPS sources are typically powerful and recently triggered, perhaps as result of mergers. Therefore there is a stronger possibility that they are high excitation, and will have more powerful emission lines.

It has already been shown that GPS/CSS sources are more likely to be located at high redshift (cf. Figure 5.11). Relations between GPS/CSS peak frequency, peak flux and source size have also been known for some time [e.g. Snellen *et al.*, 2000] for GPS/CSS radio galaxies. These are fully consistent with the expectations of classical synchrotron radiation theory, whereby radio source angular size is proportional to peak frequency, peak flux density, and

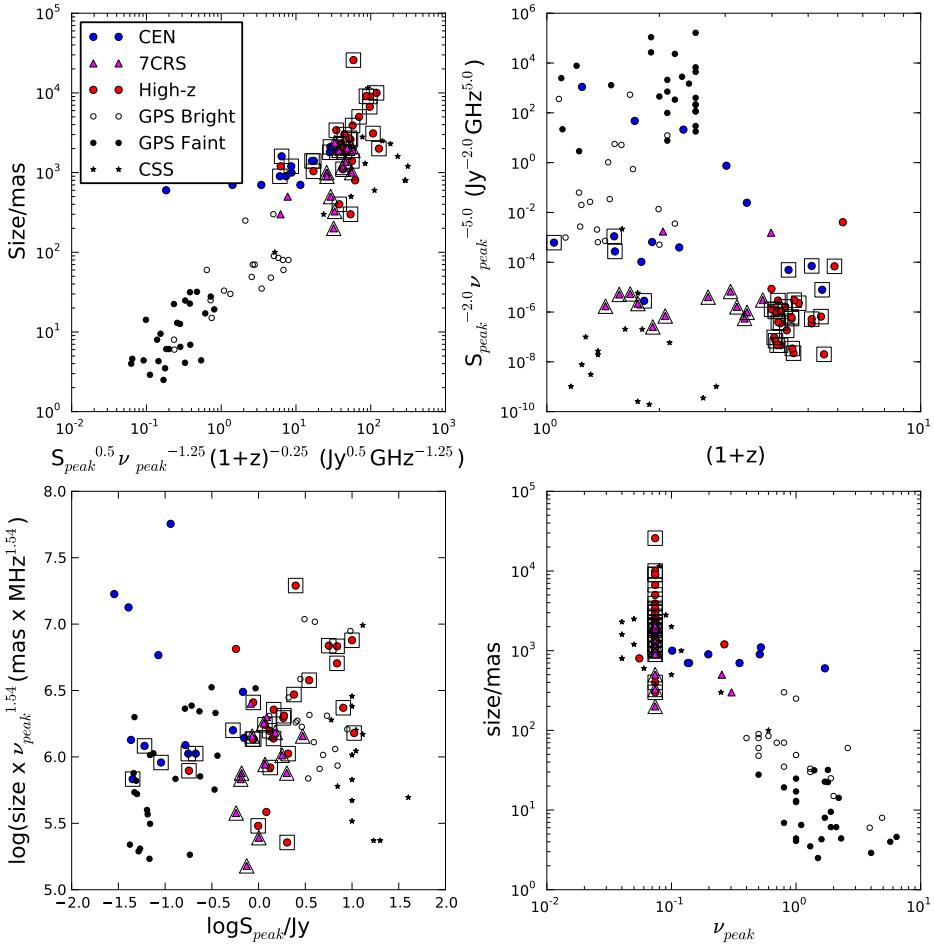

Figure 5.12: This Figure reproduces some of the diagnostic plots presented by Snellen *et al.* [2000], demonstrating that GPS/CSS sources have observable characteristics fully compatible with what would be expected from classical synchrotron radiation theory. The top left panel plots angular size against peak frequency and flux, demonstrating the strong linear dependence, as given by Equation 5.7. It can clearly be seen that CENSORS, 7CRS and the High-z sample all follow the same relation between observed peak frequency, peak flux and size (although note some of these are upper limits - these are indicated by boxed points). The top right panel plots the product of peak frequency and flux against redshift, again according to Equation 5.7. It can clearly be seen that the dependence on redshift is much much weaker. On the bottom left, the fundamental plane of GPS/CSS radio sources proposed by Falcke *et al.* [2004] (as discussed in the text) is presented. High-z sources are expected to lie in the bottom left-hand corner, however known sources at z>3 are not easily distinguishable from this plot.

more weakly dependent on source redshift and magnetic field strength, as follows:

$$\theta \propto B^{0.25} S_p^{0.5} (1+z)^{0.25} \nu_p^{1.25} \tag{5.7}$$

More recently, Falcke *et al.* [2004] presented an alternative fundamental plane based on source size, peak frequency and peak flux for GPS/CSS radio galaxies, and highlight the regions where very high redshift (z>6) sources would be expected. The key assumption behind this, is that the radio power at 5 GHz for known GPS/CSS sources appears to be fairly constant [O'Dea, 1998], and hence as in equation 5.7 above, the peak flux, in conjunction with the peak frequency and angular size provides an implicit estimate of the source redshift. It is possible to attempt to test this for the first time with high redshift GPS/CSS sources found in the samples presented here.

To provide a comparison with the known relations, the GPS/CSS samples used in Snellen *et al.* [2000] are also used in the analysis. In addition, as was noted in Chapter 4, several of the highest redshift known radio galaxies are consistent with being GPS/CSS sources. To this end, the literature was searched for radio galaxies at z=3 or greater (using the list presented by Ishwara-Chandra *et al.* [2010] as a starting point), with 47 such sources found. Radio sizes were obtained where possible from the literature, and radio spectra were compiled for these also from the NASA Extragalactic Database (NED), and the same fitting process run on the sample. Note that this sample is not in any way complete, and the flux data come from a heterogeneous range of sources, but the sample is designed to give a good estimate of what is currently known about radio galaxies at z>3. One source, TNJ0924-2201, is consistent with being a GPS source. A further nine are classed as CSS sources. Twenty have sizes less than 20 kpc, a curved spectrum, but with no visible peak. This gives a minimum of 20% of all known z>3 radio galaxies being GPS or CSS sources, possibly extending up to 60%.

In Figure 5.12, the Snellen *et al.* [2000] diagnostic plots for GPS/CSS sources are plotted, with their samples, and the GPS/CSS sources from CENSORS, 7CRS, and the High-z sample just defined also plotted. It can clearly be seen that the GPS/CSS sources from CENSORS, 7CRS and the High-z sample follow almost exactly the same relations as the GPS/CSS samples (over a redshift range z≤2) used by Snellen *et al.* [2000]. This has interesting implications: classical synchrotron theory shows that the spectral peak and size of the radio source can be used to inform on the magnetic fields present in such sources. As the relations are similar for both high and low redshift sources, this suggests that there are no major differences in the magnetic fields of GPS/CSS sources at high redshift, as compared to low.

In the bottom left hand corner, the fundamental plane postulated by Falcke *et al.* [2004] is plotted. It can clearly be seen that the faint GPS sample of Snellen *et al.* [2000] populates the bottom left-hand area of the plot where high redshift sources are expected to be seen, thus showing that the range of luminosities displayed by GPS/CSS sources is too great, and that high-z sources can display a wide range of peak flux. Therefore, analysing radio observables of GPS/CSS sources alone is unlikely to successfully highlight high redshift sources at z>3.

However, there is evidence from the complete samples of CENSORS and 7CRS that GPS/CSS become an increasingly important fraction of sources at high redshift. The high

fraction of GPS/CSS type sources amongst the highest redshift known radio galaxies is also an important indication that the shape of the radio spectrum should not be ignored. This is particularly important as GPS/CSS sources are frequently associated with recent mergers/interactions, and will be high excitation radio galaxies, with powerful observable emission lines, able to penetrate through a likely dusty medium. A potentially interesting avenue of study would be to conduct a VLBI campaign for radio galaxies known at z>4, to obtain accurate size measurements, ages and verification of the presence of jets. Merging with the results of Chapter 4, this suggests that radio size + low frequency radio spectrum as whole should be used in future high redshift searches with upcoming surveys, in conjunction with deep near-infrared cross-matching.

5.5 Implications for the Measurement of the Radio Luminosity Function

The presence of at least some degree of spectral curvature in almost every source leads naturally to the question, what is the effect of curvature on the determination of the radio luminosity function. Does assuming a simple power law spectral index lead to significant differences in the measurement? Is this particularly crucial at high redshift where source numbers are low, and the k-correction greatest? Standard cosmology gives the expression (as given in Chapter 1):

$$S(\nu_o) = \frac{L_\nu([1+z]\nu_o)}{4\pi R_o^2 S_k^2(r)(1+z)} \tag{5.8}$$

for the radio luminosity at a rest frame frequency ν and radio flux at an observed frequency ν_o. When a simple power law expression is assumed for the radio spectrum, S $\propto \nu^\alpha$, this gives:

$$L(\nu_o) = L_0 \nu_o^\alpha \tag{5.9}$$

and

$$L([1+z]\nu_o) = L_0((1+z)\nu_o)^\alpha \tag{5.10}$$

Combining these expressions gives:

$$L([1+z]\nu_o) = L(\nu_o)(1+z)^\alpha \tag{5.11}$$

leading to the well-known expression:

$$S(\nu_o) = \frac{L(\nu_o)}{4\pi D_L^2 (1+z)^{-1-\alpha}} \tag{5.12}$$

as is commonly used for calculating radio powers (e.g. Chapters 4 and 6). The same derivation can be repeated assuming a more complex radio spectral shape, in this case, a second order polynomial, incorporating the degree of spectral curvature present into the radio

power calculation. In this case, S $\propto 10^{\gamma+\alpha log\nu+\beta(log\nu)^2}$, which gives:

$$L(\nu_o) = L_0 10^{\gamma+\alpha log\nu_0+\beta(log\nu_0)^2} \tag{5.13}$$

and

$$L([1+z]\nu_o) = L_0 10^{\gamma+\alpha log((1+z)\nu_0)+\beta(log((1+z)\nu_0))^2} L(\nu_o) \tag{5.14}$$

Combining these expressions gives:

$$L([1+z]\nu_o) = L(\nu_o)(1+z)^{\alpha} 10^{\beta((log((1+z)\nu_0))^2-(log\nu_0)^2)} \tag{5.15}$$

This leads to a final expression relating flux density and luminosity:

$$S(\nu_o) = \frac{L(\nu_o)(1+z)^{\alpha} 10^{\beta((log((1+z)\nu_0))^2-(log\nu_0)^2)}}{4\pi(1+z)^3 D_A^2} \tag{5.16}$$

It is already well-known that not accounting for the spectral shape in flat spectrum radio sources can lead to erroneous measures of the flat-spectrum RLF [e.g. Jarvis and Rawlings, 2000]. What is less well-known is the effect that not accounting for radio spectral curvature has on the steep-spectrum RLF (α<-0.5). This is particularly important at high redshift, where the low numbers of sources can give rise to significant uncertainty: one of the biggest questions in current modeling efforts is how sharp the decline in number densities observed for powerful radio galaxies at redshifts of 2 or greater truly is [e.g. Rigby *et al.*, 2011].

The luminosity functions for the combined samples of CENSORS and CoNFIG1 and CoNFIG2r is shown in Figure 5.13, and likewise for 7CRS and TOOTS-00 in Figure 5.14. A spectral index cut of α=-0.5 is used to measure only the steep-spectrum sources, as in Rigby *et al.* [2011]. In each panel, there are five luminosity functions plotted. The first assumes the measured spectral index of the source (blue), the second a fixed spectral index of α=-0.8 (magenta), the third a fixed second order polynomial, with the mean values given in Figure 5.8, and the fourth uses the measured best fitting second order polynomial fit to the radio spectrum. Finally the corresponding luminosity function of Rigby *et al.* [2011] is used for comparison.

What is immediately apparent is that the form of radio spectrum chosen has little effect on the RLF at redshifts of z<1. This is as expected, as sources at low redshift require very little correction along the radio spectrum. Where the largest differences arise are at redshifts z>1. At z>1, the fixed and measured spectral index, and the fixed polynomial approximations generally provide very similar measures. The most accurate determination of the radio spectrum, the measured second order polynomial (in red) gives rise to small but noticeable differences from these. This is most likely due to the smaller numbers of sources at z>1, and possibly due to the increasing difference between the observed and rest frame frequency as redshift increases, requiring a greater correction along the radio spectrum. However the differences are random rather than systematic, occurring when sources are shifted between one luminosity bin and another. The overall effect is significant for small number samples (i.e. at high redshift, where numbers are low), but should average out for larger samples. This is also consistent with the

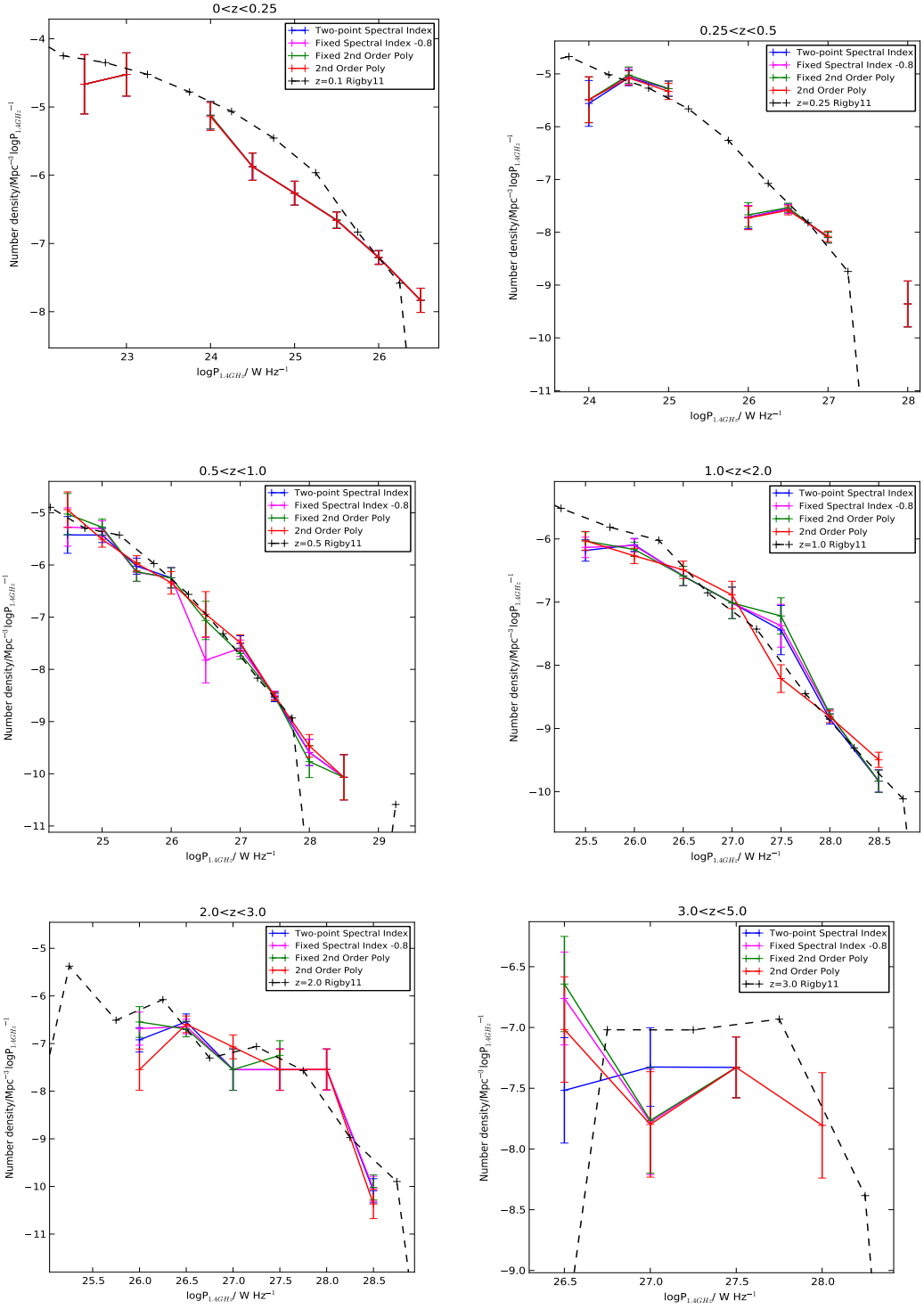

Figure 5.13: The radio luminosity functions for CoNFIG and CENSORS.There are five luminosity functions plotted. The first assumes the measured spectral index of the source (blue), the second a fixed spectral index of α=-0.8 (magenta), the third a fixed second order polynomial, with the mean values given in Figure 5.8, and the fourth uses the measured best fitting second order polynomial fit to the radio spectrum. Finally the corresponding luminosity function of Rigby *et al.* [2011] is used for comparison. Note that that the z=0.25-0.5 has low dynamic range, as there is a very sparse overlap between CENSORS and CoNFIG in this area of the P-z plane.

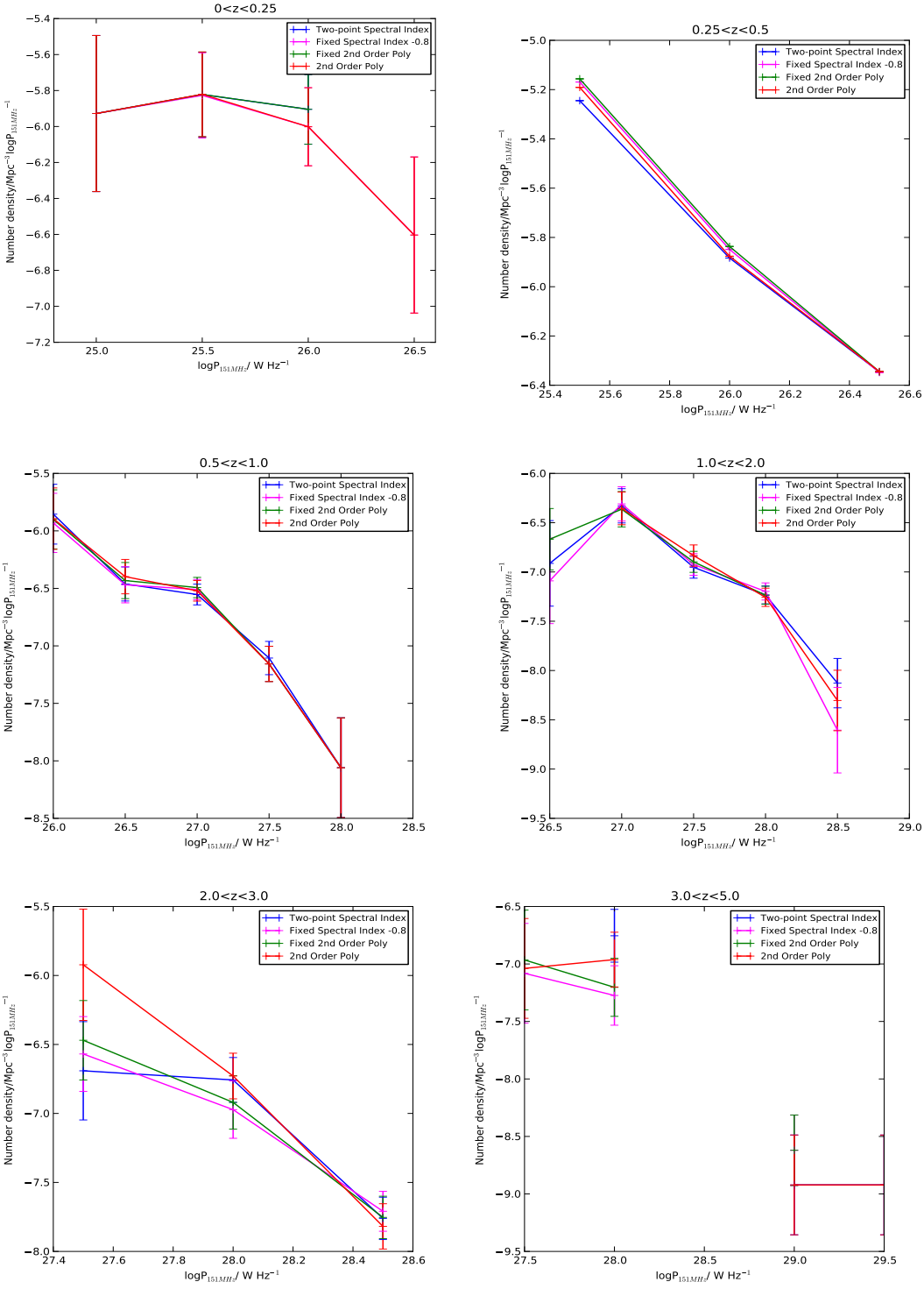

Figure 5.14: The radio luminosity functions for 7CRS and TOOTS-00. There are five luminosity functions plotted. The first assumes the measured spectral index of the source (blue), the second a fixed spectral index of α=-0.8 (magenta), the third a fixed second order polynomial, with the mean values given in Figure 5.8, and the fourth uses the measured best fitting second order polynomial fit to the radio spectrum.

reduced curvature for steep spectrum sources noted in Section 5.4.

5.6 Conclusions

- A second order polynomial in general provides a better fit to the vast majority of sources than a simple linear fit. This is in common with recent studies such as Duffy and Blundell [2012], Blundell *et al.* [1999].
- The measured curvatures of the radio spectra generally remain constant with redshift.
- The large majority of sources in CENSORS with an inverted spectrum show strong indications of being core-dominated sources.
- There is a small suggestion (limited by low number statistics) that the proportion of peaked radio spectrum, compact (GPS/CSS) sources increases with redshift. Such sources could represent a promising way of searching for young radio galaxies at very high redshift. VLBI observations of these sources as well as existing $z>4$ radio galaxies would be a useful way to gauge the feasibility of this method for future radio facilities.
- Calculating source luminosities based on a measured spectral index or measured second order polynomial gives rise to negligible difference in the measured 1.4 GHz radio luminosity functions at $z<1$, as expected. At $z>1$ there are noticeable differences where numbers of high redshift sources are low, suggesting that these should have their radio spectra fully determined when the radio luminosity function is measured. However, for larger samples, these differences will more or less average out.

Table 5.3: Fitted Radio Spectra for the CoNFIG 1 & 2r Samples [Gendre *et al.*, 2010]. Col1: Source name, Col2: 74 MHz flux, Col3: 151 MHz flux, Col4: 365 MHz flux, Col5: 408 MHz flux, Col6: 1.4 GHz flux, Col7: 2.7 GHz flux, Col8: 5 GHz flux, Col9: Reduced χ^2 value for the 2nd order polynomial fit, Col10: Fitted parameter γ, Col11: Fitted parameter α, Col12: Fitted parameter β.

Name	S_{74MHz} Jy	S_{151MHz} Jy	S_{365MHz} Jy	S_{408MHz} Jy	$S_{1.4GHz}$ Jy	$S_{2.7GHz}$ Jy	S_{5GHz} Jy	rchi2	γ	α	β
M87	729.08(74.42)	-	-	519.0	141.95	120.0	67.6	16.27	2.27	-0.64(0.16)	-0.07(0.19)
3C273	149.96(15.0)	-	66.45	55.1	54.99	41.8	44.9	3.9	1.75	-0.2(0.07)	0.14(0.09)
3C295	120.27(12.03)	90.92(1.62)	-	0.0	22.72	11.83	6.53	0.21	1.47	-0.78(0.01)	-0.23(0.02)
3C196	136.4(13.88)	84.72(0.8)	49.02	-	15.01	7.66	4.36	0.31	1.31	-0.87(0.02)	-0.14(0.03)
3C286	30.26(3.08)	-	27.48	-	14.9	10.26	7.48	0.72	1.24	-0.43(0.03)	-0.19(0.04)
3C270	46.02(4.61)	-	-	41.5	10.44	12.65	8.32	39.16	1.12	-0.44(0.24)	0.1(0.29)
3C279	30.63(3.06)	-	15.46	14.5	9.71	12.0	13.0	3.0	1.01	-0.11(0.06)	0.3(0.08)
3C327	27.42(2.79)	-	-	16.1	8.3	5.21	2.76	0.28	1.02	-0.63(0.02)	-0.24(0.02)
4C55.16	11.51(1.15)	8.57(0.12)	9.74	-	8.28	-	5.8	7.71	0.92	-0.09(0.09)	-0.08(0.13)
3C219	41.72(4.23)	56.68(0.67)	-	23.5	8.1	4.35	2.29	18.96	1.08	-1.01(0.13)	-0.25(0.2)
3C227	48.74(4.92)	-	12.0	22.1	7.62	4.16	2.6	9.02	0.98	-0.71(0.11)	-0.09(0.13)
3C310	129.86(12.95)	-	-	0.0	7.61	3.1	1.26	0.01	1.06	-1.21(0.01)	-0.25(0.01)
3C345	18.7(1.9)	10.52(0.14)	9.56	8.73	7.1	-	8.47	3.27	0.85	-0.03(0.06)	0.23(0.08)
3C287	16.05(1.61)	-	14.96	-	7.05	4.6	3.26	1.7	0.93	-0.5(0.05)	-0.21(0.06)
3C237	37.79(3.85)	-	18.05	15.4	6.52	3.66	2.01	0.13	0.93	-0.77(0.01)	-0.18(0.02)
3C298	99.61(9.96)	-	29.02	23.4	6.1	2.71	1.46	1.1	0.95	-1.09(0.04)	-0.13(0.05)
M84	28.69(2.98)	-	-	12.2	6.01	3.91	2.86	0.13	0.86	-0.57(0.01)	-0.04(0.02)
3C264	35.45(3.55)	-	-	19.3	5.69	3.1	2.0	4.85	0.89	-0.8(0.09)	-0.16(0.1)
3C234	70.88(7.12)	34.88(1.36)	15.78	-	5.6	2.92	1.54	1.55	0.87	-0.88(0.04)	-0.06(0.06)
4C12.50	-	-	8.31	8.78	5.4	3.88	2.89	0.22	0.79	-0.39(0.02)	-0.13(0.04)
3C192	-	-	-	13.1	5.33	3.3	2.6	0.56	0.82	-0.7(0.05)	0.15(0.08)
3C280	51.76(5.27)	29.74(0.44)	14.94	13.71	5.1	2.83	1.53	0.16	0.83	-0.85(0.01)	-0.07(0.02)
3C343	8.88(0.92)	16.07(0.24)	13.91	-	5.0	2.68	1.49	11.83	0.85	-0.8(0.1)	-0.45(0.16)
1607+26	-	-	2.53	-	4.91	3.04	1.56	0.88	0.7	0.12(0.05)	-1.24(0.1)
4C32.44	2.21(0.24)	3.44(0.07)	7.49	-	4.86	-	2.15	7.37	0.74	-0.21(0.09)	-0.55(0.13)
3C293	11.81(1.19)	15.72(0.2)	11.21	-	4.84	2.89	1.87	6.85	0.81	-0.69(0.08)	-0.27(0.12)
3C343.1	7.99(0.83)	14.32(0.21)	14.16	-	4.61	2.23	1.2	9.64	0.82	-0.84(0.09)	-0.53(0.14)
NGC5532	13.97(1.45)	-	-	8.3	4.45	2.7	1.7	0.13	0.74	-0.58(0.01)	-0.2(0.02)
3C315	45.21(4.55)	-	-	0.0	4.33	2.36	1.27	0.01	0.77	-0.89(0.0)	-0.09(0.0)
4C62.22	-	1.32(0.04)	5.56	-	4.31	-	1.83	27.4	0.68	-0.06(0.18)	-0.88(0.29)
3C216	40.56(4.06)	28.89(0.4)	13.93	11.9	4.23	3.39	1.81	4.49	0.76	-0.8(0.06)	0.06(0.09)
3C244.1	45.25(4.59)	26.73(0.28)	13.89	-	4.19	1.95	1.12	0.43	0.76	-0.93(0.02)	-0.14(0.03)
B1611+3420	1.94(0.2)	2.71(0.06)	2.93	-	4.02	-	2.53	3.25	0.61	-0.03(0.06)	-0.3(0.09)
4C04.51	3.83(0.46)	-	3.4	3.3	3.93	2.3	1.03	17.83	0.62	-0.37(0.15)	-0.46(0.2)

Continued on next page

Table 5.3 – continued from previous page

Name	S_{74MHz} Jy	S_{151MHz} Jy	S_{365MHz} Jy	S_{408MHz} Jy	$S_{1.4GHz}$ Jy	$S_{2.7GHz}$ Jy	S_{5GHz} Jy	rchi2	γ	α	β
3C313	59.13(5.94)	-	15.19	11.5	3.8	2.07	1.39	1.13	0.71	-0.9(0.04)	0.05(0.05)
3C300	35.78(3.63)	-	10.47	10.9	3.74	1.92	1.11	0.42	0.7	-0.87(0.02)	-0.1(0.03)
3C223	17.36(1.76)	16.38(0.43)	-	0.0	3.72	2.06	1.29	3.36	0.7	-0.77(0.06)	-0.19(0.09)
3C228	36.98(3.78)	-	10.44	9.29	3.71	1.9	1.11	0.72	0.69	-0.85(0.03)	-0.07(0.04)
3C338	112.38(11.31)	55.27(0.76)	17.39	16.73	3.68	1.24	0.49	1.37	0.76	-1.36(0.03)	-0.2(0.05)
3C346	20.81(2.08)	-	9.02	8.62	3.67	2.33	1.63	0.37	0.66	-0.64(0.02)	-0.05(0.03)
3C275	26.1(2.61)	-	10.76	10.2	3.67	1.83	0.98	0.08	0.7	-0.87(0.01)	-0.21(0.01)
3C321	26.02(2.65)	-	8.43	-	3.58	2.0	1.22	0.81	0.66	-0.75(0.03)	-0.08(0.04)
4C-05.64	15.9(1.63)	-	7.41	7.72	3.57	2.9	2.33	1.57	0.63	-0.46(0.04)	0.06(0.06)
3C325	30.41(3.09)	20.06(0.25)	12.12	-	3.56	1.84	0.83	0.36	0.69	-0.93(0.02)	-0.23(0.03)
3C349	28.59(2.89)	18.12(0.31)	9.95	8.55	3.36	1.88	1.14	0.09	0.65	-0.8(0.01)	-0.07(0.01)
3C288	35.46(3.55)	20.48(0.31)	11.74	10.06	3.36	1.76	0.99	0.44	0.66	-0.88(0.02)	-0.11(0.03)
3C225	38.58(3.92)	-	10.16	9.13	3.34	2.22	1.26	0.32	0.64	-0.79(0.02)	0.04(0.03)
3C245	31.5(3.23)	-	9.45	8.9	3.31	2.0	1.46	0.45	0.63	-0.73(0.02)	0.04(0.03)
3C351	23.58(2.41)	15.33(0.15)	8.37	-	3.26	2.03	1.21	0.04	0.62	-0.73(0.01)	-0.05(0.01)
3C236	10.67(1.1)	9.32(0.17)	7.6	-	3.24	2.01	1.4	0.87	0.6	-0.58(0.03)	-0.17(0.04)
4C01.28	6.9(0.73)	-	4.28	4.47	3.22	3.15	3.16	0.46	0.53	-0.15(0.02)	0.12(0.03)
3C326	16.03(1.67)	-	-	0.0	3.21	2.07	0.41	22.03	0.68	-1.05(0.2)	-0.52(0.23)
3C337	25.24(2.57)	17.14(0.22)	9.98	8.21	3.16	1.57	0.91	0.3	0.63	-0.87(0.02)	-0.16(0.02)
3C300.1	20.33(2.03)	-	8.81	7.21	3.16	1.83	0.94	0.42	0.62	-0.79(0.02)	-0.16(0.03)
3C299	24.94(2.5)	15.14(0.23)	8.05	8.17	3.15	1.59	0.9	0.8	0.61	-0.81(0.03)	-0.14(0.04)
3C230	41.93(4.19)	-	12.66	12.3	3.15	1.94	0.69	2.54	0.67	-1.04(0.06)	-0.16(0.07)
3C263.1	29.93(2.99)	-	16.96	-	3.13	1.49	0.78	9.01	0.67	-1.03(0.12)	-0.24(0.14)
3C254	51.25(5.21)	27.56(0.45)	12.57	10.92	3.13	1.45	0.79	0.14	0.65	-1.03(0.01)	-0.08(0.02)
4C55.17	6.47(0.65)	6.39(0.64)	5.26	-	3.08	-	2.3	2.1	0.54	-0.29(0.06)	-0.01(0.07)
3C305	33.16(3.32)	20.29(0.28)	9.82	-	3.01	1.64	0.92	0.14	0.61	-0.9(0.01)	-0.07(0.02)
4C33.38	1.85(0.2)	2.44(0.06)	2.47	-	2.99	-	2.0	1.86	0.49	-0.07(0.04)	-0.23(0.07)
4C31.38	7.64(0.8)	7.73(0.21)	7.2	-	2.98	-	1.23	2.57	0.57	-0.58(0.05)	-0.24(0.08)
4C-06.35	33.09(3.37)	-	9.91	9.74	2.96	1.79	0.98	0.83	0.61	-0.87(0.03)	-0.04(0.04)
3C238	35.13(3.58)	-	11.08	9.32	2.96	1.35	1.58	8.24	0.59	-0.79(0.1)	0.08(0.13)
3C277.3	16.33(1.64)	10.58(0.15)	6.05	-	2.92	1.93	1.24	0.31	0.55	-0.6(0.02)	-0.03(0.03)
3C274.1	29.63(2.98)	-	-	0.0	2.92	1.44	0.76	0.12	0.6	-0.94(0.01)	-0.15(0.02)
3C275.1	32.87(3.29)	-	10.88	9.35	2.9	1.56	0.95	1.07	0.6	-0.9(0.04)	-0.06(0.05)
3C265	46.46(4.69)	22.36(0.31)	12.18	-	2.89	1.39	0.63	2.03	0.61	-1.02(0.04)	-0.14(0.07)
4C39.25	10.92(1.1)	6.68(0.08)	3.92	3.33	2.88	-	11.2	11.37	0.45	0.17(0.1)	0.76(0.16)
3C247	18.45(1.88)	12.96(0.13)	7.61	7.01	2.88	1.63	0.95	0.01	0.57	-0.76(0.0)	-0.13(0.01)
3C270.1	30.8(3.08)	15.17(0.22)	9.74	-	2.85	1.49	0.87	3.24	0.57	-0.82(0.05)	-0.09(0.08)

Continued on next page

Table 5.3 – continued from previous page

Name	S_{74MHz} Jy	S_{151MHz} Jy	S_{365MHz} Jy	S_{408MHz} Jy	$S_{1.4GHz}$ Jy	$S_{2.7GHz}$ Jy	S_{5GHz} Jy	rchi2	γ	α	β
4C03.30	12.26(1.23)	-	6.08	5.16	2.8	1.97	1.28	0.24	0.53	-0.56(0.02)	-0.05(0.02)
3C249	33.13(3.39)	-	9.99	8.04	2.8	1.35	0.68	0.4	0.59	-0.97(0.02)	-0.14(0.03)
4C-00.47	2.34(0.25)	-	3.43	3.43	2.77	2.4	1.9	0.49	0.48	-0.16(0.02)	-0.21(0.03)
4C53.24	18.7(1.9)	11.95(0.29)	7.96	-	2.76	-	0.93	0.93	0.55	-0.75(0.03)	-0.12(0.05)
4C38.41	3.36(0.34)	2.86(0.05)	2.43	1.9	2.73	-	3.82	2.55	0.41	0.13(0.05)	0.23(0.07)
NGC2484	14.2(1.43)	9.23(0.13)	-	5.39	2.72	-	1.33	0.09	0.51	-0.55(0.01)	0.0(0.01)
4C03.18	15.79(1.62)	-	6.8	6.38	2.71	1.67	0.99	0.03	0.54	-0.71(0.01)	-0.11(0.01)
4C01.32	15.92(1.63)	-	6.66	5.72	2.69	1.6	0.97	0.22	0.53	-0.7(0.02)	-0.1(0.02)
3C318	20.34(2.04)	-	9.21	-	2.69	1.33	0.75	0.95	0.57	-0.89(0.04)	-0.2(0.05)
3C287.1	18.52(1.87)	-	4.77	5.29	2.65	1.93	1.43	1.1	0.49	-0.53(0.04)	0.12(0.05)
3C319	37.07(3.78)	19.62(0.22)	7.66	-	2.62	1.25	0.65	1.51	0.55	-0.97(0.04)	-0.08(0.06)
3C336	20.13(2.05)	-	7.88	-	2.61	1.4	0.69	0.04	0.55	-0.88(0.01)	-0.19(0.01)
3C207	25.66(2.61)	-	8.92	7.03	2.61	1.7	1.3	2.35	0.53	-0.72(0.05)	0.08(0.07)
3C340	17.2(1.75)	-	7.79	-	2.6	1.3	0.69	0.11	0.55	-0.87(0.01)	-0.23(0.02)
3C332	18.68(1.89)	12.19(0.14)	-	0.0	2.6	1.46	0.83	0.11	0.53	-0.78(0.01)	-0.12(0.02)
4C19.44	15.25(1.56)	-	5.29	6.0	2.59	1.5	1.49	2.4	0.49	-0.56(0.06)	0.05(0.07)
4C00.56	-	-	1.27	3.19	2.59	1.87	1.37	18.99	0.42	0.03(0.2)	-0.68(0.41)
3C303	23.22(2.32)	13.53(0.26)	7.24	-	2.54	1.55	0.94	0.04	0.52	-0.76(0.01)	-0.02(0.01)
3C324	24.67(2.47)	-	8.91	-	2.52	1.26	0.61	0.08	0.55	-0.97(0.01)	-0.19(0.01)
3C267	28.75(2.92)	-	9.07	6.97	2.52	1.29	0.59	0.74	0.54	-0.97(0.03)	-0.15(0.04)
4C33.21	13.27(1.33)	8.36(0.12)	6.75	-	2.47	-	0.92	3.77	0.49	-0.64(0.06)	-0.13(0.09)
4C14.41	-	-	3.82	3.5	2.45	1.5	1.02	0.53	0.45	-0.41(0.03)	-0.35(0.07)
1442+101	0.86(0.15)	-	1.8	1.9	2.42	1.77	1.15	2.88	0.39	-0.07(0.06)	-0.49(0.09)
B1437+6224	-	1.16(0.04)	2.91	-	2.41	-	0.79	4.33	0.44	-0.23(0.07)	-0.83(0.12)
4C04.41	10.63(1.1)	-	5.57	7.8	2.41	1.19	0.53	2.66	0.52	-0.87(0.06)	-0.38(0.07)
4C01.39	19.94(2.03)	-	7.36	6.59	2.4	1.35	0.71	0.06	0.51	-0.85(0.01)	-0.13(0.01)
3C323.1	17.75(1.81)	-	5.04	-	2.4	1.29	0.92	2.54	0.47	-0.7(0.06)	-0.03(0.07)
3C289	26.4(2.69)	15.84(0.2)	8.1	-	2.4	1.17	0.6	0.1	0.52	-0.95(0.01)	-0.15(0.01)
3C226	39.76(4.08)	-	9.34	8.19	2.39	1.22	0.64	0.03	0.53	-1.01(0.01)	-0.05(0.01)
3C212	25.27(2.57)	-	8.34	7.01	2.37	1.4	0.83	0.74	0.51	-0.85(0.03)	-0.03(0.04)
3C208	38.78(3.95)	-	10.33	7.75	2.36	1.1	0.53	0.55	0.53	-1.07(0.03)	-0.12(0.03)
3C326.1	11.93(1.2)	-	6.03	-	2.31	1.3	0.86	0.59	0.47	-0.7(0.03)	-0.14(0.04)
4C05.64	4.76(0.49)	-	2.67	2.74	2.3	1.83	2.18	1.16	0.37	-0.14(0.04)	0.1(0.05)
3C277.1	14.72(1.47)	10.7(0.26)	7.44	-	2.29	1.53	1.05	3.06	0.48	-0.7(0.05)	-0.03(0.08)
J0741+3111	1.17(0.13)	0.98(0.03)	1.36	-	2.28	-	2.68	10.21	0.3	0.32(0.11)	-0.04(0.16)
4C22.21	8.05(0.81)	5.31(0.07)	4.09	-	2.27	-	1.59	0.9	0.4	-0.34(0.03)	0.07(0.05)
4C37.24	14.52(1.45)	9.83(0.12)	5.81	5.17	2.26	-	0.77	0.09	0.46	-0.74(0.01)	-0.11(0.01)

Continued on next page

Table 5.3 – continued from previous page

Name	S_{74MHz} Jy	S_{151MHz} Jy	S_{365MHz} Jy	S_{408MHz} Jy	$S_{1.4GHz}$ Jy	$S_{2.7GHz}$ Jy	S_{5GHz} Jy	rchi2	γ	α	β
4C01.42	19.34(1.98)	-	6.86	5.56	2.26	1.28	0.68	0.36	0.48	-0.83(0.02)	-0.1(0.03)
3C205	26.91(2.74)	16.39(0.33)	9.28	-	2.26	1.11	0.67	1.37	0.5	-0.95(0.03)	-0.1(0.05)
4C11.45	15.96(1.64)	-	6.21	5.9	2.24	1.38	0.75	0.19	0.47	-0.77(0.02)	-0.11(0.02)
4C37.29	17.71(1.8)	10.56(0.12)	5.43	5.35	2.21	-	0.71	0.69	0.45	-0.76(0.03)	-0.08(0.04)
4C55.22	11.28(1.15)	-	3.7	-	2.2	-	0.0	-	0.38	-0.32(0.0)	0.24(0.0)
4C59.16	8.66(0.89)	8.14(0.09)	5.38	-	2.18	-	0.86	2.74	0.45	-0.69(0.05)	-0.16(0.08)
3C208.1	16.34(1.68)	-	6.44	5.5	2.16	1.2	0.77	0.36	0.45	-0.78(0.02)	-0.09(0.03)
4C20.24	14.83(1.51)	-	5.54	-	2.14	1.65	1.13	1.15	0.42	-0.59(0.04)	0.08(0.05)
4C-04.40	10.47(1.08)	-	4.26	4.57	2.14	1.32	0.97	0.49	0.42	-0.59(0.02)	-0.05(0.03)
4C17.71	2.95(0.31)	-	3.75	3.67	2.13	-	2.78	19.36	0.37	-0.1(0.17)	0.05(0.21)
B1225+368	-	0.29(0.02)	1.2	-	2.1	-	0.79	0.37	0.33	0.14(0.02)	-1.09(0.04)
4C52.18	14.02(1.43)	9.54(0.17)	6.04	-	2.1	-	0.8	0.61	0.44	-0.73(0.02)	-0.08(0.04)
4C-04.53	26.73(2.7)	-	5.41	6.72	2.1	0.9	0.53	3.73	0.45	-0.96(0.07)	-0.1(0.09)
4C21.35	9.21(0.93)	-	3.48	-	2.09	1.1	0.81	4.93	0.4	-0.61(0.09)	-0.12(0.1)
3C217	25.38(2.59)	16.5(0.19)	8.37	7.09	2.09	1.0	0.56	0.71	0.48	-1.01(0.02)	-0.13(0.04)
3C285	21.92(2.2)	11.1(0.14)	-	5.03	2.08	1.23	0.76	0.76	0.42	-0.75(0.03)	0.01(0.04)
4C37.32	6.7(0.7)	-	6.79	-	2.07	-	0.24	-	0.49	-1.09(0.0)	-0.7(0.0)
3C194	17.93(1.79)	11.38(0.13)	6.73	5.68	2.06	1.07	0.61	0.25	0.44	-0.86(0.01)	-0.14(0.02)
1128+455	5.23(0.55)	7.48(0.06)	5.05	4.37	2.05	-	0.65	8.6	0.44	-0.78(0.09)	-0.31(0.14)
3C284	18.27(1.86)	-	7.07	-	2.04	1.07	0.62	0.79	0.45	-0.88(0.03)	-0.13(0.04)
3C200	26.78(2.68)	12.84(0.17)	6.41	-	2.04	1.1	0.76	0.82	0.42	-0.81(0.03)	0.04(0.04)
4C29.45	5.23(0.53)	4.36(0.17)	3.11	-	2.03	-	2.17	2.87	0.34	-0.2(0.06)	0.18(0.08)
3C329	19.26(1.95)	10.8(0.13)	7.1	-	2.03	-	0.85	3.23	0.42	-0.74(0.06)	0.01(0.09)
B0710+439	-	0.15(0.02)	0.66	0.75	2.01	-	1.6	0.02	0.24	0.57(0.0)	-0.89(0.01)
3C341	19.62(1.99)	-	6.35	-	2.0	1.08	0.57	0.01	0.43	-0.89(0.0)	-0.11(0.0)
3C213.1	10.65(1.07)	8.54(0.16)	4.39	-	2.0	1.01	0.88	3.46	0.4	-0.69(0.06)	-0.07(0.09)
4C12.39	6.37(0.67)	-	3.77	3.56	1.99	1.7	1.5	1.42	0.36	-0.35(0.04)	0.06(0.05)
3C334	31.72(3.22)	-	6.71	6.8	1.99	1.32	0.57	1.67	0.44	-0.93(0.05)	0.0(0.06)
3C268.4	21.76(2.22)	12.15(0.18)	6.58	5.69	1.98	1.06	0.6	0.24	0.42	-0.87(0.01)	-0.08(0.02)
3C223.1	17.1(1.74)	10.14(0.11)	3.96	4.88	1.98	1.23	0.87	1.8	0.39	-0.69(0.04)	0.07(0.06)
4C03.33	5.52(0.56)	-	4.17	4.15	1.96	1.22	0.69	0.21	0.39	-0.62(0.02)	-0.27(0.02)
3C277.2	20.4(2.09)	-	7.09	5.83	1.95	0.91	0.58	1.0	0.43	-0.92(0.04)	-0.12(0.05)
4C29.41	9.84(1.01)	6.14(0.15)	3.16	-	1.93	-	0.85	3.3	0.35	-0.54(0.06)	-0.01(0.09)
1355+01	-	-	4.74	4.73	1.92	1.0	0.49	0.08	0.41	-0.79(0.01)	-0.34(0.03)
4C17.44	7.23(0.73)	-	4.57	4.56	1.88	1.11	0.68	0.7	0.38	-0.68(0.03)	-0.21(0.04)
4C07.32	-	-	-	5.5	1.88	1.2	0.82	0.01	0.39	-0.82(0.01)	0.2(0.01)
3C220.2	15.63(1.57)	10.64(0.24)	5.74	-	1.88	0.99	0.59	0.28	0.4	-0.85(0.02)	-0.11(0.02)

Continued on next page

Table 5.3 – continued from previous page

Name	S_{74MHz} Jy	S_{151MHz} Jy	S_{365MHz} Jy	S_{408MHz} Jy	$S_{1.4GHz}$ Jy	$S_{2.7GHz}$ Jy	S_{5GHz} Jy	rchi2	γ	α	β
3C202	13.33(1.34)	-	5.64	5.15	1.88	1.0	0.55	0.08	0.4	-0.84(0.01)	-0.18(0.01)
3C352	24.98(2.55)	15.41(0.19)	7.85	6.44	1.87	0.95	0.47	0.48	0.43	-1.02(0.02)	-0.12(0.03)
S4_1413+34	-	1.11(0.05)	2.16	-	1.86	-	0.95	3.57	0.31	-0.13(0.07)	-0.53(0.11)
3C322	22.27(2.26)	13.12(0.14)	6.94	-	1.85	0.85	0.46	0.37	0.41	-0.98(0.02)	-0.15(0.03)
1543+005	-	-	2.28	2.13	1.83	1.24	0.84	0.31	0.31	-0.27(0.03)	-0.42(0.05)
3C320	15.89(1.59)	10.95(0.37)	6.59	-	1.82	0.91	0.5	0.63	0.4	-0.92(0.02)	-0.18(0.04)
4C20.33	14.06(1.41)	-	5.54	-	1.81	1.14	0.6	0.76	0.38	-0.79(0.03)	-0.09(0.04)
4C13.56	11.23(1.13)	-	4.94	4.21	1.81	1.1	0.61	0.19	0.37	-0.74(0.02)	-0.12(0.02)
3C210	24.46(2.49)	14.75(0.34)	6.74	-	1.81	0.93	0.48	0.27	0.41	-1.0(0.02)	-0.09(0.02)
B1031+567	-	0.82(0.02)	1.77	-	1.8	-	1.3	5.5	0.26	0.06(0.08)	-0.44(0.13)
3C211	20.8(2.11)	9.99(0.18)	6.05	-	1.8	-	0.54	4.01	0.37	-0.83(0.06)	-0.07(0.1)
3C229	15.31(1.56)	-	4.95	-	1.79	1.2	0.63	0.7	0.37	-0.76(0.03)	-0.03(0.04)
3C197.1	16.06(1.61)	10.21(0.11)	5.53	4.68	1.79	1.16	0.86	1.29	0.37	-0.73(0.03)	0.06(0.05)
4C32.25A	6.48(0.67)	7.11(0.14)	-	0.0	1.77	-	0.75	17.19	0.37	-0.7(0.14)	-0.15(0.21)
4C23.41	-	-	2.4	-	1.77	1.2	0.75	0.02	0.31	-0.34(0.01)	-0.39(0.01)
1502+106	1.22(0.18)	-	1.39	1.55	1.77	1.74	2.04	0.46	0.23	0.12(0.02)	-0.02(0.03)
4C47.29	6.55(0.66)	4.62(0.08)	3.2	2.81	1.75	-	1.3	0.33	0.3	-0.36(0.02)	0.1(0.03)
3C333	12.36(1.27)	-	5.31	-	1.75	1.0	0.55	0.34	0.37	-0.81(0.02)	-0.14(0.03)
4C54.25	10.7(1.07)	7.3(0.07)	4.51	-	1.74	-	0.69	0.16	0.34	-0.69(0.01)	-0.07(0.02)
4C20.23	0.6(0.1)	-	2.77	-	1.73	-	0.69	11.02	0.31	-0.31(0.14)	-0.61(0.18)
4C12.59	7.56(0.76)	-	3.58	3.71	1.73	1.04	0.8	0.59	0.33	-0.58(0.03)	-0.08(0.03)
3C255	16.54(1.69)	-	9.25	7.73	1.73	0.57	0.2	0.9	0.45	-1.31(0.03)	-0.54(0.04)
4C43.21	14.51(1.48)	9.01(0.1)	4.69	4.52	1.72	-	0.0	0.05	0.35	-0.78(0.01)	-0.06(0.02)
4C07.36	6.69(0.77)	-	-	5.8	1.72	1.06	0.66	9.32	0.36	-0.71(0.12)	-0.22(0.15)
3C257	17.61(1.8)	-	5.9	5.08	1.72	0.9	0.52	0.25	0.37	-0.89(0.02)	-0.1(0.02)
NGC6109	-	-	1.51	-	1.71	-	0.66	-	0.27	-0.12(0.0)	-0.74(0.0)
4C48.29A	5.45(0.61)	8.32(0.11)	-	0.0	1.7	-	0.0	-	0.46	-1.4(0.0)	-1.02(0.0)
B1308+326	2.1(0.23)	1.24(0.02)	1.16	-	1.69	-	1.67	17.23	0.18	0.16(0.13)	0.08(0.2)
3C297	15.6(1.56)	-	4.58	4.17	1.69	1.0	0.63	0.05	0.34	-0.76(0.01)	-0(0.01)
3C241	17.83(1.82)	-	7.18	-	1.69	0.8	0.35	0.9	0.39	-1.06(0.04)	-0.25(0.04)
0756+377	12.62(1.26)	8.36(0.12)	5.37	4.54	1.69	-	0.45	0.48	0.36	-0.86(0.02)	-0.2(0.03)
4C41.32	3.14(0.33)	2.41(0.06)	2.47	1.99	1.68	-	1.4	1.47	0.25	-0.15(0.04)	0.02(0.06)
4C09.44	13.1(1.37)	-	3.7	3.99	1.68	1.0	0.51	1.96	0.33	-0.77(0.05)	-0.09(0.06)
DA240	7.83(0.82)	6.26(0.09)	2.64	-	1.66	-	0.0	14.71	0.3	-0.59(0.28)	0.01(0.39)
4C43.35	14.4(1.47)	10.53(0.14)	4.46	4.77	1.66	-	0.52	2.29	0.35	-0.88(0.05)	-0.08(0.07)
4C00.52	9.67(1.0)	-	4.15	4.12	1.65	1.0	0.55	0.12	0.33	-0.74(0.01)	-0.14(0.02)
4C-02.55	18.0(1.8)	-	4.12	3.87	1.65	1.19	0.9	0.02	0.31	-0.63(0.01)	0.19(0.01)

Continued on next page

Table 5.3 – continued from previous page

Name	S_{74MHz} Jy	S_{151MHz} Jy	S_{365MHz} Jy	S_{408MHz} Jy	$S_{1.4GHz}$ Jy	$S_{2.7GHz}$ Jy	S_{5GHz} Jy	rchi2	γ	α	β
4C00.46	21.36(2.17)	-	4.53	5.1	1.64	0.86	0.47	1.22	0.34	-0.9(0.04)	-0.04(0.05)
B2_1502+28	3.28(0.42)	-	-	1.92	1.63	-	0.37	25.21	0.29	-0.63(0.21)	-0.44(0.25)
4C29.44	16.21(1.66)	11.29(0.41)	5.34	-	1.62	-	0.54	2.06	0.35	-0.89(0.05)	-0.05(0.07)
4C59.13	11.32(1.16)	7.23(0.07)	4.76	-	1.61	-	0.47	1.14	0.32	-0.79(0.03)	-0.17(0.05)
4C34.47	-	-	2.47	-	1.61	-	1.24	-	0.25	-0.29(0.0)	0.1(0.0)
4C53.18	16.16(1.65)	9.39(0.14)	6.01	-	1.6	-	0.43	2.13	0.34	-0.9(0.05)	-0.15(0.07)
4C40.24	3.21(0.33)	3.16(0.05)	2.94	2.43	1.6	-	1.6	5.5	0.26	-0.24(0.07)	0.07(0.11)
4C05.57	11.4(1.17)	-	3.68	3.83	1.6	1.1	0.78	0.3	0.3	-0.62(0.02)	0.05(0.02)
4C02.34	13.36(1.37)	-	4.67	4.13	1.6	0.95	0.55	0.05	0.32	-0.79(0.01)	-0.07(0.01)
3C253	16.54(1.69)	-	4.85	4.58	1.6	0.91	0.5	0.04	0.33	-0.85(0.01)	-0.06(0.01)
4C59.17	11.44(1.17)	7.17(0.1)	4.35	-	1.59	-	0.54	0.4	0.31	-0.75(0.02)	-0.1(0.03)
3C215	28.78(2.95)	-	5.06	6.3	1.59	0.7	0.42	2.4	0.35	-1.02(0.06)	-0.04(0.07)
4C49.22	11.09(1.11)	6.91(0.09)	3.94	-	1.57	-	1.0	1.76	0.28	-0.56(0.04)	0.14(0.06)
4C43.22	10.49(1.08)	8.24(0.08)	4.22	3.9	1.57	-	0.47	1.28	0.32	-0.84(0.03)	-0.15(0.05)
4C17.56	8.44(0.85)	-	4.08	3.83	1.57	1.1	0.62	0.85	0.31	-0.67(0.03)	-0.1(0.04)
4C39.49	2.16(0.25)	1.71(0.04)	1.92	1.81	1.56	-	1.28	2.13	0.2	-0.08(0.05)	-0.05(0.07)
4C24.31	12.65(1.29)	-	4.45	-	1.56	1.0	0.51	0.57	0.31	-0.79(0.03)	-0.08(0.04)
3C239	31.57(3.16)	18.48(0.24)	7.37	6.55	1.56	0.65	0.33	0.76	0.37	-1.19(0.02)	-0.12(0.04)
4C50.30	12.76(1.28)	8.5(0.1)	5.25	-	1.55	-	0.44	0.63	0.32	-0.87(0.02)	-0.16(0.04)
3C311	14.03(1.44)	10.16(0.12)	5.22	-	1.55	-	0.44	1.3	0.34	-0.93(0.04)	-0.14(0.05)
NGC2656	8.63(0.89)	6.2(0.1)	2.92	-	1.54	-	0.66	2.63	0.28	-0.64(0.05)	-0.02(0.08)
4C11.46	1.88(0.33)	-	3.44	3.62	1.54	0.78	0.41	2.34	0.31	-0.68(0.06)	-0.56(0.08)
4C45.17	12.87(1.31)	7.14(0.11)	-	3.35	1.53	-	0.0	0.01	0.27	-0.62(0.01)	0.11(0.01)
4C17.48	17.27(1.75)	-	4.61	4.44	1.53	0.84	0.45	0.13	0.31	-0.88(0.01)	-0.06(0.02)
4C12.42	11.86(1.22)	-	-	3.49	1.53	0.9	0.46	1.02	0.3	-0.8(0.04)	-0.11(0.05)
4C32.24	10.67(1.09)	5.91(0.08)	4.27	-	1.52	-	0.46	5.49	0.28	-0.72(0.07)	-0.16(0.11)
4C-05.60	23.72(2.41)	-	6.26	5.49	1.52	0.64	0.35	0.48	0.34	-1.08(0.02)	-0.14(0.03)
1227+119	6.21(0.88)	-	-	4.31	1.52	1.04	0.49	3.66	0.3	-0.72(0.08)	-0.23(0.1)
4C35.28	3.73(0.38)	2.48(0.06)	2.32	-	1.51	-	1.1	3.26	0.21	-0.22(0.06)	0.03(0.09)
3C356	28.95(2.93)	14.66(0.22)	6.39	-	1.51	0.66	0.38	0.47	0.33	-1.07(0.02)	-0.06(0.03)
0851+202	0.62(0.08)	-	1.13	-	1.51	-	2.61	2.41	0.14	0.34(0.06)	0.05(0.08)
4C53.16	9.68(0.99)	5.78(0.09)	3.91	-	1.5	-	0.63	1.42	0.27	-0.63(0.04)	-0.04(0.06)
4C04.40	15.59(1.56)	-	4.36	4.67	1.5	0.87	0.43	0.6	0.31	-0.88(0.03)	-0.09(0.03)
3C288.1	15.73(1.57)	11.0(0.17)	5.07	-	1.49	0.81	0.4	1.2	0.33	-0.97(0.03)	-0.12(0.05)
4C39.23	6.59(0.66)	5.53(0.07)	-	2.59	1.48	-	1.0	7.13	0.25	-0.51(0.08)	0.1(0.13)
4C31.32	6.29(0.66)	7.18(0.13)	-	0.0	1.48	-	0.29	5.74	0.33	-0.99(0.08)	-0.44(0.12)
1614+26	1.14(0.13)	-	1.71	-	1.48	1.2	0.96	0.09	0.2	-0.15(0.01)	-0.24(0.01)

Continued on next page

Table 5.3 – continued from previous page

Name	S_{74MHz} Jy	S_{151MHz} Jy	S_{365MHz} Jy	S_{408MHz} Jy	$S_{1.4GHz}$ Jy	$S_{2.7GHz}$ Jy	S_{5GHz} Jy	rchi2	γ	α	β
1107+10	-	-	2.43	2.4	1.48	0.8	0.4	0.08	0.26	-0.54(0.01)	-0.59(0.03)
B0711+35	-	0.52(0.03)	0.84	-	1.47	-	0.89	4.06	0.16	0.11(0.07)	-0.54(0.12)
4C-00.50	9.1(0.91)	-	3.75	3.37	1.47	1.01	0.63	0.3	0.27	-0.65(0.02)	-0.03(0.02)
0757+503	19.0(1.9)	11.27(0.25)	5.81	-	1.47	-	0.47	1.48	0.31	-0.93(0.04)	-0.04(0.06)
4C09.45	24.53(2.5)	-	6.18	5.21	1.46	0.7	0.32	0.08	0.33	-1.08(0.01)	-0.13(0.01)
4C56.16A	1.95(0.21)	2.15(0.04)	2.03	-	1.45	-	1.2	2.13	0.2	-0.19(0.05)	-0.04(0.07)
1133+432	-	-	0.71	0.88	1.45	-	0.45	0.38	0.17	0.14(0.03)	-1.25(0.06)
4C46.21	12.56(1.29)	8.27(0.1)	3.31	4.09	1.44	-	0.0	3.58	0.28	-0.81(0.12)	-0.04(0.17)
4C32.44B	7.15(0.72)	4.49(0.09)	3.33	-	1.42	-	0.7	1.63	0.23	-0.53(0.04)	-0.02(0.06)
4C20.27	9.11(0.92)	-	4.68	-	1.42	0.8	0.36	0.95	0.29	-0.88(0.04)	-0.25(0.05)
3C344	16.19(1.65)	9.79(0.13)	4.95	4.21	1.42	-	1.38	12.83	0.26	-0.6(0.11)	0.35(0.17)
3C266	23.07(2.31)	13.91(0.21)	6.91	-	1.42	0.58	0.32	1.42	0.33	-1.13(0.03)	-0.16(0.06)
4C44.19	13.82(1.41)	8.71(0.09)	4.49	4.18	1.41	-	0.0	0.01	0.29	-0.91(0.01)	-0.13(0.01)
4C29.50	10.31(1.03)	6.83(0.18)	3.66	-	1.41	-	0.49	0.1	0.26	-0.76(0.01)	-0.08(0.01)
4C06.41	1.5(0.18)	-	1.59	1.63	1.41	-	1.4	0.82	0.16	-0.05(0.03)	-0.01(0.04)
0840+424A	0.58(0.09)	1.61(0.03)	2.5	2.28	1.41	-	0.58	7.49	0.24	-0.41(0.09)	-0.55(0.13)
3C331	17.89(1.83)	-	5.36	-	1.4	0.7	0.37	0.28	0.29	-0.98(0.02)	-0.11(0.02)
1211+33	2.25(0.24)	1.64(0.04)	1.64	-	1.4	-	0.0	3.08	0.14	0.05(0.13)	0.18(0.18)
4C45.13	9.77(1.01)	5.96(0.1)	3.19	2.91	1.39	-	0.0	0.1	0.23	-0.61(0.02)	0.06(0.03)
4C41.19	14.03(1.44)	9.25(0.11)	5.07	4.25	1.39	-	0.45	1.05	0.29	-0.9(0.03)	-0.08(0.05)
4C39.29	7.79(0.81)	5.35(0.06)	3.81	3.08	1.39	-	0.49	0.66	0.25	-0.7(0.02)	-0.14(0.04)
4C14.60	5.77(0.58)	-	2.79	2.35	1.39	1.98	1.73	7.75	0.19	-0.18(0.1)	0.33(0.12)
4C10.45	0.94(0.13)	-	-	2.11	1.39	1.1	1.7	15.91	0.16	-0(0.16)	-0.08(0.2)
4C03.27	14.97(1.52)	-	2.66	3.68	1.39	0.79	0.41	6.47	0.24	-0.8(0.09)	-0.02(0.11)
3C306	-	-	0.71	-	1.39	-	0.45	-	0.15	0.14(0.0)	-1.22(0.0)
4C33.26	2.03(0.22)	3.17(0.06)	-	0.0	1.38	-	0.4	8.12	0.26	-0.68(0.09)	-0.47(0.14)
4C16.33	12.66(1.5)	-	1.86	3.88	1.38	1.0	0.71	12.51	0.21	-0.57(0.13)	0.16(0.17)
4C29.47	8.32(0.9)	-	-	2.43	1.37	-	0.55	4.19	0.22	-0.63(0.08)	-0.03(0.1)
4C16.27	14.85(1.49)	-	4.43	4.48	1.37	0.6	0.35	0.79	0.28	-0.97(0.03)	-0.16(0.04)
3C280.1	18.62(1.86)	10.29(0.15)	5.72	4.51	1.37	0.62	0.36	0.94	0.28	-0.99(0.03)	-0.12(0.04)
4C31.30	14.06(1.43)	5.95(0.08)	2.45	-	1.36	-	1.01	1.46	0.18	-0.45(0.04)	0.33(0.06)
4C28.24	3.53(0.41)	-	2.98	-	1.36	-	0.58	2.09	0.22	-0.54(0.06)	-0.21(0.07)
3C256	18.41(1.88)	-	5.48	-	1.36	0.62	0.34	0.63	0.29	-1.02(0.03)	-0.13(0.04)
4C61.34	8.9(0.93)	6.72(0.1)	3.83	-	1.35	-	0.53	1.74	0.25	-0.75(0.04)	-0.07(0.06)
4C14.40	1.47(0.18)	-	2.96	2.72	1.35	0.82	0.53	4.79	0.23	-0.52(0.08)	-0.45(0.1)
3C272	16.4(1.67)	8.72(0.15)	4.75	4.02	1.35	0.7	0.36	0.59	0.26	-0.92(0.02)	-0.11(0.03)
S4_1242+41	0.57(0.09)	1.49(0.04)	2.04	2.01	1.34	-	0.71	7.06	0.2	-0.31(0.09)	-0.43(0.13)

Continued on next page

Table 5.3 – continued from previous page

Name	S_{74MHz} Jy	S_{151MHz} Jy	S_{365MHz} Jy	S_{408MHz} Jy	$S_{1.4GHz}$ Jy	$S_{2.7GHz}$ Jy	S_{5GHz} Jy	rchi2	γ	α	β
4C38.21	32.53(3.25)	15.75(0.18)	6.58	-	1.34	-	0.25	0.23	0.3	-1.2(0.01)	-0.13(0.02)
4C13.46	4.89(0.51)	-	2.52	2.38	1.34	0.95	0.88	0.6	0.19	-0.42(0.03)	0.03(0.04)
3C342	12.38(1.27)	-	4.34	-	1.34	0.8	0.34	1.09	0.27	-0.91(0.04)	-0.16(0.05)
3C323	20.96(2.13)	10.62(0.11)	5.43	-	1.34	0.65	0.33	0.72	0.27	-1.0(0.02)	-0.1(0.04)
3C316	8.34(0.86)	-	4.06	3.4	1.34	0.72	0.4	0.31	0.25	-0.82(0.02)	-0.19(0.03)
3C252	31.52(3.19)	12.87(0.34)	6.56	-	1.34	0.58	0.3	2.93	0.28	-1.09(0.05)	-0.08(0.08)
3C225A	12.67(1.3)	-	-	0.0	1.34	-	0.38	-	0.26	-0.89(0.0)	-0.12(0.0)
4C20.29	6.34(0.73)	-	3.08	-	1.33	0.83	0.39	0.84	0.24	-0.73(0.04)	-0.21(0.04)
4C02.29	5.38(0.55)	-	3.15	2.73	1.33	0.83	0.54	0.28	0.22	-0.62(0.02)	-0.14(0.02)
B1532+016	0.94(0.16)	-	1.14	-	1.32	-	1.3	0.23	0.11	0.06(0.02)	-0.07(0.03)
4C06.32	5.91(0.62)	-	-	2.54	1.32	0.7	0.36	2.0	0.23	-0.75(0.05)	-0.25(0.07)
3C294	31.03(3.16)	14.22(0.25)	6.12	-	1.32	0.54	0.28	0.76	0.28	-1.14(0.03)	-0.09(0.04)
4C61.23	4.74(0.5)	-	1.72	-	1.31	-	0.0	-	0.13	-0.1(0.0)	0.34(0.0)
4C51.25	15.74(1.6)	9.14(0.11)	4.22	-	1.31	-	0.32	0.41	0.26	-0.96(0.02)	-0.13(0.03)
4C14.49	11.46(1.18)	-	4.68	3.54	1.3	0.68	0.35	0.68	0.25	-0.91(0.03)	-0.17(0.04)
3C350	16.04(1.64)	9.28(0.13)	5.13	3.85	1.3	-	0.32	0.7	0.26	-0.98(0.03)	-0.14(0.04)
3C268.2	12.47(1.29)	7.84(0.14)	2.89	-	1.3	0.73	0.38	3.55	0.23	-0.85(0.06)	-0.06(0.09)
1311+552	-	0.78(0.04)	1.64	-	1.3	-	0.54	4.46	0.17	-0.2(0.08)	-0.64(0.12)
1239+577	-	-	2.13	-	1.3	-	0.24	-	0.22	-0.61(0.0)	-0.84(0.0)
4C33.30	8.57(0.91)	5.39(0.09)	-	0.0	1.29	-	0.41	1.66	0.22	-0.74(0.04)	-0.13(0.07)
4C03.23	-	-	0.52	-	1.28	1.08	1.02	2.8	0.06	0.43(0.1)	-0.76(0.17)
4C-00.45	1.37(0.16)	-	2.72	2.88	1.27	0.76	0.44	4.87	0.21	-0.56(0.08)	-0.51(0.1)
3C240	9.45(0.98)	-	3.48	-	1.27	-	0.52	0.43	0.21	-0.71(0.03)	-0.02(0.03)
4C32.34	14.19(1.46)	8.71(0.1)	4.74	-	1.26	-	0.28	0.28	0.25	-1.0(0.02)	-0.2(0.03)
4C21.28	3.09(0.32)	-	1.84	-	1.25	1.4	1.19	1.67	0.13	-0.16(0.05)	0.15(0.06)
3C242	17.4(1.76)	-	4.23	3.6	1.25	0.62	0.31	0.61	0.23	-0.97(0.03)	-0.09(0.04)
3C232	7.0(0.74)	5.06(0.07)	3.62	-	1.25	-	0.83	6.92	0.19	-0.55(0.08)	0.1(0.13)
4C29.46	13.35(1.38)	-	3.45	-	1.23	-	0.38	0.99	0.21	-0.85(0.04)	-0.05(0.05)
4C20.20	10.43(1.07)	-	2.96	-	1.23	0.71	0.39	1.29	0.2	-0.79(0.04)	-0.07(0.05)
1152+551	14.46(1.47)	-	3.7	-	1.23	-	0.0	-	0.21	-0.81(0.0)	0.03(0.0)
B21106+37	2.77(0.29)	1.99(0.08)	-	1.29	1.22	-	0.86	3.31	0.11	-0.21(0.06)	0.04(0.09)
4C13.41	12.31(1.27)	-	1.83	2.74	1.22	0.8	0.42	11.29	0.16	-0.68(0.12)	0.07(0.15)
4C-00.37	17.57(1.79)	-	4.55	4.22	1.22	0.58	0.31	0.1	0.24	-1.01(0.01)	-0.1(0.01)
4C56.18	12.7(1.3)	7.81(0.08)	4.18	-	1.21	-	0.41	0.85	0.21	-0.86(0.03)	-0.04(0.04)
4C-01.20	4.3(0.44)	-	2.75	2.42	1.21	0.72	0.42	0.1	0.18	-0.65(0.01)	-0.22(0.01)
4C49.25	4.18(0.42)	3.37(0.05)	2.48	-	1.2	-	0.58	0.24	0.16	-0.52(0.02)	-0.09(0.02)
WSTB_14W26	-	0.81(0.03)	1.94	-	1.19	-	0.4	11.97	0.15	-0.32(0.12)	-0.74(0.19)

Continued on next page

Table 5.3 – continued from previous page

Name	S_{74MHz} Jy	S_{151MHz} Jy	S_{365MHz} Jy	S_{408MHz} Jy	$S_{1.4GHz}$ Jy	$S_{2.7GHz}$ Jy	S_{5GHz} Jy	rchi2	γ	α	β
4C00.30	6.41(0.65)	-	2.86	3.24	1.19	0.75	0.42	0.97	0.19	-0.72(0.04)	-0.14(0.04)
1108+201	-	-	0.68	-	1.19	0.89	0.55	0.23	0.07	0.15(0.03)	-0.91(0.05)
4C14.35	10.43(1.07)	-	3.48	3.06	1.17	0.68	0.36	0.11	0.19	-0.83(0.01)	-0.09(0.02)
B0952+1757	2.98(0.3)	-	1.73	1.97	1.16	0.94	0.74	0.54	0.12	-0.34(0.03)	-0.02(0.03)
4C46.25	1.89(0.2)	2.77(0.04)	3.0	-	1.16	-	0.31	3.94	0.19	-0.72(0.06)	-0.51(0.1)
3C277	5.75(0.59)	8.51(0.4)	4.37	-	1.16	-	0.0	11.99	0.29	-1.44(0.28)	-0.85(0.36)
AO_1200+04	-	-	1.61	1.39	1.15	0.85	0.52	0.63	0.11	-0.3(0.04)	-0.36(0.07)
4C05.50	13.15(1.35)	-	4.21	3.25	1.15	0.66	0.35	0.65	0.19	-0.89(0.03)	-0.06(0.04)
3C261	15.57(1.59)	8.03(0.15)	4.4	-	1.15	-	0.36	1.33	0.19	-0.9(0.04)	-0.03(0.06)
B3_1151...	1.86(0.2)	1.45(0.05)	0.95	0.88	1.14	-	0.38	24.11	0.06	-0.31(0.16)	-0.22(0.23)
4C17.52	6.2(0.65)	-	2.32	2.47	1.14	0.75	0.57	0.37	0.14	-0.57(0.02)	0.01(0.03)
4C40.25	4.34(0.46)	3.0(0.04)	2.21	1.77	1.12	-	0.78	0.64	0.11	-0.38(0.02)	0.08(0.04)
4C22.25	8.07(0.83)	-	3.11	-	1.12	0.74	0.39	0.67	0.16	-0.75(0.03)	-0.08(0.04)
3C281	12.36(1.27)	-	3.54	3.37	1.12	-	0.34	0.06	0.18	-0.88(0.01)	-0.07(0.01)
4C12.41	14.51(1.49)	-	3.72	3.33	1.11	-	0.4	0.24	0.17	-0.85(0.02)	0.03(0.02)
4C23.24	6.45(0.67)	-	2.0	-	1.1	0.74	0.63	0.99	0.1	-0.5(0.04)	0.1(0.05)
4C20.31	4.34(0.44)	-	2.67	-	1.1	0.63	0.4	0.46	0.14	-0.67(0.03)	-0.2(0.03)
4C52.27	9.12(0.94)	6.24(0.11)	3.13	-	1.09	-	0.65	5.82	0.15	-0.67(0.08)	0.14(0.12)
4C-00.48	13.97(1.43)	-	3.69	2.73	1.09	0.57	0.3	1.33	0.17	-0.91(0.04)	-0.06(0.05)
3C250	24.96(2.53)	-	4.77	-	1.09	0.6	0.25	0.97	0.2	-1.09(0.04)	-0.03(0.05)
B0953+254	0.76(0.11)	-	-	0.0	1.08	-	0.85	-	0.04	-0.05(0.0)	-0.17(0.0)
4C59.11	10.14(1.04)	6.83(0.08)	3.53	-	1.08	-	0.39	1.68	0.17	-0.84(0.04)	-0.04(0.06)
4C59.10	9.06(0.93)	6.2(0.09)	3.69	-	1.08	-	0.33	0.82	0.17	-0.87(0.03)	-0.13(0.04)
4C41.22	10.78(1.11)	6.56(0.13)	-	0.0	1.08	-	0.0	-	0.16	-0.87(0.0)	-0.09(0.0)
4C00.35	6.78(0.71)	-	2.71	2.72	1.08	0.6	0.36	0.15	0.14	-0.76(0.01)	-0.13(0.02)
4C18.29	6.14(0.62)	-	3.45	3.21	1.07	0.53	0.33	1.88	0.17	-0.84(0.05)	-0.23(0.06)
4C15.34	4.83(0.52)	-	2.95	2.44	1.07	0.55	0.39	1.46	0.14	-0.72(0.04)	-0.19(0.06)
4C-00.43	9.18(0.96)	-	2.63	2.44	1.07	0.59	0.44	0.68	0.12	-0.71(0.03)	0.02(0.04)
4C17.49	10.09(1.03)	-	3.3	3.53	1.06	0.58	0.33	0.83	0.16	-0.88(0.03)	-0.11(0.04)
4C09.41	22.61(2.27)	-	4.68	4.17	1.06	0.57	0.28	0.4	0.19	-1.06(0.02)	-0.01(0.03)
4C01.31	11.73(1.18)	-	3.53	3.16	1.06	0.59	0.31	0.06	0.16	-0.9(0.01)	-0.08(0.01)
4C20.28	8.2(0.87)	-	2.87	-	1.05	0.58	0.35	0.08	0.14	-0.79(0.01)	-0.09(0.01)
4C08.31	5.48(0.56)	-	2.81	2.55	1.04	0.49	0.38	2.03	0.13	-0.74(0.05)	-0.17(0.06)
4C55.21	16.46(1.67)	8.76(0.12)	3.74	-	1.03	-	0.26	0.1	0.16	-1.01(0.01)	-0.07(0.01)
4C35.23	2.2(0.24)	2.92(0.09)	2.44	-	1.03	-	0.44	7.62	0.12	-0.61(0.09)	-0.25(0.13)
3C221	13.59(1.39)	7.3(0.1)	3.63	3.16	1.03	-	0.4	0.68	0.14	-0.84(0.03)	0.05(0.04)
B0917+449	1.47(0.21)	1.39(0.04)	1.68	0.83	1.02	-	1.0	8.14	0.02	-0.09(0.09)	0.07(0.14)

Continued on next page

Table 5.3 – continued from previous page

Name	S_{74MHz} Jy	S_{151MHz} Jy	S_{365MHz} Jy	S_{408MHz} Jy	$S_{1.4GHz}$ Jy	$S_{2.7GHz}$ Jy	S_{5GHz} Jy	rchi2	γ	α	β
4C03.21	14.37(1.48)	-	4.05	3.4	1.02	0.46	0.24	0.23	0.16	-1.04(0.02)	-0.14(0.02)
1155+251	-	-	0.91	0.74	1.02	1.07	0.88	1.75	-0.0	0.1(0.06)	-0.24(0.13)
4C17.54	2.15(0.25)	-	2.4	2.47	1.01	0.59	0.32	2.0	0.12	-0.67(0.05)	-0.39(0.07)
1223+099	3.92(0.49)	-	2.29	2.26	1.01	0.63	0.34	0.13	0.11	-0.67(0.01)	-0.21(0.02)

Table 5.4: Fitted Radio Spectra for the CENSORS sample [Brookes *et al.*, 2008]. Col1: Source name, Col2: 74 MHz flux, Col3: 151 MHz flux, Col4: 325 MHz flux, Col5: 352 MHz flux, Col6: 365 MHz flux, Col7: 408 MHz flux, Col8: 610 MHz flux, Col9: 1.4 GHz flux, Col10: 8 GHz flux, Col10: Reduced χ^2 value for the 2nd order polynomial fit, Col11: Fitted parameter γ, Col12: Fitted parameter α, Col13: Fitted parameter β. A * indicates that the 618 MHz flux is listed rather than the 610 MHz (cf. Chapter 2). A † indicates the flux value is an upper limit.

CEN	S_{74MHz} Jy	S_{151MHz} Jy	S_{325MHz} Jy	S_{352MHz} Jy	S_{365MHz} Jy	S_{408MHz} Jy	S_{610MHz} Jy	$S_{1.4GHz}$ Jy	S_{8GHz} Jy	rchi2 Jy	γ	α	β
1	5.38(0.59)	3.29(0.822)	2.045(0.205)	2.172(0.217)	2.181(0.221)	1.988(0.216)	1.399(0.14)	0.66(0.02)	-	0.32	-0.04	-0.91(0.03)	-0.21(0.04)
2	0.473(0.14)†	0.641(0.16)	0.636(0.064)	0.731(0.073)	0.718(0.08)	-	0.572(0.057)*	0.452(0.014)	0.163(0.003)	0.61	-0.29	-0.34(0.02)	-0.24(0.03)
3	0.208(0.104)†	0.755(0.189)	0.639(0.064)	0.627(0.063)	-	-	0.493(0.061)	0.355(0.011)	0.086(0.001)	0.15	-0.37	-0.51(0.01)	-0.29(0.02)
4	3.56(0.44)	2.109(0.527)	0.937(0.094)	1.023(0.102)	1.086(0.123)	1.041(0.121)	0.427(0.045)*	0.283(0.01)	-	3.07	-0.42	-0.9(0.11)	-0.03(0.14)
5	2.67(0.37)	2.063(0.516)	0.906(0.091)	0.915(0.092)	1.018(0.121)	0.801(0.096)	0.527(0.056)	0.245(0.008)	-	0.55	-0.46	-1.01(0.05)	-0.2(0.06)
6	1.04(0.17)	0.748(0.187)	0.529(0.053)	0.56(0.056)	0.518(0.073)	-	0.381(0.039)	0.24(0.001)	0.101(0.003)	0.49	-0.54	-0.52(0.01)	0.02(0.02)
7	3.46(0.43)	1.537(0.384)	0.616(0.062)	0.652(0.065)	0.49(0.057)	-	0.384(0.047)*	0.148(0.005)	-	1.09	-0.69	-0.98(0.07)	0.09(0.09)
8	0.29(0.145)†	0.543(0.136)	0.322(0.032)	-	-	-	0.29(0.033)	0.126(0.004)	-	3.21	-0.76	-0.86(0.22)	-0.44(0.51)
9	0.24(0.12)†	0.018(0.005)†	0.038(0.006)	-	-	-	0.047(0.005)*	0.118(0.004)	0.053(0.001)	22.03	-0.98	0.34(0.23)	-0.74(0.24)
84.85	0.254(0.127)†	0.016(0.004)†	0.373(0.039)	-	-	-	0.127(0.013)	0.092(0.004)	-	66.14	-0.84	-1.16(1.01)	-1.63(2.25)
10	0.86(0.15)	0.485(0.121)	0.25(0.025)	0.282(0.028)	-	-	0.14(0.014)*	0.079(0.003)	-	1.04	-0.98	-0.82(0.08)	-0.01(0.11)
11	0.254(0.127)†	0.039(0.01)†	0.07(0.008)	0.069(0.008)	-	-	0.053(0.007)	0.078(0.002)	0.11(0.002)	2.52	-1.13	0.17(0.06)	0.03(0.07)
12	0.94(0.14)	0.563(0.141)	0.282(0.028)	0.295(0.03)	-	-	0.156(0.019)*	0.07(0.003)	0.007(0.0)	0.37	-0.99	-1.09(0.01)	-0.23(0.02)
13	0.94(0.16)	0.513(0.128)	0.234(0.024)	0.267(0.027)	0.249(0.039)	-	0.123(0.014)	0.066(0.003)	-	1.03	-1.05	-0.92(0.08)	-0.01(0.11)
14	0.274(0.2)†	0.346(0.087)	0.224(0.023)	0.23(0.023)	-	-	0.135(0.014)	0.066(0.002)	-	0.37	-1.03	-0.97(0.06)	-0.35(0.14)
15	1.18(0.17)	0.585(0.146)	0.292(0.029)	0.324(0.033)	0.27(0.044)	-	0.155(0.016)*	0.063(0.002)	-	0.52	-1.03	-1.15(0.05)	-0.16(0.07)
17	0.38(0.19)†	0.106(0.026)	0.179(0.018)	0.194(0.02)	-	-	0.144(0.027)	0.062(0.002)	-	0.3	-1.0	-1.24(0.07)	-1.45(0.17)
16	0.501(0.147)†	0.467(0.117)	0.216(0.022)	0.217(0.022)	-	-	0.152(0.02)	0.062(0.002)	-	0.55	-1.06	-0.99(0.06)	-0.27(0.11)
18	0.32(0.162)†	0.126(0.031)	0.13(0.013)	0.124(0.013)	-	-	0.09(0.01)	0.058(0.002)	0.072(0.002)	3.18	-1.19	-0.34(0.06)	0.42(0.08)
19	0.28(0.14)†	0.288(0.072)	0.227(0.023)	0.232(0.023)	-	-	0.125(0.014)	0.055(0.002)	-	0.86	-1.08	-1.14(0.1)	-0.5(0.25)
21	0.27(0.135)†	0.139(0.035)	0.133(0.014)	0.138(0.014)	-	-	0.091(0.01)*	0.054(0.002)	0.008(0.0)	0.43	-1.15	-0.74(0.02)	-0.37(0.03)
20	0.26(0.125)†	0.281(0.07)	0.153(0.016)	0.177(0.018)	-	-	0.114(0.014)*	0.054(0.002)	-	1.06	-1.13	-0.88(0.12)	-0.26(0.29)
22	0.22(0.11)†	0.403(0.101)	0.212(0.022)	-	-	-	0.151(0.018)	0.053(0.002)	0.012(0.0)	4.5	-1.14	-0.89(0.08)	0.02(0.09)
23	1.2(0.19)	0.476(0.119)	0.249(0.025)	0.253(0.025)	-	-	0.1(0.012)	0.052(0.002)	-	1.79	-1.13	-1.05(0.11)	0.02(0.14)
24	0.28(0.14)†	0.1(0.025)	0.133(0.014)	0.144(0.015)	-	-	0.096(0.01)	0.051(0.002)	0.01(0.0)	2.6	-1.18	-0.71(0.06)	-0.23(0.07)
25	0.248(0.124)†	0.033(0.008)†	0.086(0.009)	0.111(0.011)	-	-	0.074(0.008)*	0.049(0.002)	0.006(0.0)	5.5	-1.2	-0.57(0.08)	-0.63(0.11)
26	0.274(0.137)†	0.295(0.074)	0.182(0.018)	0.173(0.018)	-	-	0.109(0.014)	0.044(0.001)	0.005(0.0)	0.15	-1.2	-1.02(0.01)	-0.18(0.02)
28	0.25(0.125)†	0.183(0.046)	0.112(0.012)	0.102(0.011)	-	-	0.051(0.006)*	0.04(0.002)	-	2.29	-1.34	-0.5(0.18)	0.43(0.43)
27	0.3(0.15)†	0.259(0.065)	0.149(0.017)	-	-	-	0.08(0.009)	0.04(0.002)	-	0.33	-1.27	-0.87(0.08)	-0.02(0.17)
30	0.27(0.135)†	0.066(0.016)	0.132(0.014)	0.104(0.011)	-	-	0.056(0.008)*	0.038(0.002)	-	7.16	-1.26	-1.01(0.34)	-0.86(0.79)
29	0.248(0.124)†	0.196(0.049)	0.123(0.013)	0.116(0.012)	-	-	0.07(0.009)*	0.038(0.002)	-	0.17	-1.3	-0.82(0.05)	-0.08(0.12)
31	0.43(0.125)†	0.33(0.083)	0.154(0.016)	0.164(0.017)	-	-	0.097(0.014)*	0.037(0.002)	-	0.39	-1.26	-1.13(0.06)	-0.3(0.1)
32	0.27(0.135)†	0.155(0.039)	0.137(0.014)	0.106(0.011)	-	-	0.089(0.016)	0.035(0.002)	-	1.16	-1.28	-1.07(0.14)	-0.6(0.34)
35	0.33(0.11)†	0.017(0.004)†	0.086(0.009)	0.098(0.01)	-	-	0.052(0.006)	0.034(0.001)	-	8.99	-1.37	-0.66(0.27)	-0.12(0.49)
34	0.24(0.12)†	0.042(0.01)†	0.042(0.005)	-	-	-	0.028(0.003)*	0.034(0.001)	0.009(0.0)	7.32	-1.43	-0.26(0.12)	-0.45(0.14)
33	0.374(0.162)†	0.119(0.03)	0.124(0.013)	0.122(0.013)	-	-	0.071(0.009)	0.034(0.001)	-	1.64	-1.31	-0.98(0.12)	-0.33(0.24)
39	0.272(0.136)†	0.242(0.06)	0.134(0.014)	0.13(0.013)	-	-	0.07(0.007)	0.032(0.001)	-	0.3	-1.35	-1.03(0.06)	-0.12(0.15)
38	0.28(0.14)†	0.19(0.048)	0.1(0.01)	0.109(0.012)	-	-	0.069(0.007)	0.032(0.001)	-	0.56	-1.36	-0.92(0.08)	-0.22(0.2)
37	0.405(0.17)†	0.203(0.051)	0.097(0.01)	0.094(0.01)	-	-	0.045(0.005)*	0.032(0.001)	-	1.25	-1.42	-0.62(0.11)	0.33(0.2)
36	0.28(0.14)†	0.047(0.012)†	0.062(0.007)	-	-	-	0.028(0.003)*	0.032(0.001)	0.014(0.0)	7.92	-1.44	-0.35(0.12)	-0.13(0.14)
66.82	0.27(0.135)†	0.257(0.064)	0.123(0.013)	0.06(0.007)	-	-	0.037(0.005)	0.031(0.001)	-	9.14	-1.48	-0.36(0.38)	1.03(0.9)
40	0.32(0.17)†	0.104(0.026)	0.076(0.008)	0.089(0.01)	-	-	0.05(0.006)	0.031(0.001)	-	1.36	-1.41	-0.66(0.12)	-0(0.24)
41	0.28(0.14)†	0.014(0.004)†	0.074(0.008)	0.055(0.007)	-	-	0.042(0.006)	0.028(0.002)	-	3.55	-1.42	-0.85(0.26)	-0.93(0.58)
45	0.218(0.19)†	0.127(0.032)	0.094(0.01)	0.085(0.009)	-	-	0.042(0.006)	0.026(0.001)	-	1.95	-1.47	-0.87(0.18)	-0.08(0.41)
44	0.244(0.122)†	0.019(0.005)†	0.013(0.002)	-	-	-	0.024(0.003)	0.026(0.001)	0.033(0.001)	9.3	-1.6	0.07(0.16)	0.08(0.17)
43	0.24(0.12)†	0.08(0.02)	0.068(0.007)	0.084(0.009)	-	-	0.045(0.005)	0.026(0.001)	-	2.43	-1.45	-0.83(0.18)	-0.41(0.43)
42	0.26(0.13)†	0.136(0.034)	0.083(0.009)	0.072(0.008)	-	-	0.065(0.007)	0.026(0.001)	-	1.64	-1.43	-0.95(0.14)	-0.44(0.35)

Continued on next page

Table 5.4 – continued from previous page

CEN	S_{74MHz} Jy	S_{151MHz} Jy	S_{325MHz} Jy	S_{352MHz} Jy	S_{365MHz} Jy	S_{408MHz} Jy	S_{610MHz} Jy	$S_{1.4GHz}$ Jy	S_{8GHz} Jy	rchi2	γ	α	β
47	0.432(0.121)†	0.122(0.031)	0.083(0.009)	0.076(0.008)	-	-	0.049(0.005)*	0.025(0.001)	-	0.77	-1.49	-0.75(0.08)	0.15(0.13)
46	0.248(0.124)†	0.02(0.005)†	0.026(0.004)	-	-	-	0.016(0.002)	0.025(0.001)	0.007(0.0)	23.45	-1.58	-0.25(0.23)	-0.45(0.26)
49	0.288(0.144)†	0.031(0.008)†	0.056(0.007)	-	-	-	0.023(0.003)	0.024(0.001)	0.057(0.001)	12.55	-1.62	-0.1(0.16)	0.57(0.18)
48	0.24(0.12)†	0.068(0.017)†	0.062(0.007)	0.05(0.006)	-	-	0.029(0.003)	0.024(0.001)	0.018(0.0)	2.58	-1.56	-0.43(0.06)	0.26(0.08)
53	0.274(0.137)†	0.084(0.021)†	0.059(0.006)	-	-	-	0.044(0.005)	0.022(0.001)	-	0.32	-1.53	-0.85(0.08)	-0.39(0.16)
52	0.24(0.12)†	0.047(0.012)†	0.015(0.002)†	-	-	-	0.005(0.001)*†	0.022(0.001)	0.024(0.001)	33.15	-1.69	0.04(0.29)	0.03(0.32)
51	0.262(0.131)†	0.087(0.022)†	0.064(0.007)	0.06(0.007)	-	-	0.038(0.004)	0.022(0.001)	-	0.43	-1.55	-0.75(0.08)	-0.12(0.18)
50	0.254(0.127)†	0.142(0.036)	0.113(0.012)	0.112(0.012)	-	-	0.046(0.005)	0.022(0.001)	-	3.64	-1.48	-1.18(0.22)	-0.32(0.53)
57	0.274(0.137)†	0.039(0.01)†	0.069(0.008)	0.064(0.007)	-	-	0.03(0.004)	0.021(0.001)	-	7.34	-1.54	-0.96(0.35)	-0.71(0.79)
56	0.268(0.134)†	0.108(0.027)	0.071(0.008)	-	-	-	0.036(0.005)	0.021(0.001)	-	1.43	-1.57	-0.79(0.17)	0.01(0.36)
55	0.489(0.138)†	0.072(0.018)†	0.055(0.006)	0.047(0.006)	-	-	0.032(0.004)	0.021(0.001)	-	2.21	-1.62	-0.41(0.14)	0.56(0.23)
54	0.232(0.116)†	0.051(0.013)†	0.052(0.006)	-	-	-	0.028(0.003)	0.021(0.001)	0.009(0.0)	1.98	-1.6	-0.5(0.06)	-0(0.07)
60	0.536(0.128)†	0.02(0.005)†	0.045(0.005)	-	-	-	0.031(0.004)	0.019(0.001)	0.005(0.0)	10.9	-1.63	-0.78(0.1)	0.06(0.12)
59	0.25(0.125)†	0.077(0.019)	0.081(0.009)	0.052(0.006)	-	-	0.018(0.003)*	0.019(0.001)	-	15.48	-1.65	-0.63(0.53)	0.36(1.19)
65	0.24(0.12)†	0.049(0.012)†	0.042(0.006)	0.048(0.006)	-	-	0.023(0.003)	0.018(0.001)	-	3.34	-1.66	-0.61(0.24)	-0.07(0.53)
64	0.266(0.133)†	0.196(0.049)	0.116(0.012)	0.085(0.009)	-	-	0.048(0.007)	0.018(0.001)	-	1.4	-1.55	-1.26(0.16)	-0.23(0.36)
63	0.82(0.14)	0.427(0.107)	0.154(0.016)	0.159(0.016)	-	-	0.064(0.009)*	0.018(0.001)	-	0.34	-1.5	-1.61(0.05)	-0.32(0.07)
62	0.266(0.133)†	0.072(0.018)†	0.046(0.006)	-	-	-	0.024(0.003)*	0.018(0.001)	-	1.87	-1.68	-0.42(0.19)	0.37(0.4)
61	0.264(0.132)†	0.08(0.02)	0.081(0.009)	0.068(0.008)	-	-	0.034(0.005)	0.018(0.001)	-	2.53	-1.56	-1.09(0.2)	-0.5(0.48)
70	0.308(0.117)†	0.018(0.004)†	0.068(0.008)	-	-	-	0.048(0.009)†	0.017(0.002)	-	8.28	-1.6	-0.96(0.48)	-0.28(0.64)
71	0.256(0.128)†	0.084(0.021)	0.053(0.006)	-	-	-	0.031(0.003)	0.017(0.001)	-	0.33	-1.66	-0.78(0.07)	-0.05(0.16)
69	0.244(0.122)†	0.062(0.015)	0.082(0.009)	0.06(0.007)	-	-	0.04(0.004)	0.017(0.001)	0.002(0.0)	3.6	-1.61	-0.96(0.07)	-0.17(0.1)
68	0.196(0.124)†	0.016(0.004)†	0.033(0.004)	0.032(0.005)	-	-	0.017(0.002)	0.017(0.001)	0.005(0.0)	4.1	-1.7	-0.53(0.08)	-0.19(0.1)
67	0.242(0.121)†	0.082(0.02)†	0.061(0.007)	0.032(0.004)	-	-	0.034(0.004)	0.017(0.001)	-	5.37	-1.65	-0.73(0.29)	-0.05(0.66)
75	0.262(0.131)†	0.031(0.008)†	0.082(0.01)	0.046(0.006)	-	-	0.028(0.005)*†	0.016(0.001)	-	9.79	-1.59	-1.34(0.47)	-1.33(1.01)
74	0.278(0.139)†	0.068(0.017)†	0.062(0.007)	-	-	-	0.023(0.003)*	0.016(0.001)	0.003(0.0)	5.02	-1.68	-0.82(0.1)	-0.09(0.13)
73	0.22(0.11)†	0.064(0.016)	0.062(0.007)	0.039(0.005)	-	-	0.031(0.003)	0.016(0.001)	-	3.5	-1.66	-0.86(0.22)	-0.26(0.51)
72	0.264(0.132)†	0.018(0.004)†	0.04(0.005)	0.036(0.005)	-	-	0.025(0.003)	0.016(0.001)	0.002(0.0)	0.72	-1.68	-0.72(0.03)	-0.41(0.04)
79	0.232(0.116)†	0.18(0.045)	0.092(0.011)	0.078(0.008)	-	-	0.054(0.007)*	0.015(0.001)	-	1.24	-1.6	-1.46(0.16)	-0.6(0.33)
78	0.256(0.128)†	0.016(0.004)†	0.042(0.005)	0.032(0.005)	-	-	0.024(0.003)	0.015(0.001)	-	1.44	-1.72	-0.73(0.15)	-0.33(0.33)
77	0.26(0.13)†	0.041(0.01)†	0.05(0.006)	0.043(0.006)	-	-	0.037(0.004)	0.015(0.001)	0.043(0.001)	14.56	-1.75	-0.35(0.15)	0.85(0.21)
76	0.206(0.103)†	0.016(0.004)†	0.049(0.006)	-	-	-	0.03(0.004)	0.015(0.001)	-	1.29	-1.66	-0.97(0.17)	-0.73(0.34)
138	0.2(0.1)†	0.017(0.004)†	0.041(0.005)	-	-	-	0.019(0.002)	0.015(0.0)	-	6.59	-1.76	-0.53(0.35)	0.08(0.75)
83	0.156(0.118)†	0.036(0.009)†	0.056(0.006)	0.033(0.005)	-	-	0.031(0.003)	0.014(0.001)	0.002(0.0)	3.84	-1.73	-0.86(0.08)	-0.22(0.1)
81	0.25(0.125)†	0.019(0.005)†	0.053(0.007)	0.043(0.006)	-	-	0.027(0.003)	0.014(0.001)	-	1.81	-1.69	-0.98(0.21)	-0.54(0.41)
80	0.226(0.113)†	0.017(0.004)†	0.042(0.005)	-	-	-	0.028(0.004)	0.014(0.001)	-	0.33	-1.69	-0.9(0.08)	-0.6(0.17)
92	0.274(0.127)†	0.02(0.005)†	0.08(0.009)	-	-	-	0.016(0.003)	0.013(0.001)	-	27.91	-1.7	-1.39(0.95)	-0.83(1.85)
91	0.324(0.162)†	0.014(0.004)†	0.008(0.002)†	-	-	-	0.003(0.001)†	0.013(0.001)	0.004(0.0)	41.22	-1.88	-0.3(0.37)	-0.35(0.42)
90	0.21(0.105)†	0.086(0.021)	0.039(0.005)	-	-	-	0.025(0.003)*	0.013(0.001)	-	0.41	-1.78	-0.77(0.09)	0.08(0.19)
89	0.274(0.137)†	0.073(0.018)†	0.056(0.007)	0.046(0.006)	-	-	0.018(0.003)	0.013(0.001)	-	4.16	-1.76	-0.92(0.32)	-0.04(0.66)
88	0.274(0.137)†	0.04(0.01)	0.03(0.005)	-	-	-	0.035(0.006)*	0.013(0.001)	0.003(0.0)	3.81	-1.77	-0.66(0.11)	-0.16(0.12)
87	0.294(0.147)†	0.057(0.014)†	0.056(0.007)	0.064(0.007)	-	-	0.021(0.003)*	0.013(0.001)	-	6.44	-1.7	-1.18(0.34)	-0.59(0.78)
86	0.268(0.134)†	0.054(0.013)†	0.032(0.004)	-	-	-	0.022(0.003)	0.013(0.001)	-	0.0	-1.79	-0.6(0.0)	0.04(0.0)
100	0.24(0.12)†	0.139(0.035)	0.058(0.007)	0.061(0.007)	-	-	0.025(0.003)	0.012(0.001)	-	1.28	-1.79	-1.07(0.15)	0.14(0.33)
99	0.26(0.13)†	0.042(0.011)†	0.023(0.004)	-	-	-	0.021(0.003)	0.012(0.001)	-	1.44	-1.84	-0.62(0.2)	-0.13(0.39)
98	0.24(0.12)†	0.015(0.004)†	0.014(0.004)	-	-	-	0.011(0.002)*†	0.012(0.001)	0.005(0.0)	5.08	-1.89	-0.42(0.14)	-0.04(0.16)
97	0.262(0.131)†	0.015(0.004)†	0.039(0.005)	0.038(0.005)	-	-	0.014(0.002)	0.012(0.001)	-	8.63	-1.84	-0.71(0.49)	-0.02(0.92)
96	0.282(0.141)†	-	0.054(0.007)	0.051(0.006)	-	-	0.012(0.003)	0.012(0.001)	0.002(0.0)	5.84	-1.77	-1.05(0.13)	-0.09(0.17)
95	0.268(0.134)†	0.015(0.004)†	0.045(0.007)	-	-	-	0.019(0.003)	0.012(0.001)	0.002(0.0)	3.19	-1.8	-0.81(0.1)	-0.26(0.15)
94	0.286(0.143)†	0.108(0.027)	0.06(0.007)	-	-	-	0.029(0.005)*	0.012(0.001)	-	0.25	-1.74	-1.15(0.08)	-0.23(0.17)
93	0.284(0.142)†	0.064(0.016)†	0.034(0.004)	-	-	-	0.026(0.005)* †	0.012(0.001)	-	0.97	-1.8	-0.79(0.17)	-0.12(0.34)

Continued on next page

Table 5.4 – continued from previous page

CEN	S_{74MHz} Jy	S_{151MHz} Jy	S_{325MHz} Jy	S_{352MHz} Jy	S_{365MHz} Jy	S_{408MHz} Jy	S_{610MHz} Jy	$S_{1.4GHz}$ Jy	S_{8GHz} Jy	rchi2	γ	α	β
105	0.28(0.14)†	0.122(0.03)	0.058(0.006)	0.062(0.007)	-	-	0.029(0.004)	0.011(0.001)	-	0.63	-1.78	-1.29(0.1)	-0.27(0.23)
104	0.38(0.19)†	0.078(0.019)†	0.061(0.008)	0.04(0.005)	-	-	0.018(0.003)†	0.011(0.001)	-	4.33	-1.82	-1.04(0.3)	-0.07(0.66)
103	0.27(0.135)†	0.136(0.034)	0.068(0.008)	0.059(0.007)	-	-	0.03(0.004)*	0.011(0.001)	-	0.11	-1.77	-1.32(0.04)	-0.25(0.1)
102	0.26(0.13)†	0.027(0.007)†	0.028(0.004)	-	-	-	0.011(0.002)*†	0.011(0.001)	-	8.88	-1.93	-0.32(0.58)	0.29(1.01)
101	0.26(0.13)†	0.016(0.004)†	0.035(0.005)	0.022(0.004)	-	-	0.019(0.003)	0.011(0.001)	-	1.58	-1.84	-0.71(0.2)	-0.17(0.41)
117	0.26(0.13)†	0.015(0.004)†	0.02(0.003)	-	-	-	0.005(0.001)†	0.01(0.001)	-	14.12	-2.09	0.2(0.78)	1.36(1.44)
116	0.23(0.115)†	0.014(0.004)†	0.019(0.003)†	-	-	-	0.008(0.001)†	0.01(0.001)	0.008(0.0)	3.81	-1.99	-0.35(0.1)	0.29(0.13)
115	0.24(0.12)†	0.015(0.004)†	0.055(0.011)	0.014(0.003)	-	-	0.008(0.001)	0.01(0.001)	-	17.76	-1.99	-0.4(0.84)	0.57(1.48)
114	0.262(0.131)†	0.015(0.004)†	0.017(0.004)	-	-	-	0.019(0.003)	0.01(0.001)	0.006(0.0)	2.5	-1.94	-0.49(0.09)	0.17(0.11)
113	0.292(0.146)†	0.032(0.008)†	0.058(0.007)	0.039(0.005)	-	-	0.017(0.003)*	0.01(0.001)	-	10.14	-1.81	-1.33(0.45)	-0.9(0.98)
112	0.252(0.126)†	0.015(0.004)†	0.045(0.006)	0.038(0.005)	-	-	0.023(0.003)	0.01(0.001)	0.002(0.0)	3.92	-1.85	-0.87(0.09)	-0.01(0.13)
111	0.27(0.135)†	0.04(0.01)†	0.018(0.003)	0.018(0.004)	-	-	0.015(0.002)	0.01(0.001)	-	0.36	-1.96	-0.35(0.1)	0.35(0.2)
110	0.23(0.115)†	0.018(0.004)†	0.039(0.005)	0.027(0.004)	-	-	0.011(0.002)	0.01(0.001)	-	5.88	-1.92	-0.74(0.48)	0.1(0.84)
109	0.248(0.124)†	0.02(0.005)†	0.038(0.005)	0.029(0.005)	-	-	0.012(0.003)	0.01(0.001)	-	2.44	-1.87	-0.83(0.27)	-0.08(0.56)
108	0.22(0.11)†	0.014(0.004)†	0.012(0.004)	-	-	-	0.003(0.001)	0.01(0.001)	0.015(0.0)	13.05	-2.0	-0.17(0.22)	0.39(0.26)
107	0.246(0.123)†	0.039(0.01)†	0.034(0.006)	0.028(0.004)	-	-	0.006(0.001)*†	0.01(0.001)	-	16.08	-1.97	-0.39(0.74)	0.6(1.38)
106	0.247(0.124)†	0.02(0.005)†	0.025(0.004)	0.019(0.003)	-	-	0.015(0.002)	0.01(0.001)	-	0.41	-1.93	-0.4(0.09)	0.44(0.19)
124	0.26(0.13)†	0.017(0.004)†	0.036(0.006)	-	-	-	0.014(0.003)	0.009(0.001)	-	3.64	-1.93	-0.92(0.38)	-0.21(0.71)
122	0.248(0.124)†	0.015(0.004)†	0.018(0.004)	-	-	-	0.01(0.001)	0.009(0.001)	-	0.47	-2.05	-0.12(0.11)	0.8(0.21)
120	0.266(0.133)†	0.017(0.004)†	0.012(0.002)†	-	-	-	0.003(0.001)†	0.009(0.001)	0.007(0.0)	21.81	-2.05	-0.31(0.25)	0.22(0.32)
119	0.264(0.132)†	0.058(0.015)	0.034(0.004)	-	-	-	0.019(0.002)	0.009(0.001)	-	0.03	-1.89	-0.9(0.03)	-0.11(0.05)
118	0.25(0.125)†	0.106(0.027)	0.049(0.006)	0.043(0.005)	-	-	0.025(0.004)	0.009(0.001)	-	0.06	-1.85	-1.16(0.04)	-0.12(0.08)
123	0.22(0.11)†	0.018(0.005)†	0.017(0.003)	-	-	-	0.012(0.002)	0.009(0.0)	0.003(0.0)	2.51	-1.99	-0.59(0.08)	0.03(0.11)
121	0.26(0.13)†	0.02(0.005)†	0.015(0.003)	-	-	-	0.012(0.002)	0.009(0.0)	0.014(0.0)	0.71	-2.01	-0.33(0.05)	0.55(0.06)
136	0.2(0.1)†	0.018(0.004)†	0.036(0.005)	-	-	-	0.013(0.002)	0.008(0.001)	-	7.36	-2.0	-0.92(0.44)	0.01(0.84)
135	0.26(0.13)†	0.015(0.004)†	0.016(0.003)	-	-	-	0.016(0.003)	0.008(0.001)	-	2.47	-2.01	-0.62(0.31)	0.03(0.56)
134	0.272(0.136)†	0.033(0.008)†	0.051(0.007)	0.018(0.004)	-	-	0.009(0.002)*	0.008(0.001)	-	16.99	-1.96	-1.04(0.72)	-0.29(1.41)
133	0.224(0.112)†	0.02(0.005)†	0.029(0.005)	-	-	-	0.013(0.002)	0.008(0.001)	-	0.94	-2.0	-0.8(0.23)	0.09(0.36)
132	0.26(0.13)†	0.009(0.002)†	0.017(0.003)†	-	-	-	0.006(0.001)*†	0.008(0.001)	-	7.14	-2.11	-0.08(0.53)	0.72(0.96)
131	0.24(0.12)†	0.018(0.004)†	0.018(0.003)	-	-	-	0.006(0.002)†	0.008(0.001)	-	3.5	-2.11	-0.02(0.44)	1.17(0.78)
129	0.26(0.13)†	0.024(0.006)†	0.026(0.005)	-	-	-	0.01(0.002)†	0.008(0.001)	-	5.31	-1.97	-0.73(0.49)	-0.28(0.89)
126	0.26(0.13)†	0.013(0.003)†	0.039(0.007)	-	-	-	0.028(0.004)*	0.008(0.001)	-	0.02	-1.82	-1.53(0.03)	-1.36(0.05)
130	0.2(0.1)†	0.014(0.003)†	0.018(0.003)†	-	-	-	0.011(0.002)†	0.008(0.0)	0.003(0.0)	0.57	-2.01	-0.57(0.04)	0.04(0.05)
128	0.22(0.11)†	0.033(0.008)†	0.022(0.004)	-	-	-	0.012(0.002)	0.008(0.0)	0.004(0.0)	0.39	-2.0	-0.56(0.03)	0.15(0.04)
127	0.28(0.14)†	0.015(0.004)†	0.05(0.006)	0.029(0.005)	-	-	0.023(0.003)	0.008(0.0)	0.002(0.0)	5.95	-1.91	-0.96(0.11)	-0(0.16)
125	0.24(0.12)†	0.016(0.004)†	0.037(0.005)	0.028(0.004)	-	-	0.021(0.003)	0.008(0.0)	-	0.68	-1.89	-1.18(0.12)	-0.71(0.26)
137	0.28(0.14)†	0.015(0.004)†	0.029(0.006)	-	-	-	0.009(0.002)†	0.007(0.001)	-	5.54	-2.07	-0.61(0.63)	0.32(0.94)

Table 5.5: Fitted Radio Spectra for the 7CRS sample. Col1: Source name, Col2: 4.85 GHz flux, Col3: 1.4 GHz flux, Col4: 408 MHz flux, Col5: 365 MHz flux, Col6: 327 MHz flux, Col7: 151 MHz flux, Col8: 74 MHz flux, Col9: 38 MHz flux, Col10: Reduced χ^2 value for the 2nd order polynomial fit, Col11: Fitted parameter γ, Col12: Fitted parameter α, Col13: Fitted parameter β.

name	$S_{4.85GHz}$ Jy	$S_{1.4GHz}$ Jy	S_{408MHz} Jy	S_{365MHz} Jy	S_{327MHz} Jy	S_{151MHz} Jy	S_{74MHz} Jy	S_{38MHz} Jy	rchi2	γ	α	β
5C6.8	0.395(0.04)	0.676(0.02)	1.3(0.35)	1.325(0.022)	-	1.625(0.064)	1.29(0.17)	-	5.31	-0.07	-0.5(0.06)	-0.21(0.09)
5C6.19	0.157(0.016)	0.44(0.013)	1.421(0.142)	1.259(0.026)	-	2.035(0.037)	2.93(0.31)	-	2.58	-0.22	-0.8(0.04)	-0.18(0.05)
5C6.24	0.097(0.01)	0.273(0.008)	0.71(0.071)	0.771(0.021)	-	1.282(0.036)	1.59(0.18)	-	0.95	-0.43	-0.79(0.03)	-0.16(0.04)
5C6.29	0.034(0.003)	0.107(0.003)	0.309(0.026)	0.344(0.02)	-	0.571(0.023)	0.332(0.1)†	-	3.86	-0.83	-0.87(0.06)	-0.19(0.1)
5C6.33	0.03(0.003)	0.09(0.0)	0.343(0.06)	0.42(0.04)	-	0.589(0.018)	1.26(0.16)	-	6.4	-0.91	-0.9(0.08)	-0.06(0.12)
5C6.34	0.039(0.004)	0.088(0.003)	0.245(0.018)	0.345(0.044)	-	0.505(0.025)	0.86(0.13)	-	2.59	-0.93	-0.77(0.05)	0.02(0.08)
5C6.39	0.036(0.004)	0.101(0.003)	0.272(0.016)	0.29(0.021)	-	0.532(0.022)	1.13(0.14)	-	1.26	-0.88	-0.79(0.03)	-0.03(0.05)
5C6.62	0.044(0.004)	0.131(0.005)	0.402(0.023)	0.444(0.044)	-	0.953(0.026)	1.66(0.19)	-	0.18	-0.75	-0.9(0.01)	-0.02(0.02)
5C6.63	0.051(0.005)	0.13(0.004)	0.439(0.12)	-	-	0.787(0.019)	1.36(0.18)	-	0.44	-0.77	-0.79(0.02)	0.02(0.04)
5C6.83	0.038(0.004)	0.207(0.007)	0.677(0.049)	0.824(0.047)	-	1.396(0.043)	2.14(0.23)	-	0.79	-0.52	-1.08(0.03)	-0.32(0.04)
5C6.78	0.087(0.009)	0.492(0.006)	1.276(0.024)	0.854(0.05)	-	2.623(0.085)	5.21(0.33)	-	41.0	-0.2	-0.81(0.13)	-0.06(0.18)
5C6.95	0.044(0.004)	0.127(0.004)	0.337(0.034)	0.412(0.021)	-	0.865(0.022)	1.01(0.14)	-	3.39	-0.76	-0.88(0.06)	-0.05(0.08)
5C6.160	0.054(0.005)	0.191(0.006)	0.544(0.035)	0.577(0.024)	-	0.998(0.026)	1.49(0.17)	-	0.12	-0.59	-0.87(0.01)	-0.19(0.01)
5C6.201	0.049(0.005)	0.133(0.005)	0.791(0.177)	0.645(0.044)	-	1.304(0.041)	2.58(0.35)	-	5.7	-0.7	-0.99(0.08)	0.02(0.12)
5C6.217	0.169(0.017)	0.414(0.014)	1.128(0.109)	1.072(0.04)	-	1.921(0.04)	2.8(0.29)	-	0.72	-0.27	-0.72(0.02)	-0.06(0.03)
5C6.233	0.058(0.006)	0.176(0.005)	0.597(0.06)	0.644(0.021)	-	1.266(0.029)	1.89(0.21)	-	1.98	-0.6	-0.95(0.04)	-0.11(0.06)
5C6.237	0.612(0.061)	0.922(0.028)	1.402(0.062)	1.59(0.025)	-	1.749(0.055)	2.41(0.25)	-	6.04	0.05	-0.39(0.06)	-0.14(0.08)
5C6.251	0.03(0.003)	0.096(0.003)	0.358(0.036)	0.391(0.032)	-	0.565(0.017)	1.07(0.14)	-	5.79	-0.87	-0.91(0.08)	-0.16(0.12)
5C6.258	0.085(0.008)	0.186(0.006)	0.45(0.08)	0.407(0.025)	-	0.693(0.022)	0.93(0.13)	-	0.4	-0.64	-0.61(0.02)	-0.04(0.03)
5C6.264	0.066(0.007)	0.189(0.006)	0.599(0.14)	0.64(0.053)	-	1.047(0.025)	1.78(0.2)	-	1.22	-0.6	-0.82(0.04)	-0.08(0.05)
5C6.279	0.047(0.005)	0.131(0.004)	0.402(0.04)	0.412(0.045)	-	0.63(0.02)	1.09(0.14)	-	2.03	-0.76	-0.78(0.05)	-0.11(0.07)
5C6.282	0.037(0.004)	0.133(0.003)	0.413(0.041)	0.998(0.121)	-	0.707(0.029)	1.3(0.17)	-	18.21	-0.72	-0.93(0.15)	-0.24(0.21)
7C0221+3417	0.15(0.015)	0.436(0.015)	-	1.531(0.063)	-	2.565(0.036)	4.61(0.47)	-	5.21	-0.21	-0.87(0.07)	-0.13(0.1)
5C6.288	0.242(0.024)	0.476(0.014)	0.883(0.168)	1.156(0.073)	-	1.367(0.045)	2.28(0.24)	-	4.54	-0.24	-0.53(0.07)	-0.07(0.1)
5C6.287	0.032(0.003)	0.161(0.005)	0.626(0.09)	0.729(0.054)	-	1.575(0.069)	3.25(0.34)	-	0.55	-0.62	-1.15(0.02)	-0.16(0.03)
5C6.291	1.515(0.152)	2.894(0.087)	-	3.799(0.034)	-	3.775(0.049)	5.44(0.55)	-	10.76	0.5	-0.27(0.07)	-0.2(0.08)
5C6.292	0.032(0.003)	0.118(0.004)	0.775(0.078)	0.441(0.02)	-	0.928(0.021)	2.15(0.23)	-	16.95	-0.77	-1.01(0.12)	-0.12(0.18)
5C6.5	0.04(0.004)	0.157(0.006)	0.5(0.05)	0.542(0.042)	-	0.782(0.023)	1.35(0.19)	-	2.43	-0.66	-0.91(0.05)	-0.27(0.08)
5C7.8	0.078(0.008)	0.299(0.01)	1.092(0.109)	0.885(0.054)	-	1.737(0.034)	3.46(0.37)	-	4.2	-0.4	-0.9(0.06)	-0.14(0.09)
5C7.9	0.156(0.016)	0.484(0.011)	-	0.845(0.026)	-	2.042(0.055)	4.23(0.48)	-	38.44	-0.27	-0.55(0.17)	0.17(0.25)
5C7.10	0.029(0.003)	0.15(0.006)	0.589(0.142)	0.644(0.054)	-	1.35(0.083)	3.09(0.31)	-	1.52	-0.66	-1.13(0.04)	-0.15(0.06)
7C0808+2854	0.05(0.005)	0.102(0.004)	-	-	-	0.646(0.019)	1.4(0.15)	-	0.04	-0.89	-0.71(0.01)	0.18(0.01)
5C7.15	0.047(0.005)	0.175(0.005)	0.533(0.08)	0.616(0.027)	-	0.918(0.068)	1.61(0.17)	-	2.01	-0.61	-0.94(0.04)	-0.22(0.06)
5C7.17	0.037(0.004)	0.129(0.002)	0.304(0.034)	-	-	0.62(0.025)	1.31(0.24)	-	2.74	-0.77	-0.82(0.06)	-0.15(0.09)
5C7.23	0.06(0.006)	0.18(0.006)	0.763(0.076)	0.551(0.055)	-	1.032(0.018)	1.87(0.2)	-	6.3	-0.61	-0.85(0.08)	-0.11(0.12)
5C7.25	0.064(0.006)	0.191(0.006)	0.44(0.058)	0.413(0.022)	-	0.568(0.019)	0.67(0.09)	-	0.25	-0.62	-0.66(0.02)	-0.25(0.02)
5C7.70	0.088(0.009)	0.316(0.01)	1.44(0.144)	1.106(0.026)	-	1.981(0.036)	3.95(0.4)	-	8.01	-0.34	-0.95(0.07)	-0.19(0.1)
5C7.78	0.064(0.006)	0.317(0.011)	1.411(0.141)	1.164(0.07)	-	2.327(0.04)	4.83(0.49)	-	5.17	-0.34	-1.05(0.07)	-0.22(0.1)
5C7.85	0.088(0.009)	0.272(0.009)	0.7(0.027)	0.64(0.062)	-	1.334(0.049)	2.54(0.26)	-	2.08	-0.46	-0.78(0.04)	-0.07(0.06)
5C7.87	0.031(0.003)	0.104(0.003)	0.297(0.045)	0.286(0.024)	-	0.834(0.032)	1.83(0.19)	-	2.8	-0.86	-0.91(0.06)	0.06(0.08)
5C7.95	0.033(0.003)	0.086(0.003)	0.234(0.052)	0.391(0.065)	-	0.672(0.028)	1.78(0.22)	-	2.04	-0.95	-0.86(0.05)	0.13(0.08)
5C7.106	0.083(0.008)	0.24(0.008)	0.616(0.021)	0.488(0.093)	-	1.138(0.114)	2.32(0.24)	-	1.7	-0.51	-0.78(0.04)	-0.03(0.06)
5C7.111	0.127(0.013)	0.369(0.011)	0.913(0.033)	1.086(0.063)	-	1.664(0.118)	3.44(0.35)	-	2.24	-0.32	-0.77(0.04)	-0.05(0.06)
5C7.118	0.12(0.012)	0.255(0.008)	0.661(0.021)	0.657(0.027)	-	1.32(0.119)	2.82(0.29)	-	1.5	-0.49	-0.71(0.03)	0.09(0.05)
5C7.125	0.093(0.009)	0.185(0.006)	0.436(0.031)	0.476(0.028)	-	0.702(0.044)	1.2(0.14)	-	1.77	-0.63	-0.63(0.04)	-0.01(0.06)
5C7.145	0.06(0.006)	0.137(0.005)	0.349(0.015)	0.389(0.046)	-	0.705(0.03)	1.32(0.14)	-	0.41	-0.75	-0.72(0.02)	0.03(0.03)
5C7.170	0.038(0.004)	0.145(0.005)	0.386(0.028)	0.459(0.061)	-	0.906(0.046)	1.8(0.19)	-	1.57	-0.72	-0.91(0.04)	-0.08(0.06)
5C7.178	0.027(0.003)	0.117(0.004)	0.585(0.058)	0.478(0.068)	-	0.98(0.019)	2.3(0.24)	-	6.67	-0.77	-1.05(0.08)	-0.14(0.13)

Continued on next page

Table 5.5 – continued from previous page

name	$S_{4.85GHz}$ Jy	$S_{1.4GHz}$ Jy	S_{408MHz} Jy	S_{365MHz} Jy	S_{327MHz} Jy	S_{151MHz} Jy	S_{74MHz} Jy	S_{38MHz} Jy	rchi2	γ	α	β
5C7.194	0.111(0.011)	0.324(0.01)	0.752(0.043)	0.845(0.024)	-	1.546(0.073)	3.15(0.32)	-	1.93	-0.39	-0.74(0.04)	-0.01(0.05)
5C7.205	0.076(0.008)	0.263(0.008)	0.709(0.209)	0.819(0.031)	-	1.536(0.039)	2.7(0.28)	-	0.35	-0.45	-0.88(0.02)	-0.12(0.02)
5C7.245	0.071(0.007)	0.223(0.007)	0.685(0.047)	0.731(0.023)	-	1.381(0.113)	2.95(0.3)	-	0.8	-0.52	-0.89(0.02)	-0.04(0.04)
7C0825+2930	0.152(0.015)	0.308(0.009)	-	-	-	0.722(0.034)	0.92(0.12)	-	0.25	-0.44	-0.46(0.02)	-0.11(0.03)
7C0825+2443	0.096(0.01)	0.217(0.005)	-	-	-	1.302(0.034)	1.88(0.24)	-	4.24	-0.55	-0.76(0.07)	0.05(0.11)
5C7.271	0.075(0.008)	0.219(0.007)	0.475(0.048)	0.518(0.027)	-	0.835(0.049)	1.26(0.14)	-	0.43	-0.56	-0.7(0.02)	-0.13(0.03)
5C7.7	0.108(0.011)	0.258(0.008)	0.574(0.057)	0.591(0.023)	-	0.804(0.041)	1.29(0.14)	-	1.52	-0.49	-0.62(0.04)	-0.12(0.05)
5C6.17	-	0.135(0.004)	0.46(0.046)	0.535(0.037)	-	0.973(0.022)	1.48(0.18)	-	0.23	-0.71	-1.08(0.03)	-0.29(0.04)
5C6.25	-	0.098(0.003)	0.543(0.054)	0.403(0.041)	-	0.79(0.026)	1.77(0.21)	-	12.08	-0.83	-1.13(0.25)	-0.26(0.33)
5C6.43	-	0.132(0.004)	0.469(0.104)	0.396(0.039)	-	0.792(0.02)	1.99(0.38)	-	2.16	-0.77	-0.75(0.14)	0.09(0.2)
5C6.75	-	0.092(0.003)	0.263(0.034)	0.322(0.067)	-	0.611(0.015)	0.72(0.12)	-	1.23	-0.88	-1.05(0.11)	-0.3(0.15)
5C6.214	-	0.109(0.004)	0.497(0.136)	0.645(0.044)	-	0.877(0.024)	1.8(0.2)	-	14.91	-0.76	-1.25(0.27)	-0.44(0.35)
5C6.239	-	0.098(0.002)	0.211(0.032)	-	-	0.707(0.023)	1.0(0.15)	-	7.54	-0.87	-0.92(0.28)	-0.06(0.4)
5C6.242	-	0.085(0.003)	0.262(0.017)	0.457(0.052)	-	0.548(0.026)	0.84(0.14)	-	6.74	-0.91	-1.06(0.18)	-0.32(0.25)
5C6.267	-	0.103(0.003)	0.286(0.078)	0.413(0.059)	-	0.504(0.018)	1.01(0.14)	-	5.02	-0.87	-0.77(0.21)	-0.07(0.3)
5C6.286	-	0.084(0.003)	0.372(0.049)	-	-	0.643(0.072)	1.21(0.15)	-	2.71	-0.9	-1.16(0.2)	-0.28(0.23)
5C7.47	-	0.063(0.002)	0.232(0.061)	0.28(0.025)	-	0.529(0.024)	0.75(0.1)	-	0.05	-1.02	-1.21(0.02)	-0.37(0.03)
5C7.57	-	0.079(0.002)	0.315(0.022)	0.258(0.023)	-	0.648(0.027)	1.21(0.14)	-	3.85	-0.95	-1.05(0.12)	-0.14(0.16)
5C7.82	-	0.104(0.003)	0.401(0.04)	-	-	0.822(0.036)	1.28(0.15)	-	0.33	-0.81	-1.13(0.05)	-0.3(0.06)
5C7.208	-	0.126(0.004)	0.37(0.053)	0.495(0.063)	-	0.873(0.033)	1.8(0.19)	-	1.5	-0.77	-0.88(0.1)	0.0(0.13)
5C7.223	-	0.058(0.002)	0.239(0.012)	0.306(0.031)	-	0.543(0.047)	1.06(0.12)	-	1.52	-1.05	-1.22(0.07)	-0.25(0.09)
5C7.242	-	0.089(0.003)	0.184(0.018)	0.273(0.023)	-	0.477(0.017)	0.22(0.1)†	-	6.88	-0.94	-0.79(0.23)	-0.06(0.33)
5C7.269	-	0.067(0.002)	0.25(0.025)	0.25(0.027)	-	0.535(0.034)	1.18(0.13)	-	1.36	-1.03	-0.99(0.09)	-0.04(0.11)
7C0825+2446	-	0.647(0.012)	-	-	-	4.299(0.112)	10.58(1.07)	-	-	-0.1	-0.63(0.0)	0.32(0.0)
5C7.79	-	0.042(0.001)	0.156(0.013)	-	-	0.535(0.056)	0.53(0.08)	-	9.86	-1.19	-1.24(0.28)	-0.3(0.36)
5C7.195	-	0.15(0.004)	0.438(0.028)	0.434(0.022)	-	0.889(0.09)	1.63(0.17)	-	0.78	-0.7	-0.82(0.05)	-0.01(0.06)
1731+6641	0.04(0.004)	0.108(0.003)	-	-	0.317(0.004)	0.52(0.015)	0.2(0.1)†	-	3.66	-0.85	-0.75(0.06)	-0.15(0.09)
1732+6535	0.239(0.024)	0.727(0.025)	-	-	3.004(0.004)	6.17(0.083)	8.82(0.89)	19.6(0.409)	2.55	0.0	-0.92(0.03)	-0.01(0.02)
1733+6719	0.068(0.007)	0.233(0.007)	-	-	0.944(0.004)	1.55(0.025)	2.04(0.21)	6.1(0.353)	21.69	-0.52	-0.81(0.1)	0.03(0.11)
1736+6710	-	0.191(0.008)	-	-	0.484(0.004)	0.82(0.02)	1.09(0.12)	2.0(0.22)	1.31	-0.63	-0.6(0.05)	0.02(0.05)
1740+6640	0.069(0.007)	0.168(0.005)	-	-	0.379(0.004)	0.54(0.017)	0.2(0.1)†	-	2.52	-0.68	-0.6(0.05)	-0.19(0.08)
1741+6704	-	0.084(0.002)	-	-	0.364(0.004)	0.72(0.015)	0.93(0.11)	1.9(0.238)	2.18	-0.92	-1.04(0.06)	-0.17(0.07)
1742+6346	-	0.064(0.002)	-	-	0.29(0.004)	0.62(0.028)	0.82(0.14)	2.5(0.25)	4.26	-1.05	-1.0(0.09)	-0.02(0.09)
1743+6344	0.062(0.006)	0.215(0.007)	-	-	0.865(0.004)	1.59(0.026)	2.13(0.32)	5.5(0.55)	5.82	-0.53	-0.9(0.06)	-0.05(0.08)
1743+6431	0.052(0.005)	0.235(0.007)	-	-	0.948(0.004)	1.89(0.027)	2.43(0.26)	8.2(0.385)	18.49	-0.53	-0.89(0.09)	0.05(0.09)
1743+6639	0.174(0.017)	0.435(0.016)	-	-	1.238(0.004)	1.97(0.027)	2.42(0.25)	4.9(0.257)	5.98	-0.27	-0.64(0.06)	0.01(0.05)
1745+6415	0.053(0.005)	0.128(0.004)	-	-	0.408(0.004)	0.59(0.018)	0.98(0.16)	2.1(0.368)	9.24	-0.78	-0.7(0.09)	-0.05(0.12)
1745+6422	0.174(0.017)	0.287(0.01)	-	-	0.827(0.004)	1.41(0.022)	2.1(0.23)	5.2(0.323)	6.51	-0.45	-0.55(0.06)	0.17(0.06)
1745+6624	-	0.089(0.003)	-	-	0.284(0.004)	0.51(0.016)	0.2(0.1)†	-	5.58	-0.92	-0.88(0.16)	-0.22(0.23)
1747+6533	0.13(0.013)	0.417(0.012)	-	-	1.575(0.004)	2.72(0.041)	3.52(0.36)	7.3(0.29)	6.39	-0.26	-0.83(0.05)	-0.04(0.05)
1748+6657	0.199(0.02)	0.584(0.018)	-	-	1.479(0.004)	1.15(0.027)	0.2(0.1)†	-	24.79	-0.09	-0.67(0.15)	-0.64(0.24)
1748+6703	-	0.249(0.009)	-	-	1.167(0.004)	2.17(0.036)	3.18(0.32)	7.5(0.318)	12.87	-0.46	-0.93(0.11)	-0.01(0.09)
1748+6731	0.034(0.003)	0.111(0.002)	-	-	0.376(0.003)	0.64(0.027)	0.481(0.1)†	1.7(0.258)	5.16	-0.83	-0.85(0.06)	-0.13(0.09)
1751+6455	0.058(0.006)	0.149(0.005)	-	-	0.421(0.003)	0.65(0.019)	0.259(0.1)†	1.8(0.254)	7.66	-0.73	-0.68(0.08)	-0.07(0.1)
1751+6809	-	0.32(0.004)	-	-	0.867(0.003)	1.03(0.026)	0.89(0.11)	4.1(0.42)	54.21	-0.43	-0.47(0.23)	0.06(0.3)
1753+6311	0.036(0.004)	0.12(0.004)	-	-	0.539(0.003)	1.06(0.019)	1.55(0.19)	4.4(0.301)	7.56	-0.78	-0.93(0.07)	0.02(0.07)
1753+6543	0.192(0.019)	0.401(0.013)	-	-	1.072(0.004)	1.62(0.027)	2.18(0.32)	4.6(0.299)	8.29	-0.32	-0.55(0.07)	0.07(0.07)
1754+6420	-	0.075(0.003)	-	-	0.294(0.003)	0.5(0.017)	0.263(0.1)†	2.0(0.267)	14.84	-0.99	-0.85(0.17)	-0.03(0.2)
1755+6314	-	0.188(0.006)	-	-	0.702(0.003)	1.19(0.021)	0.78(0.13)	4.8(0.338)	34.67	-0.61	-0.73(0.19)	0.09(0.19)
1755+6830	0.08(0.008)	0.276(0.002)	-	-	0.914(0.003)	1.52(0.03)	2.04(0.15)	3.8(0.302)	4.95	-0.44	-0.8(0.05)	-0.1(0.06)
1756+6520	0.043(0.004)	0.146(0.004)	-	-	0.46(0.003)	0.67(0.019)	0.8(0.14)	2.6(0.426)	12.51	-0.73	-0.76(0.1)	-0.14(0.14)

Continued on next page

Table 5.5 – continued from previous page

name	$S_{4.85GHz}$ Jy	$S_{1.4GHz}$ Jy	S_{408MHz} Jy	S_{365MHz} Jy	S_{327MHz} Jy	S_{151MHz} Jy	S_{74MHz} Jy	S_{38MHz} Jy	rchi2	γ	α	β
1758+6307	0.101(0.01)	0.304(0.009)	-	-	1.155(0.003)	1.86(0.03)	2.46(0.26)	4.9(0.292)	8.44	-0.39	-0.82(0.07)	-0.06(0.07)
1758+6535	0.069(0.007)	0.232(0.002)	-	-	0.739(0.003)	1.13(0.026)	1.98(0.43)	3.3(0.33)	10.28	-0.53	-0.74(0.08)	-0.08(0.1)
1758+6553	0.054(0.005)	0.222(0.004)	-	-	0.715(0.003)	1.3(0.045)	0.485(0.1)†	3.7(0.231)	22.73	-0.54	-0.82(0.12)	-0.07(0.12)
1758+6719	0.029(0.003)	0.102(0.003)	-	-	0.4(0.003)	0.76(0.016)	1.03(0.12)	2.0(0.274)	1.26	-0.85	-0.94(0.03)	-0.12(0.04)
1801+6902	0.132(0.013)	0.224(0.008)	-	-	0.673(0.004)	1.37(0.03)	2.02(0.21)	4.1(0.315)	2.19	-0.53	-0.68(0.04)	0.1(0.04)
1802+6456	0.025(0.002)	0.14(0.005)	-	-	0.857(0.003)	1.97(0.032)	3.25(0.41)	9.9(0.402)	9.99	-0.7	-1.17(0.07)	-0(0.06)
1804+6313	-	0.067(0.002)	-	-	0.195(0.003)	0.62(0.018)	0.92(0.13)	3.1(0.517)	11.01	-1.08	-0.74(0.16)	0.3(0.19)
1804+6625	0.026(0.003)	0.076(0.002)	-	-	0.301(0.003)	0.55(0.016)	0.99(0.13)	1.4(0.269)	2.43	-0.97	-0.89(0.04)	-0.07(0.06)
1805+6332	-	0.12(0.004)	-	-	0.561(0.004)	1.04(0.022)	1.52(0.18)	5.4(0.529)	20.49	-0.78	-0.89(0.17)	0.05(0.19)
1807+6719	0.036(0.004)	0.129(0.004)	-	-	0.44(0.003)	0.71(0.016)	0.84(0.11)	-	1.09	-0.75	-0.89(0.03)	-0.25(0.05)
1807+6831	0.124(0.012)	0.368(0.013)	-	-	1.216(0.003)	2.12(0.034)	3.37(0.34)	7.0(0.35)	7.81	-0.34	-0.73(0.06)	0.05(0.06)
1807+6841	0.034(0.003)	0.103(0.004)	-	-	0.34(0.003)	0.6(0.019)	0.93(0.11)	2.3(0.354)	4.23	-0.87	-0.79(0.06)	-0.03(0.08)
1811+6321	0.034(0.003)	0.126(0.002)	-	-	0.452(0.004)	0.95(0.028)	1.64(0.3)	3.0(0.395)	1.16	-0.77	-0.91(0.03)	-0.05(0.04)
1812+6814	0.037(0.004)	0.111(0.004)	-	-	0.372(0.003)	0.59(0.017)	1.04(0.13)	-	5.17	-0.82	-0.81(0.07)	-0.15(0.1)
1813+6439	-	0.05(0.002)	-	-	0.237(0.003)	0.5(0.013)	0.38(0.1)†	1.9(0.317)	6.91	-1.14	-1.06(0.13)	-0.11(0.16)
1813+6846	0.068(0.007)	0.195(0.006)	-	-	0.754(0.003)	1.51(0.026)	2.5(0.29)	4.6(0.333)	1.11	-0.57	-0.88(0.03)	-0.01(0.03)
1814+6529	0.038(0.004)	0.151(0.003)	-	-	0.629(0.003)	1.22(0.034)	2.18(0.39)	4.7(0.331)	6.01	-0.69	-0.93(0.06)	-0.01(0.07)
1814+6702	0.056(0.006)	0.236(0.008)	-	-	1.107(0.003)	2.26(0.03)	3.6(0.37)	8.0(0.402)	4.85	-0.49	-1.01(0.05)	-0.04(0.05)
1815+6805	0.173(0.017)	0.388(0.014)	-	-	1.188(0.003)	1.96(0.028)	2.79(0.32)	5.9(0.388)	6.07	-0.31	-0.65(0.06)	0.05(0.06)
1815+6815	0.028(0.003)	0.195(0.0)	-	-	0.725(0.003)	1.37(0.051)	1.78(0.13)	3.8(0.325)	14.85	-0.56	-1.0(0.09)	-0.21(0.11)
1816+6605	0.051(0.005)	0.182(0.006)	-	-	0.723(0.003)	1.29(0.021)	1.59(0.18)	3.8(0.38)	5.47	-0.6	-0.91(0.06)	-0.11(0.07)
1816+6710	0.112(0.011)	0.395(0.012)	-	-	1.429(0.003)	2.36(0.032)	3.18(0.33)	3.6(0.343)	1.34	-0.26	-0.91(0.03)	-0.23(0.04)
1819+6550	0.07(0.007)	0.234(0.007)	-	-	0.751(0.003)	1.17(0.021)	1.52(0.18)	2.8(0.373)	4.46	-0.51	-0.79(0.06)	-0.15(0.07)
1820+6657	0.059(0.006)	0.317(0.01)	-	-	0.862(0.003)	0.83(0.02)	0.2(0.1)†	-	4.35	-0.34	-0.87(0.06)	-0.73(0.1)
1822+6601	0.077(0.008)	0.224(0.008)	-	-	0.607(0.003)	0.97(0.019)	0.98(0.15)	2.5(0.342)	4.62	-0.55	-0.69(0.06)	-0.1(0.08)
1825+6602	0.047(0.005)	0.268(0.005)	-	-	0.982(0.003)	1.63(0.036)	1.84(0.14)	3.3(0.375)	5.57	-0.43	-0.98(0.06)	-0.3(0.07)
1826+6510	0.061(0.006)	0.223(0.007)	-	-	0.852(0.004)	1.39(0.025)	2.15(0.24)	3.0(0.357)	3.79	-0.51	-0.9(0.05)	-0.18(0.07)
1826+6704	0.079(0.008)	0.124(0.004)	-	-	0.355(0.003)	0.6(0.021)	1.06(0.13)	-	5.23	-0.8	-0.59(0.07)	0.1(0.1)
1827+6709	0.034(0.003)	0.159(0.006)	-	-	0.608(0.003)	1.1(0.022)	1.76(0.19)	2.7(0.314)	2.97	-0.67	-0.97(0.05)	-0.18(0.06)

Table 5.6: Fitted Radio Spectra for the TOOTS-00 sample [Vardoulaki *et al.*, 2010]. Col1: Source name, Col2: 74 MHz flux, Col3: 151 MHz flux, Col4: 327 MHz flux, Col5: 1.4 GHz flux, Col6: Reduced χ^2 value for the 2nd order polynomial fit, Col7: Fitted parameter γ, Col8: Fitted parameter α, Col9: Fitted parameter β.

TOOT	S_{74MHz} Jy	S_{151MHz} Jy	S_{327MHz} Jy	$S_{1.4GHz}$ Jy	rchi2	γ	α	β
TOOT00_1140	0.58	0.53	0.347	0.1211	2.101	-0.803	-0.836(0.129)	-0.264(0.105)
TOOT00_1099	0.22	0.17	0.035	0.0179	8.728	-1.754	-0.156(0.471)	1.099(0.699)
TOOT00_1125	1.09	0.76	0.395	0.0935	1.751	-0.88	-1.085(0.118)	-0.207(0.095)
TOOT00_1143	0.21	0.22	0.035	0.0094	13.097	-1.95	-0.699(0.569)	0.831(0.856)
TOOT00_1233	0.2	0.09	0.101	0.0512	2.509	-1.201	-0.552(0.187)	-0.273(0.336)
TOOT00_1022	0.33	0.15	0.065	0.0156	0.0060	-1.67	-0.953(0.0080)	0.087(0.0070)
TOOT00_1204	0.23	0.12	0.088	0.0313	0.61	-1.385	-0.774(0.091)	-0.202(0.149)
TOOT00_1235	0.24	0.34	0.254	0.0993	0.898	-0.889	-0.752(0.091)	-0.298(0.093)
TOOT00_1224	0.2	0.24	0.107	0.0326	3.506	-1.379	-0.788(0.201)	0.122(0.265)
TOOT00_1291	0.22	0.2	0.104	0.0316	0.843	-1.379	-0.838(0.099)	-0.04(0.138)
TOOT00_1107	0.16	0.17	0.057	0.0057	2.93	-1.99	-1.717(0.217)	-0.333(0.305)
TOOT00_1180	0.16	0.11	0.069	0.0158	0.053	-1.625	-1.147(0.028)	-0.398(0.041)
TOOT00_1027	0.22	0.11	0.581	0.6643	24.954	-0.08	-0.381(0.533)	-1.448(0.887)
TOOT00_1195	0.26	0.1	0.044	0.0151	0.0030	-1.738	-0.615(0.0080)	0.351(0.013)
TOOT00_1069	0.17	0.09	-	0.0036	-	-2.18	-1.738(0.0)	-0.434(0.0)
TOOT00_1094	3.37	2.21	1.154	0.248	0.427	-0.44	-1.153(0.058)	-0.243(0.045)
TOOT00_1149	0.26	0.27	0.142	0.0295	4.947	-1.346	-1.281(0.205)	-0.505(0.176)
TOOT00_1298	0.4	0.14	0.091	0.0304	3.789	-1.416	-0.672(0.186)	0.185(0.164)
TOOT00_1200	2.6	1.59	0.897	0.2724	0.0	-0.439	-0.847(0.0010)	-0.081(0.0)
TOOT00_1215	0.64	0.35	0.193	0.0428	0.752	-1.199	-1.089(0.078)	-0.191(0.066)
TOOT00_1240	0.21	0.13	-	0.0074	-	-1.885	-1.612(0.0)	-0.481(0.0)
TOOT00_1289	0.41	0.17	0.098	0.0218	4.206	-1.499	-1.026(0.194)	-0.065(0.171)
TOOT00_1072	0.89	0.55	0.361	0.1111	1.929	-0.813	-0.853(0.124)	-0.188(0.102)
TOOT00_1134	2.75	1.43	0.811	0.2374	2.168	-0.484	-0.838(0.13)	-0.059(0.103)
TOOT00_1244	0.4	0.1	0.048	0.0324	0.795	-1.515	0.061(0.102)	0.92(0.095)
TOOT00_1066	0.18	0.19	0.057	0.0144	1.845	-1.705	-0.95(0.191)	0.018(0.346)
TOOT00_1261	0.14	0.2	0.039	0.0142	14.48	-1.799	-0.502(0.576)	0.778(0.871)
TOOT00_1252	0.19	0.13	0.077	0.018	0.0070	-1.576	-1.109(0.01)	-0.324(0.014)
TOOT00_1214	0.19	0.14	0.032	0.0113	4.507	-1.886	-0.54(0.361)	0.669(0.553)
TOOT00_1152	0.19	0.24	0.138	0.0383	1.428	-1.273	-0.972(0.125)	-0.246(0.168)
TOOT00_1129	1.45	1.16	0.626	0.1566	5.156	-0.67	-1.077(0.201)	-0.238(0.159)
TOOT00_1090	0.24	0.2	0.097	0.0279	0.613	-1.427	-0.877(0.092)	-0.045(0.152)
TOOT00_1267	1.45	0.52	0.337	0.0995	26.905	-0.841	-0.756(0.462)	-0.0050(0.377)
TOOT00_1188	0.15	0.11	0.039	0.0147	1.638	-1.761	-0.564(0.195)	0.377(0.31)
TOOT00_1196	-	0.11	-	9.0E-4	-	-2.73	-2.158(0.0)	0.0(0.0)
TOOT00_1173	0.28	0.15	0.099	0.0288	1.137	-1.406	-0.878(0.102)	-0.12(0.09)
TOOT00_1228	0.16	0.25	0.191	0.0791	1.055	-0.992	-0.723(0.105)	-0.33(0.141)
TOOT00_1034	1.45	0.61	0.385	0.1405	11.985	-0.73	-0.61(0.308)	0.074(0.25)
TOOT00_1255	0.29	0.13	0.092	0.0338	3.273	-1.37	-0.646(0.174)	0.062(0.154)
TOOT00_1048	1.18	0.86	0.466	0.1041	1.185	-0.821	-1.149(0.097)	-0.288(0.077)
TOOT00_1029	0.21	0.11	0.039	0.0241	1.161	-1.625	-0.082(0.168)	0.792(0.262)
TOOT00_1115	0.25	0.32	0.22	0.0561	3.394	-1.078	-1.18(0.166)	-0.641(0.14)
TOOT00_1132	0.62	0.42	0.258	0.0883	0.0030	-0.939	-0.777(0.0050)	-0.114(0.0040)
TOOT00_1250	0.51	0.41	0.202	0.054	6.176	-1.137	-1.005(0.224)	-0.181(0.188)
TOOT00_1268	0.3	0.11	0.072	0.0612	0.407	-1.234	0.076(0.077)	0.539(0.12)
TOOT00_1251	0.3	0.21	0.074	0.0196	9.373	-1.583	-0.966(0.303)	0.014(0.275)
TOOT00_1203	1.07	1.06	0.666	0.1646	4.007	-0.629	-1.15(0.177)	-0.447(0.14)

Chapter 6

The Cosmic Evolution of Low-Excitation Radio Sources and the Nature of Infra-red Faint Radio Sources

6.1 Introduction

With the notable exception of 3CRR, there are very few complete radio samples in existence with 100% spectroscopic completeness. As demonstrated aptly by the spectroscopic follow-up of CENSORS, whilst the vast majority of radio sources may be matched with an optical or near-infrared host, a surprising proportion ($\sim$20%) cannot be successfully spectroscopically identified. This may be because these sources show no emission lines or identifiable absorption features in their observed spectra, or that they have faint or undetectable continuum in the optical or near-infrared (these are often noted in the literature as infra-red faint radio sources, or IFRS). Understanding the nature of such sources is crucial to obtain accurate and complete redshift estimates for studying the radio luminosity function, and to distinguish very high redshift candidates. It is difficult to measure precisely how common such sources are - whether an object has simply not been targeted, was undetected, or in fact has continuum with no identifiable features is often not made clear in the literature, as the spectra of such sources are usually not published. However, some attempts have been made to study such 'no-z' sources [see for example Reuland *et al.*, 2003], and De Breuck *et al.* [2001] find that 24% of a sample of USS radio sources (with additional faint optical and K-band selection criteria) do not show any strong emission lines.

There are several possible explanations for the nature of such sources:

- Radio sources without optical continuum may be pulsars. This is more likely for sources observed close to the galactic plane.

- They could lie in the 'redshift desert', whereby [OII] has been shifted out of the optical passband, but Lyα has not yet entered it.
- They could be very highly obscured by dust, as might be expected for young, recently triggered AGN.
- They may lie at very high redshift, such that Lyα is redshifted outwith the optical window.
- They may be Low Excitation Radio Sources, or LERGs, perhaps at moderate redshifts, where identifiable absorption features such as the 4000$\AA$ break are shifted out of the optical range. These are a type of AGN associated with old passive galaxies, often in the centre of groups or clusters, and show weak or no emission lines (see Chapter 1).

The first possibility, that of pulsars, is very unlikely for the majority of spectroscopically unidentified sources in radio galaxy samples. The majority of radio samples are located away from galactic plane and recent work by Cameron *et al.* [2011], and Middelberg *et al.* [2011] present some detailed observations of samples of IFRS, and conclude that the majority of IFRS are inconsistent with being pulsars.

The comprehensive optical and near-infrared spectral data collected for CENSORS outlined in Chapter 3 give a unique opportunity to investigate the prevalence of the second possibility, that sources may lie within the 'redshift desert'. This is a narrow range in redshift, $1 \lesssim z \lesssim 2$ where [OII] is shifted out of the typically accessible optical range, but Lyα has not yet entered it. As only two sources out of the remaining 28 unidentified CENSORS sources targeted with SINFONI have emission lines within the 'redshift desert' range that is covered by SINFONI, this explanation cannot account for all, or even the majority of, 'missing redshifts'.

This then leaves three plausible explanations, that of extreme redshift, youth and dust obscuration, or a LERG at more moderate redshift ($z \gtrsim 1$). Using CENSORS again as an example, there are 9 extended radio sources with continuum, but no measurable emission lines or absorption features in either the optical or infrared that could naively assumed to be LERGs. Determining the number of LERGs that might be expected in a sample of this size at $z \gtrsim 1$ is difficult, as there has been little work done on measuring the luminosity function of LERGs out to high redshift. The most recent work in this area was presented by Best and Heckman [2012], who measure the luminosity function for LERGs at low redshift ($z<0.3$), and find evidence for strong evolution in the HERG population, but little evidence for evolution of LERGs. Theoretical predictions for the evolution of LERGs support this finding - suggesting that the LERGs as a population don't evolve substantially over cosmic time [cf Merloni and Heinz, 2008], but this is as yet unproven beyond $z=0.3$.

A good example of the youth nature can be found in Reuland *et al.* [2003], who have carried out millimetre and submillimetre observations of one such missing redshift source, and concluded that it is consistent with being a very young radio source, heavily obscured by dust, at $z \sim 3 \pm 1$. In contrast, another strong radio source with no optical detection, and only a very faint mid-infrared detection has recently been identified with a $z=4.88$ host, the second highest redshift radio galaxy known [Jarvis *et al.*, 2009]. It is also possible that these 'missing-z' sources may be both young and dust obscured, and located at high redshift - as pointed out in Chapter

4, the highest redshift radio galaxy known is a GPS radio source; GPS sources are, as discussed in Chapter 5, generally thought to be young and recently triggered.

In this Chapter, two complementary investigations are presented with the aim of providing useful constraints on the nature of these 'missing redshift' objects. Firstly, the LERG luminosity function is derived out to much higher redshift than is currently known, in order to place constraints on the number of such sources that might be expected at high redshift. Secondly, a multiwavelength spectroscopic study of a sample of IFRS is carried out, aiming to detect Lyα if present and confirm whether they do indeed lie at high redshift.

6.2 Measuring the Cosmic Evolution of Low Excitation Radio Sources

Low-excitation objects are a population of low luminosity radio sources, variably referred to as low-excitation (LERG), hot-mode or radio-mode sources, in which the accretion process is radiatively inefficient and most of the AGN energy emerges in the form of radio jets [e.g. Hardcastle *et al.*, 2007, , Chapter 1]. These are generally believed to be fueled directly from the hot gas halos surrounding massive galaxies or clusters, at low accretion rates, and energetic feedback from these sources is widely used in galaxy formation models as a means to switch off star formation in the most massive galaxies. It has recently been shown that, in the local Universe, the time-averaged energetic output of these sources is indeed sufficient to counter-balance gas cooling in early type galaxies of all masses [Best *et al.*, 2006]. Distinct from the LERG population are the high excitation (or quasar-mode) HERG radio sources that dominate at higher radio powers; these are believed to be fueled by cold gas, perhaps brought in through mergers and interactions. HERGs, together with their radio-quiet counterparts (quasars), are thought to be important in curtailing star formation at high redshifts, and setting up the tight relationship between black hole and bulge masses observed in the nearby Universe [e.g. Silk and Rees, 1998].

Theoretical models have been constructed in an attempt to fully understand AGN evolution and the growth of supermassive black holes [e.g. Croton *et al.*, 2006; Merloni and Heinz, 2008]. The latter are based on the premise that the differences observed between radiatively efficient (HERG/quasar) and inefficient (LERG) sources arises as a result of the Eddington-scaled accretion rate onto the black hole. This hypothesis has recently been borne out by recent investigations of a local radio source sample [Best and Heckman, 2012]. A prediction of these theoretical models that lends itself well to observational testing is the cosmic evolution of the LERG population: both Merloni and Heinz [2008] and Croton *et al.* [2006] predict this to be essentially flat out to redshift one.

It has been well-known for some time that there is differential cosmic evolution of the radio luminosity function (RLF) as a function of radio power, with high power radio sources showing strong evolution, and low power sources only weak evolution [cf Rigby *et al.*, 2011; Willott *et al.*, 2001; Dunlop and Peacock, 1990, and references therein]. A common assumption leading on from this has been to categorise all low radio power sources as LERGs and high power sources

as HERGs. However, the first separate RLF determination has recently been determined locally for the two populations, and has shown that although LERGs do dominate at low powers and HERGs begin to dominate at the highest powers, both populations exist over all studied radio powers [Best and Heckman, 2012] with strong evidence to suggest that HERGs evolve strongly and LERGs don't. This behaviour is in line with the theoretical predictions and, coupled with the increasing fraction of HERGs found at higher powers, may account for the differential evolution observed in the RLF as a whole. However, in order to properly test the theoretical predictions and to fully understand and model the evolving AGN feedback mechanisms, a much more precise measure of the RLF of the LERG population to much higher redshift is required than is currently known.

6.3 The Sample Compilation and Classification

To address this goal, six existing radio samples, including CENSORS and a new recently published very faint radio sample by Simpson *et al.* [2012], all with high redshift completeness, were combined to select a complete sample of around 200 radio sources with $0.5<z<1.0$, over a wide range in luminosity. Spectroscopic observations can easily tell the HERG/LERG radio galaxy populations apart, due to the presence or otherwise of strong emission lines [cf Laing *et al.*, 1994].

6.3.1 The Samples

The first five samples were compiled from those already studied in this thesis, namely Wall & Peacock (1985), Parkes Selected Regions, ConFIG 1 & CoNFIG2r, CENSORS and Hercules. All samples have the same selection criteria as outlined in Chapter 4, with the exception of the Parkes Selected Regions sample, for which in this case the reselected sample of Rigby *et al.* [2011] containing all sources brighter than 0.3 Jy at 1.4 GHz is used (this is a different, fainter selection to that used in Chapter 4 to maximise the number of sources in the smaller redshift range studied here).

The 200μJy SXDF Sample

The sixth sample, the 200 μJy SXDF sample is a subset of the 100μJy Subaru/XMM-Newton Deep Field Radio Source Sample first presented in Simpson *et al.* [2006], which selects all radio sources above 200 μJy over a 0.81 square degree area of sky in the SXDF (the brighter flux limit was chosen to ensure that the number of unclassifiable sources did not dominate the sample). There are 59 sources in total in this sample within the redshift range of $0.5\leq z\leq 1.0$. Simpson *et al.* [2012] present classifications for these based on observed emission line properties as follows:

- BLAGN - sources with broad permitted emission lines (2 sources).
- Abs - sources displaying no emission lines, but identifiable absorption features (18 sources).

- NLAGN - sources diagnosed according to the [NII]/Hα vs [OIII]/Hβ diagram following Simpson et al. (2005) and Baldwin et al. (1981), or alternatively, having strong, high-ionisation emission lines such as CIV or [NeIII] present (11 sources).
- Strong - sources where the rest-frame equivalent width of the [OII] line is greater than 15$\mathring{A}$ (6 sources).
- Weak - sources where the rest-frame equivalent width of the [OII] line is less than 15$\mathring{A}$ (3 sources).
- SB - sources with [OII] and strong MgII absorption were assumed to indicate a star-forming galaxy (7 sources).

For the purposes of this study, sources classified in Simpson *et al.* [2012] as starbursts (SB) were excluded from the analysis, as were the two sources classified as BLAGN as they are likely to be beamed quasars (no spectral index cut could be applied to this sample, so it is important to remove any sources which show indications of being heavily beamed). Of the 50 remaining sources, 38 had spectroscopic redshifts and accompanying classifications. 10 had only photometric redshifts and no spectra or classification available, and the remaining two had spectra with featureless continuum. These two sources have been classified as LERGs, having no identifiable [OII] emission.

All sources between z=0.5 and z=1.0 and with α<-0.5 (excepting SXDF) were selected from these samples. A spectral index limit of α < -0.5 is applied where possible to exclude the majority of highly beamed sources (steep spectrum quasars are classed as HERGs). This was done in order to match as closely as possible the local RLF study by Best and Heckman [2012] who use the SDSS galaxies sample to cross match with the FIRST radio sample, thereby excluding highly beamed quasars. A spectral index cut of -0.5 is also required by the definition of some of the samples. A redshift range of 0.5≤z≤1.0 was selected to investigate. The upper limit was chosen as z∼1 as it is the highest practical to be able to still view [OII] within the optical spectrum if present (the majority of the samples have optical spectra within the wavelength range of 4000-8000$\mathring{A}$, and sky lines become much more problematic beyond ∼7000$\mathring{A}$). The lower limit was chosen to obtain a good balance between unmanageably large numbers of unclassified sources, and studying a large enough range to extend and compare with the results of Best and Heckman [2012] in the local Universe, over the redshift range 0.01 to 0.3. Details of the samples used in the compilation, and their classifications are presented in Tables 6.4 - 6.9, located at the end of this Chapter.

6.3.2 Sample Classification

Traditional approaches to the classification of high and low excitation radio galaxies have used combinations of emission line observables, typically [OII] and [OIII] line ratios and equivalent widths to separate the populations [as in e.g. Laing *et al.*, 1994; Jackson and Rawlings, 1997; Heckman *et al.*, 2004]. Typically adopted values for separating the populations are an equivalent width of 5$\mathring{A}$ for [OIII] and/or a flux ratio f[OII]/f[OIII]<1. In Figure 6.1, this is illustrated with

[OII]/[OIII] line ratios and equivalent widths for HERGs and LERGs within the SDSS-FIRST sample of Best and Heckman [2012]. It can be clearly seen that the combination of emission line flux ratio and equivalent widths allow a reasonably clean separation of HERGs, and LERGs, particularly in the case of [OIII] equivalent width. An equivalent width of 5$\mathring{A}$ in [OIII], and a log([OII]/[OIII]) ratio less than 0.0 as outlined above cleanly separates the vast majority of HERGs from LERGs [as used in, e.g. Jackson and Rawlings, 1997]). However, as also shown in Figure 6.1 (left panel) the work of Best and Heckman [2012] shows that an even cleaner separation can be achieved by using the equivalent width of [OIII] and the f[OII]/f[OIII] flux ratio in combination. This is given by a line logEW([OIII]) = 0.25 + 0.25log(f([OII])/f([OIII])) in the EW[OIII]-f[OII]/f[OIII] plane, calibrated using the Best and Heckman [2012] data.

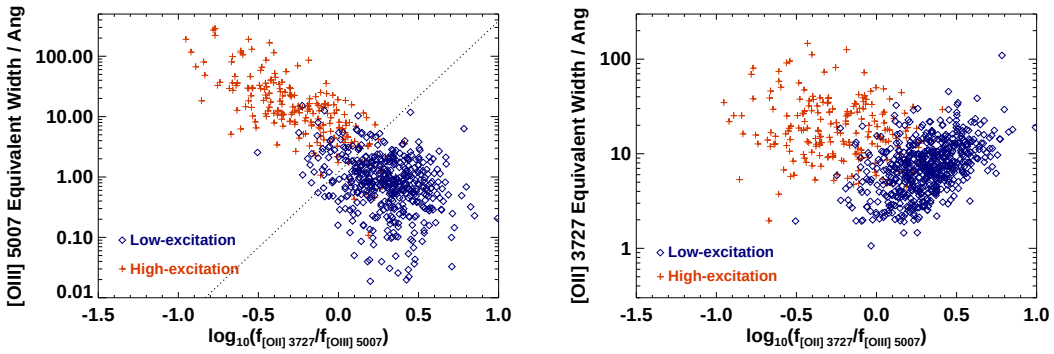

Figure 6.1: The [OII] and [OIII] equivalent widths vs f[OII]/f[OIII] for the SDSS-FIRST sample of Best and Heckman [2012], which demonstrate that the equivalent widths of both lines may be used to separate HERGs and LERGs. The [OIII] trend is clearly stronger, and hence the [OIII] EW criteria is used in preference to the [OII] line where possible in this study. The separating line on the [OIII] plot is given by logEW([OIII]) = 0.25 + 0.25log(f([OII])/f([OIII])).

However, many sources may only display one line (e.g. [OIII] quickly moves out of the optical window at z>0.8, or spectra may not be flux-calibrated, making flux ratios unreliable). If the detected line is [OIII], then it is clearly apparent that a cut based solely on [OIII] equivalent width is acceptable for classifying HERGs and LERGs (this is similar to the classification used in Grimes *et al.* [2004]). If there is no other information present in the spectrum other than the [OII] emission line, a cut based on [OII] equivalent width may also separate out HERGs from LERGs, but as there is significantly more overlap between the populations of HERGs and LERGs, there is a region of [OII] equivalent width where sources cannot be classified.

Hence, where flux data for both [OII] and [OIII], along with [OIII] equivalent width were available for a source, the source was classified according to the relation given above (Figure 6.1): sources lying on or above the line as HERGs, and sources below the line as LERGs. For sources without full [OII] and [OIII] data, the classification was as follows:

- HERG: EW[OIII]>5$\mathring{A}$ or EW[OII]>30.0
- LERG: EW[OIII]<5$\mathring{A}$ or EW[OII]<5.0
- U(unclassifiable): 5$\mathring{A}$<EW[OII]<30$\mathring{A}$

where the equivalent widths (EW) of the lines are measured in the rest frame (EW(rest) = EW(obs)/(1+z)). For sources without full line information, the equivalent width of the [OIII] was the preferred criteria, followed by the [OII] equivalent width.

An extensive literature search was carried out to locate spectra for sources within the samples used. For sources with available spectra in either electronic form, or with tabulated data, the above criteria were applied. For sources with only published paper spectra, a 'by eye' estimate of [OII] and/or [OIII] line equivalent widths was made as a best-estimate to enable a classification. In published tables of emission line properties where there was no information as to whether the spectrum was in the observed or rest frame, measured equivalent widths were assumed to be in the observed frame, and subsequently converted to rest-frame values for classification. Note, however, in the vast majority of cases, this does not matter - most of the 'paper' spectra are for bright, powerful 3C type sources, virtually all of which are clearly HERGs, and would be classified as such whether the EW was measured in the rest or observed frame. Spectra for the SXDF 200μJy sample were obtained from Chris Simpson to enable line measurements to made in a consistent fashion with the other samples. These were not flux calibrated so only equivalent width classifications were used. The full samples and associated classifications may be seen in Tables 6.4 - 6.9 at the end of this Chapter.

6.4 New Spectroscopic Data

Figure 6.2 displays the unclassifiable sources within the combined sample. From this, it is clear that there are several peak areas within the P-z plane where the number of unclassified sources introduces a large uncertainty. To this end the unclassified sources which had no spectroscopic data available within the sample were split into two groups according to Right Ascension (similar times of year for optimal observations) and proposals submitted for spectroscopic observations in the 2012 semesters. The first group was observed with the William Herschel Telescope (WHT) on La Palma over three nights on the 22nd - 24th May 2012, with unclassified sources with RAs from 08-17 from CoNFIG, Hercules and PSR observed. The second group is scheduled for observation in October 2012, also on the WHT.

Data reduction followed standard procedures in IRAF, as outlined for CENSORS in Chapter 3, with the standard star HZ21 observed each night for flux calibration. A single standard star was sufficient for the purposes of an approximate flux calibration, as the primary aim of these observations was to obtain line widths, redshifts and line flux ratios, not to measure precise fluxes, and indeed, some of the sources have very extended line emission (see Figure 6.9), and so the flux calibration will probably be less accurate for these regardless. The resultant spectra were analysed using a custom IDL script (cf Chapter 2), and the spectra and measured parameters can be seen in Figures 6.5-6.12, and Table 6.1. Of the 34 sources observed in total, redshifts were obtained for 28, with 4 less certain redshifts, and 2 undetected. 15 are classified as HERGs, 4 as LERGs, 8 originally included in the sample on the basis of their photometric redshifts had in fact redshifts outwith the z=0.5-1.0 band, and 7 were unclassified (e.g. having only narrow [OII] in the ambiguous range of 5$\mathring{A}$<EW<30$\mathring{A}$, or undetected). The

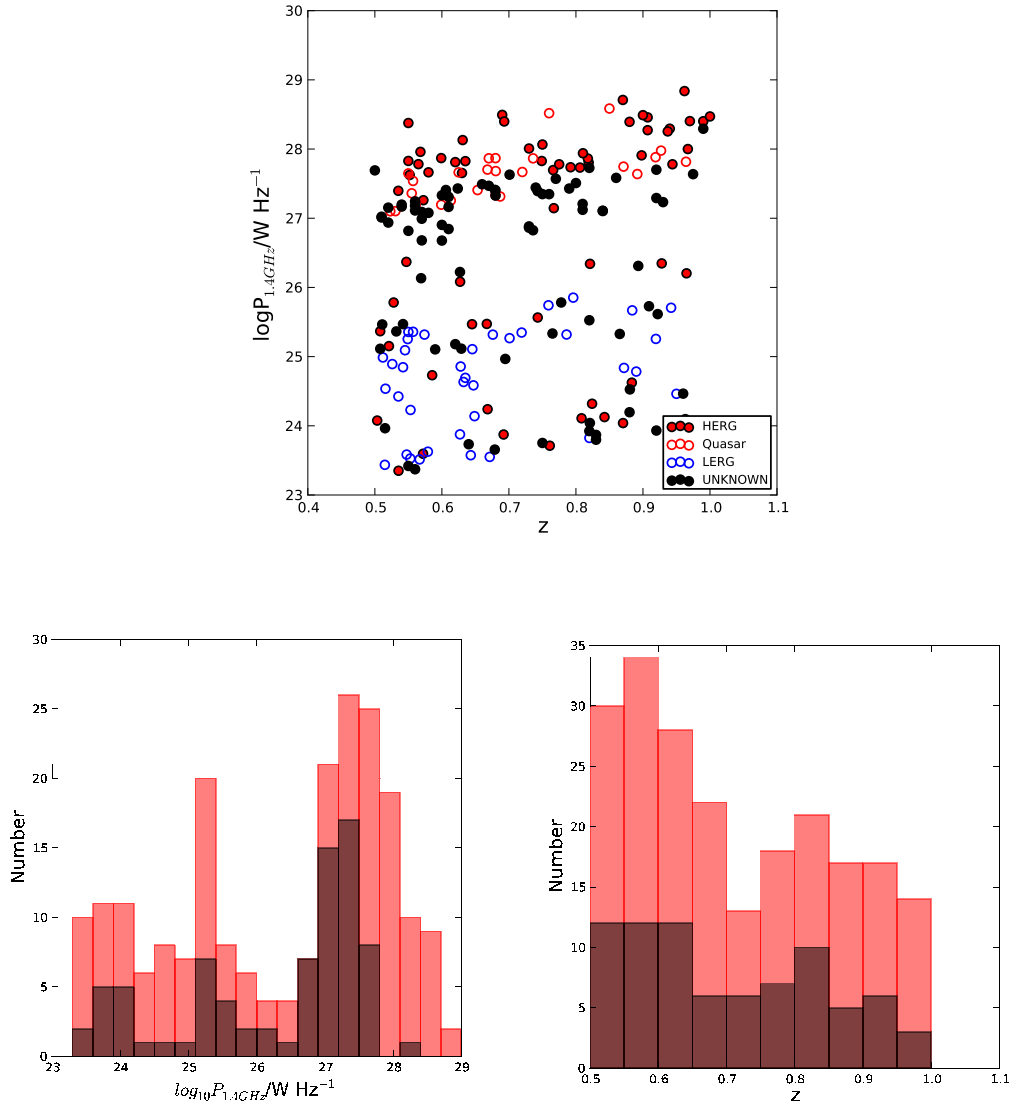

Figure 6.2: The top figure plots the radio power - redshift plane for the six combined samples, along with the source classifications able to be made with already published data. The bottom two figures show histograms of radio power and redshift for the entire sample (red), and for the unclassified sources (black). Whilst the unclassified sources are fairly evenly distributed in redshift, there is a clear deficit of classified sources in the range logP$\sim$27-28 W Hz^{-1}. The P-z plane also highlights areas which are sparse in sources, and for which it is important to gain as many classifications as possible in order to constrain the luminosity function in these regions (e.g, the area defined by logP$\sim$25.5-26.5 W Hz^{-1}). It also highlights the need to obtain as high a spectroscopic completeness as possible, in order to ensure these sparse areas are the result of the combination of samples, and not a bias introduced by the use of photometric redshifts (photometric redshifts comprise 68/220 sample sources in total).

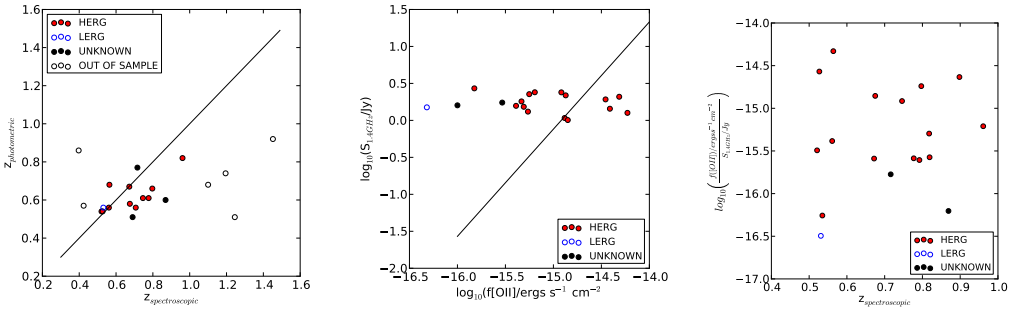

Figure 6.3: The figure on the top displays the spectroscopic vs photometric redshifts for the CoNFIG sources targeted in the new WHT spectroscopic campaign. It illustrates that whilst they are in generally good agreement, there is a small tendency for the photometric redshifts to underestimate the true redshifts. The final two figures illustrate the radio and [OII] flux of the new spectroscopic data, the middle figure showing the relation between radio flux and [OII] emission line flux as given by Rigby [2007] overplotted (as also shown in Chapter 3 for CENSORS). As the CoNFIG sources cover a narrow range in flux, a correlation is not seen, but HERGs generally lie close to the line, and LERGs and unclassified sources are offset, as would be expected.

two undetected sources were very faint, i=25, 26 Hercules sources. Given the faint i-band magnitudes of these sources, it is likely that if they are AGN, then they lie at z>1 (despite the quoted photometric redshifts). If the photometric redshifts are correct, then they are likely to be star-forming galaxies. Either way, both would hence be unlikely to be included in the sample, and are removed.

6.4.1 Notes on Individual Sources

4C59.10 The spectrum of this source reveals faint continuum and one strong emission line, along with a further possible faint extended emission line in a region of sky emission. If the faint line is real, it would be consistent with MgII and [OII], and the redshift is hence assumed to be z=1.245, greater than the photometric redshift of 0.51, and which places the source out of the sample.

4C54.25 This source has faint continuum, and a possible very faint line feature, which if identified as [OII], places the source at z=0.716. The photometric estimate of z=0.77 adds weight to this, although the line is too faint to be positively identified from this spectrum.

4C17.49 this source has featureless continuum, and a possible very faint line feature, which if identified as [OII], places the source at z=0.69. However, this is next to a sky line, and cannot be confirmed. The photometric estimate of z=0.51 adds weight to this.

PKS1337 The spectra for the host for this source identified in Dunlop and Peacock [1990] is very faint, with only a very faint possible emission line candidate (too faint to be confirmed). If this was [OII], it would place the source at z=0.69, consistent with the

photometric redshift of z=0.79. However, the flux of the [OII] line is very faint for a 1 Jy (1.4 GHz) radio source of HERG classification (cf. the radio luminosity-emission line relation discussed in Chapter 3), and it is unlikely to be a LERG at this redshift, as its radio power would lie in a range where there are very few LERGs seen. As shown in Figure 6.11, there is another bright galaxy with strong emission lines about 20 arcseconds away, offset slightly from the centre of the radio source. This galaxy also fits the K-z relationship, with a 2MASS K = 15.36. The flux of this source's [OII] emission line, and [OII]/[OIII] emission line ratio would be consistent with a powerful 1 Jy radio source. There is no evidence for another radio lobe in the FIRST radio image, however, the radio flux does appear extended towards this galaxy. In light of this, the host for PKS1337 was taken as the bright galaxy, which gives a z = 0.487, placing the source out of the sample.

6.5 Sample Status

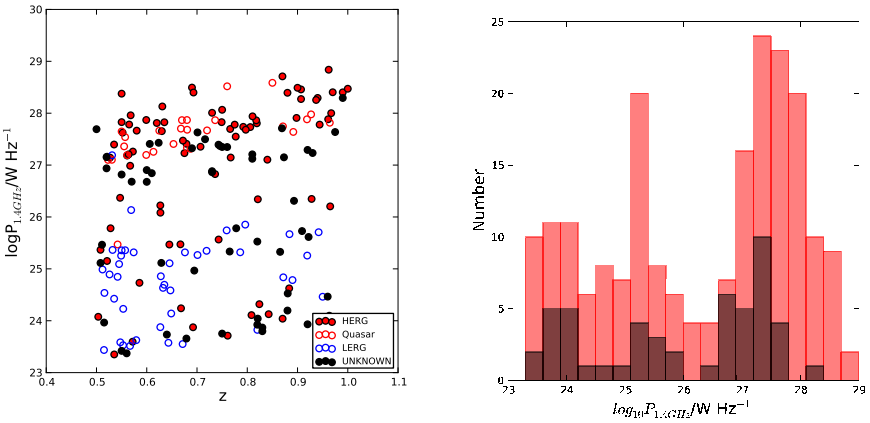

Figure 6.4: With the addition of the new spectroscopic data, it can clearly be seen that the number of unclassified sources is substantially reduced, particularly in the previously problematic region between logP=27-28 W Hz^{-1}, enabling the luminosity functions of both HERGs and LERGs to be constrained with much higher precision. The number of sources with photometric redshifts now stands at 41 out of 210 sources.

With the addition of these new data (cf. Figure 6.3), the uncertainty in the classifications is reduced substantially, particularly in the high luminosity range, logP=27-28 W Hz^{-1}. Figure 6.4 shows the new distribution of HERGs, LERGs and unclassified sources in the sample. Regions of high uncertainty in the P-z plane are clearly reduced. The narrow range between logP=26-27 W Hz^{-1}, and the area around logP=23 W Hz^{-1} still have a high associated uncertainty. These are mainly represented by bright PSR sources with only photometric redshifts, and RAs between 21-02, and faint SXDF sources without spectroscopic data, again around 02 in RA. These sources are due to be observed with the WHT in October 2012, and the addition of these data will ensure that the contribution of unclassified sources to the analysis is minimal.

Table 6.1: Optical Spectroscopy Results for the Northern RA Range sample.Col1: Source Name, Col2: Photometric redshift, Col3: Exposure time, Col4: Emission line, Col5: Emission line observed wavelength, Col6: Observed emission line flux, Col7: δv_{FWHM} (observed frame), Col8: Equivalent Width (observed frame), Col9: Spectroscopic redshift - a ? indicates the redshift is uncertain, Col10: Class, where O=outside redshift selection, U=unclassifiable, HERG=high excitation, LERG=low excitation. Values in brackets indicate uncertainties. Note that there are no photometric redshifts listed for the Hercules sources, which already had spectroscopic redshifts, but no published spectra to enable a classification.

Name	zphot	Exp. Time s	Line	λ Obs $\AA$	Flux x 10^{-16} ergs s^{-1} cm^{-2}	δv_{FWHM} km s^{-1}	EW $\AA$	z(δz)	Class	Note
4C20.28	0.57	1200	NeV	4765	0.45(0.25)	-	-	0.424(0.001)	O	
			[OII]	5314	8.15	-	60(7)			
			Hβ	6921	-	-	-			
			[OIII]	7061	18.07(1.81)	-	56(6)			
			[OIII]	7130	53.05(5.31)	290(167)	163(17)			
4C59.10^N	0.51	1200	MgII	6246	0.32(0.09)	3407(2384)	9(3)	1.245(0.001)?	O	Lines very faint
			[OII]	8369	5.33(0.55)?	974(242)	99(20)			Probable [OII],
										obscured by sky.
4C53.18	0.60	1200	[OII]	6967	1.00(0.12)	320(209)	11(1)	0.869(0.001)	U	
			H	7420	-	-	-			
			K	7353	-	-	-			
PKS1352	0.8	1200	[OII]	8076	1.72(0.18)	536(191)	26(3)	1.167(0.001)	O	
53W023	-	2400	K	6176	-	-	-	0.569(0.01)	LERG	
			H	6217	-	-	-			
53W031	-	2400	[OII]	6066	0.97(0.1)	601(248)	13(1)	0.627(0.001)	HERG	Borderline.
			[OIII]	8074	0.72(0.09)	314(276)	3(1)			Classed on basis
			[OIII]	8147	1.65(0.18)	292(169)	7(1)			of line ratio.
53W008	-	2400	[OII]	6470	3.17(0.32)	718(192)	12(1)	0.736(0.001)	HERG	
			[NeIII]	6724	1.78(0.19)	1302(427)	6(1)			
			Hβ	8434	1.73(0.19)	413(344)	5(1)			
			[OIII]	8610	3.22(0.33)	472(199)	9(1)			
			[OIII]	8688	8.81(0.89)	541(143)	23(2)			
53W080	-	2400	[OII]	5746	12.28(1.23)	234(208)	10(1)	0.542(0.001)	HERG	
			[OIII]	6710	17.29(1.74)	3773(404)	17(2)			
			Hβ	7495	53.30(5.33)	2381(192)	49(5)			

Continued on next page

Table 6.1 – continued from previous page

Name	zphot	Exp. Time s	Line	λ Obs $\AA$	Flux x 10^{-16} ergs s^{-1} cm^{-2} $\AA^{-1}$	δv_{FWHM} km s^{-1}	EW $\AA$	z(δz)	Class	Note
			[OIII]	7654	-	-	-			Sky obscured.
			[OIII]	7718	36.06(3.61)	304(154)	36(4)			
53W077	-	2400	H	7094	-	-	-	0.786(0.01)	LERG	
			K	7031	-	-	-			
53W047	-	2400	H	6084	-	-	-	0.532(0.01)	LERG	
			K	6034	-	-	-			
53W005	-	2400	[OII]	6576	3.7(0.42)	1048(317)	23(3)	0.765(0.002)	U	[OII] emission
			H	6990	-	-	-			contaminated
			K	6948	-	-	-			by sky line.
4C54.25	0.77	1200	[OII]	6395	2.93(0.40)	248(247)	18(3)	0.716(0.001)?	U	[OII] I.D.
										faint, uncertain.
PKS1355	0.66	1200	[OII]	6699	34.95(3.52)	905(184)	113(13)	0.797(0.001)	HERG	
			[NeIII]	6952	12.14(1.32)	-	32(4)			
			[OIII]	8911	30.98(3.27)	633(197)	45(6)			
			[OIII]	8998	90.77(9.17)	1115(163)	158(21)			
PKS1336	0.57	1200	[OII]	5842	32.26(3.30)	620(213)	44(5)	0.567(0.001)	HERG	
			[NeIII]	6063	13.74(1.44)	476(213)	18(2)			
			[OIII]	7772	112.83(11.31)	427(154)	87(9)			
			[OIII]	7847	335.85(33.59)	585(152)	261(27)			
4C59.11	0.56	1200	[OII]	6364	-	-	-	0.707(0.0002)	HERG	
			[NeIII]	6603	12.82(1.44)	483(204)	4(1)			
			[OIII]	8466	28.53(2.96)	-	9(1)			
			[OIII]	8548	72.38(7.33)	396(142)	25(3)			
4C51.25	0.56	1200	[OII]	5817	5.43(0.79)	545(307)	16(3)	0.561(0.001)	HERG	
			[OIII]	7816	22.30(2.36)	413(173)	28(3)			
4C00.35	0.61	1200	[OII]	6505	13.10(1.35)	245(187)	34(4)	0.746(0.0002)	HERG	
			[OIII]	8740	9.57(1.21)	-	12(2)			
4C32.34	0.68	1200	[OII]	5826	59.08(6.01)	249(207)	126(20)	0.564(0.0002)	HERG	
			[NeIII]	6048	16.62(1.82)	-	35(5)			
			[OIII]	7755	132.37(13.28)	233(154)	142(16)			

Continued on next page

Table 6.1 – continued from previous page

Name	zphot	Exp. Time s	Line	λ Obs $\AA$	Flux x 10^{-16} ergs s^{-1} cm^{-2} $\AA^{-1}$	δv_{FWHM} km s^{-1}	EW $\AA$	z(δz)	Class	Note
			[OIII]	7829	401.59(40.18)	415(152)	428(49)			
4C46.21	0.54	1200	[OII]	5689	38.79(3.94)	-	69(8)	0.527(0.0001)	HERG	
			[OIII]	7570	43.41(4.40)	-	41(4)			[OIII] lies in
			[OIII]	7643	68.75(6.91)	-	67(7)			7600$\AA$ absorp.
PKS1337	0.79	1200	[OII]	5544	1.61(0.28)	-	-	0.487(0.0001)	O	See Fig. 6.9.
(Host 2)			[NeIII]	5752	1.23(0.2)	-	-			
			[OIII]	7375	1.7(0.18)	-	66(13)			
			[OIII]	7447	4.91(0.50)	-	192(38)			
PKS1329	0.84	2400	[OII]	6981	1.09(0.13)	557(233)	19(2)	0.873(0.001)	U	
4C04.40	0.56	1200	K	6051	-	-	-	0.531(0.002)	LERG	
			H	6108	-	-	-			
4C13.56	0.67	1200	[OII]	6228	4.65(0.48)	754(204)	26(3)	0.672(0.004)	HERG	
			[OIII]	8353?	-	-	-			[OII] lines
			[OIII]	8358	21.79(2.22)	2000(336)	52(5)			in sky area
4C16.27	0.92	1200	[OII]	9139	3.4(0.43)	437(175)	25(4)	1.452(0.001)	O	extended [OII]
4C17.49	0.51	1200	[OII]?	6284	-	-	-	0.69(0.0002)?	U	Poss [OII]
										Next to sky line.
4C17.48	0.54	1200	[OII]	5663	4.91(0.55)	545(250)	24(3)	0.521(0.001)	HERG	
			[OIII]	7537	8.33(0.86)	588(170)	26(3)			[OIII] lies in
			[OIII]	7616	5.28(0.55)	-	16(2)			7600$\AA$ absorp.
4C17.54	0.58	1200	[OII]	6241	14.12(1.41)	769(191)	134(14)	0.675(0.001)	HERG	
			[NeIII]	6474	1.57(0.16)	-	14(2)			
			[OIII]	8300	5.36(0.57)	473(175)	27(3)			
			[OIII]	8385	14.52(1.47)	516(147)	73(8)			
4C17.56	0.61	1800	[OII]	6623	4.08(0.42)	702(195)	37(4)	0.777(0.0003)	HERG	
			[OIII]	8894	4.50(0.57)	501(273)	18(3)			
4C29.46	0.86	1200	Hβ	6794	15.55(1.56)	-	16(2)	0.397(0.0002)	O	
			[OIII]	6930	54.61(5.46)	-	56(6)			
			[OIII]	6997	177.01(17.70)	-	184(18)			
			Hα+NII	9165	300.5(30.06)	3738(174)	306(31)			

Continued on next page

Table 6.1 – continued from previous page

Name	zphot	Exp. Time s	Line	λ Obs $\AA$	Flux x 10^{-16} ergs s^{-1} cm^{-2} $\AA^{-1}$	δv_{FWHM} km s^{-1}	EW $\AA$	z(δz)	Class	Note
4C59.16	0.82	1200	[OII]	7307	13.43(1.35)	722(166)	44(5)	0.961(0.0002)	HERG	
			[NeIII]	7583	0.50(0.13)	-	-			
			[OIII]	9720	6.61(0.76)	425(202)	43(7)			
			[OIII]	9818	13.07(1.37)	541(138)	105(21)			
4C12.41	0.68	1200	MgII	5885	-	-	-	1.10(0.002)	O	
			[NeV]	7021	1.36(0.15)	-	5(1)			
			[NeV]	7188	2.43(0.26)	460(183)	8(1)			
			[OII]	7820	10.02(1.01)	624(159)	33(3)			
			[NeIII]	8118	2.48(0.29)	459(183)	9(1)			
			[NeIII+Hϵ]	5.23(0.54)	344(154)	18(2)				
TXS1152	0.74	1800	[OII]	8181	8.07(1.06)	382(215)	21(4)	1.195	O	

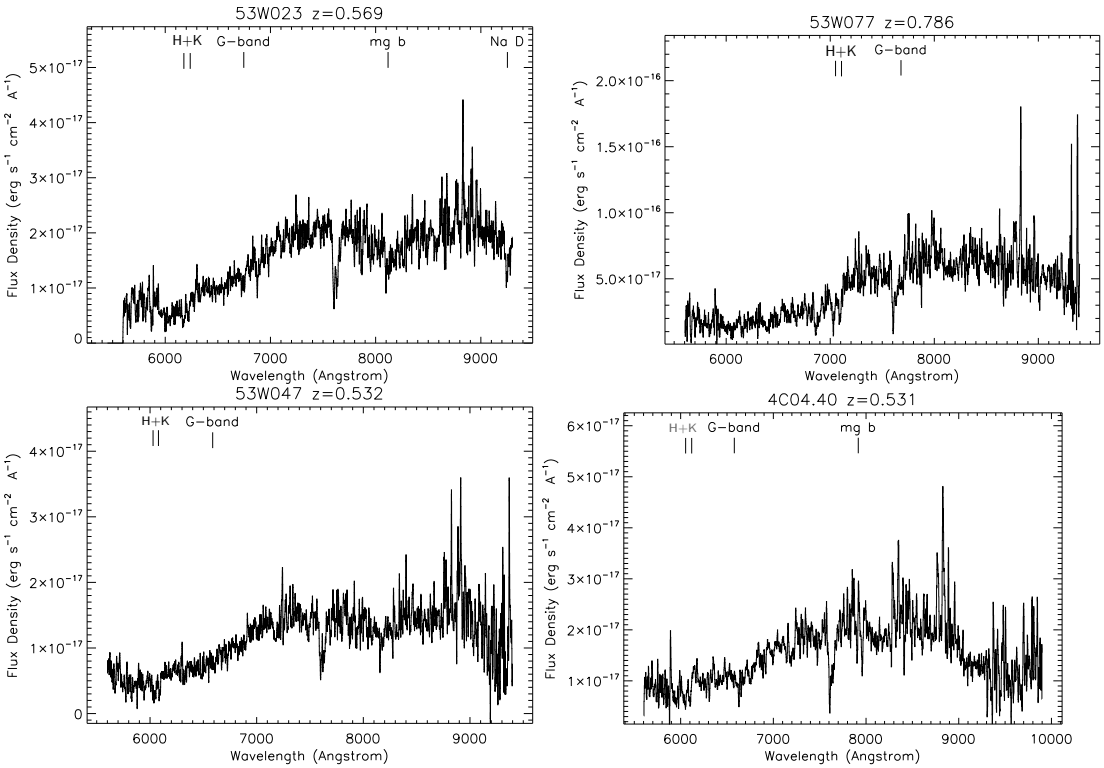

Figure 6.5: Sources identified as LERGs from the new spectroscopic data.

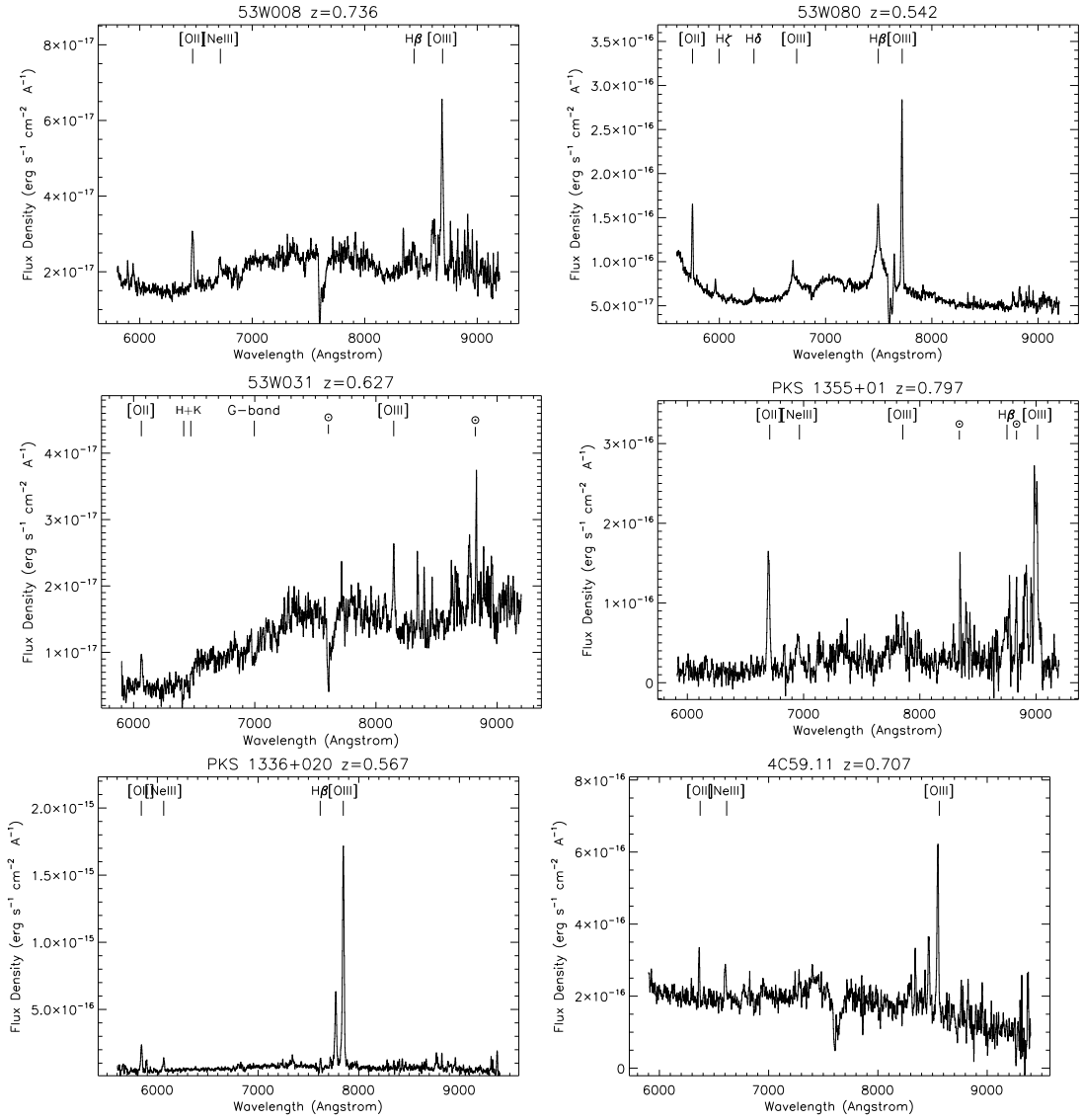

Figure 6.6: Sources identified as HERGs from the new spectroscopic data.

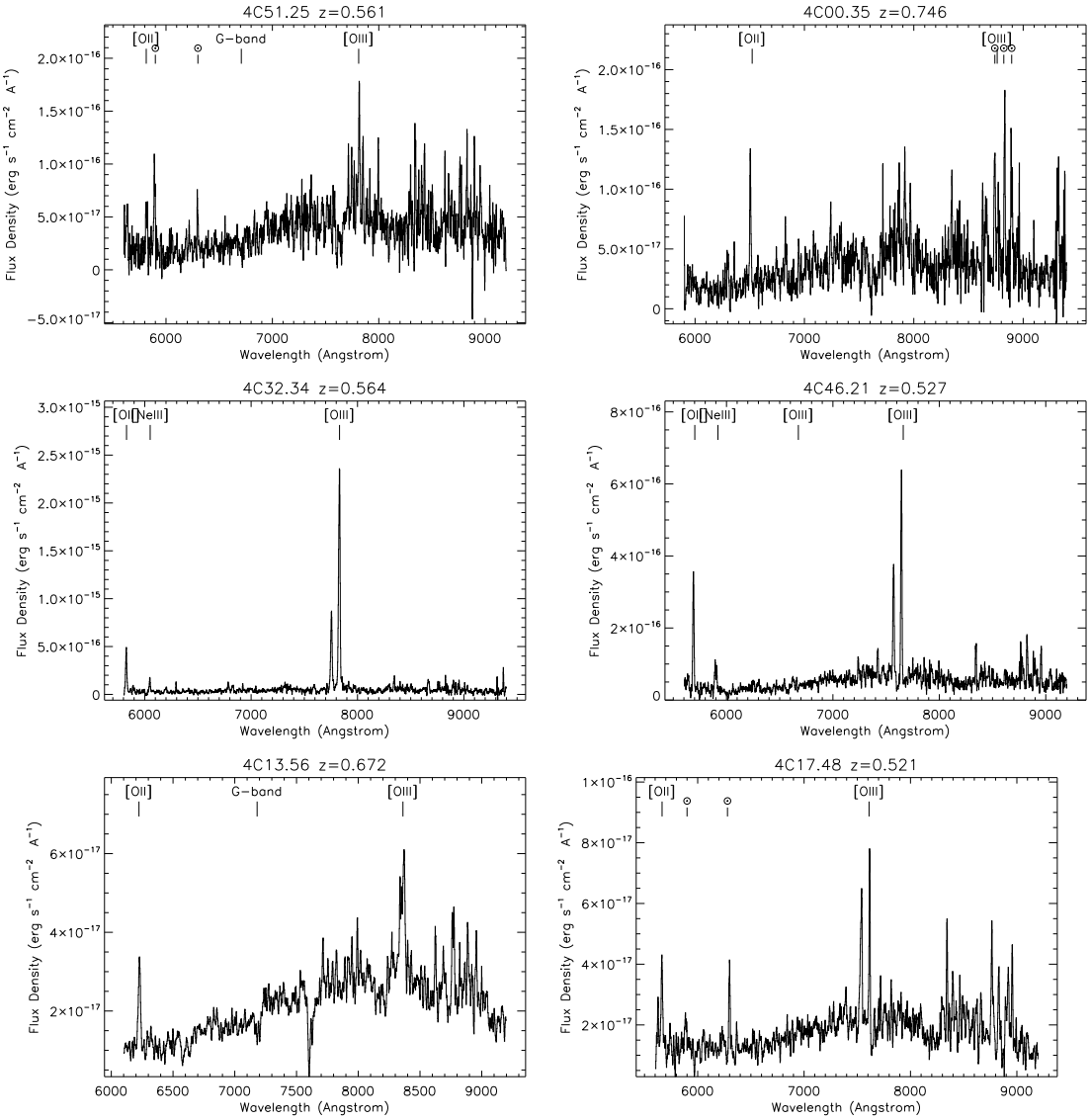

Figure 6.7: Sources identified as HERGs from the new spectroscopic data.

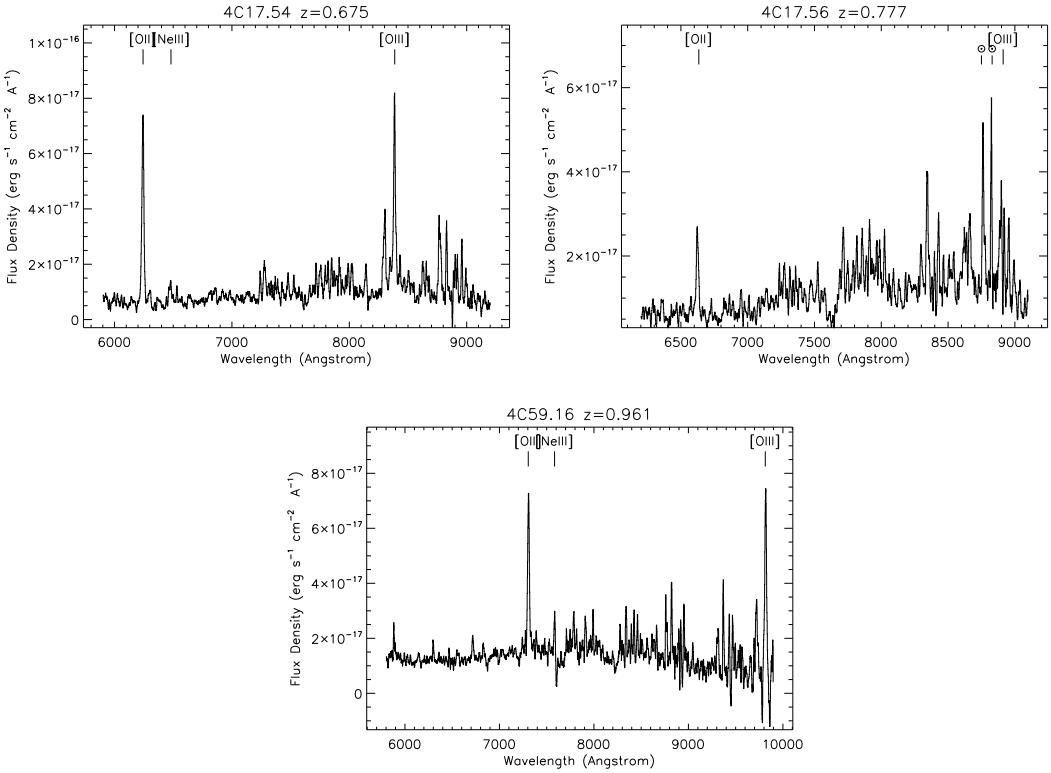

Figure 6.8: Sources identified as HERGs from the new spectroscopic data.

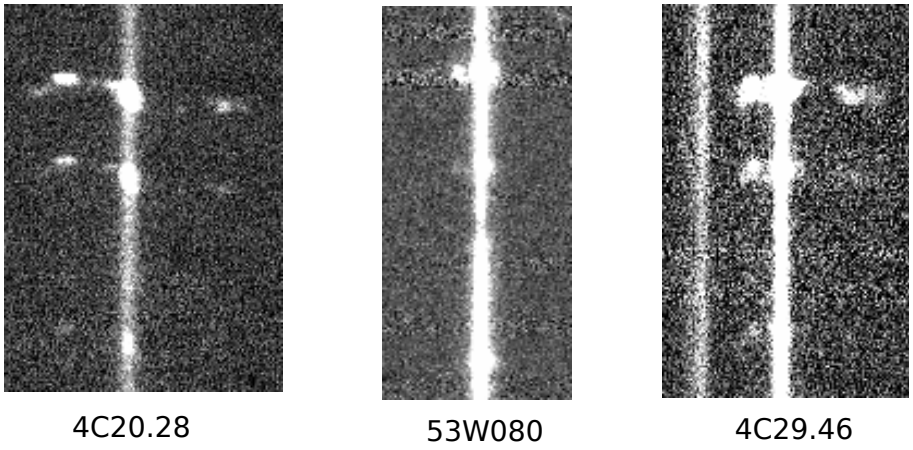

Figure 6.9: Spectra for three sources 53W080 (z=0.542), 4C20.28 (z=0.424) and 4C29.46 (z=0.397) showed substantially extended line emission ([OIII] lines illustrated here).

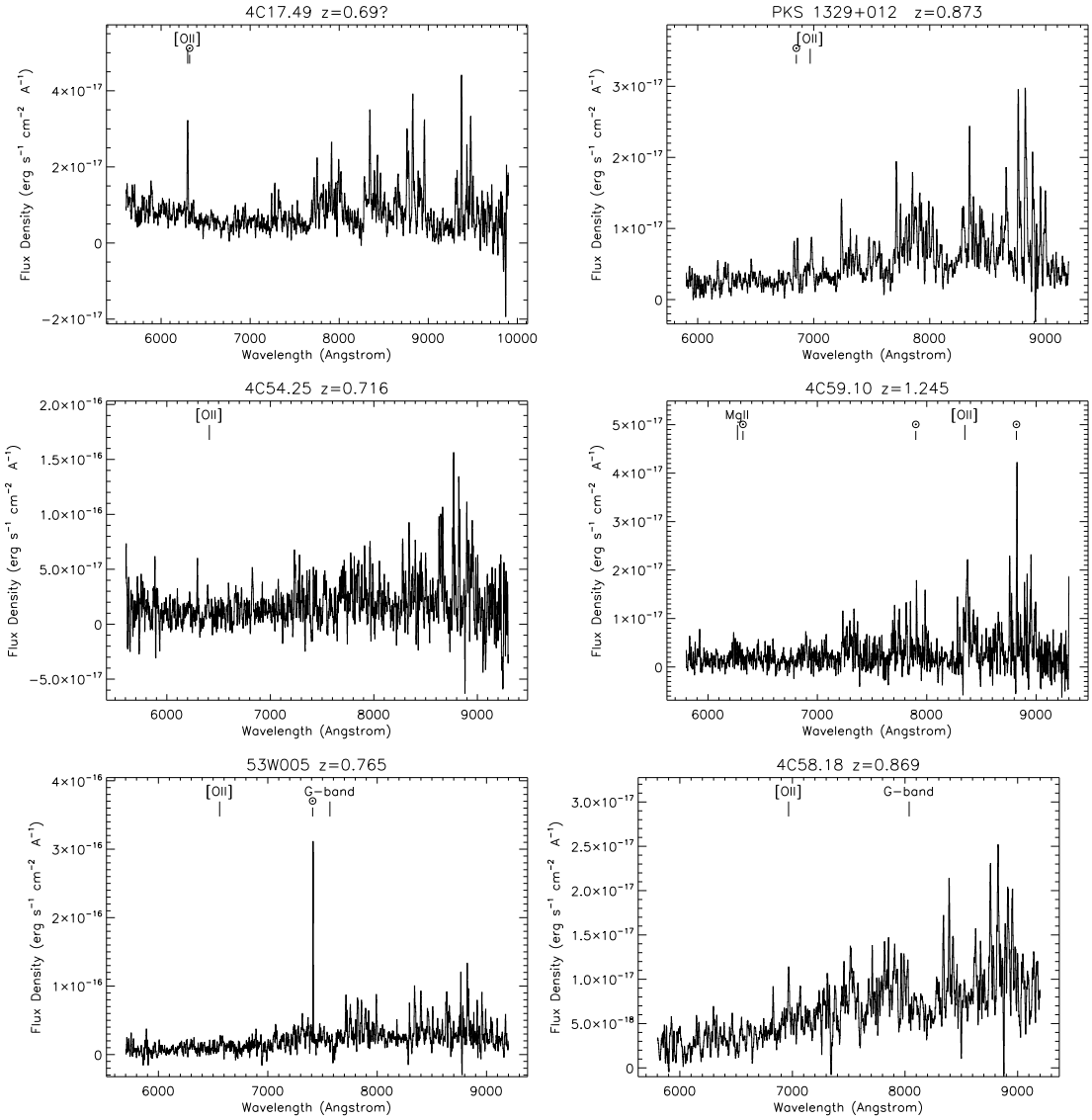

Figure 6.10: Sources for which the new spectroscopic observations do not allow a classification to be made.

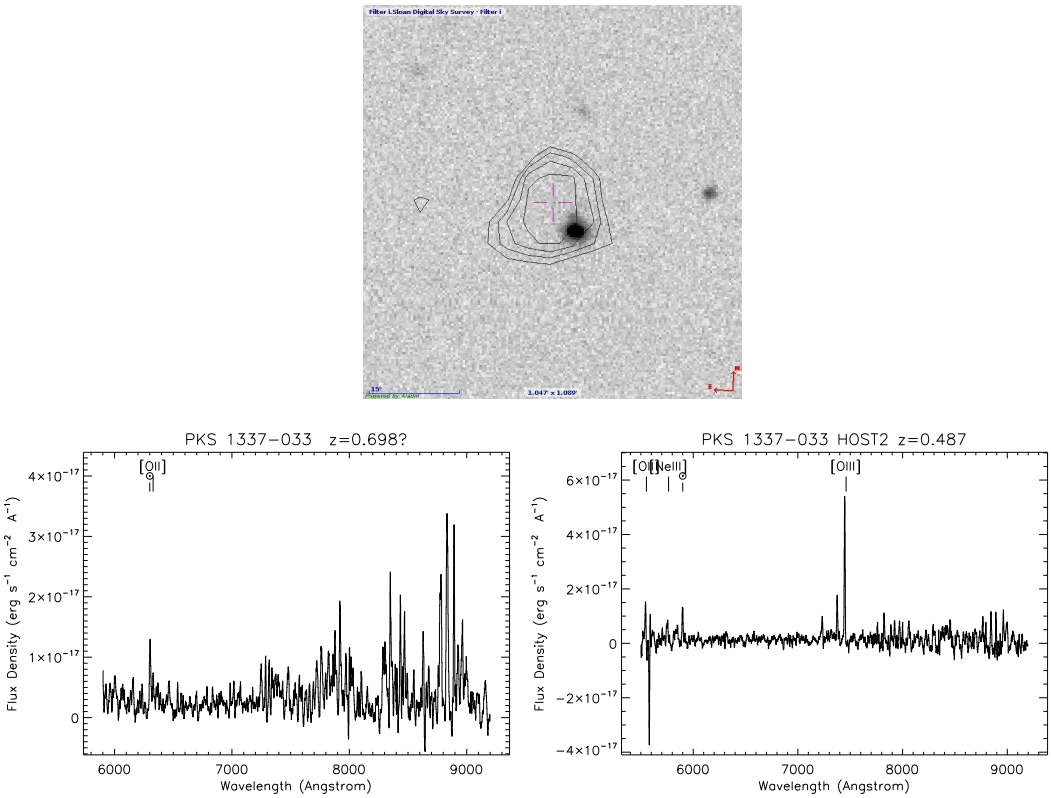

Figure 6.11: New Spectroscopy and host identification for PKS 1337-033.

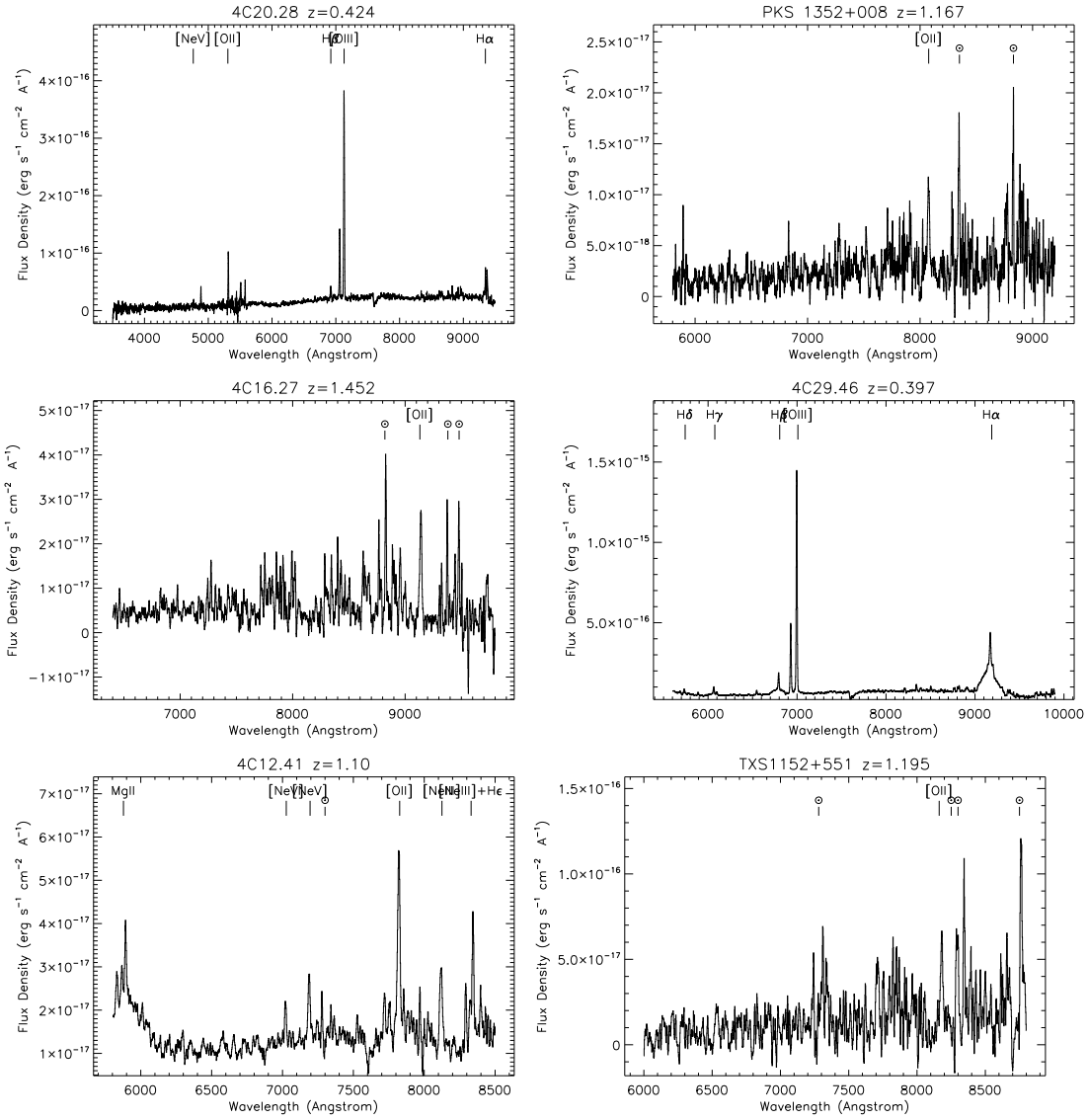

Figure 6.12: New Spectroscopy showing that these sources have redshifts outside of the z=0.5-1.0 selection, and are hence excluded from the analysis.

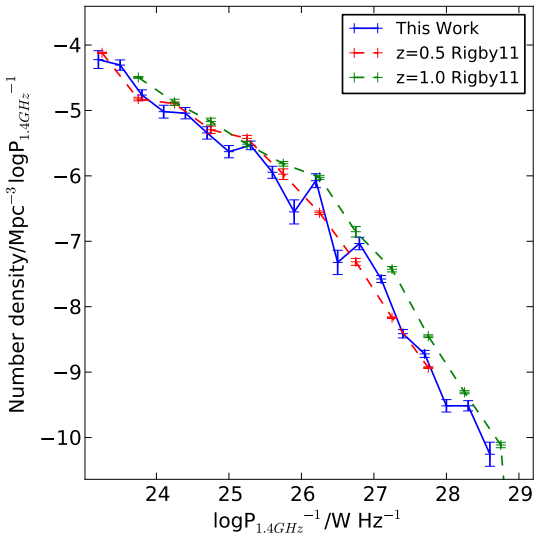

Figure 6.13: The luminosity function for all the combined samples. Plotted for comparison are the z=0.5 and z=1 luminosity functions from Rigby *et al.* [2011], which are in excellent agreement.

6.6 Luminosity Functions

Luminosity functions were constructed for the entire sample, and the HERG and LERG populations individually, with the number density in a given luminosity bin

$$\rho_m = \sum_N \frac{1}{V_{MAX} - V_{MIN}} \pm \left[\sum_N \left(\frac{1}{V_{MAX} - V_{MIN}} \right)^2 \right]^{0.5} \tag{6.1}$$

in Mpc^{-3}, and in log form,

$$log\rho_m = log_{10}\left(\frac{\rho_m}{m}\right) \pm \frac{1}{m}\frac{1}{ln10}\frac{\delta\rho_m}{\rho_m} \tag{6.2}$$

for all N sources within the set luminosity bin m, with V_{MAX} and V_{MIN} being the maximum and minimum co-moving volumes enclosed by the upper and lower redshift limits at which each source would be included in the sample. For each source, V_{MAX}-V_{MIN} was calculated as the sum over all surveys of (the sky area of the survey/total sky area) * (volume enclosed over all sky between z=0.5 and z = zmax(survey)). zmax(survey) is either the maximum redshift to which the source could be observed at that radio luminosity in the survey, or z = 1 (as per the redshift constraint), whichever was least. If zmax(survey) was less than 0.5, the volume contribution of the associated survey was ignored.

Figure 6.13 shows the combined luminosity function for all samples, and the luminosity function at z=0.5 and z=1 recently presented by Rigby *et al.* [2011] for comparison. The Rigby

et al. [2011] luminosity function determination is derived in a different fashion to this study, and whilst it uses some of the same samples, it does not use the CoNFIG or SXDS samples, and includes the VLA Cosmos sample, which this study does not. The luminosity functions of

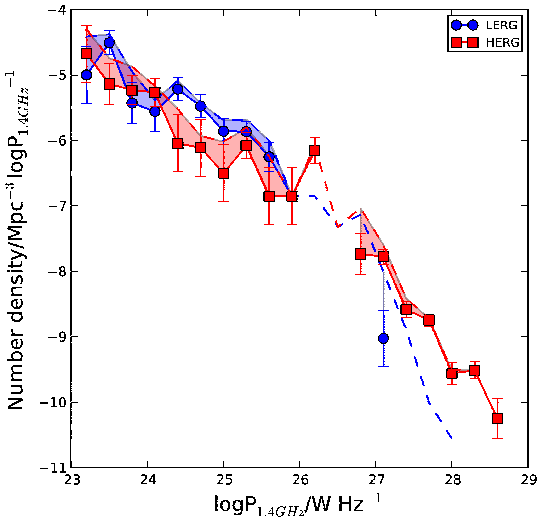

Figure 6.14: The luminosity functions for HERGs only and LERGs only in the sample (red and blue solid lines), plus the associated Poissonian error. The dashed lines, and shading up to them show both the HERG (red) and LERG (blue) luminosity functions plus the unclassified sources, thereby indicating the maximum potential increase in each from the unclassified sources.

logP$_{1.4GHz}$ W Hz^{-1}	All		HERG		LERG		Unclassified	
	N	ρ	N	ρ	N	ρ	N	ρ
23.2-23.5	4	5.99(3.14)e-5	1	2.12(2.12)e-5	1	1.00(1.00)e-5	2	2.87(2.08)e-5
23.5-23.8	12	4.93(1.50)e-5	2	7.30(5.3)e-6	6	3.11(1.28)e-5	4	1.09(0.56)e-5
23.8-24.1	11	1.72(0.52)e-5	4	5.89(2.96)e-6	2	3.73(2.65)e-6	5	7.56(3.34)e-6
24.1-24.4	7	9.58(0.36)e-5	4	5.43(2.71)e-6	2	2.77(1.96)e-6	1	1.38(1.38)e-6
24.4-24.7	9	9.08(3.04)e-6	1	9.01(9.01)e-7	6	6.07(2.49)e-6	2	2.11(1.49)e-6
24.7-25.0	8	4.53(1.64)e-6	1	7.74(7.74)e-7	6	3.36(1.39)e-6	1	4.02(4.02)e-7
25.0-25.3	8	2.34(0.84)e-6	1	3.15(3.15)e-7	5	1.39(0.63)e-6	2	6.41(4.55)e-7
25.3-25.6	16	2.93(0.74)e-6	5	8.37(3.75)e-7	7	1.36(0.52)e-6	4	7.30(3.72)e-7
25.6-25.9	8	1.13(0.40)e-6	1	1.41(1.41)e-7	4	5.62(2.81)e-7	3	4.30(2.49)e-7
25.9-26.2	2	2.81(1.99)e-7	1	1.41(1.41)e-7	1	1.41(1.41)e-7	0	-
26.2-26.5	6	8.43(3.44)e-7	5	7.03(3.14)e-7	0	-	1	1.41(1.41)e-7
26.5-26.8	2	4.75(3.39)e-8	0	-	0	-	2	4.75(3.38)e-8
26.8-27.1	8	9.24(3.37)e-8	2	1.84(1.32)e-8	0	-	6	7.39(3.10)e-8
27.1-27.4	30	2.65(0.53)e-8	19	1.67(0.43)e-8	1	9.43(9.43)e-10	10	8.87(3.03)e-9
27.4-27.7	21	3.87(0.95)e-9	15	2.58(0.75)e-9	0	-	6	1.29(0.54)e-9
27.7-28.0	25	1.90(0.39)e-9	24	1.80e-9(0.38)	0	-	1	9.81(9.81)e-11
28.0-28.3	8	3.05(1.11)e-10	7	2.78(1.08)e-10	0	-	1	2.78(2.78)e-11
28.3-28.6	11	3.06(0.92)e-10	11	3.06(0.92)e-10	0	-	0	-
28.6-28.9	2	5.56(3.93)e-11	2	5.56(3.92)e-11	0	-	0	-

Table 6.2: The HERG, LERG and Unclassified luminosity functions at 0.5<z<1.0, as plotted in 6.14 above. The space densities ρ are given in units of number per Mpc^3 per $\log_{10}$P$_{1.4GHz}$. The first column gives the luminosity range considered in each bin. The second, third, fourth and fifth columns give the number of sources and space densities for all sources in the combined sample, the HERGs only, the LERGs only and the Unclassified sources only respectively.

Rigby *et al.* [2011] at z=0.5 and z=1.0 are in excellent agreement with this work, and provide reassurance that the contribution of photometric redshift errors in the samples used here are low.

Figure 6.14 shows the luminosity functions for the classified HERGs and LERGs within the sample, in addition to the luminosity functions obtained if the unclassified sources are added to either the HERG or LERG classification. The most striking feature is that, regardless of the uncertainty introduced by the unclassified sources, in the redshift range 0.5-1.0, the number density of HERGs and LERGs is similar at lower luminosities. At higher luminosities, above $\log P_{1.4GHz} \sim 26$ W Hz^{-1} HERGs clearly dominate.

Best and Heckman [2012] find that locally in the redshift range 0.01<z<0.3 that LERGs dominate below $\log P_{1.4GHz} \sim 26$ W Hz^{-1}, and using the V/V_{MAX} test, found that the HERGs in the sample showed strong signs of evolution, whilst the LERGs did not. They then suggested that the combination of these two factors, the changing relative numbers with luminosity, and the weakly or not evolving LERGs, and the strongly evolving HERGs, would account for the strong luminosity dependence of evolution seen the overall radio luminosity function [e.g Rigby *et al.*, 2011]. The results seen in Figure 6.14 confirm this, with the number density of HERGs increasing at higher redshifts out to z=1 to be comparable to the number of LERGs at low luminosities, as would be expected for a strongly evolving HERG population, and a more weakly evolving LERG one.

The Best and Heckman [2012] RLFs provide an excellent reference point for comparison with these higher redshift observations. Using the CENSORS sample between z=0.5-1.0 as an example (as it covers similar luminosities and is 85% spectroscopically complete, and 79% classified), and assuming that there is no redshift evolution in either the LERG or HERG population, the Best and Heckman [2012] RLFs would predict a total of 3 LERGs and 1 HERG between the redshifts of 0.5 and 1.0 for a survey of the CENSORS area and flux density limit. As there are a minimum of 11 LERGs and nine HERGs in this sample, this is a clear indication that both RLFs must evolve with redshift.

In Figure 6.15, the left panel shows the luminosity functions at 0.5<z<1, and locally, and the right panel gives the ratio of the luminosity functions with the local ones for HERGs and LERGs determined by Best and Heckman [2012] over a luminosity range $P_{1.4GHz}$ = 22-26 W Hz^{-1}. This highlights the strongly evolving HERG and the weaker evolution of the LERG population clearly. Note that over this luminosity range, the unclassified sources introduce an uncertainty comparible to the error bars. Also noteworthy is the fact that the evolution of HERGs appears to be stronger at low luminosity than high, and LERGs show the opposite trend, albeit much more weakly. It is possible that there may be more radio-quiet quasar interlopers present at the very lowest luminosities: the SXDF sample which covers this range has no spectral index cut applied, unlike the other samples, and whilst obvious broad-line quasars have been removed, it is possible other highly beamed sources have been missed (particularly as the samples are selected at 1.4 GHz, and are more likely to contain highly beamed sources, cf. Chapter 5). In order to investigate this further, radio spectral indices would be required for the SXDF sample.

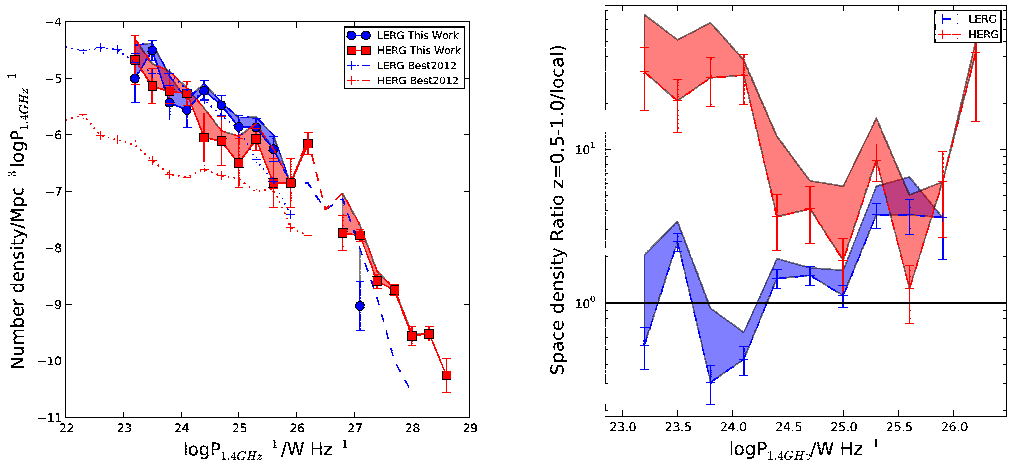

Figure 6.15: The radio luminosity functions of HERGs and LERGs from this work, as compared to the local HERG/LERG luminosity functions from Best and Heckman [2012]. The evidence for evolution of HERGs is clear. Note that the points and shading are as for Figure 6.14.

6.7 The V/V_{MAX} Test for Evolution

Having established that evolution is present for the HERG population, at z=0.5 - 1.0 compared to locally, it is interesting to test whether there is any indication that the evolution of both HERGs and LERGs changes over the interval z=0.5 - 1.0. The V/V_{MAX} test can be used to ascertain if there are any indications of evolution within a complete galaxy sample. Considering some limiting volume V_{MAX}, beyond which sources cannot be detected, if there is no evolution present, then the sources are expected to be distributed homogeneously, and half of the sources would be expected to lie in the inner half of the volume considered, and half in the outer. Hence the average of the ratio source volume V to maximum volume V_{MAX} for all sources over a given luminosity range should be 0.5. If it is greater than 0.5, this suggests evolution in the sense that there were more sources located at larger distances than smaller, and for less than 0.5, vice versa.

$$V/V_{MAX} = \frac{1}{N}\sum_{N}\frac{V}{V_{MAX}} \pm (12N)^{-0.5} \tag{6.3}$$

In the case that the galaxy sample has some constraints, for example flux limits and redshift limits, a banded V/V_{MAX} test must be used. For each source in the sample, the volume of the source V is calculated similarly to the above, and the maximum and minimum volume in which the source could be observed are also calculated, taking into account the redshift constraints as follows:

$$V/V_{MAX} = \frac{1}{N}\sum_{N}\frac{V - V_{MIN}}{V_{MAX} - V_{MIN}} \pm (12N)^{-0.5} \tag{6.4}$$

where V is the co-moving volume out to the redshift of the source. V-V_{MIN} is calculated as the sum over all surveys of (the sky area of the survey/total sky area) * (volume enclosed

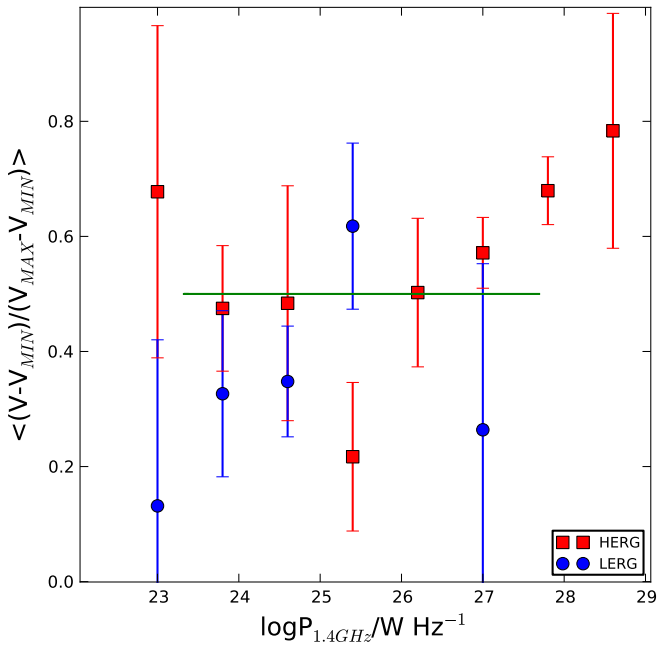

Figure 6.16: The V/V_{MAX} test for evolution on the HERG and LERG sources.

between z=0.5 and z = zmax(survey) or the redshift of the source, whichever is lower). As for the luminosity function, V_{MAX}-V_{MIN} was calculated as the sum over all surveys of (the sky area of the survey/total sky area) * (volume enclosed between z=0.5 and z = zmax(survey)). zmax(survey) is either the maximum redshift at which the source could be observed to at that radio luminosity in the survey, or z = 1 (as per the redshift constraint), whichever was least. Again, if zmax(survey) was less than 0.5, the volume contribution of the associated survey was ignored.

The results of the V/Vmax test may be seen in Figure 6.16. The low number statistics in some areas of the P-z clearly have an effect (cf. Figure 6.4), most notably at logP$\sim$25.5-26.5 W Hz^{-1}, so data points in these luminosities ranges should be treated with caution. The LERG population shows little, or even slightly negative evolution over this redshift range, and the HERG population shows clear positive evolution, particularly towards the highest luminosities. The slight negative evolution seen in the LERG population over this redshift range, coupled with no evolution of the HERGs, at low luminosities would be consistent with recent findings of a turnover in the radio luminosity function at low luminosity (logP$\sim$25-26 W Hz^{-1}), whereby the space density of low luminosity sources declines at z>0.7 [Rigby *et al.*, 2011]. However, note that the V/Vmax test as presented here is very reliant on accurate classifications and redshifts for the entire sample, as there are some areas of the P-z plane naturally low in sources, so a more precise result should be obtained with the additional spectroscopic data due to be taken

in October 2012.

6.8 LERG Evolution: Discussion

This initial determination of the RLF for both HERGs and LERGs shows strong evolution in the HERG population out to z=1, with the V/V_{MAX} test indicating continued positive evolution to higher redshift, whilst there is weaker evolution in the LERG population out to z=1 and indications of a turnover at lower powers. For the HERGs this result is consistent with recent theoretical work but for the LERG population the situation is less clear. Croton *et al.* [2006] presented simulations of central supermassive black hole growth through a set of semi-analytic models run on the output of the Millenium Simulation. In these models, they incorporate both 'quasar mode' and 'radio mode' feedback, and find that both are required in order to accurately reproduce the observed galaxy luminosity function, and predict that LERG evolution remains flat out to z=1 (cf. Figure 6.17, and see discussion Chapter 1, Section 1.3).

Other complementary work, such as that of Merloni and Heinz [2008] use synthesis models for AGN evolution incorporating both high and low excitation modes, and also predict that the evolution of low excitation, radio-mode sources remains more or less flat, although their uncertainties would allow a small increase, perhaps a factor 2-3 in space density out to z=1. The results obtained here for LERGs are more or less consistent with this, especially at lower radio powers, but the factor 2-3 increase in LERG space density found at higher powers is weakly at variance with the model predictions.

There are still some remaining sources of uncertainty in this study, which could conceivably lead to an erroneous LERG RLF measurement. These are the number of unclassified sources, and the contribution of photometric redshifts. The upcoming spectroscopic campaign should reduce the number of unclassified sources further. For unclassified sources at higher redshift, i.e. with only [OII] with an unclassifiable equivalent width in the range $5\mathring{A}$ - $30\mathring{A}$ (51 sources) further observations would need to be taken to measure or rule out the presence of [OIII]. However, the unclassified sources will only act to increase the number density for both HERGs and LERGs, not decrease it, so the unclassified sources do not contribute to the observed evolution in both populations.

The contribution of photometric redshift error is more difficult to measure, as sources may be shifted in and out of the sample when measured spectroscopically. However, this effect is likely to be small (cf. Figure 6.3), particularly for the LERG population because the spectroscopic completeness of the z=0.5-1.0 samples at luminosities below logP$\sim$26 W Hz^{-1} is very high - any photometric redshift errors present would add a net gain to the density. The most recent spectroscopic campaign showed that only 8 photometric redshift selected sources (all high luminosity HERGs) had spectroscopic redshifts outside the z=0.5-1.0 range. In Figure 6.3, the photometric vs spectroscopic redshift is plotted for the CoNFIG sources targeted in this campaign, illustrating the scatter present. These results indicate that the high luminosity section of the P-z plane is most susceptible to photometric redshift errors. However, the addition of new spectroscopic redshifts will only serve to increase the space densities measured: existing

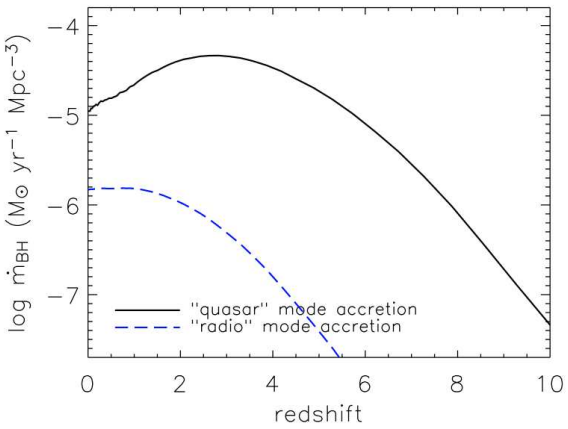

Figure 6.17: This Figure from Croton *et al.* [2006] shows their predicted evolution (traced by black hole accretion rate) of LERGs (radio mode) and HERGs (quasar mode). The evolution of LERGs is expected to be flat out to z∼1. Figure reproduced from Croton *et al.* [2006].

unclassified sources will be classified and added, and any objects with a photometric redshift outside the range considered but with a spectroscopic redshift within the considered range will also increase the measured space densities. Quantifying this effect further awaits completion of the spectroscopic data acquisition for the samples, but the key finding of weak LERG evolution and strong HERG evolution remains robust regardless of this uncertainty.

An interesting possibility to explain the weak evolution of LERGs seen in this study between z=0.5 and locally lies in the evolution of the host galaxy luminosity functions. Janssen *et al.* [2012] recently presented a study of HERG and LERG host colours, and the relations with mass and star formation rate. They note that whilst HERGs are predominantly found in massive blue galaxies, and LERGs in massive red galaxies (as found also by e.g. Tasse *et al.* [2008]), there are examples of the opposite occurring for both HERGs and LERGs. Massive red galaxies are generally thought to show little evolution in cosmic space density out to z∼ 1.0 [Cool *et al.*, 2008], but massive blue (star-forming) galaxies have been shown to evolve strongly with redshift [Matsuoka and Kawara, 2010]. Interestingly, Janssen *et al.* [2012] find that the fraction of massive red galaxies with a LERG present decreases strongly for increasing radio luminosity, but this dependence is substantially weaker for massive blue galaxies hosting either a HERG or a LERG. If the density of massive blue galaxies increases with redshift, then one would expect correspondingly increased numbers of the relatively rare LERGs hosted by a massive blue galaxy, in addition to a strongly evolving HERG population.

This could contribute to the weak evolution seen in LERGs, especially at higher radio powers, and, although outside the scope of this thesis, is a promising avenue for further investigation (e.g. Janssen *et al.* [2012] split their sample into blue, green and red galaxies by the strength of the 4000$\mathring{A}$ break, data which are available for at least CENSORS, and a moderate proportion of the other samples). If the interpretation of Best and Heckman [2012] is correct, LERGs simply reflect low accretion rates. Red LERGs are most probably cooling flow driven, but blue

LERGs could be the starting/end point of a HERG when the gas density is decreasing, or an interaction/merger that brought in little gas (indeed Janssen *et al.* [2012] find that several of their blue LERGs show signs of an early merging event). These would be expected to evolve like HERGs.

If the trend of strongly evolving HERGs and weakly evolving LERGs continues out to higher redshift, and especially if the LERG RLF peaks and declines as the results would suggest, then overall, the likelihood of detecting LERGs at higher redshifts falls. The measurement of the luminosity function of LERGs and HERGs out to redshift 1 allows some predictions to be made for the numbers expected in flux-limited radio surveys, and provides a useful tool for measuring the contribution of LERGs to the 'missing redshift' population, particularly for those sources with featureless continuum. In the entire, complete, CENSORS sample as presented in Chapter 3, there are 21 sources for which there is no confirmed spectroscopic redshift. 16 of these have a confirmed host galaxy identification, have featureless continuum, and lie at estimated (photometric) redshifts between 0.8 and 2.7. Six of these are consistent with being GPS or CSS radio sources, and the remaining 10 are associated with more steep extended radio sources. The LERG RLF measured at z=0.5 - 1.0 suggests that the LERG RLF shows slight positive evolution (of a factor 2-3) in comparison with the locally determined RLF. However, the V/V_{MAX} test hints at slight negative evolution being present over the redshift range 0.5 -1.0. If no further evolution is assumed in either the LERG population, the RLFs presented here give a minimum of 4 LERGs between redshift 0.8 and 3.

This suggests that at least some of the ten extended radio sources without a spectroscopic redshift are indeed LERGs, and that continued weak positive evolution of the LERG luminosity function cannot be ruled out, contrary to the findings of the V/V_{MAX} test. In order to determine the evolution of the LERG RLF past z=1, the RLF would need to be measured out to even higher redshift, z=1-3. This is more technically challenging, as the majority of spectra available for radio sources are in the optical, and the [OIII] and [OII] emission lines are shifted out of this range at z>1.2. One possibility would be to use SINFONI (cf. Chapter 3), or the new MOONs instrument on the VLT to target [OIII] in the near-infrared range.

6.9 Infrared Faint Radio Sources (IFRS): High Redshift Radio Galaxies?

If the LERG interpretation holds for at least some of the featureless continuum objects, then what about those with no continuum detection at all in the optical/NIR? Could these be good candidates for high redshift radio galaxies, or are they more likely to be obscured sources at more moderate redshift?

Extending the frontier of the most distant known powerful radio galaxies is of great interest for a number of reasons. Locating the highest redshift radio sources will allow investigation of the characteristics of early unknown populations of radio galaxies, and offer a probe of the most massive structures in the early Universe, since powerful distant radio galaxies are almost always found in massive galaxies in protoclusters, [cf. Venemans *et al.*, 2007]. Perhaps most

excitingly, any powerful radio source found at z>6 can be used to constrain how conditions in the Epoch of Reionisation evolved with cosmic time by studying redshifted 21cm absorption features along its line of sight (analogous to the Lyman-alpha forest towards bright quasars). This is one of the key science drivers of both LOFAR and the Square Kilometre Array. However for this method to succeed, a substantial number of distant radio sources with secure redshifts must be assembled.

Significant progress has been made identifying galaxies at redshifts comparible to the EoR, with likely z∼7-9 galaxies recently identified in deep Hubble Space telescope data and the UltraVista survey [e.g. Bowler *et al.*, 2012; McLure *et al.*, 2011]. However there has been little progress in identifying high-redshift AGN within the EoR - a quasar at z=7.085 has the highest spectroscopically confirmed redshift [Mortlock *et al.*, 2011], and very little is known about the types and numbers of AGN during this epoch. Powerful radio sources should be easily detectable out to the redshift of reionisation, but despite this, there is only one radio galaxy known at a redshift greater than 5, at redshift 5.2 [van Breugel *et al.*, 1999].

Any high redshift powerful radio sources will have been detected already in current radio surveys, but the main difficulty lies in successfully identifying them. In recent years, a popular method for filtering out high z candidates in various radio surveys was to utilise the redshift-spectral index (z-α) correlation, with α<-1.3. However as has been shown in Chapter 4, many of the highest redshift radio galaxies currently known have relatively average α∼-0.8, and would not have been selected by this method.

Bright radio emitters which are not detected in deep optical or infrared images (Infrared Faint Radio Sources or IFRSs) may provide a unique, unbiased means of locating such high redshift sources. The crucial advantage of this method is that it allows a clean selection of candidate high-z radio sources: essentially, any radio-loud AGN which is optically undetected, and is faint or undetected in deep near-IR imaging is extremely likely to be at high z (see Chapter 4), given the tight K - z correlation seen for radio sources [e.g. Willott *et al.*, 2003]. Jarvis *et al.* [2009] have successfully utilised this technique, and detected the Lyα line in a normal radio galaxy at z=4.88, undetected in K, optical and only weakly in the mid-infrared, demonstrating the feasibility of this method.

Spectral energy distributions of infrared faint radio sources by Garn and Alexander [2008] suggest that these sources are consistent with being compact FRII radio galaxies at high redshift. VLBI observations have been used to verify the presence of a compact high brightness temperature radio core in one of the objects selected using this technique [cf. Middelberg *et al.*, 2011] again suggesting an AGN origin of the radio emission. Nevertheless, despite this, there is only one confirmed spectroscopic redshift for a high redshift IFRS at z=4.88 available in the literature [Jarvis *et al.*, 2009].

However as outlined above, there are other explanations for the nature of IFRSs. In order to maximise the likelihood of sources selected for follow-up being at high redshift, the number of star-forming and low-excitation radio galaxies must be minimised in any selected sample. From extensive studies of radio source counts, down to the sub-mJy level, it is now accepted that star-forming galaxies begin to be significant below 1mJy at 1.4 GHz, and to dominate

Table 6.3: The IFRS High Redshift Candidates.

Source	RA	DEC	PA	Lyα Flux x 10^{-17} ergs s^{-1} cm^{-2}	$S_{1.4GHz}$ mJy	α	Filter	Mag	Sample
J171404.0+595317	17:14:03.986	+59:53:17.54	-96	<7.05	2.48	-0.69	R	>24.5	Garn08
J171149.8+591727	17:11:49.817	+59:17:28.17	145	<3.01	1.4	-0.99	R	>24.5	Garn08
J171436.6+594456	17:14:36.552	+59:44:57.08	-1.4	<6.18	4.11	-1.38	R	23.31	Garn08
J172046.5+584729	17:20:46.548	+58:47:28.91	-77	<12.5	3.71	-0.35	R	>24.5	Garn08
J171453.8+594329	17:14:53.688	+59:43:30.43	-40	<10.3	3.74	-0.05	R	24.70	Garn08
J171315.5+590302	17:13:15.408	+59:03:03.63	-22	<51.2	2.58	-1.37	R	24.31	Garn08
J172057.6+601558	17:20:57.637	+60:15:57.85	43	<11.9	0.65	-0.21	R	>24.5	Garn08
J171909.8+585346	17:19:09.804	+58:53:46.03	-58	<9.62	0.84	-0.29	R	>24.5	Garn08
RID151	03:32:33.44	-27:52:28.1	90	<4.76	0.13	-1.3	i	28.2	CDF-S
RID87	03:32:09.85	-27:50:15.5	90	<0.912	0.05	-0.22	R	>27.5	CDF-S
RID216	03:33:03.31	-27:53:28.0	90	<3.63	0.18	-1.3	R	>25.5	CDF-S
RID97	03:32:13.09	-27:43:50.7	90	<13.9	1.4	-1.0	-	-	CDF-S
RID100	03:32:13.36	-27:39:34.8	135	<24.6	0.06	-1.1	R	>25.5	CDF-S
CENSORS26	09:52:17.69	-20:08:36.20	90	<7.07	38.7	-0.97	K	>20.6	CENSORS

below 0.1 mJy [e.g. Padovani *et al.*, 2009; Mainieri *et al.*, 2008]. As presented earlier in this Chapter, the number of LERGs above 10^{26} W Hz^{-1} is negligible (10^{26} W Hz^{-1} corresponds to a flux density of $\sim$ 5, 1, 0.3, and 0.2 mJy at z = 2, 4, 6, and 8 respectively). Sources above this luminosity are essentially all high-excitation radio galaxies, and hence should have powerful line emission, enabling detection of the Lyα line. Local AGN and star forming galaxies with any reasonable amount of dust absorption will be bright in thermal dust emission in the Spitzer mid-infrared surveys (e.g. 24 μm), leading to the likelihood that any sources without mid-infrared counterparts are moderately powerful AGN at very high redshift. This all suggests that an optimal selection would involve a $\sim$1mJy cut at 1.4 GHz, searching for sources without an optical or near/mid-infrared counterpart, as has been recently successfully trialled by, e.g. Jarvis *et al.* [2009]. Also of interest is whether extending the radio flux cut down to 0.1 mJy would offer any improvement in selecting very high redshift radio galaxies - this would potentially probe out to higher redshift, but would be more at risk of contamination by star-forming galaxies and more moderate redshift LERGs. This is a particularly timely area of investigation, as recently submillimetre μJy radio galaxies have been identified for the first time at z>4, with at least one that meets the broad criteria for an IFRS, along with evidence for hosting both a starburst and an AGN, at a moderate radio luminosity of $\log P_{1.4GHz}\sim$24.5 W Hz^{-1} [Coppin *et al.*, 2009], these are another possible population behind IFRS.

6.10 Spectroscopic Follow-Up of Infrared Faint Radio Sources (IFRS)

Two samples of Infra-red Faint Radio Sources were hence selected, based on these criteria, for spectroscopic targeting during two observing runs.

The first was a sample of 14 sources selected by Garn and Alexander [2008] by cross-matching deep 1.4GHz and 610 MHz radio data of the xFLS field with Spitzer. These display a variety of spectral indices, from flat to USS spectra, and are faint or undetected in the R band, and Spitzer wavelengths. Eight of these sources, selected to be representative of as wide range in radio and infrared properties as possible, were observed as part of a two night observing run with the William Herschel Telescope on La Palma in July 2010. Each source was observed for up to two hours, with a succession of 15 minute exposures, nodded to improve sky subtraction. The

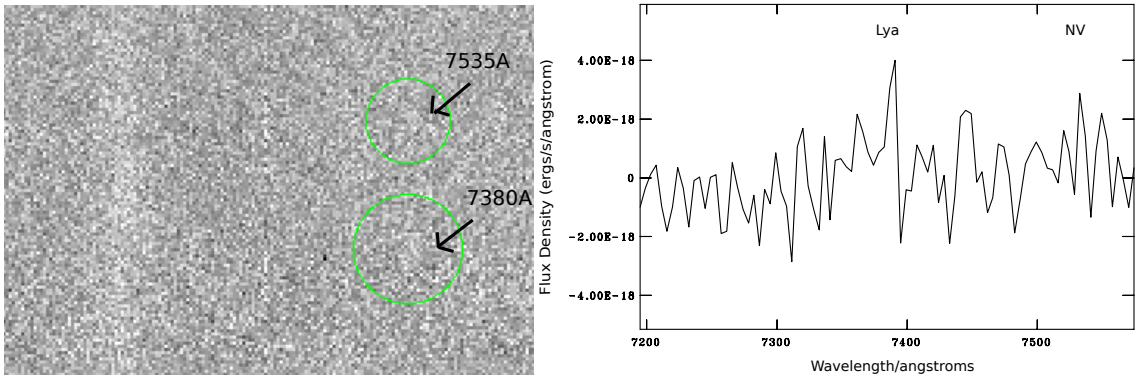

Figure 6.18: The 2D and 1D EFOSC2 spectra for RID87.

weather conditions during the run were variable, with Saharan dust and thin cloud affecting much of the second night. Each spectrum was fully reduced in IRAF following the same procedure as detailed for the CENSORS sources in Chapter 3, and carefully double checked to ensure the source candidate positioning was correct. Unfortunately, none of the eight sources were successfully detected in the WHT spectra: upper limits in Lyα (or any other emission line) flux from measuring the noise in the middle of the red arm (around 7000$\mathring{A}$) exposures are listed in Table 6.3.

Concurrently, another independent sample of Infra-red Faint Radio Sources was observed during the EFOSC2 CENSORS run (as detailed in Chapter 3) in February 2011. This seven source sample was compiled from all radio sources in the Chandra Deep Field-South (CDF-S) with a radio flux above 0.05μJy and detected only in Spitzer 3.6μm or 4.5μm imaging, or undetected. The CDF-S has been observed deeply at optical, near-IR and Spitzer wavelengths [Mainieri *et al.*, 2008], as part of the Great Observatories Origins Deep Survey (see Kellermann *et al.* [2008] for a full description). Five of these were observed for 1.5 hours each during the run, and were reduced following the same reduction procedure in IRAF as for the CENSORS sources, detailed in Chapter 3. CENSORS 26 was also observed as part of the same run, and is also an IFRS. Four of the CDF-S sources and CENSORS 26 were confirmed non-detections, and again, as for the Garn and Alexander [2008] sample, upper limits in Lyα flux are listed in Table 6.3. The fifth source, RID 87, showed a possible very faint line detection, as is highlighted in Figure 6.18.

6.10.1 RID 87: EFOSC2 Spectrum

RID 87 is undetected in the optical or K band [see Brusa *et al.*, 2009], and has a flat spectral index between 4.8 and 1.4GHz of -0.22. The source also has a faint X-ray detection, logL_X = 42.7 [Tozzi *et al.*, 2009], along with a firm faint detection in most of the IRAC Spitzer bands (the CDFS is covered by some of the deepest Spitzer data ever taken - the SIMPLE survey, Damen *et al.* [2011]). The Spitzer colours of RID 87 taken from Cardamone *et al.* [2008], log(S8.0 /S4.5)=0.52 and log(S5.8 /S3.6)=0.37, place the source firmly on the AGN loci, in the Spitzer colour-

colour plot from Lacy *et al.* [2004]. By fitting spectral energy distributions to this source, Brusa *et al.* [2009] determine a photometric redshift of z>5. The X-ray detection, in conjunction with the flat radio spectral index, Spitzer colours and no optical or K-band detection verify the AGN nature of the source, and allow us to firmly rule out a heavily obscured star forming galaxy at moderate redshift. The 1.5 hour observation with EFOSC2 shows two faint line features located exactly on the radio position, which are consistent with Lyα and NV at S/N of 4 and 2 respectively, implying a redshift of 5.08 (see Figure 6.18). These features are not CCD artifacts or cosmic rays but yet are too weak to be secure. Note that given the expected line fluxes for these sources, this is consistent with what might be expected. As this feature was too faint to be a confirmed line detection, 3 hours of XSHOOTER time on the VLT was proposed for and successfully obtained in order to follow up the source.

6.10.2 X-SHOOTER Observations

X-SHOOTER is an echelle spectrograph with three arms covering the UVB, VIS and NIR wavelength ranges, and is currently the most sensitive ground-based instrument covering both the optical and near-infrared wavebands. The UV, visible and NIR arms were used with a slit width of 1.3, 1.5 and 1.2 arcsec respectively, as use of a 1.5" slit in the optical for centering to the radio position has been demonstrated to be successful in previous observations. The time on each source was split into four observing blocks of 3x0.5 hour and 1x0.75 hour, in order to maximise exposure time and minimise overheads within the individual Observation Block time constraint of 1 hour on X-SHOOTER. Each half-hour block was composed of 2x15 minute exposures with nodding along the slit to improve sky subtraction, with the final 15 minute exposure completed in stare mode. All four observing blocks were completed in period 88A in Service mode between October 2011 and February 2012 (ESO program 088.A-0455(A)).

6.10.3 Reduction Procedure

The reduction of the X-SHOOTER spectrum was completed using the XSHOOTER pipeline v1.3.7[1] from ESO which contains a series of recipes designed for optimal reduction of both nodding and stare science exposures, and the ESO Gasgano GUI.

Firstly, for the optical (VIS), bias frames were combined into a Master bias frame using the recipe **xsh_bias** in all necessary frame configurations. **xsh_predict** was then run to generate a guess order solution for the raw frames, and **xsh_order** run to refine the the guess order predictions into an order table for use as input in subsequent reduction steps. A master flat was then created using **xsh_mflat**, and then the recipe **xsh_2dmap** run to create a table of the dispersion solution coefficients and the 2d instrument bidimensional mapping. At this point, several test scripts available with the pipeline were run to confirm that all the order prediction steps had produced correct output. The recipe **xsh_flexcomp** was run to compute instrument flexures: this is an optional step for nodding/stare mode, but can help in improving sky subtraction, important for a faint target as in this case. Finally the standard

[1]The XSHOOTER User Manual can be found here: `http://www.eso.org/sci/facilities/paranal/instruments/xshooter/doc/`

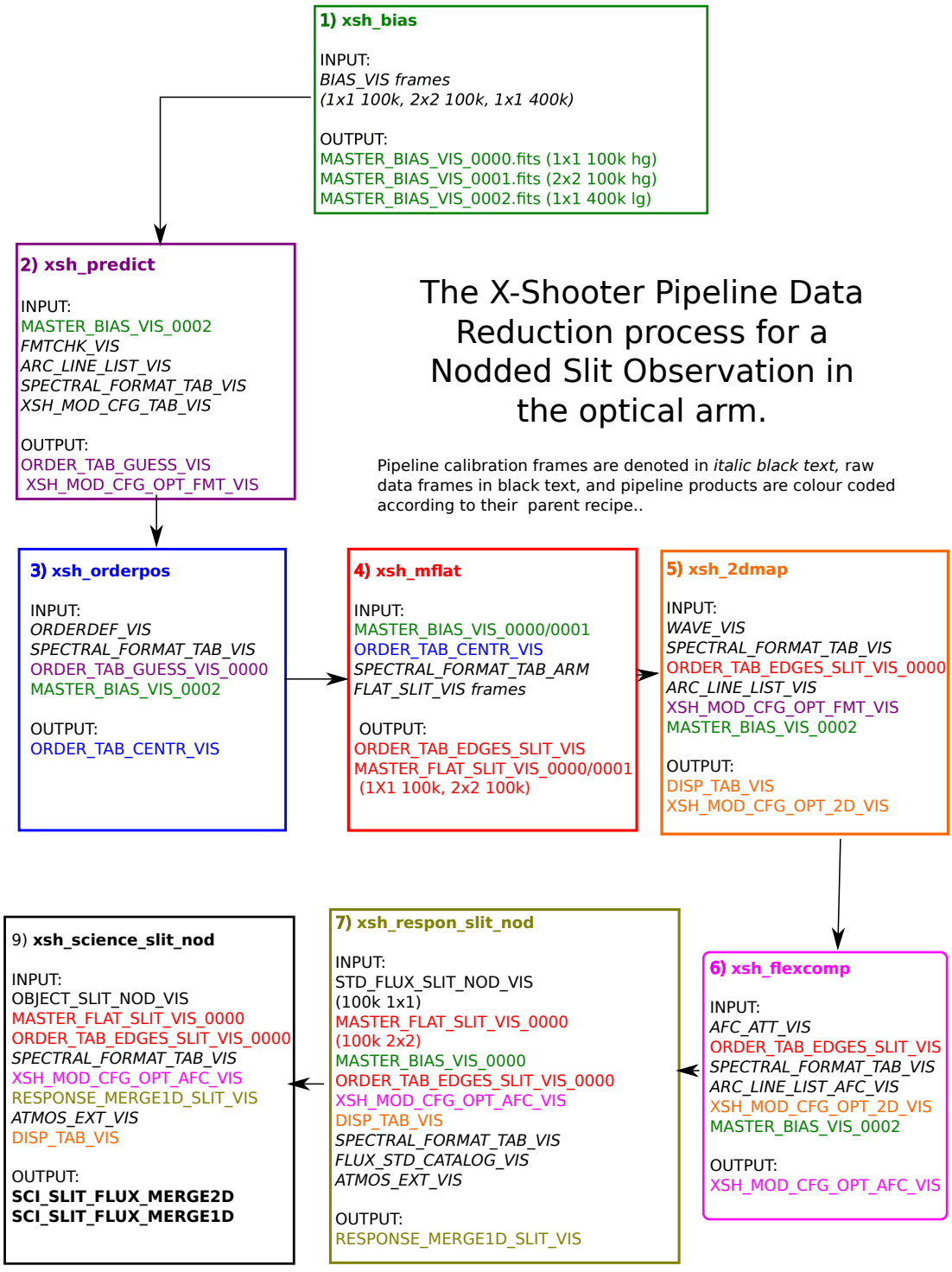

Figure 6.19: The XSHOOTER Data Reduction Process Illustrated.

star data were reduced using **xsh_respon_slit_nod**, and the science frames shifted, combined, and wavelength and flux calibrated using **xsh_science_slit_nod**. The sequence of these recipes, and the necessary inputs, and important products produced by each are illustrated in Figure 6.19.

Reduction of the near-infrared (NIR) arm frames follows the same procedure, with the exception that a master dark frame is needed, created using **xs_dark**, and a master bias frame is not, and a map of non-linear pixels (created automatically as part of the calibration products) needs to be included in the reduction steps. One frame of the UVB arm was reduced in a similar fashion to the VIS arm data to confirm no features were present there.

The resulting images from each of the three long observation blocks in the optical and infrared arms were mean combined using the IRAF task incombine. It was decided not to include the final observation block (45 minute) nod + stare exposures, as the seeing was poor during this observation in comparison with the others.

6.10.4 Results

The resulting spectrum in the VIS arm is shown in Figures 6.20 and 6.21. The spectrum should fall in the central area (where the two nodded frames are combined, and where the sky background subtraction is best[2]. The maximum upper limit in flux, measured from the combined exposures is 9.12e-18 ergs s^{-1} cm^{-2}, a factor of 6 times deeper than the EFOSC2 observations of RID87 at 7380$\mathring{A}$. There is no clear detection of the line present at the expected wavelength. A visual examination of the UVB and NIR frames shows no detection of any line features or continuum at the expected central position either. The only feature present in the frames is in the optical at 7575$\mathring{A}$, offset from the target position by a few arcseconds, consistent with an [OII] doublet.

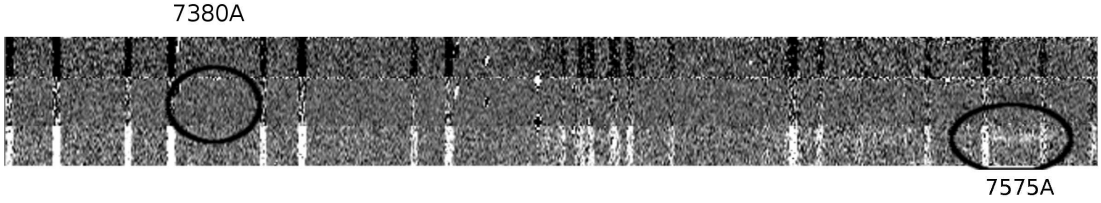

Figure 6.20: The XSHOOTER spectrum of RID 87 in the visible arm. The faint line visible in the EFOSC2 spectrum should be seen at 7380A, however the only clearly detected feature is an [OII] doublet several arcseconds away from the target position.

6.11 IFRS Discussion

Unfortunately, for RID 87 the faint detection noted in the EFOSC2 spectrum cannot be confirmed with the deeper XSHOOTER data, in both the optical and near-infrared arms.

[2]Note that good sky line background subtraction is still difficult to achieve with the pipeline: see, for example, `http://www.eso.org/public/abouteso/committees/uc/uc-35th.html`

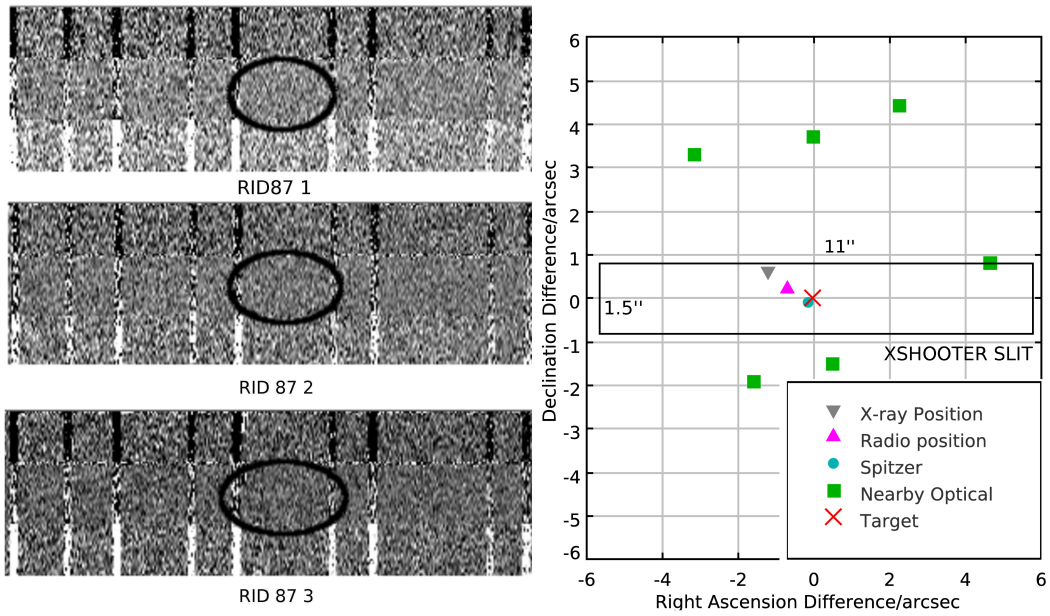

Figure 6.21: Left: The XSHOOTER spectrum of RID 87 in the visible arm. The reduced frame from each of the three 30 minute observations are shown. The third observation shows a faint feature at the expected wavelength, but this does not appear in the other two observations (observing conditions similar). Right: The distribution of the Spitzer, Radio and X-ray detections of RID87 on the sky, and the XSHOOTER target position. Also plotted are the positions of several nearby optical sources from the MUSYC catalogue (the deepest optical catalogue available over this area).

The only feature visible is a clear [OII] doublet, approximately three arcseconds away from the target position on the spectrum, giving a redshift of z = 1.033. There is one MUSYC source located about this distance along the slit. This gives rise to two possibilities, that either the true host is undetected in the XSHOOTER observations, or that that the host is in fact the other nearby MUSYC source close to the target position (the source perhaps being a radio lobe, or astrometric errors occurring between the respective catalogues).

Either way, this 'null' result gives rise to several interesting points.

- Firstly, if the true host is undetected to this level, does it still seem likely that it lies at very high redshift? In Figure 6.22, the ratio of Lyα flux to radio flux vs radio size and redshift is plotted for radio galaxies within the CENSORS sample for which there is a Lyα measurement, along with six of the highest redshift powerful radio sources known (cf. Chapter 4) and 2 μJy z>4 radio sources reported in the literature for comparison. For the majority of the IFRS sources, if the true Lyα flux was many times fainter than the assumed upper limit, then it could still be consistent with the Lyα/ratio flux ratios shown by high-z radio galaxies, and thus it is not possible to rule a high-z nature out for any particular source. However, given that approximately half of the IFRS Lyα limit/radio ratios fall within an area occupied by known high-z radio galaxies, it is surprising that no

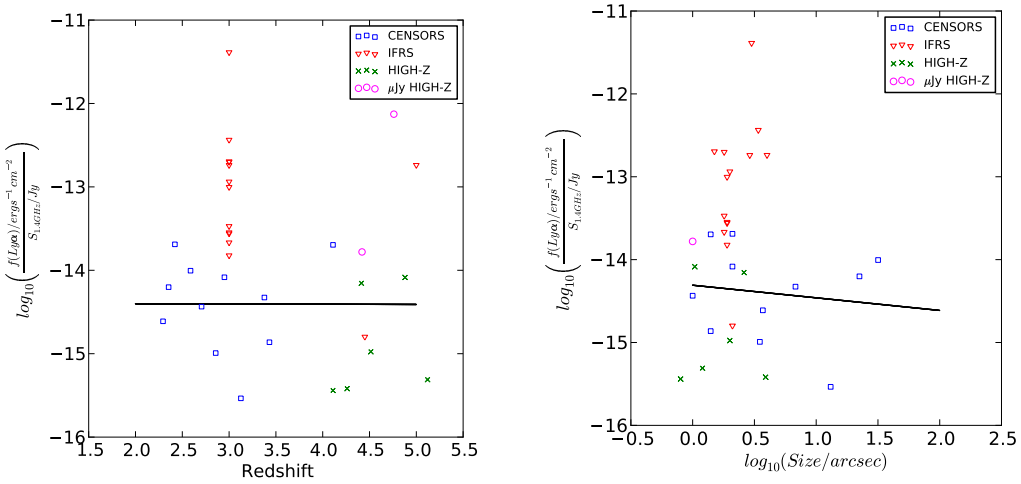

Figure 6.22: Plotted above is the ratio of Lyα flux to radio flux against redshift and radio size for all radio galaxies in the CENSORS sample with measured Lyα (blue squares). The IFRS Lyα flux limits are plotted as red triangles (note only two of these have an associated redshift limit estimate, for the rest a z=3 is assumed, in order that the distribution of Lyα limit/radio ratios may be compared to known high-z galaxies. For comparison, also plotted are the Lyα/radio flux ratios and sizes for the six highest redshift powerful radio galaxies known, and two μJy radio sources also at z>4 [Waddington *et al.*, 1999; Coppin *et al.*, 2009]. The CENSORS, and high redshift sources have similar Lyα to radio ratios, distributed around $\sim$-14.5. The μJy radio sources have higher ratios (the source from Coppin *et al.* [2009] in particular), most likely due to more star-formation, and a smaller contribution from the central AGN). Despite the poor conditions for some of the observations, roughly half the IFRS reach Lyα/radio ratios comparable to known high-z radio galaxies.

Lyα emission was successfully detected in any of the sources.

- It is possible that IFRS sources could be LERGs at moderate redshifts (z>2), where continuum emission shortward of the 4000$\mathring{A}$ break is too weak to be detected in the optical. Taking the CDF-S field as an example, where there are 7 IFRS sources, over an area of 0.11 square degrees with a limiting flux of 0.05mJy, and assuming no further evolution in the RLF over the redshift range of z=1-5 the RLF determined previously gives 16 LERGs (and only 8 HERGs) between z=1-5. If there is weak redshift evolution in the LERG RLF, this number will be higher, and could conceivably explain the presence of the seven 'IFRS' sources (although note that many of the LERGs would have host galaxy identifications, and hence not be classified as IFRS). However, as shown earlier, there are indications of a turnover in the LERG RLF, consistent with theoretical predictions, so the true number of LERGs expected will be lower. A more precise prediction awaits a direct measurement of the LERG RLF out to high redshift.

- From Figure 6.21, it is clear that the astrometric solutions become less reliable for successively fainter catalogues. In the case of RID 87, the X-ray, radio, Spitzer and

optical positions span a range of ∼2-3 arcseconds. Offsets of up to 2 arcseconds are also observed between GMRT, VLA, IRAC and optical positions for the Garn et al sample. This is very different to the case of brighter radio samples, e.g. CENSORS, where host galaxy association between radio and optical is achievable with ≤1 arcsecond accuracy when the host galaxy is successfully detected.

- Related to the issue of correct host galaxy identification, is the possiblity of faint very steep spectrum radio lobes being missed, and leading to an incorrect identification. This is an area where the low frequency, deep surveys of LOFAR will become invaluable in ruling out the presence of any ultra-steep spectrum lobes.

The results strongly suggest that in future studies of IFRS, bright, mJy samples should be preferred, in order to cover as much of the log(Lyα/radio)-z plane as possible within the capability of existing ground-based spectrometers, and thus definitively ascertain whether IFRS are indeed analogous to known high-z radio galaxies.

All the currently known z>4 powerful radio galaxies have $S_{1.4GHz}$>10 mJy. The very few known μJy radio sources at z>4 have higher Lyα/radio ratios, most likely due to a significant star-forming component, and a relatively smaller AGN contribution (i.e. they are not analogues of classical double radio galaxies). Noting low number statistics, it does appear unlikely that the μJy IFRS investigated here are similar to these sources, as no line emission was detected.

One possibility to investigate IFRS sources further could be via the combination of VLBI observations, as has been done recently for a single IFRS by Norris *et al.* [2007], enabling the accurate determination of the position of the source radio core (a high brightness temperature core would indicate a strong AGN, and hence should display powerful emission lines), or very deep low frequency radio observations (e.g. by LOFAR) in order to remove any ambiguities in the host position.

In conclusion, investigating the multiwavelength spectra of 'missing redshift' candidates has not enabled any significant constraints to be made on the nature of these sources. The possibilities that a number of these could be LERGs or sources enbedded in a dense medium, attenuating any line emission remain, as does the possibility of a high-z nature. It is however unlikely that all are high-z classical radio galaxies, as despite at least half of the IFRS sample having Lyα limits lying in the same locus as known high-z galaxies, no line emission was successfully detected.

6.12 Summary

In this Chapter, the very first determination of the HERG and LERG luminosity functions has been determined over the bulk of cosmic time, out to a redshift of 1. HERGs are shown to have strong positive evolution when comparing the RLF at z=0.5-1.0 to the local RLF at z<0.3, fully consistent with theoretical predictions. Higher luminosity LERGs are shown to have weak (a factor of 2-3) positive evolution too when compared to the local RLF, which is within the margin of error of theoretical predictions (these generally predict no evolution out

to z=1). All the evidence collated supports the HERG RLF continuing to evolve past z=1, but whether the LERG RLF also continues to evolve (positively or negatively) past z=1 remains an open question, which awaits further data.

Using these RLFs, it is shown that LERGs could account for at least some of the 'missing-z' sources, but most likely not all. An investigation of two IFRS samples detected no line emission from any of the sources, and provided little additional evidence to confirm the IFRS sources were at high redshift. It is likely that at least some of these sources are LERGs at more moderate redshifts, or are embedded in a dense, dusty medium which is attenuating any emission line flux. Optimal candidates for high-z radio galaxy searches should be sourced from bright mJy samples.

Table 6.4: The Wall & Peacock 1985 sample, with sources with α<-0.5 and 0.5<z<1.0 selected. Col1: Source name, Col2: redshift, Col3: redshift type S-spectroscopic, P-photometric, Col4: 1.4 GHz radio flux, Col5: Class HERG - high excitation, LERG - low excitation, Q - quasar, S - starburst, U - unclassifiable, O - out of sample (a photo-z in range 0.5<z<1, but new spectroscopy places source outwith this range), Col6: Equivalent width [OII], Col7: Equivalent width [OIII] (observed frame) Lawrence96 measures are assumed to be in the rest-frame & are converted to observed frame, Col8: [OII] flux, Col9: [OIII] flux, Col10: Spectrum D - measured directly from raw spectrum, P - measured from published paper spectrum/tabulated line data, N - no spectral data is currently available for this source, Col11: Reference, Lawrence96 - Lawrence *et al.* [1996], 2DF-QSO/SDSS - spectrum taken from 2DF/SDSS online repository,Aldcroft94 - Aldcroft *et al.* [1994], Gelderman94 - Gelderman and Whittle [1994], Hirst03 - Hirst *et al.* [2003], Holt09 - Holt *et al.* [2009], Johnson05 - Johnson & Best, priv. com, Labiano07 - Labiano *et al.* [2007], Rigby2011 - Rigby *et al.* [2011],Tadhunter93 - Tadhunter *et al.* [1993], deVries95 -de Vries *et al.* [1995], diSerego94 - di Serego-Alighieri *et al.* [1994], Col12: Notes on individual source - 'BE' indicates that the line equivalent widths have been estimated by eye from published spectra.

Name	z	ztype	$S_{1.4GHz}$ Jy	Class	EW[OII] Å	EW[OIII] Å	f[OII]x10^{-16} ergs s^{-1} cm^{-2}	f[OIII]x10^{-16} ergs s^{-1} cm^{-2}	Spectrum	Reference	Note
0538+49	0.55	S	21.79	HERG	41.1	157.3	-	-	P	Lawrence96	-
1828+48	0.69	S	16.69	HERG	5.1	102.1	-	-	P	Lawrence96	-
1328+30	0.85	S	14.7	Q	0.67	-	-	-	P	SDSS	Possible quasar.
0809+48	0.87	S	14.37	HERG	25.3	172.4	-	-	P	Lawrence96	-
0407-65	0.962	S	13.47	HERG	157.0	-	-	-	D	Rigby11	-
0518+16	0.76	S	12.99	Q	-	205.0	-	-	P	Geraldman94	-
0409-75	0.693	S	12.72	HERG	20.0	-	-	-	P	Tadhunter93	BE, marginal - has extended OII, but weak OIII
1458+71	0.9	S	8.89	HERG	10.5	-	-	-	P	Lawrence96	-
0316+16	0.907	S	8.01	HERG	-	50.0	5.4	33.0	P	Labiano07	BE (EWs), fluxes taken from paper.
2032-35	0.631	S	7.62	HERG	-	-	-	-	D	Johnson05	-
1005+07	0.88	S	6.62	HERG	-	-	-	-	P	Hirst03	NIR Spectrum, Ha detected. Hirst03 classify as HERG.
0252-71	0.568	S	6.55	HERG	-	10.0	-	-	P	Tadhunter93	BE,noted as high ionisation
1157+73	0.97	S	6.41	HERG	123.7	409.0	-	-	P	Lawrence96	-
1609+66	0.55	S	6.19	HERG	296.5	829.1	-	-	P	Lawrence96	-
0404+76	0.599	S	6.01	HERG	153.0	65.7	-	-	P	Lawrence96	-
1254+47	1.0	S	5.59	HERG	338.4	-	-	-	P	Lawrence96	-
1634+62	0.99	S	5.09	HERG	548.4	-	-	-	P	Lawrence96	-
1526-423	0.5	P	5.08	U	-	-	-	-	N	-	-
0117-15	0.565	S	4.91	HERG	-	20.0	-	-	P	Tadhunter93	BE,noted as high ionisation with extended emission lines.
2128+04	0.99	S	4.84	U	-	-	-	-	P	-	-
2331-41	0.907	S	4.84	HERG	-	-	3.94	25.43	P	diSerego94	-
0022-42	0.937	S	4.71	HERG	50.0	50.0	-	-	P	deVries95	BE
1453-10	0.94	S	4.6	HERG	-	-	-	-	P	Aldcroft94	MgII detected only.
1637+62	0.75	S	4.45	HERG	3.15	20.3	-	-	P	Lawrence96	-

Continued on next page

Table 6.4 – continued from previous page

Name	z	ztype	$S_{1.4GHz}$ Jy	Class	EW[OII] $\AA$	EW[OIII] $\AA$	f[OII]x10^{-16} ergs s^{-1} cm^{-2}	f[OIII]x10^{-16} ergs s^{-1} cm^{-2}	Spectrum	Reference	Note
2342+82	0.73	S	4.35	HERG	39.6	237.7	-	-	P	Lawrence96	-
1136-13	0.55	S	4.29	Q	-	20.0	-	-	P	Tadhunter93	BE,noted as having broad lines, quasar-like spectrum
2135-20	0.635	S	4.27	HERG	-	25.0	-	-	P	Holt09	BE
0235-19	0.62	S	4.27	HERG	-	20.0	-	-	P	Tadhunter93	BE,noted as high ionisation
0157-31	0.68	S	4.03	Q	-	-	-	-	P	2DF_QSO	-

Table 6.5: The combined CoNFIG 1 and 2r sample, selected with α<-0.5 and a redshift range of 0.5<z<1.0. Col1: Source name, Col2: redshift, Col3: redshift type S-spectroscopic, P-photometric, Col4: 1.4 GHz radio flux, Col5: Class HERG - high excitation, LERG - low excitation, Q - quasar, S - starburst, U - unclassifiable, O - out of sample (a photo-z in range 0.5<z<1, but new spectroscopy places source outwith this range), Col6: Equivalent width [OII], Col7: Equivalent width [OIII] (observed frame), Col8: Spectrum D - measured directly from raw spectrum, P - measured from published paper spectrum/tabulated line data, N - no spectral data is currently available for this source, Col9: Reference, SDSS - spectrum taken from SDSS online repository, Best99 - Best *et al.* [1999], Bremer92 - Bremer *et al.* [1992],Grimes03 - Grimes *et al.* [2004] ,Hewitt89 - Hewitt and Burbidge [1989],Hewitt93 - Hewitt and Burbidge [1993], Jackson97 - Jackson and Rawlings [1997], Kuraszk2002 - Kuraszkiewicz *et al.* [2002], Lahulla91 - Lahulla *et al.* [1991], Marziani96 - Marziani *et al.* [1996], Maxfield95 - Maxfield *et al.* [1995], Schmidt1974 - Schmidt [1974], WHT12 - new data as presented in Section 6.4.

Name	z	ztype	$S_{1.4GHz}$ Jy	Class	EW[OII] $\AA$	EW[OIII] $\AA$	f[OII]x10^{-16} ergs s^{-1} cm^{-2}	f[OIII]x10^{-16} ergs s^{-1} cm^{-2}	Spectrum	Reference	Note
3C196	0.871	S	15.01	Q*	-	-	-	-	P	None	Source excluded as in WP85
3C237	0.88	S	6.52	HERG*	-	-	-	-	P	None	Source excluded as in WP85
3C280	0.996	S	5.1	HERG*	-	-	-	-	N	Grimes2003	Source excluded as in WP85
3C216	0.67	S	4.23	Q	154.0	28.0	-	-	P	SDSS	None
3C228	0.552	S	3.71	HERG	-	-	-	-	N	Grimes2003	None
3C225	0.58	S	3.34	HERG	-	-	-	-	N	Jackson1997	None
3C337	0.63	S	3.16	HERG	-	-	-	-	N	Jackson1997	None
3C254	0.7361	S	3.13	Q	-	-	-	-	N	Grimes2003	None
4C-06.35	0.625	S	2.96	Q	-	-	-	-	N	Best1999	None
3C275.1	0.557	S	2.9	Q	-	-	-	-	N	Grimes2003	None
3C265	0.8105	S	2.89	HERG	-	-	-	-	N	Jackson1997	None
3C247	0.749	S	2.88	HERG	-	-	-	-	N	Grimes2003	None
4C03.18	0.535	S	2.71	HERG	30.0	-	1.5	-	P	Best1999	None
3C336	0.927	S	2.61	Q	-	-	-	-	N	Jackson1997	None
3C207	0.6804	S	2.61	Q	-	-	-	-	P	Marziani96	None
3C340	0.775	S	2.6	HERG	-	-	-	-	N	Jackson1997	None
4C19.44	0.72	S	2.59	Q	-	-	-	-	P	Kuraszk2002	None
4C33.21	0.701	P	2.47	U	-	-	-	-	P	None	None
4C01.39	0.819	S	2.4	HERG	95.0	-	6.4	-	P	Best1999	None
3C289	0.967	S	2.4	HERG	-	-	-	-	N	Grimes2003	None
3C226	0.8178	S	2.39	HERG	159.0	-	12.1	-	P	Best2000	None
4C37.24	0.9188	S	2.26	Q	-	-	-	-	P	SDSS	None
4C01.42	0.792	S	2.26	HERG	108.0	-	5.6	-	P	Best1999	None
4C59.16	0.961	S	2.18	HERG	44.0	105.0	13.43	13.07	D	WHT12	None
3C217	0.898	S	2.09	HERG	544.0	-	48.5	-	P	Best2000	None
3C334	0.555	S	1.99	Q	-	-	-	-	N	Jackson1997	None
3C277.2	0.766	S	1.95	HERG	-	-	-	-	N	Grimes2003	None
1355+01	0.797	S	1.92	HERG	113.0	158.0	34.95	90.77	D	WHT12	None
3C202	0.6237	P	1.88	U	-	-	-	-	N	None	None

Continued on next page

Table 6.5 – continued from previous page

Name	z	ztype	$S_{1.4GHz}$ Jy	Class	EW[OII] Å	EW[OIII] Å	f[OII]x10^{-16} ergs s^{-1} cm^{-2}	f[OIII]x10^{-16} ergs s^{-1} cm^{-2}	Spectrum	Reference	Note
3C352	0.806	S	1.87	HERG	-	-	-	-	N	Grimes2003	None
4C20.33	0.871	S	1.81	Q	-	-	-	-	P	Hewitt89	None
4C13.56	0.672	S	1.81	HERG	26.0	47.0	4.65	-	D	WHT12	Some [OIII] flux lost by sky absorption
4C54.25	0.716	S	1.74	U	18.0	-	2.93	-	D	WHT12	Uncertain z.
4C53.18	0.869	S	1.6	U	11.0	-	1.0	-	D	WHT12	None
4C43.22	0.5724	S	1.57	HERG	30.4	-	-	-	P	Maxfield95	None
4C17.56	0.777	S	1.57	HERG	37.0	18.0	4.08	4.5	D	WHT12	None
4C24.31	0.6532	S	1.56	Q	-	-	-	-	P	SDSS	None
4C17.48	0.521	S	1.53	HERG	24.0	16.0	4.91	-	D	WHT12	Some [OIII] flux lost by sky absorption
4C04.40	0.531	S	1.5	LERG	4.0	-	0.48	-	D	WHT12	Absorption features only.
3C288.1	0.9642	S	1.49	Q	-	-	-	-	N	Jackson1997	None
4C-00.50	0.8916	S	1.47	Q	-	-	-	-	P	SDSS	None
4C46.21	0.527	S	1.44	HERG	69.0	67.0	38.79	-	D	WHT12	None
3C344	0.52	S	1.42	U	-	-	-	-	P	None	None
4C16.27	1.452	S	1.37	O	25.0	-	3.4	-	D	WHT12	None
4C61.34	0.523	S	1.35	Q	-	-	-	-	P	None	None
3C272	0.944	S	1.35	HERG	-	-	-	-	N	Jackson1997	None
3C342	0.561	S	1.34	Q	-	-	-	-	P	Schmidt	None
3C323	0.679	S	1.34	HERG	-	-	-	-	N	Jackson1997	None
4C20.29	0.68	S	1.33	Q*	-	-	-	-	P	None	Duplicate source in catalogues of Gendre2010
4C51.25	0.561	S	1.31	HERG	16.0	28.0	5.43	22.3	D	WHT12	None
4C20.29	0.68	S	1.27	Q	-	-	-	-	P	Hewitt93	None
4C32.34	0.564	S	1.26	HERG	126.0	428.0	59.08	401.59	D	WHT12	None
3C232	0.5306	S	1.25	Q	-	-	-	-	P	SDSS	None
4C29.46	0.397	S	1.23	O	-	184.0	-	177.01	D	WHT12	None
1152+551	1.195	S	1.23	O	21.0	-	8.07	-	D	WHT12	None
4C46.25	0.7428	S	1.16	U	29.0	-	-	-	P	Maxfield95	None
3C261	0.6133	S	1.15	Q	-	-	-	-	P	Schmidt1974	None
3C281	0.599	S	1.12	Q	-	-	-	-	N	Bremer92	None
4C12.41	1.1	S	1.11	O	33.0	-	10.02	-	D	WHT12	None
4C59.11	0.707	S	1.08	HERG	-	25.0	-	72.38	D	WHT12	None
4C59.10	1.245	S	1.08	O	99.0	-	5.33	-	D	WHT12	None
4C00.35	0.746	S	1.08	HERG	34.0	12.0	13.1	9.57	D	WHT12	[OIII] next to sky line.
4C15.34	0.9748	I	1.07	U	-	-	-	-	P	None	None

Continued on next page

Table 6.5 – continued from previous page

Name	z	ztype	$S_{1.4GHz}$ Jy	Class	EW[OII] $\AA$	EW[OIII] $\AA$	f[OII]x10^{-16} ergs s^{-1} cm^{-2}	f[OIII]x10^{-16} ergs s^{-1} cm^{-2}	Spectrum	Reference	Note
4C17.49	0.69	S	1.06	U	-	-	-	-	D	WHT12	Uncertain z.
4C20.28	0.424	S	1.05	O	60.0	163.0	8.15	53.05	D	WHT12	None
4C17.54	0.675	S	1.01	HERG	134.0	73.0	14.12	14.52	D	WHT12	None

Table 6.6: The Parkes Selected Regions sample, selected with α<-0.5 and a redshift range of 0.5<z<1.0. Col1: Source name, Col2: redshift, Col3: redshift type 1-spectroscopic, 2-4-photometric, Col4: 1.4 GHz radio flux, Col5: Class HERG - high excitation, LERG - low excitation, Q - quasar, S - starburst, U - unclassifiable, O - out of sample (a photo-z in range 0.5<z<1, but new spectroscopy places source outwith this range), Col6: Equivalent width [OII], Col7: Equivalent width [OIII] (observed frame), Col8: [OII] flux, Col9: [OIII] flux, Col10: Spectrum D - measured directly from raw spectrum, P - measured from published paper spectrum/tabulated line data, N - no spectral data is currently available for this source, Col11: Reference, Dunlop89 - Dunlop *et al.* [1989] , Allington91 - Allington-Smith *et al.* [1991], Wright77 - Wright *et al.* [1977], WHT12 - new data as presented in Section 6.4, Col12: Notes on individual sources.

Name	z	ztype	$S_{1.4GHz}$ Jy	Class	EW[OII] $\AA$	EW[OIII] $\AA$	f[OII]x10^{-16} ergs s^{-1} cm^{-2}	f[OIII]x10^{-16} ergs s^{-1} cm^{-2}	Spectrum	Reference	Note
2154-184	0.668	S	2.39	Q	-	-	-	-	P	Dunlop89	None
0010+005	0.606	S	1.74	U	-	-	-	-	N	None	None
1352+008	1.167	S	1.17	O	26.0	-	1.72	-	D	WHT12	None
0222-008	0.687	S	1.11	Q	-	50.0	-	-	P	Wright77	None
1337-033	0.487	S	1.01	O	-	192.0	-	4.91	D	WHT12	See Figure 6.9.
2355-010	0.76	P	0.83	U	-	-	-	-	N	None	None
0059+017	0.52	P	0.8	U	-	-	-	-	N	None	None
1336+020	0.567	S	0.74	HERG	44.0	261.0	32.26	335.85	D	WHT12	None
2159-201	0.75	P	0.6	U	-	-	-	-	N	None	None
2158-177	0.81	P	0.54	U	-	-	-	-	N	None	None
0242+028	0.767	S	0.53	HERG	194.0	-	-	-	P	Allington91	None
0043+000	0.6	P	0.53	U	-	-	-	-	N	None	None
2155-202	0.55	P	0.49	U	-	-	-	-	N	None	None
2213-156	0.81	P	0.48	U	-	-	-	-	N	None	None
0003+006	0.92	P	0.47	U	-	-	-	-	N	None	None
0223-023	0.93	P	0.41	U	-	-	-	-	N	None	None
0235-019	0.84	S	0.4	HERG	68.0	179.0	-	-	P	Allington91	None
1329+012	0.873	S	0.39	U	19.0	-	1.09	-	D	WHT12	None
2356+033	0.57	P	0.38	U	-	-	-	-	N	None	None
0000+035	0.61	P	0.37	U	-	-	-	-	N	None	None
2354+008	0.73	P	0.31	U	-	-	-	-	N	None	None
2157-214	0.73	P	0.31	U	-	-	-	-	N	None	None
0045-009	0.6	P	0.3	U	-	-	-	-	N	None	None

Table 6.7: The CENSORS sample, selected with α<-0.5 and a redshift range of 0.5<z<1.0. Col1: Source name, Col2: redshift, Col3: redshift type 1-spectroscopic, 2-photometric, Col4: 1.4 GHz radio flux, Col5: Class HERG - high excitation, LERG - low excitation, Q - quasar, S - starburst, U - unclassifiable, O - out of sample (a photo-z in range 0.5<z<1, but new spectroscopy places source outwith this range), Col6: Equivalent width [OII], Col7: Equivalent width [OIII] (observed frame), Col8: [OII] flux, Col9: [OIII] flux, Col10: Spectrum D - measured directly from raw spectrum, P - measured from published paper spectrum/tabulated line data, N - no spectral data is currently available for this source, Col11: Notes on individual sources. Data for sources not already presented in this thesis were taken from Brookes *et al.* [2008]

Name	z	ztype	$S_{1.4GHz}$ Jy	Class	EW[OII] $\AA$	EW[OIII] $\AA$	f[OII]x10^{-16} ergs s^{-1} cm^{-2}	f[OIII]x10^{-16} ergs s^{-1} cm^{-2}	Spectrum	Note
6.0	0.547	S	0.2397	HERG	-	14.0	-	11.0	D	None
12.0	0.821	S	0.0704	HERG	31.0	-	-	-	D	None
17.0	0.893	S	0.0615	U	16.0	-	-	-	D	None
22.0	0.928	S	0.0529	HERG	86.0	-	0.94	-	D	None
29.0	0.965	S	0.0382	HERG	-	-	-	-	D	MgII, NeV in optical. [OII] obscured by sky.
37.0	0.511	S	0.0318	U	-	-	-	-	D	MgII, NeV in optical. No [OII].
43.0	0.778	S	0.0264	U	18.0	-	0.53	-	D	Weak [OII].
45.0	0.796	S	0.0255	LERG	-	-	-	-	D	Absorption features only.
47.0	0.508	S	0.0252	HERG	-	24.0	-	-	D	None
55.0	0.557	S	0.0214	LERG	-	-	-	-	D	Absorption features only.
62.0	0.574	S	0.0184	LERG	-	-	-	-	D	Absorption features only.
65.0	0.549	S	0.0179	LERG	-	-	-	-	D	Absorption features only.
70.0	0.645	S	0.017	HERG	23.0	10.0	-	-	D	None
74.0	0.667	S	0.016	HERG	30.0	14.0	-	-	D	None
138.0	0.508	S	0.0147	U	10.0	-	1.1	-	D	None
83.0	0.521	S	0.0135	HERG	49.0	13.0	2.31	1.1	D	Sky absorption in [OIII]5007 line?
86.0	0.82	P	0.0132	U	-	-	-	-	D	None
89.0	0.909	S	0.013	U	22.0	-	0.17	-	D	None
92.0	0.743	S	0.0126	HERG	3.0	28.0	-	-	D	None
104.0	0.884	P	0.0107	LERG	-	-	-	-	D	No lines in optical or NIR. Faint continuum
107.0	0.512	S	0.0103	LERG	-	-	-	-	D	Absorption features only.
109.0	0.719	P	0.0101	LERG	-	-	-	-	D	Possible weak [OII]
113.0	0.942	P	0.0097	LERG	-	-	-	-	D	No lines in optical or NIR. Faint continuum
115.0	0.545	S	0.0096	LERG	-	-	-	-	D	Absorption features only.
125.0	0.701	S	0.0084	LERG	-	-	-	-	D	Absorption features. No [OII]. Weak NeV
127.0	0.922	S	0.0083	U	21.0	-	1.8	-	D	None
136.0	0.629	S	0.0075	U	19.0	-	1.0	-	D	None
137.0	0.526	S	0.0074	LERG	-	-	-	-	D	Absorption features only.

Table 6.8: The Hercules sample, selected with α<-0.5 and a redshift range of 0.5<z<1.0. Col1: Source name, Col2: redshift, Col3: redshift type S-spectroscopic, P-photometric, Col4: 1.4 GHz radio flux, Col5: Class HERG - high excitation, LERG - low excitation, Q - quasar, S - starburst, U - unclassifiable, O - out of sample (a photo-z in range 0.5<z<1, but new spectroscopy places source outwith this range), Col6: Equivalent width [OII], Col7: Equivalent width [OIII] (observed frame), Col8: [OII] flux, Col9: [OIII] flux, Col10: Spectrum D - measured directly from raw spectrum, P - measured from published paper spectrum/tabulated line data, N - no spectral data is currently available for this source, Col11: Notes on individual sources. WHT12 indicates new spectra have been taken as presented in Section 6.4. The remaining spectra come from Waddington *et al.* [2001].

Name	z	ztype	$S_{1.4GHz}$ Jy	Class	EW[OII] $\AA$	EW[OIII] $\AA$	f[OII]x10^{-16} ergs s^{-1} cm^{-2}	f[OIII]x10^{-16} ergs s^{-1} cm^{-2}	Spectrum	Note
53W008	0.736	S	0.3066	HERG	12.0	23.0	3.17	8.81	D	WHT12
53W031	0.627	S	0.1165	HERG	13.0	7.0	0.97	1.65	D	WHT12.
53W023	0.569	S	0.1099	LERG	-	-	-	-	D	WHT12. Absorption features only.
53W046	0.528	S	0.0631	HERG	-	-	-	-	P	Published spectra with NV, no cover of OII wavelength
53W080	0.542	S	0.0276	Q	10.0	17.0	12.28	17.29	D	WHT12.
53W047	0.532	S	0.0239	LERG	-	-	-	-	D	WHT12. Absorption features only.
53W067	0.759	S	0.0232	LERG	-	-	-	-	D	Absorption only. Possible faint detection OII?
53W026	0.55	S	0.0211	LERG	-	-	-	-	D	Absorption features only.
53W048	0.676	S	0.0115	LERG	-	-	-	-	D	Absorption features only
53W060	0.62	P	0.0097	U	-	-	-	-	N	possible LERG, but uncertain faint single line spectrum
53W041	0.59	P	0.0094	U	-	-	-	-	N	None
53W077	0.786	S	0.0078	LERG	-	-	-	-	D	Absorption features only.
53W005	0.765	S	0.0076	U	23.0	-	3.7	-	D	WHT12
53W019	0.542	S	0.0068	LERG	-	2.0	-	0.3	D	None
53W083	0.628	S	0.0050	LERG	-	-	-	-	D	absorption features only
53W089	0.635	S	0.0025	LERG	-	-	-	-	D	None

Table 6.9: The SXDF sample, selected with a redshift range of 0.5<z<1.0. Col1: Source name, Col2: Source SXDF ID. Col3: redshift Col4: ztype - S = spectroscopic, P = photometric, Col5: 1.4 GHz radio flux, Col6: Type as defined in Simpson *et al.* [2012], Col7: Class HERG - high excitation, LERG - low excitation, Q - quasar, S - starburst, U - unclassifiable, O - out of sample (a photo-z in range 0.5<z<1, but new spectroscopy places source outwith this range),Col8: Equivalent width [OII], Col9: Equivalent width [OIII] (observed frame).

Name	SXDF_ID	z	ztype	$S_{1.4GHz}$ Jy	Type	Class	EW[OII] $\AA$	EW[OIII] $\AA$
J021827-04546	1	0.6272	S	0.08025	NLAGN	HERG	13.0	95.0
J021823-05250	11	0.6454	S	0.00795	Abs	LERG	-	-
J021634-04550	12	0.8654	S	0.00659	Weak	U	-	16.0
J021724-05128	18	0.9193	S	0.00484	Abs	LERG	-	-
J021757-05279	19	0.6946	S	0.00483	Weak	U	-	19.0
J021754-05128	23	0.5855	S	0.0042	Strong	HERG	-	109.0
J021906-04590	24	0.5158	S	0.00361	Abs	LERG	-	-
J021755-05370	25	0.9626	S	0.00323	BLAGN	Q	-	-
J021718-05293	28	0.6324	S	0.0028	Abs_BL	LERG	-	-
J021822-05168	30	0.5351	S	0.00256	Abs	LERG	-	-
J021737-05134	33	0.6471	S	0.00237	Abs_len	LERG	-	-
J021932-05129	36	0.8717	S	0.002092	Abs	LERG	-	-
J021758-04329	39	0.89	P	0.001763	U	LERG	-	-
J021848-05083	45	0.5532	S	0.001511	Abs	LERG	-	-
J021722-05349	50	0.5035	S	0.001324	NLAGN	HERG	67.0	25.0
J021855-04434	54	0.8834	S	0.001241	Strong	HERG	-	140.0
J021822-05291	60	0.8805	S	9.98E-4	Weak	U	-	13.0
J021702-05163	61	0.6682	S	9.93E-4	Strong	HERG	154.1	19.0
J021849-04595	64	0.5152	S	9.72E-4	Strong	U	3.1	38.0
J021834-04580	67	0.6487	S	8.45E-4	Abs	LERG	-	-
J021935-05054	79	0.8241	S	7.26E-4	NLAGN	HERG	80.0	21.0
J021625-04522	80	0.95	P	7.2E-4	U	LERG	-	-
J021801-05373	83	0.96	P	7.07E-4	U	U	-	-
J021720-05027	108	0.627	S	5.0E-4	Abs	LERG	-	-
J021705-05100	115	0.88	P	4.68E-4	U	U	-	-
J021809-05311	116	0.8084	S	4.68E-4	NLAGN	HERG	-	54.0
J021837-04488	120	0.8426	S	4.41E-4	Strong	HERG	14.1	21.0
J021830-05009	127	0.8797	S	4.19E-4	SB	S	-	-
J021826-05277	132	0.6921	S	3.94E-4	NLAGN	HERG	-	60.0
J021717-05016	136	0.8208	S	3.86E-4	NLAGN	U	-	10.0
J021638-05113	145	0.5474	S	3.51E-4	Abs	LERG	-	-
J021659-05109	148	0.64	P	3.43E-4	U	U	-	-
J021707-04521	151	0.5791	S	3.38E-4	Abs	LERG	-	-
J021920-05051	154	0.8703	S	3.35E-4	NLAGN	HERG	24.0	16.0
J021803-04476	160	0.5719	S	3.25E-4	NLAGN	HERG	-	-
J021839-05308	166	0.7612	S	3.11E-4	SB	S	-	-
J021757-05030	169	0.5529	S	3.01E-4	Abs	LERG	-	-
J021941-05074	170	0.9632	S	3.0E-4	NLAGN	HERG	-	234.0
J021808-05222	175	0.82	P	2.96E-4	U	U	-	-
J021740-04516	177	0.5149	S	2.88E-4	Abs	LERG	-	-
J021800-05380	186	0.5668	S	2.75E-4	Abs	LERG	-	-
J021743-04364	190	0.784	S	2.72E-4	BLAGN	Q	-	-
J021925-05125	195	0.8848	S	2.63E-4	SB	S	-	-
J020458-04468	202	0.83	P	2.53E-4	U	U	-	-
J021742-05370	205	0.6789	S	2.5E-4	Strong	U	-	14.0
J021842-04347	209	0.75	P	2.46E-4	U	U	-	-
J021923-05130	214	0.6259	S	2.38E-4	SB	S	-	-
J021728-04389	215	0.55	P	2.37E-4	U	U	-	-
J021900-05267	218	0.8697	S	2.35E-4	SB	S	-	-
J021729-05187	217	0.6431	S	2.35E-4	Abs	LERG	-	-
J021659-05063	219	0.8201	S	2.35E-4	Abs	LERG	-	-
J021645-05180	220	0.8019	S	2.31E-4	SB	S	-	-
J021634-04512	221	0.92	P	2.29E-4	U	U	-	-

Continued on next page

Table 6.9 – continued from previous page

Name	SXDF_ID	ztype	z	$S_{1.4GHz}$ Jy	Type	Class_1	EW[OII] $\AA$	EW[OIII] $\AA$
J021853-04517	228	0.518	S	2.19E-4	SB	S	-	-
J021936-04588	231	0.761	S	2.17E-4	NLAGN	HERG	-	84.0
J021759-05209	236	0.5353	S	2.16E-4	NLAGN	HERG	149.0	29.0
J021728-04354	238	0.83	P	2.15E-4	U	U	-	-
J021845-05081	247	0.56	P	2.04E-4	U	U	-	-
J021806-05342	252	0.6714	S	2.01E-4	Abs	LERG	-	-

Chapter 7

LOFAR: The Next Generation

7.1 The Low Frequency Array (LOFAR)

In this thesis, I have presented several complementary novel approaches to exploring the influence of radio AGN at high redshift. However, further progress is hampered by a lack of sufficiently wide and sensitive multi-frequency radio surveys. This will soon change with the advent of a radio telescope of much greater angular resolution and sensitivity at low frequencies than is possible with any current instrument, the LOw Frequency ARray, or LOFAR. In this chapter, I outline the capabilities of this revolutionary new telescope and the software pipeline in development for reducing radio interferometric data for the first time automatically, describe my contributions to several LOFAR commissioning activities, and finally present some early results from some of the very first commissioning observations with the LOFAR interferometer.

LOFAR [van Haarlem *et al.*, to be submitted 2012] is a multi-purpose sensor array, with its main usage being in radio interferometric observations at the very lowest frequencies, between 10 and 240 MHz, in addition to geophysical and agricultural applications, as diverse as subsidence monitoring and potato crop control. LOFAR is composed of 'stations', each consisting of many small individual and inexpensive antennas (cf Figure 7.1), of which there are 36 in the Netherlands (40 eventually), with a further 9 international stations in Germany, France, Sweden and the UK, with the largest baselines of order ∼1500 km. On completion, LOFAR will be the largest low frequency radio telescope in the world. This unique design ensures that the door is kept firmly open for easy expansion - individual stations are relatively inexpensive, and could potentially enable many smaller European countries to purchase a relatively inexpensive stake in the project (e.g. Poland are almost certainly going to have three stations, and Ireland have recently expressed an interest[1]), that they would simply not be able to afford to do with more expensive instruments, whilst all the time substantially improving the sensitivity and angular resolution of the instrument.

LOFAR is a 'software telescope', being composed of relatively simple hardware components, and relying on fast network connections and significant advanced automated processing both at

[1] `http://www.lofar.ie/Home.html`

An example of a LOFAR core station, with the Low Band Antenna array (LBA) in the middle, and the two High Band Antenna Arrays (HBA) at either side. To the left is a map displaying the location of the remote LOFAR stations across Europe, with the central `Superterp' located in Exloo, the Netherlands. Images copyright ASTRON.

The left image shows the HBA antennas, which are arranged in 4x4 tiles covered with tarpaulin and are sensitive to radio signals in the range 120 to 240 MHz. The LBA antennas (right) are simple dipoles, sensitive to the frequency range 10 to 80 MHz.

Figure 7.1: The LOFAR Radio Telescope

station-level and by a central high performance computing cluster for managing and storing the observed data. Each individual antenna is sensitive to radio emission from the whole sky. In order to target a particular source in the sky, the LOFAR software carries out 'beam-forming' at the individual station level - it varies the relative phases of the signals recieved by the antennas such that the signal is enhanced (in phase) in the desired direction, and suppressed in the others. LOFAR operates in three major observing modes: interferometric (for surveys, wide-field imaging), beam-formed (for observing e.g. pulsars, the Sun), and direct storage (e.g. monitoring of cosmic ray showers, single station all-sky observing). In this Chapter, only the interferometric mode is discussed further.

7.2 Observing with LOFAR

A 'raw' LOFAR interferometric dataset consists of up to 244 subbands of 0.195 MHz bandwidth (256 individual 0.76 kHz channels) interferometric data with a user specified integration time and frequency resolution, delivered in Measurement Set (MS) format. Frequency ranges of 15-78 MHz in the LBA, and 120-158, 115-185, and 215-245 MHz in the HBA can be observed currently (the LOFAR planned setup for observations in the first half of 2012), and bandwidth can be swapped for sky coverage, e.g. 1 beam of 244 subbands (48 MHz), or 8 beams of 31 subbands (6 MHz), each beam targetting a different area of the sky. This is useful for targeting for example, a bright calibrator and a faint source field simutaneously.

7.3 The LOFAR Imaging Pipeline

The LOFAR Imaging Pipeline is ultimately designed to take the raw observed data from LOFAR, and calibrate and image these data in an automated fashion, with no human intervention. Automating the process of interferometric reduction is the single greatest challenge for the LOFAR telescope, and significant gains towards this goal have been made over the last three years. As yet, the noise levels achievable for the data processed by the Imaging Pipeline are not approaching the theoretical levels. In early 2011, a typical 6 hour observation in the LBA reached 80mJy/beam, and in the HBA, 6mJy/beam[2]. This will improve as the number of stations increases, a problem with the synchronisation of observations is corrected (in September 2012) and improvements are made in the Imaging Pipeline, e.g. determining optimal processing settings, correcting for ionospheric effects and station clock drift. The pipeline is currently composed of three main steps: Flagging and Compression, Calibration, and Imaging.

7.3.1 Data Flagging

An average observation produces 244 subbands of data, several terabytes in size, dependent on the integration time, and with large amounts of Radio Frequency Interference (RFI) present, particularly towards the lower frequencies, which needs to be removed. In the LOFAR pipeline, this process is completed using NDPPP - the New Default Pre-Processing Pipeline. NDPPP runs with an associated parset, in which all desired steps to be carried out are entered by the user. NDPPP can complete flagging operations with several different flagging algorithms (including flag statistics), averaging of the data (in both time and frequency), concatenation of subbands, phase shifting to another phase centre, and demixing (see next section). For the processing of a typical subband, in NDPPP the first and last channels of a dataset are usually not usable, and hence are excluded, one or two flagging steps are completed, normally with AOFlagger [Offringa *et al.*, 2010] or the MADFlagger algorithms, and the data averaged in time and frequency. Typically the subband is averaged to one channel, with a 3 or 5 second averaging in time - although this increases slightly bandwidth smearing issues: at the current

[2] `http://www.astron.nl/radio-observatory/astronomers/technical-information/data-products/examples-deliverable-lofar-product`

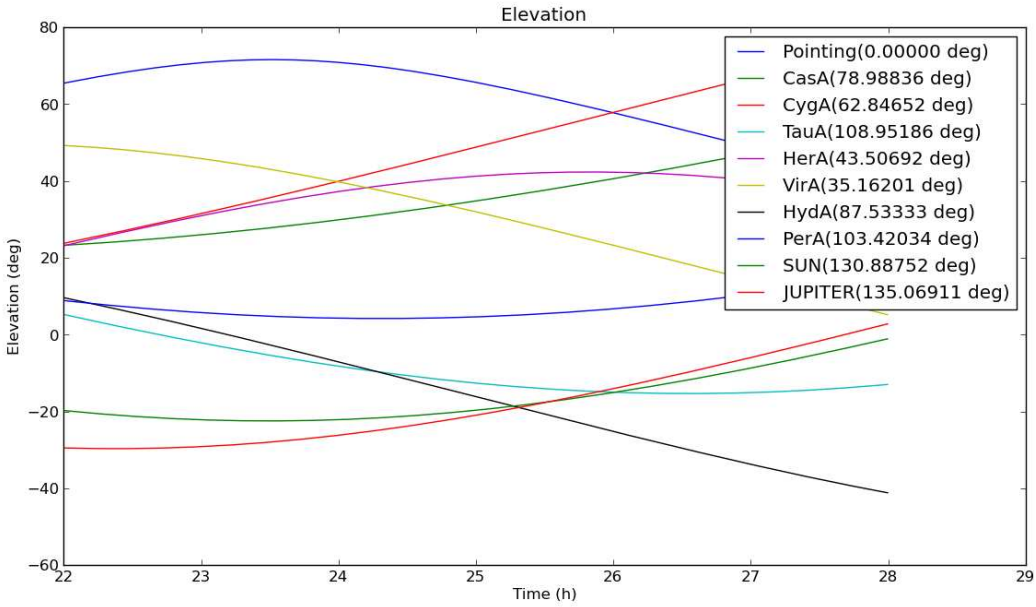

Figure 7.2: The elevation of the brightest radio sources in the sky with time for the LBA observation of the Bootes field as outlined in section 7.4.3. Cygnus A, Casseopia A, Virgo A and Hercules A are all well above the horizon for the duration of the observation, and need to be 'demixed', or removed from the dataset (cf Section 7.3.2).

time, some subsequent processing tasks run only on one channel subbands, and significant compression is helpful regardless to keep processing time to a reasonable level.

7.3.2 Demixing

The process of 'demixing' was developed in an attempt to remove the influence of the brightest radio sources in the sky from LOFAR observations [van der Tol *et al.*, 2007]. In the LBA, LOFAR stations are sensitive to almost the entire sky above the horizon and when bright radio sources rise during an observation, their sidelobes can severely adversely affect the calibration of the target field, particularly on the shortest baselines. The algorithm estimates and subtracts the contribution of user specified very bright radio sources present in the observation. Demixing must be run on all LBA datasets, and in some cases HBA datasets, in order to achieve a good calibration. Originally, demixing was run automatically on all observed datasets after NDPPP, and had to be run on datasets that had not been compressed in either time or frequency, and before any calibration. After initial successful testing, demixing is now incorporated into, and run as part of NDPPP.

Some caveats exist with the current demixing process. Firstly, bright radio sources to be removed must be outside a critical radius from the phase centre of the observation. This is because the removal of bright sources via demixing too close to the target can corrupt the target calibration solutions. Testing has shown that the size of this critical radius varies with

frequency, with higher frequencies having smaller critical radii. A good rule of thumb in the LBA is that sources to be demixed should be greater than 30 degrees away from the target field. In Fig 7.2, a plot of elevation vs time is plotted for some of the brightest radio sources in the sky: Cassiopeia A, Cygnus A, Taurus A, Hercules A, The Sun, for an observation of the Bootes field (see Section 7.4.3). This plot illustrates that for the duration of the observation, Cassiopeia A, Cygnus A, Virgo A and Hercules A are all well above the horizon, and need to be demixed (generally bright sources greater than 15 degrees above the horizon should be removed). Methods for removing bright sources closer than the critical radius in new obervations are currently being tested, using e.g. Sagecal (cf. Section 7.4.3).

7.3.3 Calibration

The essence of all radio interferometric calibration is to take a model of the sky, the observed radio signal, and solve to find the set of parameters which minimises the difference between the two. Calibration of the flagged, compressed and demixed data is completed using Black-Board Selfcal, or BBS. As detailed in Chapter 2, raw radio interferometric data must be calibrated, to correct for distortions to the radio signal ocurring between the radio source and the observer. In practical terms, this means correcting for instrumental effects such as the station beam, clock drift, and atmospheric effects such as ionospheric distortions, and differential faraday rotation described by the instrument Measurement Equation (cf Chapter 2, Section 2.1.3).

BBS is designed to process multiple subbands of data across the entire computing cluster - it can find a solution for each subband individually, or be run 'globally' on multiple subbands for parameter estimation, if the signal to noise in a single subband is too low. It takes as input a user created sky model - a text file of sources and their associated fluxes expected to be seen in the observation (often taken from existing all-sky surveys such as the VLSS), the flagged subbands, and a parset file, which specifies the steps required to be run by BBS, and procedes to find the optimum set of parameters that minimise the difference between the sky simulated from the model, and the observed data.

BBS includes multiple options for calibration, which can be optionally switched on and off in the accompanying parset, dependent on the type of solution to be carried out. Subsections of the measurement set can be selected by polarisation, timerange and baseline, along with the option of both direction dependent and independent gain solving. For the direction independent gain, there is the option of solving for amplitude and phase independently, as is used in e.g. AIPS and CASA, but for automated pipeline calibration it is envisaged to solve for both amplitude and phase together in a single cycle of calibration (self-calibration is highly computationally expensive, and whether the improvement offered by self-calibration is worth the cost in computation time is still an area of active investigation). Note too that whilst direction dependent solving can also be used to solve for the influence of bright interfering 'A-Team' sources, this is very slow in comparison to the demixing process (timescale of days as opposed to hours).

BBS can also include various other components of the Measurement Equation when solving, such as station beamshape, differential TEC (changes in the total electron content in the

overhead ionosphere), ionospheric Faraday rotation etc. Several of these are still undergoing active development and testing, for example the current version of the LOFAR station beam model has only been recently implemented, and whilst tests on simulated data suggest that this is working, tests on flux measurement on real data show that some further refinement may be required. For example, work on the LOFAR station beam recently highlighted a previously unknown problem with asynchronous clocks in some stations. The LOFAR HBA and LBA bandpasses are still being actively determined (Rafferty et al, in prep), and with a new imager recently completed, more substantial testing of ionospheric calibration will be able to take place.

7.3.4 Imaging

The final piece of the LOFAR pipeline, the Imager, has taken an enormous step forward in the last year. Up until the end of 2011, there was no full capacity imager available as part of the pipeline, and alternatives had to be used. The first MWImager (or CImager) used for the first few months of LOFAR interferometric operation had no working clean function, and it and subsequent versions were very slow, and there was very little documentation available on usage options. The imager available in CASA, whilst fast and with clean capacity, could not correct for the LOFAR beamshape, and therefore it was not possible to image correctly wide field areas. The AWImager (Tasse et al, in prep) was made available for testing towards the latter half of 2011, and is parallelised (fast), has full IQUV Stokes capacity, dirty/clean image options, in addition to other data selection parameters. Provided the beam model has been enabled previously in BBS, it applies the LOFAR beam correction, and has a suitable framework for straightforward addition of image-plane based calibration routines (e.g. ionospheric correction.)

7.4 The Imaging Team Commissioning Tests

Fully automated interferometric data reduction has never been achieved before. Thus extensive testing is required to understand optimal calibration techniques for the data. In the summer of 2009, the first three stations of LOFAR were connected, enabling the first interferometric observations to be taken. Commissioning LOFAR is a uniquely challenging project, as all aspects of the instrument, both hardware and software, are actively being developed whilst testing is taking place. LOFAR also involves project members from multiple countries and disciplines being able to work efficiently together, and several novel ways of working have sprung up around this. Commissioning tests have progressed through a series of 'busyweeks' and 'busydays', where commissioners (both end-user astronomers and developers/engineers) come together to work on specific problems. Given the wide geographical area, members often participate remotely through video conferencing, or via the usage of an online forum, wiki and cookbook to feed back results into the project community.

In the following two sections, I outline commissioning observations of three targets, analysed by myself. Firstly, observations of 3C196 and Cygnus A, which serve to illustrate the considerable technical challenges in commissioning, and the great strides in progress made by the LOFAR telescope over the last three years, and secondly, more recent observations of

the well-studied Bootes field.

Note that many of the raw and processed datasets discussed in this Chapter no longer exist. This is due to the LOFAR policy of deleting early datasets once the commissioning and testing objectives have been achieved - raw and processed commissioning datasets (for which the aims of the specific tests have been achieved and results fed back into the project), are too large to be stored permanently on the LOFAR compute cluster.

7.4.1 The First Three Stations: 3C196

In June 2009[3], the first three stations of LOFAR came online.

The aims of these first interferometric observations were three-fold:

- Do the individual components of the imaging pipeline work as expected?
- Is the output understood?
- What are the optimal parameters for each, in order to inform future automated processing?

One of the first observations to be taken was a 60 hour long integration in the HBA (observation L2009_13306) on 3C196, a bright unresolved quasar, and a source which is often used as a calibrator for other radio interferometers. The purpose of this observation was to test the functionality of the various components of the Imaging pipeline, which had never been tested as a whole on interferometric LOFAR data before, and to ascertain whether the stations, now functioning for the first time as an interferometer, were working as they should. I selected one subband at 141 MHz to reduce, the chosen subband having the standard total bandwidth of $\sim$0.2 MHz (256x$\sim$0.8kHz channels) and 1s integration time. The sparse uv-coverage may be seen in Figure 7.3. I then flagged the subband using IDPPP (an older version of the current NDPPP), and compressed it in frequency to 15 channels. Considerable experimentation was used to find the optimal set of parameters for flagging, and the resulting measurement set had to be split, removing the first and last few timeslots due to a bug in IDPPP, as these timeslots were corrupted. Approximately 2-3% was flagged in total.

With three stations available, it was then possible to conduct a simple test to look for any baseline-dependent errors present. The concept of 'closure phase' was first outlined by Roger Jennison in 1958, and works as follows. The phase measured by each antenna is corrupted by e.g. clock delays and ionospheric distortions. For the triangle formed by the three baselines between CS3, RS5 and RS3, by adding a combination of these phases, the phase errors at each individual antenna cancel, with the closure phase defined as:

$$\theta_{CL} = \theta_{CS3-RS5} + \theta_{RS5-RS3} - \theta_{CS3-RS3} \tag{7.1}$$

[3]Data reduction of 3C196, and the four station Cygnus A observation, were completed at ASTRON, The Netherlands Institute for Radio Astronomy, in Dwingeloo, Summer 2009 and was made possible by an ASTRON International Summer Student award. I gratefully acknowledge the assistance and team effort of my fellow LOFAR summer student Francesco de Gasperin, my ASTRON supervisors and pipeline software developers for their assistance in both learning and testing this new system from the ground up.

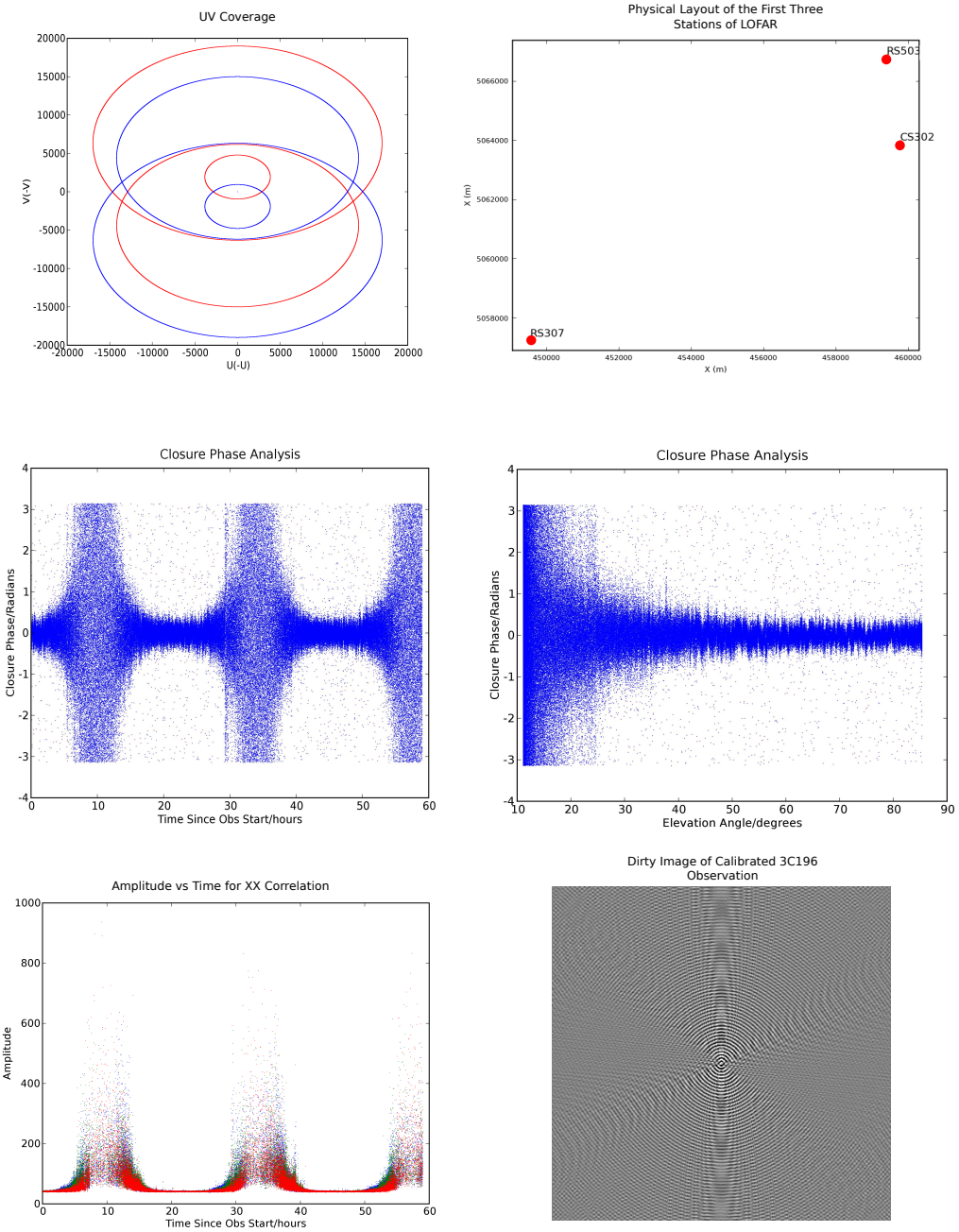

Figure 7.3: This figure illustrates the results of one of the very first interferometric observations of 3C196 to be taken with the first three stations to come online.

where $\theta_{CS3-RS5}$, $\theta_{RS5-RS3}$, $\theta_{CS3-RS3}$ are the measured phases for each baseline. Note that the nomenclature used here is consistent with the Measurement Set format - only one visibility is recorded per baseline in the MS (with two associated points in the UV plane), with the first antenna in the measurement set (ANTENNA1) being the lower number. For example, taking antenna 1 & 2, 2&1, one visibility will be listed in the measurement set with ANTENNA1 = 1, ANTENNA2 = 2.

Hence, this observable quantity depends only on the phase of the observed visibility, and is unaffected by phase errors at any of the antennas. In the case of a point source like 3C196, this value should tend to zero - any deviations being suggestive of baseline errors. In Figure 7.3, I plot the closure phase between stations CS302, RS503 and RS307 vs time and elevation. During the times when 3C196 is well above the horizon ($\geq$30 degrees) the closure phase behaves more or less as expected, suggesting that this initial 'mini-LOFAR' was working as expected. The closure phase plots also highlighted that at least initially, target sources should be 30 degrees above the horizon or greater in order to obtain enough signal to noise on the individual baselines. This finding was fed back to the commissioning team, along with several bugs and issues with the pipeline identified during the reduction to the developers.

I then calibrated the subband using a simple gain calibration and point source sky model in BBS, and imaged in MWImager (an older version of the current AWImager, as described in 7.3.4). The resulting dirty image of 3C196 may also be seen in Figure 7.2 (note no clean capacity in the pipeline imager was available at this time).

7.4.2 Cygnus A Imaging

As the array hardware rollout progressed, futher commissioning observations were undertaken with the goals of continuing to test the Imaging Pipeline, to determine optimal calibration strategies, and to start to build good sky models of the brightest complex sources in the sky, the so-called 'A-Team' of supernova remnant Cassiopeia A, radio galaxy Cygnus A, radio cluster Virgo A, Hercules A and Taurus A across the LOFAR frequency range.

The First Stations: Cygnus A at 30 MHz

In July 2009, a 10 hour observation of Cygnus A in the LBA was taken (observation L2009_13244), again with the first three stations online (the old test station CS010 was also available for this observation). I processed one subband at 30 MHz, using the same procedure as detailed above for 3C196. The UV-coverage of the observation can be seen in Figure 7.4.

I compressed the dataset to 15 channels in frequency, with no time averaging, using IDPPP, and $\sim$2-3% of the data was subsequently flagged. I inspected the data using CASA and several custom python scripts (written by both myself and several other commissioners), and completed several rounds of testing the flagger with different parameters, in order to identify the parameter set in IDPPP which provided the most robust removal of RFI present. After splitting the dataset to remove the first and last timeslots (an IDPPP bug, detailed above), the data were calibrated in BBS, using a gain solve, and a simple two point source model to represent Cygnus A. At such low frequency, with only three stations (+1 old test station), Cygnus A is expected to be barely

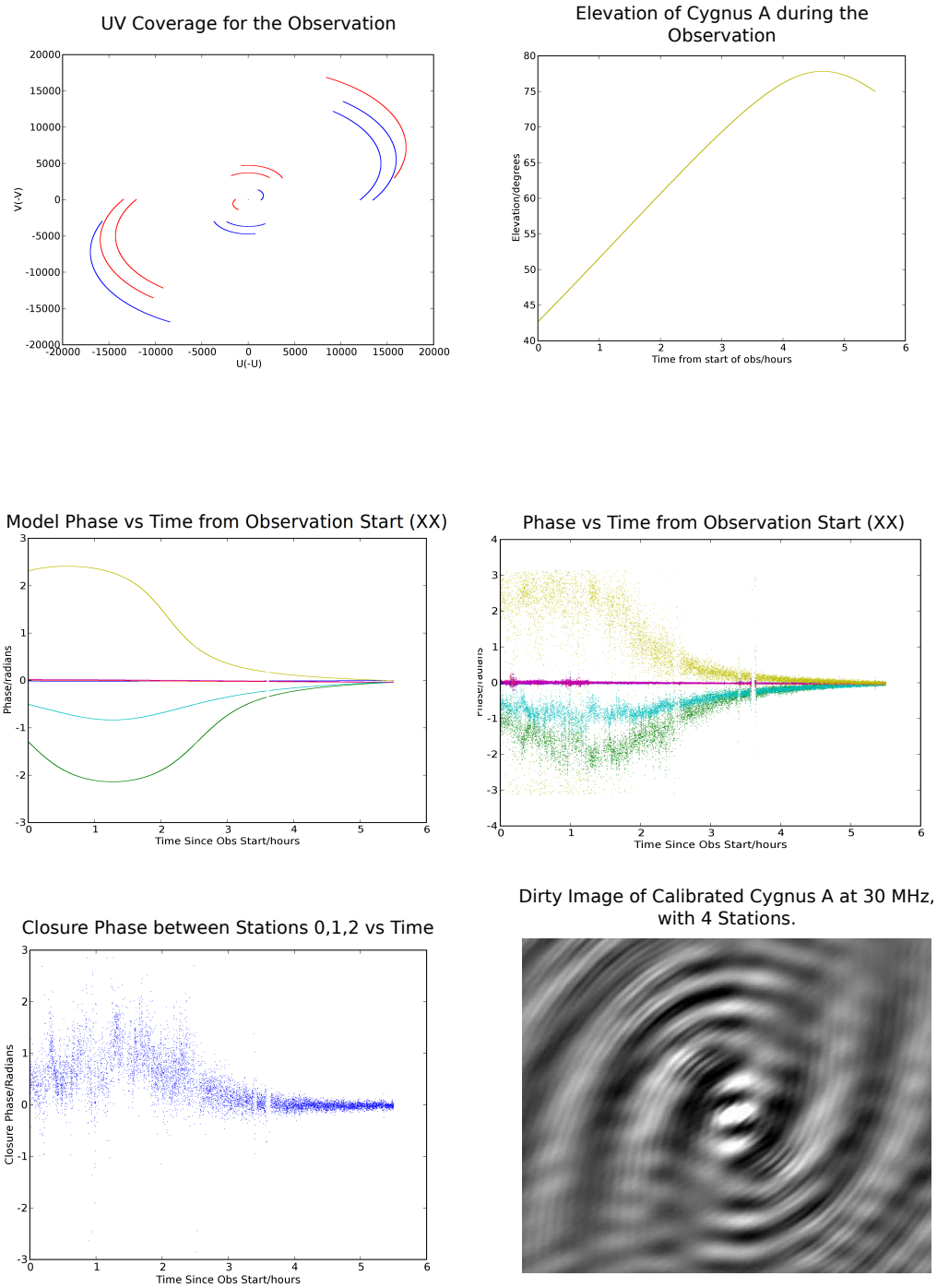

Figure 7.4: This figure illustrates the results of one of the very first interferometric observations of Cygnus A to be processed with the LOFAR imaging pipeline during the summer of 2009.

resolved. After calibration, the CORRECTED_DATA needed to be flagged again. However, IDPPP did not have the capacity to flag on the CORRECTED_DATA column, and so custom Python scripts provided by the BBS developer for flagging of calibration solutions had to be used instead (given the sparse uv-coverage provided by only four stations, it is not unexpected to get a large proportion of bad solutions after calibration). BBS also has a facility for simulating data - given an input sky model, it can simulate the visibilities that LOFAR would expect to observe. Figures of the simulated data, and the actual observed calibrated data can be seen in Figure 7.4, showing good agreement. After calibration, the newly calibrated data was flagged again using custom python scripts for flagging outlying gain solutions, and a dirty image made of the data, showing the unresolved Cygnus A, consistent with BBS model predictions for the dataset, and thus again demonstrating that at least at a basic level, 'mini-LOFAR' was working as expected.

As a result of both this reduction and that of 3C196, as might reasonably be expected for the pipeline which had only previously been tested on data from a single station, several problems with the pipeline had become immediately apparent. There were issues with IDPPP corrupting measurement sets, IDPPP being unable to run on its own output (e.g. for a second round of flagging), and with some RFI still being missed. Both IDPPP and BBS were at this stage very slow to run (hours) dependent on parameters chosen, and the imager too had problems with both a lack of clean option, and very sparse documentation, making it difficult to understand all the options available (it should be noted that CASA, an alternative to processing and imaging measurement sets in the traditional fashion, by hand, was still in development at this time). These findings were communicated to the developers and commissioners at subsequent busyweeks (and through version 1.1 of the LOFAR Imaging Cookbook, which I contributed not long after completing the analysis of these observations).

Eleven Stations 236 MHz

In May 2010, an observation of Cygnus A in the HBA was completed using seventeen stations (L2010_07678). I selected 28 subbands for imaging, covering a frequency range between 233 and 239 MHz. At this time, the progress in software development was not keeping pace with the hardware development. With a seventeen station array, both the existing BBS and Imager versions on the cluster were very slow to run. Whilst the Imager now had clean capacity, it still required significant experimentation to determine optimal parameters, and could not be used in a self-calibration loop. Although the pipeline was not designed with self-calibration in mind, it was a necessary tool at this stage in order to gain the best models possible of the 'A-Team' as seen by LOFAR. CASA was the only software suite available that offered the possibility of self-calibration, and hence the capacity to create a good model of Cygnus A, that could be used as a starting point for future observations. The decision was therefore taken to use CASA for the data reduction, which whilst still under development, by this stage had full capacity in calibration and imaging. I first flagged and compressed the data to one channel per subband in NDPPP, and inspected the data. There were six problematic stations in the observation, which subsequently had to be flagged. One station failed to take data, and the others were all central

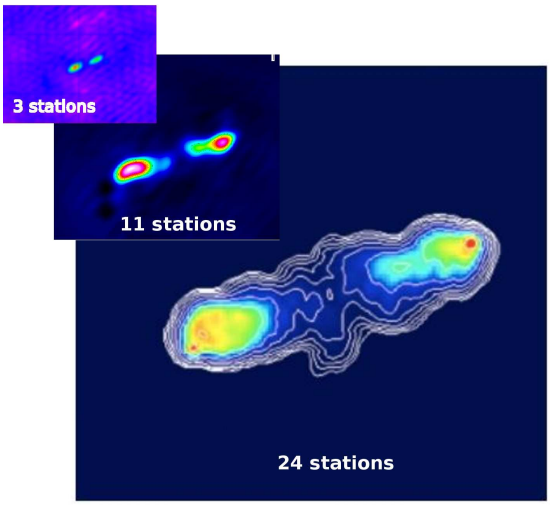

Figure 7.5: This figure illustrates the substantial progress made by the LOFAR hardware rollout and software development over the period 2009-2011. The smallest image on the left shows Cygnus A imaged in the HBA (120 MHz) by Sarod Yatawatta with the first three stations to come online. The middle image is my image of Cygnus A with eleven stations in the HBA at 236 MHz, and the final image on the right is that of Cygnus A in the HBA with 24 stations, made by John McKean.

Superterp stations, where a clock delay was thought to be present during the observations. The subbands were then concatenated together. A VLA image of Cygnus A at 325 MHz was used as a starting model in the CASA task **setjy**, before running the task **gaincal** with a phase only calibration and a solution interval of 10 minutes, and finally applying the calibration with **applycal**. An initial image was then made with the task **clean**. Several further rounds of phase only self-calibration were then run, followed by a final round of amplitude and phase self-calibration. The final image had a dynamic range of ∼1000:1.

Whilst this observation did not succeed in generating a very high dynamic range image, it did provide a useful learning experience on how to identify potential hardware issues - problems like clock delays would not have been easily apparent with lower numbers of stations, or with earlier versions of the pipeline, illustrating the importance of continuing to take test observations as the hardware rollout continued. The issues with the superterp stations in this observations almost certainly adversely affected the image quality possible with this observation. However, in Figure 7.5, my final image from this observation is shown, along with a three station image made by Sarod Yatawatta in the HBA at 120 MHz, and an HBA image made later by John McKean [McKean *et al.*, 2011] with 24 stations, showing the vast improvement in hardware and software imaging capability over the last three years.

7.4.3 The Bootes Field

By 2011, substantial progress had been made in imaging successfully individual bright 'A-Team' and 3C radio sources, and fields surrounding these. What was less well known however was whether it was possible to image successfully a field without a bright source in, or close to, the centre. The Bootes field (RA: 14:32:06.00, DEC: 34:16:48.00) was observed for six hours in LBA on the night of the 30th April 2011. I initially processed four subbands around 58MHz. At this stage the flagging through NDPPP was deemed reliable enough to be run automatically on all acquired datasets, and with automatic compression, also ensured datasizes were kept to a managable size on the cluster. After careful inspection of the subbands, no further flagging was needed. Each subband was then demixed, to remove the effects of bright 'A-Team' sources CassA, HerA, VirA and CygA (cf Figure 7.2). After successful demixing, station 17 was flagged, as this did not record data.

The data were calibrated in BBS with a global calibration, using a direction independent gain, and correcting for the beam towards the centre of the field. The sky model used was constructed from a VLSS image of the Bootes field at 74MHz, using PyBDSM (the LOFAR source-finder), and converting to an appropriate BBS model format. The calibrated data underwent further flagging in CASA, and were then imaged using the CASA **clean** task. The initial images were relatively poor, showing only the brightest sources included in the model. A further two subbands were added, and processed together with the original four subbands, again with a BBS global calibration, to see if the additional data offered any improvement. However, although there was some improvement in visible image quality, the LOFAR images did not show any additional sources not included in the initial model.

Given that imaging was completed in CASA, the fluxes obtained were in error, more so the further away from the phase centre they were, as CASA cannot correct for the LOFAR beamshape, included in the calibration. It was difficult to ascertain whether the poor images were due to the aforementioned lack of bright source in the centre of the field for calibration, lack of signal to noise (short time range/more subbands needed), the imaging process, or a problem with the dataset itself.

However, given that work on the AWImager, which would be able to image the dataset correctly, fully accounting for the beam was almost complete, it was decided to wait to perform another observation of the Bootes field in December 2011 for both a longer time (12 hours) and simultaneously with a beam on a calibrator source, 3C295. Experimentation by several commissioners had proved that the transfer of gain solutions from a bright 3C source was a viable option for calibration. The calibration of the entire Bootes field dataset was completed in automated pipeline mode by Cyril Tasse in January 2012, and an average image of the entire dataset, imaged in distributed mode over the new cluster (not available to general commissioners) showed that the transfer of gains method was working, with plenty of bright sources visible.

Initially, I utilised the calibrated dataset to test both the newly functioning AWImager, and the usage of Sagecal, a complementary self-calibration software to BBS, to assess whether it gave measurable improvement to the image quality. Sagecal [Yatawatta *et al.*, 2009], was

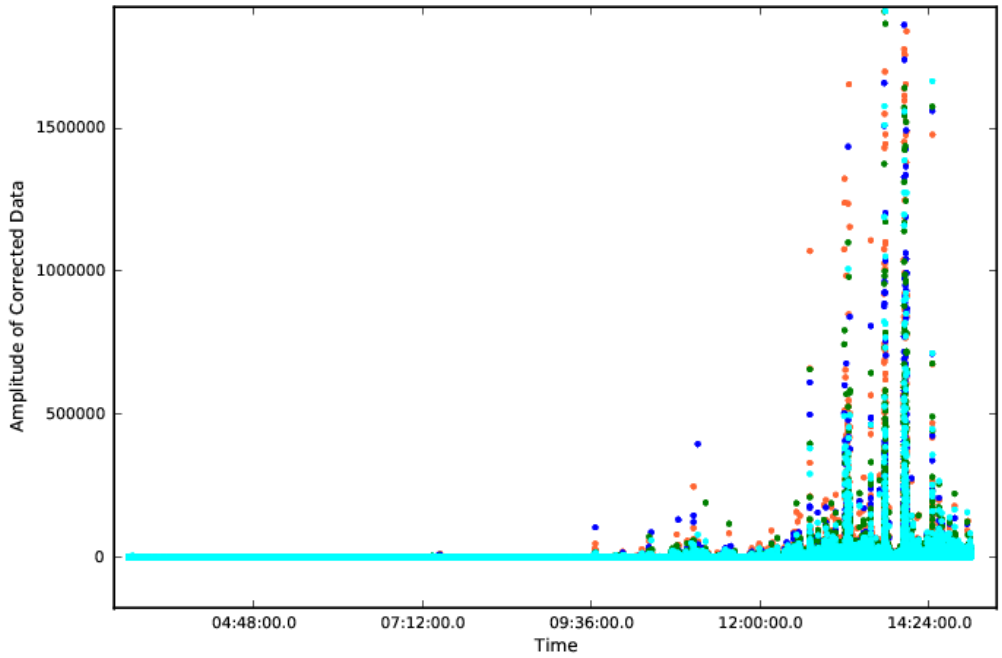

Figure 7.6: This figure illustrates for a single subband of the December 2011 Bootes field observation at 43 MHz, a zoomed in plot of amplitude vs time for the entire observation. The strong interference induced by the Sun, and the time of Sunrise can clearly be seen, and the latter 4 hours of the observation was hence flagged.

developed as part of the Epoch of Reionisation Key Science Project, and is designed for optimal subtraction of radio sources from an image, allowing bright sidelobes and remaining artifacts to be calibrated out. Sagecal is optimised for GPU usage and is extremely fast, and would therefore be an attractive option to add into the pipeline calibration process, if it significantly improves image quality. It has also recently been explored as a potentially useful alternative to 'demixing' for bright 'A-Team' sources closer than 30 degrees to the phase centre of an observation (cf Section 7.3.2).

I started initial testing using only one subband at 48 MHz. The latter third of the observation (4 hours) had to be removed (flagged in CASA), as these data were taken during sunrise, and were too noisy to be used (cf. Figure 7.6). The CORRECTED_DATA column was then flagged and clipped at 200 Jy, and an initial image made with AWImager, with the following parameters:

*a*wimager ms=sub1.MS image=test.img weight=uniform wprojplanes=256 npix =1500 cellsize =30arcsec data=CORRECTED_DATA padding =1. niter =10000 timewindow =1200 stokes=IQUV threshold =0. operation=csclean wmax=3000

Note that the parameters chosen above may not be the most optimal - AWImager at this point was a new development, and progress was by 'trial and error', with the aim of obtaining a good image in a reasonable timeframe. The parameters used above produced a reasonably good image over $\sim$ 12 degrees, in $\sim$1 hour, and subsequent processing with Sagecal produced a noticable reduction in sidelobes in the image, and a small reduction in noise.

Later, 10 subbands were assessed, between 43 MHz and 54 MHz. For each subband, again the CORRECTED_DATA column was flagged and clipped at 200 Jy, and the latter third (4 hours) of the observation flagged entirely, as described above. Each subband was then imaged individually with the AWImager (version 21483) using the above parameters. Duchamp [Whiting, 2012] was used to extract all bright sources above 1 Jy in the image, and create an associated mask file, and Buildsky (v0.02) used to model these sources, and group into clusters. A total of 6 clusters (directions) was selected to solve for. This represents a compromise between achieving optimal calibration solutions and a manageable computing time - it is not computationally practical to solve for every possible direction on the sky, so sources close together on the sky are grouped into 'clusters'. Sagecal was then run on each subband, modelling and subtracting the sources identified by buildsky, and the resulting residuals written back to the respective subband measurement sets. These were then re-imaged using the same settings as given above in AWImager, and the subtracted sources restored. Finally, the resulting images were averaged using the CASA task **immath**.

Bootes Field Results

After the first round of imaging, the Bootes field image had a restoring beam of 100x70 arcseconds, and an rms noise level of $\sim$ 40 mJy at 48.5 MHz (Figure 7.7), roughly a factor of two deeper than the VLSS 74 MHz survey, previously the deepest survey available below 100 MHz. After Sagecal was run, the rms noise on the final image was reduced to $\sim$ 30 mJy, and visually, the sidelobes in the image are reduced. As can be seen from Figure 7.8, the vast majority of sources in the VLSS survey are detected at 48.5 MHz, and some additional

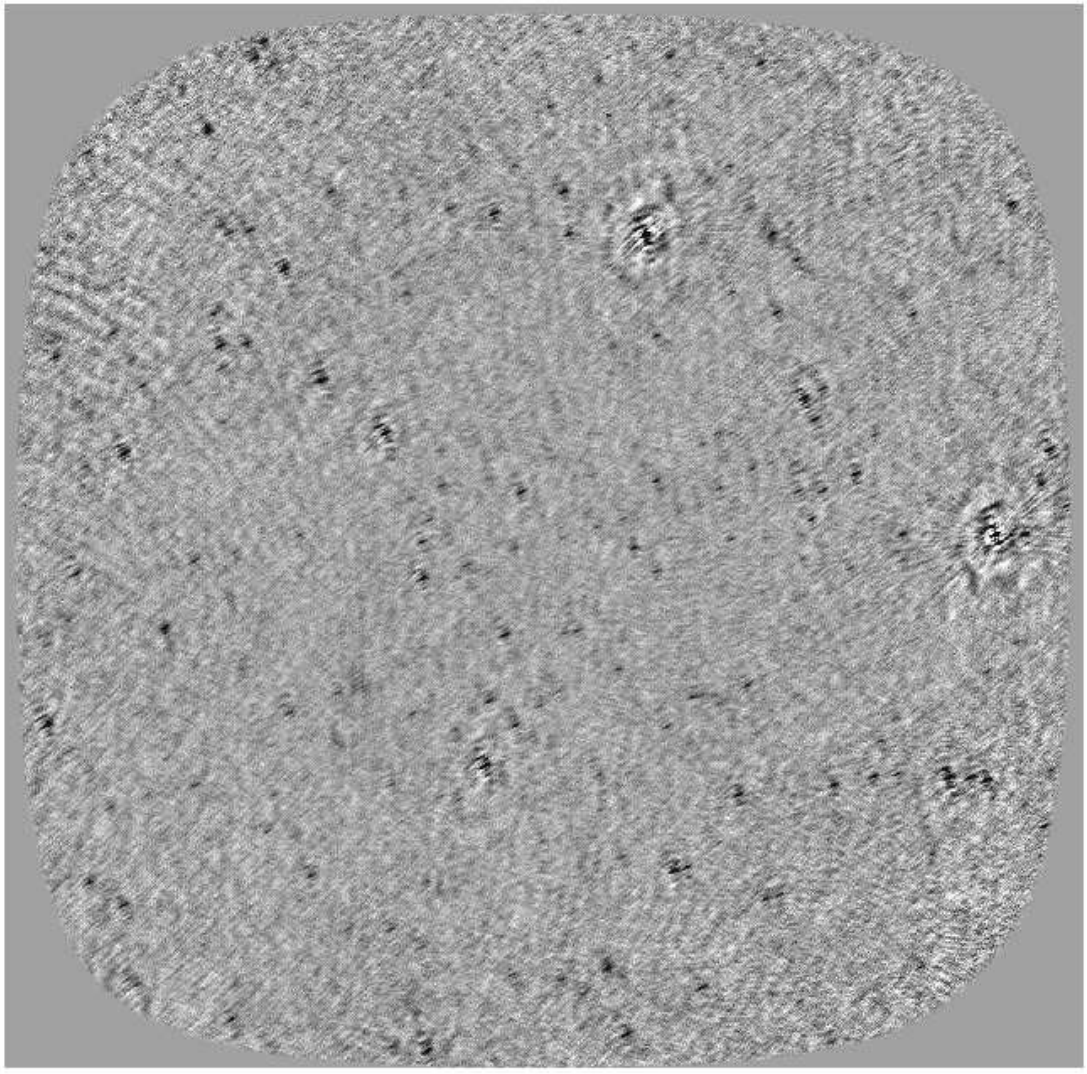

Figure 7.7: A 10 subband (between 43 MHz and 53 MHz) initial averaged image of the Bootes field after imaging with AWImager. The image covers an area of approximately 12.5 x 12.5 degrees. The minimum background rms noise as measured by PyBDSM is ∼40 mJy.

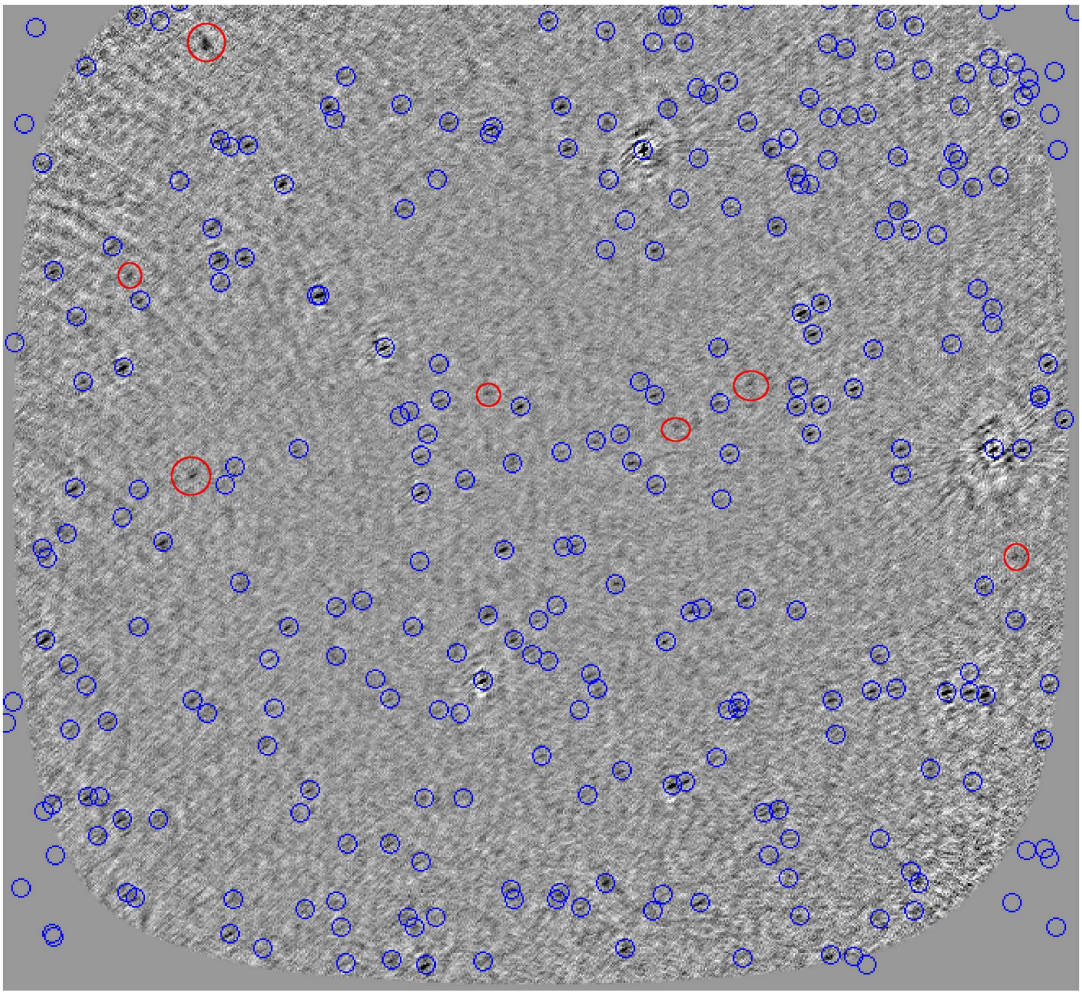

Figure 7.8: A 10 subband (between 43 MHz and 53 MHz) averaged image of the Bootes field after a Sagecal run and subsequent imaging with AWImager. The sidelobe levels in the resulting image are visibly reduced after a cycle of self-calibration with Sagecal. The image covers an area of approximately 12.5 x 12.5 degrees. Overplotted is the VLSS 74 MHz catalogue for the same area, showing clearly that the majority of sources within the VLSS are detected, in addition to several others not detected by the VLSS (red circles). The minimum background rms noise as measured by PyBDSM is ∼30 mJy.

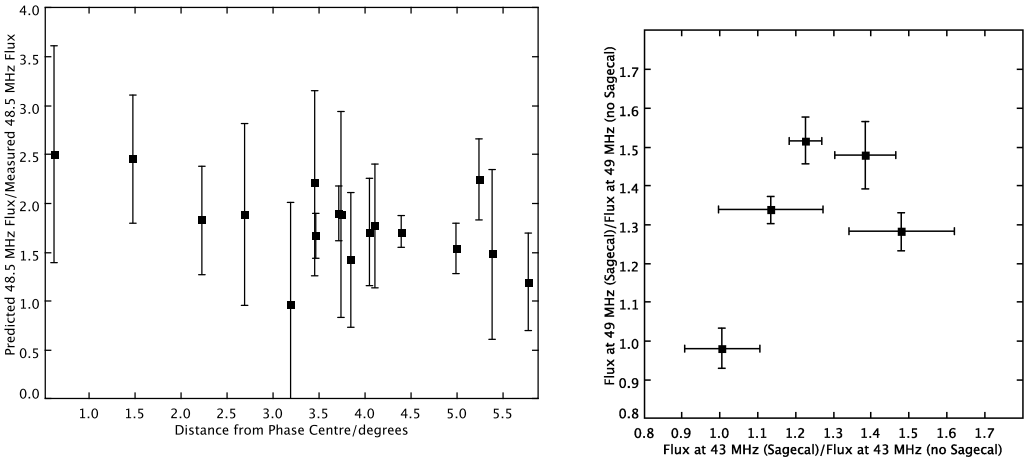

Figure 7.9: The figure on the left plots the ratio of predicted flux to measured flux at 48 MHz for the 17 sources detected in the averaged image, and in more than one individual subband, showing a clear ∼40% underestimation in flux. The figure on the right shows for the five brightest sources to be detected in the individual images, the ratio of flux before and after Sagecal was applied, for the 43 MHz vs 49 MHz subbands. These two subbands showed larges differences in flux, but as shown, this is not introduced by Sagecal, which produces consistent proportional increases in flux as expected.

sources, highlighted in red, are detected which are not present in the VLSS catalogue. The most noticable of these is the bright extended giant radio galaxy 4C39.42, at the top left hand corner. The extended emission of this source is barely detected in the VLSS maps, but is clearly detected by LOFAR. This type of extended, steep spectrum emission will be easily detectable by LOFAR, and gives a good foretaste of discoveries to come. PyBDSM was then used to extract the fluxes of the 17 sources in total detected in the averaged image, in addition to at least two of the individual subband images.

Data at 1.4 GHz (NVSS), 327 MHz (WENSS), 151 MHz (7C) and 74 MHz (VLSS) was assembled and matched for these sources, and a 2nd order polynomial (as per Chapter 5) was fitted, in order to predict the expected flux at 48 MHz. In Figure 7.9, the ratio of predicted flux to measured flux is shown for the selected sample of 17 sources, versus the distance of the source from the phase centre. If the fluxes are reasonably correct, this ratio should be around 1. It can clearly be seen that the LOFAR fluxes are underestimated consistently, by around $\sim$ 40%. However, reassuringly, there appears to be no measurable correlation with distance from the phase centre, suggesting that the beam correction is working well. Both of these findings are consistent with previous, and ongoing work on the first LOFAR sky survey, MSSS. Commissioning work in progress on MSSS has also found various issues with the flux calibration, with some calibrator observations showing variations of up to 40%, and some fields showing unusually steep spectral indices. The latter has very recently been traced to an issue with source extraction, with the extraction software utilising the wrong beam shape for a stacked image. However, there also appears to be variations in flux present in individual subbands.

I investigated this further by using PyBDSM to measure the fluxes (where detected) in each individual subband. The spectra for the six of the brightest sources (as measured at 74 MHz) are shown in Figure 7.10 to illustrate the results. Firstly, source extraction does appear to be an issue, with the fluxes measured from the averaged image being significantly lower than those extracted from the individual subbands. The source extraction software uses the beamshape from the image to fit gaussian models to sources. As the beamshape varies in each individual subband image, assumption of the same beamshape as in the first individual subband to be included in the averaging as PyBDSM does leads to incorrect modelling of sources in the averaged image. For bright sources that are detectable in individual subbands this is less of an issue, but to detect many fainter sources the averaging of several subbands is required. A solution to this awaits the availability of multi-frequency imaging in the pipeline.

Secondly, it is also clear that there is substantial variation in measured fluxes from subband to subband. To check firstly that this was not introduced by any process associated with Sagecal, I took two subbands where the measured fluxes were very different, at 43 MHz and 49 MHz respectively, and measured the fluxes for the five brightest sources, before and after Sagecal was run, and took the ratio. As can be seen from Figure 7.9, Sagecal gives as expected similar proportional increases in flux for both subbands. Note that this also demonstrates the effectiveness of Sagecal in improving the quality of the image - more flux ends up correctly distributed in the bright sources, as opposed to surrounding sidelobes.

The variation from subband to subband thus seems real. There is currently a known hardware issue with $\sim$ 5 nanosecond clock delays present in stations, which could lead to frequency-dependent differences in expected beamshape and sensitivity in the observed data. This is expected to be solved with hardware upgrades planned for September. It is also possible that self-calibration may improve this, or that there is still some remaining low-level RFI present in the dataset. In order to investigate further, it would be necessary to reduce the entire LBA dataset, in order to study the low frequency spectral behaviour across all subbands. Some work on the flux calibration and source spectral behaviours is already underway using MSSS data, and findings from both this observation and the MSSS work will be used to inform the subsequent processing of the next Bootes field observation, planned for later this year.

7.5 Outstanding Issues & Future Work

At the time of writing, the LOFAR hardware has progressed much more quickly than the software, and the latter is where several key challenges still remain. Only very recently has the first, full version (Version 1.0) of the imaging pipeline been released, and this is still undergoing substantial testing. Priorities over the next year will be implementing and improving image-based calibration (e.g. correcting for clock delays, ionospheric effects), and optimising the automated calibration cycle to improve the sensitivity of the images towards expected theoretical levels. A major step towards this goal is currently underway with MSSS, the first extensive survey to be carried out by LOFAR, and which will contribute the first sky model at LOFAR frequencies for subsequent observations.

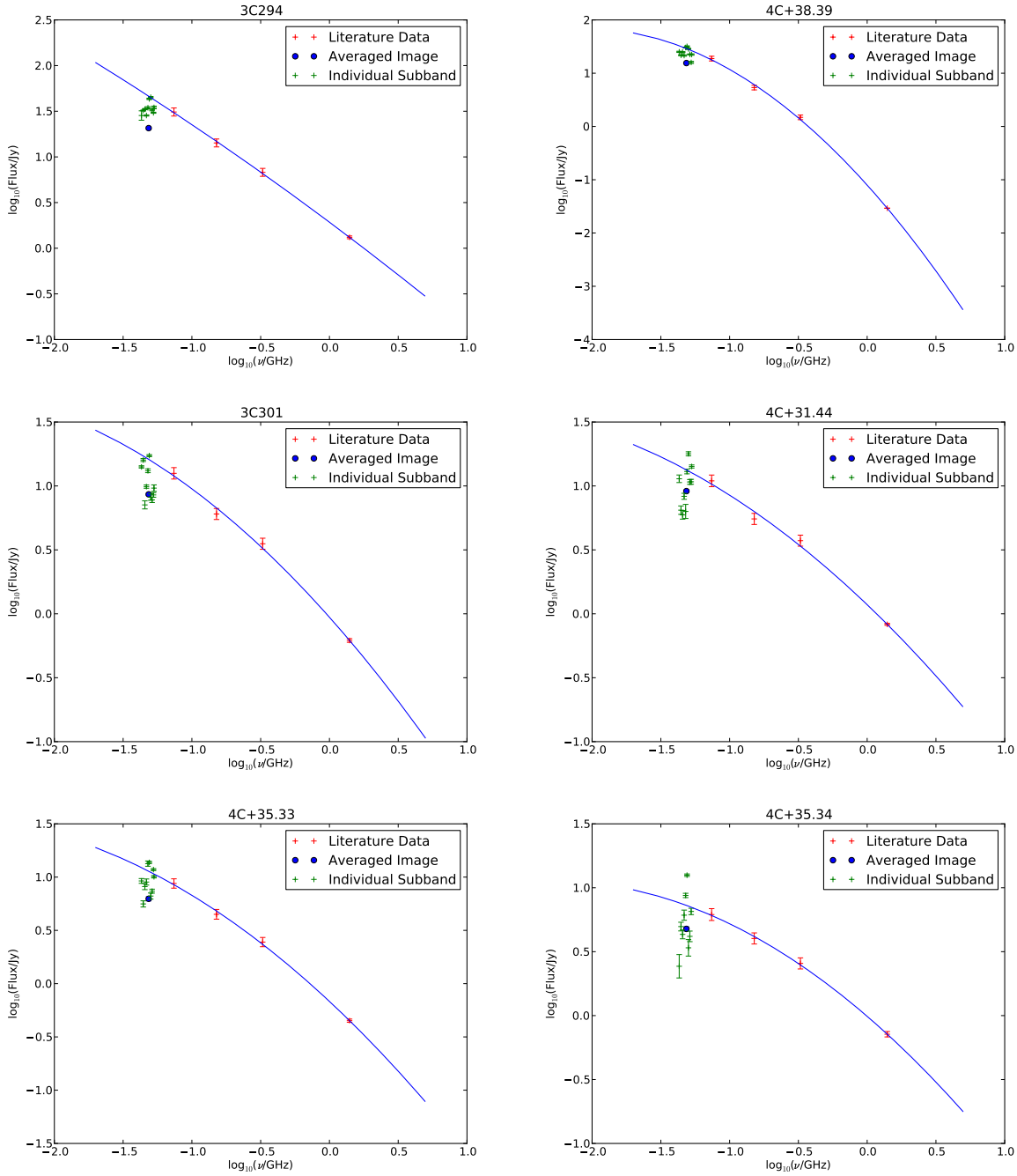

Figure 7.10: Radio spectra for the six brightest sources (at 74 MHz) in the area of the Bootes field imaged. The spectrum has been fitted (blue line) to literature data (red points) as described in the text, and the individual subband fluxes from the LOFAR data are plotted in green. The flux measured from the averaged image is plotted as a large blue circle, demonstrating clearly the difference in measuring the flux from individual and averaged images, and also the subband to subband variation in flux. However, more positively, the fluxes as a whole correspond well to what is expected from the existing spectrum for each of these sources.

LOFAR is already starting to produce useful science: the very first LOFAR science papers having recently been accepted for publication [e.g. Hassall *et al.*, 2012; van Weeren *et al.*, 2012; Singh *et al.*, 2012; Stappers *et al.*, 2011]. In July 2012, ASTRON issued a 'Cycle 0' open call for proposals to the astronomical community, signaling the start of the phased array radio telescope era.

Chapter 8

Conclusions & Future Directions

In this thesis the evolution of radio-AGN feedback modes, and methods to locate and study such systems at the very highest redshifts have been investigated, using complete radio samples along with extensive new multi-wavelength data in the radio, optical and near-infrared. This thesis is built around four key questions, as outlined in Chapter 1.

- What are the most efficient means of assembling samples of very high redshift radio-AGN?
- What effect does the shape of the radio spectrum have on the determination of the radio luminosity function, particularly at high redshift?
- How does the relative number density of the two main AGN fueling modes (HERG, and LERG) evolve over the bulk of cosmic time (z$\sim$1)?
- How can the findings above be used to inform efficiently future studies with data intensive instruments such as LOFAR and the SKA?

8.1 Locating High Redshift radio-loud AGN

In Chapter 4, radio-based and K-band magnitude methods for the efficient selection of high redshift radio-loud AGN are analysed, using nine of the most highly spectroscopically complete radio galaxy samples in existence. The existence of a weak correlation between z and α is confirmed, which remains even when Malmquist bias is removed. The strength of this correlation depends on both the k-correction and sample selection frequency, in addition to the frequency at which α is measured, and consistent results for both high and low frequency selected samples are only seen if analysis is restricted to just extended radio galaxies.

The efficiency and the completeness of the techniques of radio size, α and K-band selection used to locate high-z radio galaxies is then successfully quantified. A steep-spectrum cut applied to low-frequency selected samples can more than double the fraction of high-z sources, but at a cost of excluding over half of the high-z sources present in the original sample. An angular size cut is an almost as equally effective method as a steep-spectrum cut, and works for both high

and low frequency selected samples. In multi-wavelength data, selection first of infrared-faint radio sources remains by far the most efficient method of selecting high-z sources.

A short spectroscopic investigation of several samples of Infra-red faint radio sources, which are radio sources with faint or no detection in the optical or infrared was presented in Chapter 6, but detected no Lyα emission. The majority of these sources were at the sub-mJy flux level at 1.4 GHz, and comparing the upper limits in line flux for these sources with known Lyα emitting radio galaxies showed that a high-redshift nature could not be ruled out. It also remains possible from the radio luminosity functions of HERGs and LERGs presented in Chapter 6 that these sources could be low excitation radio galaxies at more moderate redshifts, although the possible turnover identified in the LERG RLF makes this more unlikely. As the Lyα flux/ radio flux ratio for known radio sources covers a fairly constant range out to high redshift, selecting bright, mJy radio sources at 1.4 GHz should increase the chance of successfully detecting Lyα emission, and hence confirming the source redshift and the nature of these sources.

It is also noted in Chapter 4 that many of the highest redshift radio galaxies are very compact and often display a negatively curved or peaked spectrum, which is corroborated by the findings from Chapter 5, where the proportion of GPS/CSS sources in complete samples shows indications of increasing with redshift. As discussed in Chapter 5, whilst the radio characteristics of GPS/CSS sources cannot be used to locate high-z radio galaxies alone, in combination with a near-infrared magnitude cut, this method could prove to be a promising way of filtering out the highest redshift radio galaxies in upcoming surveys.

Drawing these conclusions together, the combination of the upcoming LOFAR Medium-Deep surveys at 30, 60, 120 and 200 MHz, with the planned WRST APERTIF 1.4 GHz survey [Röttgering *et al.*, 2011] would provide instantaneous spectral coverage with the high angular resolution required to pick out small, peaked sources at lower frequencies (high redshift GPS sources would be expected to be peak around a few hundred MHz), and at relatively bright (mJy) 1.4 GHz fluxes. Combining this with near-infrared surveys, such as e.g. UKIDSS LAS [Lawrence *et al.*, 2007], which reaches a limiting K magnitude K $\sim$ 18, will allow good high-z candidates to be selected efficiently for follow-up, and to hopefully successfully allow the location of radio galaxies at z>6, enabling direct study of the neutral 21 cm hydrogen line in sources within the Epoch of Reionisation.

8.2 The Radio Luminosity Function: Contribution of the Radio Spectrum

Building on this work, it was noted that many high redshift sources display a curved radio spectrum. Traditionally, a two-point spectral index is used to calculate source luminosities, and it was unknown what effect incorporating spectral curvature has on source luminosities, and subsequent measurement of the radio luminosity function.

In Chapter 5 it is shown that the vast majority of sources within the four complete samples studied are better fitted by a 2nd order polynomial than by a simple power-law. Radio spectral curvature remains relatively constant with redshift, but there are also indications that the

fraction of compact, peaked sources increases at higher redshift (both GPS and CSS in high frequency selected samples, and CSS in low frequency selected samples).

For flat spectrum sources, curvature is shown to correlate with spectral index, which confirms that curvature should be fully taken into account with measuring the radio luminosity function of these sources (as was also found by Jarvis and Rawlings [2000]). For steep spectrum sources, incorporating the shape of the radio spectrum into calculations of source luminosity gives negligible differences from those calculated from a two-point spectral index at z<1, but at higher redshifts these differences can become more significant, of order 0.1-0.2 dex. Incorporating these into a calculation of the radio luminosity function can give rise to differences in individual measured space densities of order a factor 2-3, where source numbers are low, showing that the shape of the radio spectrum should not be neglected for high redshift sources in low numbers. However, for large samples, this effect should average out.

8.3 Measuring the Evolution of Low Excitation Radio Galaxies Across the Bulk of Cosmic Time

In Chapter 6 the question of how low excitation radio galaxies evolve is addressed. The very first measurement of the HERG and LERG radio luminosity functions out to a redshift of one is presented. Comparison with locally determined RLFs shows that there is significant evolution in the HERG RLF, and weaker evolution in the LERG RLF (typically a factor 2 higher than locally at higher luminosities). For the HERGs, this is what is expected from theoretical predictions. The evolution in LERGs is expected to be broadly flat out to z=1, but the theoretical predictions do allow an evolution of this magnitude within their uncertainty range, and there is a weak suggestion from the V/V_{MAX} test that the LERG luminosity function may begin to turnover in the range z=0.5-1.0. There are still uncertainties present in the RLF determinations due to the presence of unclassified sources, and sources with photometric redshifts. However, these are shown to have little effect on the measured RLFs, particularly for the LERG population, suggesting the weak evolution compared to locally, and the possible turnover at higher redshift seen is real. It is tentatively suggested that the weak evolution in the high radio luminosity LERG population could be attributed to greater numbers of rare LERGs hosted by massive blue galaxies at higher redshifts.

These luminosity functions are then utilised in an investigation of the nature of a sample of infra-red faint radio sources as summarised earlier. The numbers of IFRS are not inconsistent with the number of LERGs expected at z>1, assuming no further evolution in the LERG luminosity function, but as there are indications that the LERG RLF begins to turnover at z=0.5-1.0, this number will likely be reduced. In order to determine whether this turnover is genuine, further observations are required. Further spectroscopic observations are planned in October 2012, to gather classifications and redshifts for the remaining unclassified sources with only photometric redshift information. This should enable a more precise measurement of the LERG RLF, and any turnover present in the observed redshift range.

The results presented here have given exciting hints that the RLF of the two different

accretion modes do indeed evolve differently. In order to progress this further, the RLF for both HERGs and LERGs would need to measured out to higher redshifts, at z=1-3. This is much more technically difficult, as the majority of historical spectra available for radio sources are in the optical, and the [OIII] and [OII] emission lines are shifted out of this range at z>1.2. However, with the next generation of ground-based spectrometers, this may become less of a challenge. For example, SINFONI (as used in Chapter 3), or the new MOONs instrument on the VLT both have the appropriate wavelength range and capacity to target [OIII] in the near-infrared range, using non-prohibitive amounts of telescope time.

8.4 LOFAR: The Final Frontier

The findings outlined above have made significant strides in three inter-related strands of radio-AGN studies. However, there are three main limitations to further progress in these areas.

Small Sky Area Coverage Despite the rapid progress in understanding of the numbers and evolution of radio-AGN offered by studies of existing complete samples and 'deep-fields', the vast majority of these datasets with large amounts of high quality multi-wavelength data cover only very small areas of sky. This means only a negligible number of high redshift (z>4) sources can be studied, and the behaviour of the RLF at higher redshifts cannot be constrained.

Poor Radio Spectral Coverage Most current radio surveys have been taken decades apart, with differing resolutions. The behaviour of the low frequency end of the radio spectrum (ν<100 MHz) for radio sources is essentially unknown.

Lack of Radio Source Size Measurements VLBI measurements of radio source sizes, particularly those of high redshift candidates would enable sources to be confirmed as genuine young GPS or CSS sources, in addition to allowing detailed studies of the environments around them, and determine whether there is any change in the magnetic fields of sources at high redshift compared to low.

To obtain a complete picture of radio-loud AGN evolution, future studies must cover wide sky areas in order to incorporate the highest redshifts and rarest environments of AGN. The low frequency end of the radio spectrum is one of the last few areas of the observable electromagnetic spectrum that has yet to be fully explored. In Chapter 7, details of a brand new innovative low-frequency radio telescope with the capacity to do all of this are outlined. LOFAR will provide high resolution, high sensitivity wide area surveys over a substantial low frequency range. Several examples of software commissioning tests are presented, demonstrating that LOFAR is now leaving the construction phase, and will be ready to begin substantial science campaigns by late 2012.

The LOFAR Surveys KSP [Röttgering *et al.*, 2011] has guaranteed time on LOFAR during the first five years of operation, and will deliver a series of unique surveys ideally suited for this purpose. The extragalactic surveys will provide all sky surveys at a range of frequencies between

15 - 200 MHz, at the highest resolution (suitable for direct optical/infrared cross-matching) and sensitivity ever achieved at these frequencies, and with a survey speed outstripping all other radio telescopes in use today. This will enable a diverse and broad range of science to be studied, from nearby galaxies to cosmology, including detecting essentially all radio-loud AGN in the Universe. The first planned survey, the Multifrequency Snapshot Sky Survey (MSSS), designed to provide an all-sky calibration model for LOFAR, is already underway, and full science operations are expected to begin within the next year.

Auspiciously, there are several next-generation optical/near-infrared surveys just becoming available/underway. Wide-area optical and near-infrared surveys such as Pan-STARRS medium-deep, and the public UKIRT UKIDSS-LAS/DXS and ESO VLT VISTA and VST surveys, provide a fantastic opportunity for cross-matching with the LOFAR surveys to obtain photometric redshift estimates. These will provide a powerful resource for studying high redshift AGN and radio-AGN feedback on a much larger scale than is currently possible.

Extending the lines of investigation outlined above, such a combination of next-generation radio + optical/near-infrared datasets would allow several other aspects of AGN-feedback to be studied to unprecedented depth. For example, observations of the brightest cluster galaxies in recent years suggest that associated radio sources are responsible for heating the intra-cluster medium, and terminating cooling flows, illustrated most strongly by X-ray cavities in the gas being coincident with the radio lobes [e.g Fabian *et al.*, 2006]. Utilising LOFAR surveys data in combination with optical or near-infrared surveys would give a unique opportunity to study LERGs within (proto-)cluster environments, and determine how the radio source duty-cycle and heating vary both as a function of redshift and environment.

Bibliography

J. Afonso, L. Bizzocchi, E. Ibar, M. Grossi, C. Simpson, S. Chapman, M. J. Jarvis, H. Röttgering, R. P. Norris, J. Dunlop, R. J. Ivison, H. Messias, J. Pforr, M. Vaccari, N. Seymour, and P. Best. Ultra Steep Spectrum radio sources in the Lockman Hole: SERVS identifications and redshift distribution at the faintest radio fluxes. *ArXiv e-prints*, August 2011.

T. L. Aldcroft, J. Bechtold, and M. Elvis. MG II absorption in a sample of 56 steep-spectrum quasars. ApJS, 93:1–46, July 1994.

D. M. Alexander, W. N. Brandt, I. Smail, A. M. Swinbank, F. E. Bauer, A. W. Blain, S. C. Chapman, K. E. K. Coppin, R. J. Ivison, and K. Menéndez-Delmestre. Weighing the Black Holes in z $\sim$ 2 Submillimeter-Emitting Galaxies Hosting Active Galactic Nuclei. AJ, 135:1968–1981, May 2008.

S. W. Allen, R. J. H. Dunn, A. C. Fabian, G. B. Taylor, and C. S. Reynolds. The relation between accretion rate and jet power in X-ray luminous elliptical galaxies. MNRAS, 372:21–30, October 2006.

J. R. Allington-Smith, J. A. Peacock, and J. S. Dunlop. Spectroscopy of radio sources from the Parkes Selected Regions. MNRAS, 253:287–294, November 1991.

H. Andernach. Internet Resources for Radio Astronomy. In M. R. Kidger, I. Perez-Fournon, and F. Sanchez, editors, *Internet Resources for Professional Astronomy*, pages 67–130, 1999.

R. Andrae, T. Schulze-Hartung, and P. Melchior. Dos and don'ts of reduced chi-squared. *ArXiv e-prints*, December 2010.

R. Athreya. A New Approach to Mitigation of Radio Frequency Interference in Interferometric Data. ApJ, 696:885–890, May 2009.

J. W. M. Baars, R. Genzel, I. I. K. Pauliny-Toth, and A. Witzel. The absolute spectrum of CAS A - an accurate flux density scale and a set of secondary calibrators. A&A, 61:99–106, October 1977.

R. D. Baldi and A. Capetti. Radio and spectroscopic properties of miniature radio galaxies: revealing the bulk of the radio-loud AGN population. A&A, 508:603–614, December 2009.

Paramita Barai and Paul J. Wiita. Testing models of radio galaxy evolution and the cosmological impact of fr ii radio galaxies. ApJ, 658:217–231, 2007.

C. M. Baugh. A primer on hierarchical galaxy formation: the semi-analytical approach. *Rept.Prog.Phys.*, 69:3101–3156, 2006.

S. A. Baum, E. L. Zirbel, and C. P. O'Dea. Toward Understanding the Fanaroff-Riley Dichotomy in Radio Source Morphology and Power. ApJ, 451:88–+, September 1995.

R. H. Becker, R. L. White, and A. L. Edwards. A new catalog of 53,522 4.85 GHz sources. ApJS, 75:1–229, January 1991.

P. N. Best and T. M. Heckman. On the fundamental dichotomy in the local radio-AGN population: accretion, evolution and host galaxy properties. MNRAS, 421:1569–1582, April 2012.

P. N. Best and the LOFAR-UK Consortium. Lofar-uk white paper: A science case for uk involvement in lofar. February 2008.

P. N. Best, H. J. A. Röttgering, and M. D. Lehnert. A 98 per cent spectroscopically complete sample of the most powerful equatorial radio sources at 408MHz. MNRAS, 310:223–254, November 1999.

P. N. Best, J. N. Arts, H. J. A. Röttgering, R. Rengelink, M. H. Brookes, and J. Wall. Censors: A combined eis-nvss survey of radio sources. i. sample definition, radio data and optical identifications. MNRAS, 346:627, 2003.

P. N. Best, C. R. Kaiser, T. M. Heckman, and G. Kauffmann. Agn-controlled cooling in elliptical galaxies. MNRAS.*Lett.*, 368:L67–L71, 2006.

P. N. Best, A. von der Linden, G. Kauffmann, T. M. Heckman, and C. R. Kaiser. On the prevalence of radio-loud agn in brightest cluster galaxies: implications for agn heating of cooling flows. MNRAS, 379:894–908, 2007.

P. Best. Feedback from radio loud agn. *New Astronomy Reviews*, 51:168–173, 2007.

L. Birzan, D. A. Rafferty, B. R. McNamara, M. W. Wise, and P. E. J. Nulsen. A systematic study of radio-induced x-ray cavities in clusters, groups, and galaxies. ApJ, 607:800–809, 2004.

Roger D. Blandford. Active galaxies and quasistellar objects, accretion. Astronomy and Astrophysics Encyclopedia.

K. M. Blundell and S. Rawlings. High-z Radio Galaxies and the 'Youth-Redshift Degeneracy'. *ASPC Series*, 193:75–+, 1999.

K.M. Blundell, S. Rawlings, and C.J. Willott. The nature and evolution of classical double radio sources from complete samples. ApJ, 117:677–706, 1999.

C. G. Bornancini, C. De Breuck, W. de Vries, S. Croft, W. van Breugel, H. Röttgering, and D. Minniti. Imaging and spectroscopy of ultrasteep spectrum radio sources. MNRAS, 378:551–562, June 2007.

R. G. Bower, A. J. Benson, R. Malbon, J. C. Helly, C. S. Frenk, C. M. Baugh, S. Cole, and C. G. Lacey. The broken hierarchy of galaxy formation. MNRAS, 370:645–655, 2006.

R. A. A. Bowler, J. S. Dunlop, R. J. McLure, H. McCracken, B. Milvang-Jensen, H. Furusawa, J. P. U. Fynbo, O. Le Fevre, J. Holt, Y. Ideue, Y. Ihara, A. B. Rogers, and Y. Taniguchi. Discovery of bright z ˜ 7 galaxies in the UltraVISTA survey. *ArXiv e-prints*, May 2012.

M. N. Bremer, C. S. Crawford, A. C. Fabian, and R. M. Johnstone. Extended optical emission around radio-loud quasars at Z of about 1. MNRAS, 254:614–626, February 1992.

M. H. Brookes, P. N. Best, R. Rengelink, and H. J. A. Röttgering. A combined eis-nvss survey of radio sources ii: Infrared imaging and the k-z relation. MNRAS, 366:1265, 2006.

M. H. Brookes, P. N. Best, J. A. Peacock, H. J. A. Röttgering, and J. S. Dunlop. A combined eis-nvss survey of radio sources (censors) iii: Spectroscopic observations. MNRAS, 385:1297–1326, February 2008.

Mairi Brookes. *The Cosmological Evolution of Radio Sources*. PhD thesis, Institute for Astronomy, The University of Edinburgh, 2005.

M. Brusa, F. Fiore, P. Santini, A. Grazian, A. Comastri, G. Zamorani, G. Hasinger, A. Merloni, F. Civano, A. Fontana, and V. Mainieri. Black hole growth and starburst activity at z = 0.6-4 in the Chandra Deep Field South. Host galaxies properties of obscured AGN. A&A, 507:1277–1289, December 2009.

J. J. Bryant, H. M. Johnston, J. W. Broderick, R. W. Hunstead, C. De Breuck, and B. M. Gaensler. A new search for distant radio galaxies in the Southern hemisphere - III. Optical spectroscopy and analysis of the MRCR-SUMSS sample. MNRAS, 395:1099–1120, May 2009.

A. D. Cameron, M. Keith, G. Hobbs, R. P. Norris, M. Y. Mao, and E. Middelberg. Are the infrared-faint radio sources pulsars? MNRAS, 415:845–848, July 2011.

C. N. Cardamone, C. M. Urry, M. Damen, P. van Dokkum, E. Treister, I. Labbé, S. N. Virani, P. Lira, and E. Gawiser. Mid-Infrared Properties and Color Selection for X-Ray-Detected Active Galactic Nuclei in the MUSYC Extended Chandra Deep Field-South. ApJ, 680:130–142, June 2008.

C. L. Carilli, R. A. Perley, J. W. Dreher, and J. P. Leahy. Multifrequency radio observations of Cygnus A - Spectral aging in powerful radio galaxies. ApJ, 383:554–573, December 1991.

C. L. Carilli, Ran Wang, M. van Hoven, K. Dwarakanath, J. Chengalur, and S. Wyithe. A search for hi 21cm absorption toward the highest redshift radio loud objects. AJ, 133:2841–2845, 2007.

T. D. Carozzi and G. Woan. A generalized measurement equation and van Cittert-Zernike theorem for wide-field radio astronomical interferometry. MNRAS, 395:1558–1568, May 2009.

A. Cattaneo, S. M. Faber, J. Binney, A. Dekel, J. Kormendy, R. Mushotzky, A. Babul, P. N. Best, M. Brüggen, A. C. Fabian, C. S. Frenk, A. Khalatyan, H. Netzer, A. Mahdavi, J. Silk, M. Steinmetz, and L. Wisotzki. The role of black holes in galaxy formation and evolution. Nature, 460:213–219, July 2009.

K. C. Chambers, G. K. Miley, W. J. M. van Breugel, M. A. R. Bremer, J.-S. Huang, and N. A. Trentham. Ultra–Steep-Spectrum Radio Sources. II. Radio, Infrared, Optical, and HST Imaging of High-Redshift 4C Objects. ApJ, 106:247, October 1996.

C. C. Cheung and A. Springmann. FIRST "Winged" and "X"-shaped Radio Source Candidates. In L. C. Ho and J.-W. Wang, editors, *The Central Engine of Active Galactic Nuclei*, volume 373 of *Astronomical Society of the Pacific Conference Series*, page 259, October 2007.

A. S. Cohen, W. M. Lane, W. D. Cotton, N. E. Kassim, T. J. W. Lazio, R. A. Perley, J. J. Condon, and W. C. Erickson. The vla low-frequency sky survey. AJ, 134:1245–1262, June 2007.

J. J. Condon, W. D. Cotton, E. W. Greisen, Q. F. Yin, R. A. Perley, G. B. Taylor, and J. J. Broderick. The NRAO VLA Sky Survey. AJ, 115:1693–1716, May 1998.

J. J. Condon. Radio emission from normal galaxies. *Ann.Rev.Astron.Astrophys.*, 30:575–611, 1992.

R. J. Cool, D. J. Eisenstein, X. Fan, M. Fukugita, L. Jiang, C. Maraston, A. Meiksin, D. P. Schneider, and D. A. Wake. Luminosity Function Constraints on the Evolution of Massive Red Galaxies since z ˜ 0.9. ApJ, 682:919–936, August 2008.

K. E. K. Coppin, I. Smail, D. M. Alexander, A. Weiss, F. Walter, A. M. Swinbank, T. R. Greve, A. Kovacs, C. De Breuck, M. Dickinson, E. Ibar, R. J. Ivison, N. Reddy, H. Spinrad, D. Stern, W. N. Brandt, S. C. Chapman, H. Dannerbauer, P. van Dokkum, J. S. Dunlop, D. Frayer, E. Gawiser, J. E. Geach, M. Huynh, K. K. Knudsen, A. M. Koekemoer, B. D. Lehmer, K. M. Menten, C. Papovich, H.-W. Rix, E. Schinnerer, J. L. Wardlow, and P. P. van der Werf. A submillimetre galaxy at z = 4.76 in the LABOCA survey of the Extended Chandra Deep Field-South. MNRAS, 395:1905–1914, June 2009.

J. H. Croston, M. J. Hardcastle, and M. Birkinshaw. Evidence for radio-source heating of groups. MNRAS, 357:279–294, February 2005.

Darren J. Croton, Volker Springel, Simon D. M. White, G. De Lucia, C. S. Frenk, L. Gao, A. Jenkins, G. Kauffmann, J. F. Navarro, and N. Yoshida. The many lives of active galactic nuclei: cooling flows, black holes and the luminosities and colours of galaxies. MNRAS, 365:11–28, 2006.

Maria J. Cruz, Matt J. Jarvis, Steve Rawlings, and Katherine M. Blundell. The 6c** sample of steep-spectrum radio sources: Ii - redshift distribution and the space density of high-redshift radio galaxies. MNRAS, 375:1349–1363, 2007.

E. Daddi, D. M. Alexander, M. Dickinson, R. Gilli, A. Renzini, D. Elbaz, A. Cimatti, R. Chary, D. Frayer, F. E. Bauer, W. N. Brandt, M. Giavalisco, N. A. Grogin, M. Huynh, J. Kurk, M. Mignoli, G. Morrison, A. Pope, and S. Ravindranath. Multiwavelength Study of Massive Galaxies at z∼2. II. Widespread Compton-thick Active Galactic Nuclei and the Concurrent Growth of Black Holes and Bulges. ApJ, 670:173–189, November 2007.

M. Damen, I. Labbé, P. G. van Dokkum, M. Franx, E. N. Taylor, W. N. Brandt, M. Dickinson, E. Gawiser, G. D. Illingworth, M. Kriek, D. Marchesini, A. Muzzin, C. Papovich, and H.-W. Rix. The SIMPLE Survey: Observations, Reduction, and Catalog. ApJ, 727:1, January 2011.

C. de Breuck, W. van Breugel, H. Röttgering, and G. Miley. A sample of 669 ultra steep spectrum radio sources to find high redshift radio galaxies. A&A, 143:303–333, 2000.

C. De Breuck, W. van Breugel, H. Röttgering, D. Stern, G. Miley, W. de Vries, S. A. Stanford, J. Kurk, and R. Overzier. Spectroscopy of Ultra-steep-Spectrum Radio Sources. AJ, 121:1241–1265, March 2001.

C. de Breuck, Y. Tang, A. G. de Bruyn, H. Röttgering, and W. van Breugel. A sample of ultra steep spectrum sources selected from the Westerbork In the Southern Hemisphere (WISH) survey. A&A, 394:59–69, October 2002.

F. de Gasperin, H. T. Intema, and E. Orrú. Estimating gmrt pointing errors. Technical report, June 2011.

G. De Lucia. "Ab initio" models of galaxy formation: successes and open problems. In G. Giobbi, A. Tornambe, G. Raimondo, M. Limongi, L. A. Antonelli, N. Menci, and E. Brocato, editors, *American Institute of Physics Conference Series*, volume 1111 of *American Institute of Physics Conference Series*, pages 3–10, May 2009.

W. H. de Vries, P. D. Barthel, and R. Hes. Identifications of Gigahertz Peaked Spectrum radio sources. A&AS, 114:259, December 1995.

S. di Serego-Alighieri, I. J. Danziger, R. Morganti, and C. N. Tadhunter. New Identifications and Redshifts for Southern 2-JANSKY Radio Sources. MNRAS, 269:998, August 1994.

J. N. Douglas, F. N. Bash, F. A. Bozyan, G. W. Torrence, and C. Wolfe. The Texas Survey of Radio Sources Covering -35.5 degrees < declination < 71.5 degrees at 365 MHz. AJ, 111:1945–+, May 1996.

A. J. B. Downes, J. A. Peacock, A. Savage, and D. R. Carrie. The Parkes selected regions - Powerful radio galaxies and quasars at high redshifts. MNRAS, 218:31–62, January 1986.

P. Duffy and K. M. Blundell. The non-thermal emission of extended radio galaxy lobes with curved electron spectra. MNRAS, 421:108–115, March 2012.

J. Dunkley, E. Komatsu, M. R. Nolta, D. N. Spergel, D. Larson, G. Hinshaw, L. Page, C. L. Bennett, B. Gold, N. Jarosik, J. L. Weiland, M. Halpern, R. S. Hill, A. Kogut, M. Limon, S. S. Meyer, G. S. Tucker, E. Wollack, and E. L. Wright. Five-year wilkinson microwave anisotropy probe (wmap) observations: Likelihoods and parameters from the wmap data. *Astrophys.J.Suppl.*, 180:306–329, March 2008.

J. S. Dunlop and J. A. Peacock. The Redshift Cut-Off in the Luminosity Function of Radio Galaxies and Quasars. MNRAS, 247:19–+, November 1990.

J. S. Dunlop, J. A. Peacock, A. Savage, S. J. Lilly, J. N. Heasley, and A. J. B. Simon. The Parkes Selected Regions - Deep optical and infrared observations of radio galaxies and quasars at high redshifts. MNRAS, 238:1171–1231, June 1989.

S.A. Eales. A sample of the 6c radio sources selected at the peak of the source counts. i - a search for extended sources and multifrequency radio observations. ii - optical identifications. iii - an investigation of the variation of the sizes of radio sources with cosmic epoch. MNRAS, 217:149–177, November 1985.

Richard S Ellis. Observations of the high redshift universe. 2007.

D. A. Evans, M. J. Hardcastle, and J. H. Croston. X-Ray Nuclei in Radio Galaxies: Exploring the Roles of Hot and Cold Gas Accretion. In T. A. Rector and D. S. De Young, editors, *Extragalactic Jets: Theory and Observation from Radio to Gamma Ray*, volume 386 of *Astronomical Society of the Pacific Conference Series*, page 161, June 2008.

A. C. Fabian, J. S. Sanders, G. B. Taylor, S. W. Allen, C. S. Crawford, R. M. Johnstone, and K. Iwasawa. A very deep chandra observation of the perseus cluster: shocks, ripples and conduction. MNRAS, 366:417–428, 2006.

A. C. Fabian. Observational Evidence of Active Galactic Nuclei Feedback. ARA&A, 50:455–489, September 2012.

H. Falcke, E. Körding, and N. M. Nagar. Compact radio cores: from the first black holes to the last. *NAR*, 48:1157–1171, December 2004.

B. L. Fanaroff and J. M. Riley. The morphology of extragalactic radio sources of high and low luminosity. MNRAS, 167:31P–36P, May 1974.

L. Ferrarese and D. Merritt. A Fundamental Relation between Supermassive Black Holes and Their Host Galaxies. ApJ, 539:L9–L12, August 2000.

T. Garn and P. Alexander. Deep 610-MHz Giant Metrewave Radio Telescope observations of the Spitzer extragalactic First Look Survey field - III. The radio properties of infrared-faint radio sources. MNRAS, 391:1000–1008, December 2008.

Timothy Garn, David A. Green, Sally E. G. Hales, Julia M. Riley, and Paul Alexander. Deep 610-mhz gmrt observations of the spitzer extragalactic first look survey field - i. observations, data analysis and source catalogue. MNRAS, 376:1251–1260, 2007.

Timothy Garn, Dominic Ford, Paul Alexander, David A. Green, and Julia M. Riley. Magnetic fields in star-forming galaxies at high and low redshift. *From Planets to Dark Energy: the Modern Radio Universe. October 1-5 2007, The University of Manchester, UK. Published online at SISSA, Proceedings of Science*, page p.73, June 2008.

Timothy Garn. *610MHz Observations of Galaxy Evolution*. PhD thesis, University of Cambridge, September 2008.

R.A. Perley G.B. Taylor, C.L. Carilli, editor. *Synthesis Imaging in Radio Astronomy II*, volume 180. Astronomical Society of the Pacific Conference Series, 1999.

K. Gebhardt, R. Bender, G. Bower, A. Dressler, S. M. Faber, A. V. Filippenko, R. Green, C. Grillmair, L. C. Ho, J. Kormendy, T. R. Lauer, J. Magorrian, J. Pinkney, D. Richstone, and S. Tremaine. A Relationship between Nuclear Black Hole Mass and Galaxy Velocity Dispersion. ApJ, 539:L13–L16, August 2000.

R. Gelderman and M. Whittle. An optical study of compact steep-spectrum radio sources. 1: The spectroscopic data. ApJS, 91:491–505, April 1994.

M. A. Gendre, P. N. Best, and J. V. Wall. The Combined NVSS-FIRST Galaxies (CoNFIG) sample - II. Comparison of space densities in the Fanaroff-Riley dichotomy. MNRAS, 404:1719–1732, June 2010.

M. A. Gendre, P. N. Best, J. V. Wall, and L. M. Ker. The relation between morphology, accretion modes and environmental factors in local radio agn. in prep., 2012.

Gopal-Krishna, M. Mhaskey, and A. Mangalam. On the Injection Spectrum of Relativistic Electrons in High-redshift Radio Galaxies. ApJ, 744:31, January 2012.

E. Greison. *AIPS Cookbook*. The National Radio Astronomy Observatory, 2007.

Jennifer A. Grimes, Steve Rawlings, and Chris J. Willott. Implications for unified schemes from the quasar fraction and emission-line luminosities in radio-selected samples. MNRAS, 349:503, 2004.

K. Gültekin, D. O. Richstone, K. Gebhardt, T. R. Lauer, S. Tremaine, M. C. Aller, R. Bender, A. Dressler, S. M. Faber, A. V. Filippenko, R. Green, L. C. Ho, J. Kormendy, J. Magorrian, J. Pinkney, and C. Siopis. The M-σ and M-L Relations in Galactic Bulges, and Determinations of Their Intrinsic Scatter. ApJ, 698:198–221, June 2009.

S. E. G. Hales, J. M. Riley, E. M. Waldram, P. J. Warner, and J. E. Baldwin. A final non-redundant catalogue for the 7C 151-MHz survey. MNRAS, 382:1639–1642, December 2007.

J. P. Hamaker, J. D. Bregman, and R. J. Sault. Understanding radio polarimetry. I. Mathematical foundations. A&A. *Supp.*, 117:137–147, May 1996.

M. J. Hardcastle, D. A. Evans, and J. H. Croston. Hot and cold gas accretion and feedback in radio-loud active galaxies. MNRAS, 376:1849–1856, 2007.

T. E. Hassall, B. W. Stappers, J. W. T. Hessels, M. Kramer, A. Alexov, K. Anderson, T. Coenen, A. Karastergiou, E. F. Keane, V. I. Kondratiev, K. Lazaridis, J. van Leeuwen, A. Noutsos, M. Serylak, C. Sobey, J. P. W. Verbiest, P. Weltevrede, K. Zagkouris, R. Fender, R. A. M. J. Wijers, L. Bähren, M. E. Bell, J. W. Broderick, S. Corbel, E. J. Daw, V. S. Dhillon, J. Eislöffel, H. Falcke, J.-M. Grießmeier, P. Jonker, C. Law, S. Markoff, J. C. A. Miller-Jones, R. Osten, E. Rol, A. M. M. Scaife, B. Scheers, P. Schellart, H. Spreeuw, J. Swinbank, S. ter Veen, M. W. Wise, R. Wijnands, O. Wucknitz, P. Zarka, A. Asgekar, M. R. Bell, M. J. Bentum, G. Bernardi, P. Best, A. Bonafede, A. J. Boonstra, M. Brentjens, W. N. Brouw, M. Brüggen, H. R. Butcher, B. Ciardi, M. A. Garrett, M. Gerbers, A. W. Gunst, M. P. van Haarlem, G. Heald, M. Hoeft, H. Holties, A. de Jong, L. V. E. Koopmans, M. Kuniyoshi, G. Kuper, G. M. Loose, P. Maat, J. Masters, J. P. McKean, H. Meulman, M. Mevius, H. Munk, J. E. Noordam, E. Orrú, H. Paas, M. Pandey-Pommier, V. N. Pandey, R. Pizzo, A. Polatidis, W. Reich, H. Röttgering, J. Sluman, M. Steinmetz, C. G. M. Sterks, M. Tagger, Y. Tang, C. Tasse, R. Vermeulen, R. J. van Weeren, S. J. Wijnholds, and S. Yatawatta. Wide-band simultaneous observations of pulsars: disentangling dispersion measure and profile variations. A&A, 543:A66, July 2012.

T. M. Heckman, E. P. Smith, S. A. Baum, W. J. M. van Breugel, G. K. Miley, G. D. Illingworth, G. D. Bothun, and B. Balick. Galaxy collisions and mergers - The genesis of very powerful radio sources? ApJ, 311:526–547, December 1986.

T. M. Heckman, G. Kauffmann, J. Brinchmann, S. Charlot, C. Tremonti, and S. D. M. White. Present-Day Growth of Black Holes and Bulges: The Sloan Digital Sky Survey Perspective. ApJ, 613:109–118, September 2004.

J. F. Helmboldt, N. E. Kassim, A. S. Cohen, W. M. Lane, and T. J. Lazio. Radio Frequency Spectra of 388 Bright 74 MHz Sources. ApJS, 174:313–336, February 2008.

A. Hewitt and G. Burbidge. A new optical catalog of Quasi-Stellar Objects. In *A new optical catalog of QSO (1989)*, page 0, 1989.

A. Hewitt and G. Burbidge. A revised and updated catalog of quasi-stellar objects. ApJS, 87:451–947, August 1993.

R. G. Hine and M. S. Longair. Optical spectra of 3CR radio galaxies. MNRAS, 188:111–130, July 1979.

P. Hirst, N. Jackson, and S. Rawlings. Near-infrared spectroscopy of powerful compact steep-spectrum radio sources. MNRAS, 346:1009–1020, December 2003.

David W. Hogg, Ivan K. Baldry, Michael R. Blanton, and Daniel J. Eisenstein. The k correction. 2007.

J. Holt, C. N. Tadhunter, and R. Morganti. The ionization of the emission-line gas in young radio galaxies. MNRAS, 400:589–602, December 2009.

Eduardo Ibar. *Deep Multi-frequency radio observations of the SHADES fields and the nature of the faint radio sources population*. PhD thesis, Institute for Astronomy, The University of Edinburgh, 2008.

H. T. Intema, S. van der Tol, W. D. Cotton, A. S. Cohen, I. M. van Bemmel, and H. J. A. Röttgering. Ionospheric calibration of low frequency radio interferometric observations using the peeling scheme. I. Method description and first results. A&A, 501:1185–1205, July 2009.

C. H. Ishwara-Chandra, S. K. Sirothia, Y. Wadadekar, S. Pal, and R. Windhorst. Deep GMRT 150-MHz observations of the LBDS-Lynx region: ultrasteep spectrum radio sources. MNRAS, 405:436–446, June 2010.

N. Jackson and S. Rawlings. [O III] 500.7 spectroscopy of 3C galaxies and quasars at redshift z>1. MNRAS, 286:241–256, March 1997.

J.D. Jackson. *Classical electrodynamics*. Wiley, 1962.

C. A. Jackson. Radio source evolution and unified schemes. *Electronic Publications of the Astronomical Society of Australia*, 16:2, 2006.

R. M. J. Janssen, H. J. A. Röttgering, P. N. Best, and J. Brinchmann. The triggering probability of radio-loud AGN. A comparison of high and low excitation radio galaxies in hosts of different colors. A&A, 541:A62, May 2012.

Matt J. Jarvis and Ross J. McLure. On the black-hole mass – radio luminosity relation for flat-spectrum radio-loud quasars. MNRAS, 336:L38, 2002.

Matt J. Jarvis and Steve Rawlings. On the redshift cut-off for flat-spectrum radio sources. MNRAS, 319:121, 2000.

Matt J. Jarvis, Steve Rawlings, Steve Eales, Katherine M. Blundell, Andrew J. Bunker, Steve Croft, Ross J. McLure, and Chris J. Willott. A sample of 6c radio sources designed to find objects at redshift ¿ 4: Iii — imaging and the radio galaxy k-z relation. MNRAS, 326:1585, 2001.

Matt J. Jarvis, Hanifa Teimourian, Chris Simpson, Daniel J. B. Smith, Steve Rawlings, and David Bonfield. The discovery of a typical radio galaxy at z = 4.88. MNRAS.*Lett*, July 2009.

T.L. Wilson K. Rohlfs. *Tools of Radio Astronomy*. Astronomy and Astrophysics Library. Springer, 2000.

C. R. Kaiser and P. N. Best. Luminosity function, sizes and FR dichotomy of radio-loud AGN. MNRAS, 381:1548–1560, November 2007.

C. R. Kaiser. The environments and ages of extragalactic radio sources inferred from multi-frequency radio maps. A&A, 362:447–464, October 2000.

Nimisha Kantharia. Working towards a pointing model for gmrt antennas -i. Technical report, Tata Institute for Fundamental Research, 2005.

Guinevere Kauffmann, Timothy M. Heckman, Christy Tremonti, Jarle Brinchmann, Stephane Charlot, Simon D. M. White, Susan Ridgway, Jon Brinkmann, Masataka Fukugita, Patrick Hall, Zeljko Ivezic, Gordon Richards, and Donald Schneider. The host galaxies of agn. MNRAS, 346:1055, 2003.

K. I. Kellermann, I. I. K. Pauliny-Toth, and P. J. S. Williams. The Spectra of Radio Sources in the Revised 3c Catalogue. ApJ, 157:1, July 1969.

K. I. Kellermann, E. B. Fomalont, V. Mainieri, P. Padovani, P. Rosati, P. Shaver, P. Tozzi, and N. Miller. The vla survey of the chandra deep field south: I. overview of the radio data. *Astrophys.J.*, June 2008.

G. L. Kellermann, K. I.; Verschuur. *Galactic and Extragalactic Radio Astronomy*. Number Chapter 13. Berlin and New York, Springer-Verlag, 1998.

M. L. Khabibullina and O. V. Verkhodanov. Catalog of radio galaxies with z¿0.3. i:construction of the sample. *Astrophys. Bull.,*, 64,:No3, 263, 2009.

S. Khochfar and J. Silk. The specific star formation rate of high redshift galaxies: the case for two modes of star formation. MNRAS, 410:L42–L46, January 2011.

I. J. Klamer, R. D. Ekers, J. J. Bryant, R. W. Hunstead, E. M. Sadler, and C. De Breuck. A search for distant radio galaxies from sumss and nvss: Iii. radio spectral energy distributions and the z-alpha correlation. MNRAS, 371:852–866, 2006.

E. Komatsu, K. M. Smith, J. Dunkley, C. L. Bennett, B. Gold, G. Hinshaw, N. Jarosik, D. Larson, M. R. Nolta, L. Page, D. N. Spergel, M. Halpern, R. S. Hill, A. Kogut, M. Limon, S. S. Meyer, N. Odegard, G. S. Tucker, J. L. Weiland, E. Wollack, and E. L. Wright. Seven-year Wilkinson Microwave Anisotropy Probe (WMAP) Observations: Cosmological Interpretation. ApJS, 192:18, February 2011.

J. Kormendy. Supermassive Black Holes in Disk Galaxies. In J. G. Funes and E. M. Corsini, editors, *Galaxy Disks and Disk Galaxies*, volume 230 of *Astronomical Society of the Pacific Conference Series*, pages 247–256, 2001.

J. K. Kuraszkiewicz, P. J. Green, K. Forster, T. L. Aldcroft, I. N. Evans, and A. Koratkar. Emission Line Properties of Active Galactic Nuclei from a pre-COSTAR Faint Object Spectrograph Hubble Space Telescope Spectral Atlas. ApJS, 143:257–276, December 2002.

F. La Franca, G. Melini, and F. Fiore. Tools for Computing the AGN Feedback: Radio-loudness Distribution and the Kinetic Luminosity Function. ApJ, 718:368–379, July 2010.

A. Labiano, P. D. Barthel, C. P. O'Dea, W. H. de Vries, I. Pérez, and S. A. Baum. GPS radio sources: new optical observations and an updated master list. A&A, 463:97–104, February 2007.

M. Lacy, S. Rawlings, G. J. Hill, A. J. Bunker, S. E. Ridgway, and D. Stern. Optical spectroscopy of two overlapping, flux-density-limited samples of radio sources in the North Ecliptic Cap, selected at 38 and 151MHz. MNRAS, 308:1096–1116, October 1999.

M. Lacy, L. J. Storrie-Lombardi, A. Sajina, P. N. Appleton, L. Armus, S. C. Chapman, P. I. Choi, D. Fadda, F. Fang, D. T. Frayer, I. Heinrichsen, G. Helou, M. Im, F. R. Marleau, F. Masci, D. L. Shupe, B. T. Soifer, J. Surace, H. I. Teplitz, G. Wilson, and L. Yan. Obscured and Unobscured Active Galactic Nuclei in the Spitzer Space Telescope First Look Survey. ApJS, 154:166–169, September 2004.

J. F. Lahulla, R. Merighi, G. Vettolani, and M. Vigotti. The B-3 VLA sample - Quasar redshifts. II. A&AS, 88:525–534, June 1991.

R. A. Laing and J. A. Peacock. The relation between radio luminosity and spectrum for extended extragalactic radio sources. MNRAS, 190:903–924, March 1980.

R. A. Laing, J. M. Riley, and M. S. Longair. Bright radio sources at 178 MHz - Flux densities, optical identifications and the cosmological evolution of powerful radio galaxies. MNRAS, 204:151–187, July 1983.

R. A. Laing, C. R. Jenkins, J. V. Wall, and S. W. Unger, editors. *Spectrophotometry of a Complete Sample of 3CR Radio Sources: Implications for Unified Models*, volume 54 of *Astronomical Society of the Pacific Conference Series*, 1994.

D. V. Lal and A. P. Rao. Spectral structure of X-shaped radio sources. *Bulletin of the Astronomical Society of India*, 32:247, September 2004.

C. R. Lawrence, J. R. Zucker, A. C. S. Readhead, S. C. Unwin, T. J. Pearson, and W. Xu. Optical Spectra of a Complete Sample of Radio Sources. I. The Spectra. ApJS, 107:541, December 1996.

A. Lawrence, S. J. Warren, O. Almaini, A. C. Edge, N. C. Hambly, R. F. Jameson, P. Lucas, M. Casali, A. Adamson, S. Dye, J. P. Emerson, S. Foucaud, P. Hewett, P. Hirst, S. T. Hodgkin, M. J. Irwin, N. Lodieu, R. G. McMahon, C. Simpson, I. Smail, D. Mortlock, and M. Folger. The ukirt infrared deep sky survey (ukidss). MNRAS, 379:1599–1617, 2007.

T. J. W. Lazio, N.E. Kassim, and R.A. Perley. *Low-Frequency Data Reduction at the VLA: A Tutorial for New Users*, revision: 1.13 edition, January 2005.

S. J. Lilly and M. S. Longair. Infrared studies of a sample of 3C radio galaxies. MNRAS, 199:1053–1068, June 1982.

M.S. Longair. *High Energy Astrophysics*. Cambridge University Press, 2011.

J. Machalski, M. Jamrozy, and D. J. Saikia. A multifrequency study of giant radio sources - III. Dynamical age versus spectral age of the lobes of selected sources. MNRAS, 395:812–822, May 2009.

J. Magorrian, S. Tremaine, D. Richstone, R. Bender, G. Bower, A. Dressler, S. M. Faber, K. Gebhardt, R. Green, C. Grillmair, J. Kormendy, and T. Lauer. The Demography of Massive Dark Objects in Galaxy Centers. AJ, 115:2285–2305, June 1998.

V. Mainieri, K. I. Kellermann, E. B. Fomalont, N. Miller, P. Padovani, P. Rosati, P. Shaver, J. Silverman, P. Tozzi, J. Bergeron, G. Hasinger, C. Norman, and P. Popesso. The VLA Survey of the Chandra Deep Field-South. II. Identification and Host Galaxy Properties of Submillijansky Sources. ApJS, 179:95–113, November 2008.

A. Martínez-Sansigre and S. Rawlings. Observational constraints on the spin of the most massive black holes from radio observations. MNRAS, 414:1937–1964, July 2011.

P. Marziani, J. W. Sulentic, D. Dultzin-Hacyan, M. Calvani, and M. Moles. Comparative Analysis of the High- and Low-Ionization Lines in the Broad-Line Region of Active Galactic Nuclei. ApJS, 104:37, May 1996.

Y. Matsuoka and K. Kawara. Witnessing the active assembly phase of massive galaxies since z = 1. MNRAS, 405:100–110, June 2010.

L. Maxfield, D. Thompson, S. Djorgovski, M. Vigotti, and G. Grueff. Optical Identifications of Radio Galaxies from the B3VLA Survey. PASP, 107:369, April 1995.

J. McKean, L. Ker, R. J. van Weeren, F. Batejat, L. Birzan, A. Bonafede, J. Conway, F. De Gasperin, C. Ferrari, G. Heald, N. Jackson, G. Macario, E. Orrù, R. Pizzo, D. Rafferty, H. Rottgering, A. Shulevski, C. Tasse, S. van der Tol, I. van Bemmel, G. van Diepen, J. E. van Zwieten, and for the LOFAR collaboration. LOFAR: Early imaging results from commissioning for Cygnus A. *ArXiv e-prints*, June 2011.

R. J. McLure and J. S. Dunlop. On the black hole-bulge mass relation in active and inactive galaxies. MNRAS, 331:795–804, April 2002.

R. J. McLure, M. J. Jarvis, T. A. Targett, J. S. Dunlop, and P. N. Best. On the evolution of the black-hole:spheroid mass ratio. New A Rev., 50:782–785, November 2006.

R. J. McLure, J. S. Dunlop, L. de Ravel, M. Cirasuolo, R. S. Ellis, M. Schenker, B. E. Robertson, A. M. Koekemoer, D. P. Stark, and R. A. A. Bowler. A robust sample of galaxies at redshifts 6.0<z<8.7: stellar populations, star formation rates and stellar masses. MNRAS, 418:2074–2105, December 2011.

A. Meiksin. The micro-structure of the intergalactic medium - I. The 21 cm signature from dynamical minihaloes. MNRAS, 417:1480–1509, October 2011.

A. Merloni and S. Heinz. A synthesis model for AGN evolution: supermassive black holes growth and feedback modes. MNRAS, 388:1011–1030, August 2008.

D. Merritt and G. D. Quinlan. Dynamical Evolution of Elliptical Galaxies with Central Singularities. ApJ, 498:625, May 1998.

E. Middelberg, R. P. Norris, C. A. Hales, N. Seymour, M. Johnston-Hollitt, M. T. Huynh, E. Lenc, and M. Y. Mao. The radio properties of infrared-faint radio sources. A&A, 526:A8+, February 2011.

G. Miley and C. De Breuck. Distant radio galaxies and their environments. A&A Rev., 15:67–144, February 2008.

R. Mohan, K. S. Dwarakanath, G. Srinivasan, and J. N. Chengalur. GMRT observations of interstellar clouds in the 21cm line of atomic hydrogen. *Journal of Astrophysics and Astronomy*, 22:35–50, March 2001.

D. J. Mortlock, S. J. Warren, B. P. Venemans, M. Patel, P. C. Hewett, R. G. McMahon, C. Simpson, T. Theuns, E. A. Gonzáles-Solares, A. Adamson, S. Dye, N. C. Hambly, P. Hirst, M. J. Irwin, E. Kuiper, A. Lawrence, and H. J. A. Röttgering. A luminous quasar at a redshift of z = 7.085. Nature, 474:616–619, June 2011.

M. Murgia, C. Fanti, R. Fanti, L. Gregorini, U. Klein, K.-H. Mack, and M. Vigotti. Synchrotron spectra and ages of compact steep spectrum radio sources. A&A, 345:769–777, May 1999.

M. Murgia. Spectral Ages of CSOs and CSS Sources. PASA, 20:19–24, 2003.

N. P. H. Nesvadba, M. D. Lehnert, C. De Breuck, A. Gilbert, and W. van Breugel. Compact radio sources and jet-driven AGN feedback in the early universe: constraints from integral-field spectroscopy. A&A, 475:145–153, November 2007.

J.E. Noordam. The measurement equation of a generic radio telescope. Technical report, ASTRON, NFRA, 1996.

O.E. Noordam, J.E. Smirnov. Meqtrees: A software module for implementing an arbitrary measurement equation and solving for its parameters. Project Doculmentation Version 0.991, ASTRON, Dwingeloo, 2009.

R. P. Norris, S. Tingay, C. Phillips, E. Middelberg, A. Deller, and P. N. Appleton. Very long baseline interferometry detection of an Infrared-Faint Radio Source. MNRAS, 378:1434–1438, July 2007.

C. P. O'Dea. The Compact Steep-Spectrum and Gigahertz Peaked-Spectrum Radio Sources. PASP, 110:493–532, May 1998.

A. R. Offringa, A. G. de Bruyn, S. Zaroubi, and M. Biehl. A lofar rfi detection pipeline and its first results. July 2010.

P. Ogle, D. Whysong, and R. Antonucci. Spitzer Reveals Hidden Quasar Nuclei in Some Powerful FR II Radio Galaxies. ApJ, 647:161–171, August 2006.

E. Orrú, M. Murgia, L. Feretti, F. Govoni, G. Brunetti, G. Giovannini, M. Girardi, and G. Setti. Low-frequency study of two clusters of galaxies: A2744 and A2219. A&A, 467:943–954, June 2007.

E. Orrù, M. Murgia, L. Feretti, F. Govoni, G. Giovannini, W. Lane, N. Kassim, and R. Paladino. Low-frequency study of two giant radio galaxies: 3C 35 and 3C 223. A&A, 515:A50, June 2010.

P. Padovani, V. Mainieri, P. Tozzi, K. I. Kellermann, E. B. Fomalont, N. Miller, P. Rosati, and P. Shaver. The Very Large Array Survey of the Chandra Deep Field South. IV. Source Population. ApJ, 694:235–246, March 2009.

P. Padovani, N. Miller, K. I. Kellermann, V. Mainieri, P. Rosati, and P. Tozzi. The VLA Survey of Chandra Deep Field South. V. Evolution and Luminosity Functions of Sub-millijansky Radio Sources and the Issue of Radio Emission in Radio-quiet Active Galactic Nuclei. ApJ, 740:20, October 2011.

J. A. Peacock and 2dFGRS Team. Measuring Large-Scale Structure with the 2dF Galaxy Redshift Survey (Plenary Talk). In J. C. Wheeler and H. Martel, editors, *20th Texas Symposium on relativistic astrophysics*, volume 586 of *American Institute of Physics Conference Series*, page 245, October 2001.

John A. Peacock. *Cosmological Physics*. Cambridge University Press, 1998.

T. J. Pearson and A. J. Kus. The 5C 6 and 5C 7 surveys of radio sources. MNRAS, 182:273–274, January 1978.

M. Pedani. On the efficiency of the ultra steep spectrum technique in finding high-z radiogalaxies. *New Astron.*, 8:805–815, 2003.

W. H. Press and P. Schechter. Formation of Galaxies and Clusters of Galaxies by Self-Similar Gravitational Condensation. ApJ, 187:425–438, February 1974.

D. A. Rafferty, W. N. Brandt, D. M. Alexander, Y. Q. Xue, F. E. Bauer, B. D. Lehmer, B. Luo, and C. Papovich. Supermassive Black Hole Growth in Starburst Galaxies over Cosmic Time: Constraints from the Deepest Chandra Fields. ApJ, 742:3, November 2011.

Steve Rawlings, Steve Eales, and Mark Lacy. A sample of 6c radio sources with virtually complete redshifts. ii - optical spectroscopy. MNRAS, 322:523, 2001.

N. Rees. A deep 38-MHz radio survey of the area delta greater than + 60 degrees. MNRAS, 244:233–246, May 1990.

R. B. Rengelink, Y. Tang, A. G. de Bruyn, G. K. Miley, M. N. Bremer, H. J. A. Röttgering, and M. A. R. Bremer. The Westerbork Northern Sky Survey (WENSS), I. A 570 square degree Mini-Survey around the North Ecliptic Pole. A&AS, 124:259–280, August 1997.

M. Reuland, W. van Breugel, H. Röttgering, W. de Vries, C. De Breuck, and D. Stern. An Obscured Radio Galaxy at High Redshift. ApJ, 582:L71–L74, January 2003.

A. G. Riess, L. Macri, S. Casertano, M. Sosey, H. Lampeitl, H. C. Ferguson, A. V. Filippenko, S. W. Jha, W. Li, R. Chornock, and D. Sarkar. A Redetermination of the Hubble Constant with the Hubble Space Telescope from a Differential Distance Ladder. ApJ, 699:539–563, July 2009.

E. E. Rigby, P. N. Best, M. H. Brookes, J. A. Peacock, J. S. Dunlop, H. J. A. Röttgering, J. V. Wall, and L. Ker. The luminosity-dependent high-redshift turnover in the steep spectrum radio luminosity function: clear evidence for downsizing in the radio-AGN population. MNRAS, 416:1900–1915, September 2011.

E. E. Rigby. *Measuring the high redshift space density of FRI radio galaxies: investigating the nature of the FRI/II divide*. PhD thesis, The University of Edinburgh, 2007.

I. Robson. *Active Galactic Nuclei*. Wiley-Praxis Series in Astronomy & Astrophysics. John Wiley & Sons, Inc., 1996.

R. S. Roger, C. H. Costain, and A. H. Bridle. The low-frequency spectra of nonthermal radio sources. AJ, 78:1030, December 1973.

H. J. A. Röttgering, M. J. West, G. K. Miley, and K. C. Chambers. The optical counterparts and the environments of ultra-steep-spectrum radio sources. A&A, 307:376–384, March 1996.

H. Röttgering, J. Afonso, P. Barthel, F. Batejat, P. Best, and for the LOFAR Collaboration. LOFAR and APERTIF surveys of the radio sky: probing shocks and magnetic fields in galaxy clusters. *arXiv:1107.1606*, July 2011.

M. T. Sargent, E. Schinnerer, E. Murphy, H. Aussel, E. Le Floc'h, D. T. Frayer, A. Martínez-Sansigre, P. Oesch, M. Salvato, V. Smolčić, G. Zamorani, M. Brusa, N. Cappelluti, C. L. Carilli, C. M. Carollo, O. Ilbert, J. Kartaltepe, A. M. Koekemoer, S. J. Lilly, D. B. Sanders, and N. Z. Scoville. The VLA-COSMOS Perspective on the Infrared-Radio Relation. I. New Constraints on Selection Biases and the Non-Evolution of the Infrared/Radio Properties of Star-Forming and Active Galactic Nucleus Galaxies at Intermediate and High Redshift. ApJS, 186:341–377, February 2010.

A. M. M. Scaife and G. H. Heald. A broad-band flux scale for low-frequency radio telescopes. MNRAS, 423:L30–L34, June 2012.

R. T. Schilizzi, W. Tschager, I. A. G. Snellen, A. G. de Bruyn, G. K. Miley, H. J. A. Röttgering, H. J. van Langevelde, C. Fanti, and R. Fanti. A Morphological and Spectral Study of GPS Galaxies and Quasars. *Advances in Space Research*, 26:709–714, 2000.

S. J. Schmidt, A. J. Connolly, and A. M. Hopkins. The DRaGONS Survey: A Search for High-Redshift Radio Galaxies and Heavily Obscured Active Galactic Nuclei. ApJ, 649:63–78, September 2006.

M. Schmidt. Optical spectra and redshifts of 4C quasi-stellar radio sources. ApJ, 193:505–507, November 1974.

P. A. Shaver, J. V. Wall, K. I. Kellermann, C. A. Jackson, and M. R. S. Hawkins. Decrease in the space density of quasars at high redshift. Nature, 384:439–441, December 1996.

J. Silk and M. J. Rees. Quasars and galaxy formation. A&A, 331:L1–L4, March 1998.

Chris Simpson, Alejo Martinez-Sansigre, Steve Rawlings, Rob Ivison, Masayuki Akiyama, Kazuhiro Sekiguchi, Tadafumi Takata, Yoshihiro Ueda, and Mike Watson. Radio imaging of the subaru/xmm-newton deep field - i. the 100-microjy catalogue, optical identifications, and the nature of the faint radio source population. MNRAS, 372:741–757, 2006.

C. Simpson, S. Rawlings, R. Ivison, M. Akiyama, O. Almaini, E. Bradshaw, S. Chapman, R. Chuter, S. Croom, J. Dunlop, S. Foucaud, and W. Hartley. Radio imaging of the Subaru/XMM-Newton Deep Field- III. Evolution of the radio luminosity function beyond z= 1. MNRAS, 421:3060–3083, April 2012.

K. Singh, M. Mevius, O. Scholten, J. M. Anderson, A. van Ardenne, M. Arts, M. Avruch, A. Asgekar, M. Bell, P. Bennema, M. Bentum, G. Bernadi, P. Best, A.-J. Boonstra, J. Bregman, R. van de Brink, C. Broekema, W. Brouw, M. Brueggen, S. Buitink, H. Butcher, W. van Cappellen, B. Ciardi, A. Coolen, S. Damstra, R. Dettmar, G. van Diepen, K. Dijkstra, P. Donker, A. Doorduin, M. Drost, A. van Duin, J. Eisloeffel, H. Falcke, M. Garrett, M. Gerbers, J.-M. Grießmeier, T. Grit, P. Gruppen, A. Gunst, M. van Haarlem, M. Hoeft, H. Holties, J. Hörandel, L. A. Horneffer, A. Huijgen, C. James, A. de Jong, D. Kant, E. Kooistra, Y. Koopman, L. Koopmans, G. Kuper, P. Lambropoulos, J. van Leeuwen, M. Loose, P. Maat, C. Mallary, R. McFadden, H. Meulman, J.-D. Mol, J. Morawietz, E. Mulder, H. Munk, L. Nieuwenhuis, R. Nijboer, M. J. Norden, J. Noordam, R. Overeem, H. Paas, V. N. Pandey, M. Pandey-Pommier, R. Pizzo, A. Polatidis, W. Reich, J. de Reijer, A. Renting, P. Riemers, H. Roettgering, J. Romein, J. Roosjen, M. Ruiter, A. Schoenmakers, G. Schoonderbeek, J. Sluman, O. Smirnov, B. Stappers, M. Steinmetz, H. Stiepel, K. Stuurwold, M. Tagger, Y. Tang, S. Ter Veen, R. Vermeulen, M. de Vos, C. Vogt, E. van der Wal, H. Weggemans, S. Wijnholds, M. Wise, O. Wucknitz, S. Yattawatta, and J. van Zwieten. Optimized trigger for ultra-high-energy cosmic-ray and neutrino observations with the low frequency radio array. *Nuclear Instruments and Methods in Physics Research A*, 664:171–185, February 2012.

Oleg M. Smirnov. Revisiting the radio interferometer measurement equation. i. a full-sky jones formalism. A&A, 2011,:527,A106, January 2011.

Oleg M. Smirnov. Revisiting the radio interferometer measurement equation. ii. calibration and direction-dependent effects. A&A, 2011,:527,A107, January 2011.

Oleg M. Smirnov. Revisiting the radio interferometer measurement equation. iii. addressing direction-dependent effects in 21 cm wsrt observations of 3c 147. A&A, 2011,:527,A108, January 2011.

Oleg M. Smirnov. Revisiting the radio interferometer measurement equation. iv. a generalized tensor formalism. A&A, 2011,:531,A159, June 2011.

V. Smolčić. The Radio AGN Population Dichotomy: Green Valley Seyferts Versus Red Sequence Low-Excitation Active Galactic Nuclei. ApJ, 699:L43–L47, July 2009.

I. A. G. Snellen, R. T. Schilizzi, G. K. Miley, A. G. de Bruyn, M. N. Bremer, and H. J. A. Röttgering. On the evolution of young radio-loud AGN. MNRAS, 319:445–456, December 2000.

Volker Springel. The cosmological simulation code gadget-2. MNRAS, 364:1105–1134, 2005.

B. W. Stappers, J. W. T. Hessels, A. Alexov, K. Anderson, T. Coenen, T. Hassall, A. Karastergiou, V. I. Kondratiev, M. Kramer, J. van Leeuwen, J. D. Mol, A. Noutsos, J. W. Romein, P. Weltevrede, R. Fender, R. A. M. J. Wijers, L. Bähren, M. E. Bell, J. Broderick, E. J. Daw, V. S. Dhillon, J. Eislöffel, H. Falcke, J. Griessmeier, C. Law, S. Markoff, J. C. A. Miller-Jones, B. Scheers, H. Spreeuw, J. Swinbank, S. Ter Veen, M. W. Wise, O. Wucknitz, P. Zarka, J. Anderson, A. Asgekar, I. M. Avruch, R. Beck, P. Bennema, M. J. Bentum, P. Best, J. Bregman, M. Brentjens, R. H. van de Brink, P. C. Broekema, W. N. Brouw, M. Brüggen, A. G. de Bruyn, H. R. Butcher, B. Ciardi, J. Conway, R.-J. Dettmar, A. van Duin, J. van Enst, M. Garrett, M. Gerbers, T. Grit, A. Gunst, M. P. van Haarlem, J. P. Hamaker, G. Heald, M. Hoeft, H. Holties, A. Horneffer, L. V. E. Koopmans, G. Kuper, M. Loose, P. Maat, D. McKay-Bukowski, J. P. McKean, G. Miley, R. Morganti, R. Nijboer, J. E. Noordam, M. Norden, H. Olofsson, M. Pandey-Pommier, A. Polatidis, W. Reich, H. Röttgering, A. Schoenmakers, J. Sluman, O. Smirnov, M. Steinmetz, C. G. M. Sterks, M. Tagger, Y. Tang, R. Vermeulen, N. Vermaas, C. Vogt, M. de Vos, S. J. Wijnholds, S. Yatawatta, and A. Zensus. Observing pulsars and fast transients with LOFAR. A&A, 530:A80, June 2011.

M. Susperregi. Breaking the Degeneracy of Cosmological Parameters in Galaxy Redshift Surveys. ApJ, 546:85–99, January 2001.

C. N. Tadhunter, R. Morganti, S. di Serego-Alighieri, R. A. E. Fosbury, and I. J. Danziger. Optical Spectroscopy of a Complete Sample of Southern 2-JY Radio Sources. MNRAS, 263:999, August 1993.

T. A. Targett, J. S. Dunlop, and R. J. McLure. The host galaxies and black hole-to-galaxy mass ratios of luminous quasars at z$\sim$ 4. MNRAS, 420:3621–3631, March 2012.

C. Tasse, P. N. Best, H. Röttgering, and D. Le Borgne. Radio-loud AGN in the XMM-LSS field. II. A dichotomy in environment and accretion mode? A&A, 490:893–904, November 2008.

George W. Thompson, A.R. Moran James M. Swenson. *Interferometry and Synthesis in Radio Astronomy*. John Wiley & Sons, Inc., 1986.

A. G. G. M. Tielens, G. K. Miley, and A. G. Willis. Westerbork Observations of 4C Sources with Steep Radio Spectra. A&AS, 35:153–+, February 1979.

D. F. Torres and L. A. Anchordoqui. Astrophysical origins of ultrahigh energy cosmic rays. *Reports on Progress in Physics*, 67:1663–1730, September 2004.

P. Tozzi, V. Mainieri, P. Rosati, P. Padovani, K. I. Kellermann, E. Fomalont, N. Miller, P. Shaver, J. Bergeron, W. N. Brandt, M. Brusa, R. Giacconi, G. Hasinger, B. D. Lehmer, M. Nonino, C. Norman, and J. Silverman. The VLA Survey of the Chandra Deep Field-South. III. X-Ray Spectral Properties of Radio Sources. ApJ, 698:740–755, June 2009.

C. Megan Urry and Paolo Padovani. Unified schemes for radio-loud active galactic nuclei. *Publ.Astron.Soc.Pac.*, 107:803, 1995.

W. van Breugel, C. De Breuck, S. A. Stanford, D. Stern, H. Röttgering, and G. Miley. A Radio Galaxy at Z = 5.19. ApJ, 518:L61–L64, June 1999.

S.. van der Tol, B.D. Jeffs, and A.-J.. van der Veen. Self-calibration for the lofar radio astronomical array. *Signal Processing, IEEE Transactions on*, 55(9):4497 –4510, sept. 2007.

M. P. van Haarlem, M. W. Wise, A. Gunst, G. Heald, J.P. McKean, and for the LOFAR Collaboration. LOFAR: The Low Frequency Array. A&A, to be submitted, 2012.

R. J. van Weeren, H. J. A. Röttgering, D. A. Rafferty, R. Pizzo, A. Bonafede, M. Brüggen, G. Brunetti, C. Ferrari, E. Orrù, G. Heald, J. P. McKean, C. Tasse, F. de Gasperin, L. Bîrzan, J. E. van Zwieten, S. van der Tol, A. Shulevski, N. Jackson, A. R. Offringa, J. Conway, H. T. Intema, T. E. Clarke, I. van Bemmel, G. K. Miley, G. J. White, M. Hoeft, R. Cassano, G. Macario, R. Morganti, M. W. Wise, C. Horellou, E. A. Valentijn, O. Wucknitz, K. Kuijken, T. A. Enßlin, J. Anderson, A. Asgekar, I. M. Avruch, R. Beck, M. E. Bell, M. R. Bell, M. J. Bentum, G. Bernardi, P. Best, A.-J. Boonstra, M. Brentjens, R. H. van de Brink, J. Broderick, W. N. Brouw, H. R. Butcher, W. van Cappellen, B. Ciardi, J. Eislöffel, H. Falcke, R. Fender, M. A. Garrett, M. Gerbers, A. Gunst, M. P. van Haarlem, J. P. Hamaker, T. Hassall, J. W. T. Hessels, L. V. E. Koopmans, G. Kuper, J. van Leeuwen, P. Maat, R. Millenaar, H. Munk, R. Nijboer, J. E. Noordam, V. N. Pandey, M. Pandey-Pommier, A. Polatidis, W. Reich, A. M. M. Scaife, A. Schoenmakers, J. Sluman, B. W. Stappers, M. Steinmetz, J. Swinbank, M. Tagger, Y. Tang, R. Vermeulen, M. de Vos, and M. P. van Haarlem. First LOFAR observations at very low frequencies of cluster-scale non-thermal emission: the case of Abell 2256. A&A, 543:A43, July 2012.

E. Vardoulaki, S. Rawlings, G. J. Hill, T. Mauch, K. J. Inskip, J. Riley, K. Brand, S. Croft, and C. J. Willott. The TexOx-1000 redshift survey of radio sources I: the TOOT00 region. MNRAS, 401:1709–1759, January 2010.

B. P. Venemans, H. J. A. Röttgering, G. K. Miley, W. J. M. van Breugel, C. de Breuck, J. D. Kurk, L. Pentericci, S. A. Stanford, R. A. Overzier, S. Croft, and H. Ford. Protoclusters associated with $z > 2$ radio galaxies . I. Characteristics of high redshift protoclusters. A&A, 461:823–845, January 2007.

I. Waddington, R. A. Windhorst, S. H. Cohen, R. B. Partridge, H. Spinrad, and D. Stern. NICMOS Imaging of the Dusty Microjansky Radio Source VLA J123642+621331 at $Z = 4.424$. ApJ, 526:L77–L80, December 1999.

I. Waddington, J. S. Dunlop, J. A. Peacock, and R. A. Windhorst. The lbds hercules sample of mjy radio sources at 1.4 ghz - ii. redshift distribution, radio luminosity function, and the high-redshift cut-off. MNRAS, 328:882, 2001.

J. V. Wall and J. A. Peacock. Bright extragalactic radio sources at 2.7 GHz. III - The all-sky catalogue. MNRAS, 216:173–192, September 1985.

J. V. Wall, D. J. Cole, and D. K. Milne. A summary of recent observations with the Parkes interferometer. *Proceedings of the Astronomical Society of Australia*, 1:98–+, February 1968.

L. Wan and R. Daly. *FRII radio sources in rich clusters of galaxies*, page 240. 1996.

M. Way and H. Nussbaumer. Lemaitre's Hubble relationship. *Physics Today*, 64(8):080000, 2011.

Z. L. Wen and J. L. Han. Galaxy Clusters at High Redshift and Evolution of Brightest Cluster Galaxies. ApJ, 734:68, June 2011.

R. L. White and R. H. Becker. A new catalog of 30,239 1.4 GHz sources. ApJS, 79:331–467, April 1992.

S. D. M. White and C. S. Frenk. Galaxy formation through hierarchical clustering. ApJ, 379:52–79, September 1991.

S. D. M. White and M. J. Rees. Core condensation in heavy halos - A two-stage theory for galaxy formation and clustering. MNRAS, 183:341–358, May 1978.

M. T. Whiting. DUCHAMP: a 3D source finder for spectral-line data. MNRAS, 421:3242–3256, April 2012.

C. J. Willott, S. Rawlings, K. M. Blundell, and M. Lacy. The emission line-radio correlation for radio sources using the 7C Redshift Survey. MNRAS, 309:1017–1033, November 1999.

Chris J. Willott, Steve Rawlings, Katherine M. Blundell, Mark Lacy, and Stephen A. Eales. The radio luminosity function from the low-frequency 3crr, 6ce & 7crs complete samples. MNRAS, 322:536–552, 2001.

Chris J. Willott, Steve Rawlings, Matt J. Jarvis, and Katherine M. Blundell. Near-infrared imaging and the k-z relation for radio galaxies in the 7c redshift survey. MNRAS, 339:173–188, 2003.

R. J. Wilman, L. Miller, M. J. Jarvis, T. Mauch, F. Levrier, F. B. Abdalla, S. Rawlings, H.-R. Klöckner, D. Obreschkow, D. Olteanu, and S. Young. A semi-empirical simulation of the extragalactic radio continuum sky for next generation radio telescopes. MNRAS, 388:1335–1348, August 2008.

Andrew S. Wilson and Edward J. M. Colbert. The difference between radio-loud and radio-quiet active galaxies. ApJ, 438:62–71, 1995.

A. E. Wright, D. L. Jauncey, B. A. Peterson, and J. J. Condon. Redshifts of southern radio sources. II. ApJ, 211:L115–L119, February 1977.

E. L. Wright. A Cosmology Calculator for the World Wide Web. PASP, 118:1711–1715, December 2006.

S. Yatawatta, S. Zaroubi, G. de Bruyn, L. Koopmans, and J. Noordam. Radio interferomietric calibration using te sage algorithm. In *Digital Signal Processing Workshop and 5th IEEE Signal Processing Education Workshop, 2009. DSP/SPE 2009. IEEE 13th*, pages 150 –155, jan. 2009.

A. J. Young, A. S. Wilson, and C. G. Mundell. Chandra Imaging of the X-Ray Core of the Virgo Cluster. ApJ, 579:560–570, November 2002.

G. Zhao. Large Astronomical Facilities in China - Current Status and Future Projects. In *Bulletin of the American Astronomical Society*, volume 41 of *Bulletin of the American Astronomical Society*, pages 405–+, January 2009.

Publications

Journals:
L.M. Ker, P.N. Best, E.E. Rigby, H.J.A. Rottgering, M. Gendre. "New Insights on the z-α Correlation from Complete Radio Samples" In *MNRAS*, 420, 2644-2661, 2012.

E. E. Rigby, P. N. Best, M. H. Brookes, J. A. Peacock,J. S. Dunlop, H. J. A. Rottgering, J. V. Wall, **L. Ker**. "The luminosity-dependent high-redshift turnover in the steep spectrum radio luminosity function: clear evidence for downsizing in the radio-AGN population" In *MNRAS*, 416, 1900-1915, 2011.

Technical:
"The LOFAR Imaging Cookbook v1.1" I contributed v1.1 of the LOFAR Imaging Cookbook. The most recent version, v8.0 can by found here: http://www.astron.nl/radio-observatory/lofar/lofar-imaging-cookbook

Conference:
J. McKean, **L. Ker**, R. J. van Weeren, F. Batejat, L. Birzan, A. Bonafede, J. Conway, F. De Gasperin, C. Ferrari, G. Heald, N. Jackson, G. Macario, E. Orr, R. Pizzo, D. Rafferty, H. Rottgering, A. Shulevski, C. Tasse, S. van der Tol, I. van Bemmel, G. van Diepen, J. van Zwieten, for the LOFAR collaboration. "LOFAR: Early imaging results from commissioning for Cygnus A" ,In *Proceedings of Science, 2010.* 10th European VLBI Network Symposium and EVN Users Meeting: VLBI and the new generation of radio arrays, Manchester.

G. Heald, J. McKean, G. van Diepen, J. van Zwieten, R. van Weeren, S. van der Tol, A. Shulevski, J. Swinbank, E. Orru, F. e Gasparin, **L. Ker**, A. Bonafede, G. Macario,C. Ferrari."Progress with the LOFAR Imaging Pipeline", In *Proceedings of Science, 2010.* International SKA Forum 2010, The Netherlands.

H. Rottgering, R. van Weeren, G. Miley, I. Snellen, D. Rafferty, S. van der Tol, L. Birzan, A. Shulevski, G. Heald, J. McKean, R. Morganti, M. Haverkorn, R. Pizzo, G. van Diepen, M. Wise, J. van Zwieten, P. Best, **L. Ker**, and 16 others. "LOFAR and the low frequency universe.Probing the formation and evolution of massive galaxies, AGN and clusters" In *Proceedings of Science, 2010.* International SKA Forum 2010, The Netherlands.